A THEORETICAL AND EXPERIMENTAL INVESTIGATION OF THE H_3 SYSTEM

Thesis by
Mary Theresa Rodgers

In Partial Fulfillment of the Requirements
for the Degree of
Doctor of Philosophy

California Institute of Technology
Pasadena, California
1992

(Defended February 24, 1992)

In memory of my parents, Nancy and Joseph Rodgers

Acknowledgements

I take great pleasure in thanking all of the people that have made a contribution to my graduate studies at Caltech. In addition, I would also like to thank those who have made my personal life during graduate school more enjoyable.

First, I would like to thank my thesis advisor Aron Kuppermann. My first experiences with him were in Chemistry 125a (Quantum Mechanics) where I learned of his expert teaching skills. Thoughout my graduate years he has been committed to providing me as well as the other students in the group thorough and complete training. I also wish to thank Professor Jack Beauchamp for the interest he has shown in my work and in my future especially during the last year of my doctoral work. In addition, special thanks goes to Professor Fred Anson for his friendly and financial support of my last year and a half at Caltech.

This project would not have been possible without the enormous help, both technical and spiritual, which I received from the Caltech staff. The major players include the staff of the Chemistry Instrument shop; Guy Duremberg, Tony Stark, Ray Garcia and Delmer Dill. Their help in the design, construction, and maintence of my apparatus is most heartily appreciated. Special thanks to Guy Duremberg for his patience and guidance while trying to teach me how to machine the simpler parts of my apparatus. The Chemistry Electronics shop also played a major role in my experimental work. Many thanks to Tomm Dunn for his help in designing and building the arc source control panel, the arc source translation-rotation assembly control box and for his help in reviving the mass spectrometer electronics. In addition, Tom Dunn and Jack Guledjian worked very hard to help me keep the remaining electronics in my apparatus operational. The staff of the Chemistry Maintence shop; Jim Olson, Jim Gangwer, Pavel Svitek, Jess Miller and Darryl

Riley also deserve special thanks for their efforts in keeping my pumping systems in working condition. I would like to thank the guys in the Aeronautics shop George Lundgren and Phil Wood for their help when the Chemistry Instrument shop was overloaded with jobs. The Central Engineering shop personnel, Lou Johnson, Norm Keidel, Ralph Ortega and the machinists deserve special thanks for their help in building the new source and differential stage chambers. I would like to thank Fran Bennett for her friendly and efficient handling of my purchase orders, and Al Taylor for his prompt and friendly delivery of liquid nitrogen which my apparatus required on a nearly daily basis. Special thanks to the people in the Chemistry stockroom especially Louis Borbon and Steve Gould. In addition there are many other people that contributed to making my stay at Caltech easier and more interesting. Thanks to all of you.

I wish to thank the other members of the Kuppermann group, both past and present, Maria Giorgi, Qiu Jin, Zhengwei Peng, Garth Parker, Mark Wu, Sandor Kristyan, Isaac Xavier, Steve Cuccaro, Carrie Stroud, Paul Hipes, Kerry Walzl, Bruno Lepetit, Viadehi Nagarajan, Soren Padkjaer, Joseph Wong and Amy Shaw. Maria deserves special thanks for her friendship throughout our years here, and for babysitting my lab and cats when I was out of town. Thanks to Qui and Peng for providing my initial training in the lab as well as a friendly atmosphere to work in. Thanks to Garth for his guidance and willingness to help me with anything I asked about. Thanks to Mark, Peng and Sandor for their help with the computational portion of my work. In addition Lena Lenore and Ann Strieber, the Kuppermann group secretaries, deserve thanks for their help. Thanks to all of you for providing friendship and support.

Among my friends and colleagues outside the Kuppermann group, special mention must go to Russ Bowers and his wife Bambi, Matt Braunstein and his wife Waverly, and Larry Peng. Their friendship has made my stay at Caltech much more enjoyable. Other friends deserving special thanks are Captain Mobody and the entire Dog Nuts Motley Crew and their associated significant others for the fun times we have had together. I would also like to thank the people that have attended my aerobics classes or have subbed for me when I was unable to teach. My involvement with aerobics has been a great deal of fun and has helped to keep my stress level under control.

I wish to thank my family for all of the love and support that they have provided me throughout my life. My parents deserve special thanks for the encouragement they provided early on in my advanced schooling without which I may never made it to graduate school, this thesis is dedicated to their memory. I would also like to thank my new family (by marriage) for their love and encouragement.

Most importantly, I would like to thank my husband Cliff Frieler. His love and support thoughout my years at Caltech gave me the strength and encouragement to make it through all of the ordeals associated with graduate school. In addition, his technical advice and physical strength helped to accelerate my progress in the lab, while performing calculations and writing this thesis. I love you very much.

Abstract

The H_3 system is the simplest triatomic neutral molecular species. It possesses only three electrons and three protons. As a result of its simplicity, the H_3 system has received a great deal of attention in *ab initio* quantum mechanical as well as experimental studies.

This dissertation consists of two parts. The first part is a theoretical investigation of the H_3 molecular system. Results of the *ab initio* quantum mechanical calculations for the lowest three electronic potential energy surfaces are given, as well as electronically nonadiabatic coupling elements between these states. The calculated nonadiabatic coupling elements compare well in some regions of configuration space with previous calculations performed on this system. Discrepancies in other regions can be attributed to the method of calculation. In our study these coupling elements were calculated by an *ab initio* method whereas analytic continuation was used in previous work. Calculation of the nonadiabatic coupling surfaces represents notable progress and will improve the fidelity of dynamics calculations of the H_3 system. All 3-D quantum mechanical theoretical investigations to date invoke the Born-Oppenheimer approximation and neglect nonadiabatic coupling of the nearby states. Although this is justified in many cases, the H_3 system exhibits a conical intersection near which this approximation breaks down. To obtain theoretical estimates of predissociative lifetimes of excited states of the H_3 system, accurate bound state wavefunctions and energies of the excited states of H_3 and accurate differential and integral cross sections in quantum mechanical scattering studies of the $H + H_2$ system above 2.75 eV, these nonadiabatic terms must be included.

The second part of this dissertation involves the development and characterization of an intense source of trihydrogen molecules. The ultimate goal of this work

is to fully characterize the metastable H_3 molecules formed in this beam and to create a source of monoenergetic trihydrogen molecules whose translational energy would be continuously tunable from ~1-12 eV. Once developed, it could be utilized in crossed beam experiments and would enable many reactions to be studied that might not otherwise take place due to low reaction probability. The H_3 molecule in its $2p_z^2A_2''$ electronic state is 5.85 eV higher and the $2p_{x,y}^2E'$ repulsive ground state is 2.65 eV higher in energy than H + H_2.[17-20] Therefore, upon a vertical transition to the ground state, the $2p_z^2A_2''$ state of H_3 will liberate about 3 eV of electronic energy with the remaining energy being channeled into vibration and rotation of the H + H_2 dissociated system. In a collision with another molecule, this energy could become available for reaction along with some fraction of the translational energy of these molecules (1-12 eV). This species can be expected to exhibit unusual dynamics, in that it may undergo novel chemical reactions as well as unique partitioning of the available energy into electronic, vibrational, rotational and translational energy of the products.

Table of Contents

Chapter 1.

Prologue

I. Introduction

Quantum mechanics holds the key to many interesting chemical and physical questions however, unlocking the answers to many of these questions is very difficult if not impossible with the present knowledge. Since the advent of quantum mechanics, a great effort has been made to understand the structure and dynamics of molecular systems. The Schrödinger equation which fully describes the motion of any system has been known for a long time, however most chemical systems of interest possess a large number of electrons and nuclei making solutions of this equation very difficult to obtain. Only recently have accurate solutions to the Schrödinger equation been obtained as a result of the great advances in computer technology.

The H_3 system is the simpliest triatomic neutral molecular species. It possesses only three electrons and three protons. As a result of its simplicity, the H_3 system has received a great deal of attention in *ab initio* quantum mechanical studies as well as experimental studies.

This dissertation consists of two parts. The first part is a theoretical investigation of the H_3 molecular system. This study involves the *ab initio* quantum mechanical calculation of the potential energy surfaces and nonadiabatic coupling elements of the three lowest electronic states of the H_3 system. This information is useful for several reasons:

1. The nonadiabatic coupling elements are necessary to obtain theoretical estimates of the predissociative lifetimes of the excited states of the H_3 system.[1-4]
2. The nonadiabatic coupling elements must be included to obtain accurate rovibrational bound state wave functions and energies of the excited states

of H_3.[5-7] These terms tend to shift the positions of the eigen-energies of the discrete states involved in the coupling.[8-11]

3. The electrically nonadiabatic terms can introduce new chemical reaction channels and would therefore be important as well as interesting to include in quantum mechanical scattering studies of the H + H_2 system at high energies ($\geq$2.75 eV).[12-16]

The second part of this dissertation involves the development and characterization of an intense source of trihydrogen molecules. The ultimate goal of this work is to fully characterize the metastable H_3 molecules formed in this beam and to create a source of monoenergetic trihydrogen molecules whose translational energy would be continuously tunable from ~1-12 eV. Once achieved, it could be utilized in crossed beam experiments and would enable many reactions that might not otherwise take place (due to very low reaction probability) to be studied. The H_3 molecule in its $2p_z^2A_2''$ electronic state is approximately 5.85 eV above that of H + H_2 [17-20] whereas the potential energy of the $2p_{x,y}^2E'$ repulsive ground state is approximately 2.65 eV higher in energy than H + H_2.[17-20] Therefore, upon a vertical transition to the ground state, the $2p_z^2A_2''$ state of H_3 will liberate about 3 eV of electronic energy with the remaining energy being channelled into vibration and rotation of the H + H_2 dissociated system. In a collision with another molecule, this energy could become available for reaction. In addition, the translational energy of these molecules (1-12 eV) could provide an additional source of energy. Therefore, this species can be expected to exhibit unusual dynamics in that it may undergo novel chemical reactions as well as various partitioning of the available energy into electronic, vibrational, rotational and translational energy of the products.

II. Overview

This dissertation is organized as follows. It consists of two main parts, a theoretical and an experimental investigation of the H_3 system. Chapters 3 through 5 comprise the theoretical portion of this thesis. Chapters 6 through 9 summarize the experimental portion. Chapter 2 presents background information on previous theoretical and experimental investigations of the H_3 system. Chapter 3 presents background material on the formulation of the quantum mechanical study of the H_3 system presented in this thesis. Chapter 4 presents background information on the methodology used in the calculations performed in this thesis. Chapter 5 presents the results and discussion of the the *ab initio* quantum mechanical calculations performed. Chapter 6 presents a description of the apparatus designed, built and used for the experimental work done. Chapter 7 describes the rovibrational population measurements. Chapter 8 describes the radiative lifetimes measurements. Chapter 9 discusses the preliminary experiments performed, the results and future work. Chapter 10 is a summary of the results of this dissertation and a discussion of future work. Appendix 1 is a series of tables of the energies and nonadiabatic coupling elements calculated in this work.

III. References

1. A.C. Hurley, *Introduction to the Electron Theory of Small Molecules*, (Academic Press, 1976), Chapter 1.
2. E.E. Nikitin and L. Zülicke, *Theory of Elementary Processes, Lecture Notes in Chemistry*, (Springer-Verlag, 1978).
3. U. Fano, *Phys. Rev.* **124**, 1866 (1961).
4. S.H. Lin (editor), *Radiationless Transitions*, (Academic Press, 1980).
5. Z. Peng, *Ph.D. Thesis*, California Institute of Technology, 1991.
6. Z. Peng, A. Kuppermann and J.S. Wright, *Chem. Phys. Lett.* **175**, 242 (1990).
7. B. Lepetit, Z. Peng and A. Kuppermann, *Chem. Phys. Lett.* **166**, 572 (1990).
8. H.R. King and K. Morokuma, *J. Chem. Phys.* **71**, 3213 (1979).
9. R.L. Martin, *J. Chem. Phys.* **71**, 3541 (1979).
10. M. Jungen, *J. Chem. Phys.* **71**, 3540 (1979).
11. C.G. Freeman, T.I. Quickenden and D.F. Sangster, *J. Photochemistry* **24**, 403 (1984).
12. Hélène Lefebvre-Brion and R.W. Field, *Perturbations in the Spectra of Diatomic Molecules*, (Academic Press, 1986).
13. G. Herzberg, *Spectra of Diatomic Molecules*, Van Nostrand, Princeton, 2nd edition, 1950.
14. G. Herzberg, *Electronic Spectra and Electronic Structure of Polyatomic Molecules*, Van Nostrand, Princeton, 2nd. edition, 1950.

15. B.C. Garrett and D.G. Truhlar, in *Theoretical Chemistry: Theory of Scattering: Papers in Honor of Henry Eyring*, edited by D. Henderson, **Vol. 6A**, (Academic Press, 1981), pp. 216-289.
16. F. Rebentrost, in *Theoretical Chemistry: Theory of Scattering: Papers in Honor of Henry Eyring*, edited by D. Henderson, **Vol. 6B**, (Academic Press, 1981), pp. 3-77.
17. M. Baer, in *Theory of Chemical Reaction Dynamics*, edited by M. Baer, **Vol. II**, (CRC Press, 1985), pp. 219-280.
18. J.C. Tulley and R.K. Preston, *J. Chem. Phys.* **55**, 562 (1971).
19. J.P. Braga, H. Guo, J.N. Murrell and L.J. Dunne, *Molec. Phys.* **65**, 909 (1988).
20. B. Lepetit, J.M. Launay and M. Le Dourneuf, *Chem. Phys.* **117**, 17 (1987).

Chapter 2.

Background on H_3

I. Introduction

The H_3 system is the simplest triatomic neutral molecular species, possessing only three electrons and three protons. As a result of its simplicity, the H_3 system has received a great deal of attention in *ab initio* quantum mechanical studies as well as experimental studies. These studies can be broken down into two main groups, those associated with the hydrogen exchange reaction ($H + H_2 \longrightarrow H_2 + H$) and those associated with the H_3 species itself. The hydrogen exchange reaction has been extensively reviewed in several papers.[1-3] Results of these investigations both theoretical and experimental, are discussed in the sections that follow.

II. Theoretical Studies of H_3

A. Introduction

There are two classes of theoretical investigations involved with the study of the H_3 system. The first class deals with explicitly examining the hydrogen exchange reaction. Included in this group are potential energy surface calculations, quasiclassical trajectory calculations and quantum mechanical scattering calculations. The second class deals with examining the H_3 species itself. Potential energy surface and wavefunction calculations play the key role here, however excited surfaces are now also involved. The potential energy surfaces and wavefunctions are used to calculate the Rydberg spectra, transition state spectroscopy, bound rovibrational states, transition dipole moments, and nonadiabatic coupling elements. In the following sections, a discussion of the results of these studies will be presented.

B. Potential Energy Surface Calculations

The ground state potential energy surface of H_3, relevant to the symmetric hydrogen exchange reaction

$$H + H_2 \longrightarrow H_3 \longrightarrow H_2 + H \tag{2.1}$$

has been calculated by many workers using a variety of techniques. The first such calculations were performed by London[4] in 1929, and by Eyring and Polyani[5] in 1930. London presented a formula for the energy of the lowest adiabatic electronic state of H_3 as a function of Q_{ij} andJ_{ij}, the Coulomb and exchange integrals respectively for each pair of atoms. Eyring and Polyani developed a semi-empirical method to evaluate the integrals in the London formulation in terms of the properties of the diatoms. This methodology results in the LEP potential. One of the terms in the calculation is the fraction, ρ, which is equal to the ratio of the Coulomb integral to the sum of the Coulomb and exchange integrals. At large distances $\rho \approx 0.14$, however, it is often treated as an adjustable parameter with values ranging from 0.00 to 0.20.[2] For any ρ, the method predicts that the lowest energy reaction path is linear. For low values of ρ, the barrier to reaction is symmetric and much too large. For larger values of ρ, the symmetric configuration is a local minimum situated between twin nonsymmetric barriers.

In 1955, Sato[6-8] modified the LEP method to give the LEPS method. This method introduces a new parameter, δ, which is varied in an attempt to obtain agreement between theory and experiment.[2] The LEPS surface for the H_3 system has a symmetric saddle point for all values of δ. For $\delta = 0.1475$ the best value for the barrier height is obtained and is 0.358 eV at an internuclear separation of 1.76 a_o.

Porter and Karplus[9] used a different semi-empirical method which also includes multiple exchange integrals and predicts a symmetric saddle point. They generated 4 different surfaces, one of which, PK2, has been used extensively in dynamics calculations. The barrier height of this surface is 0.398 eV at an internuclear distance of 1.70 a_o.

In addition to the semi-empirical methods used, there have been *ab initio* calculations of the H_3 surface. The first such calculation was the minimal basis set calculation performed by Coolidge and James[10] in 1934. A flurry of similar calculations found that the saddle point is symmetric for the collinear reaction and that the potential energy rose for bent configurations. Hirschfelder *et al.*[11] found that the binding energy of H_3 is -2.94 eV, 1.08 eV above that for H_2 calculated using the same level of theory.

The accuracy of the potential energy surface calculations was improved by using an extended basis set of s orbitals on each H atom. In 1956 Boys *et al.*[12–13] performed the first such caculation. They found a binding energy of -3.48 eV and an estimated barrier height of 0.66 eV. Later calculations were performed including p and d orbitals, multiple ζ's, pseudo-natural orbitals, and configuration interactions.[2] The most accurate results published of such calculations are the results of Liu[14] in 1973. He examined the potential energy surface for linear H_3 using a contracted basis set consisting of 4 s-type, 3 p-type and 2 d-type Slater orbitals for each H atom and included an almost complete CI calculation. He found that the symmetric saddle point occurred at an internuclear separation of 1.757 a_o with a binding energy of -4.302 eV. This represents an absolute upper bound for the barrier height of 0.446 eV by comparison with the exact H_2 binding energy of -4.748 eV as determined by Kolos and Wolniewicz.[15] By comparing his H_2 results (-4.727 eV) with the exact results, he concluded that the actual binding energy was -4.323 eV with a barrier height of 0.425 eV, with "best" values of -4.327 eV and 0.420 eV, respectively.

Liu's work was later extended to nonlinear geometries by Seigbahn and Liu.[16] To simplify the calculations they used a contracted basis set consisting of 4 s-type, 3 p-type and 1 d-type Gaussian orbitals. Their calculation yielded a barrier of 0.429 eV; however, the collinear portion of their surface was parallel to the previous one within 0.001 eV for all points examined with a separation between 1.4 and 3.5 a_o.

Truhlar and Horowitz[17] parametrized the results of the Lui and Seigbahn and Liu calculations. They fitted all 267 *ab initio* points to an analytic expression using 8 nonlinear parameters and 15 linear parameters with a global root-mean-square (rms) error of 0.007 eV and a maximum deviation of 0.024 eV. The rms error of this fit for the collinear geometry is only 0.004 eV. This surface was coined as the

LSTH surface and is believed to be the first potential energy surface to achieve chemical accuracy of 1.0 kcal/mole. The barrier height of this surface is 0.425 eV.

The LSTH surface is repulsive except for a shallow van der Waals well of 1.6 meV at an atom-diatom separation of 6.59 a_o. This is in agreement with the experimental results of Welz[18]. He found a well depth of 2.6 meV at 6.56 a_o from measurements of the integral cross section at energies as low as $E_{rel} \approx 1$ meV.

More recent *ab initio* calculations suggest that the LSTH barrier is slightly too large. Liu[19] performed new calculations on several geometries in the vicinity of the saddle point using a contracted basis set consisting of 3 s-type, 3 p-type, 2 d-type and 1 f-type Slater orbitals on each H atom. In these calculations, the symmetric saddle point occurred at an internuclear separation of 1.759 a_o with a binding energy of -4.320 eV. This implies an absolute upper bound for the barrier height of 0.428 eV. After corrections for errors in the H_2 calculation, the barrier height is estimated to be 0.418 eV with a "best" value of 0.416 eV.

A new parameterization of the H_3 surface based upon a double many-body expansion (DMBE) was performed by Varandas *et al.*[20-21] This new parameterization was designed to be more accurate at higher energies than the LSTH surface. In addition, long-range forces are treated more accurately, and therefore it is believed that the base of the barrier and the van der Waals well are more accurate. The barrier height on the DMBE surface is 0.418 eV. This surface, like the LSTH surface, is based primarily on the 267 *ab initio* points calculated by Lui[14] and Seigbahn and Liu.[16] In addition, 31 points calculated by Blomberg and Liu[22] were included. These 298 points were corrected by a semiempirical formula to reduce the barrier height by 0.007 eV. An additional 18 points were calculated by Varandas *et al.*[20-21] resulting in the fit being based on a total of 316 *ab initio* points. The DMBE fit had a global rms error of 0.010 eV with an rms error of 0.008 eV for collinear configurations.

More recently, Petsalakis *et al.*[23] have performed multi-reference single and double excitation configuration interaction MRD-CI calculations on the ground and excited electronic states of H_3 for limited D_{3h}, $D_{\infty h}$, $C_{\infty v}$, and C_{2v} geometries. The AO basis set used consisted of the (6s/4s) basis of Huzinaga[24] augmented with two p functions with exponents 0.7 and 0.2 for each H atom. The Rydberg basis was of double-zeta quality (for functions up to 4s) with the folowing exponents (0.01875, 0.0475, 0.00525, 0.0133, 0.0013875, and 0.003515 for the s set, and 0.026255, 0.0665, 0.005025, and 0.01273 for the p set and 0.01275 and 0.02603 for the d set). The Rydberg functions were centered at the center of the triangle for D_{3h}, at the central H atom for $D_{\infty h}$, and at the midpoint of the distance of the H atom from the center of the H_2 bond for $C_{\infty h}$ and C_{2v} geometries. Only C_s symmetry was embedded in the calculation, as it is the common symmetry of all H_3 geometries. The best D_{3h} structure for the ground state is obtained at 1.972 bohr and 2.74 eV, compared to 1.973 bohr and 2.75 eV for the DMBE surface obtained by Varandas and coworkers.[20-21] The ground state saddle point occurs at $R_1 = R_2 = 1.767$ bohr with a barrier of 0.432 eV which is very close to the values obtained by Liu[14] and Seigahn and Liu.[16] The collinear geometries were essentially parallel to those of Liu[14] being slightly higher in energy (~0.11eV).

Even more recently, members of this group have undertaken the task of obtaining high quality potential energy surfaces for the lowest four electronic states of H_3. Peng and coworkers[25-27] have published preliminary results, however a thoroughly complete calculation is still underway which will include over 1000 *ab initio* points.[28] The reliability of the basis set used was tested to obtain

1. Accurate atomic excitation energies for the 1s→2s and 1s→2p transitions.
2. Accurate values for the H_2 energy in its ground electronic $X^1\Sigma_g^+$ state and excited $b^3\Sigma_u^+$ state.

3. A ground-state surface for H_3 of accuracy comparable to that of the LSTH surface.
4. Reasonably good agreement with the known Rydberg spectrum of H_3 and the results of recent calculations of Petsalakis *et al.*[23] and Diercksen.[29]

A more detailed discussion of the basis set used will be given in Chapter 4, since it is this basis set that was used for the present work.

C. Quasiclassical Trajectories Calculations

Hirschfelder *et al.*[31] calculated the first classical trajectories in 1936. Karplus *et al.*[32] calculated the first detailed quasiclassical trajectories using the PK2 surface in the 1960's. They observed a threshold energy of $E_{rel} = 0.25$ eV for $\nu = j = 0$. The reaction cross section was found to increase slowly to 0.01 a_o^2 at $E_{rel} = 0.30$ eV, then increases nearly linearly with energy until it reaches a plateau of 4.5 a_o^2 at $E_{rel} = 1.1$ eV. Later, higher energies and other isotopes were studied using this surface.[33-34]

Later, Mayne and coworkers[35-37] carried out a detailed QCT study of the hydrogen exchange reaction using the LSTH surface. On this surface, the reaction threshold for the $H + H_2$ reaction occurred at $E_{rel} = 0.31 \pm 0.01$ eV. In their first paper, they studied isotope effects. Their second and fourth papers dealt with the effects of vibrational and rotational excitation on reactivity, and the third paper compared the calculated rate constants and angular distributions with experimental results.

A summary of their results follows. For the reaction series H,D,T + H_2, T is the most reactive and H is the least reactive. For the reaction series H + H_2, D_2, T_2, H_2 is the most reactive and T_2 is the least reactive. The reactivity at a given translational energy is increased and the final rotational and angular distributions are broadened if the initial diatom is vibrationally excited. Small amounts of initial rotational excitation of the diatom reduces the reactivity near the threshold and broadens the final rotational distributions. However, the angular distributions are not broadened. Large amounts of initial rotational excitation increase reactivity. Theoretical and experimental rate constants agreed quite well considering that quantum mechanical effects such as tunneling are neglected.

Other QCT have been calculated at energies also studied in experiments. Blais and Truhlar[39−43] calculated state-to-state reactive cross sections for the H + D_2 system at relative translational energies of 0.55, 0.98, 1.1 and 1.3 eV. These energies correspond to the energies studied by Gerrity and Valentini[44−46] and by Marinero, Rettner and Zare[47,48] in hot atom/single collision condition experiments. The earlier work of Mayne and coworkers[35−37] was extended by Mayne and Prasad[49] to energies up to 10 eV for comparison with D + H_2 crossed molecular beam experiments. Their calculations on the LSTH surface agree with experiment to better than 30% for all but the lowest temperatures where tunnelling is expected to contribute a significant fraction to the total reaction.

Later, Blais and Truhlar extended their studies to higher energies to compare with the experiments of Rinnen, Kliner, Blake and Zare[50] at 1.5, 1.6, 2.25 and 2.4 eV translational energy. The DMBE surface was used in these studies, and the calculated HD rotational distributions agreed very well with the experimental results.

Aoiz *et al.*[51−53] calculated differential and state-to-state integral cross sections for the D + H_2 system over the range from 0.35 to 1.1 eV. Their results agreed well with those of Blais and Truhlar[39−43] and qualitative agreement with the exact quantum results of Zhang and Miller[54] was achieved. In addition, the rotational distributions agreed well with the experimental results of Buntin *et al.*[55], Phillips *et al.*[56] and Kliner *et al.*[57] However, their results did not confirm the resonant behavior observed by Phillips *et al.*[56]

D. Quantum Mechanical Scattering Calculations

In the quantum mechanical treatment of reactive scattering, the Schrödinger equation is solved to determine the motion of the particles subject to a given potential energy surface.[3] Solution of the complete problem for the hydrogen exchange reaction in 3-dimensional space requires 6 mathematical degrees of freedom.

The Schrödinger equation can be solved exactly using the coupled channel (CC) method.[3] In this method a reaction coordinate is chosen and the other five degrees of freedom constitute the internal coordinates. The complete wavefunction is expanded in a basis set consisting of wavefunctions of the internal coordinates. Plugging this expansion into the Schrödinger equation leads to a set of coupled ordinary differential equations in the reaction coordinate which can be solved by standard methods. Solution of this set of coupled ODEs results in a scattering matrix, from which all observable quantities may be exhumed. Various CC methods differ in the reaction coordinate chosen and in the choice of basis set.

The best approximation to the CC method is the coupled states (CS) method which neglects the kinematic coupling between different projection quantum states.[3] Further simplifications involve approximations to the rotational motion, either the infinite-order sudden approximation (IOSA) in which the atom-diatom angle is fixed in the reagent and product channels or the reduced dimensionality exact quantum (RDEQ) method which the coupled rotational and bending motion is treated adiabatically.

Schatz and Kuppermann[58,59] performed the first 3-dimensional CC calculation in 1975. They studied the H + H_2 reaction on the PK2 surface for energies of E_{rel} = 0.03 to 0.43 eV. Their results can be summarized as follows: 1) the reactive differential cross sections are backwards peaked, 2) inelastic nonreactive differential cross sections are both backwards and sideways peaked, and 3) elastic nonreactive differential cross sections are forward peaked and decrease monotonically with increasing scattering angle. The product rotational angular momentum is significantly polarized in the integral cross sections, the dominant nonreactive transition is from $m_j = 0$ to $m'_j = 0$ for low reagent rotational quantum number j. Elkowitz and Wyatt[60] also performed quantum mechanical scattering calculations for the H_3 system on the PK2 surface.

Walker *et al.*[61] performed calculations on the LSTH surface. Changing from the PK2 to the LSTH surface caused the reaction threshold to shift to higher energy by approximately 0.05 eV while the location of the first resonance is shifted by only 0.015 eV. For all energies in the range E_{rel} = 0.33 to 0.73 eV, the reaction cross section from the LSTH calculation is approximately 20 to 30% lower than the corresponding results using the PK2 surface.

Coltan and Schatz[62,63] performed CS calculations for the H + H_2 reaction on the LSTH surface for translational energies below 1.4 eV. Schatz[64] studied the H + D_2 reaction at E_{rel} = 0.55 eV using the CS method on the LSTH surface. Schatz[62,63] studied the D + H_2, H + DH, and H + HD reactions using the CS method on the PK2 surface for $E_{rel} < 0.25$ eV.

Distorted wave theory is another approach that has been used to approximate CC and CS reactive scattering. In this method, the reaction is treated as a minor perturbation to the nonreactive collision. The reactive scattering matrix can be approximated by the matrix element of a perturbed Hamiltonian. This method has been used by Tang and coworkers[66−71] to study the D + H_2 reaction. This method is only accurate for reaction probabilities of less than 0.1 making studies beyond 0.6 eV for the H + H_2 system unfeasible.

In the last seven years, several groups have presented new results using the CC method. Webster and Light[72,73] calculated reaction probabilities for total angular momentum $J = 0$ for the H/D + H_2, H + D_2, H/D + HD, and H/D + DH reactions for $0.50 < E_{tot} < 1.50$ eV on the LSTH surface. They used R-matrix propagation to solve the coupled equations for reactive scattering, with three sets of Jacobi coordinates. They obtained reaction probabilities for the J=0 partial wave, and observed resonances in all 7 systems.

Another method which has been used to study the H_3 system takes advantage of the use of hyperspherical coordinates, which have been described in several papers.[74–77] Hipes and Kuppermann[78,79] presented reaction probabilities and lifetimes for $J = 0$ for H + H_2 for $0.40 < E_{tot} < 1.60$ eV on the PK2 surface. Six resonances were observed at 0.61, 0.847, 0.971, 1.170, 1.382 and 1.56 eV. These calculations were repeated on the LSTH surface.[80] The resonance energies on this surface occurred at 0.65, 0.880, 0.981, 1.193, 1.363, and 1.55 eV. These resonances have been identified with progressions on the symmetric stretching and bending motions of the H_3 transition state. Parker *et al.*[81–83] calculated reaction probabilities for $J = 0,1$ for H + H_2 and for $J = 0$ for D + H_2 on the PK2 surface for energies up 1.0 eV.

During the past several years, converged calculations for the H + H_2 and D + H_2 systems have been published. Several investigators have employed the hyperspherical propagation method mentioned earlier including: Kuppermann and coworkers,[78–80,84–85] Shatz,[86] Linderberg and coworkers,[87] Pack *et al.*[81–83] and Launay and LeDourneuf.[88] A second method of choice is the variational method using Jacobi coordinates. This method has been employed by Manolopoulos and Wyatt,[89–95] Miller,[96,97] and Truhlar, Kouri and coworkers.[98–106] Webster and

Light[72–73] have also published converged results with the method they previously developed using a natural collision coordinate system. The converged theoretical cross sections agree very well with one another.

E. Transition State Spectroscopy of the H_3 System

In a series of papers, Polanyi and coworkers[107–109] examined the transition state spectroscopy of the $H + H_2$ system. Absorption spectra of transition state configurations in the collinear reaction $H + H_2 \longrightarrow H_3^\ddagger \longrightarrow H_2 + H$ were calculated.[107–108] They obtained the density of $H_3^\ddagger$ in configuration space from a classical trajectory study of collinear reaction on the LSTH *ab initio* potential energy surface. Vertical transitions were assumed to one of four upper PESs of H_3 modeled using limited *ab initio* data. They studied the effects of reagent collision energy, reagent vibrational excitation, isotopic mass and optical transition moment. Spectra were also computed for thermal distributions of $H+H_2$, at 300 K and 1000 K. The density distributions showed marked accumulation of density at translational and vibrational turning points in the entry and exit valleys of the ground state PES.

Later, they extended this study to three dimensions.[109] The density of $H_3^\ddagger$ in configuration space was computed by means of a 3D classical trajectory calculation on the LSTH potential energy surface. Optically induced transitions were assumed to occur, with constant transition moment, to a 3D upper PES fitted to points obtained from a DIM calculation. They examined the effect of collision energy. The computed spectra showed a single peak with a wavelength related to the distance of closest approach of the collision partners and width related to the range of angles present in $H_3^\ddagger$ at closest approach. With increasing collision energy, the location of the transition-state spectral peak shifted to lower

ν by ≈ 27000 cm^{-1}. They attributed the existence of this spectral peak to the accumulation of trajectories at a tranlsational turning point, a region of configurations in which the momentum along the coordinate of approach has been largely converted into potential energy. Linear and bent configurations were found to contribute to a comparable extent to the total absorption.

F. Rydberg Spectra of the H_3 Molecule

The observation of the emission spectra of triatomic hydrogen by Herzberg and coworkers[110–119] (for more details see section 2.III.C) sparked interest in this species and several groups set out to calculate the Rydberg spectra of this molecule. Jungen[120] calculated the energies of the Rydberg states of H_3 for the equilibrium geometry of the ion H_3^+ (D_{3h} with R=1.650 bohr, see Ref. 121). Their study was carried out using a frozen core approximation,[122] *i.e.*, solving the one electron problem in the field of the Hartree-Fock solution for H_3^+. He used a basis which consisted of 196 Gaussian lobes contracted to 74 functions with exponents as small as 0.00025. Reorganization and polarization effects were included for the lower Rydberg states. Their results were in good agreement with the spectrum observed by Herzberg *et al.*[110–119] Their results are summarized as follows: calculated quantum defects were small for all series except for the npE$'$ series which has a quantum defect of about 0.4. As a consequence of this, the ns series in H_3 lies between the npE$'$ and npA$''$ series. The Rydberg states of H_3 are all stable with respect to the separation limit $H + H + H^*(n = 2)$ (-1.125 hartree); any separation limit into H + bound H_2^+ is still higher. Except for the $1^2E'$ electronic state, all states are unstable with respect to H + H + H. Since the only states arising from this limit are $^2E' + {}^4A_1'$ the potential surfaces of the excited Rydberg states of H_3 are all bonding. However, the $^4A_1'$ state is antibonding and has for the equilibrium geometry of H_3^+ a total electronic energy of -1.0926 hartree, about 11 eV above the H + H + H limit.

Shortly afterwards, Martin[123] performed similar calculations. He again used the equilibrium geometry of H_3^+ for the Rydberg H_3 geometries. Wavefunctions for the excited states were generated by optimizing a single orbital in the presence of a fixed H_3^+ core. The basis set used consisted of a (4s,1p) contracted Gaussian set on each hydrogen. The s space used was the (9s/4s) contraction used by Seigbahn and Liu,[16] the single p function used had an exponent of 1.0. The Rydberg orbitals were described by an additional (7s,7p,3d) set of functions located at the center of the H_3^+ core. Again, their results were in good agreement with the spectrum observed by Herzberg.

Later, King and Morokuma[124] calculated the spectrum of triatomic hydrogen. They calculated the fifteen lowest Rydberg states of H_3 using Koopmans theorem with a large Gaussian basis set constructed to represent both core and Rydberg orbitals. All excited electronic states were calculated using a simple but realistic frozen core approximation to have geometries and vibrational force constants close to those of H_3^+. The states with A symmetry, especially A_1' have shorter bond lengths, and the E' states are somewhat expanded as compared to the ion. Jahn-Teller effects were small. Small quantum defects and nearly integer values of electronic angular momenta indicate atomlike character for the Rydberg states. The most significant departure from atomic behavior is the lowering of the npE' levels. Their results predict six vibronic transitions which are in good agreement with the spectrum observed by Herzberg.

Zaitsevskii *et al.*[125] used a diatomics-in-molecules (DIM) approach to calculate the ground and low lying excited electronic states of the H_3 molecule, corresponding to a C_{2v} geometry. They used seven potential surfaces of the H_2 molecule and cubic spline fits to these surfaces. Their results showed qualitative agreement with *ab initio* results for potential surfaces of excited states as well as for ground states. Quantitative discrepancies did not exceed 0.05 hartree for all states and geometrical configurations considered.

Later, Raynor and Herschbach[126] used a diatomics-in-molecules approximation and spline fits to calculate the Rydberg states of H_3 in D_{3h} or C_{2v} nuclear configurations. They employed all available accurate diatomic data, a total of 22 potential curves. In their application, they used three customary approximations: (1) valence bond wave functions were constructed from linear combinations of Slater determinants. (2) All overlap integrals between atomic orbitals on different centers were neglected. (3) The Coulomb and exchange integrals are evaluated from spline fits to accurate diatomic potentials, derived from either *ab initio* results or experimental data. To treat the Rydberg states, they adopted three further approximations: (4) The only Slater determinants retained have two electrons residing in the ground 1s orbital on each of two protons and the third electron in an excited s or p orbital on the third proton. (5) The same approximation is made in representing the ground and excited states of diatomic fragments. (6) both for H_3 and its component diatomic parts, mixing between wave functions representing different types of atomic excitation is neglected. They obtained simple explicit formulas relating the H_3 Rydberg levels to the H_2 potential curves. Comparison of their results to those obtained previously showed that for almost all the levels, the DIM energies agree with the *ab initio* values within 0.01 hartree or better. The exception in the 3pE′ level which DIM predicts to be more stable by ≈ 0.05 hartree. This difference is attributed to the inaccuracy of the diatomic potential used for this state. The DIM method results in less reliable bond lengths, the bond lengths exceed the *ab initio* values by 0.09-0.14 bohr for most states. In another study,[127] they adopted the strategy used by King and Morokuma.[124] A basis set of core orbitals was selected to represent the parent ion, and the geometry and orbital exponents were optimized. Rydberg-like orbitals centered on the second-row atom were then added. They determined virtual orbital energies and added them to the energy of the parent ion to obtain Rydberg energies of the molecule via Koopmans theorem. They used Slater type orbitals (STOs) rather than Gaussian functions employed in previous calculations. The STOs offer the advantage that fewer orbitals are required for convergence to a good representation of the parent ion. The long range behavior is also better than for Gaussians, and this becomes important for the higher Rydberg orbitals. The major disadvantage of STOs is the increased difficultly of computing multicenter or large STO integrals. They used a floating spherical Slater orbital (FSSO) basis for the core orbitals. Their results were essentially equivalent to those of King and Morokuma,[124] the transition wavelengths to within 70 Å and emission rates agreed to within 10% . Agreement with the spectra observed by Herzberg and coworkers[110−119] was satisfactory. Transition wavelengths agreed to within 50-150 Å for the transitions near 5600 and 7100 Å. Agreement was less satisfactory (only within ~ 500 Å for transitions near 5900 and 6025 Å.

More recently, Petsalakis *et al.*[23] have performed multi-reference single and double excitation configuration interaction MRD-CI calculations on the first nine Rydberg states of H_3 using D_{3h} geometry with a bond length of 1.64 bohr. Their work represents the first all-electron configuration interaction treatment of the Rydberg states of H_3. The basis set used was previously discussed in section II.B. The Rydberg functions were centered at the center of the triangle. Their results are in excellent agreement with the results of Herzberg and coworkers,[110−119] and are significantly better (by approximately 800cm^{-1}) than has previously been calculated. They also calculated transition frequencies, transition dipole moments and Einstein coeffiecients. The transitions moments were similar to those calculated by King and Morokuma[124] differing only by ~ 15% for most transitions. The lifetimes of the $2p_z^2A_2''$ and $2s^2A_1'$ states were calculated to be 70 μs and 2.16 μs respectively.

Most recently Diercksen *et al.*[29] have performed large-scale multi-reference configuration-interaction (CI) calculations using basis sets of contracted Gaussian functions and obtained energies for the ground state and for eight excited states of H_3 in an equilateral triangle geometry with a bond length of 1.633 bohr. They examined the effects on the resulting spectrum due to the change of the basis-set and the many particle wavefunction. They used five different basis sets for their study. The first was the basis set used by King and Morokuma[124] which consists of 98 orbitals: 4 contracted s- and 2p- type orbitals at each of the protons and 2 s-, 8 p- and 7 d- type orbitals at the center of the molecule. The orbitals at the center of the molecule describe the Rydberg states and were very carefully chosen for an accurate description of the 15 lowest Rydberg states of the H_3 molecule at the one-electron level. The second was the basis set used by Dykstra *et al.*[121] which consists of 63 orbitals: 6 contracted s-type, 3 p-type and 1 d-type orbitals centered at each of the protons. It was constructed for determining a very accurate ground-state energy of the H_3^+ ion. The third was constructed by combining the basis set of Dykstra *et al.*[121] with 23 orbitals (2 s-, 3 p- and 2 d-type) at the center of the molecule. This basis set consists of 86 orbitals. The exponents were partially optimized to result in the lowest values for the first Rydberg states of H_3. The exponents used were 0.118 and 0.003 for the s-, 0.128, 0.064 and 0.032 for the p-, 2.9 and 0.01 for the d-type functions. The fourth was the final basis set of Seigbahn and Lui[16] which consists of 57 contracted orbitals: 4 s-, 3 p- and 1 d-type at each proton. This basis was designed to obtain very accurate ground state energies of the H_3 molecule. The fifth was constructed by combining the basis set of Siegbahn and Lui with 38 orbitals (2 s-, 6 p- and 3 d-type) at the center of the molecule. These 38 orbitals were obtained by reducing the basis set of King and Morokuma and then optimizing the exponents. The final values of the exponents are: 0.118 and 0.031 for the s-, 0.160, 0.080, 0.040, 0.020, 0.010 and 0.005 for the p-, 0.100, 0.033, and 0.010 for the d-type orbitals. This basis set consists of 95 orbitals. The ground state and excited state energies of H_3 were obtained by either full CI calculations or by calculations taking all singly and doubly excited states from a multi-reference space consisting of an internal space containing the most important configurations. The first ground state energy of the H_3 molecule showed a strong dependence upon the correlation energy of the one-electron basis. Basis 1 accounts for only 25% whereas bases 2 through 5 account for 97.5% to 98.4% of the exact correlation energy. The behavior of the correlation energy versus the number of basis functions used vary regularly and are similar for all bases used (E_{corr} increases with the number of basis functions). The sequence of the Rydberg states was found to depend strongly on the electron correlation. The calculated transistion energies for bases 1 and 5 is very good. In addition, the agreement remains good if the CI procedure is entirely neglected, due to cancellations of errors. Very poor agreement was obtained for basis 3, probably due to the smaller number of orbitals specifically designed to describe the Rydberg states in this basis. Their results demonstrate that very large and carefully selected basis sets are necessary in order to obtain an adequate description of both ground and excited (Rydberg) states of a molecule if reliable results are needed to make predictions about the system.

G. Bound Ro-vibrational States of the H_3 Molecule

The bound ro-vibrational states of H_3 in its first excited electronic state have been calculated by Peng and coworkers.[25–26] They performed this calculation using two different methods. The first method employed the variational method of Tennyson and Sutcliffe[128–129] and the DMBE surface of Varandas and coworkers[20–21] under the assumption that electronically nonadiabatic coupling of the first excited electronic state to the electronic ground state vanishes. They calculated the 10 lowest vibrational states for J=0, and the 12 lowest vibrational states for J=1. However, due to the memory limitations of the computer system used, the basis set could not be further expanded and the calculations were not well converged.

Later, because of the geometric phase effect (or the molecular Aharanov-Bohm effect)[130–132] related to the conical intersection[133–135] between the ground and first excited electronic states, they developed a hyperspherical coordinate propagation method to study the ro-vibrational states on the DMBE surface including this effect. In addition, this method also incorporated the full nuclear permutation symmetry P_3 of H_3. Using this method, they calculated the ro-vibrational bound states of H_3 on the first excited electronic state with and without the inclusion of the geometrical phase. The eigenenergies obtained neglecting the geometrical phase are in good agreement with those obtained using the variational method of Tennyson and Sutcliffe.[128–129] The geometric phase was shown to be very important as it significantly changed the quantum numbers, eigenenergies and the wavefunctions of those bound ro-vibrational states.

In equilateral triangular geometries, the ground and the first excited electronic states of H_3 are degenerate. When the nuclear configuration deviates away from the equilateral triangle configuration, the degeneracy is lifted. As Longguet-Higgins, Herzberg and co-workers[133–136] have pointed out, the effect of the conical intersection causes the real-valued electronic wavefunctions of both electronic states to change sign as an arbitrary closed path in the internal nuclear configuration space around the line of the conical intersection configuration is traversed. Since the total electronic and nuclear wave function must be single valued, a change in the nuclear wave function must also occur.

The Hypersherical propagation (HS) method produced better results than the variational method for several reasons. First, the symmetry assignments and degeneracy of an eigen-level in the HS method are exact, while in in the TS method, the symmetry assignments were difficult to make for closely spaced eigenstates. In addition, the convergence of the energy levels was always better with the HS method than with the TS method. For example the lowest energy J=0 state is the A_1 (0,0,0) state. The TS method gives an energy of 3.7218 eV, whereas the HS method gives 3.7210 eV (where (ν_1, ν_2, ℓ) are the quantum numbers of the symmetric mode, anti-symmetric mode and vibrational rotational quantum numbers used in the normal mode analysis). Typical improvements in the energy were approximately 0.001 eV, with the greatest improvement for any of the states calculated being 0.02 eV.

Inclusion of the geometrical phase results in bending modes having half-odd-integer quantum numbers and significant changes in the ro-vibrational state energies and their symmetry properties. The A_1 states are no longer allowed by the Pauli exclusion principle, and the lowest J=0 state is the E $(0, \frac{1}{2}, \frac{1}{2})$ state which occurs at an energy of 4.0215 eV. These results suggest that the conical intersection and therefore the geometrical phase play an important role in the chemistry of the H_3 system.

The bound ro-vibrational states of H_3 in the third excited state $2p_z^2 A_2''$ were also calculated by Peng and coworkers[25–26] For this calculation, they used the TS method with their *ab initio* results fitted by a rotated Morse cubic-curve spline (RMCS). This surface has features similar to the ground electronic state of H_3^+ ion, with a deep smooth well at an internuclear distance of 1.642 bohr (1.662 bohr for H_3^+ [137]). Because of the similarity of this surface to the ground state surface of H_3^+ , the TS variational method is believed to be very effective as it has been successively used for the H_3^+ ion in its ground electronic state.[128–129] The Rydberg nature of this electronic state led to nuclear motion similar to that of the H_3^+ ion. Comparison between the calculated values of the rovibrational constants and the corresponding experimental results suggest that the $2p_z^2A_2''$ surface calculated needs improvement. They calculated values of $\nu_E = 2533\ \text{cm}^{-1}$ and $\nu_{A_1} = 3227\ \text{cm}^{1}$. Although these values are similar to those calculated for H_3^+, ($\nu_E = 2521.6\ \text{cm}^{-1137}$ and $\nu_{A_1} = 3178.28\ \text{cm}^{-1138}$), the experimental values for H_3 are $\nu_E = 2602\ \text{cm}^{-1}$,[139] and $\nu_E = 2618.34\ \text{cm}^{-1}$,[138] and $\nu_{A_1} = 3255.4\ \text{cm}^{-1}$.[140] Their calculated value of ν_E is off by 85 cm^{-1} and ν_{A_1} by 28 cm^{-1} from the experimental values.

H. Transition Dipole Moments of H_3

The transition dipole moments between the four lowest electronic states of H_3 were calculated by Petsalakis *et al.*[23] using the same method MRD-CI and basis described earlier. They calculated the transition moments along linear and insertion paths. On the basis of calculated oscillator strengths they predict two types of transition state spectra. One type, corresponding to absorption to the 2p state, would show high intensity at high frequencies near the atomic 1s-2p frequency and no appreciable intensity at frequencies lower than 70,000 cm^{-1}. The other type corresponding to 2s absorption is predicted to be stronger than that to the 2p everywhere except at the dissociation limits. This compares well with the TSS calculated by Mayne and coworkers[107–108] that display intensity maxima at both low and high frequencies and thus give a composite picture of the spectra expected from their results. However, the present data is likely to lead to a more accurate prediction of the transition state spectra if employed in treatments such as those used by Mayne and coworkers.[107-109]

The transition dipole moments between the four lowest electronic states of H_3 were also calculated Peng *et al.*[25,27] Their study covered a much larger range of geometries than that of Petsalakis *et al.*[23] Although only C_s symmetry was embedded in their calculation, when the three nuclei formed an equilateral triangle, the full molecular point group D_{3h} associated with this geometry manifested itself in the results of the electronic calculations via the following features:

1. The electric dipole transition moments $\mathbf{T}_{41}$, $\mathbf{T}_{42}$ from the $2p_z^2A_2''$ state to the $2p_{x,y}^2E'$ states vanish due to symmetry reasons, and were close to zero in the actual calculations due to inherent innaccuracies of the calculations.
2. Because of the degeneracy of the $2p_{x,y}^2E'$ states under D_{3h} symmetry, these states can always be written as:

$$|2p_x^2E'\rangle = \cos\varphi|\phi_1\rangle + \sin\varphi|\phi_2\rangle \tag{2.2}$$

$$|2p_y^2E'\rangle = -\sin\varphi|\phi_1\rangle + \cos\varphi|\phi_2\rangle \tag{2.3}$$

where $|\phi_1\rangle$, $|\phi_2\rangle$ are solutions of the electronic wave equation with the same energy, which form another E' representation of the D_{3h} symmetry group. The phase angle φ is not determined by the variational method alone, and can have an arbitrary value. However, the D_{3h} symmetry ensures that:

a. The magnitudes of $\mathbf{T}_{31}$, $\mathbf{T}_{32}$, and $\mathbf{T}_{21}$ do not depend upon the phase φ and therefore should change smoothly with internuclear distance.

b. $|\mathbf{T}_{31}| = |\mathbf{T}_{32}|$, $|T_{31}(x)| = |T_{32}(y)|$, and $|T_{31}(y)| = |T_{32}(x)|$.

Their results confirmed these features. These results could be used in a study similar to that performed by Mayne and coworkers[107-109] to predict the transition state spectra of H_3. As in the case of the results of Petsalakis *et al.*, the increased accuracy of the transition dipole moments calculated here should provide a more accurate prediction of the transition state spectra.

I. Nonadiabatic Coupling Elements of H_3

The major terms of the electrically nonadiabatic coupling elements near the equilateral triangle configuration of H_3 between the upper and lower sheets of the DMBE surface have been obtained through a functional analysis by Varandas and coworkers.[20–21] As discussed above, the DMBE surface is an analytic fit to the *ab initio* results of several studies. They calculated potential energy and first derivative nonadiabatic coupling elements along six cuts in nuclear configuration space. The variables chosen for the description of the nuclear geometry were r (the distance between two of the nuclei, or diatom), R (the distance between the center of mass of the diatom and the third nuclei), and χ (the angle between r and R). A pictorial representation of the coordinate geometry variables they used is shown in Figure 1. The cuts chosen for their study were

1. $\chi = 89°$, r = 1.4 bohr and R was varied between 0 and 3.0 bohr.
2. $\chi = 89°$, r = 2.0 bohr and R was varied between 0 and 3.0 bohr.
3. $\chi = 89°$, R = 0.7 bohr and r was varied between 0.4 and 3.0 bohr.
4. $\chi = 89°$, R = 0.9 bohr and r was varied between 0.4 and 3.0 bohr.
5. r = 2.0 bohr, R = 0.7 bohr and χ was varied between 0 and 90°.
6. r = 1.4 bohr, R = 1.9 bohr and χ was varied between 0 and 90°.

The first four cuts correspond to points where the conical intersection is replaced by an avoided crossing and cusps are replaced by maxima and minima with continuous derivatives. The nonadiabatic coupling elements were found to exhibit the behavior expected if it just passes an odd-ordered pole without going through the pole. The last two cuts show that even when $\chi = 90°$ the configuration does not correspond to a conical intersection, but instead it corresponds to a local maximum in the angular coupling. Of noteworthy importance is that all three components of the nonadiabatic coupling elements are large in the same regions of space. Their graphs of the potential energy surface cuts and nonadiabatic coupling elements are shown in Figures 2-4. A more detailed discussion of their results will be given in Chapter 4 as they are compared to the results obtained in the present study.

III. Experimental Studies of H_3

A. Introduction

There have been two classes of experiments performed on the H_3 system. The first class of experiments deals with explicitly examining the hydrogen exchange reaction. Included in this group are crossed molecular beam experiments and hot atom experiments. The second class of experiments deals with examining the H_3 species itself. Included in this group are spectroscopic experiments, neutralized ion beam and neutral H_3 beam experiments. In the following sections, a discussion of the results of these studies will be presented.

B. Crossed Molecular Beam Experiments

Crossed molecular beam experiments provide several useful pieces of information about the reaction which is being investigated. The most direct result is the differential cross section (DSC) which can be used to determine the potential energy function for the reaction being studied. In addition, the time-scale of the reaction (fast or slow compared to rotation) and the reaction mechanism can be determined. The product internal energy distribution can also be obtained by measuring the velocity distribution of the products given a sufficiently narrow velocity distribution of the reagents.

The D + H_2 system has been the system of choice for these experiments. A beam of D atoms produced in a gas discharge or high temperature oven were crossed at right angles with an effusive jet of H_2 molecules.The product HD molecules were detected using a rotatable mass spectrometer tuned to mass 3. Complications arise from background mass 3 resulting from HD produced in wall reactions, HD impurities in the D atom source, and to a lesser extent in the

H_2 beam, and from H_3^+ ions formed by ion-molecule reactions in the ionizer region of the mass spectrometer.

Datz and Taylor[141] performed the first such experiments in 1963. However due to severe HD background, the only conclusions they were able to make was that in the center of mass frame, the molecular products are backwards scattered with respect to the D atom.

Geddes *et al.*[142] repeated the experiments in 1970. They were able to conclude that the reaction products were backwards scattered and that the observed velocity distributions were consistent with low internal excitation of the products.

Götting *et al.*[143–144] added a chopper and time-of-flight detection to enable them to measure the product velocity distribution. The differential cross section they measured was peaked at 125° rather than backwards peaked. A QCT analysis of their results led them to conclude that although less than 10% of the available energy went into product vibration a significant fraction $\approx$ 40% went into product rotation.

Kwei and Lo[145] studied the H + T_2 reaction. They used MoO_3 coated buttons located at 10° intervals to act as getter surfaces for H and T atoms. Liquid scintillation counting was used to determine the number of T atoms at each button. Their results indicated that the T atoms were scattered forward and therefore the molecular product was scattered backward.

Buntin *et al.*[146] were able to reduce the uncertainty in the atomic beam velocity by photolyzing D_2S under nearly collisionless conditions with an ArF eximer laser at 193 nm. The resulting D atom beam had a velocity resolution of $\Delta v/v = 11\%$, which was a factor of four improvement over that obtained using a thermal D atom source. Preliminary analysis of their results indicates that a greater percentage than was observed previously of the available energy is present as vibration in the molecular product.

Recently Continetti *et al.*[147] used photodissociation of DI at 248 nm as a source of D atoms. The measured DH integral cross sections agreed with theoretical results,[89,96] however the measured differential cross sections for rotationally excited DH were significantly different. The observed differences were attributed to the lack of the LSTH surface to accurately describe the bending potential at high energies. The differential cross sections seem to be much more sensitive to the features of the potential energy surface than are the integral cross sections. This is a result of the washing out of dynamical resonances which have been observed when averaged over the orbital angular momentum states of the reactants.[89,96]

C. Hot Atom Experiments

In these experiments, hydrogen halides or H_2S are photolyzed to produce H atoms with excess translational energy and a very narrow energy range. The hot H atoms are reacted with H_2 under single collision conditions and pulsed lasers are used to detect the nascent internal state distributions of the products.

Gerrity and Valentini[44-46] photolyzed HI at 266 nm, 280 nm and 291 nm. The products were detected by Coherent Anti-Stokes Raman Spectroscopy (CARS). For the H + D_2 reaction at 1.3 eV relative energy, they detected J=1-10,12 for v=0, J=1-9 for v=1, and J=2-5 for v=2. The rotational distribution in all three cases was peaked at J=3.

Zare and coworkers[47-48] repeated the experiments of Gerrity and Valentini using a different detection technique. The products were detected using resonance enhanced multiphoton ionization (REMPI). For the same relative energy, they observed J=0-6 for v=1 and J=0-6 for v=2. A large HD background prevented measurement of the rotational distribution for v=0. The rotational distribution was peaked at J=4 for v=1 and J=2 for v=2. Their results compared better with the QCT results of Blais and Truhlar[38−39] that predicted peaks at J=8 for v=0, J=4 for v=1 and J=5 for v=2.

In 1988 Nieh and Valentini[148−149] observed dynamical Feshbach resonances in the H + p-H_2 $\longrightarrow$ o,p-H_2 + H reaction. Such resonances have also been observed in 3-D quantum scattering calculations.[78,98] These resonances are the result of interference between direct and resonant scattering. The resonant scattering is the result of nonadiabatic coupling between the relative motion and the internal degrees of freedom, which leads to the formation of quasibound excited states. The vibrational modes of the H_3 transition state that are perpendicular to the relative motion of the reactants and products in the vicinity of the transition are responsible for these resonant states. However, fully converged quantum calculations[96−97] including 19 partial waves (J=0-18) do not show such resonances. Averaging over angular momemtum states leads to a washing-out of the partial wave resonances in the integral cross sections.

This discrepancy was first explained by the inadequacy of the LSTH surface in the region of the conical intersection (barrier is too high and van der Waals region is not accurately described). However, the DMBE surface was constructed to more accurately describe this region and calculations by Manolopoulos and Wyatt[89] using the DMBE surface are in agreement with results using the LSTH surface.

Zare and coworkers[150] repeated these experiments and observed no resonance structure in the integral cross sections. Their results agreed well with the results of Zhang and Miller.[96−97] In addition, Zare and coworkers[151−153] studied the H + D_2 and the D + H_2 systems. These studies complemented the earlier work by Marinero, Rettner and Zare.[47−48] Their results agreed well with those of Gerrity and Valentini,[44−46] the QCT results of Blais and Truhlar (although the experimental rotational distributions were slightly colder), and the CC quantum mechanical results of Wyatt and coworkers.[95]

D. Properties of Rydberg Molecules

Rydberg states derive their name from the Swedish physicist, J. R. Rydberg, who established that most excited states of atoms are similar to the excited states of the H atom. Rydberg states occur in simple series and give rise to line series of the form

$$E_n = T_\infty - \frac{R}{(n - \delta_{eff})^2} , \tag{2.4}$$

where T_∞ is the ionization limit, $R = 109717.39\ cm^{-1}$ is the Rydberg constant and δ_{eff} is the Rydberg correction or quantum defect. For molecules built-up from atoms of the first period, n must be at least 3 to obtain a Rydberg orbital, and δ_{eff} is small (≤ 0.1) for states derived from nd electrons, somewhat larger (0.3 – 0.5) for np electrons and appreciably larger (0.9 – 1.2) for ns electrons. The separation of successive lines in these series changes rapidly, approximately as the inverse third power of the principle quantum number, n.[115]

Conditions which seem necessary for the existence of a Rydberg molecule are:

1) the corresponding ion must be very stable,

2) the ground state of the neutral molecule must be only weakly bound or entirely repulsive, and

3) the energy difference between the ground state of the neutral molecule and the first Rydberg state must be large.

To satisfy these conditions, there must be no valence states between the ground state and the first Rydberg state. Otherwise interactions between Rydberg and non-Rydberg states would lead to predissociation or mixing and therefore deviations from Rydberg character.[115] The H_3 molecule is an example of a Rydberg molecule, and of the few Rydberg molecules that have been observed, it has recieved the most attention. Experimental studies of this species will be discussed in the sections that follow.

E. Early Neutralized Ion Beam Experiments

A powerful method for studying Rydberg molecules is that of neutralized ion beams. Several important results have come out of studies using this method. First, this method provides a means of producing neutral species which may be difficult, if not impossible, to form in any other way. It provides an opportunity for measurement of the energetics of fragmentation. It also allows an estimation of their lifetimes and hence stabilities to be made. Lastly, this method lends itself to the study of spectra of the individual isotopes.[154]

This method involves the neutralization of fast moving ions R^+ in a charge transfer reaction

$$R^+ + G_1 \longrightarrow R + G_1^+ \ , \tag{2.5}$$

where G_1 represents a gas atom or molecule. Detection of these species can be accomplished in many ways, but most studies have employed reionization of the fast moving species in a collisional ionization reaction

$$R + G_2 \longrightarrow R^+ + G_2 + e^- \ , \tag{2.6}$$

where G_2 may or may not be an atom or molecule of the same gas used in the neutralization step.

This method was first developed by Devienne.[155–156] In his experiments a high energy (12.0 keV) beam of stable H_3^+ ions were sent through a gas target (H_2)

such that electron-capture processes result in the production of a neutral beam of H_3. He observed the neutral to exist with appreciable intensity for flight times as long as a fraction of a μs. The neutral H_3 molecules were detected by reionization with a target gas and detected with a Faraday cup. Variations of this technique have since been examined by several investigators. Shortly afterwards, Gray and Tomlinson[157] investigated the HeH system using the same method as Devienne and found HeH molecules with a lifetime of at least 10^{-8} s. However, when they attempted to neutralize and re-ionize either D_2H^+ or D_3^+ they observed no signal, suggesting that no neutral species had been generated. With this result, it appeared that Devienne's result was not neutral H_3 but rather due to the presence of HD. It was thought that in Devienne's experiment an unavoidable contamination of deuterium in the hydrogen of the accelerator source produced HD^+ ions since the intensity of the observed H_3^+ signal was of the same order of magnitude as the intensity expected from the natural abundance of HD in hydrogen gas.Since HD^+ can not be distinguished from H_3^+ electromagnetically at the resolution used by Devienne, his results were attributed to the HD contamination. Then in 1972, Barnett and Ray[158] observed highly excited states of H_3 ($n \geq 11$) produced in a similar set up, however in their study the second charge exchange was replaced by electric field ionization. In their experimental procedure they took several precautions to minimize the contamination of the H_3^+ beam by any HD^+. Despite the fact that HD and H_3 would behave similarly in the electrostatic-stripping field, they concluded that the precautions they took to minimize contamination were sufficient to conclude that the signal they observed was due solely to the generation of an H_3 neutral species. Because these studies had the problem that H_3^+ and HD^+ could not be distinguished by the detection technique, the existence of a longlived H_3 species was still questioned. To clear up this question Nagasaki *et al.*,[159] looked at D_3 molecules using the successive charge exchange technique of Devienne combined with solid-state detection through a gold foil. Species with the same mass and energy were distinguished by their energy loss through the foil. They observed neutral D_3 with a half-life longer than 10^{-7} s. However, H_3 and D_3 are not exactly equivalent since differences between the rovibrational states can affect the stability of the Rydberg states formed by electron capture. This study was repeated by Castro de Faria *et al.*,[160] to observe H_3, their results presented no ambiguity since H_3^+ and HD^+ were clearly distinguished by their energy loss just before being detected. Gaillard *et al.*,[161] carried out a similar study and obtained estimates for the dissociation cross section, the electron capture, and the electron-loss cross sections. Volger,[162] observed H_3 and determined its vibrational level structure by measuring the translational energy structure of H, H_2 fragment pairs arising from predissociation of H_3. Cisneros *et al.*,[163] measured differential cross sections for the production of D_3^- and $D + D_2 \rightarrow D_3$ by electron capture into the repulsive states of D_3^- and D_3 by bombardment of D_3^+ with Cs. They used an electrostatic analyzer to distinguish neutral and ionic species. Gellene *et al.*,[164] observed excited dissociative and metastable states of H_3 and were the first to identify these states. Charge exchange with Mg produced primarily H_3 in its $2p_{x,y}^2E'$ electronic state, whereas exchange with K produced H_3 in its $2s^2A_1'$ and $2p_z^2A_2''$ states. They obtained estimates for the cross sections for both of these processes. Figger *et al.*,[165] examined laser spectroscopy of D_3 and observed transitions between the $3p^2E'$, $3p^2A_2''$ and $2s^2A_1'$ states. They were able to observe several previously unobserved transitions. In another study Figger *et al.*[166] observed these same transitions in D_3 and D_2H and measured total lifetimes of rotational sublevels by radiative decay.

F. Spectroscopic Experiments

Herzberg and coworkers[110–119] made the first spectroscopic measurements of the electronic structure of H_3. Herzberg originally set out to observe and characterize the rovibrational spectrum of H_3^+ using an ordinary hollow cathode discharge tube. They found that when operated at a pressure of H_2 of 1 torr and at liquid nitrogen temperatures, the emission spectrum observed at the cathode end was different than at the anode end. Further examination of these emission spectra showed that the emission spectrum observed at the anode end was due solely to H_2. However, the emission spectrum observed at the cathode end was due to H_2 as well as H_3. By superimposing a negative print of the anode spectrum they were able to eliminate all of the features resulting from H_2. The resulting spectrum consisted of a series of broad bands at 5600, 6025 and 7100 Å.

Further analysis of this spectrum found that the bands at 5600, 6025 and 7100 Å were due to transitions between several Rydberg states of H_3. The lines of the 5600 and 7100 Åbands are very broad and have the same width. This suggests they correspond to the same lower state and that this state is strongly predissociated ($\sim 0.8 \times 10^{-12}$s). The assignment of these bands has since been verified, with the 5600 Å band being due to the parallel transition

$$3d^2A_2'' \longrightarrow 2s^2A_1' \tag{2.7}$$

and the 7100 Å band being due to the perpendicular transition

$$3p^2E' \longrightarrow 2s^2A_1'. \tag{2.8}$$

The lines of the 6025 Å band are much sharper than those of the 5600 and 7100 Å bands (by more than 2 orders of magnitude). This band has been assigned to the perpendicular transition

$$3d^2E'' \longrightarrow 2p^2A_2'', \tag{2.9}$$

the lower state being the second excited state of H_3 .

The longest lived Rydberg excited state of H_3 is the $2p^2A_2''$ state. This is due to the fact that the

$$2p^2A_2'' \longrightarrow 2p^2E' \tag{2.10}$$

predissociation is both electronically and vibronically forbidden. Only rovibronic interaction can result in predissociation of this state. The predissociation of the $2p^2A_2''$ state must occur through a rotational motion about an axis perpendicular to the symmetry axis of the molecule.

Since spontaneous emission to the ground state is strongly forbidden, the only other means to relax radiatively from this state is by the process

$$2p^2A_2'' \longrightarrow 2s^2A_1' \longrightarrow 2p^2E'. \tag{2.11}$$

An Einstein emission coefficient of $\sim 1.2 \times 10^4\ s^{-1}$ for the

$$2p^2A_2'' \longrightarrow 2s^2A_1' \tag{2.12}$$

process was calculated using the results of King and Morokuma,[124] implying a lifetime of $\sim$ 87 μsec. An energy level diagram including the Rydberg excited states of H_3 and the levels of H_2 $(X^1\Sigma_g{}^+)$ with n = 1,2,3 and ∞ are given in Figure 5.[112,167]

The work of Herzberg and coworkers stimulated a flurry of theoretical calculations[120,123-127,168-170] which have successfully described the spectra they observed. These calculations have concluded that the Rydberg electron for the $^2A_2''$ state is in a $2p_z$ hydrogenic orbital perpendicular to the plane of the equilateral triangle H_3^+ ground state core.[171] The 90% contour surface for the probability density of this orbital in atomic hydrogen superimposed on the equilateral triangle representing the equilibrium position of the nuclei in H_3 is shown in Figure 6.[172]

For the H_3 molecule in the $2p^2A_2''$ state the following process is exoergic by 7.8 eV

$$H_3\ (2p^2A_2'') \longrightarrow \frac{3}{2}H_2\ (X^1\Sigma_g{}^+). \qquad (2.13)$$

The equilibrium geometry of the H_3 molecule is an equilateral triangle whose side measures $1.63a_o$.[112] This is only slightly smaller than the value of $1.66a_o$ for H_3^+ in the ground state. It can be seen from this figure that the $2p_z$ orbital extends significantly beyond the three protons. Thus the cross sections for H_3 undergoing various kinds of dynamical process should turn out to be substantial, as indeed has been found experimentally in limited cases and is discussed in section 2.III.D.[173−174] In addition, the lack of vibronic coupling of this $^2A_2''$ state of H_3 with the ground $2E'$ state is in part caused by the fact that the Rydberg electron is in a $2p_z$ orbital which is perpendicular to the plane containg the H_3^+ ion core. The channels available for the decay of the $2p^2A_2''$ state of H_3 are therfore: (i) radiative transition to the $^2A_1'$ state, which has been calculated to be 87 μsec;[124] (ii) rovibronic coupling to the ground state, resulting in rovibronic predissociation; (iii) magnetic dipole or electric quadrupole radiative transitions to the ground state, resulting in dissociation. The lifetime of the $^2A_2''$ state of H_3 will therefore depend upon the lifetime of these decay channels. The ability of metastable H_3 molecules to act as high energy species in practical applications depends partly upon its lifetime.

G. Neutral H_3 Beam Experiments

Using a high-temperature arc-discharge source, Garvey *et al.*[173−176] were able to produce an intense beam of neutral H_3 molecules. The laboratory energy distribution function of this beam of H_3 molecules was found to span the range from 0.1 to 15 eV with a maximum at about 8 eV. Its intensity lies in the range from 10^{21} to 10^{22} molecules sterad^{-1} s^{-1}. A lower limit for the lifetime of these molecules was estimated as 40 μs corresponding to the flight time of an 8 eV H_3 molecule from the source to the detector. Garvey *et al.*[174–175] measured the emission spectrum emanating from the source in the wavelength region between 5000 Å and 7500 Å. He observed several broad bands in the 7100 Å region corresponding to the perpendicular transition of $3p^2E' \longrightarrow 2s^2A_1'$ observed by Herzberg. In addition, He observed a band at 7480 Å which corresponds to the frequency calculated by King and Morokuma[124] for the transition $2s^2A_1' \longrightarrow 2p^2E'$. Garvey also performed total scattering, surface ionization, and photoionization experiments on the beam of H_3 molecules.[173–174] In the total scattering experiments, two target gases were used. Scattering of H_3 molecules at a source stagnation pressure of 65 torr by Ar led to a total attenuation cross section of 30 ± 7 Å^2 almost a factor of 10 greater than that found for scattering of Ar by H. Results with n-propane led to a total cross section of 25.4 ± 1.6 Å^2 only a factor of 1.2 greater than that found for scattering of n-propane by H. In the surface ionization experiments, the ionization efficiency was measured as a function of filament temperature using both tungsten and platinum filaments at several stagnation pressures. In all cases, the ionization efficiency was low, typically less than 10^{-6}, but increased with increasing filament temperature and decreasing stagnation pressure (increasing translational energy of the H_3 species). In the photoionization experiments, they were able to observe photoionization of H_3 molecules, however due to large background signals, an estimation of the radiative lifetime was not possible.

H. Recent Neutralized Ion Beam Experiments

Helm[139–140] has combined the neutralized ion beam of H_3 coaxially with a tunable laser beam and excited from the metastable $2p^2A_2''$(J=0,K=0) state the higher Rydberg ns, nd states up to n=40. He observed four series of Rydberg states converging to vibrationally excited H_3^+ and one series converging to H_3^+ in its ground vibrational state. He labeled these series A, B, B′, C and D, from the lowest vibrational level or from states with either one or the other of the two fundamental vibrations excited (but with N=0, K=0, since all other rotational levels predissociate rapidly). He found that the line positions in these series could be represented with a precision of better than 0.5 cm^{-1} using Equation 2.4. In a more accurate experiment, Helm[177] was able to observe the Rydberg series of H_3 which converges to the lowest rotational level of ortho-H_3^+ for values of n ranging from 27 to 100 (this is the series he labels D) using field ionization. Extrapolation of this series yields an ionization potential of 29562.6 ± 0.5 cm^{-1} for H_3 in its $\tilde{B}$ ($2p^2A_2''$,N=K=0) state. In addition, Cosby and Helm[178–179] made the first observation of photodissociation of H_3 molecules. They detected predissociation of optically prepared $3s^2A_1'$ and $3d^2E''$ states by the $\tilde{\chi}^2E'$ ground state by monitoring the production of rovibrationally excited H_2 molecules and H atoms. Six transitions were observed and excitation in the products was highly dependent upon the electronic and nuclear configuration of H_3. Recently, Helm and coworkers[179] have measured the lifetime of the $\tilde{B}(2p^2A_2''$,N=K=0) state by probing its population as a function of elapsed time from formation by photoionization. They found a lifetime for this state of only 0.64 μs and of 0.74 μs for the symmetric stretch-excited level. These lifetimes are about 2 orders of magnitude shorter than those expected on the basis of the allowed radiative transition $2p_z^2A_2'' \longrightarrow 2s^2A_1'$. They attributed the faster decay to weakly allowed radiative transitions between the metastable state and the degenerate mode-excited ground state of H_3, as well as to predissociation of the metastable levels by the repulsive ground state of H_3 induced by spin-orbit coupling. In their latest study Helm and coworkers[180] observed the f-electron series of H_3 converging to the two lowest rotational levels of H_3^+ by two photon excitation of the metastable $2p^2A_2''$ (J=0,K=0) state of H_3 through the d-electron Rydberg states with total angular momentum N=1. They determined the quantum defects, ionization potentials and their excitation intensity.

Bjerre *et al.*[181] have also used the fast neutral beam laser spectroscopy technique to measure fine structure splittings of the $3d^2E''$ and $3d^2A_1'$ states of H_3. They measured spin-orbit coupling constants for $3d^2E''$ and $3d^2A_1'$ states of H_3 of 409 and 427 MHz respectively, very close to those of the H (433 MHz) and Li (434 MHz) atoms. They estimated a spin-orbit limited lifetime for this state of 8 μs, implying that the main decay mechanism for this longlived state is optical decay to vibrationally asymmetric continuum levels in the $2p^2E'$ electronic ground state. This lifetime estimate is much shorter than previously published values of $40 - 90$ μs, but does agree well with recent measurements by Helm and coworkers.[179]

IV. References

1. D. G. Truhlar and R. E. Wyatt, *Ann. Rev. Phys. Chem.* **27** 1 (1976).
2. D. G. Truhlar and R. E. Wyatt, *Adv. Chem. Phys.* **36** 141 (1977).
3. G. C. Schatz, in *The Theory of Chemical Reaction Dynamics*, edited by D. C. Clary, (D. Reidel Publishing, Boston, 1986) p.1-26.
4. F. London, *Z. electrochem.* **35**, 552 (1929).
5. H. Eyring and M. Polanyi, *Naturwiss* **18**, 914 (1930).
6. S. Sato, *Bull. Chem. Soc. Jpn.* **28**, 450 (1955).
7. S. Sato, *J. Chem. Phys.* **23**, 592 (1955).
8. S. Sato, *J. Chem. Phys.* **23**, 2465 (1955).
9. R.N. Porter and M. Karplus, *J. Chem. Phys.* **40**, 1105 (1964).
10. A.S. Coolidge and H.M. James, *J. Chem. Phys.* **2**, 811 (1934).
11. J.O. Hirschfelder, H. Diamond and H. Eyring, *J. Chem. Phys.* **5**, 695 (1937).
12. S.F. Boys, G.B. Cook, C.M. Reeves and I. Shavitt, *Nature* **178**, 1207 (1956).
13. S.F. Boys and I. Shavitt, *Univ. of Wis. NRL Tech. Rep. WIS-AF-13*, 1959.
14. B. Liu, *J. Chem. Phys.* **58**, 1925 (1973).
15. W. Kolos and L. Wolniewicz, *J. Chem. Phys.* **43**, 2429 (1965).
16. D. Seigbahn and B. Liu, *J. Chem. Phys.* **68**, 2457 (1978).
17. D.G. Truhlar and C.J. Horowitz, *J. Chem. Phys.* **68**, 2466 (1978).
18. W. Welz, Ph.D. Thesis, Bonn, 1976.
19. B. Liu, *J. Chem. Phys.* **80**, 581 (1984).
20. A.J.C. Varandas, F.B. Brown, C.A. Mead, D.G. Truhlar and N.C. Blais, *J. Chem. Phys.* **86(11)**, 6258 (1987).
21. B.C. Garrett, D.G. Truhlar, A.J.C. Varandas and N.C. Blais, *Int. J. Chem. Kinet.* **18**, 1065 (1986).

22. M.R.A. Blomberg and B. Liu, *J. Chem. Phys.* **82**, 1050 (1985).
23. I. Petsalakis, J. Theodorakopoulos and J.S. Wright, *J. Chem. Phys.* **89**, 6850 (1988).
24. S. Huzinaga, *J. Chem. Phys.* **42**, 1293 (1965).
25. Z. Peng, Ph.D. Thesis, California Institute of Technology, Pasadena, CA, 1991.
26. B. Lepetit, Z. Peng and A. Kuppermann, *Chem. Phys. Lett.* **166(5,6)**, 572 (1990).
27. Z. Peng, A. Kuppermann and J.S. Wright, *Chem. Phys. Lett.* **175(3)**, 242 (1990).
28. S. Kristyan, Z. Peng and A. Kuppermann, to be published.
29. G.H.F. Diercksen, W. Duch and J. Karwowski, *Chem. Phys. Lett.* **168**, 69 (1990).
30. L.M. Raff and D.L. Thompson, in *Theory of Chemical Reaction Dynamics*, Vol. III, edited by M. Baer (CRC Press, Florida) pp. 1-121.
31. J. O. Hirschfelder, H. Eyring and B. Topley, *J. Chem. Phys.* **4**, 170 (1936).
32. M. Karplus, R. N. Porter and R. D. Sharma, *J. Chem. Phys.* **40**, 2033 (1964).
33. M. Karplus, R. N. Porter and R. D. Sharma, *J. Chem. Phys.* **43**, 3259 (1965).
34. M. Karplus, R. N. Porter and R. D. Sharma, *J. Chem. Phys.* **45**, 3871 (1966).
35. H. R. Mayne, *J. Chem. Phys.* **73**, 217 (1980).
36. G. D. Barg, H. R. Mayne and J. P. Toennies, *J. Chem. Phys.* **74**, 1017 (1981).
37. H. R. Mayne and J. P. Toennies, *J. Chem. Phys.* **75**, 1794 (1981).
38. C. A. Boonenberg and H. R. Mayne, *Chem. Phys. Lett.* **108**, 67 (1984).

40. N. C. Blais and D. G. Truhlar, *J. Chem. Phys.* **83**, 2201 (1985).

41. N. C. Blais and D. G. Truhlar, *J. Chem. Phys.* **88**, 5457 (1988).

42. N. C. Blais and D. G. Truhlar, *Chem. Phys. Lett.* **162**, 503 (1989).

43. N. C. Blais, M. Zao, M. Mladenovic, D. G. Truhlar, D. W. Schwenke, Y. Sun and D. J. Kouri, *J. Chem. Phys.* **91**, 1038 (1989).

44. D. P. Gerrity and J. J. Valentini, *J. Chem. Phys.* **79**, 5202 (1983).

45. D. P. Gerrity and J. J. Valentini, *J. Chem. Phys.* **81**, 1298 (1984).

46. D. P. Gerrity and J. J. Valentini, *J. Chem. Phys.* **82**, 1323 (1985).

47. C. T. Rettner, E. E. Marinero and R. N. Zare, in *Physics of Electronic and Molecular Collisions*, edited by J. Eichler, I. V. Hertel and N. Stolterfoht (North Holland, Amsterdam, 1984), p.51

48. E. E. Marinero, C. T. Rettner and R. N. Zare, *J. Chem. Phys.* **80**, 4142 (1984).

49. H.R. Mayne and S.S. Prasad, *INt. J. Chem. Kinetics* **18**, 977 (1986).

50. K. D. Rinnen, D. A. V. Kliner, R. S. Blake and R. N. Zare, *Chem. Phys. Lett.* **153**, 371 (1988).

51. F. J. Aoiz, V. Candela, V. J. Herrero and V. Saez Rabanos, *Chem. Phys. Lett.* **169**, 243 (1990).

52. F. J. Aoiz, V. J. Herrero and V. Saez Rabanos, *J. Chem. Phys.* **94**, 7991 (1991).

53. F. J. Aoiz, V. J. Herrero and V. Saez, *Chem. Phys. Lett.* **161**, 270 (1989).

54. J. Z. H. Zhang and W. H. Miller, *Chem. Phys. Lett* **140**, 329 (1987); *J. Chem. Phys.* **88**, 3202 (1988).

55. S. A. Buntin, C. F. Giese and W. R. Gentry, *J. Chem. Phys.* **87**, 1443 (1987).

56. D. L. Phillips, H. B. Levene and J. J. Valentini, *J. Chem. Phys.* **90**, 1600 (1989).

57. D. A. V. Kliner, K. D. Rinnen and R. N. Zare, *Chem. Phys. Lett.* **166**, 107 (1990).

58. G. C. Schatz and A. Kuppermann, *J. Chem. Phys.* **65**, 4668 (1976).

59. A. Kuppermann and G. C. Schatz, *J. Chem. Phys.* **62**, 2502 (1975).

60. A. B. Elkowitz and R. E. Wyatt, *J. Chem. Phys.* **63**, 702 (1975).

61. R. B. Walker, E. B. Stechel and J. C. Light, *J. Chem. Phys.* **69**, 2922 (1978).

62. M. C. Colton and G. C. Schatz, *Chem. Phys. Lett.* **124**, 256 (1986).

63. M. C. Colton and G. C. Schatz, *Int. J. Chem. Kin.* **18**, 961 (1986).

64. G. C. Schatz, *Chem. Phys. Lett.* **108**, 532 (1984).

65. L. M. Hubbard, S. Shi and W. H. Miller, *J. Chem. Phys.* **78**, 2381 (1983).

66. K. T. Tang and B. H. Choi, *J. Chem. Phys.* **62**, 3642 (1975).

67. B. H. Choi and K. T. Tang, *J. Chem. Phys.* **63**, 2854 (1975).

68. Y. Y. Yung, B. H. Choi and K. T. Tang, *J. Chem. Phys.* **72**, 621 (1980).

69. J. C. Sun, B. H. Choi, R. T. Poe and K. T. Tang, *J. Chem. Phys.* **73**, 6095 (1980).

70. B. H. Choi, R. T. Poe and K. T. Tang, *J. Chem. Phys.* **81**, 4979 (1984).

71. M. S. Bowers, B. H. Choi, R. T. Poe and K. T. Tang, *Chem. Phys. Lett.* **116**, 239 (1985).

72. F. Webster and J. C. Light, *J. Chem. Phys.* **85**, 4744 (1986).

73. F. Webster and J. C. Light, *J. Chem. Phys.* **90**, 265 (1989); *J. Chem. Phys.* **90**, 300 (1989).

74. A. Kuppermann, J. A. Kaye and J. P. Dwyer, *Chem. Phys. Lett.* **74**, 257 (1980); J. A. Kaye and A. Kuppermann, *Chem. Phys. Lett.* **77**, 573 (1981).

75. A. Kuppermann, *Theor. Chem.: Advances and Perpectives*, **6A**, 79 (1981).

76. G. Hauke, J. Manz and J. Römelt, *J. Chem. Phys.* **73**, 5040 (1980).

76. G. Hauke, J. Manz and J. Römelt, *J. Chem. Phys.* **73**, 5040 (1980).

77. J. Römelt, *Chem. Phys. Lett.* **74**, 263 (1980); *Chem. Phys. Lett.* **87**, 259 (1982).

78. A. Kuppermann and P. G. Hipes, *J. Chem. Phys.* **84**, 5962 (1986).

79. P. G. Hipes and A. Kuppermann, *Chem. Phys. Lett.* **133**, 1 (1987).

80. S. A. Cuccaro, P. G. Hipes and A. Kuppermann, *Chem. Phys. Lett.* **157**, 440 (1989).

81. G. A. Parker, R. T. Pack, B. J. Archer and R. B. Walker, *Chem. Phys. Lett.* **137**, 564 (1987).

82. R. T. Pack and G. A. Parker, *J. Chem. Phys.* **90**, 3511 (1989).

83. J. D. Kress, Z. Bačić, G. A. Parker and R. T. Pack, *Chem. Phys. Lett.* **157**, 585 (1989); *Chem. Phys. Lett.* **170**, 306 (1990).

84. S. A. Cuccaro, P. G. Hipes and A. Kuppermann, *Chem. Phys. Lett.* **154**, 155 (1989).

85. Y. M. Wu, S. A. Cuccaro, P. G. Hipes and A. Kuppermann, *Chem. Phys. Lett.* **168**, 429 (1990).

86. G. C. Schatz, *Chem. Phys. Lett.* **151**, 409 (1988); *J. Chem. Phys.* **90**, 3582 (1989); *Chem. Phys. Lett.* **150**, 92 (1988).

87. J. Linderberg, S. B. Padkjaer, Y. Öhrn and B. Vessal, *J. Chem. Phys.* **90**, 6254 (1989).

88. J. M. Launay and M. Le Dourneuf, *Chem. Phys. Lett.* **163**, 178 (1989).

89. D. E. Manolopoulos and R. E. Wyatt, *Chem. Phys. Lett.* **159**, 123 (1989).

90. D. E. Manolopoulos, R. E. Wyatt, *Chem. Phys. Lett.* **152**, 23 (1988).

91. D. E. Manolopolous and R. E. Wyatt, *J. Chem. Phys.* **92**, 810 (1990).

92. D. E. Manolopoulos M. D'Mello and R. E. Wyatt, *J. Chem. Phys.* **93**, 403 (1990).

93. M. D'Mello, D. E. Manolopoulos and R. E. Wyatt, *Chem. Phys. Lett.* **168**, 113 (1990).

94. D. E. Manolopoulos, M. D'Mello, R. E. Wyatt and R. B. Walker, *Chem. Phys. Lett.* **169**, 482 (1990).

95. M. D'Mello, d. E. Manolopoulos and R. E. Wyatt, *J. Chem. Phys.* **94**, 5985 (1991).

96. J. H. Z. Zhang and W. H. Miller, *J. Chem. Phys.* **91**, 1528 (1989); W. H. Miller, *Ann. Rev. Phys. Chem.* **41**, 245 (1990); *J. Chem. Phys.* **92**, 1811 (1990).

97. J. H. Z. Zhang and W. H. Miller, *J. Chem. Phys.* **88**, 4549 (1988); *J. Chem. Phys.* **90**, 7610 (1989); *Chem. Phys. Lett.* **159**, 130 (1989); *Chem. Phys. Lett.* **153**, 465 (1988).

98. M. Zhao, D. G. Truhlar, D. W. Schwenke and D. J. Kouri, *J. Phys. Chem.* **94**, 7074 (1990).

99. J. Z. H. Zhang, D. J. Kouri, K. Haug, D. W. Schwenke, Y. Shima and D. G. Truhlar, *J. Chem. Phys.* **88**, 2492 (1988).

100. M. Mladenovic, M. Zhao, D. G. Truhlar, D. W. Schwenke, Y. Sun, D. J. Kouri, *Chem. Phys. Lett.* **146**, 358 (1988).

101. M. Zhao, M. Mladenovic, D. G. Truhlar, D. W. Schwenke, Y. Sun, D. J. Kouri, and N. C. Blais, *J. Amer. Chem. Soc.* **111**, 852 (1989).

102. M. Mladenovic, M. Zhao, D. G. Truhlar, D. W. Schwenke, Y. Sun and D. J. Kouri, *J. Phys. Chem.* **92**, 7035 (1988).

103. M. Zhao, M. Mladenovich, D. G. Truhlar, D. W. Schwenke, O. Sharafeddin, Y. Sun and D. J. Kouri, *J. Chem. Phys.* **91**, 5302 (1989).

104. K. Haug, D. W. Schwenke, Y. Shima, D. G. Truhlar, J. Z. H. Zhang and D. J. Kouri, *J. Phys. Chem.* **90**, 6757 (1986).

105. M. Zhao, D. G. Truhlar, Y. Sun, D. J. Kouri and D. W. Schwenke, *Chem. Phys. Lett.* **156**, 281 (1989).

106. N. C. Blais, M. Zhao, M. Mladenovich, D. G. Truhalr, D. W. Schwenke, Y. Sun and D. J. Kouri, *J. Chem. Phys.* **91**, 1038 (1989).

107. H.R. Mayne, J.C.Polanyi and N. Sathyamurthy, *J. Phys. Chem.* **88**, 4064 (1984).

108. H.R. Mayne, R.A. Poirier and J.C. Polanyi, *J. Chem. Phys.* **80**, 4025 (1984).

109. H.J. Foth, H.R. Mayne, R.A. Poirier, J.C. Polanyi and H.H. Telle, *Laser Chem.* **2**, 229 ().1983

110. G. Herzberg, *J. Chem. Phys.* **70**, 4806 (1979).

111. I. Dabrowski and G. Herzberg, *Can. J. Phys.* **58**, 1238 (1980).

112. G. Herzberg and J. K. Watson, *Can. J. Phys.* **58**, 1250 (1980).

113. G. Herzberg, H. Lew, J. J. Sloan and J. K. G. Watson, *Can. J. Phys.* **60**, 1261 (1981).

114. G. Herzberg, J. T. Hougen and J. K. G. Watson, *Can. J. Phys.* **60**, 1261 (1982).

115. G. Herzberg, *Ann. Rev. Phys. Chem.* **38**, 27 (1987).

116. G. Herzberg, *Faraday Discuss. Chem. Soc.* **71**, 165 (1981).

117. G. Herzberg and J. T. Hougen, *J. Molec. Spec.* **97**, 430 (1983).

118. G. Herzberg, *J. Mol. Structure* **113**, 1 (1984).

119. G. Herzberg, *J. Astrophys. Astr.* **5**, 131 (1984).

120. M. Jungen, *J. Chem. Phys.* **71**, 3540 (1971).

121. C.E. Dykstra, A.S. Gaylord, W.D. Gwinn, W.C. Swope and H.F. Schaefer, *J. Chem. Phys.* **68**, 3951 (1978).

122. D. Demoulin and M. Jungen, *Theor. Chim. Acta* **34**, 1 (1974).

123. R. L. Martin, *J. Chem. Phys.* **71**, 3541 (1979).

124. H. R. King and K. Morokuma, *J. Chem. Phys.* **71**, 3213 (1979).

125. A.V. Zaitsevskii, A.V. Nemukhin and N.F. Stepanov, *Molec. Phys.* **41(2)**, 377 (1980).

126. S. Raynor and D.R. Herschbach, *J. Phys. Chem.* **86**, 1214 (1982).

127. S. Raynor and D.R. Herschbach, *J. Chem. Phys.* **86**, 3592 (1982).

128. J. Tennyson and B.T. Sutcliffe, *Molec. Phys.* **51**, 887 (1984).

129. J. Tennyson and B.T. Sutcliffe, *J. Chem. Soc. Faraday Trans. 2* **82**, 1151 (1986).

130. M.V. Berry, *Proc. Royal Soc. London Ser. A* **392**, 45 (1984).

131. C.A. Mead and D.G. Truhlar, *J. Chem. Phys.* **49**, 23 (1979).

132. C.A. Mead, *Chem. Phys.* **49**, 23 (1980).

133. H.C. Longguet-Higgins, U. Opik, M.H.L. Pryce and R.A. Sack, *Proc. Royal Soc. London Ser. A* **244**, 1 ().1958

134. G. Herzberg and H.C.Longguet-Higgins, *Diss. Faraday Soc.* **35**, 77 (1963).

135. H.C. Longguet-Higgins, *Adv. in Spec.* **2**, 429 (1961).

136. H.C. Longguet-Higgins, *Proc. Royal Soc. London Ser. A* **344**, 147 (1975).

137. T. Oka, *Phys. Rev. Lett.* **45**, 531 (1980).

138. W. Ketterle, H.P. Messmer and H. Walther, *Europhys. Lett.* **8**, 333 (1989).

139. H. Helm, *Phys. Rev. Lett.* **56(1)**, 42 (1986).

140. H. Helm, L. J. Lembo, P. C. Cosby and D. L. Huestis, in *Fundamentals of Laser Interactions*, (Springer-Verlag, 1989)

141. S. Datz and E.H. Taylor, *J. Chem. Phys.* **39**, 1896 (1963).

142. J. Geddes, H. F. Krause and W. L. Fite, *J. Chem. Phys* **52**, 3297 (1970); *J. Chem. Phys.* **56**, 3298 (1972).

143. R. Götting, H. R. Mayne and J. P. Toennies, *J. Chem. Phys.* **80**, 2230 (1984); *J. Chem. Phys.* **85**, 6396 (1986).

144. R. Götting, J. P. Toennies and M. Vodegel, *Int. J. Chem. Kin.* **18**, 949 (1986).

145. G. H. Kwei and V. W. S. Lo, *J. Chem. Phys.* **72**, 6265 (1980).

146. S. A. Buntin, C. F. Giese and W. R. Gentry, *J. Chem. Phys.* **87**, 1443 (1987).

147. R. E. Continetti, B. A. Balko and Y. T. Lee, *J. Chem. Phys.* **93**, 5719 (1990).

148. J. C. Nieh and J. J. Valentini *Phys. Rev. Lett.* **60**, 519 (1988).

149. J. C. Nieh, and J. J. Valentini, *J. Chem. Phys.* **92**, 1083 (1990).

150. D. A. V. Kliner, D. A. Adelman and R. N. Zare, *J. Chem. Phys.* **94**, 1069 (1991).

151. R. S. Blake, K. D. Rinnen, D. A. V. Kliner and R. N. Zare, *Chem. Phys. Lett.* **153**, 365 (1988).

152. K. D. Rinnen, D. A. V. Kliner, R. N.'Blake and R. N. Zare, *Chem. Phys. Lett.* **153**, 371 (1988).

153. K. D. Rinnen, D. A. V. Kliner and R. N. Zare, *J. Chem. Phys.* **91**, 7514 (1989).

154. W.J. Griffiths, F.M. Harris and J.H. Beynon, *Int. J. Mass Spec. and Ion Proc.* **77**, 233 (1987).

155. F. M. Devienne and J. C. Roustau, *C. R. Acad. Sci. Paris*, **263**, B-1389 (1966).

156. F. M. Devienne, a) *C .R. Acad. Sci. Paris*, **264**, B-1400 (1967); b) **267** B-1279 (1968); c)**268**, B-1303 (1969); d) *Entropie*, **24**, 35 (1968); VI th Intern. Conf. on the Phys. of Electron and Atom Collisions (MIT Press, Cambridge, 1969) p. 789.

157. J. Gray and R.H. tomlinson, *Chem. Phys. Lett.* **4**, 251 (1969).

158. C. F. Barnett and J. A. Ray, *Phys. Rev. A* **5**, 2120 (1972).

159. T. Nagasaki, H. Doi, K. Wada, K. Higashi, and F. Fukuzawa, *Phys. Lett.*, **38A**, 381 (1972).

160. N. V. Castro deFaria, M. J. Gaillard, J. C. Poizat and J. Remillieux, *Ann. Israel Phys. Soc.*, **4**, 134 (1981).

161. M. J. Galliard, A. G. dePinho, J. C. Poizat, J. Remillieux and R. Saoudi, *Phys. Rev.* **A28**, 1267 (1983).

162. M. Volger, *Phys. Rev. A* **19**, 1 (1979).

163. C. Cisneros, I. Alvarez, R. Garcia. C. F. Barnett, J. A. Ray and A. Russek, *Phys. Rev.* **A19**, 631 (1979).

164. G. I. Gellene and R. F. Porter, *J. Chem. Phys.* **79**, 5975 (1983).

165. H. Figger, H. Moller, W. Schrepp and H. Walther, *Chem. Phys. Lett.* **90**, 90 (1982).

166. H. Figger, M. N. Dixit, R. Maier, W. Schrepp, H. Walther, I. R. Peterkin and J. K. G. Watson, *Phys. Rev. Lett.* **52**, 906 (1984).

167. K. C. Kulander and M. F. Guest, *J. Phys. B: Atom. Molec. Phys.*, **12**, L501 (1979).

168. G. Calzaferri, *Chem. Phys. Lett.* **87**, 443 (1982).

169. J. Tennyson, *Chem. Phys. Lett.* **86**, 181 (1982).

170. K. Hirao and S. Yamake, *Chem. Phys.* **80**, 237 (1983).

171. G. I. Gellene, D. A. Cleary, R. F. Porter, C. E. Burkhardt, and J. J. Leventhal, *J. Chem. Phys.* **77**, 1354 (1982).

172. M. Karplus and R. N. Porter, *Atoms and Molecules: An Introduction for Students of Physical Chemistry*, (Benjamin/Cummings Publishing Co., 1970) p. 139.

173. J. F. Garvey and A. Kuppermann, *J. Chem. Phys.* **85**, (1986).

174. J. F. Garvey, Ph. D. thesis, California Institute of Technology, 1985.

175. J. F. Garvey and A. Kuppermann, *Chem. Phys. Lett.* **107**, 491 (1984).

176. J. F. Garvey and A. Kuppermann, *Rev. Sci. Instrum.*, **57**, 1061 (1986).

177. H. Helm, *Phys. Rev. A* **38(7)**, 3425 (1988).

178. P. C. Cosby and H. Helm, *Phys. Rev. Lett.* **61(3)**, 298 (1988).

179. C. Bordas, P.C. Cosby and H. Helm, *J. Chem. Phys.* **93**, 6303 (1990).

180. L.J. Lembo, M.C. Bordas and H. Helm, *Phys. Rev. A* **42**, 6660 (1990).

181. N. Bjerre, I. Hazell and D.C. Lorents, *Chem. Phys. Lett.* **181**, 301 (1991).

V. Figure Captions

Figure 1. Coordinate system used by Varandas and coworkers[20−21] for the calculation of the electrically nonadiabatic coupling elements near the equilateral triangular configuration of H_3 between the upper and lower sheets of the DMBE surface. P_i is the ith proton of H_3. The three protons are all in the xy-plane. The bond distance r between P_1 and P_2, R the distance between the center of mass of P_1P_2 and P_3, and the bond angle χ between r and R are used as the variables describing the shape of the triangle.

Figure 2. Potential surface cuts and components of nonadiabatic coupling elements along the unit vector $\hat{R}$ from the center of mass of H_2 to H for $\chi = 89°$ as functions of R(H-H_2). (a) E_1 and E_2 for r(H_2) = 1.4a_o, (b) $d_{12} \cdot \hat{R}$ (H-H_2) for r(H_2) = 1.4a_o, (c) E_1 and E_2 for r(H_2) = 2.0a_o, (d) $d_{12} \cdot \hat{R}$ (H-H_2) for r(H_2) = 2.0a_o.

Figure 3. Potential surface cuts and components of nonadiabatic coupling elements along the H_2 axis direction $\hat{r}$ for $\chi = 89°$ as functions of R(H-H_2). (a) E_1 and E_2 for R(H-H_2) = 0.70a_o, (b) $d_{12} \cdot \hat{r}$ for R(H-H_2) = 0.70a_o, (c) E_1 and E_2 for R(H-H_2) = 1.90a_o, (d) $d_{12} \cdot \hat{r}$ for R(H-H_2) = 1.90a_o.

Figure 4. Potential surface cuts and components of nonadiabatic coupling elements d_{12}^{χ} as a function of χ (a) E_1 and E_2 for R(H-H_2) = 0.7a_o and r(H_2) = 2.00a_o, (b) d_{12}^{χ} for R(H-H_2) = 0.7a_o and r(H_2) = 2.00a_o, (c) E_1 and E_2 for R(H-H_2) = 1.9a_o andr(H_2) = 1.4a_o, (d) d_{12}^{χ} for R(H-H_2) = 1.9a_o and r(H_2) = 1.4a_o.

Figure 5. Energy level diagram for H_3. The ground and excited states of H_3 are scaled with respect to their dissociation products as determined by Ref. 110. The scaling of the ground state of H_3^+ with respect to

H_2 (X $^1\Sigma_g^+$) + H^+ is taken from Ref 167. On this energy level diagram H_2 (X $^1\Sigma_g^+$) + H(n = 1) is taken as the zero of energy.

Figure 6. Representation of H_3 molecules in the $2p^2A_2''$ electronic state. The bond distance for the nuclei were taken from Ref. 111. The Rydberg orbital perperdicular to the plane of the nuclei is represented by a 90 % boundary surface of a hydrogenic $2p_z$ orbital.[74]

Figure 7. Summary of Helm's results: a) Table 1; the observed Rydberg series of the H_3 molecule. The state designation is (ν_1, ν_2, N, K) for the lower state and (ν_1, ν_2, N^+, G) for the H_3^+ core. b) Excitation spectrum of n=7 states of H_3. c) Excitation spectrum of hign-n Rydberg states of H_3. Five series are marked at the top of the figure. The series B′ is indicated by small tick marks along with series B.

Figure 1.

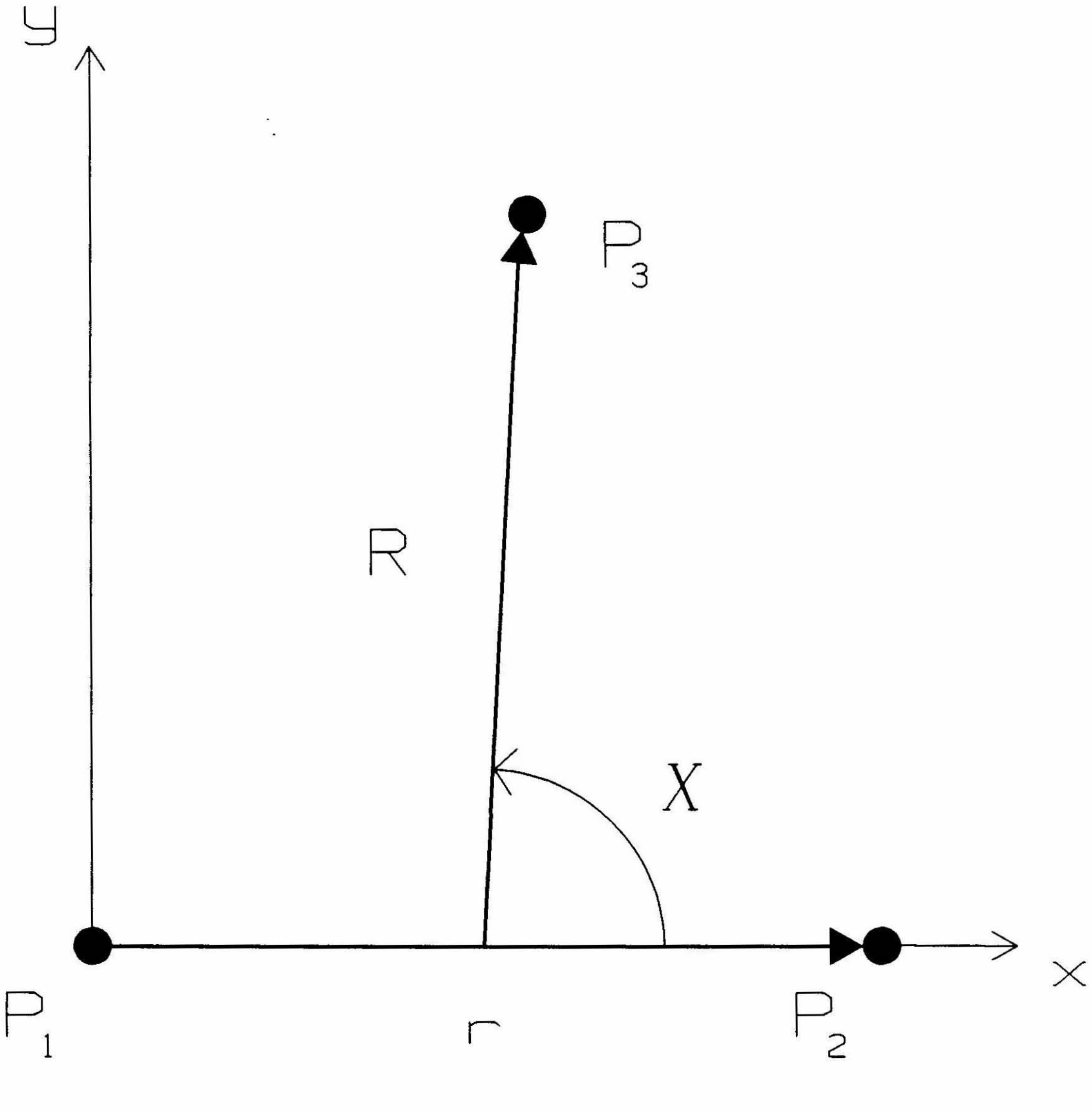

Figure 2.

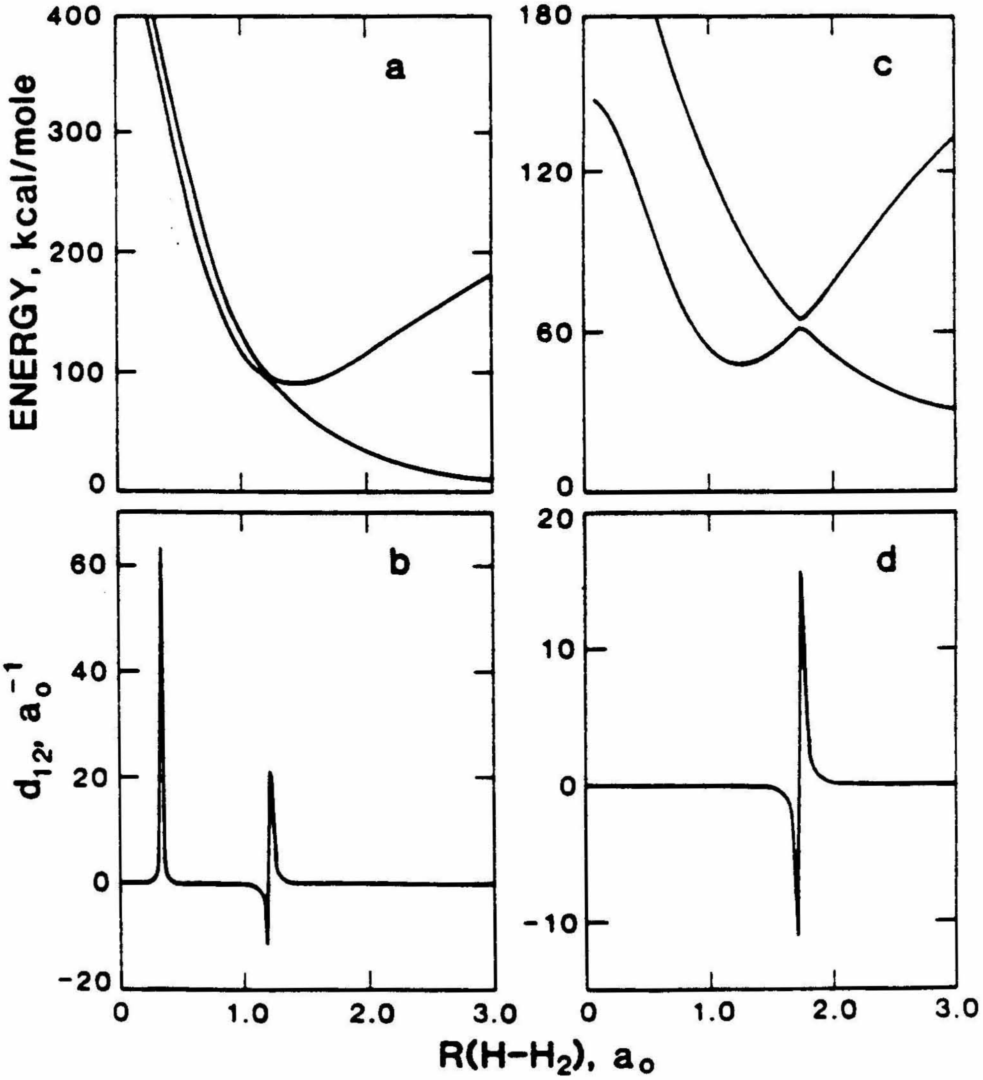
ENERGY, kcal/mole
400
300
200
100
0
a
180
120
60
0
c
d_{12}, a_o^{-1}
60
40
20
0
-20
b
20
10
0
-10
d
0
1.0
2.0
3.0
0
1.0
2.0
3.0
R(H-H_2), a_o

Figure 3.

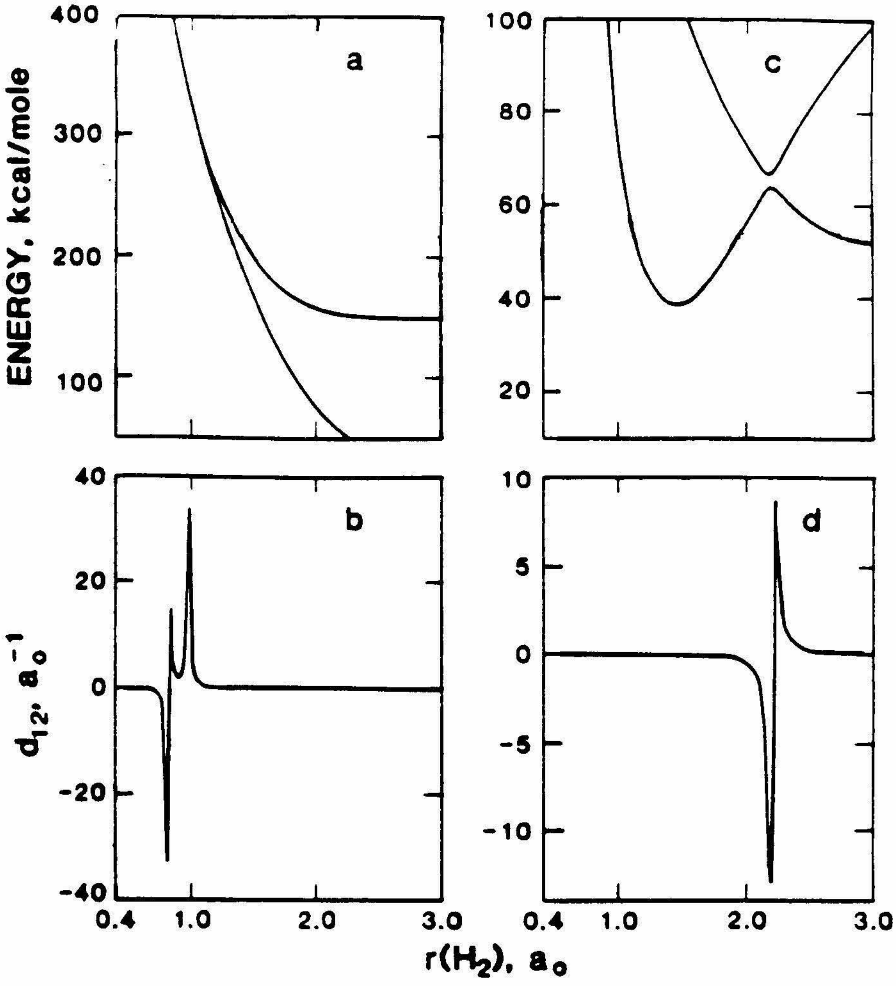
ENERGY, kcal/mole
400
300
200
100
a
100
80
60
40
20
c
d_{12}, a_o^{-1}
40
20
0
-20
-40
b
10
5
0
-5
-10
d
0.4
1.0
2.0
3.0
0.4
1.0
2.0
3.0
r(H$_2$), a_o

Figure 4.

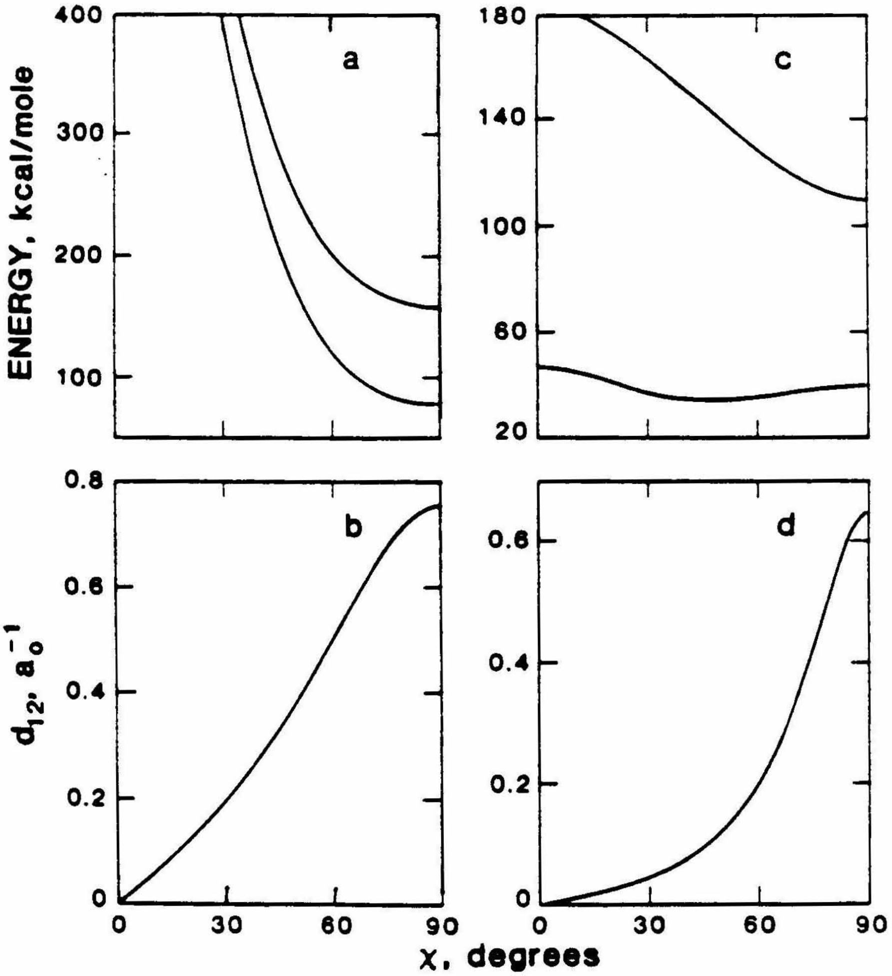
ENERGY, kcal/mole
400
300
200
100
a
180
140
100
60
20
c
d_{12}, a_o^{-1}
0.8
0.6
0.4
0.2
0
b
0.6
0.4
0.2
0
d
0
30
60
90
0
30
60
90
χ, degrees

Figure 5.

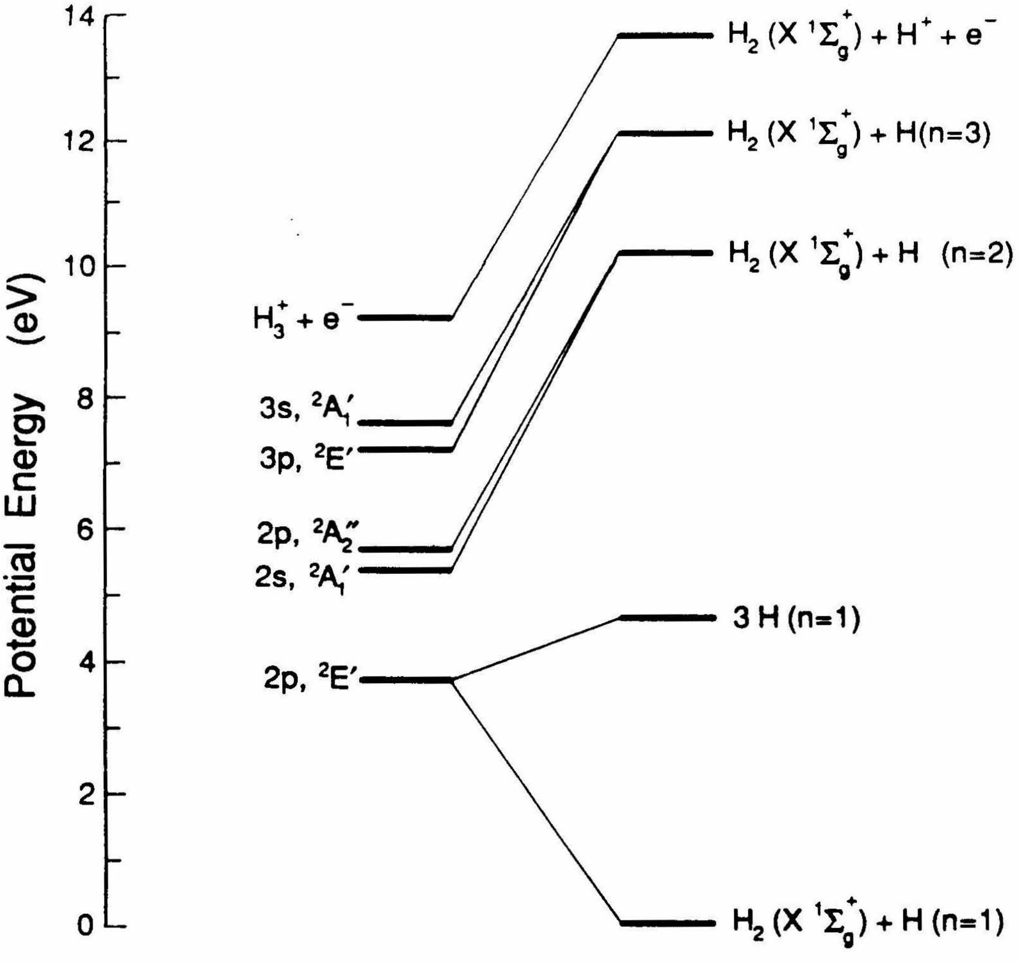
Potential Energy (eV)
14
12
10
8
6
4
2
0
$H_3^+ + e^-$
3s, $^2A_1'$
3p, $^2E'$
2p, $^2A_2''$
2s, $^2A_1'$
2p, $^2E'$
$H_2(X\,^1\Sigma_g^+) + H^+ + e^-$
$H_2(X\,^1\Sigma_g^+) + H(n=3)$
$H_2(X\,^1\Sigma_g^+) + H\ (n=2)$
3 H (n=1)
$H_2(X\,^1\Sigma_g^+) + H\ (n=1)$

Figure 6.

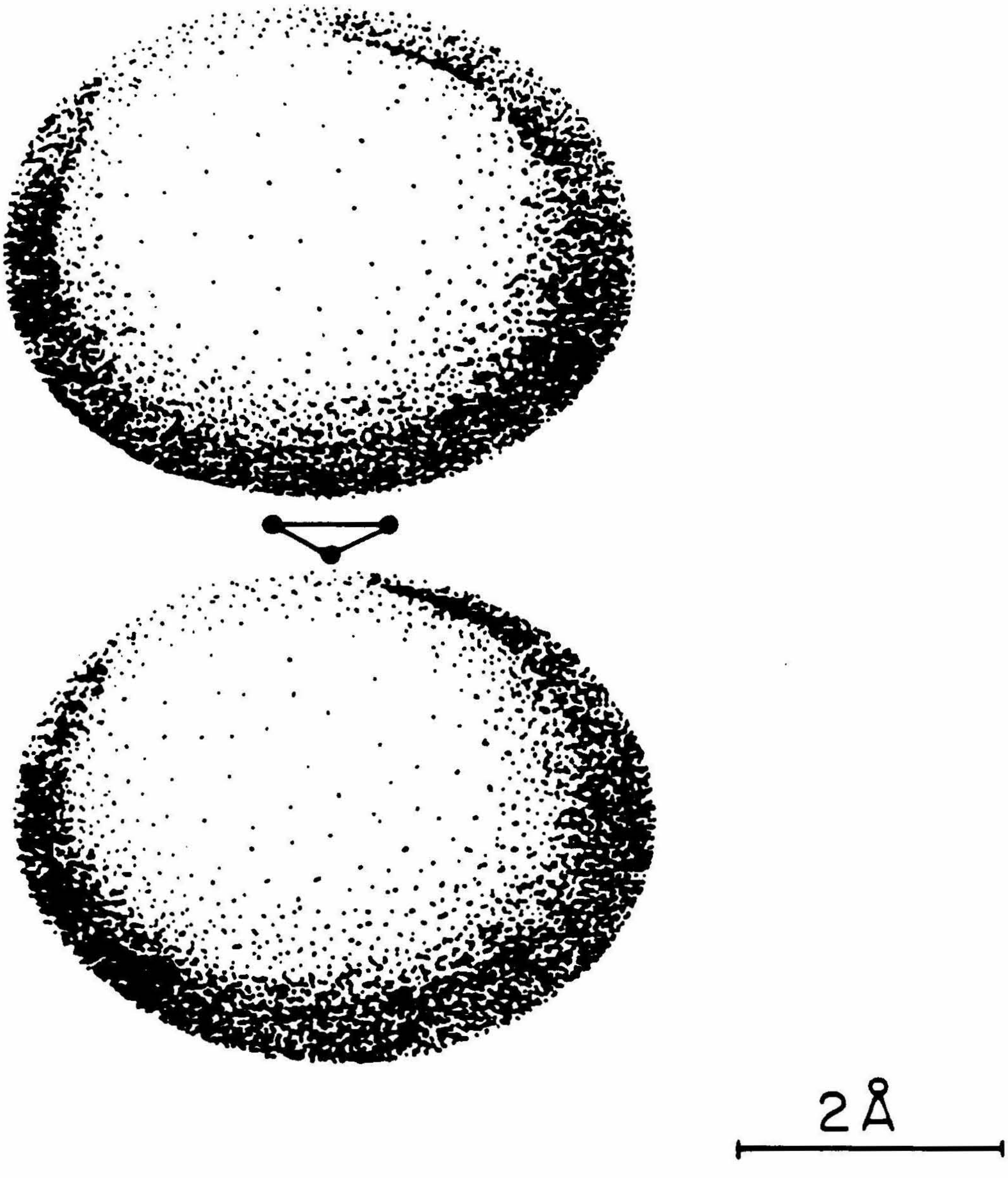

Figure 7.

TABLE I. Observed Rydberg series of H_3 molecule. The state designation is (ν_1, ν_2, N, K) for the lower state and (ν_1, ν_2, N^+, G) for the H_3^+ core.

Series	$\tilde{B}\,2p\,^2A_2''$	Upper state H_3^+ core		T_∞ (cm^{-1})	δ_{eff}	Observed n range
A	(0,0,0,0)	(0,0,1,0)	· · ·	29 566.0	[a]	33–40
B	(0,1,0,0)	(0,1,1,1)	*nd*	29 485.5	0.022	7,8,12–40
B'	(0,1,0,0)	(0,1,1,1)	*ns*	29 485.5	0.073	7,12–32
C	(· · ·)	(· · ·)	*nd*	29 402.0	0.02	13–36
D	(1,0,0,0)	(1,0,1,0)	*nd*	29 469.5	0.02	7,12–32

[a] When series *A* is fitted together with the *R*0 ($3s \leftarrow 2p$) transition (Ref. 2) a value $\delta_{eff} = 0.0803$ is obtained. When fitted together with the *R*0 ($3d \leftarrow 2p$) transition (Ref. 5) $\delta_{eff} = 0.0095$ is obtained.

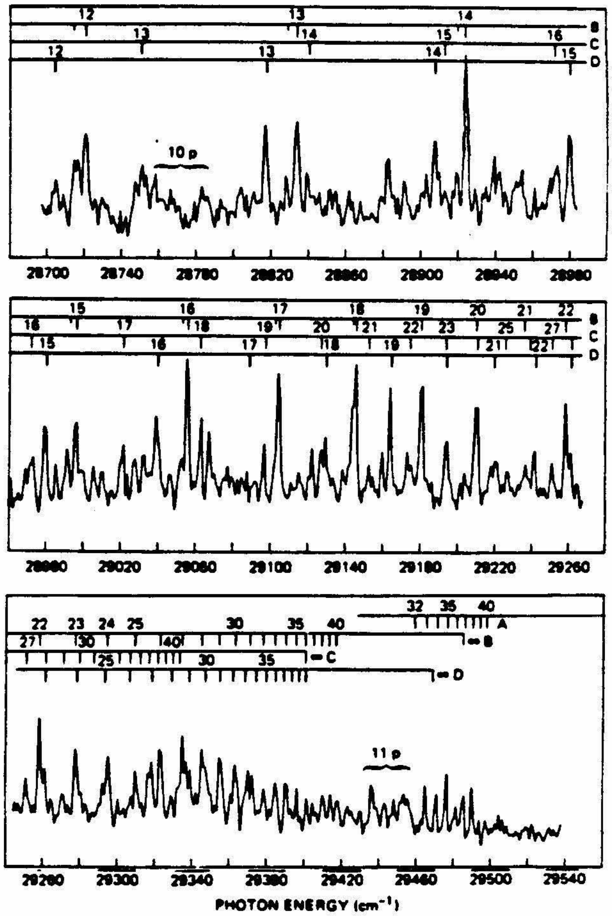

FIG. 3. Excitation spectrum of high-n states of H_3. Four series are marked in the top of the figure. The series *B'* is indicated by the small tick marks along with series *B*.

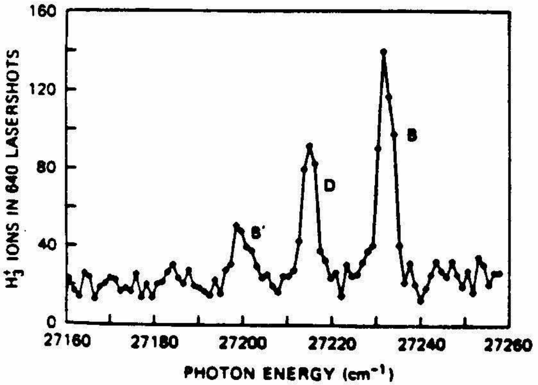

FIG. 2. Excitation spectrum of $n = 7$ states of H_3.

Chapter 3.

Formulation of the Quantum Mechanical Study of the Electronically NonAdiabatic Chemical Reaction Dynamics of the H_3 System

I. Introduction

An overview of the quantum mechanics of polyatomic molecules is presented in this chapter. Several important concepts including the form of the Hamiltonian operator, the Born-Oppenheimer (or adiabatic) approximation, potential energy surfaces, electronically nonadiabatic coupling elements, and the construction of diabatic states are discussed. Dynamical processes of molecular systems are also discussed. This discussion serves as a starting point for the *ab initio* calculations to be presented in this thesis.

Most chemical processes can be understood by considering the dynamics on a single potential energy surface. The equilibrium structure of a molecule in a given electronic state can be obtained by locating local and global minima on the potential energy surface. Given a deep enough potential well, the surface may support bound nuclear ro-vibrational states having discrete energy levels, and transitions between these levels may be observed. Scattering processes can be studied if the surface is repulsive or if the total energy of the system is large enough, to gain information about the dynamics of molecular collisions and the breaking and formation of chemical bonds.[1–20]

Two molecular states on two distinct non-interacting potential energy surfaces may be coupled by a radiation field. If the radiation field is very weak, the perturbation coupling strength can be obtained using Fermi's Golden Rule[21]

$$\langle \chi_{k\nu}\phi_k|\hat{\mathrm{O}}_{\mathrm{r}}|\phi_{k'}\chi_{k',\nu'}\rangle \ ,$$

where $|\chi_{k\nu}\phi_k\rangle$ and $|\phi_{k'}\chi_{k'\nu'}\rangle$ are the total initial and final wave functions and $\hat{\mathrm{O}}_{\mathrm{r}}$ is the coupling operator between the molecule and the field. The electric dipole interaction is usually the dominant term in $\hat{\mathrm{O}}_{\mathrm{r}}$. Once again, the nuclear wave functions may be discrete or continuous. Ordinary spectroscopic experiments generally examine bound-to-bound transitions which produce discrete lines in the spectrum. Transitions from bound-to-continuous states produce continuous spectra with the possibility of fine structure embedded in the continuous background, as is observed in Transition State Spectroscopy experiments.[22−30] To date, continuum-to-continuum transitions have not received much attention due mainly to the lack of discrete features in the spectra and the difficulty of the experimental procedures.[31−35]

However, there are many dynamical processes which are not confined to a single potential energy surface and do not require an external field to take place. These processes occur as a result of nonadiabatic coupling between the states involved. When the two interacting electronic states are discrete, the electronically nonadiabatic coupling elements produce a shift in the positions of the eigen-energies of the discrete states. These shifts caused by the electronically nonadiabatic couplings have been observed in spectroscopic experiments as irregularities in the spectral line positions.[36−38] One of the many interesting aspects of quantum scattering studies occurs when two interacting electronic states are continuous. New chemical reaction channels may be introduced through the electronically nonadiabatic coupling.[39−44]

For the case of a discrete bound state interacting with a continuous state, the nonadiabatic coupling results in a finite probability that the bound state will decay into the continuous state and become a quasi-bound metastable state. Such a process is known as predissociation.

The Born-Oppenheimer adiabatic approximation[45−47] provides a means by which the calculation of dynamical processes in molecules can be greatly simplified. This approximation is based upon the large difference in mass of electrons and nuclei, while in general the forces they are subject to are of the same order of magnitude. As a consequence, the nuclei move much more slowly than the electrons, and to a good approximation the electronic and nuclear motions can be treated separately. The validity of Born-Oppenheimer approximation relies upon the fact that the spacing of electronic eigenvalues is generally large compared to typical spacings associated with nuclear motion. When this condition is violated, the residual coupling via the kinetic energy operator induces transitions between the adiabatic electronic states. Ordinarily only two electronic states lie close in energy, and only over a limited range of nuclear coordinate space. It is not necessary to abandon the Born-Oppenheimer approximation, however, one must cope with the near-degeneracy of electronic states in these localized regions. The most successful means of dealing with nonadiabatic phenomena has been through the use of appropriate "diabatic" electronic states which may cross as a function of the internuclear distances, whereas the adiabatic electronic states are subject to the noncrossing rule.[48-52]

II. The Hamiltonian

The Hamiltonian of an isolated molecular system containing N_e electrons and N_n nuclei can be expressed as[53-54]

$$\hat{H}_t = \hat{T}_N + \hat{T}_e + V_{Ne} \ , \tag{3.1}$$

where $\hat{T}_N$ and $\hat{T}_e$ are the kinetic energy operators of the nuclei and the electrons respectively. V_{Ne} is the Coulomb interaction potential between all charged particles in the system. These operators can be expressed as

$$\hat{T}_N = \sum_{\alpha=1}^{N_n} -\frac{\hbar^2}{2M_\alpha}\nabla_\alpha^2 \tag{3.2}$$

$$\hat{T}_e = \sum_{i=1}^{N_e} -\frac{\hbar^2}{2m_e}\nabla_i^2 \tag{3.3}$$

$$V_{N_e} = \sum_{\alpha>\beta=1}^{N_n} \frac{Z_\alpha Z_\beta e^2}{|\mathbf{R}_\alpha - \mathbf{R}_\beta|} - \sum_{\alpha=1,i=1}^{N_n,N_e} \frac{Z_\alpha e^2}{|\mathbf{R}_\alpha - \mathbf{r}_i|} + \sum_{i>j=1}^{N_e} \frac{e^2}{|\mathbf{r}_i - \mathbf{r}_j|} \ , \tag{3.4}$$

where i, j and α, β are indexes for the electrons and nuclei respectively. The Q_α and M_α are the charge and mass of the α^{th} nucleus. $\mathbf{R}_\alpha$ and $\mathbf{r}_i$ are the coordinate vectors of the α^{th} nucleus and the i^{th} electron with respect to a laboratory reference frame. The Coulombic interaction depends solely upon the relative positions of all charged particles, hence it is invariant to rigid translation or rotation of the molecule. All spin containing and relativistic terms have been neglected in Equation 3.1. For light molecules, these terms are small, and their effects can be accurately included *a posteriori* by low order perturbation methods.

The Schrödinger equation for the molecular system is given by

$$\hat{\mathrm{H}}_t\Psi(\mathbf{r},\mathbf{R}) \;=\; \mathrm{E}\Psi(\mathbf{r},\mathbf{R}) \; . \tag{3.5}$$

This eigenvalue problem is a second order partial differential equation in a $3(\mathrm{N}_n + \mathrm{N}_e)$-dimensional space. For H_3, $\mathrm{N}_n = 3$, $\mathrm{N}_e = 3$, $3(\mathrm{N}_n + \mathrm{N}_e) = 18$. The dimensionality of the problem is reduced to $3(\mathrm{N}_n + \mathrm{N}_e - 1)$ in the center of mass reference frame. Therefore even for very simple systems such as H_3, obtaining solutions of the Schrödinger is difficult.

III. The Adiabatic Representation

Finding solutions to the Schrödinger equation (Equation 3.5) can be greatly simplified by making use of the large difference in the mass of the electrons and the nuclei. The electronic Hamiltonial $\hat{\mathrm{H}}_e$ is defined as

$$\hat{\mathrm{H}}_e \;=\; \hat{\mathrm{T}}_e + \mathrm{V}_{\mathrm{N}e} \;. \tag{3.6}$$

For each set of fixed nuclear coordinate variables $\{\mathbf{R}\}$, there exists a set of adiabatic solutions $\left[|\phi_k(\mathbf{r};\mathbf{R}\rangle\right]$ that satisfy

$$\hat{\mathrm{H}}_e|\phi_k(\mathbf{r};\mathbf{R})\rangle = \mathrm{E}_k(\mathbf{R})|\phi_k(\mathbf{r};\mathbf{R})\rangle \;, \tag{3.7}$$

where $\mathbf{r}$ and $\mathbf{R}$ represent all electronic and nuclear coordinate variables respectively. The ; in the above equation is used to denote the parametric dependence of ϕ_k and E_k on $\mathbf{R}$, the nuclear coordinates. The index k represents the set of all quantum numbers needed to specify the eigenfunctions $|\phi_k(\mathbf{r};\mathbf{R})\rangle$. In general the electronic spectra E_k may include a discrete and a continuous part as occurs in ionization processes. Typically only the discrete electronic spectrum is considered, and used to form a discrete orthonormal electronic basis set which satisfies

$$\langle\phi_k(\mathbf{r};\mathbf{R})|\phi_{k'}(\mathbf{r};\mathbf{R})\rangle = \delta_{kk'}. \tag{3.8}$$

In Equation 3.8, the integration is performed over all electronic coordinate variables, and this expression is valid for all nuclear configurations $\{\mathbf{R}\}$.

Using this electronic basis set, the total wavefunction can be written as

$$\Psi(\mathbf{r},\mathbf{R}) = \sum_k \chi_k(\mathbf{R})|\phi_k(\mathbf{r};\mathbf{R})\rangle. \tag{3.9}$$

The coefficients $\chi_k(\mathbf{R})$ are the nuclear wave functions and depend only upon the nuclear coordinate variables. Using Equations 3.5 through 3.9, the set of coupled differential equations that $\chi_k(\mathbf{R})$ must satisfy is given by

$$\begin{aligned}\{\hat{\mathrm{T}}_{\mathrm{N}} + \mathrm{E}_k(\mathbf{R})\}\chi_k(\mathbf{R}) + \sum_{k'}\{F_{kk'}(\mathbf{R})\chi_{k'}(\mathbf{R}) + G_{kk'}(\mathbf{R})\chi_{k'}(\mathbf{R})\}& \\ = E\chi_k(\mathbf{R})\ ,& \qquad (3.10)\end{aligned}$$

where

$$F_{kk'}(\mathbf{R}) = \sum_{\alpha=1}^{\mathrm{N}_n}\langle\phi_k| - \frac{\hbar^2}{\mathrm{M}_\alpha}\nabla_\alpha|\phi_{k'}\rangle\cdot\nabla_\alpha \qquad (3.11)$$

$$G_{kk'}(\mathbf{R}) = \sum_{\alpha=1}^{\mathrm{N}_n}\langle\phi_k| - \frac{\hbar^2}{2\mathrm{M}_\alpha}\nabla_\alpha^2|\phi_{k'}\rangle\ , \qquad (3.12)$$

where integration is over all electronic coordinates. The coupling terms $\mathrm{F}_{kk'}(\mathbf{R})$ and $\mathrm{G}_{kk'}(\mathbf{R})$ are the electronically nonadiabatic coupling terms.

If these electronically nonadiabatic coupling terms are neglected, Equation 3.10 reduces to the well known Born-Oppenheimer approximation[45]

$$\{\hat{\mathrm{T}}_{\mathrm{N}} + \mathrm{E}_k(\mathbf{R})\}\chi_{k\nu}(\mathbf{R}) = \mathrm{E}\chi_{k\nu}(\mathbf{R}) \qquad (3.13)$$

and the total wave function expansion in Equation 3.9 reduces to a single term which is the product of the electronic wave function and the nuclear wave function

$$\Psi_{k\nu}(\mathbf{r},\mathbf{R}) = \chi_{k\nu}(\mathbf{R})|\phi_k(\mathbf{r},\mathbf{R})\rangle. \qquad (3.14)$$

In Equation 3.14, ν is the set of quantum numbers which describe the nuclear wave function. The wave function can be discrete for bound rotational and vibrational molecular motions, or continuous for scattering processes and chemical reactions.

$E_k(\mathbf{R})$ is the potential energy surface of the $|\phi_k(\mathbf{r};\mathbf{R})\rangle$ electronic state. It can be thought of as the effective interaction potential between the nuclei.

Use of the Born-Oppenheimer approximation results in the decomposition of the total wave function into an electronic and nuclear wave function, each of which can be obtained by solving the corresponding simpler Schrödinger equation (Equations 3.7 and 3.13). This separation of electronic and nuclear motions simplifies solution of the full Schrödinger equation (Equation 3.5) and is a fundamental building block of molecular physics. Although the adiabatic approximation is a very attractive and often useful technique, it may fail when the potential energy surfaces of different electronic states approach one another. In general only two (at most a few) electronic states lie close in energy, but for these states the nonadiabatic coupling cannot be neglected in the Hamiltonian.

A. The Two-State Approximation

Consider now the two-state approximation to Equation 3.10. Within this approximation, the summation over k is restricted to two terms and Equation 3.10 can be written explicitly as

$$\begin{aligned}\{\hat{T}_N + E_1(\mathbf{R})\}\chi_1(\mathbf{R}) + G_{11}(\mathbf{R})\chi_1(\mathbf{R}) + F_{12}(\mathbf{R})\chi_2(\mathbf{R}) + G_{12}(\mathbf{R})\chi_2(\mathbf{R}) \\ = E\chi_1(\mathbf{R}) \qquad (3.15)\end{aligned}$$

$$\begin{aligned}\{\hat{T}_N + E_2(\mathbf{R})\}\chi_2(\mathbf{R}) + F_{21}(\mathbf{R})\chi_1(\mathbf{R}) + G_{21}(\mathbf{R})\chi_1(\mathbf{R}) + G_{22}(\mathbf{R})\chi_2(\mathbf{R}) \\ = E\chi_2(\mathbf{R}). \qquad (3.16)\end{aligned}$$

The diagonal terms F_{11} and F_{22} are absent from Equations 3.15 and 3.16 since they are identically zero. To see this, consider the identity

$$\nabla_\alpha \langle \phi_k | \phi_k \rangle = 0 \ , \tag{3.17}$$

where α corresponds to any nuclear particle, derivatives are taken with respect to all components of $\mathbf{R}_\alpha$ and the integration is performed over all electronic variables. Differentiation may be passed inside the integration which leads to

$$\langle \phi_k | \nabla_\alpha | \phi_k \rangle = 0 \ . \tag{3.18}$$

It is important to note that the nonadiabatic coupling terms in the adiabatic representation are Hermitian with respect to their operation on the nuclear coordinates. Considering first the identity

$$\nabla_\alpha \langle \phi_1 | \phi_2 \rangle = 0, \tag{3.19}$$

Equation 3.19 implies that

$$\langle \phi_2 | \nabla_\alpha | \phi_1 \rangle^* = -\langle \phi_1 | \nabla_\alpha | \phi_2 \rangle. \tag{3.20}$$

For future use, it is convenient to define the quantity

$$\mathbf{g}_{kk'\alpha} \equiv \langle \phi_k | \nabla_\alpha | \phi_{k'} \rangle. \tag{3.21}$$

The quantity $\mathbf{g}_{kk'\alpha}$ is the vector whose components are given by Equation 3.21. The assertion that the nonadiabatic coupling terms are Hermitian is given by the equality

$$\langle \chi_1 | \mathrm{F}_{12} + \mathrm{G}_{12} | \chi_2 \rangle = \langle \chi_2 | \mathrm{F}_{21} + \mathrm{G}_{21} | \chi_1 \rangle^* \ , \tag{3.22}$$

where the integration is with respect to the nuclear coordinates $\{\mathbf{R}\}$. Consider the first integral involving the operator F_{12}; $\langle \chi_1 | \mathrm{F}_{12} | \chi_2 \rangle$. By definition

$$\langle \chi_1 | \mathrm{F}_{12} | \chi_2 \rangle = \langle \chi_1 \mid \sum_{\alpha=1}^{\mathrm{N}_n} -\frac{\hbar^2}{\mathrm{M}_\alpha} \mathbf{g}_{12\alpha} \cdot \nabla_\alpha \mid \chi_2 \rangle. \tag{3.23}$$

Examining an individual term of the right hand side of Equation 3.23, we have that

$$\langle \chi_1 | \mathbf{g}_{12\alpha} \cdot \nabla_\alpha | \chi_2 \rangle = \int \mathrm{d}\beta ... \int \mathrm{d}\alpha \; \chi_1^* \; \mathbf{g}_{12\alpha} \cdot \nabla_\alpha \; \chi_2 . \tag{3.24}$$

Since the integrations over each component of **R** are independent, we can perform the α integration by parts to obtain,

$$\int \mathrm{d}\alpha \; \chi_1^* \; \mathbf{g}_{12\alpha} \cdot \nabla_\alpha \; \chi_2 = \chi_1^* \; \mathbf{g}_{12\alpha} \; \chi_2 \; |_{\alpha^{\mathrm{min}}}^{\alpha^{\mathrm{max}}} - \int \mathrm{d}\alpha \; \chi_2 \big[\mathbf{g}_{12\alpha} \cdot \nabla_\alpha \chi_1^* + \chi_1^* \nabla_\alpha \cdot \mathbf{g}_{12\alpha} \big] . \tag{3.25}$$

The first term on the right hand side of Equation 3.25 vanishes since the nonadiabatic coupling term $\mathbf{g}_{12\alpha}$ vanishes for large values of the nuclear coordinate α^{max}. At small values of the coordinate α^{min} either $\mathbf{g}_{12\alpha}$, χ_1, χ_2 or both χ_1 and χ_2 vanish due to the repulsive nature of the potentials E_1 and E_2. Thus

$$\langle \chi_1 | \mathbf{g}_{12\alpha} \cdot \nabla_\alpha | \chi_2 \rangle = - \langle \chi_2 | \mathbf{g}_{12\alpha}^* \cdot \nabla_\alpha | \chi_1 \rangle^* - \langle \chi_2 | \nabla_\alpha \cdot \mathbf{g}_{12\alpha}^* | \chi_1 \rangle^* . \tag{3.26}$$

Equation 3.26 is true for all components of **R** by similar reasoning. Making use of Equation 3.20, Equation 3.26 can be written as

$$\langle \chi_1 | \mathbf{g}_{12\alpha} \cdot \nabla_\alpha | \chi_2 \rangle = \langle \chi_2 | \mathbf{g}_{21\alpha} \cdot \nabla_\alpha | \chi_1 \rangle^* + \langle \chi_2 | \nabla_\alpha \cdot \mathbf{g}_{21\alpha} | \chi_1 \rangle^* . \tag{3.27}$$

Therefore, we have the important result that

$$\langle \chi_1 | \mathrm{F}_{12} | \chi_2 \rangle = \langle \chi_2 | \mathrm{F}_{21} | \chi_1 \rangle^* + \left\langle \chi_2 \left| \sum_{\alpha=1}^{\mathrm{N}_n} -\frac{\hbar^2}{\mathrm{M}_\alpha} \mathbf{g}_{21\alpha} \cdot \nabla_\alpha \right| \chi_1 \right\rangle^* , \tag{3.28}$$

and hence the operator F_{12} is not Hermitian except in cases where $\nabla_\alpha \cdot \mathbf{g}_{12\alpha}$ vanishes for all components of **R**.

From the definition of $\mathbf{g}_{12\alpha}$,

$$\nabla_\alpha \cdot \mathbf{g}_{12\alpha} = \nabla_\alpha \cdot \langle \phi_2 | \nabla_\alpha | \phi_1 \rangle = \langle \nabla_\alpha \phi_2 | \nabla_\alpha \phi_1 \rangle + \langle \phi_2 | \nabla_\alpha^2 | \phi_1 \rangle \; . \tag{3.29}$$

Therefore, Equation 3.28 can be written as

$$\begin{aligned} \langle \chi_1 | \mathrm{F}_{12} | \chi_2 \rangle = & \left\langle \chi_2 \left| \sum_{\alpha=1}^{\mathrm{N}_n} -\frac{\hbar^2}{\mathrm{M}_\alpha} \{ \langle \nabla_\alpha \phi_2 | \nabla_\alpha \phi_1 \rangle + \langle \phi_2 | \mathbf{g}_{12\alpha} \cdot \nabla_\alpha | \phi_1 \rangle \} \right| \chi_1 \right\rangle^* \\ & + \langle \chi_2 | \mathrm{F}_{21} | \chi_1 \rangle^* . \end{aligned} \tag{3.30}$$

To complete the proof of the Hermicity of the nonadiabatic coupling terms, we make use of the following identity

$$\nabla_\alpha^2 \langle \phi_1 | \phi_2 \rangle = 0 \tag{3.31}$$

to establish that

$$-\frac{\hbar^2}{2\mathrm{M}_\alpha} \langle \phi_1 | \nabla_\alpha^2 | \phi_2 \rangle = \frac{\hbar^2}{\mathrm{M}_\alpha} \langle \nabla_\alpha \phi_2 | \nabla_\alpha \phi_1 \rangle^* + \frac{\hbar^2}{2\mathrm{M}_\alpha} \langle \phi_2 | \nabla_\alpha^2 | \phi_1 \rangle^* . \tag{3.32}$$

Thus,

$$\begin{aligned} -\frac{\hbar^2}{2\mathrm{M}_\alpha} \left\langle \chi_1 \left| \langle \phi_1 | \nabla_\alpha^2 | \phi_2 \rangle \right| \chi_2 \right\rangle = & \frac{\hbar^2}{\mathrm{M}_\alpha} \left\langle \chi_2 \left| \langle \nabla_\alpha \phi_2 | \nabla_\alpha \phi_1 \rangle \right| \chi_1 \right\rangle^* \\ & + \frac{\hbar^2}{2\mathrm{M}_\alpha} \left\langle \chi_2 \left| \langle \phi_2 | \nabla_\alpha^2 | \phi_1 \rangle \right| \chi_1 \right\rangle^* . \end{aligned} \tag{3.33}$$

Summing Equation 3.33 over all α and adding this to Equation 3.30 leads to

$$\left\langle \chi_1 \left| \sum_{\alpha=1}^{N_n} -\frac{\hbar^2}{2M_\alpha} \langle \phi_1 | \nabla_\alpha^2 | \phi_2 \rangle \right| \chi_2 \right\rangle + \langle \chi_1 | F_{12} | \chi_2 \rangle$$

$$= \left\langle \chi_2 \left| \sum_{\alpha=1}^{N_n} -\frac{\hbar^2}{2M_\alpha} \langle \phi_2 | \nabla_\alpha^2 | \phi_1 \rangle \right| \chi_1 \right\rangle + \langle \chi_2 | F_{21} | \chi_1 \rangle^*. \quad (3.34)$$

This can be rewritten in terms of $G_{kk'}$ as

$$\langle \chi_1 | F_{12} + G_{12} | \chi_2 \rangle = \langle \chi_2 | F_{21} + G_{21} | \chi_1 \rangle^*. \quad (3.35)$$

This derivation shows that the sum of the nonadiabatic coupling terms $F_{12} + G_{12}$ is Hermitian, however, in general the quantities F_{12} and G_{12} are not individually Hermitian. This point is important for rigorous quantum mechanical calculations. In semi-classical descriptions of the two-state problem the G_{12} term is absent in the formalism,[55−56] hence there may be a temptation to omit this term in the rigorous quantum mechanical description.[57] This omission must be carefully justified or non-Hermitian coupling may result, which will lead to a nonunitary scattering matrix.[58]

IV. The Diabatic Representation

In the previous section the adiabatic representation of electronically nonadiabatic chemical reactions was discussed. The critical point which led to this representation is expressed in Equation 3.7. That is, the electronic wavefunctions ϕ_k were required to be eigenfunctions of the full and complete electronic Hamiltonian $\hat{\mathrm{H}}_e$ at all nuclear configurations. Eigenfunctions which satisfy this condition are termed molecular wavefunctions.

If instead of using the exact solutions to Equation 3.7 a different set of electronic wavefunctions is employed in the expansion of $\Psi(\mathbf{r},\mathbf{R})$ then the representation is termed diabatic.[49] The choice of diabatic wavefunctions (denoted ϕ_k^{d}) is not specified, therefore the diabatic representation is not unique. Two examples of how ϕ_k^{d} might be chosen are:

(i) eigenfunctions of $\hat{\mathrm{H}}_e$ for isolated atoms (and/or molecules) "frozen" at all other atomic (and/or molecular) geometries.

(ii) a second more realistic possibility would be if the ϕ_k^{d} were allowed to slowly change as the nuclei are moved without being exact eigenfunctions of $\hat{\mathrm{H}}_e$.[49]

Frozen orbitals, as in the first case would not in general satisfy Equation 3.7. The second diabatic picture, although it is not unique, is more realistic since it produces a set of coupled equations for the diabatic nuclear wavefunctions χ_k^{d}. The procedure for developing these equations is analogous to that used in the adiabatic representation, however, Equation 3.7 can no longer be used. In place of Equations 3.10 through 3.12, we have the following set of coupled equations

$$\sum_k \left[\langle \phi_{k'}^{\mathrm{d}} | \hat{\mathrm{T}}_{\mathrm{N}} | \phi_k^{\mathrm{d}} \rangle + \hat{\mathrm{H}}_e^{kk'} - \mathrm{E} \right] \chi_k^{\mathrm{d}} = 0 \ , \tag{3.36}$$

where $\hat{\mathrm{H}}_e^{kk'}$ is given by

$$\hat{\mathrm{H}}_e^{kk'} = \langle \phi_{k'}^{\mathrm{d}} | \hat{\mathrm{H}}_e | \phi_k^{\mathrm{d}} \rangle . \tag{3.37}$$

When compared to the adiabatic representation, this use of approximate electronic wavefunctions has introduced new coupling (through the off diagonal matrix elements $\hat{\mathrm{H}}_e^{kk'}$) in the coupled equations for χ_k^{d} Next, we assume that

$$\langle \phi_{k'}^{\mathrm{d}} | \hat{\mathrm{T}}_{\mathrm{N}} | \phi_k^{\mathrm{d}} \rangle = \delta_{kk'} \hat{\mathrm{T}}_{\mathrm{N}} \ . \tag{3.38}$$

This simplifies Equation 3.36 to

$$\sum_k [(\hat{\mathrm{T}}_{\mathrm{N}} - \mathrm{E})\delta_{kk'} + \hat{\mathrm{H}}_e^{kk'}] \chi_k^{\mathrm{d}} = 0 \ . \tag{3.39}$$

Validation of Equation 3.38 has not appeared in the literature and this assumption is given only cursory mention.[55–56] This approximation could be justified if the ϕ_k^{d} are frozen orbitals, which by definition change very little with $\mathbf{R}$ and therefore have derivatives with respect to $\mathbf{R}$ which are small. These equations are simpler in nature than Equations 3.10 through 3.12, since the coupling has a tidier form than that in the adiabatic representation which involves nuclear kinetic energy and velocity operators. However, the simplicity of Equation 3.39 relies on the validity of Equation 3.38. In the time-dependent impact parameter approximation to Equation 3.36, it is argued that the nuclear velocity coupling is negligible for high energy collisions.[59] To validate Equation 3.39 in choosing a good diabatic representation, one should seek the ϕ_k^{d} for which Equation 3.38 is best satisfied. Smith[52] has shown that a diabatic representation can be found such that Equation 3.38 can be satisfied exactly. This procedure will be discussed in the following section.

A. The Two-State Approximation

In the two-state approximation Equation 3.39 becomes

$$\left[\hat{\mathrm{T}}_{\mathrm{N}} + \hat{\mathrm{H}}_e^{11} - \mathrm{E}\right]\chi_1^{\mathrm{d}} = \hat{\mathrm{H}}_e^{12}\chi_2^{\mathrm{d}} \tag{3.40}$$

$$\left[\hat{\mathrm{T}}_{\mathrm{N}} + \hat{\mathrm{H}}_e^{22} - \mathrm{E}\right]\chi_2^{\mathrm{d}} = \hat{\mathrm{H}}_e^{21}\chi_1^{\mathrm{d}} \ . \tag{3.41}$$

The functions $\hat{\mathrm{H}}_e^{11}$ and $\hat{\mathrm{H}}_e^{22}$ are the diabatic potential curves and in many cases these curves cross. Since the diabatic wavefunctions ϕ_k^{d} are not exact eigenfunctions of $\hat{\mathrm{H}}_e$, the non-crossing rule does not apply.

It is straightforward to show that the coupling terms in Equations 3.40 and 3.41 are Hermitian. By definition

$$\hat{\mathrm{H}}_e^{12} = \langle \phi_1^{\mathrm{d}} | \hat{\mathrm{H}}_e | \phi_2^{\mathrm{d}} \rangle$$

and

$$\hat{\mathrm{H}}_e^{21} = \langle \phi_2^{\mathrm{d}} | \hat{\mathrm{H}}_e | \phi_1^{\mathrm{d}} \rangle. \tag{3.42}$$

Since $\hat{\mathrm{H}}_e$ is Hermitian , we have that

$$\hat{\mathrm{H}}_e^{12} = \hat{\mathrm{H}}_e^{21*} \ . \tag{3.43}$$

Therefore, the following matrix elements are equal

$$\langle \chi_1 | \hat{\mathrm{H}}_e^{12} | \chi_2 \rangle = \langle \chi_2 | \hat{\mathrm{H}}_e^{21} | \chi_1 \rangle^* \ . \tag{3.44}$$

Thus, the Hermicity of the coupling terms is established.

A second approach to a diabatic representation is to employ the adiabatic representations for those regions of space where the nonadiabatic coupling terms

$F_{kk'}$ and $G_{kk'}$ are negligible. When these coupling terms are not small, such as in the vicinity of a conical intersection or avoided crossing, the representation is changed to a diabatic representation via a unitarity transformation. The most suitable choice for the diabatic representation is one which best satisfies Equation 3.38.[56]

Since the approximation given in Equation 3.38 was introduced to simplify the form of the coupled equations given in Equation 3.39, the diabatic representation presented here is not rigorous. The adiabatic and diabatic representations as presented are not equivalent, with the adiabatic description being the exact one. The next section discusses a procedure for developing equivalent adiabatic and diabatic formalisms.[52]

V. On the Equivalence of the Adiabatic and Diabatic Representations

As mentioned previously, the diabatic representation discussed is not rigorously equivalent to the exact adiabatic representation. However, it has been shown that there exists a procedure which uniquely determines a diabatic representation and in which Equation 3.38 is satisfied. The procedure is outlined below.

Consider a compact notation for the coupled equations in an unspecified representation, *i.e.*, adiabatic or diabatic. Let the matrix P be defined as follows:[52]

$$\mathrm{P}_{kk'} = \langle \phi_k | P_{\mathrm{N}} | \phi_{k'} \rangle \ , \tag{3.45}$$

where P_{N} is the nuclear momentum operator and let $\mathcal{P}$ be a generalized momentum matrix operator

$$\mathcal{P} = \mathrm{P} + \mathrm{I}P_{\mathrm{N}} \ , \tag{3.46}$$

where I is the identity matrix. The dimensionality of these momentum operators should be large enough to ensure the completeness of the set of functions ϕ_k, *i.e.*,

$$\sum_k |\phi_k\rangle\langle\phi_k| = \hat{1} \ , \tag{3.47}$$

where $\hat{1}$ is the identity operator. Let the potential matrix $\mathcal{U}$ be defined as

$$\mathcal{U}_{kk'} = \langle \phi_k | \hat{\mathrm{H}}_e | \phi_{k'} \rangle \ . \tag{3.48}$$

Using the above expresions for $\mathcal{P}$, $\mathcal{U}$ and the total energy matrix IE the coupled equations can be written as

$$[\frac{1}{2\mathrm{M}}\mathcal{P} \cdot \mathcal{P} + \mathcal{U} - \mathrm{IE}]\chi = 0 \ . \tag{3.49}$$

Substituting Equation 3.46 into Equation 3.49 leads to

$$[\mathrm{I}\hat{\mathrm{T}}_{\mathrm{N}} + \frac{1}{2\mathrm{M}}(\mathrm{P}\cdot\mathrm{P} + \mathcal{P}_{\mathrm{N}}\cdot\mathrm{P}) + \frac{1}{\mathrm{M}}\mathrm{P}\cdot\mathcal{P}_{\mathrm{N}} + \mathcal{U} - \mathrm{IE}]\mathcal{X} = 0 \ . \tag{3.50}$$

$\mathcal{X}$ in Equations 3.49 and 3.50 is a column vector of nuclear wavefunctions $\mathcal{X}_k$. The set of coupled equations given by Equation 3.50 must be satisfied by the nuclear wavefunctions for any diabatic or adiabatic representation. This set of coupled equations is equivalent to those given in Equation 3.36. The matrix $\mathrm{I}\hat{\mathrm{T}}_{\mathrm{N}}$ is the diagonal nuclear kinetic energy operator matrix. The matrix $\frac{1}{2\mathrm{M}}\mathrm{P}\cdot\mathrm{P}$ is diagonal, its elements are given by

$$[\frac{1}{2\mathrm{M}}\mathrm{P}\cdot\mathrm{P}]_{kk'} = \langle\phi_k|\hat{\mathrm{T}}_{\mathrm{N}}|\phi_{k'}\rangle\delta_{kk'} \ . \tag{3.51}$$

The coupling matrices $\frac{1}{2\mathrm{M}}\mathcal{P}_{\mathrm{N}}\cdot\mathrm{P}$ and $\frac{1}{\mathrm{M}}\mathrm{P}\cdot\mathcal{P}_{\mathrm{N}}$ are given by

$$\begin{aligned}[\frac{1}{2\mathrm{M}}\mathcal{P}_{\mathrm{N}}\cdot\mathrm{P}]_{kk'} &= \langle\phi_k|\hat{\mathrm{T}}_{\mathrm{N}}|\phi_{k'}\rangle \quad && k \neq k' \\ &= 0 && k = k'\end{aligned} \tag{3.52}$$

and

$$\begin{aligned}[\frac{1}{\mathrm{M}}\mathrm{P}\cdot\mathcal{P}_{\mathrm{N}}]_{kk'} &= \frac{1}{\mathrm{M}}\langle\phi_k|\mathrm{P}|\phi_{k'}\rangle\cdot\mathcal{P}_{\mathrm{N}} \quad && k \neq k' \\ &= 0 && k = k'.\end{aligned} \tag{3.53}$$

The form of the coupled equations given by Equation 3.49 is particularly useful since it provides a transparent adiabatic or diabatic transformation. The requirement that the potential matrix $\mathcal{U}$ be diagonal for all internuclear distances leads directly to the adiabatic representation so long as the electronic basis is complete. Under these conditions Equation 3.49 (or more clearly Equation 3.50) is equivalent to Equations 3.10 through 3.12. If instead, the $\mathcal{P}$ matrix operator is required to be diagonal for all internuclear separations, then the $\mathcal{U}$ matrix will not in general be diagonal. This results in the diabatic representation. This procedure is less restrictive than Equation 3.38 which states that $\mathcal{P} \equiv 0$. Therefore, in the diabatic representation coupling occurs solely through the potential matrix $\mathcal{U}$.

Using this procedure for construction of adiabaitic and diabatic representations establishes that these representations provide equivalent descriptions of electroincally nonadiabatic collisions within the framework outlined above. A discussion of the relationship between these two representations in the two-state approximation follows.

VI. The Adiabatic and Diabatic Representations in the Two-State Approximation

For simplicity of discussion and without loss of generality, we limit our discussion to two interacting states. We assume that two adiabatic electronic eigenfunctions form a complete expansion for the electronic coordinates for all internuclear distances. The coupled equations for the adiabatic nuclear wavefunctions are given according to Equations 3.15 and 3.16 by

$$\left[\hat{T}_N + E_1(\mathbf{R}) + G_{11}(\mathbf{R}) - E\right]\chi_1(\mathbf{R}) = -\left[F_{12}(\mathbf{R}) + G_{12}(\mathbf{R})\right]\chi_2(\mathbf{R}) \tag{3.54}$$

$$\left[\hat{T}_N + E_2(\mathbf{R}) + G_{22}(\mathbf{R}) - E\right]\chi_2(\mathbf{R}) = -\left[F_{21}(\mathbf{R}) + G_{21}(\mathbf{R})\right]\chi_1(\mathbf{R}) \ , \tag{3.55}$$

where $F_{kk'}$ and $G_{kk'}$ are the nonadiabatic coupling terms defined by Equations 3.11 and 3.12, and E is the total energy of the system. Explicity in the two state approximation

$$F_{12} = -\sum_{\alpha=1}^{N_n} \frac{\hbar^2}{M_\alpha} \mathbf{g}_{12\alpha}(\mathbf{R}) \cdot \nabla_\alpha, \tag{3.56}$$

$$F_{21} = \sum_{\alpha=1}^{N_n} \frac{\hbar^2}{M_\alpha} \mathbf{g}_{12\alpha}(\mathbf{R}) \cdot \nabla_\alpha, \tag{3.57}$$

$$G_{12} = -\sum_{\alpha=1}^{N_n} \frac{\hbar^2}{2M_\alpha} \nabla_\alpha \cdot \mathbf{g}_{12\alpha}(\mathbf{R}), \tag{3.58}$$

$$G_{21} = \sum_{\alpha=1}^{N_n} \frac{\hbar^2}{2M_\alpha} \nabla_\alpha \cdot \mathbf{g}_{12\alpha}(\mathbf{R}), \tag{3.58}$$

and

$$G_{11} = G_{22} = \sum_{\alpha=1}^{N_n} \frac{\hbar^2}{2M_\alpha} \mathbf{g}_{12\alpha}^2(\mathbf{R}) \ . \tag{3.60}$$

Equations 3.58 through 3.60 are valid only for the two-state approximation, and a derivation of these equations follows. By definition,

$$\mathbf{g}_{12\alpha} = \langle \phi_k | \nabla_\alpha | \phi_{k'} \rangle \ , \tag{3.61}$$

$$\mathrm{G}_{12} = \sum_{\alpha=1}^{\mathrm{N}_n} -\frac{\hbar^2}{2\mathrm{M}_\alpha} \langle \phi_k | \nabla_\alpha^2 | \phi_{k'} \rangle \ , \tag{3.62}$$

Therefore, to derive Equations 3.58 through 3.60, it must be shown that

$$\langle \phi_1 | \nabla_\alpha^2 | \phi_2 \rangle = \ \nabla_\alpha \cdot \mathbf{g}_{12\alpha} \tag{3.63}$$

$$\langle \phi_2 | \nabla_\alpha^2 | \phi_1 \rangle = -\nabla_\alpha \cdot \mathbf{g}_{12\alpha} \ . \tag{3.64}$$

Differentiating $\mathbf{g}_{12\alpha}$ in the definition above gives

$$\nabla_\alpha \cdot \mathbf{g}_{12\alpha} = \langle \nabla_\alpha \phi_1 | \nabla_\alpha | \phi_2 \rangle + \langle \phi_1 | \nabla_\alpha^2 | \phi_2 \rangle \ . \tag{3.65}$$

The first term on the right hand side of Equation 3.65 is identically zero in the two state approximation. This follows from the fact that

$$\langle \phi_k | \nabla_\alpha | \phi_k \rangle = 0 \tag{3.66}$$

which states that $\nabla_\alpha \phi_k$ has a non-zero projection on the state $\phi_{k'}$ only when $k \neq k'$. This establishes Equation 3.63. Using this result and Equation 3.20 proves Equation 3.64, therefore, Equations 3.58 and 3.59 hold in the two-state approximation. To prove Equation 3.60 we make use of Equation 3.66 to get

$$\nabla_\alpha \cdot \langle \phi_k | \nabla_\alpha | \phi_k \rangle = 0 \tag{3.67}$$

and therefore,

$$-\langle\nabla_\alpha\phi_k|\nabla_\alpha\phi_k\rangle = \langle\phi_k|\nabla^2_\alpha|\phi_k\rangle \ . \tag{3.68}$$

However, we know that

$$\nabla_\alpha\phi_k = \mathbf{g}_{kk'\alpha}\phi_{k'} \tag{3.69}$$

which gives the result that

$$\langle\phi_k|\nabla^2_\alpha|\phi_{k'}\rangle = -\mathbf{g}^2_{kk'\alpha} \ . \tag{3.70}$$

Finally making use of Equation 3.20 we have the result that

$$\langle\phi_1|\nabla^2_\alpha|\phi_2\rangle = \langle\phi_2|\nabla^2_\alpha|\phi_1\rangle = -\mathbf{g}^2_{12\alpha} \tag{3.71}$$

and hence

$$\mathrm{G}_{11} = \mathrm{G}_{22} = \sum_{\alpha=1}^{\mathrm{N}_n} \frac{\hbar^2}{2\mathrm{M}_\alpha}\mathbf{g}^2_{12\alpha} \tag{3.72}$$

which is equivalent to Equation 3.60. We now make use of these results to obtain the coupled equations. Substituting Equations 3.56 through 3.60 into Equations 3.54 and 3.55 leads to the following two coupled equations.

$$\begin{aligned}
&[\hat{\mathrm{T}}_\mathrm{N} - \mathcal{U}_1(\mathbf{R}) + \mathrm{k}^2 - \sum_{\alpha=1}^{\mathrm{N}_n} \frac{\hbar^2}{2\mathrm{M}_\alpha}\mathbf{g}^2_{12\alpha}(\mathbf{R})]\chi_1(\mathbf{R}) \\
&\qquad = \sum_{\alpha=1}^{\mathrm{N}_n} \frac{\hbar^2}{2\mathrm{M}_\alpha}\{2\mathbf{g}_{12\alpha}(\mathbf{R})\cdot\nabla_\alpha + \nabla_\alpha\cdot\mathbf{g}_{12\alpha}(\mathbf{R})\}\chi_2(\mathbf{R}), \qquad (3.73) \\
&[\hat{\mathrm{T}}_\mathrm{N} - \mathcal{U}_2(\mathbf{R}) + \mathrm{k}^2 - \sum_{\alpha=1}^{\mathrm{N}_n} \frac{\hbar^2}{2\mathrm{M}_\alpha}\mathbf{g}^2_{12\alpha}(\mathbf{R})]\chi_2(\mathbf{R}) \\
&\qquad = \sum_{\alpha=1}^{\mathrm{N}_n} \frac{\hbar^2}{2\mathrm{M}_\alpha}\{2\mathbf{g}_{12\alpha}(\mathbf{R})\cdot\nabla_\alpha + \nabla_\alpha\cdot\mathbf{g}_{12\alpha}(\mathbf{R})\}\chi_1(\mathbf{R}), \qquad (3.74)
\end{aligned}$$

where

$$\mathcal{U}_k(\mathbf{R}) = \frac{2\mathrm{ME}_k(\mathbf{R})}{\hbar^2} \ , \quad k = 1, 2$$

$$\mathrm{k}^2 = -\frac{2\mathrm{ME}}{\hbar^2} \tag{3.75}$$

and

$$\mathrm{M} = \sum_{\alpha=1}^{\mathrm{N}_n} \mathrm{M}_\alpha \ . \tag{3.76}$$

The coupling operators which appear on the right hand side of Equations 3.73 and 3.74 are Hermitian. Their Hermicity has already been shown in Section III for a more general example, *i.e.*, one for which Equations 3.58 through 3.60 were not assumed. A proof in this more specialized example can be developed following these same methods.

Let us now turn our attention to the diabatic representation within the two-state approximation. As stated previously we assume that the generalized momentum matrix $\mathcal{P}$ is diagonal. Note that, in the two-state approximation, it can be shown that a diabatic representation exists for which $\mathcal{P}$ vanishes for all internuclear distances.[52] The diabatic equations are then given by

$$\left[\hat{\mathrm{T}}_\mathrm{N} + \hat{\mathrm{H}}_e^{11}(\mathbf{R}) - \mathrm{E}\right]\chi_1^\mathrm{d} = -\hat{\mathrm{H}}_e^{12}\chi_2^\mathrm{d} \ , \tag{3.77}$$

$$\left[\hat{\mathrm{T}}_\mathrm{N} + \hat{\mathrm{H}}_e^{22}(\mathbf{R}) - \mathrm{E}\right]\chi_2^\mathrm{d} = -\hat{\mathrm{H}}_e^{12}\chi_1^\mathrm{d} \ . \tag{3.78}$$

According to the equivalence relationship established in Section V, (for a complete expansion) diagonalization of the matrix

$$\mathcal{U}^\mathrm{d} = \begin{pmatrix} \hat{\mathrm{H}}_e^{11} & \hat{\mathrm{H}}_e^{12} \\ \hat{\mathrm{H}}_e^{12} & \hat{\mathrm{H}}_e^{22} \end{pmatrix} \tag{3.79}$$

yields the adiabatic Equations 3.73 and 3.74. The details of this diagonalization as well as the relationship between the $\mathcal{U}^\mathrm{d}$ matrix and the nonadiabatic coupling terms of Equations 3.73 and 3.74 are discussed in the following section.

VII. The Transformation From The Diabatic to the Adiabatic Representations in the Two-State Approximation

To transform the diabatic representation given by Equations 3.77 and 3.78 to the adiabatic representation given by Equations 3.73 and 3.74 a unitarity transformation, $\mathcal{C}$, is applied to the basis functions ϕ_1^{d} and ϕ_2^{d}. This matrix transformation can be written as[52]

$$\begin{pmatrix} \phi_1 \\ \phi_2 \end{pmatrix} = \mathcal{C} \begin{pmatrix} \phi_1^2 \\ \phi_2^{\mathrm{d}} \end{pmatrix} = \begin{pmatrix} \cos\tau & \sin\tau \\ -\sin\tau & \cos\tau \end{pmatrix} \begin{pmatrix} \phi_1^{\mathrm{d}} \\ \phi_2^{\mathrm{d}} \end{pmatrix} . \tag{3.80}$$

Rewriting the diabatic coupled equations in matrix form gives

$$\left[\begin{pmatrix} \hat{\mathrm{T}}_{\mathrm{N}} & 0 \\ 0 & \hat{\mathrm{T}}_{\mathrm{N}} \end{pmatrix} + \begin{pmatrix} \hat{\mathrm{H}}_e^{11} & \hat{\mathrm{H}}_e^{12} \\ \hat{\mathrm{H}}_e^{21} & \hat{\mathrm{H}}_e^{22} \end{pmatrix} - \mathrm{E} \begin{pmatrix} 1 & 0 \\ 0 & 1 \end{pmatrix} \right] \begin{pmatrix} \phi_1^{\mathrm{d}} \\ \phi_2^{\mathrm{d}} \end{pmatrix} = 0 . \tag{3.81}$$

The theorem of representation theory[60] states that the transformed kinetic energy operator matrix $\mathcal{T}'$, is related to the original kinetic energy operator $\mathcal{T}$ by

$$\mathcal{T}' = \mathcal{C}\mathcal{T}\mathcal{C}^{\dagger} , \tag{3.82}$$

where $\mathcal{C}^{\dagger}$ is the adjoint of $\mathcal{C}$. Since $\mathcal{C}$ is real, $\mathcal{C}^{\dagger} = \mathcal{C}^{T}$ the transpose of $\mathcal{C}$. Therefore, $\mathcal{T}'$ is given by

$$\mathcal{T}' = \begin{pmatrix} \cos\tau(\mathbf{R}) & \sin\tau(\mathbf{R}) \\ -\sin\tau(\mathbf{R}) & \cos\tau(\mathbf{R}) \end{pmatrix} \begin{pmatrix} \hat{\mathrm{T}}_{\mathrm{N}} & 0 \\ 0 & \hat{\mathrm{T}}_{\mathrm{N}} \end{pmatrix} \begin{pmatrix} \cos\tau(\mathbf{R}) & -\sin\tau(\mathbf{R}) \\ \sin\tau(\mathbf{R}) & \cos\tau(\mathbf{R}) \end{pmatrix} . \tag{3.83}$$

The unitary transformation, $\mathcal{C}$, of this Equation 3.81 leaves the identity matrix unchanged and diagonalizes the $\mathcal{U}^{\mathrm{d}}(\mathbf{R})$ at all $\mathbf{R}$. Therefore, τ is a function of $\mathbf{R}$.

By performing the above matrix multiplications (remembering that $\mathcal{T}$ is not a simple matrix, but an operator), it is straightforward to show that $\mathcal{T}'$ is given by

$$\mathcal{T}' = \begin{pmatrix} \hat{\mathrm{T}}_{\mathrm{N}} + \sum_{\alpha=1}^{\mathrm{N}_n} \frac{\hbar^2}{2\mathrm{M}_\alpha}(\nabla_\alpha \tau)^2 & -\sum_{\alpha=1}^{\mathrm{N}_n} \frac{\hbar^2}{2\mathrm{M}_\alpha}(2\tau\nabla_\alpha + \nabla_\alpha \tau) \\ \sum_{\alpha=1}^{\mathrm{N}_n} \frac{\hbar^2}{2\mathrm{M}_\alpha}(2\tau\nabla_\alpha + \nabla_\alpha \tau) & \hat{\mathrm{T}}_{\mathrm{N}} - \sum_{\alpha=1}^{\mathrm{N}_n} \frac{\hbar^2}{2\mathrm{M}_\alpha}(\nabla_\alpha \tau)^2 \end{pmatrix} \tag{3.84}$$

With this, the transformed coupled equations are given by

$$\left[\hat{\mathrm{T}}_{\mathrm{N}} + \sum_{\alpha=1}^{\mathrm{N}_n} \frac{\hbar^2}{2\mathrm{M}_\alpha}(\nabla_\alpha \tau)^2 + \mathrm{E}_1(\mathbf{R}) - \mathrm{E}\right]\chi_1^{\mathrm{d}} = \sum_{\alpha=1}^{\mathrm{N}_n} \frac{\hbar^2}{2\mathrm{M}_\alpha}(2\tau\nabla_\alpha + \nabla_\alpha \tau)\chi_2^{\mathrm{d}} \tag{3.85}$$

$$\left[\hat{\mathrm{T}}_{\mathrm{N}} + \sum_{\alpha=1}^{\mathrm{N}_n} \frac{\hbar^2}{2\mathrm{M}_\alpha}(\nabla_\alpha \tau)^2 + \mathrm{E}_2(\mathbf{R}) - \mathrm{E}\right]\chi_2^{\mathrm{d}} = \sum_{\alpha=1}^{\mathrm{N}_n} \frac{\hbar^2}{2\mathrm{M}_\alpha}(2\tau\nabla_\alpha + \nabla_\alpha \tau)\chi_1^{\mathrm{d}} \ . \tag{3.86}$$

$\mathrm{E}_1(\mathbf{R})$ and $\mathrm{E}_2(\mathbf{R})$ are the eigenvalues of the $\mathcal{U}^{\mathrm{d}}$ matrix and within the two-state approximation, they are identical to the adiabatic potential energy curves of Equations 3.54 and 3.55. In order to establish the equivalence of these sets of coupled equations (3.54, 3.55 and 3.85, 3.86), it must be shown that

$$\nabla_\alpha \tau = \mathbf{g}_{12\alpha}(\mathbf{R}) = \langle \phi_1 | \nabla_\alpha | \phi_2 \rangle \ . \tag{3.87}$$

The general proof of Equation 3.87 is rather involved, therefore it will be shown that it is true at the crossing point of the two diabatic curves $\hat{\mathrm{H}}_e^{11}$ and $\hat{\mathrm{H}}_e^{22}$. The function τ is determined from the eigenvalue equation that must be solved to diagonalize the $\mathcal{U}^{\mathrm{d}}$ matrix and is given by

$$\tan 2\tau = \frac{2\hat{\mathrm{H}}_e^{12}(\mathbf{R})}{\hat{\mathrm{H}}_e^{22}(\mathbf{R}) - \hat{\mathrm{H}}_e^{11}(\mathbf{R})} \ . \tag{3.88}$$

Therefore, at the crossing point $\nabla_\alpha \tau$ is given by

$$\nabla_\alpha \tau = \nabla_\alpha \left[\frac{\hat{\mathrm{H}}_e^{11} - \hat{\mathrm{H}}_e^{22}}{4\hat{\mathrm{H}}_e^{12}}\right] . \tag{3.89}$$

In the two-state approximation it can be shown that

$$\mathrm{g}_{12\alpha}(\mathbf{R}) = \frac{\langle\phi_1|\nabla_\alpha \hat{\mathrm{H}}_e|\phi_2\rangle}{\mathrm{E}_2(\mathbf{R}) - \mathrm{E}_1(\mathbf{R})} \tag{3.90}$$

and from the diagonalization of $\mathcal{U}^{\mathrm{d}}$ that

$$\mathrm{E}_1 = \frac{\hat{\mathrm{H}}_e^{11} + \hat{\mathrm{H}}_e^{22}}{2} + \left[\frac{(\hat{\mathrm{H}}_e^{11} - \hat{\mathrm{H}}_e^{22})^2}{4} + (\hat{\mathrm{H}}_e^{12})^2\right]^{\frac{1}{2}} \tag{3.91}$$

$$\mathrm{E}_2 = \frac{\hat{\mathrm{H}}_e^{11} + \hat{\mathrm{H}}_e^{22}}{2} - \left[\frac{(\hat{\mathrm{H}}_e^{11} - \hat{\mathrm{H}}_e^{22})^2}{4} + (\hat{\mathrm{H}}_e^{12})^2\right]^{\frac{1}{2}} . \tag{3.92}$$

Therefore, at the crossing point

$$\mathrm{E}_1 - \mathrm{E}_2 = 2\hat{\mathrm{H}}_e^{12} . \tag{3.93}$$

Plugging this result into Equation 3.90 we have that

$$\mathrm{g}_{12\alpha}(\mathbf{R}) = \frac{\langle\phi_1|\nabla_\alpha \hat{\mathrm{H}}_e|\phi_2\rangle}{2\hat{\mathrm{H}}_e^{12}} . \tag{3.94}$$

Using Equation 3.80, ϕ_1 and ϕ_2 can be expressed in terms of ϕ_1^{d} and ϕ_2^{d}. If the resulting expressions for ϕ_1 and ϕ_2 are substituted into Equation 3.94, this equation becomes

$$\begin{aligned}\mathrm{g}_{12\alpha}(\mathbf{R}) = {} & \sin\tau\,\cos\tau\big[\langle\phi_1^{\mathrm{d}}|\nabla_\alpha \hat{\mathrm{H}}_e|\phi_1^{\mathrm{d}}\rangle - \langle\phi_2^{\mathrm{d}}|\nabla_\alpha \hat{\mathrm{H}}_e|\phi_2^{\mathrm{d}}\rangle\big] \\ & + \cos^2\tau\langle\phi_1^{\mathrm{d}}|\nabla_\alpha \hat{\mathrm{H}}_e|\phi_2^{\mathrm{d}}\rangle - \sin^2\tau\langle\phi_2^{\mathrm{d}}|\nabla_\alpha \hat{\mathrm{H}}_e|\phi_1^{\mathrm{d}}\rangle .\end{aligned} \tag{3.95}$$

This expression can be simplified by taking advantage of the fact that

$$\langle\phi_k^{\mathrm{d}}|\nabla_\alpha \hat{\mathrm{H}}_e|\phi_{k'}^{\mathrm{d}}\rangle = \nabla_\alpha\langle\phi_k^{\mathrm{d}}|\hat{\mathrm{H}}_e|\phi_{k'}^{\mathrm{d}}\rangle , \quad k, k' = 1, 2 \tag{3.96}$$

to give

$$\mathbf{g}_{12\alpha}(\mathbf{R}) = \sin\tau\ \cos\tau\ \nabla_\alpha\left[\hat{\mathrm{H}}_e^{11} - \hat{\mathrm{H}}_e^{22}\right] + [\cos^2\tau\ - \sin^2\tau]\nabla_\alpha\hat{\mathrm{H}}_e^{12}\ . \tag{3.97}$$

From Equation 3.88, at the crossing point, we have that

$$\cot 2\tau = 0\ . \tag{3.98}$$

Using the identity

$$\cot 2\tau = \frac{\cos^2\tau - \sin^2\tau}{\sin\tau\cos\tau} \tag{3.99}$$

Equation 3.98 implies that

$$\cos^2\tau - \sin^2\tau = 0 \tag{3.100}$$

and

$$\sin\tau\ \cos\tau = \frac{1}{2}\ . \tag{3.101}$$

Using Equation 3.89 this gives the result that

$$\mathbf{g}_{12\alpha}(\mathbf{R}) = \nabla_\alpha\left[\frac{\hat{\mathrm{H}}_e^{11} - \hat{\mathrm{H}}_e^{22}}{4\hat{\mathrm{H}}_e^{12}}\right] \tag{3.102}$$

which is equivalent to Equation 3.89. Thus, it has been established that at the crossing point

$$\mathbf{g}_{12\alpha}(\mathbf{R}) = \nabla_\alpha\tau(\mathbf{R})\ . \tag{3.103}$$

Although Equation 3.103 has only been shown for the crossing point, it is valid for all nuclear configurations. Therefore, the adiabatic and diabatic representations are equivalent in the two-state approximation.

VIII. Construction of a Diabatic Basis from an Ab Initio Adiabatic CI Basis

Two methods for constructing a diabatic basis ϕ_k^d from the adiabatic (CI) solutions ϕ_k of the electronic Schrödinger equation have been developed. A summary of these methods is given by Köppel *et al.*[61] The first method is based on the nonadiabatic coupling elements $\mathbf{g}_{kk'\alpha} = \langle \phi_k | \nabla_\alpha | \phi'_k \rangle$. These coupling elements must be calculated by differentiating with respect to all internal coordinates Q of the system and then integrating along each coordinate to obtain the desired diabatic transformation matrix. This method is rigorous and the diabatic representation is equivalent to the adiabatic representation. This method has been applied in several cases. Baer and co-workers[62−63] used this method to examine the nonadiabatic effects upon the collinear reactions: $H_2 + H^+$, $H_2^+ + H$, $Ar^+ + H_2$ and $Ar + H_2^+$. The difficulty with this method is the determination of the nonadiabatic coupling elements $\mathbf{g}_{kk'\alpha}$, since a very fine mesh is required for accurate numerical integration.

In the case of a sharply avoided crossing the shape of the $\mathbf{g}_{kk'\alpha}$ coupling surface approaches a δ function and its numerical integration becomes difficult. For conical intersections, in a polyatomic molecule singular behavior in the $\mathbf{g}_{kk'\alpha}$ coupling element has been observed.[64] In order to avoid the procedure of calculating, fitting and integrating the nonadiabatic coupling elements, a second method of diabatisation has been developed. This technique defines the diabatic basis by examining pointwise-determined molecular properties that reflect the avoided crossing in their geometric dependence. Macìas and Riera[65] have examined the possible shapes of these property curves and defined three cases for a two-state crossing:

case (a) with the diagonal elements of the one-electron operator showing extrema along the coordinate of differentiation and the off-diagonal element crossing zero;

case (b) for the opposite situation with crossing diagonal elements and extremal off-diagonal elements in the crossing region;

and

case (c) for an intermediate situation.

This method has been applied in several cases. Werner and Meyer,[66] define a diabatic basis for the two lowest $^1\Sigma^+$ states of LiF as the one which diagonalizes the corresponding dipole operator. Hirsch and Buenker[67] have also used this method to examine the nonadiabatic coupling between the two lowest $^2A'$ states of NO_2. A more general method for construction of a diabatic basis has been suggested by Hendeković.[68] In his definition, a diabatic basis maximizes the sum of the squared occupation probabilities of natural spin orbitals. A method which is in principle rigorous has been discussed by Özkan and Goodman.[69] Their method is based upon fully taking into account interactions within a primary subset of vibronically coupled states, and treating perturbatively the coupling of the primary states with the remaining states. Following the same idea, Köppel *et al.*[61] constructed an effective Hamiltonian matrix for the primary subset of states using quasi-degenerate perturbation theory. They applied this method to the study of several molecules and ions. Malrieu and coworkers[70–71] have also used this method to calculate quasi-diabatic states and dynamical couplings in the $HeNe^{2+}$ system. Recently, there has been a flurry of activity in this area and several new techniques for constructing the diabatic states have emerged.[72–86]

Since the present work deals with calculating the nonadiabatic coupling elements directly from the *ab initio* CI wavefunctions, the first method can later be used to calculate the diabatic wavefunctions and coupling elements. The nonadiabatic coupling surfaces thus obtained can be used in quantum mechanical scattering studies to provide a more accurate description of the dynamics near the conical intersection of H_3.

IX. References

1. D. C. Clary (editor), *the Theory of Chemical Reaction Dynamics*, (D. Reidel, 1985).
2. G. C. Schatz and A. Kuppermann, *J. Chem. Phys.* **65**, 4668 (1976).
3. R. T. Ling and A. Kuppermann, in *Electronic and Atomic Collisions, Abstract of the 9th International Conference on the Physics of Electronic and Atomic Collisions*, Seattle, Washington, 24-30 July, 1975, Vol. 1, eds. J. S. Risley, R. Geballe (Univ. Washington Press, Seattle, 1975) pp. 353-354.
4. A. Kuppermann and P.G. Hipes, *J. Chem. Phys.* **84**, 5962 (1986).
5. P.G. Hipes and A. Kuppermann, *Chem. Phys. Lett.* **133**, 1 (1987).
6. S.A. Cuccaro, P.G. Hipes and A. Kuppermann, *Chem. Phys. Lett.* **154**, 155 (1989).
7. S.A. Cuccaro, P.G. Hipes and A. Kuppermann, *Chem. Phys. Lett.* **157**, 440 (1989).
8. G.A. Parker, R.T. Pack, B.J. Archer and R.B. Walker, *Chem. Phys. Lett.* **137**, 564 (1987).
9. R.T. Pack and G.A. Parker, *J. Chem. Phys.* **87**, 3888 (1987).
10. J. Linderberg, S. Padkjaer, Y. Öhrn and B. Vessal, *J. Chem. Phys.* **90**, 6254 (1989).
11. B. Lepetit, J.M. Launay and M. Le Dourneuf, *Chem. Phys.* **106**, 103 (1986).
12. J.M. Launay and M. Le Dourneuf, *Chem. Phys. Lett.* **163**, 178 (1989).
13. G.C. Schatz, *Chem. Phys. Lett.* **150**, 92 (1988).
14. J.Z.H. Zhang and W.H. Miller, *Chem. Phys. Lett.* **140**, 329 (1987).
15. J.Z.H. Zhang and W.H. Miller, *Chem. Phys. Lett.* **159**, 130 (1989).
16. J.Z.H. Zhang, D.J. Kouri, K. Haug, D.W. Schwenke, Y. Shima and D.G. Truhlar, *J. Chem. Phys.* **88**, 2492 (1988).

17. M. Mladenovic, M. Zhao, D.G. Truhlar, D.W. Schwenke, Y. Sun and D.J. Kouri, *Chem. Phys. Lett.* **146**, 358 (1988).
18. C.H. Yu, D.J. Kouri, M. Zhao and D.G. Truhlar, *Chem. Phys. Lett.* **157**, 491 (1989).
19. D.E. Manopoulos and R.E. Wyatt, *Chem. Phys.* **90**, 300 (1989).
20. F. Webster and J.C. Light, *J. Chem. Phys.* **90**, 300 (1989).
21. M. Weissbluth, *Atoms and Molecules*, (Academic Press, 1978), pp. 299-301.
22. H.J. Foth, H.R. Mayne, R.A. Poirier, J.C. Polanyi and H.H. Teller, *Laser Chem.* **2**, 229 (1983).
23. H.R. Mayne, R.A. Poirier and J.C. Polyani, *J. Chem. Phys.* **80**, 4025 (1984).
24. V. Engel, Z. Bacic, R. Schinke and M. Shapiro, *J. Chem. Phys.* **82**, 4844 (1984).
25. H.R. Mayne, J.C. Polanyi, N. Sathyamurthy and S. Raynor, *J. Chem. Phys.* **88**, 4064 (1984).
26. V. Engel and R. Schinke, *Chem. Phys. Lett.* **122**, 103 (1985).
27. P.M. Agrawal, V. Mohan and N. Sathymurthy, *Chem. Phys. Lett.* **114**, 343 (1985).
28. B.A. Collings, J.C. Polyani, M.A. Stolow and J.W. Tarr, *Phys. Rev. Lett.* **59**, 2551 (1987).
29. T. Seidenman and M. Shapiro, *J. Chem. Phys.* **88**, 5525 (1988).
30. J.L. Krause and M. Shapiro, *J. Chem. Phys.* **90**, 6401 (1989).
31. M. Shapiro and P. Brumer, *J. Chem. Phys.* **84**, 4103 (1986).
32. P. Brumer and M. Shapiro, *Chem. Phys. Lett.* **126**, (1986).
33. P. Brumer and M. Shapiro, *Faraday Discuss.* **82**, 177 (1986).
34. C. Asaro, P. Brumer and M. Shapiro, *Phys. Rev. Lett.* **60**, 1634 (1988).
35. M. Shapiro and Y. Zeiri, *J. Chem. Phys.* **85**, 6449 (1986).

36. Hélène Lefebvre-Brion and R.W. Field, *Perturbations in the Spectra of Diatomic Molecules*, (Academic Press, 1986).

37. G. Herzberg, *Spectra of Diatomic Molecules*, Van Nostrand, Princeton, 2nd edition, 1950.

38. G. Herzberg, *Electronic Spectra and Electronic Structure of Polyatomic Molecules*, Van Nostrand, Princeton, 2nd. edition, 1950.

39. B.C. Garrett and D.G. Truhlar, in *Theoretical Chemistry: Theory of Scattering: Papers in Honor of Henry Eyring*, edited by D. Henderson, Vol. 6A, (Academic Press, 1981), pp. 216-289.

40. F. Rebentrost, in *Theoretical Chemistry: Theory of Scattering: Papers in Honor of Henry Eyring*, edited by D. Henderson, Vol. 6B, (Academic Press, 1981), pp. 3-77.

41. M. Baer, in *Theory of Chemical Reaction Dynamics*, edited by M. Baer, Vol. II, (CRC Press, 1985), pp. 219-280.

42. J.C. Tulley and R.K. Preston, *J. Chem. Phys.* **55**, 562 (1971).

43. J.P. Braga, H. Guo, J.N. Murrell and L.J. Dunne, *Molec. Phys.* **65**, 909 (1988).

44. B. Lepetit, J.M. Launay and M. Le Dourneuf, *Chem. Phys.* **117**, 17 (1987).

45. M. Born and J. R. Oppenheimer, *Ann. Phys.* **84**, 458 (1927).

46. M. Born, *Nachr. Acad. Wiss. Göttengen, Math-Physik Kl.* **IIa**, 1 (1957); M. born and K. Huang, *Dynamical Theory of Crystal Lattices*, (Oxford University Press, New York. 1954.

47. C.J. Ballhausen and A.E. Hansen, *Ann. Rev. Phys. Chem.* **23**, 15 (1972).

48. L.D. Landau, *Physik Z. Sowjetunion* **2**, 46 (1932); C. Zener, *Proc. Roy. Soc. London* **A137**, 696 (1932); E.C.G. Stueckelberg, *Helv. Phys. Acta* **5**, 369 (1932).

49. W. Lichten, *Phys. Rev.* **131**, 229 (1963); **139**, A27 (1965); **164**, 131 (1967).

50. H. C. Longuet-Higgens, *Advan. Spectrosc.* **2**, 429 (1961).

51. T.F. O'Malley, *Phys. Rev.* **162**, 98 (1967).

52. F.T. Smith, *Phys. Rev.* **179**, 111 (1969).

53. A. C. Hurley, *Introduction to the Electron Theory of Small Molecules*, (Academic Press, 1976) Chapter 1.

54. E. E. Nikitin and L. Zülicke, *Theory of Elementary Processes*, Lecture Notes in Chemistry, (Springer-Verlag, 1978).

55. D.R. Bates and A.A. Holt, *Proc. Royal Soc. London* **A292**, 168 (1966).

56. D.R. Bates, *Atomic and Molecular Processes*, edited by D.R. Bates (Academic, New York, 1962), Section 3.3.

57. H. Nakamura, *Molec. Phys.* **26**, 673 (1973).

58. N.F. Mott and H.S.W. Massey, *The Thoery of Atomic Collisions*, (Oxford, London, 1965), p. 370.

59. D.R. Bates, H.S.W. Massey, and A.L. Stewart, *Proc. Royal Soc. London* **A216**, 437 (1953).

60. A.S. Davydov, *Quantum Mechanics* (Addison-Wesley, Reading, Mass., 1965), Section 30.

61. H. Köppel, W. Domcke and L.S. Cederbaum, *Adv. in Chem. Phys.* **57**, 59 (1984).

62. Z.H. Top and M. Baer, *Chem. Phys.* **25**, 1 (1977).

63. M. Baer and J.A. Beswick, *Phys. Rev. A* **19**, 1559 (1979).

64. C. Petronlongo, *J. Chem. Phys.* **89**, 1297 (1988).

65. A. Macìas and A. Riera, *J. Phys. B* **11**, L489 (1978).

66. H.J. Werner and W. Meyer, *J. Chem. Phys.* **74**, 5802 (1981).

67. G. Hirsch and R.J. Buenker, *Molec. Phys.* **70**, 835 (1990); *Molec. Phys.* **73**, 1085 (1991).

68. J. Hendeković, *Chem. Phys. Lett.* **90**, 193 (1982).

69. I. Özkan and L. Goodman, *Chem. Rev.* **79**, 275 (1979).

70. R. Cimiraglia, J.P. Malrieu, M. Persico and F. Spiegelmann *J. Phys. B* **18**, 3073 (1984).

71. P. Durand and J.P. Malrieu, *Adv. in Chem. Phys.* **67**, 321 (1987).

72. J. Kucar, M. Pavlović and J. Hendeković, *Int. J. Quantum Chem.* **32**, 699 (1987); **32**, 705 (1987).

73. N. Komiha, J.P. Daudey and J.P. Malrieu, *J. Phys. B* **20**, 4375 (1987).

74. M. Desouter-Lecomte, D. Dehareng and J.C. Lorquet, *J. Chem. Phys.* **86**, 1429 (1987).

75. H.J. Werner, B. Follmeg and M.H. Alexander, *J. Chem. Phys.* **89**, 3139 (1988).

76. O.K. Kabbaj, F. Volatron and J.P. Malrieu, *Chem. Phys. Lett.* **147**, 353 (1988).

77. J.G. Frey, *Molec. Phys.* **65**, 1313 (1988); *Molec. Phys.* **71**, 659 (1990).

78. T. Pacher, H. Köppel and L.S. Cederbaum, *J. Chem. Phys.* **89**, 7367 (1988); *J. Chem. Phys.* **95**, 6668 (1991).

79. A. Russek and R.J. Furlan, *Phys. Rev. A* **39**, 5034 (1989).

80. F.X. Gadéa and M. Pélissier, *J. Chem. Phys.* **93**, 545 (1990).

81. C. Petronlongo, G. Hirsch and R.J. Buenker, *Molec. Phys.* **70**, 825 (1990).

82. M. Perić, R.J. Buenker and S.D. Peyerimhoff, *Molec. Phys.* **71**, 673 (1990).

83. U. Manthe and H. Köppel, *J. Chem. Phys.* **93**, 1658 (1990).

84. O.K. Kabbaj, M.B. Lepetit, J.P. Malrieu, G. Sini and P.C. Hiberty, *J. Amer. Chem. Soc.* **113**, 5619 (1991).

85. I.D. Petsalakis, G. Theodorakopoulos, C.A. Nicolaides and R.J. Buenker, *Chem. Phys. Lett.* **185**, 359 (1991).

86. A. Henriet, F. Masnou-Seeuws and O. Dulieu, *Z. Phys. D - Atoms, Molecules and Clusters* **18**, 287 (1991)

Chapter 4.

Ab Initio Calculation of the Lowest Three Electronic States of H_3 and the Nonadiabatic Coupling Elements Between These States

I. Introduction

To understand the structure and dynamics of a molecular system, requires knowledge of the potential energy surfaces of its electronic states. In addition, the electronically nonadiabatic coupling matrix elements and (or) the radiation assisted coupling elements between the two electronic states is needed when physical or chemical processes are of interest.

Two good global surfaces have been obtained for the $H + H_2$ reaction. The high quality ground electronic state potential energies calculated by Lui[1] and by Siegbahn and Lui[2] were fitted by Truhlar and Horowitz[3] to give the LSTH surface. The LSTH surface incorporates some scaling to produce accurate diatomic limits, and has provided a standard of accuracy in this field for several years. More recently Varandas and coworkers[4] used a double many-body expansion (DMBE) to fit the energy data of Lui and Seigbahn. Although the RMS error of the DMBE surface is larger than that of the LSTH surface, it is believed to be more accurate at higher energies.

The number of available *ab initio* calculations for excited states of the $H+H_2$ system is sparse and over a very limited range of configurations. Theoretical studies of the Rydberg excited states of H_3 include work performed by King and Morokuma,[5] Jungen,[6] Martin,[7] Kulander and Guest,[8] Nager and Jungen,[9] and Raynor and Herschbach.[10] In addition Polanyi and coworkers[11–13] have published a series of papers on transition state spectroscopy of H_3. Roach and Kuntz[14] have studied the excited electronic potential energy surfaces of H_3 using a semiempirical diatom in molecule (DIM) method. Some recent work on H_3 has also been conducted by Petsalakis, Theodorakopoulos and Wright[15] (PTW) and also by Diercksen and coworkers.[16] In general, the above mentioned studies were done over a limited range of nuclear geometric configurations, and were not sufficient to generate the full potential energy surfaces. Even more recently other members of this group have undertaken the task of obtaining complete potential energy surfaces for the lowest four electronic states of H_3 and electric dipole transition moments between these electronic states.[17-18]

The major terms of the electronically nonadiabatic coupling elements near the equilateral triangle configuration of H_3 between the upper and lower sheets of the DMBE surface have been obtained through a functional analysis by Varandas and coworkers.[4,19] Prior to the work presented here, there have been no direct calculations of the nonadiabatic coupling terms for any other pair of H_3 surfaces.

Herzberg,[20] Watson,[21] and Gellene and Porter[22] have published reviews of the Rydberg spectra of H_3. The Rydberg electronic states of H_3 in an equilateral triangle configuration and the correlation diagram to its dissociation products is shown in Figure 1. The $2p_z^2A_2''$ electronic state has drawn a great deal of attention in experimental work (as will be discussed in later chapters) because it has been found to have a life time longer than 40 μs[24] (the theoretical estimate is about 90 μs[23]). Herzberg and coworkers[25-29] first identified the decay mechanisms of the H_3 species in this electronic state. These transitions include an allowed electric dipole transition to the $2s^2A_1'$ state, and the predissociation to the repulsive ground $2p_{x,y}^2E'$ electronic states. In order to understand these decay processes, and other dynamical processes involving the three low-lying electronic states of H_3 [11-13,23-24] we have calculated the electronic energies using an *ab initio* quantum mechanical method, along with the electronically nonadiabatic coupling elements between each pair of states.

The general approach used in this work to calculate electronic states in molecular systems, Multi reference single and double excitation configuration interaction, (MRD-CI) is outlined in the following sections. The choice of atomic orbital (AO) basis set functions is discussed and the results obtained are compared with those of previous studies.

II. Methodology

A. General Considerations

In the frozen-nucleus Born-Oppenheimer approximation, the electronic Hamiltonian operator in atomic units for a molecule with n electrons and N nuclei in the absence of external fields and neglecting spin and other relativistic effects is given by[30−31]

$$\hat{\mathrm{H}} = -\frac{1}{2}\sum_{\mathrm{i=1}}^{\mathrm{n}} \nabla_{\mathrm{i}}^{2} - \sum_{\mathrm{A=1}}^{\mathrm{N}}\sum_{\mathrm{i=1}}^{\mathrm{n}} \frac{\mathrm{Z_A}}{\mathrm{r_{Ai}}} + \sum_{\mathrm{i>j=1}}^{\mathrm{n}} \frac{1}{\mathrm{r_{ij}}} + \sum_{\mathrm{A>B=1}}^{\mathrm{N}} \frac{\mathrm{Z_A Z_B}}{\mathrm{R_{AB}}} , \qquad (4.1)$$

where the indices $i,\ j$ are used to denote electrons, and the indices A, B are used to denote nuclei with charges $\mathrm{Z_A}$, $\mathrm{Z_B}$ respectively. The variables r_{ij}, $\mathrm{r}_{\mathrm{A}i}$ and $\mathrm{R_{AB}}$ are the electron-electron, the electron-nuclear and the nuclear-nuclear distances respectively. The terms in Equation 4.1 represent the electronic kinetic energy, the nuclear-electron attractive potential, the electron-electron repulsive potential, and the nuclear-nuclear repulsive potential, respectively. This Hamiltonian commutes with all symmetry operations of the molecular symmetry point group. The goal of this work is to obtain solutions of the time-independent electronic Schrödinger wave equation

$$\hat{\mathrm{H}}\phi_k(\mathbf{r};\mathbf{R}) = \mathrm{E}\phi_k(\mathbf{r};\mathbf{R}) \qquad (4.2)$$

and then to use this information to obtain nonadiabatic coupling elements between different electronic states as discussed in Chapter 3.

$$\mathrm{F}_{k,k'}(\mathbf{R}) = \sum_{\mathrm{A=1}}^{\mathrm{N}_n} \langle\phi_k| - \frac{\hbar^2}{\mathrm{M_A}}\nabla_{\mathrm{A}}|\phi_{k'}\rangle \cdot \nabla_{\mathrm{A}} \qquad (4.3)$$

$$G_{k,k'}(\mathbf{R}) = \sum_{A=1}^{N_n} \langle \phi_k | -\frac{\hbar^2}{2M_A} \nabla_A^2 | \phi_{k'} \rangle \ . \tag{4.4}$$

Equation 4.2 is a partial differential equation in $3n$ mathematical dimensions. The eigenvalue E is the potential energy of the system at a given nuclear configuration. Solution of Equation 4.2 at various nuclear configurations throughout space gives the potential energy surface. Although analytical methods have made some progress in solving Equation 4.2,[32] the procedure is difficult and does not yield accurate results. At present more accurate methods make use of basis set expansion techniques and variational approaches. The unknown eigenfunctions ϕ_k of Equation 4.2 are expressed in terms of a set of n-particle basis functions Φ. Although many possible functional forms for the Φ can be used, most often they are constructed as a product of one electron molecular orbitals (MOs), ψ;

$$\Phi_K \ = \ \hat{P} \prod_{i=1}^{n} \psi_i \ . \tag{4.5}$$

Here, a given function Φ_K is an n-fold product of MOs, in which the permutation operation has been applied to ensure that it is antisymmetric with respect to interchange of any two electrons as required by the Pauli principle. The Φs obtained in this way are generally referred to as configuration state functions or CSFs.

The molecular orbitals (MOs) are expressed as linear combinations of one-particle basis functions

$$\psi_i \ = \ \sum_{\mu} C_{i\mu} \varphi_{\mu} \ . \tag{4.6}$$

The one-particle basis functions φ_μ are often referred to as atomic orbitals (AOs). This overall scheme is generally referred to as the linear combination of atomic orbitals to produce molecular orbitals method (LCAO-MO). The MO coefficients $C_{i\mu}$ are obtained by solving an electronic structure problem that is simpler in nature than Equation 4.2, such as the independent particle (Hartree-Fock self consistent field) method. This approximation generally provides a good estimate of the solutions of Equation 4.2. However, since it is an independent particle model, the correlation of electrons is neglected. Löwdin[33] has coined the term "correlation energy" to denote the difference between the exact energy obtained from Equation 4.2 and the Hartree-Fock energy.

The most common use of the n-particle basis Φ in solving Equation 4.2 is the linear configuration interaction (CI) expansion

$$\phi_k = \sum_{\mathrm{K}} \mathrm{c_K} \Phi_{\mathrm{K}} \ . \tag{4.7}$$

Equation 4.7 yields exact eigenvalues and eigenfunctions of Equation 4.2 when the one-particle basis is complete (the basis spans the entire one-particle function space). The coefficients $\mathrm{c_K}$ are determined by making the energy stationary with respect to variations in the coefficients, subject to normalization of ϕ_k. All possible choices for the $\mathrm{c_K}$s yield an upper bound to the exact energy.

In practice, a complete one-particle function space is infinite therefore, the complete CI problem is also infinite in dimension. If a finite one-particle space is chosen, and ϕ_k is approximated as in Equation 4.7 using all of the n-particle basis functions, the result is a full CI wave function (FCI). It can be thought of as the exact solution to the Schrödinger equation projected onto the finite subspace generated by the truncated one-particle basis. The number of all of the possible n-particle basis functions has a factorial dependence upon the number of electrons correlated and the number of MOs. This can create insurmountable computational difficulties for most problems of chemical interest. For example, approximately 10^{14} CSFs are required to obtain the dissociation energy of the N_2 molecule to within 5 kcal/mole of the correct value.[31] Only a few FCI bench-mark calculations have been performed which take full advantage of the advances in the supercomputer industry.[34−39] In real applications, especially those aimed at obtaining the potential energy surface of a molecular system, the n-particle space must be truncated due to limited computer memory and speed.

Truncation of the n-particle space can be achieved by using the uncorrelated wave function (which is a very substantial fraction of the exact wavefunction) to classify terms in the n-particle space. Using the Hartree-Fock MOs, all CSFs in the full n-particle space can be constructed by successively exciting one, two,... electrons from the occupied Hartree-Fock MOs to unoccupied MOs. For cases in which several CSFs are present in the zeroth-order wave function via the Hamiltonian in Equation 4.1, a good first approximation would be to truncate the n-particle expansion at this level. Thus producing single and double excitations from Hartree-Fock (SDCI) or its multi-reference analog, multi-reference CI (MR-SDCI). The accuracy of this scheme of single and double excitation has been confirmed by recent full CI (FCI) bench-mark calculations.[31]

Since the truncated CI method is variational in nature, it yields approximate energies which are upper bounds of the true energies. This method can be formulated to handle the case in which the zeroth-order wave function is multi-configurational in character. It is also one of the most widely used methods methods for electronic state calculations today.

B. The MRD-CI Method of Buenker

The use of severely truncated CSF space can lead to an MR-SDCI expansion that in some cases is too long for practical calculations. There are several means by which the dimension of the CSF space can be further reduced.[40−46] Outlined below is the method developed by Buenker and co-workers[42−46], which we have used in our H_3 application. It is based on the individual configuration selection and energy extrapolation technique.

Since in many cases only several low-lying electronic states are of interest, the resulting eigenfunctions of those states are usually dominated by a small number of CSFs, with small contributions from the remaining CSFs. Therefore, the removal of those CSFs with small contributions is likely to have a negligible effect on the final wave functions and their eigen-energies for the electronic states of interest. This implies that the set of dominant CSFs can be used as a set of reference configurations and the full singly and doubly excited CSFs (generated with respect to this set) can be tested individually to ascertain their importance. If there are N_{ref} dominant reference configurations, a small CI calculation with this set is performed and the M eigenvaules of interest are obtained. Since this set of reference CSFs is made up of the dominant CSFs for those M eigenstates, the M eigenvalues obtained should be nearly equivalent to those obtained from a full MR-SDCI calculation. Next, each generated singly and doubly excited CSF with respect to the set of reference configurations is tested individually by adding it to the set of reference configurations and another CI calculation with $N_{ref} + 1$ CSFs is performed. The variational nature of the CI ensures that each eigenvalue obtained using $N_{ref} + 1$ CSFs is lower that the corresponding eigenvalue obtained using N_{ref} CSFs. Only those CSFs that result in a lowering of the energy of any one of the M states by an amount greater than the chosen threshold energy are included in the final CI calculation. If a very large threshold energy is chosen, all generated singly and doubly excited CSFs will fail to lower the eigenvalues enough and will be rejected. On the other hand, if the threshold is chosen to be zero, all generated CSFs will lower the eigenvalues by some amount and will be included, resulting in a full MR-SDCI calculation. In order to insure the convergence of the final CI calculation, the set of reference configurations must be chosen to include all possible dominant CSFs so that the final eigenfunction of each state of interest has at least 90 % of its contribution from the set of reference configurations. This effectively reduces the size of the final CI space without eliminating important contributions from any part of the full single and double excitation CI space.

The eigenvalues obtained using the above method decrease monotonically with decreases in the chosen threshold. Since the dominant CSFs are included in the set of reference configurations, the difference between the eigenvalues obtained using a large threshold and those obtained with the threshold equal to zero (full MR-SDCI) are small. Beunker and coworkers have found that the the eigenvalues depend linearly upon the threshold when the threshold is close to zero.[42−46] By performing two or more CI calculations with different but small (nearly zero) thresholds, the eigenvalues at zero threshold (full MR-SDCI limit) can be obtained through extrapolation.

These two features of the MRD-CI (multi-reference single and double excitation configuration interaction) method of Beunker and coworkers have been very successful in many applications.[42−46] The configuration selection procedure is well suited to all types of electronic states in any nuclear geometry, and the results of the associated CI calculations are nearly equivalent to a complete treatment in which all single and double excitation CSFs with respect to the set of dominant configurations in the given states of interest are included.[42−46]

The Cray version of the MRD-CI codes that were used in this work were supplied by Buenker's group.[42-46] The flowchart of this package with a minimal explanation of the function each code performs is presented in Figure 2. Conceptually, the following steps are taken in our H_3 application.

1. Gaussian-Type atomic orbitals (GTOs) are used.[47] The choice of the AOs will be discussed in detail in the next section.
2. A Hartree-Fock Self-Consistent-Field (SCF) calculation with the set of AOs is performed in an iterative manner. The molecular orbitals (MOs) obtained from the SCF calculation serve as a starting point for the CI calculation.
3. An appropriate set of reference configurations for a given number of electronic states and a threshold energy are chosen. All single and double excitation CSFs with respect to the reference configurations are generated and selected or rejected based upon the chosen threshold.
4. The electronic Hamiltonian including all of the configurations selected is diagonalized.
5. Steps 3 and 4 are repeated with the same set of reference configurations and a new threshold twice as large as that originally chosen. The extrapolation to zero threshold is performed based upon the CI results with two different thresholds resulting in the eigen-energies of the full single and double excitation CI (over the set of reference configurations).
6. The above process steps 1 through 5 is then repeated for a slightly different geometry (one in which only one of the input geometry variables is changed slightly) to obtain the wavefunctions and energies of this new configuration.
7. With the resulting electronic wave functions from the CI calculations with the first (smaller) threshold, and the difference in the chosen input geometry variable the nonadiabatic coupling element between two chosen states $\langle \phi_k | \frac{\mathrm{d}}{\mathrm{d}\mathbf{R}_\mathbf{a}} | \phi_{k'} \rangle$ is then calculated. $\mathbf{R}_\mathbf{a}$ is one of the three input geometry

variables R_1, R_2 or γ as shown in Figure 3. Although these are not the same variables used by Varandas and coworkers, R, r and χ), as shown in Figure 4. They are related by a simple transformation.

$$R_1 = \left\{R^2 + (\frac{r}{2})^2 - rR\cos(\pi - \chi)\right\}^{\frac{1}{2}} \tag{4.8}$$

$$R_2 = r \tag{4.9}$$

$$\gamma = \cos^{-1}\left\{\frac{(R_1^2 + (\frac{r}{2})^2 - R^2)}{rR_1}\right\} \tag{4.10}$$

The program also calculates $\langle \frac{d}{d\mathbf{R}_a}\phi_k | \frac{d}{d\mathbf{R}_a}\phi_{k'} \rangle$. Although this is not one of the coupling elements needed for the calculation of predissociative lifetimes, it is related to the second derivative coupling elements as will be shown later.

8. Performing calculations following the steps presented above gives the energies of all of the chosen states and one coupling element between two of the calculated states. Since the coupling elements with respect to each nuclear geometry variable of all of the calculated states are desired, it is more efficient to do all of this at once. Therefore, step 7. is repeated for all three desired couplings (1-2, 1-3, and 2-3). A complete flow chart for process is shown in Figure 5.
9. The entire process is then repeated for the other two input geometry variables. In this way the original configuration and the changed configurations are calculated only once. This results in a savings of CPU time by more than a factor of three.

From a formal point of view, few complications arise when calculating the second derivative coupling elements $\langle \phi_k | \frac{d^2}{d\mathbf{R}_a^2} | \phi_{k'} \rangle$ directly, however, the required numerical precision increases. To avoid the need for a third closely spaced nuclear configuration CI calculation, use of the following identity is made to obtain the nonmixed second derivative coupling elements.

$$\frac{\mathrm{d}}{\mathrm{d}\mathbf{R}_{\mathrm{a}}}\langle\phi_k|\frac{\mathrm{d}}{\mathrm{d}\mathbf{R}_{\mathrm{a}}}|\phi_{k'}\rangle = \langle\frac{\mathrm{d}}{\mathrm{d}\mathbf{R}_{\mathrm{a}}}\phi_k|\frac{\mathrm{d}}{\mathrm{d}\mathbf{R}_{\mathrm{a}}}\phi_{k'}\rangle + \langle\phi_k|\frac{\mathrm{d}^2}{\mathrm{d}\mathbf{R}_{\mathrm{a}}^2}|\phi_{k'}\rangle \tag{4.11}$$

The second derivative coupling elements therefore require knowledge of the first derivative of the first derivative coupling elements. Since the first derivative coupling elements are being calculated as a function of nuclear configuration (the 3-D grid in the R_1, R_2, γ space) nearby points are used to calculate the derivative of this quantity using a finite difference approximation.

III. Atomic Orbital Basis Set

In depth reviews on basis set selection for molecular calculations have been written by Huzinaga,[47] Wilson.[48] and Davidson *et al.*[49] General considerations for selecting a basis set for an *ab initio* calculation and several useful concepts will be discussed in this section.

A. General Considerations

All CI methods for electronic state calculations employ a variational approach. In principle a complete set of basis functions is equivalent to any other complete set of basis functions. However, in practice complete sets cannot be used since the computational effort increases very quickly with the size of the of the basis set. The basis set chosen should be large enough to produce **good** results over the range of molecular geometries of interest and small enough to make the problem computationally tractable and economically feasible.

In the early days of quantum calculations, the basis sets used generally consisted of atom-centered Slater-type orbitals.[50] Slater-type orbitals (STOs) are defined as follows:

$$\mathrm{X}_{\mathrm{n}\ell\mathrm{m}}(\mathrm{r},\theta,\phi) = \mathrm{R}_{n\ell}(\mathrm{r})\mathrm{Y}_{\ell m}(\theta,\phi) \tag{4.12}$$

$$\mathrm{R}_{n\ell}(\mathrm{r}) = (2\xi_{n\ell})^{n+\frac{1}{2}}[(2n)!]^{-\frac{1}{2}}\mathrm{r}^{n-1}\mathrm{e}^{-\xi_{n\ell}\mathrm{r}} \ , \tag{4.13}$$

where ℓ and m are angular momentum quantum numbers and the Y_{lm} are the spherical harmonics. ξ_{nl} is the orbital exponent. The coordinate variables (r,θ,ϕ) describe the position of an electron with respect to the position of the nucleus. The main advantage of STOs are that their short- and long-range behavior is very similar to the exact radial wave functions of the H atom. The major disadvantage with these types of orbitals is the difficulty of the numerical integrations required for molecular calculations.

This difficulty was overcome by introduction of Gaussian-type orbitals (GTOs) for the construction of the Hamiltonian matrix by Boys.[51] They are defined as:

$$\mathrm{X}_{n\ell m}(\mathrm{r},\theta,\phi) = \mathrm{R}_{nl}(\mathrm{r})\mathrm{Y}_{\ell m}(\theta,\phi) \tag{4.14}$$

$$\mathrm{R}_{n\ell}(\mathrm{r}) = \mathrm{N}(n,\alpha)\mathrm{r}^{n-1}\mathrm{e}^{-\alpha \mathrm{r}^2} \tag{4.15}$$

$$\mathrm{N}(n,\alpha) = 2^{n+1}[(2n-1)!!]^{-\frac{1}{2}}(2\pi)^{-\frac{1}{4}}\alpha^{\frac{(2n+1)}{2}} \tag{4.16}$$

$$n = \ell+1, \ell+3, \ell+5, ...$$

where the !! sign indicates the product $(2n-1)(2n-3)(2n-5)...$, α is a conventionally chosen range parameter and $\mathrm{N}(n,\alpha)$ is the normalization coefficient. In molecular calculations, the Cartesian coordinate system is generally used and the normalized, primitive GTOs in these coordinates are defined as:[52-54]

$$\mathrm{X}_{kmn}(\mathrm{x},\mathrm{y},\mathrm{z};\alpha) = N(k,m,n;\alpha)x^k y^m z^n e^{-\alpha r^2} \tag{4.17}$$

$$N(k,m,n;\alpha) = (\frac{2}{\pi})^{\frac{3}{4}}[(2k-1)!!(2m-1)!!(2n-1)!!]^{-\frac{1}{2}}\alpha^{\frac{[k+m+n+\frac{3}{4}]}{2}} \tag{4.18}$$

Note that (k,m,n) in Equation 4.17 are completely different from (n,ℓ,m) in Equation 4.14. The GTOs are of the following types:

$$\mathrm{X} \propto \mathrm{e}^{-\alpha \mathrm{r}^2} \qquad \mathrm{s-type}: k+m+n=0 \tag{4.19}$$

$$\mathrm{X} \propto (\mathrm{x},\mathrm{y},\mathrm{z})\mathrm{e}^{\alpha \mathrm{r}^2} \qquad \mathrm{p-type}: k+m+n=1 \tag{4.20}$$

$$\mathrm{X} \propto (\mathrm{x}^2,\mathrm{y}^2,\mathrm{z}^2,\mathrm{xy},\mathrm{xz},\mathrm{yz})\mathrm{e}^{\alpha \mathrm{r}^2} \qquad \mathrm{d-type}: k+m+n=2 \tag{4.21}$$

The choice of the Cartesian primitive GTOs has been made for ease of coding. However, this choice results in two important consequences. The first of which is a self imposed restriction on the power or r in Equation 4.15 for atomic calculations. The power is restricted to the lowest for each symmetry, $n = \ell + 1$. Only 1s-type GTOs are used to expand all s-type atomic orbitals, only 1p-type GTOs are used to expand all p-type atomic orbits, and similarly for d- and f-type atomic orbitals. This restriction can be compensated for by combining many 1s-type (or 1p-type) functions with various exponents. The second consequence of the choice of the Cartesian primitive GTOs is the redundancy in the d- and higher symmetries. The d-orbitals can be thought of as a proper 5-member d-type orbital set plus one isotropic 3s-type orbital

$$(3z^2 - r^2, x^2 - y^2, xy, xz, yz)\ e^{-\alpha r^2} \tag{4.22}$$

$$(x^2 + y^2 + z^2)\ e^{-\alpha r^2} \ = \ r^2 e^{-\alpha r^2} \tag{4.23}$$

Similarly, the 10-member f-type orbitals contain three 4p-type orbitals

$$(\mathrm{x}, \mathrm{y}, \mathrm{z},)\mathrm{r}^2 \mathrm{e}^{-\alpha \mathrm{r}^2} \tag{4.24}$$

in addition to the proper 7-member set of f-orbitals.

The exponents α and the number of GTOs used are parameters which must be tuned for a given molecular sytem under investigation. Although the use of more tunable parameters results in greater flexibility, too many can make the problem untractable. This is especially true for many exponents, since optimization is achieved using a time consuming non-linear process.

A major reason for the choice of GTOs as basis functions is that integrals involving GTOs can be evaluated analytically. However, because an individual

Gaussian-type function has the wrong behavior both near and far away from the nucleus, more GTOs are required to describe an atomic wave function than would be necessary if STOs were used. On the other hand, integrals involving STOs are computationally expensive and often intractable for molecules. The disadvantage associated with the large number of GTOs (resulting in many parameters in the basis set needing to be determined and optimized) compared to STOs is compensated for by the use of **contracted** Gaussians.[52−54] Rather than using individual Gaussian-type functions, fixed linear combinations of them are used as basis functions.

$$\mathrm{X}_{\mathrm{contr}}(k,m,n) \;=\; \sum_{i} \mathrm{C}_i \mathrm{X}_{kmn}(\alpha_i) \qquad (4.25)$$

The coefficients C_i are chosen to give a good description of the atomic wavefunctions. The use of such contracted Gaussians has the advantage of easy integration of the primitive functions, a smaller number of parameters to be optimized (and therefore a more compact basis set) as well as a good description for the behavior desired in the basis functions. The use of contracted Gaussians for basis functions has become a method of choice for molecular structure calculations.

To obtain reasonable contracted basis functions, a good set of primitive Gaussian-type functions must be chosen. Molecules can be thought of as a collection of slightly distorted atoms. Therefore, requiring that the primitive basis set provide an accurate description of the atoms is only natural. Most Gaussian primitive basis sets are constructed by optimization of the Hartree-Fock-Self-Consistent-Field (SCF) energy of the atoms. This is especially true for the H atom since it possesses only one electron. Huzinaga[55] was the first to publish an optimized Gaussian primitive set for atomic SCF energies. Since then, Davidson *et al.*[56–57] have made several improvements. Their results can be used directly as the choice of Gaussian primitives for any new calculation.

Examination of the optimum exponents of a set of Gaussian primitives reveals a nearly constant ratio between successive exponents of the Gaussian primitives in the valence region. This suggests that the use of an **even-tempered** or geometric sequence of exponents ($\alpha_i = a * \beta_i$, where a and β are two parameters) would be a good approximation for the independently optimized set.[58–59] Use of such a basis set reduces the number of parameters to be optimized and makes the construction of the basis set much easier. Ruedenberg and coworkers[60–61] found good agreement between independently optimized exponent sets and even-tempered exponent sets. The use of even-tempered exponent sets has also become a method of choice for molecular structure calculations.

Contraction coefficients for the Gaussian primitives used are generally obtained by one of the following three methods. The first method is referred to in the literature as the STO-nG scheme.[55] In this method, several Gaussian type functions are linearly combined to mimic the behavior of a single Slater-type function. The orbital exponents for STOs are chosen as the average of the best exponents found in molecular calculations. The results of the STO-nG expansion give the exponents and the contraction coefficients needed. However, this method generally produces rather poor atomic energies. The second method used to obtain contraction coefficients is direct optimization of atomic SCF calculations. In this method, the coefficients are treated as independent variables to be optimized. The third method involves the simultaneous optimization of the Gaussian exponents and contraction coefficents based on atomic SCF energies. The first method is very easy to perform, but generally leads to poor results. The third method is the most accurate, but is also the most time consuming method due to the non-linear optimization procedure.

B. The Basis Set and Selection Criteria

The goal of this work is to achieve good descriptions for the lowest three electronic states of the H_3 system for use in calculating the nonadiabatic coupling elements between these states. Previous results from an empirical diatom-in-molecule (DIM) calculation of H_3 [14] show that the lowest five states in the asymptotic region of $H_2 + H$ correlate with the following states.

$$H_2(X^1\Sigma_g^+) + H(1s)$$

$$H_2(X^1\Sigma_g^+) + H(2s, 2p_x, 2p_y, 2p_z)$$

and

$$H_2(b^3\Sigma_u^+) + H(1s) \rightarrow 3H(1s)$$

The basis set chosen for our calculations should therefore be able to describe the atomic states of H(n=1) and H(n=2), and the two lowest diatomic states $H_2(X^1\Sigma_g^+)$ and $H_2(b^3\Sigma_g^+)$. In addition, the basis set must satisfy the following criteria be satisfied.

1. Accurate atomic excitation energies for 1s → 2s and 1s → 2p transitions.
2. Accurate values for the H_2 energy in its ground state $X^1\Sigma_g^+$ and excited state $b^3\Sigma_u^+$.
3. A ground state surface for H_3 of comparable accuracy to that of the LSTH surface.
4. Reasonable agreement with the known Rydberg spectrum of H_3 and the results of recent calculations by Petsalakis *et al.*[15] and Diercksen *et al.*[16]

In addition to the above mentioned criteria, our choice of the basis set used was guided by studies of the H_3^+ and H_2 systems, both in their ground electronic states[1-2,62-64] and their Rydberg excited electronic states.[5-16,65]

The basis sets used by Lui and Sieghban[2] for the ground state of H_3 and by Talbi and Saxon[65] for the Rydberg spectrum of H_3^+ were adapted for our work. It has been shown that these two sets of basis functions provide good descriptions of the electronic valence bond and the Rydberg n = 2 states of H. The valence (9s/4s) (four s-type contracted GTO basis functions obtained from nine s-type primitive GTO functions) basis was taken from Lui and Sieghban,[2] and has an outer exponent of 0.06618. Three additional Rydberg s-functions were added, with an approximately even-tempered ratio of 2.4, resulting in exponents of 0.02758, 0.01149 and 0.00420. The polarization (Rydberg) p-basis was taken from Talbi and Saxon,[65] with exponents of 1.6, 0.4, 0.09 and 0.025. In addition, the 6-component d-function with an exponent of 1.0 was taken from Lui and Seighban.[1,2] The full basis set, denoted (12s4p1d/7s4p1d) is made up of 25 contracted AOs, of which three s-functions and two p-functions are essentially Rydberg in character. The parameters of the full basis set are listed in Table 1.

To allow for proper dissociation of the H_3 molecule, it was necessary to place the full AO set on each nuclei, resulting in a total basis set size of 75 AOs. This was necessary for mapping the potential energy and nonadiabatic coupling surfaces over a wide range of nuclear configurations.

Use of such a diffuse overlapping basis of 75 functions may have led to linear dependence problems as discussed by Talbi and Saxon.[65] However the use of the HONDO routine[66] for evaluating the necessary integrals with its high accuracy helped to eliminate this problem.

C. Basis Set Calibration

The quality of the AO basis set used for these calculations was tested by a previous student in our lab.[17-18] With the basis set of (12s4p1d/7s4p1d), the

1s → 2s transition energy of 10.2045 eV is within 0.0001 eV of the exact value. The 1s → 2p transition energy of 10.2118 eV is less accurate differing from the exact value by 0.0074 eV due to the smaller number of Rydberg p-basis, but is still reasonable.

The energy of the ground state $H_2(X^1\Sigma_g^+)$ is close to that calculated by Lui[1] and more accurate than that calculated by Lui and Seighban.[2] The D_e calculated at 1.40 bohr is 4.7255 eV, it differs from the exact value of 4.7477 eV by 0.02 eV. The excited state of $H_2(b^1\Sigma_u^+)$ which has the configuration of $\sigma_g\sigma_u$, was found to lie 10.605 eV above the ground state. Kolos and Wolniewicz[67] calculated a value of 10.623 eV, therefore this valence shell transition is also accurate to within 0.02 eV.

Table 1: (12s/7s, 4p, 1d) Gaussian-type basis set

Orbital	i	ξ_i	C_i
1s	1	837.22	.000112
	2	123.524	.000895
	3	27.7042	.004737
	4	7.82599	.019518
	5	2.6504	.065862
	6	.938258	.178008
2s	1	.372145	1.00000
3s	1	.155838	1.00000
4s	1	.066180	1.00000
5s	1	.027580	1.00000
6s	1	.011490	1.00000
7s	1	.004200	1.00000
1p	1	1.6	1.00000
2p	1	.40	1.00000
3p	1	.09	1.00000
4p	1	.025	1.00000
1d	1	1.0	1.00000

IV. References

1. B. Liu, *J. Chem. Phys.* **58**, 1925 (1973).
2. P. Seigbahn and B. Liu, *J. Chem. Phys.* **68**, 2457 (1978).
3. D.G. Truhlar and C.J. Horowitz, *J. Chem. Phys.* **68**, 2466 (1978); **71**, 1514(E) (1979).
4. A.J.C. Varandas, F.B. Brown, C.A. Mead, D.G. Truhlar and N.C. Blais, *J. Chem. Phys.* **86**, 6258 (1987).
5. H.F. King and K. Morokuma, *J. Chem. Phys.* **71**, 3213 (1979).
6. M. Jungen, *J. Chem. Phys.* **71**, 3213 (1979).
7. R.L. Martin, *J. Chem. Phys.* **71**, 3541 (1979).
8. K.C. Kulander and M.F. Guest, *J. Phys.* **B12**, L501 (1979).
9. Ch. Nager and M. Jungen, *Chem. Phys.* **70**, 189 (1982).
10. S. Raynor and D.R. Herschbach, *J. Chem. Phys.* **86**, 3592 (1982).
11. H.J. Foth, H.R. Mayne, R.A. Poirer and J.C. Polanyi, *J. Chem. Phys.* **80**, 4025 (1984).
12. H.R. Mayne, R.A. Poirer and J.C. Polanyi, *J. Chem. Phys.* **80**, 4025 (1984).
13. H.R. Mayne, J.C. Polanyi, N. Sathyamurthy and S. Raynor, *J. Chem. Phys.* **88**, 4064 (1984).
14. A.C. Roach and P.J. Kuntz, *J. Chem. Phys.* **84**, 822 (1986).
15. I. Petsalakis, J. Theodorakopoulos and J.S. Wright, *J. Chem. Phys.* **89**, 6850 (1988).
16. G.H.F. Diercksen, W. Duch and J. Karwowski, *Chem. Phys. Lett.* **168**, 69 (1990).
17. Z. Peng, A. Kuppermann and J.S. Wright, *Chem. Phys. Lett.* **175**, 242 (1990).
18. Z. Peng, *Ph.D. Thesis*, California Institute of Technology, 1991.

19. N.C. Blais, D.G. Truhlar and C. Alden Mead, *J. Chem. Phys.* **89**, 6204 (1988).
20. G. Herzberg, *Ann. Rev. Phys. Chem.* **38**, 27 (1987).
21. J.K.G. Watson, in press.
22. G.I. Gellene and R.F. Porter, *Acc. Chem. Res.* **23**, 141 (1990).
23. G. Gellene and R.F. Porter, *J. Chem. Phys.* **79**, 5975 (1983).
24. J.F. Garvey and A. Kuppermann, *Chem. Phys. Lett.* **107**, 491 (1984).
25. G. Herzberg, *J. Chem. Phys.* **70**, 4086 (1979).
26. I. Dabrowski and G. Herzberg, *Can. J. Phys.* **58**, 1238 (1980).
27. G. Herzberg and J.K.G. Watson, *Can. J. Phys.* **58**, 1250 (1980).
28. G. Herzberg, H. Lew, J.J. Sloan and J.K.G. Watson, *Can. J. Phys.* **59**, 428 (1981).
29. G. Herzberg, J.T. Hougen and J.K.G. Watson, *Can. J. Phys.* **60**, 1261 (1982).
30. K.P. Lawley, editor *Adv. in Chem. Phys.: Ab Initio Methods in Quantum Chemistry*, **Vol. 67, 69**, Wiley, New York, 1987.
31. C.W. Bauschlicher,Jr., S. Langhoff and P.R. Taylor, *Adv. in Chem. Phys.* **20**, 103 (1990).
32. K. McIsaac and E.N. Maslen, *Int. J. Quan. Chem.* **31**, 361 (1987).and references therein.
33. P.O. Löwdin, *Adv. in Chem. Phys.* **2**, 207 (1959).
34. P.E.M. Siegbahn, in *Quantum Chemistry: The State of Art*, V.R. Saunders and J. Brown, editors, Science Research Council, Didcot Oxon., 1975, p. 81.
35. P.E.M. Seigbahn, *Chem. Phys. Lett.* **109**, 417 (1984).
36. P.J. Knowles and N.C. Handy, *Chem. Phys. Lett.* **111**, 315 (1984).
37. C.W. Bauschlicher and P.R. Taylor, *J. Chem. Phys.* **85**, 2779 (1986).
38. P.J. Knowles, *Chem. Phys. Lett.* **155**, 513 (1989).
39. P.J. Knowles and N.C. Handy, *J. Chem. Phys.* **91**, 2396 (1989).

40. P.E.M. Seigbahn, *Int. J. Quan. Chem.* **23**, 1869 (1983).

41. H.J. Werner and P.J. Knowles, *J. Chem. Phys.* **89**, 5803 (1988).

42. R.J. Buenker and S.D. Peyerimhoff, *Theoret. Chim. Acta* **35**, 33 (1974).

43. R.J. Buenker, S.D. Peyerimhoff and W. Bitscher, *Molec. Phys.* **35**, 771 (1978).

44. R.J.Buenker, in: *Molecular Physics and Quantum Chemistry in the 80s*, Ed. P.G. Burton (Univ. of Wollongong, Wollongong, 1980).

45. R.J. Buenker, in: *Studies in Physical and Theoretical Chemistry*, **Vol 21** (Current Aspects of Quantum Chemistry 1981), Ed. R. Carbo (Elsevier Scientific, Amterdam, 1982), p. 17.

46. R.J. Buenker and R.A. Phillips, *J. Mol. Structure* **123**, 291 (1985).

47. S. Huzinaga, *Comp. Phys. Rep.* **2**, 279 (1985).

48. S. Wilson, in: *Methods in Computational Physics*, G.H. Diercksen and S. Wilson, Eds. (Dorrecht, The Netherlands, Reidel, 1983).

49. E.R. Davidson and D. Feller, *Chem. Rev.* **86**, 681 (1986).

50. J.C. Slater, *Phys. Rev.* **36**, 57 (1930).

51. S.F. Boys, *Proc. Royal Soc. London Ser. A* **200**, 542 (1950).

52. E. Clementi, *IBM J. Res. and Dev.* **9**, 2 (1965).

53. J.L. Whitten, *J. Chem. Phys.* **44**, 359 (1966).

54. E. Clementi and D.R. Davis, *J. Comp. Phys.* **1**, 223 (1967).

55. S. Huzinaga, *J. Chem. Phys.* **42**, 1293 (1965).

56. E.R. Davidson, L.E. McMurchie and S. Days, *J. Chem. Phys.* **74**, 739 (1981).

57. E.R. Davidson and D. Feller, *Chem. Phys. Lett.* **104**, 54 (1984).

58. K. Ruedenberg, R.C. Raffenetti, R.D. Bardo, in: *Energy, Structure and Reactivity, Proc. of the 1972 Boulder Conference*, (Wiley, New York, 1973).

59. R.D. Bardo and K. Ruedenberg, *J. Chem. Phys.* **60**, 918 (1974).

60. D. Feller and K. Ruedenberg, *Theoret. Chim. Acta* **71**, 231 (1979).

61. M.W. Schmidt and K. Ruedenberg, *J. Chem. Phys.* **71**, 3951 (1979).

62. G.D. Carney and R.N. Porter, *J. Chem. Phys.* **65**, 3547 (1976).

63. C.E. Dykstra and W.C. Swope, *J. Chem. Phys.* **70**, 1 (1979).

64. W. Meyer, P. Botschwina and P. Burton, *J. Chem. Phys.* **84**, 891 (1986).

65. D. Talbi and R.P. Saxon, *J. Chem. Phys.* **89**, 2235 (1988).

66. The program HONDO can be obtained from the Quantum Chemistry Program Exchange. In the MRD-CI package, it is used solely for the integral evaulation step.

67. W. Kolos and L. Wolniewiez, *J. Chem. Phys.* **43**, 2429 (1965).

V. Figure Captions

Figure 1. Energy level and correlation diagram for the H_3 molecule. The spacing of the H_3 energy levels was calculated for an equilateral triangle D_{3h} configuration and is shown relative to the energy of the dissociated products $H + H_2$ from a separate calculation.

Figure 2. Flow chart of the MRD-CI programs. The name of each individual routine is listed along with a brief description of the function which it performs.

Figure 3. Coordinate system used in the MRD-CI program. P_i is the ith proton of the H_3 molecule. The three protons all lie in the xy-plane. The variables describing the shape of the triangle are R_1, the bond distance between P_1 and P_3, R_2, the bond distance between P_1 and P_2, and γ, the bond angle between R_1 and R_2.

Figure 4. The coordinate system used by Varandas and coworkers.[4] P_i is the ith proton of the H_3 molecule. The three protons all lie in the xy-plane. The variables describing the shape of the triangle are r, the bond distance between P_1 and P_2, R, the bond distance between P_3 and the center of mass of P_1P_2, and γ, the bond angle between r and R.

Figure 5. Flow chart of the MRD-CI programs as used in our application. The name of each individual routine is listed along with a brief description of the function which it performs.

Figure 1.

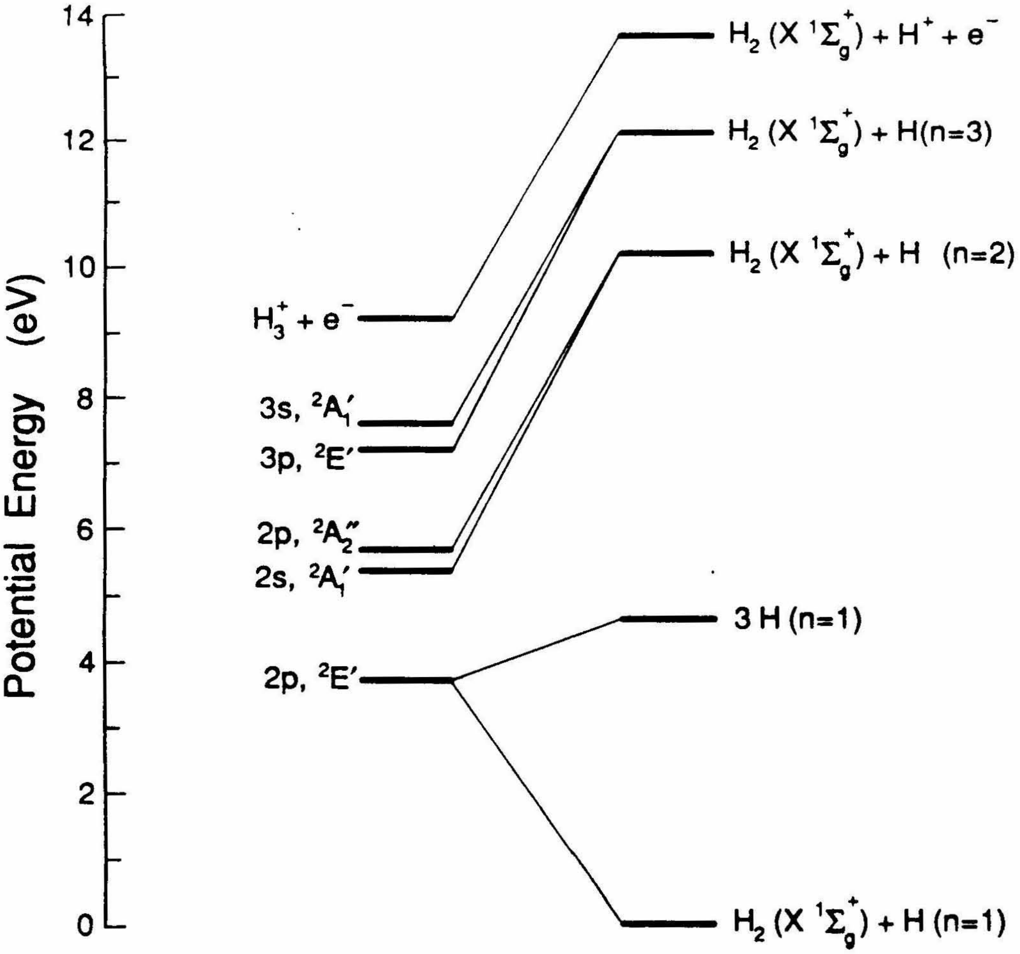
Potential Energy (eV)
14
12
10
8
6
4
2
0
$H_3^+ + e^-$
3s, $^2A_1'$
3p, $^2E'$
2p, $^2A_2''$
2s, $^2A_1'$
2p, $^2E'$
$H_2 (X\ ^1\Sigma_g^+) + H^+ + e^-$
$H_2 (X\ ^1\Sigma_g^+) + H(n=3)$
$H_2 (X\ ^1\Sigma_g^+) + H\ (n=2)$
3 H (n=1)
$H_2 (X\ ^1\Sigma_g^+) + H\ (n=1)$

Figure 2.

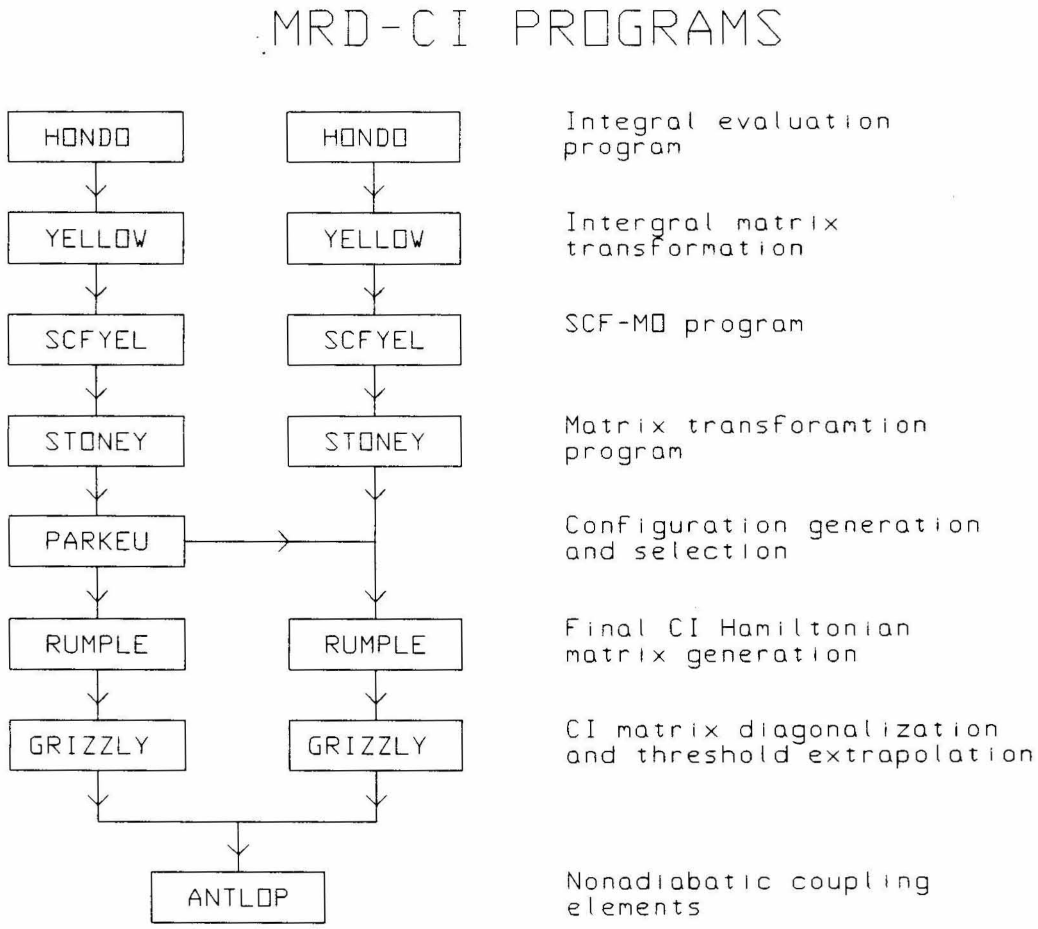
MRD-CI PROGRAMS
HONDO
HONDO
Integral evaluation program
YELLOW
YELLOW
Intergral matrix transformation
SCFYEL
SCFYEL
SCF-MO program
STONEY
STONEY
Matrix transforamtion program
PARKEU
Configuration generation and selection
RUMPLE
RUMPLE
Final CI Hamiltonian matrix generation
GRIZZLY
GRIZZLY
CI matrix diagonalization and threshold extrapolation
ANTLOP
Nonadiabatic coupling elements

Figure 3.

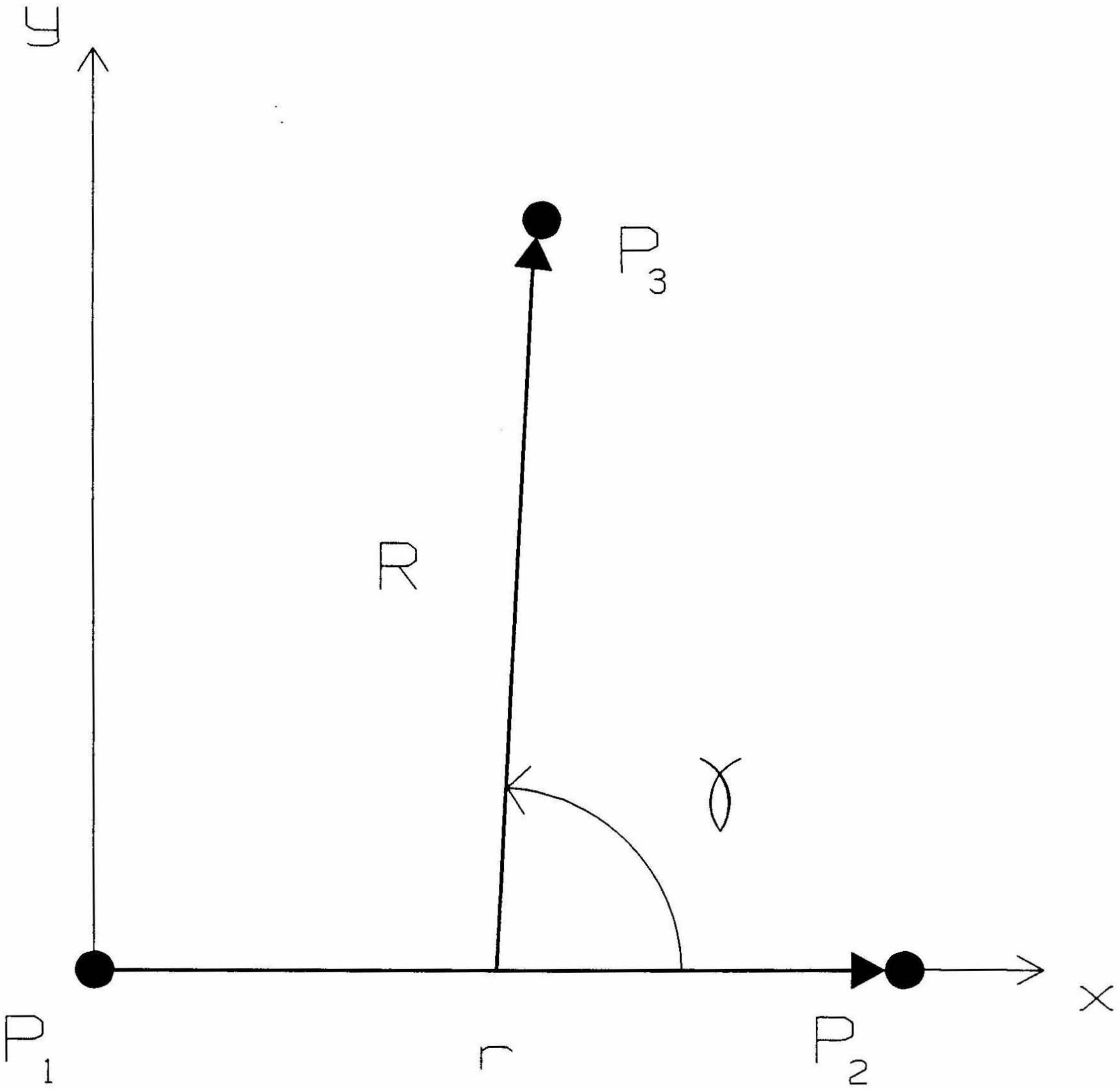

Figure 4.

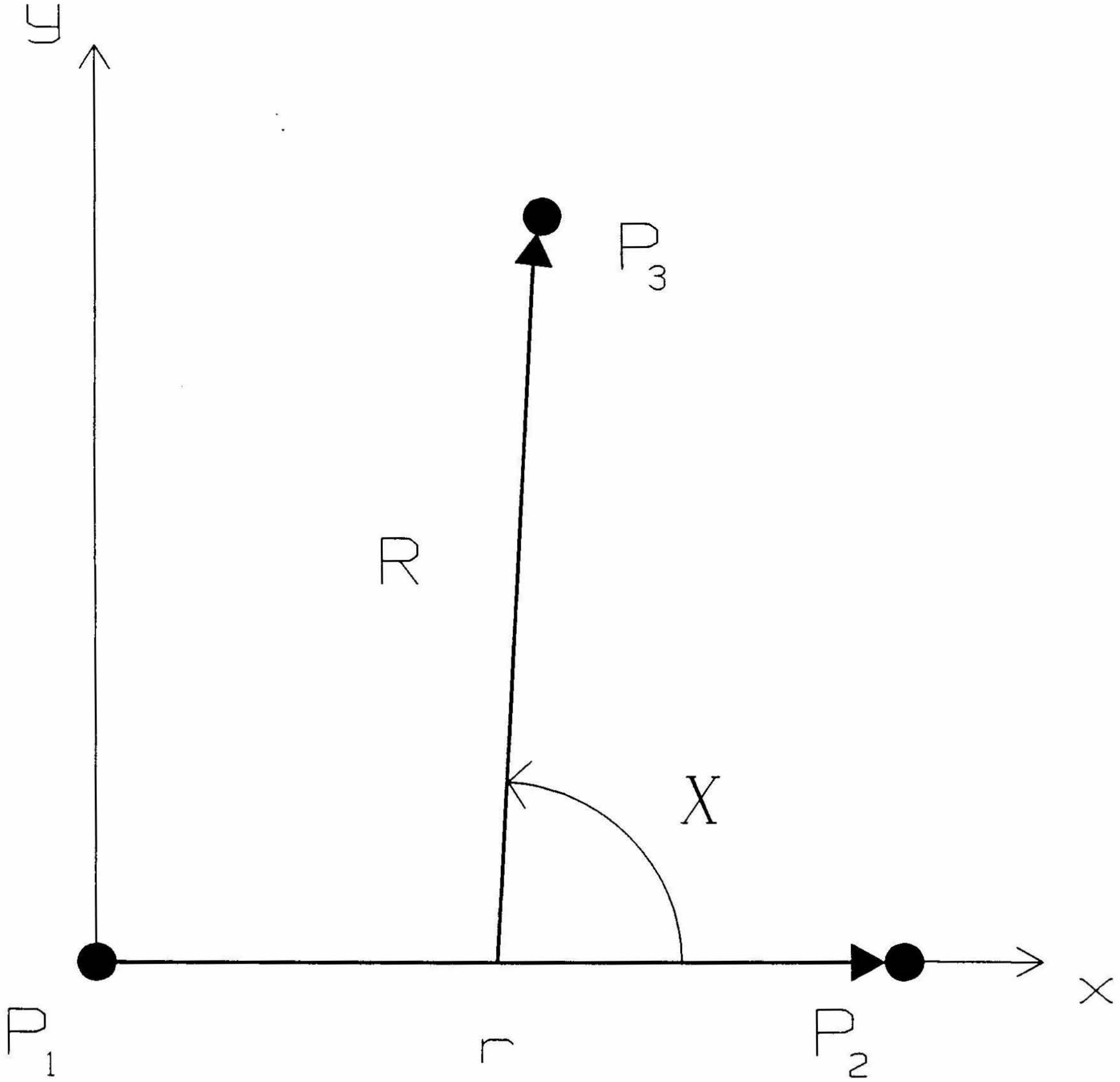

Figure 5.

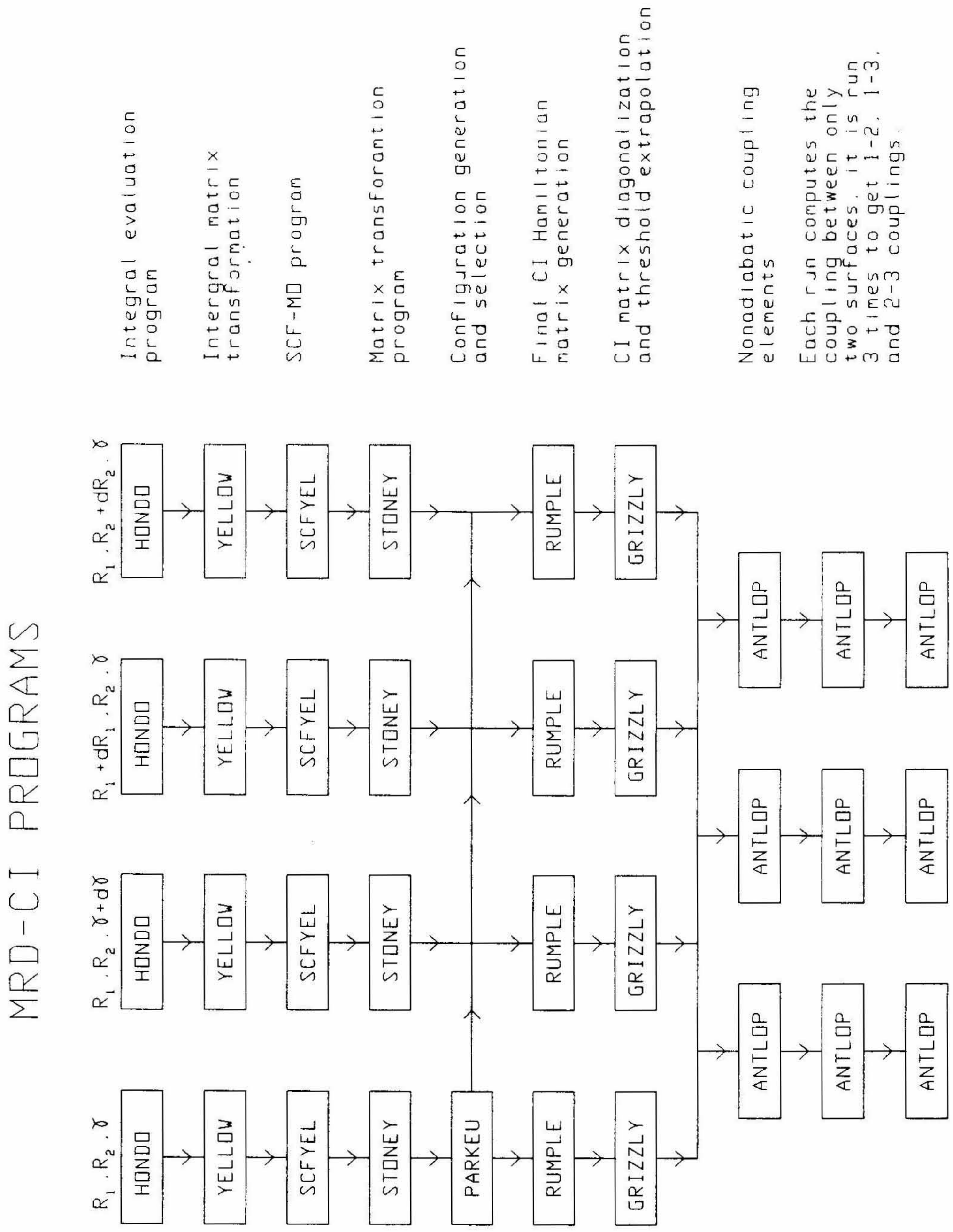
MRD-CI PROGRAMS
R1, R2, γ
R1, R2, γ+dγ
R1+dR1, R2, γ
R1, R2+dR2, γ
HONDO
YELLOW
SCFYEL
STONEY
PARKEU
RUMPLE
GRIZZLY
ANTLOP
Integral evaluation program
Intergral matrix transformation
SCF-MO program
Matrix transforamtion program
Configuration generation and selection
Final CI Hamiltonian matrix generation
CI matrix diagonalization and threshold extrapolation
Nonadiabatic coupling elements
Each run computes the coupling between only two surfaces. it is run 3 times to get 1-2, 1-3, and 2-3 couplings.

Chapter 5.

Ab Initio MRD-CI Calculation Results for H_3

I. Details of the Ab Initio Calculation

The results of the *ab initio* calculations are given in an extensive series of tables as Appendix 1 to this dissertation. Before discussing these results, some of the details of our application of the MRD-CI method for H_3 are discussed. The molecule was placed in the xy-plane, see Figure 1. All calculations were carried out using the point group C_s, even though at many of the nuclear geometries the symmetry of the molecular point group was higher (D_{3h}, C_{2v}). The reason for choosing this lower symmetry was to insure that the calculated energies and wavefunctions varied smoothly over the range of nuclear geometries calculated. Under C_s symmetry, the symmetry type A' is symmetric with respect to the xy-plane and the symmetry type A'' is antisymmetric with respect to the xy-plane.

The SCF-MOs were constructed using the occupation $(1a')^2(1a'')^1$, which is the most dominant MO configuration for the $2p_z^2A_2''$ electronic state when the molecule is in an equilateral triangle configuration which is its equilibrium configuration. This choice of occupation configuration was chosen to provide an even-handed description for the two degenerate $2p_{x,y}^2E'$ (the ground and first excited) electronic states for the equilateral triangle configurations.

The choice of 75 AOs leads to 75 AOs plus linear combinations of these AOs in the SCF step. If it were necessary to reduce the size of the CI space or to remove possible linear dependencies in the AO basis set, some of the MOs could have been deleted before the CI step. Fortunately, it was not necessary to do this in our application and all 75 MOs were kept in the final CI step.

The CI space of A' symmetry was constructed using between 45 and 49 reference configurations, depending upon the nuclear geometry. The selection threshold energy used was 2 μhartree, and the lowest three eigenvalues of this symmetry were obtained. This led to the generation of between 50,000 and 60,000 configuration functions out of which between 5,000 and 6,000 were selected for the final CI calculation.

Using the symmetry notation of the point group associated with an equilateral triangle (D_{3h}), the three lowest states of A' symmetry which were calculated correspond to:

1) E_1 the ground state $^2E'$ ($1a'^2 1e'$),

2) E_2 the state degenerate with the ground state in the equilateral triangle geometry $^2E'$ ($1a'^2 1e'$),

3) E_3 the second excited state $^2A'_1$ ($1a'^2 2s$).

Although E_1 and E_2 are degenerate in that geometry, the degeneracy is lifted as the triangle is distorted, and this leads to the conical intersection between E_1 and E_2.

Nonadiabatic coupling elements between these three states were calculated at many nuclear geometric configurations. However, all of the second derivative coupling elements could not be calculated due to the indirect way in which they are obtained and the limited number of cuts in nuclear geometry space. When a more complete 3D grid in the nuclear geometry space is calculated, all of the non-mixed second derivatives at each point can be determined. One motivation for the present calculations is to provide the nonadiabatic coupling elements for use in scattering studies. Since hyperspherical coordinates provide a simpler means of performing 3-D quantum mechanical scattering calculations,[1-4] the nonadiabatic coupling elements in terms of these variables are desired. The mixed second derivative coupling elements are needed to transform from the coordinate system used to the hyperspherical system, however the mixed second derivatives cannot be calculated with the codes used. In principle modifying these codes in such a way as to allow calculation of the mixed second derivatives should be relatively simple. However, this requires detailed knowledge of the inner workings of these codes which are very long and poorly documented. Such modifications are part of the planned future work. In addition, it would have been desirable to obtain the nonadiabatic coupling elements between E_4 ($^2A_2''$ ($1a'^2 2p_z$)) and E_1, E_2, and E_3 states. However, due to the difference in symmetries of these states and the method employed, the nonadiabatic coupling elements calculated between these states are zero. It is believed that the nonadiabatic coupling which occurs between these states is a result of rotational motion about an axis perpendicular to the symmetry axis of the molecule and such rotations are not included in the calculation.

Since the electronic wave functions have been determined by the variational calculation to within a phase factor (real electronic wave functions can only have a phase factor of ± 1), all nonadiabatic coupling elements are subject to a possible sign change. In many cases it was obvious when a change of sign was warranted. In others, it became necessary to calculate additional points around the region of question.

The calculations were performed on the CRAY Y-MPs of the Jet Propulsion Laboratory, NSF-San Diego Supercomputing Center and NASA Ames Research Center. The CPU time on the CRAY Y-MP machines for a complete calculation of 1 derivative type between two states took 9 to 15 minutes. A calculation of the 3 derivative types between 3 states (resulting in 9 first derivative coupling elements, and 9 second derivative coupling elements once a 3D grid is completed) generally took 35 to 50 minutes. The intermediate files generated during a calculation can be as large as 38 Mwords.

II. General Features of the Potential Energy Surfaces and of the Nonadiabatic Coupling Elements

A. Convergence Criteria

To speak of the convergence of the calculations performed in this work, several factors need to be taken into consideration. The first of which is the basis set used. As discussed previously, the basis set was chosen using a list of criteria to help accurately describe the lowest four electronic states of H_3 throughout nuclear configuration space. For a more detailed description of the selection criteria used see Chapter 4 Section III.B. The accuracy of the calculations using this basis set is discussed in Chapter 4 Section III.C. The second factor that should be considered is the threshold energy used for the selection or rejection of single and double excitation CSFs. As mentioned earlier, the threshold energy used in our calculations was 2 μhartree. As discussed in Chapter 4 Section II.B the MRD-CI method of Buenker used in this work calculates the wavefunctions and eigenvalues (energies) for the initially chosen threshold and for a threshold of twice that size. Since the eigen-value dependence is essentially linear for small thresholds, extrapolation to zero provides the MR-SDCI limit. The threshold used was chosen to satisfy the above criteria for linearity, making the calculations almost equivalent to the MR-SDCI limit. However, this only provides the MR-SDCI limit for the eigenvalues, not the wavefunctions and hence the nonadiabatic coupling elements.

The third factor that must be considered affects only the nonadiabatic coupling elements, not the wavefunctions or the energies. As discussed in Chapter 4 the first derivative coupling elements are calculated by repeating the MR-DCI calculation at a slightly different geometry (one in which only one of the input geometry variables is changed slightly) and a finite difference technique is used to obtain the derivative of the wavefunction. The size of the difference in the input geometry variable can have profound effects upon the calculated nonadiabatic coupling element. If the chosen difference is too large, narrow features in the nonadiabatic coupling elements can be minimized or even completely absent. If the difference chosen is too small round off in the computation can lead to erroneous results. Since the second derivative coupling elements are also calculated numerically, they also depend upon this difference as well as the grid size chosen for neighboring points. To address these difficulties, a rather large grid size was used in regions of nuclear configuration space where the first derivative coupling elements were varying slowly and a much finer grid was used in regions where the first derivative coupling elements were changing rapidly. This not only gave better estimates of the second derivative coupling elements, it helped to map out resonances in the first derivative coupling elements more completely.

To determine the appropriate size for the difference in the input geometry variable to be used, the variation of the nonadiabatic coupling element with this difference dR_a where R_a corresponds to one of the three input geometry variables R_1, R_2 and γ was examined. Ideally such a study would be done for each nuclear geometry, each input geometry variable and each different coupling examined. However, due to the large amount of time these calculations require and the limited computer time available to perform these calculations, only two geometries were examined. The first geometry examined was, $R = 0.7$ bohr, $r = 0.97$ bohr and$\chi = 89°$ (For a pictorial representation of these coordinates, see Figure 2). This corresponds to a geometry along one of the cuts examined by Varandas and coworkers[5-6] (see Chapter 2, Figure 3b). As can be seen from the present results shown in Figure 3, the nonadiabatic coupling element varies slowly for values of dr less than 0.004 bohr and then drops rapidly to large negative values for larger dr. At this geometry, any value of dr less than 0.004 bohr would give a correct qualitative picture of the behavior of the nonadiabatic coupling element. However, choosing dr to be as close to zero as possible without introducing round off error produces more accurate results since the formal equivalence between finite difference and derivative occurs at zero difference. Therefore, we chose to use a dr of 0.0001 bohr for repeating the calculations of Varandas and coworkers.

In addition to the above geometry, we examined the variation of the first derivative coupling elements at $\gamma = 59°\mathrm{and}\mathrm{R}_1 = \mathrm{R}_2 = 1.91$ bohr. The coupling elements with repect to γ oscillated somewhat as $\mathrm{d}\gamma$ was varied, and therefore a neighboring point was also examined ($\gamma = 59°$ and $\mathrm{R}_1 = \mathrm{R}_2 = 1.92$ bohr). The results for γ are shown in Figure 4. Examining these graphs, we chose to use a $\mathrm{d}\gamma$ of 0.01 degrees for our calculations. The coupling elements with respect to R_1 and R_2 are shown in Figures 5 and 6. The coupling elements between states 1 and 2, and between states 2 and 3 both showed flat regions for values of $\mathrm{dR}_1 = \mathrm{dR}_2 \geq 0.0001$ bohr. However, the coupling elements between states 1 and 3 increased with dR_1 or dR_2 for all values examined. Since we are mainly interested in the coupling elements between the first and second states, we chose to use a $\mathrm{dR}_1 = \mathrm{dR}_2 = 0.0001$ bohr for our calculations.

B. Ab Initio Results Versus DMBE Results

Since the codes used for these calculations were obtained from Buenker's group, to ensure that we understood how to use them properly and also to provide some comparison for the results obtained, we repeated some of the calculations performed by Varandas and coworkers.[5-6] We chose to repeat the cuts in nuclear configuration space that correspond to those shown in Figures 2 and 3 of Chapter 2. We did not repeat the cuts in Figure 4 of Chapter 2 since they did not display any features which suggested the conical intersection had been crossed. Since the input coordinate geometry variables used by Varandas and coworkers (see Figure 2) were different than those used in our application, we performed coordinate transformations to choose the values of nuclear geometry input variables to use. The transformation relating the variables used by Varandas and coworkers to those used in our application is given by the following equations:

$$R_1 = \left\{R^2 + (\frac{r}{2})^2 - rR\cos(\pi - \chi)\right\}^{\frac{1}{2}} \tag{5.1}$$

$$R_2 = r \tag{5.2}$$

$$\gamma = \cos^{-1}\left\{\frac{(R_1^2 + (\frac{r}{2})^2 - R^2)}{rR_1}\right\}. \tag{5.3}$$

Since R_2 and r are identical, the nonadiabatic coupling elements along the cuts where r is varying are identical to those calculated by our MRD-CI package ($(\langle 1|\frac{d}{dr}|2\rangle \equiv \langle 1|\frac{d}{R_2}|2\rangle)$). However, when R is changing, it is necessary to calculate both $\langle 1|\frac{d}{dR_1}|2\rangle$ and $\langle 1|\frac{d}{d\gamma}|2\rangle$ to obtain $\langle 1|\frac{d}{dR}|2\rangle$ since R depends upon the values of both of these variables by the above relations. The relationship between these nonadiabatic coupling elements can be obtained by differentiating the above equations.

The four cuts in nuclear configuration space corresponding to those shown in Figures 2 and 3 of Chapter 2 are defined as follows:

1. The bond angle χ between R and r was held fixed at 89°. The bond distance r was held fixed at 1.40 bohr. The bond distance R was varied. The nonadiabatic coupling element $\langle 1|\frac{d}{dR}|2\rangle$ was calculated over the ranges of bond distances 0.30 bohr $\leq R \leq$ 0.40 bohr and 1.0 bohr $\leq R \leq$ 1.4 bohr corresponding to the ranges over which Varandas and coworkers observed features in the the nonadiabatic coupling element. The results of these calculations are shown in Figures 7 through 9. The potential energy surfaces

show an avoided crossing, and the cusps are replaced by maxima and minima with continuous derivatives. As can be seen in Figure 8, the nonadiabatic coupling element is essentially flat over the range from 0.3 to 0.4 bohr; whereas Varandas and coworkers observed a sharp spike in this region. Over the region from 1.0 bohr $\leq$ R $\leq$ 1.4 bohr $\langle 1|\frac{d}{dR}|2\rangle$ behaves as if an odd-ordered pole is passed, it varies from about -1 bohr^{-1} slowly decreases to about -23.0 bohr^{-1} at R = 1.212 bohr, rapidly increases to about 23.5 bohr^{-1} and then decreases to approximately zero. The maximum intensity, and width (0.05 bohr) are approximately equal to that observed by Varandas and coworkers. Graphs of the $\langle 1|\frac{d}{dR_1}|2\rangle$, $\langle 1|\frac{d}{d\gamma}|2\rangle$ and $\langle 1|\frac{d}{d\chi}|2\rangle$ coupling elements are also shown.

2. $\chi = 89°$, r = 2.0 bohr and 1.5 bohr $\leq$ R $\leq$ 2.0 bohr. The results of these calculations are shown in Figures 10 and 11. The potential energy surfaces show an avoided crossing, and the cusps are replaced by maxima and minima with continuous derivatives. Within this range of R, $\langle 1|\frac{d}{dR}|2\rangle$ starts at 1.5 bohr^{-1} , slowly increases to a maximum of about 1.6 bohr^{-1} at 1.730 bohr and then decreases to approximately -0.5 bohr^{-1}. The maximum intensity and the width (0.06 bohr) are approximately equal to that observed by Varandas and coworkers. However, it does not behave as though it passes an odd-ordered pole as they observed. Graphs of the $\langle 1|\frac{d}{dR_1}|2\rangle$, $\langle 1|\frac{d}{d\gamma}|2\rangle$ and $\langle 1|\frac{d}{d\chi}|2\rangle$ coupling elements are also shown.

3. $\chi = 89°$, R = 0.70 bohr and 0.4 bohr $\leq$ r $\leq$ 2.9 bohr. The results of these calculations are shown in Figures 12 and 13. The potential energy surfaces are nearly parallel and lie close together for r < 1.0 bohr. For values of r > 0.975 bohr, the surfaces slowly separate and flatten out. Careful examination of Figure 12 shows that there is an avoided crossing. The geometry at the crossing point is such that the surfaces do not achieve a maxima or minima at this point. Starting from near zero at r = 0.9 bohr, $\langle 1|\frac{d}{dr}|2\rangle$ increases to 65.1 bohr^{-1} at r = 0.975 bohr and then decreases to zero again. The maximum intensity is greater, and the width (0.02 bohr) is narrower than the feature observed by Varandas and coworkers. Again, it does not behave as though it passes an odd-ordered pole.

4. $\chi = 89°$, R = 1.90 bohr and 0.8 bohr $\leq$ r $\leq$ 2.7 bohr. The results of these calculations are shown in Figures 14 and 15. The potential energy surfaces show an avoided crossing, and the cusps are replaced by maxima and minima with continuous derivatives. Over this region the coupling behaves as if an odd-ordered pole is passed, $\langle 1|\frac{d}{dr}|2\rangle$ increases from approximately -0.2 bohr^{-1} to 2.8 bohr^{-1} at r = 2.15 bohr, rapidly decreases to -13.6 bohr^{-1} at r = 2.20 bohr and then increases to -1.5 bohr^{-1} again. The maximum intensity and width (0.11 bohr) are approximately equal to that observed by Varandas and coworkers.

One explanation for the differences in our results and those of Varandas and coworkers is that ours is an *ab initio* method, whereas they obtained the nonadiabatic coupling elements by analytic continuation. Therefore, our results should be more accurate.

C. Isosceles Triangle Configurations (C_{2v})

Three cuts in nuclear configuration space along which C_{2v} symmetry is maintained were calculated. The nuclear geometry coordinate variables describing these cuts are as follows:

1. The bond angle γ between R_1 and R_2 was held fixed at 59°. The ratio of the bond distances $\frac{R_1}{R_2}$ was held fixed at 1, and these distances were simultaneously varied. The nonadiabatic coupling elements

$\langle k|\frac{d}{d\gamma}|k'\rangle$, $\langle k|\frac{d}{dR_1}|k'\rangle$, $\langle k|\frac{d}{dR_2}|k'\rangle$, were calculated over the range of bond distances 1.4 bohr $\leq R_1 = R_2 \leq$ 3.0 bohr for values of (k,k') equal to (1,2), (1,3) and (2,3). Since R_1 and R_2 were varied simultaneously, the second dervative coupling elements $\langle k|\frac{d^2}{dR_1^2}|k'\rangle$, $\langle k|\frac{d^2}{dR_2^2}|k'\rangle$, for values of (k,k') equal to (1,2), (1,3) and (2,3) could also be calculated. Since the coupling elements with respect to γ are unitless and the coupling elements with respect to R_1 and R_2 have units of bohr^{-1}, the angular coupling elements were normalized by the bond distance R_1 to provide consistent units for all of the first derivative coupling elements. The results of these calculations are shown in Figures 16 through 31.

2. R_1 and R_2 = 1.97 bohr. The nonadiabatic coupling elements $\langle k|\frac{d}{d\gamma}|k'\rangle$, $\langle k|\frac{d}{dR_1}|k'\rangle$ and $\langle k|\frac{d}{dR_2}|k'\rangle$, for values of (k,k') equal to (1,2), (1,3) and (2,3) were calculated over the range of bond angles 47° $\leq \gamma \leq$ 73°. Since only γ was varied, only the second derivative coupling elements $\langle k|\frac{d^2}{d\gamma^2}|k'\rangle$, for values of (k,k') equal to (1,2), (1,3) and (2,3) could be calculated. The second derivative angular coupling elements were normalized by the square of the bond distance R_1 to provide consistent units for the second derivative coupling elements. The results of these calculations are shown in Figures 32 through 44.

3. $R_1 = R_2 =$ 1.973 bohr and 49° $\leq \gamma \leq$ 73°. The results of these calculations are shown in Figures 45 through 57.

i. General features of the potential energy curves and nonadiabatic coupling elements along the $\gamma = 59°$ and $R_1 = R_2$ cut in nuclear configuration space.

The potential energy curves along this cut in nuclear configuration are shown in Figure 16. A blow-up of the two lowest surfaces is also shown. The potential energy curves vary smoothly over this range. The lowest two surfaces run nearly parallel to each other over this range.

The nonadiabatic coupling elements are shown in a series of graphs in Figures 17 through 31. These plots of the nonadiabatic coupling elements show three regions of strong interaction (centered at 1.652, 1.936 and 2.211 bohr). A blow-up of each of the coupling elements over these ranges are also included. As found in the convergence tests, the coupling elements involving derivatives with repect to γ showed erratic oscillatory behavior. This implies that the chosen value of $d\gamma$ was not a good one. All of the coupling elements involving first derivatives with respect to R_1 and R_2 exhibited the behavior expected if it just passes by an odd-ordered pole without going through it. In many cases this behavior was superimposed upon a background coupling so that the rapid increase (decrease) in the coupling element was not centered about zero. The coupling elements varied smoothly (except of course at the point of passing by the pole) over most of the range studied. However, over the range near 1.652, the coupling elements between the second and third states were not as well converged, implying that in this region, a better choice of $dR_1(dR_2)$ is necessary for this interaction.

ii. General features of the potential energy curves and nonadiabatic coupling elements along the $R_1 = R_2 = 1.97$ bohr cut in nuclear configuration space.

The potential energy curves along this cut in nuclear configuration space vary smoothly over the range observed and are shown in Figure 32. The lowest two surfaces show an avoided crossing, with the cusps replaced by maxima and minima with continuous derivatives. The avoided crossing occurs at $\gamma = 60°$. At this point, $E_1 = E_2 = 2.795$ eV (E_2 is greater than E_1 by an amount less than 0.001 eV).

The nonadiabatic coupling elements are shown in a series of graphs in Figures 33 through 44. These plots of the nonadiabatic coupling elements show one region of strong interaction (centered at 60°). A blow-up of each of the coupling elements over this range are also included. The coupling elements involving derivatives with respect to γ are very small over the entire range examined except at values of γ close to 60°. Due to limitations in time and computer resources, a finer grid over the range near 60° has been left for future work. All of the coupling elements involving first derivatives with respect to R_1 and R_2 behaved as if an odd-ordered pole had been passed by. Unlike the previously discussed cut in nuclear configuration space, the rapid increase (decrease) in the coupling element was centered about zero. The coupling elements varied smoothly (except of course near the pole) over the range studied.

iii. General features of the potential energy curves and nonadiabatic coupling elements along the $R_1 = R_2 = 1.973$ bohr cut in nuclear configuration space.

The potential energy curves along this cut in nuclear configuration are shown in Figure 45. The potential energy curves vary smootly over this range. The lowest two surfaces show an avoided crossing, and the cusps are replaced by maxima and minima with continuous derivatives. The avoided crossing occurs at $\gamma = 60°$. At this point, $E_1 = E_2 = 2.795$ eV (E_2 is greater than E_1 by an amount less than 0.001 eV).

D. Other Triangular Configurations (C_s)

Two cuts in nuclear configuration space along which C_s symmetry is maintained were calculated. The nuclear geometry coordinate variables describing these cuts are as follows:

1. The bond angle γ between R_1 and R_2 was held fixed at 59°. The bond distance R_1 was held fixed at 1.97 bohr, and the bond distance R_2 was varied. The nonadiabatic coupling elements $\langle k|\frac{d}{d\gamma}|k'\rangle$, $\langle k|\frac{d}{dR_1}|k'\rangle$, $\langle k|\frac{d}{dR_2}|k'\rangle$, for values of (k, k') equal to (1,2), (1,3) and (2,3) were calculated over the range of bond distances 1.45 bohr $\leq R_2 \geq$ 2.51 bohr. Since only R_2 was varied, only the second derivative coupling elements $\langle k|\frac{d^2}{dR_2^2}|k'\rangle$, for values of (k, k') equal to (1,2), (1,3) and (2,3) could be calculated. The results of these calculations are shown in Figures 58 through 70.
2. $\gamma = 60°, R_1 = 1.973$ bohr and 1.57 bohr $\leq R_2 \leq$ 2.41 bohr. The results of these calculations are shown in Figures 71 through 83.

i. General features of the potential energy curves and nonadiabatic coupling elements along the $\gamma = 59°$ and $R_1 = 1.97$ bohr cut in nuclear configuration space.

The potential energy curves along this cut in nuclear configuration are shown in Figure 58. The potential energy curves vary smoothly over this range. The lowest two surfaces show an avoided crossing, and the cusps are replaced by maxima and minima with continuous derivatives. The avoided crossing occurs at $R_2 = 1.967$ bohr, E_1 obtains it maximum value of 2.720 eV at $R_2 = 1.969$ bohr and E_2 reaches it minimum value of 2.866 eV at $R_2 = 1.964$ bohr.

The nonadiabatic coupling elements are shown in a series of graphs in Figures 59 through 70. These plots of the nonadiabatic coupling elements show one region of strong interaction (centered at ~ 1.973 bohr). Since the interesting features in these figures are rather broad, a blow-up of each of the coupling elements over this range was not necessary. The coupling elements involving derivatives with repect to γ each show unique behavior. The coupling element between the two lowest states exhibits the behavior expected if it just passes by an odd-ordered pole without passing through it. The coupling element between the lowest and third state is a rather broad peak which flattens out and then dips down slightly in the region near the conical intersection. The coupling between the second and third state slowly decreases over this region until it approaches the vicinity of the conical intersection and then dips down sharply and then increases once again. The coupling elements involving first derivatives with respect to R_1 and R_2 between the two lowest states show a smooth broad peak. The coupling between the lowest and third state exhibited behavior similar to that observed for the γ coupling between the second and third state. The behavior of the R_1 coupling element between the second and third state is particularly interesting. The coupling appears as a very broad rising peak which dips down suddenly as the conical intersection is being passed. The R_2 coupling between the second and third states increases slowly over this range with a small odd-ordered pole type oscillation embedded in this background coupling as it crosses the region of the conical intersection. The coupling elements varied smoothly (except of course near the pole) over the range studied.

ii. General features of the potential energy curves and nonadiabatic coupling elements along the $\gamma = 60°$ and $R_1 = 1.973$ bohr cut in nuclear configuration space.

The potential energy curves along this cut in nuclear configuration are shown in Figure 71. The potential energy curves vary smoothly over this range. The lowest two surfaces show an avoided crossing, and the cusps are replaced by maxima and minima with continuous derivatives. The avoided crossing occurs at $R_2 = 1.973$ bohr, at this point, E_1 achieves a maximum of 2.794 eV and E_2 a minimum of 2.795 eV.

The nonadiabatic coupling elements are shown in a series of graphs in Figures 72 through 83. These plots of the nonadiabatic coupling elements show one region of strong interaction (centered at $\sim$ 1.973 bohr). A blow-up of each of the coupling elements over this range is also included. The coupling elements involving derivatives with repect to γ show behavior very similar to that observed along the last cut discussed ($\gamma = 59°$, $R_1 = 1.97$ bohr), however, the features observed were much sharper. The coupling element with respect to R_1 between the two lowest states behaves as if an odd-ordered pole is passed by. This is different than that observed in the previous case, indicating that a sign flip of the calculated elements on one side of the peak in the last cut may be warranted although no other indication for such a change in sign was observed. The coupling element with respect to R_2 between these states exhibits the same behavior as in the last cut except the observed feature is much sharper. The coupling with respect to R_1 between the first and third state, and between the second and third state are relatively flat over the entire region and appears as a sharp spike near the region of the conical intersection. The coupling with respect to R_2 between the first and third, and the second and third states behave similarly. The coupling decreases (increases) over the observed range with a small odd-ordered pole type oscillation embedded in this background coupling as it crosses the region of the conical intersection, respectively. Most of the coupling elements varied smoothly (except of course at the point of passing by the pole) over the range studied. However, the R_1 and R_2 coupling between the first and third and second and third states does show some oscillations indicating that a better choice of dR_1 (dR_2) may be necessary. As expected, the behavior exhibited along this cut is very similar to the behavior exhibited along the previous cut since the geometries are very similar.

An interesting feature of many of the coupling elements between the first and third and between the second and the third states is illustrated by comparing Figures 39b and 43b. The behavior of the coupling elements is not symmetric about the point of greatest coupling. The features here are spiked on one side of the interaction region and curved on the other. The 1,3 coupling for $\gamma < 60°$ is nearly the mirror image of the 2,3 coupling for $\gamma > 60°$ and vice versa. This is a result of performing calculations in an adiabatic representation. In this representation the surfaces are not allowed to cross, therefore as the crossing region is traversed, the character of the wavefunction of state 1 (2) transitions to the character of the wavefuction of state 2 (1). If instead of defining state '1' as the lowest energy state, the states were denoted by their character (by which basis functions are dominant) then the states would cross and the coupling would be symmetric about the interaction region (a 'diabatic representation').

III. References

1. F. Webster and J.C. Light, *J. Chem. Phys.* **90**, 265 (1989); *J. Chem. Phys.* **90**, 300 (1989).
2. A. Kuppermann, J.A. Kaye and J.P. Dwyer, *Chem. Phys. Lett.* **74**, 257 (1980); J.A. Kaye and A. Kuppermann, *Chem. Phys. Lett.* **77**, 573 (1981).
3. A. Kuppermann, *Theor. Chem.: Advances and Perspectives*, **6A**, 79 (1981).
4. G. Hauke, J. Manz and J. Römelt, *J. Chem. Phys.* **73**, 5040 (1980).
5. A.J.C. Varandas, F.B. Brown, C.A. Mead, D.G. Truhlar and N.C. Blais, *J. Chem. Phys.* **86(11)**, 6258 (1987).
6. B.C. Garrett, D.G. Truhlar, A.J.C. Varandas and N.C. Blais, *Int. J. Chem. Kinet.* **18**, 1065 (1986).

IV. Figure Captions

Figure 1. Coordinate system used in the MRD-CI program. P_i is the ith proton of H_3. The three protons are all in the xy-plane. The bond distance R_1 between P_1 and P_3, R_2 between P_1 and P_2, and the bond angle γ between R_1 and R_2 are used as the variables describing the shape of the triangle.

Figure 2. Coordinate system used in by Varandas and coworkers.[5-6] P_i is the ith proton of H_3. The three protons are all in the xy-plane. The bond distance r between P_1 and P_3, R between the center of mass of P_1P_2 and P_3, and the bond angle χ between r and R are used as the variables describing the shape of the triangle.

Figure 3. Nonadiabatic coupling elements $\langle 1|\frac{d}{dr}|2\rangle$ for $R = 0.7$ bohr, $r = 0.97$ bohr and $\chi = 89°$ as a function of dr.

Figure 4. Nonadiabatic coupling elements $\langle k|\frac{d}{d\gamma}|k'\rangle/R_1$, where $k, k' = (1,2), (1,3)$ and (2,3) for $\gamma = 59°$, and $R_1 = R_2$ as a function of $d\gamma$. The asterisks are for 1.91 bohr, and the open boxes for 1.92 bohr.

Figure 5. Nonadiabatic coupling elements $\langle k|\frac{d}{dR_1}|k'\rangle$ where $k, k' = (1,2), (1,3)$ and (2,3) for $\gamma = 59°$, and $R_1 = R_2 = 1.91$ bohr as a function of dR_1.

Figure 6. Nonadiabatic coupling elements $\langle k|\frac{d}{dR_2}|k'\rangle$ where $k, k' = (1,2), (1,3)$ and (2,3) for $\gamma = 59°$, and $R_1 = R_2 = 1.91$ bohr as a function of dR_2.

Figure 7. Potential energy surface cuts E_1 and E_2 for $r = 1.40$ bohr and $\chi = 89°$ as a function of R.

Figure 8. Nonadiabatic coupling elements $\langle 1|\frac{d}{dR_1}|2\rangle$ for $r = 1.40$ bohr and $\chi = 89°$ as a function of R.

Figure 9. Nonadiabatic coupling elements $\langle 1|\frac{d}{dR_1}|2\rangle$, $\langle 1|\frac{d}{d\gamma}|2\rangle$, $\langle 1|\frac{d}{dR}|2\rangle$ and $\langle 1|\frac{d}{d\chi}|2\rangle$ for $r = 1.40$ bohr and $\chi = 89°$ as a function of R.

Figure 23. Nonadiabatic coupling elements $\langle 1|\frac{d}{dR_1}|3\rangle$ for $\gamma = 59°$ and $R_1 = R_2$ as a function of R_1 (or R_2).

Figure 24. Nonadiabatic coupling elements $\langle 1|\frac{d^2}{dR_1^2}|3\rangle$ for $\gamma = 59°$ and $R_1 = R_2$ as a function of R_1 (or R_2).

Figure 25. Nonadiabatic coupling elements $\langle 1|\frac{d}{dR_2}|3\rangle$ for $\gamma = 59°$ and $R_1 = R_2$ as a function of R_1 (or R_2).

Figure 26. Nonadiabatic coupling elements $\langle 1|\frac{d^2}{dR_2^2}|3\rangle$ for $\gamma = 59°$ and $R_1 = R_2$ as a function of R_1 (or R_2).

Figure 27. Nonadiabatic coupling elements $\langle 2|\frac{d}{d\gamma}|3\rangle/R_1$ for $\gamma = 59°$ and $R_1 = R_2$ as a function of R_1 (or R_2).

Figure 28. Nonadiabatic coupling elements $\langle 2|\frac{d}{dR_1}|3\rangle$ for $\gamma = 59°$ and $R_1 = R_2$ as a function of R_1 (or R_2).

Figure 29. Nonadiabatic coupling elements $\langle 2|\frac{d^2}{dR_1^2}|3\rangle$ for $\gamma = 59°$ and $R_1 = R_2$ as a function of R_1 (or R_2).

Figure 30. Nonadiabatic coupling elements $\langle 2|\frac{d}{dR_2}|3\rangle$ for $\gamma = 59°$ and $R_1 = R_2$ as a function of R_1 (or R_2).

Figure 31. Nonadiabatic coupling elements $\langle 2|\frac{d^2}{dR_2^2}|3\rangle$ for $\gamma = 59°$ and $R_1 = R_2$ as a function of R_1 (or R_2).

Figure 32. Potential energy surface cuts E_1, E_2 and E_3 for $R_1 = R_2 = 1.97$ bohr as a function of γ.

Figure 33. Nonadiabatic coupling elements $\langle 1|\frac{d}{d\gamma}|2\rangle/R_1$ for $R_1 = R_2 = 1.97$ bohr as a function γ.

Figure 34. Nonadiabatic coupling elements $\langle 1|\frac{d^2}{d\gamma^2}|2\rangle/R_1^2$ for $R_1 = R_2 = 1.97$ bohr as a function γ.

Figure 35. Nonadiabatic coupling elements $\langle 1|\frac{d}{dR_1}|2\rangle$ for $R_1 = R_2 = 1.97$ bohr as a function γ.

Figure 36. Nonadiabatic coupling elements $\langle 1|\frac{d}{dR_2}|2\rangle$ for $R_1 = R_2 = 1.97$ bohr as a function γ.

Figure 37. Nonadiabatic coupling elements $\langle 1|\frac{d}{d\gamma}|3\rangle/R_1$ for $R_1 = R_2 = 1.97$ bohr as a function γ.

Figure 38. Nonadiabatic coupling elements $\langle 1|\frac{d^2}{d\gamma^2}|3\rangle/R_1^2$ for $R_1 = R_2 = 1.97$ bohr as a function γ.

Figure 39. Nonadiabatic coupling elements $\langle 1|\frac{d}{dR_1}|3\rangle$ for $R_1 = R_2 = 1.97$ bohr as a function γ.

Figure 40. Nonadiabatic coupling elements $\langle 1|\frac{d}{dR_2}|3\rangle$ for $R_1 = R_2 = 1.97$ bohr as a function γ.

Figure 41. Nonadiabatic coupling elements $\langle 2|\frac{d}{d\gamma}|3\rangle/R_1$ for $R_1 = R_2 = 1.97$ bohr as a function γ.

Figure 42. Nonadiabatic coupling elements $\langle 2|\frac{d^2}{d\gamma^2}|3\rangle/R_1^2$ for $R_1 = R_2 = 1.97$ bohr as a function γ.

Figure 43. Nonadiabatic coupling elements $\langle 2|\frac{d}{dR_1}|3\rangle$ for $R_1 = R_2 = 1.97$ bohr as a function γ.

Figure 44. Nonadiabatic coupling elements $\langle 2|\frac{d}{dR_2}|3\rangle$ for $R_1 = R_2 = 1.97$ bohr as a function γ.

Figure 45. Potential energy surface cuts E_1, E_2 and E_3 for $R_1 = R_2 = 1.973$ bohr as a function of γ.

Figure 46. Nonadiabatic coupling elements $\langle 1|\frac{d}{d\gamma}|2\rangle/R_1$ for $R_1 = R_2 = 1.973$ bohr as a function γ.

Figure 47. Nonadiabatic coupling elements $\langle 1|\frac{d^2}{d\gamma^2}|2\rangle/R_1^2$ for $R_1 = R_2 = 1.973$ bohr as a function γ.

Figure 48. Nonadiabatic coupling elements $\langle 1|\frac{d}{dR_1}|2\rangle$ for $R_1 = R_2 = 1.973$ bohr as a function γ.

Figure 49. Nonadiabatic coupling elements $\langle 1|\frac{d}{dR_2}|2\rangle$ for $R_1 = R_2 = 1.973$ bohr as a function γ.

Figure 50. Nonadiabatic coupling elements $\langle 1|\frac{d}{d\gamma}|3\rangle/R_1$ for $R_1 = R_2 = 1.973$ bohr as a function γ.

Figure 51. Nonadiabatic coupling elements $\langle 1|\frac{d^2}{d\gamma^2}|3\rangle/R_1^2$ for $R_1 = R_2 = 1.973$ bohr as a function γ.

Figure 52. Nonadiabatic coupling elements $\langle 1|\frac{d}{dR_1}|3\rangle$ for $R_1 = R_2 = 1.973$ bohr as a function γ.

Figure 53. Nonadiabatic coupling elements $\langle 1|\frac{d}{dR_2}|3\rangle$ for $R_1 = R_2 = 1.973$ bohr as a function γ.

Figure 54. Nonadiabatic coupling elements $\langle 2|\frac{d}{d\gamma}|3\rangle/R_1$ for $R_1 = R_2 = 1.973$ bohr as a function γ.

Figure 55. Nonadiabatic coupling elements $\langle 2|\frac{d^2}{d\gamma^2}|3\rangle/R_1^2$ for $R_1 = R_2 = 1.973$ bohr as a function γ.

Figure 56. Nonadiabatic coupling elements $\langle 2|\frac{d}{dR_1}|3\rangle$ for $R_1 = R_2 = 1.973$ bohr as a function γ.

Figure 57. Nonadiabatic coupling elements $\langle 2|\frac{d}{dR_2}|3\rangle$ for $R_1 = R_2 = 1.973$ bohr as a function γ.

Figure 58. Potential energy surface cuts E_1, E_2 and E_3 for $\gamma = 59°$ and $R_1 = 1.97$ bohr as a function of R_2.

Figure 59. Nonadiabatic coupling elements $\langle 1|\frac{d}{d\gamma}|2\rangle/R_1$ for $\gamma = 59°$ and $R_1 = 1.97$ bohr as a function of R_2.

Figure 60. Nonadiabatic coupling elements $\langle 1|\frac{d}{dR_1}|2\rangle$ for $\gamma = 59°$ and $R_1 = 1.97$ bohr as a function of R_2.

Figure 61. Nonadiabatic coupling elements $\langle 1|\frac{d}{dR_2}|2\rangle$ for $\gamma = 59°$ and $R_1 = 1.97$ bohr as a function of R_2.

Figure 62. Nonadiabatic coupling elements $\langle 1|\frac{d^2}{dR_2^2}|2\rangle$ for $\gamma = 59°$ and $R_1 =$ 1.97 bohr as a function of R_2.

Figure 63. Nonadiabatic coupling elements $\langle 1|\frac{d}{d\gamma}|3\rangle/R_1$ for $\gamma = 59°$ and $R_1 =$ 1.97 bohr as a function of R_2.

Figure 64. Nonadiabatic coupling elements $\langle 1|\frac{d}{dR_1}|3\rangle$ for $\gamma = 59°$ and $R_1 =$ 1.97 bohr as a function of R_2.

Figure 65. Nonadiabatic coupling elements $\langle 1|\frac{d}{dR_2}|3\rangle$ for $\gamma = 59°$ and $R_1 =$ 1.97 bohr as a function of R_2.

Figure 66. Nonadiabatic coupling elements $\langle 1|\frac{d^2}{dR_2^2}|3\rangle$ for $\gamma = 59°$ and $R_1 =$ 1.97 bohr as a function of R_2.

Figure 67. Nonadiabatic coupling elements $\langle 2|\frac{d}{d\gamma}|3\rangle/R_1$ for $\gamma = 59°$ and $R_1 =$ 1.97 bohr as a function of R_2.

Figure 68. Nonadiabatic coupling elements $\langle 2|\frac{d}{dR_1}|3\rangle$ for $\gamma = 59°$ and $R_1 =$ 1.97 bohr as a function of R_2.

Figure 69. Nonadiabatic coupling elements $\langle 2|\frac{d}{dR_2}|3\rangle$ for $\gamma = 59°$ and $R_1 =$ 1.97 bohr as a function of R_2.

Figure 70. Nonadiabatic coupling elements $\langle 2|\frac{d^2}{dR_2^2}|3\rangle$ for $\gamma = 59°$ and $R_1 =$ 1.97 bohr as a function of R_2.

Figure 71. Potential energy surface cuts E_1, E_2 and E_3 for $\gamma = 60°$ and $R_1 =$ 1.973 bohr as a function of R_2.

Figure 72. Nonadiabatic coupling elements $\langle 1|\frac{d}{d\gamma}|2\rangle/R_1$ for $\gamma = 60°$ and $R_1 =$ 1.973 bohr as a function of R_2.

Figure 73. Nonadiabatic coupling elements $\langle 1|\frac{d}{dR_1}|2\rangle$ for $\gamma = 60°$ and $R_1 =$ 1.973 bohr as a function of R_2.

Figure 74. Nonadiabatic coupling elements $\langle 1|\frac{d}{dR_2}|2\rangle$ for $\gamma = 60°$ and $R_1 =$ 1.973 bohr as a function of R_2.

Figure 75. Nonadiabatic coupling elements $\langle 1|\frac{d^2}{dR_2^2}|2\rangle$ for $\gamma = 60°$ and $R_1 =$ 1.973 bohr as a function of R_2.

Figure 76. Nonadiabatic coupling elements $\langle 1|\frac{d}{d\gamma}|3\rangle/R_1$ for $\gamma = 60°$ and $R_1 =$ 1.973 bohr as a function of R_2.

Figure 77. Nonadiabatic coupling elements $\langle 1|\frac{d}{dR_1}|3\rangle$ for $\gamma = 60°$ and $R_1 =$ 1.973 bohr as a function of R_2.

Figure 78. Nonadiabatic coupling elements $\langle 1|\frac{d}{dR_2}|3\rangle$ for $\gamma = 60°$ and $R_1 =$ 1.973 bohr as a function of R_2.

Figure 79. Nonadiabatic coupling elements $\langle 1|\frac{d^2}{dR_2^2}|3\rangle$ for $\gamma = 60°$ and $R_1 =$ 1.973 bohr as a function of R_2.

Figure 80. Nonadiabatic coupling elements $\langle 2|\frac{d}{d\gamma}|3\rangle/R_1$ for $\gamma = 60°$ and $R_1 =$ 1.973 bohr as a function of R_2.

Figure 81. Nonadiabatic coupling elements $\langle 2|\frac{d}{dR_1}|3\rangle$ for $\gamma = 60°$ and $R_1 =$ 1.973 bohr as a function of R_2.

Figure 82. Nonadiabatic coupling elements $\langle 2|\frac{d}{dR_2}|3\rangle$ for $\gamma = 60°$ and $R_1 =$ 1.973 bohr as a function of R_2.

Figure 83. Nonadiabatic coupling elements $\langle 2|\frac{d^2}{dR_2^2}|3\rangle$ for $\gamma = 60°$ and $R_1 =$ 1.973 bohr as a function of R_2.

Figure 1.

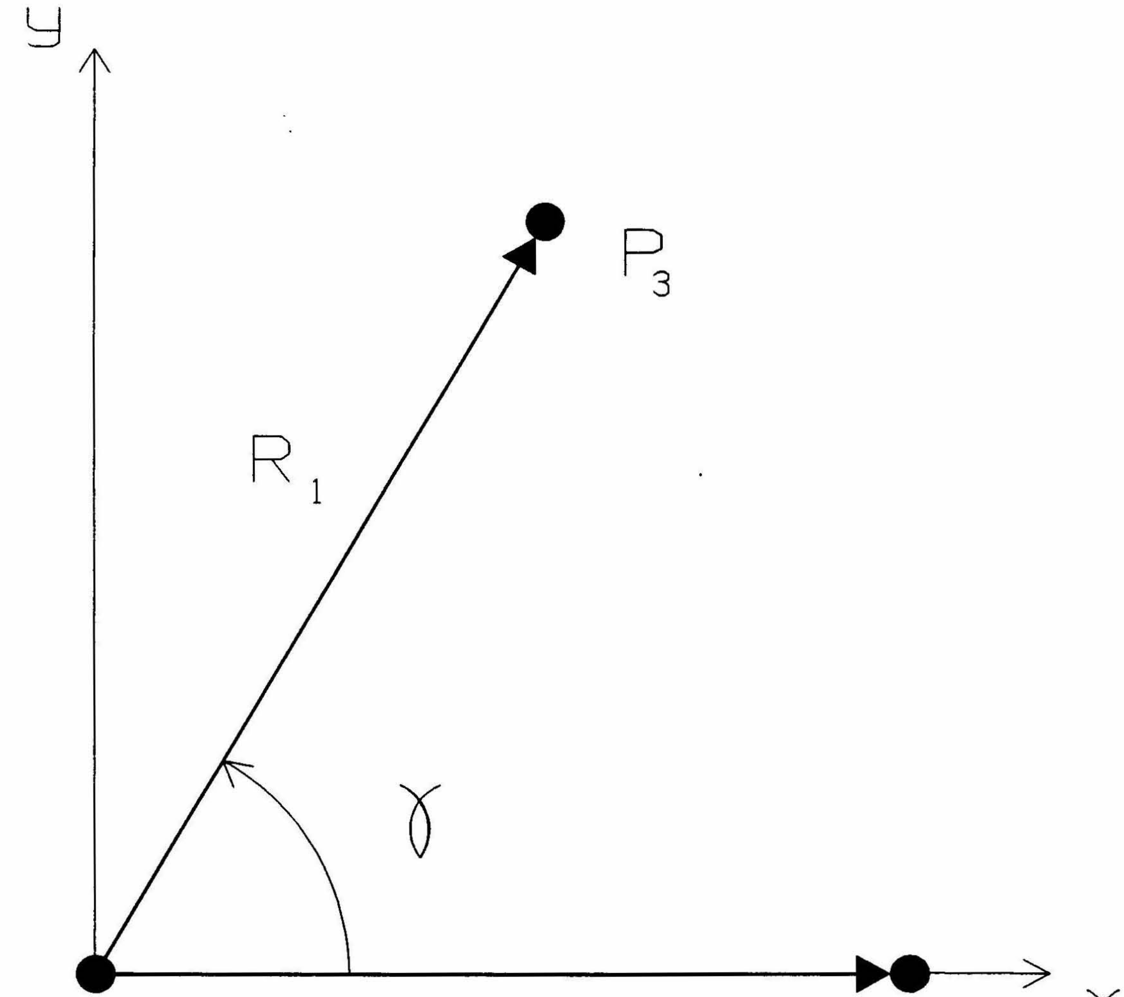

Figure 2.

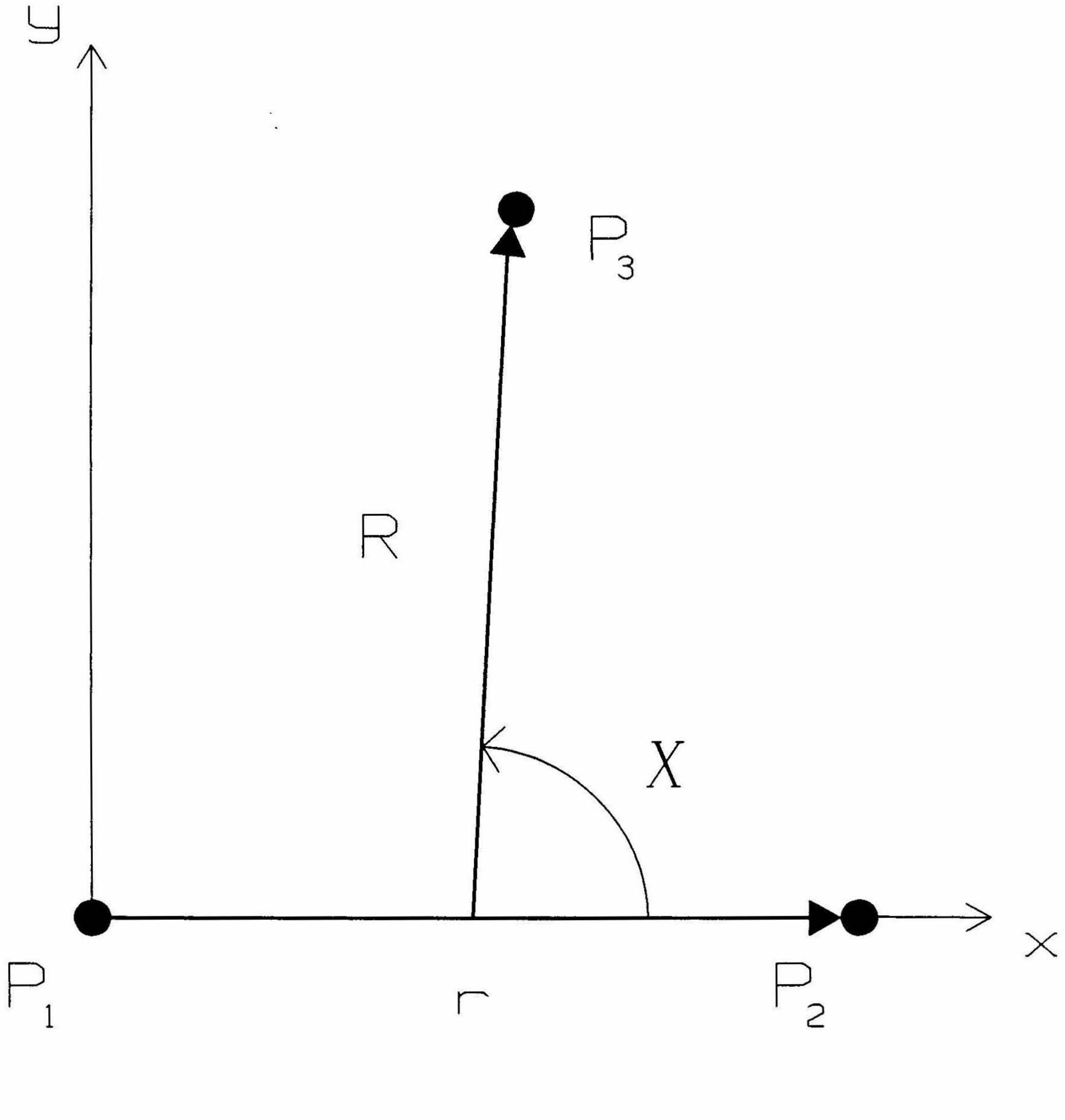

Figure 3.

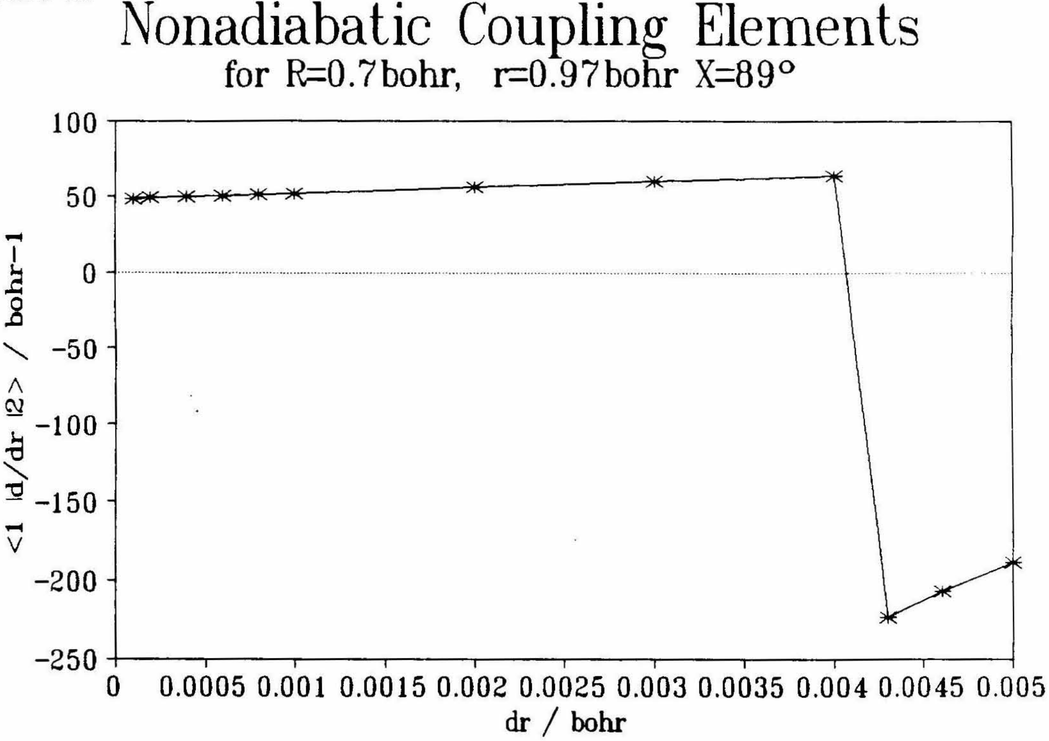

Figure 4a.

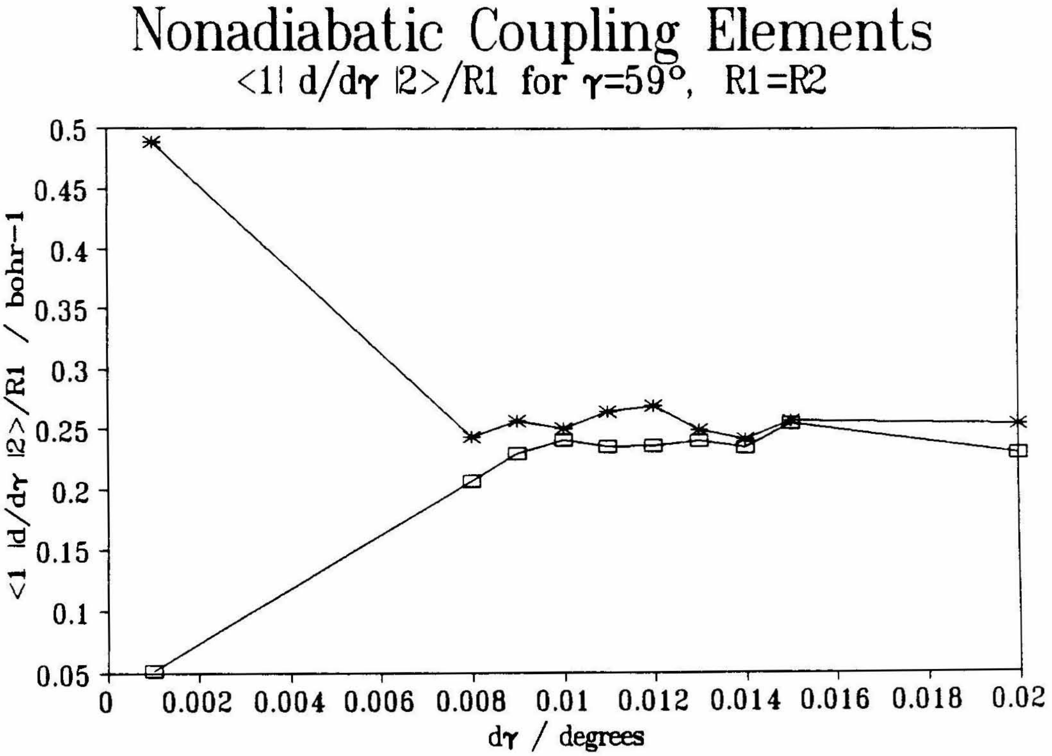

Figure 4b.

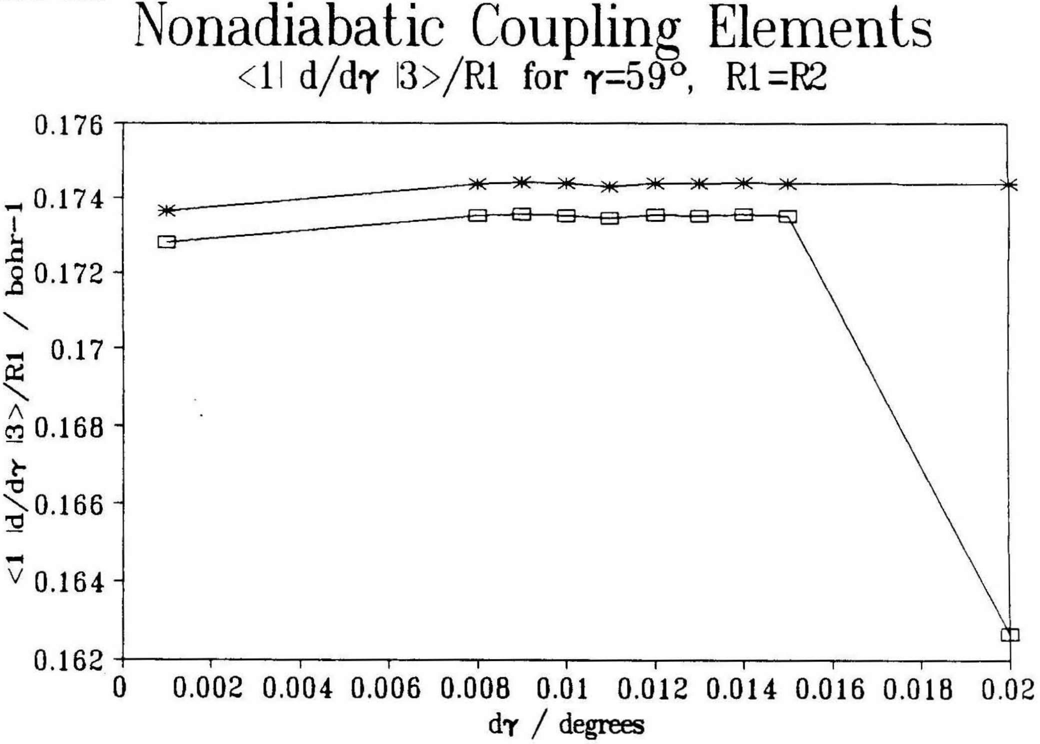

Figure 4c.

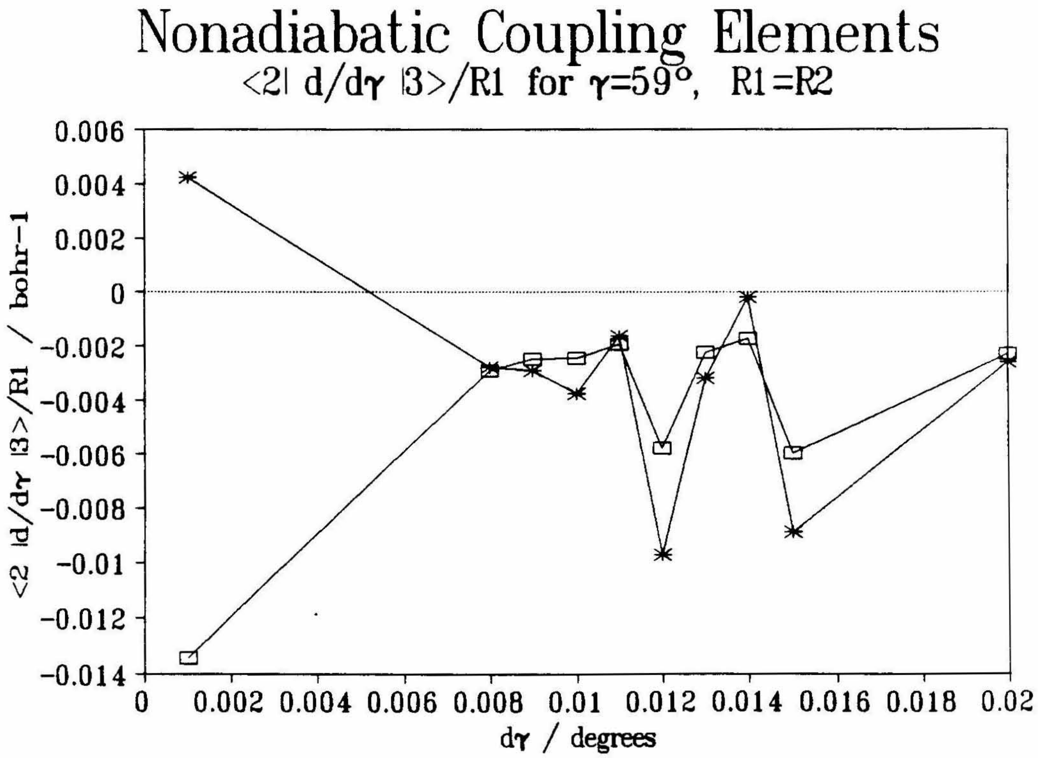

Figure 5a.

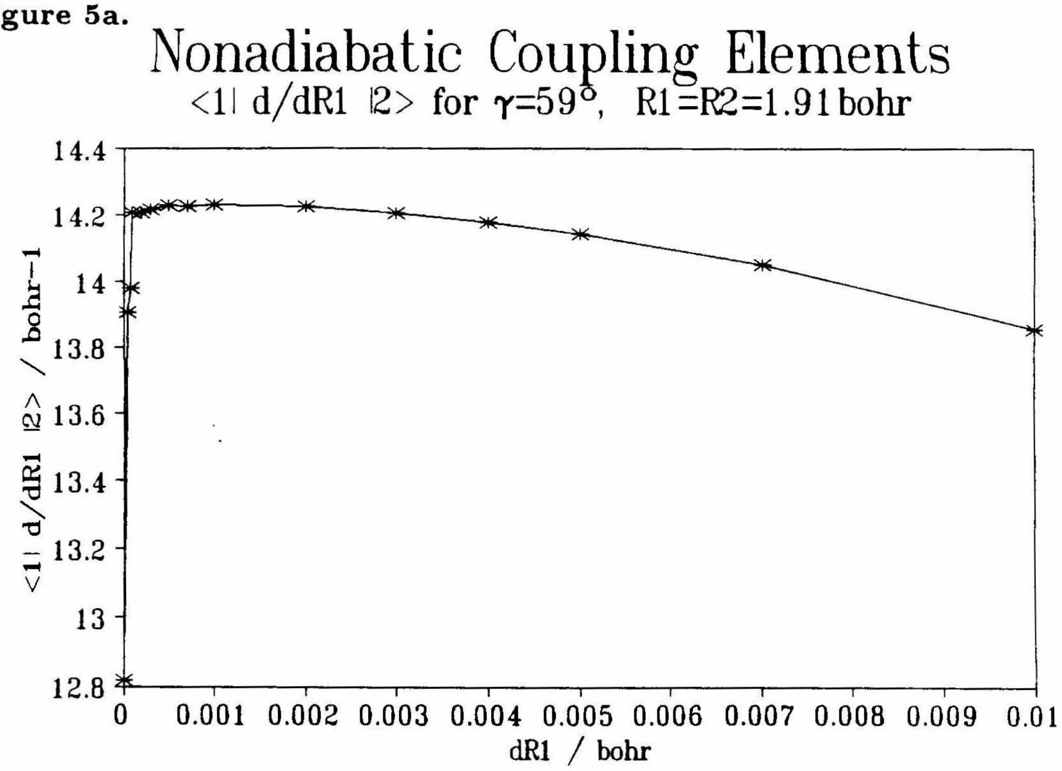

Figure 5b.

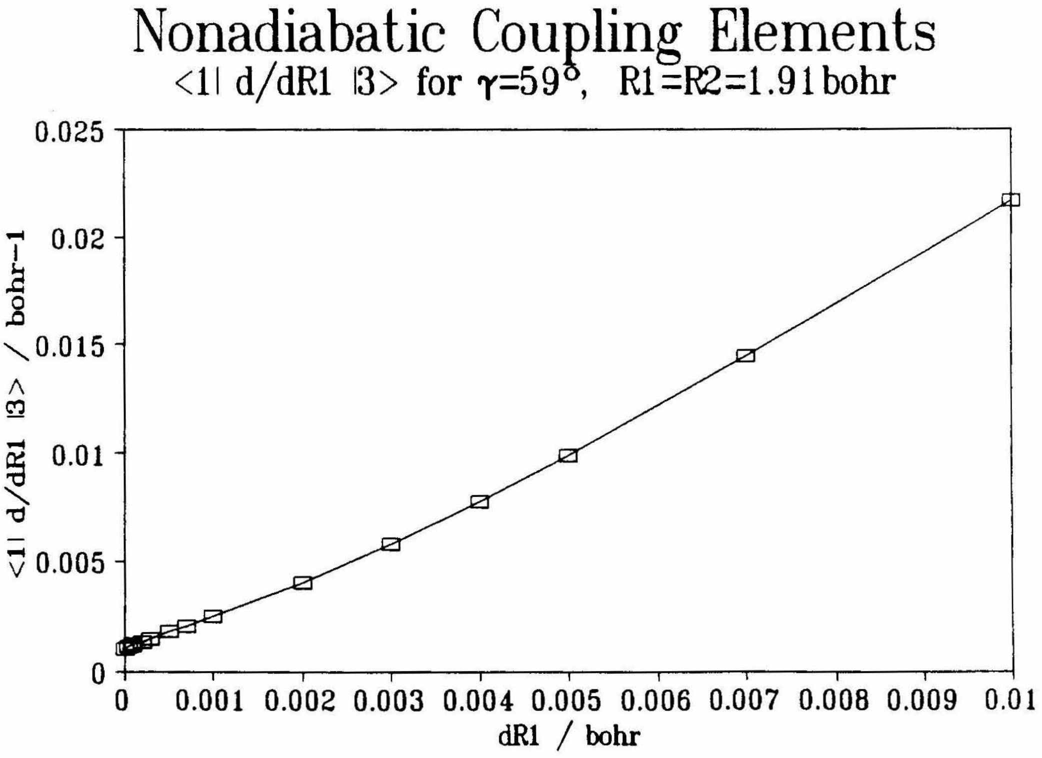

Figure 5c.

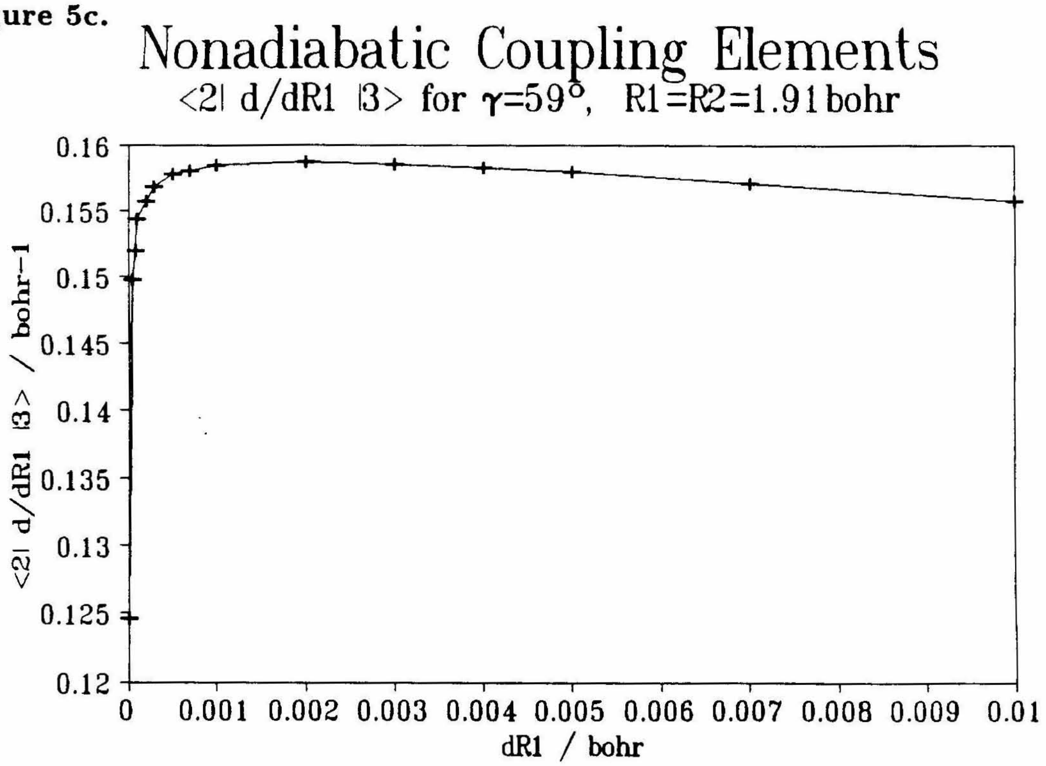

Figure 6a.

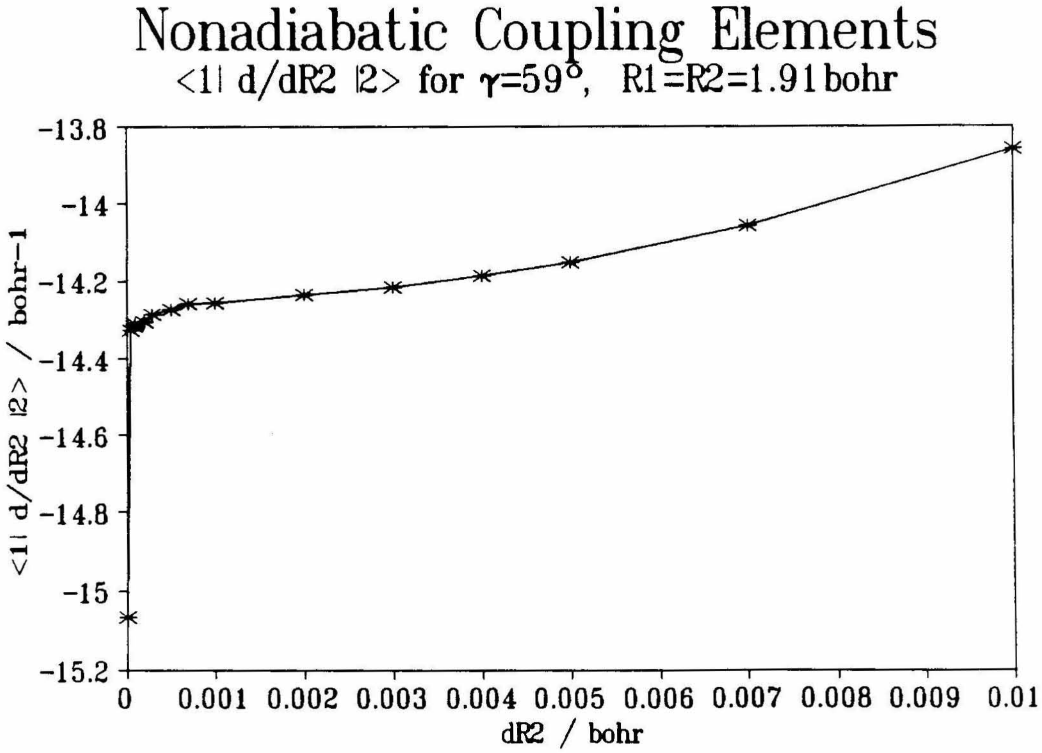

Figure 6b.

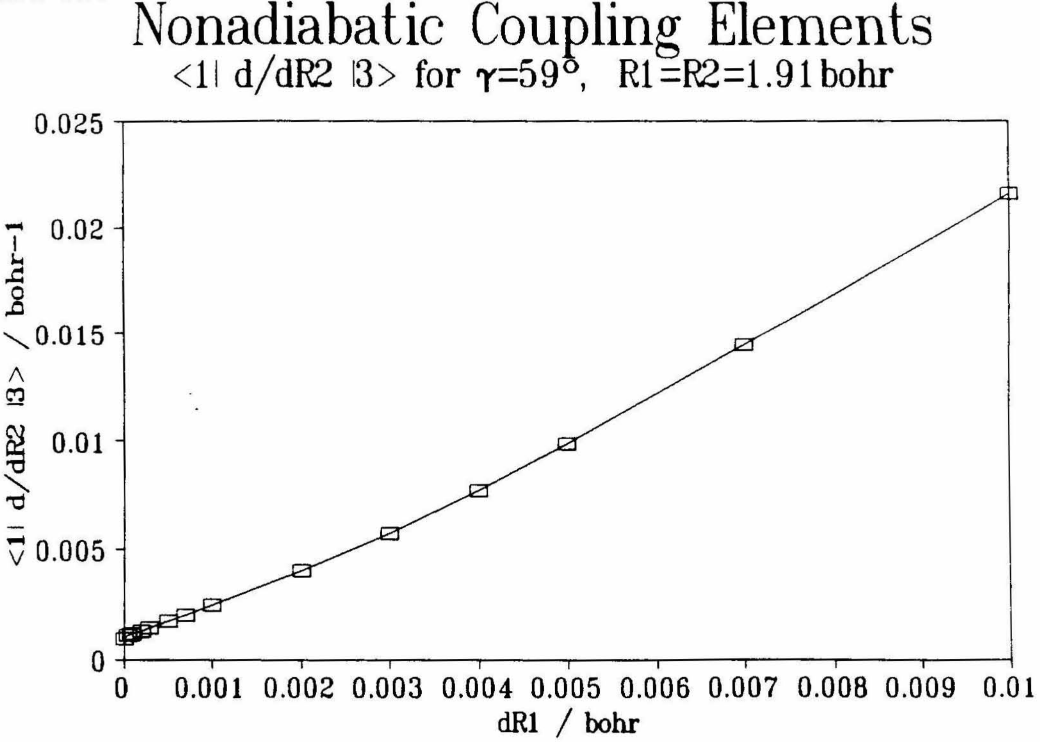

Figure 6c.

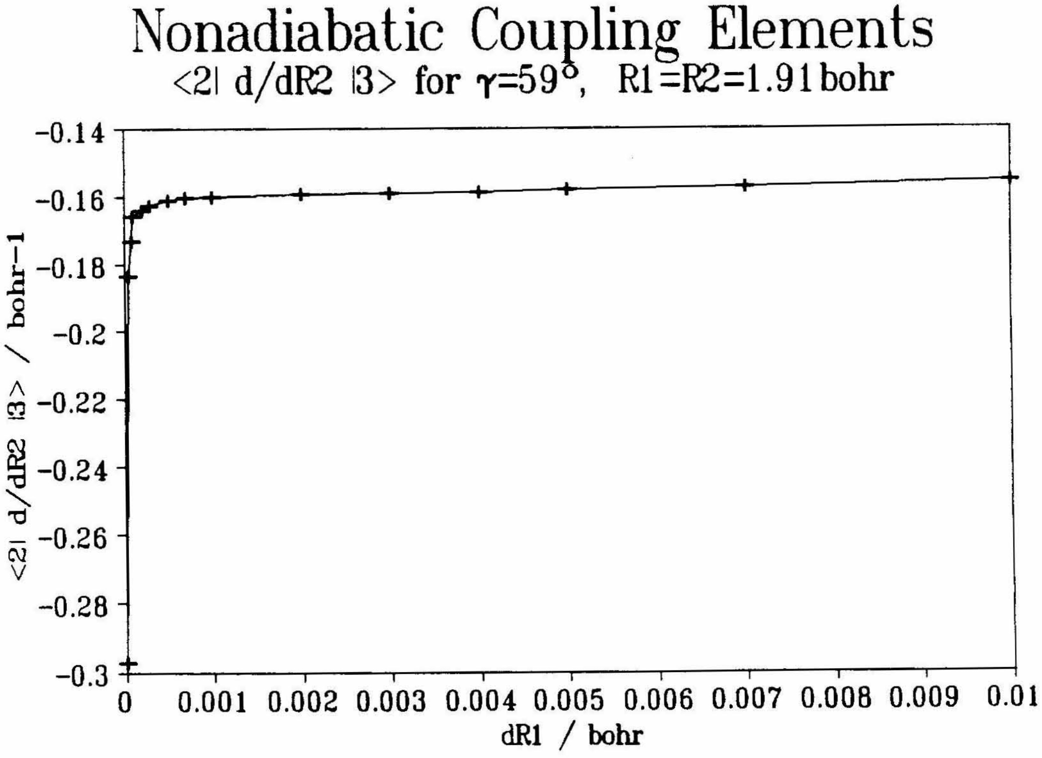

Figure 7a.

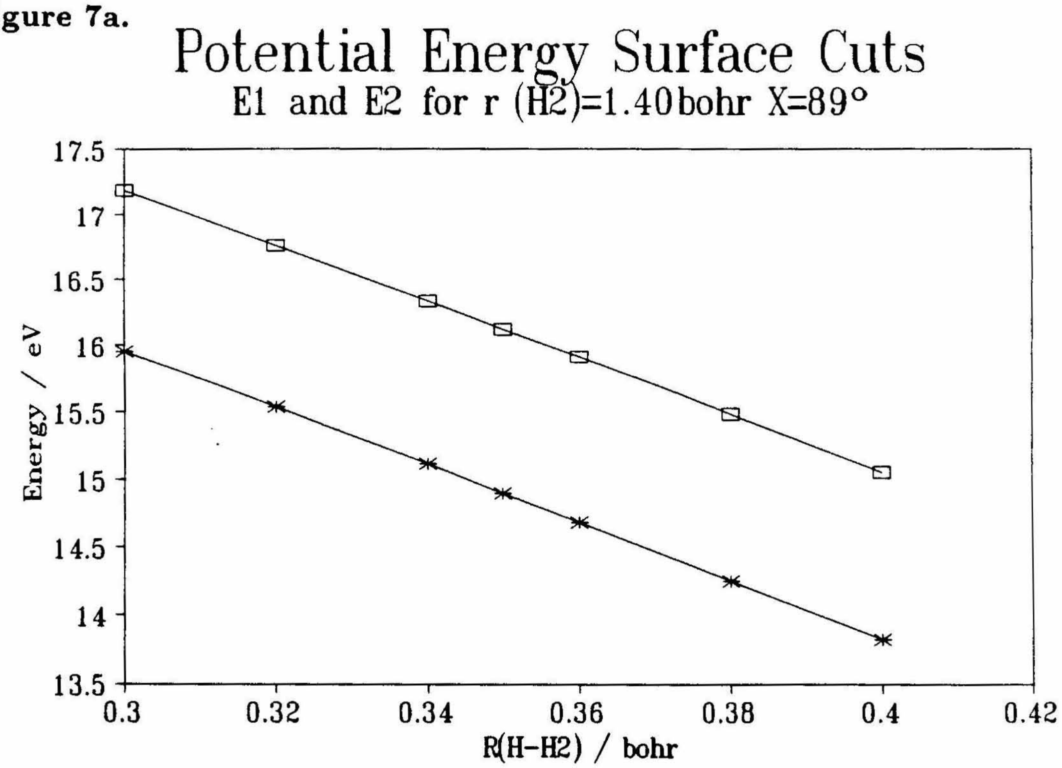

Figure 7b.

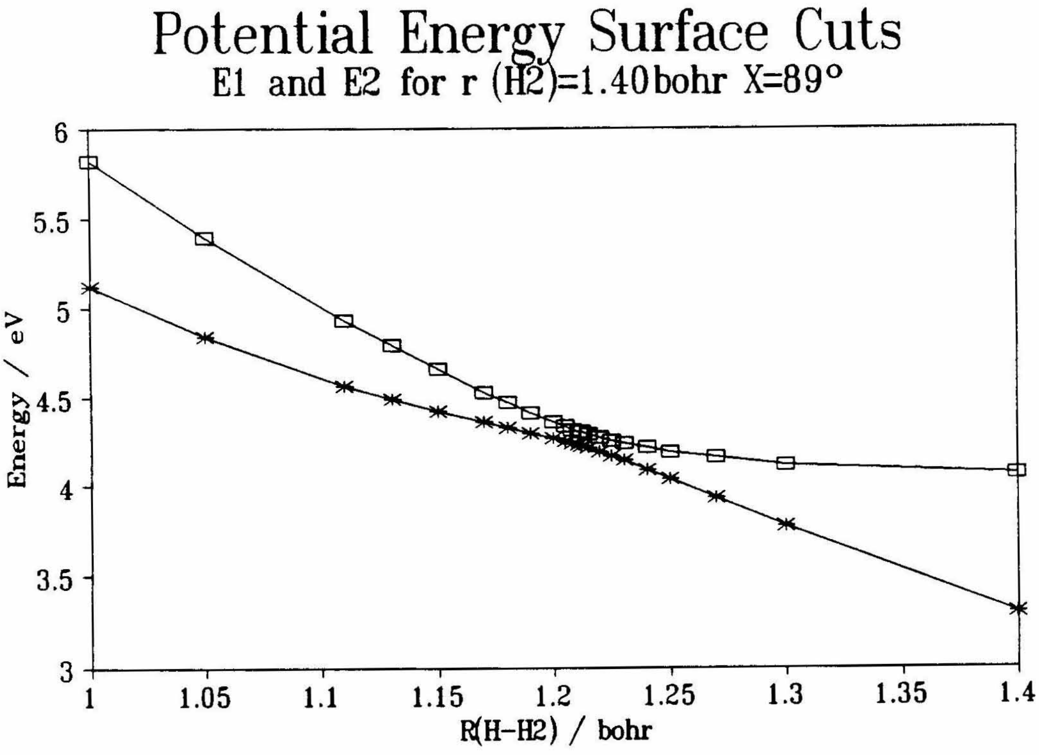

Figure 8.

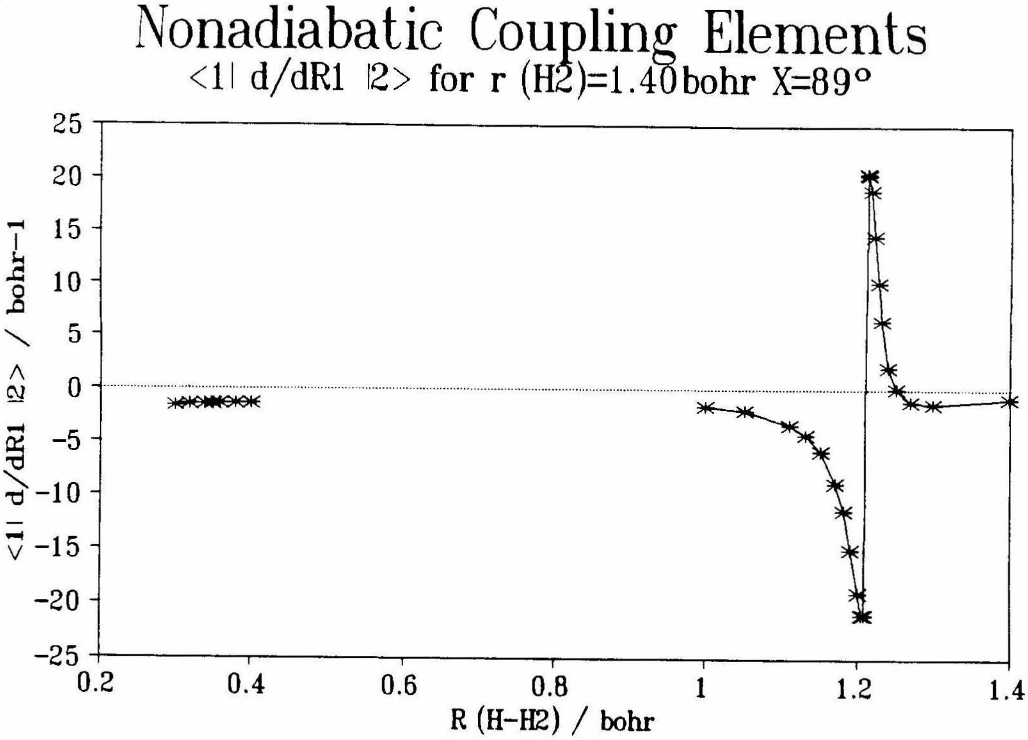

Figure 9a.

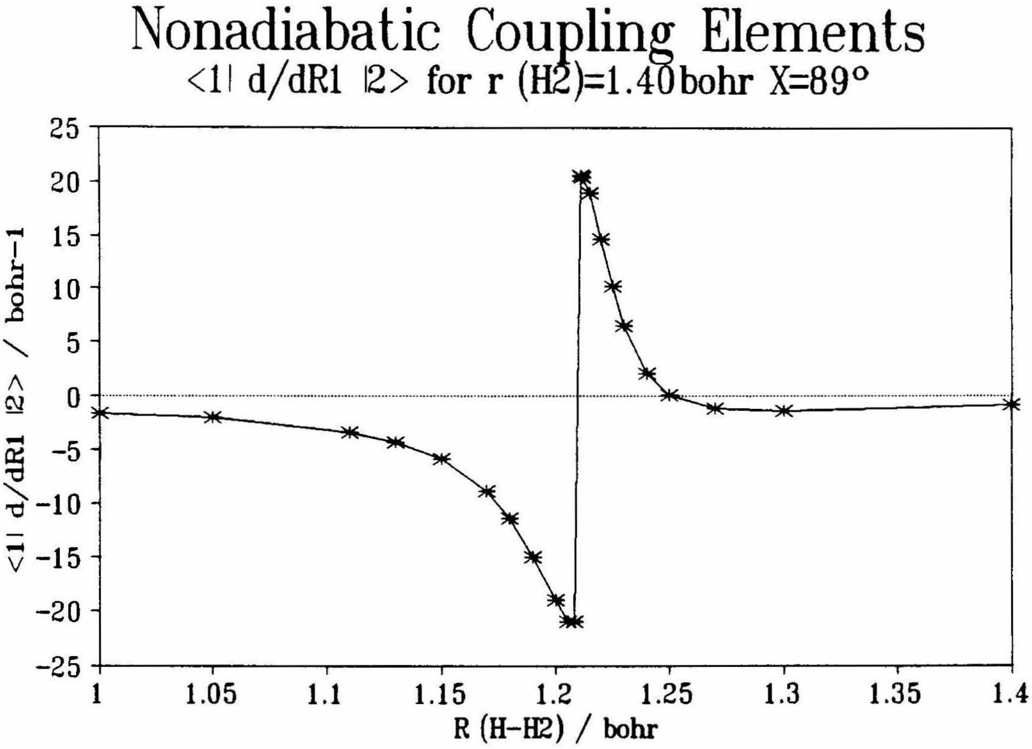

Figure 9b.

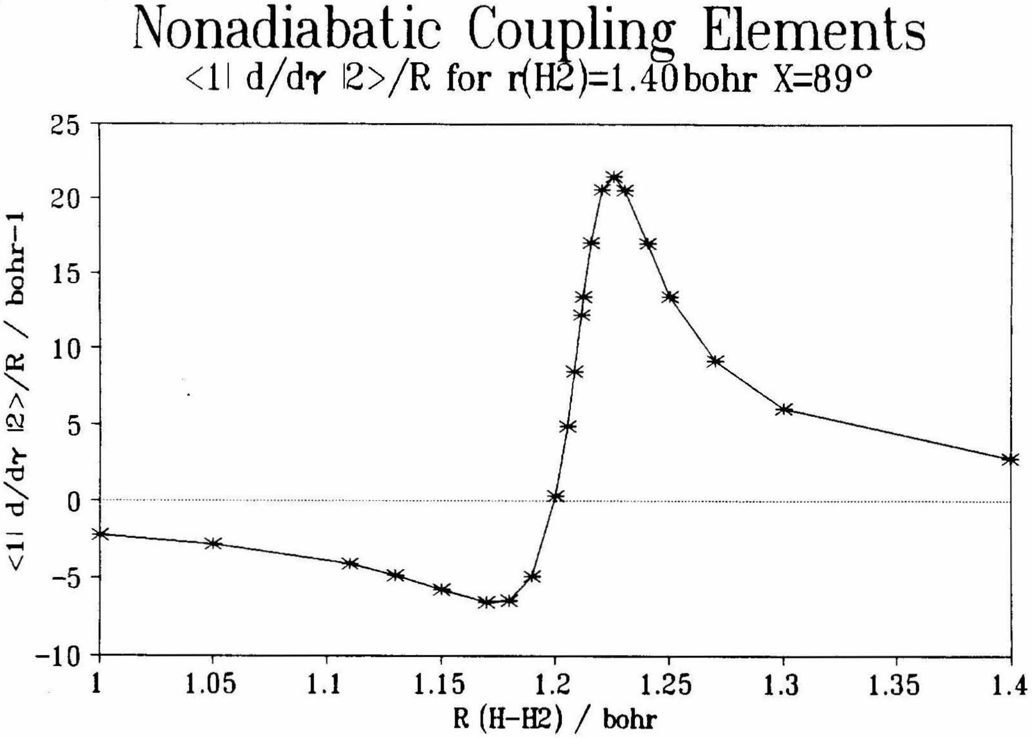

Figure 9c.

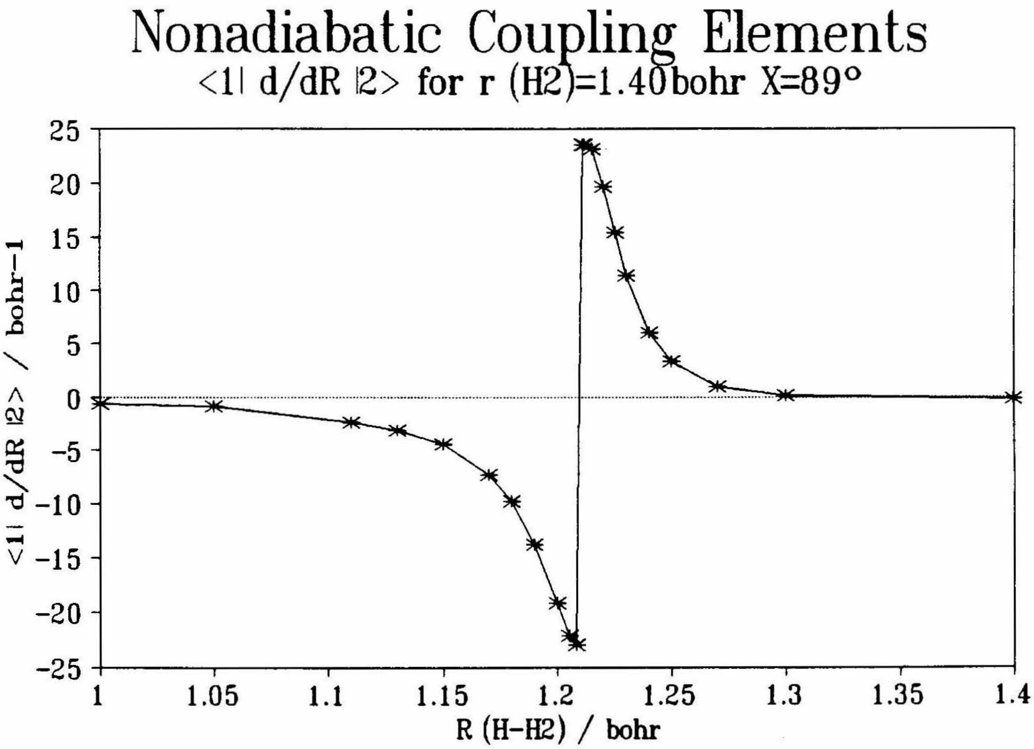

Figure 9d.

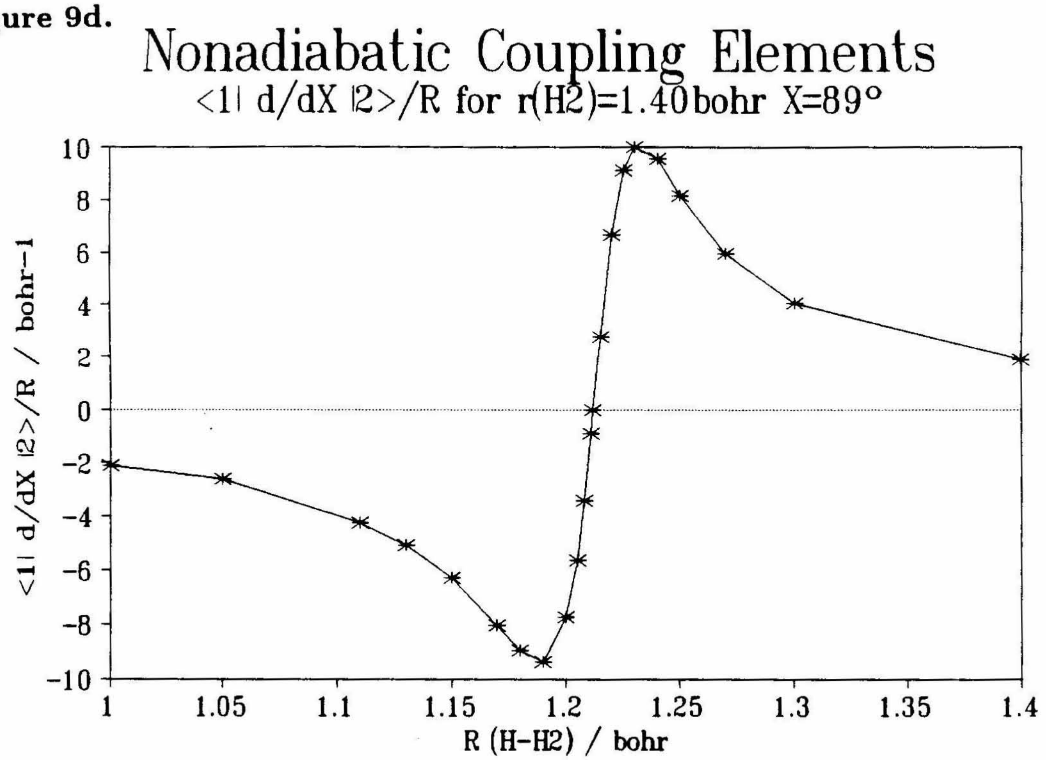

Figure 10.

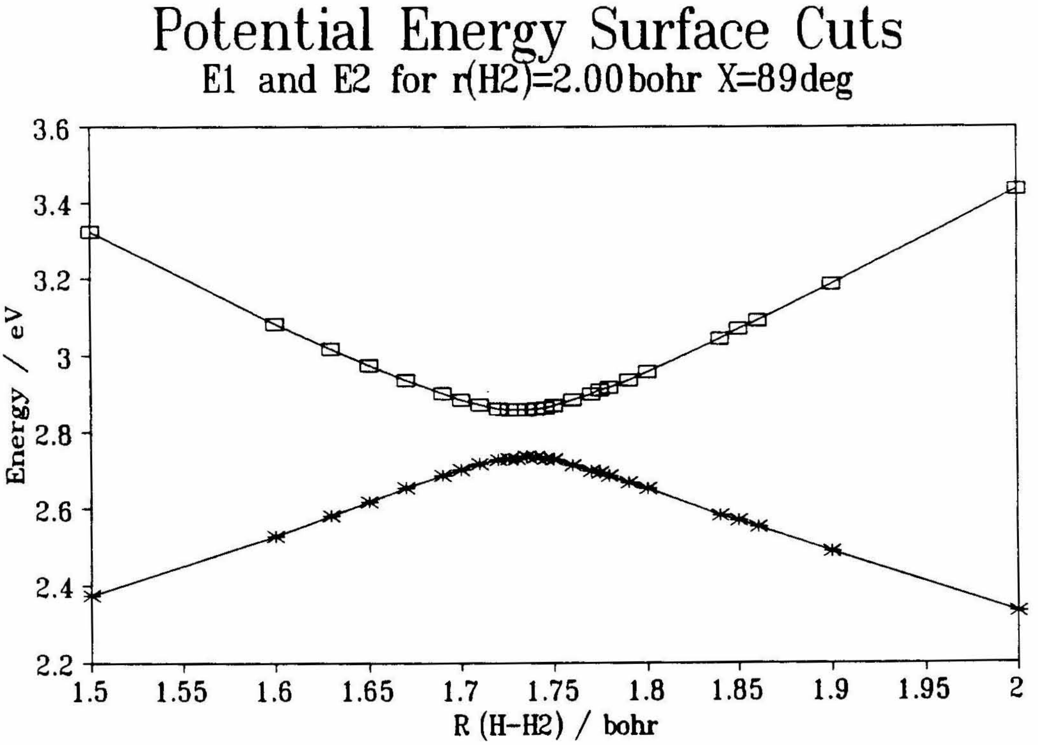

Figure 11a.

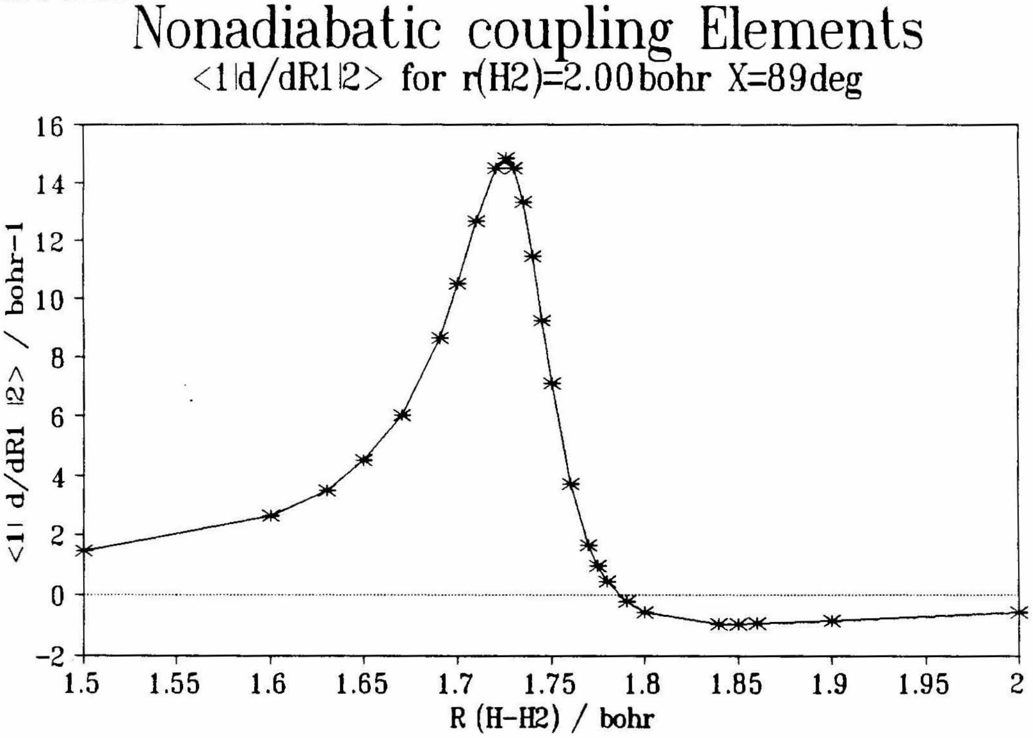

Figure 11b.

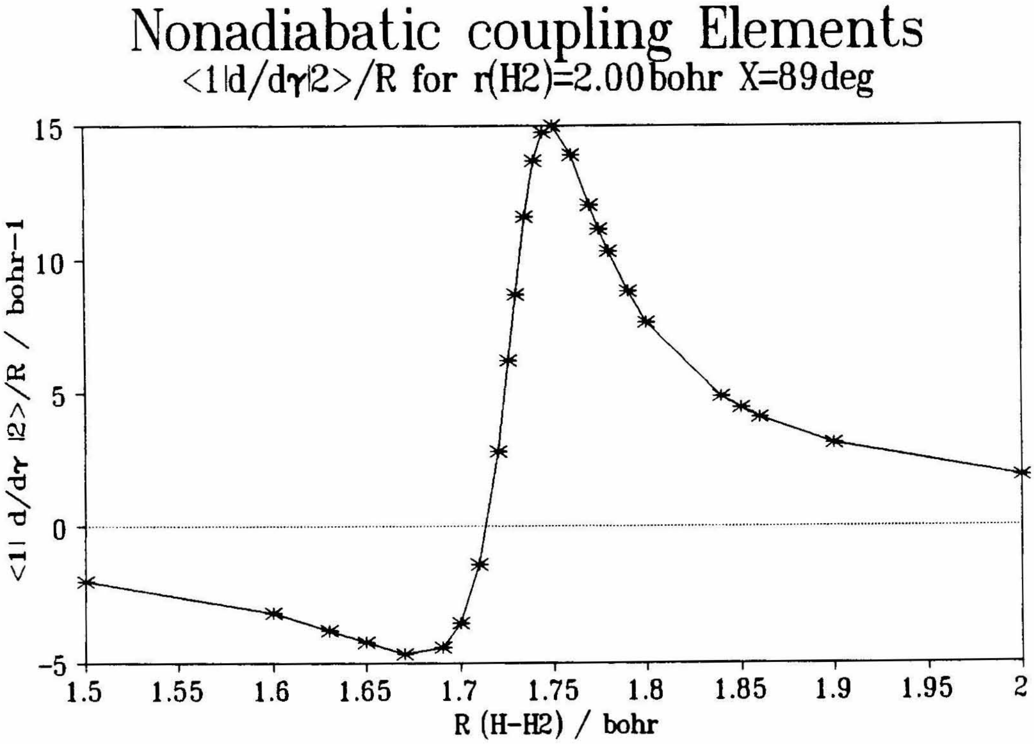

Figure 11c.

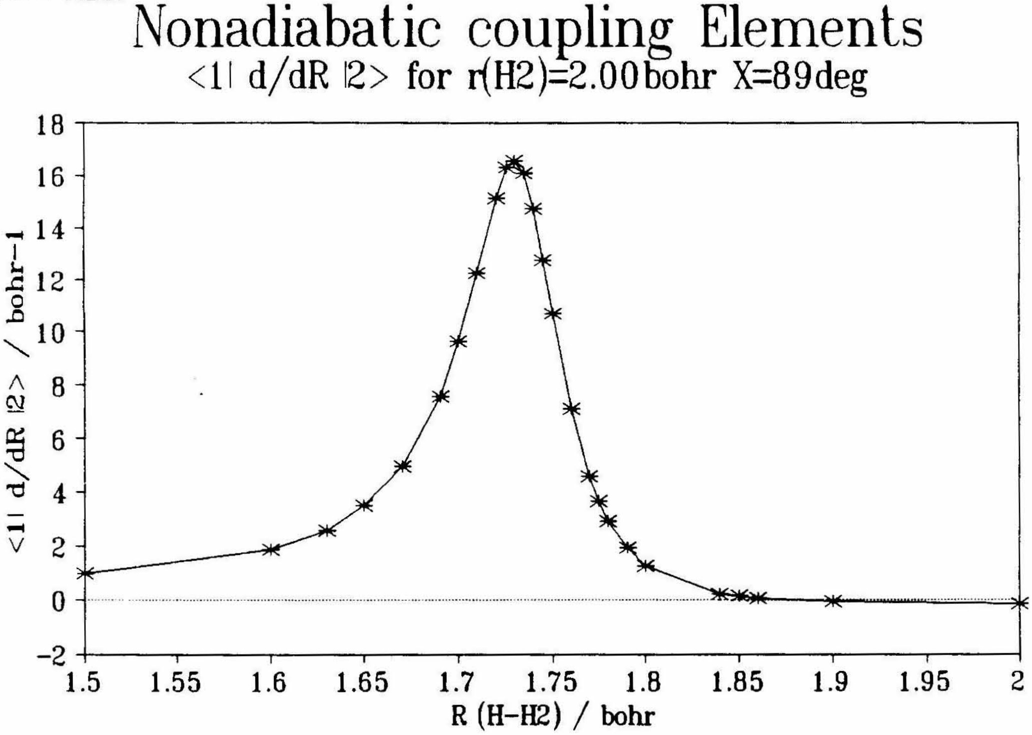

Figure 11d.

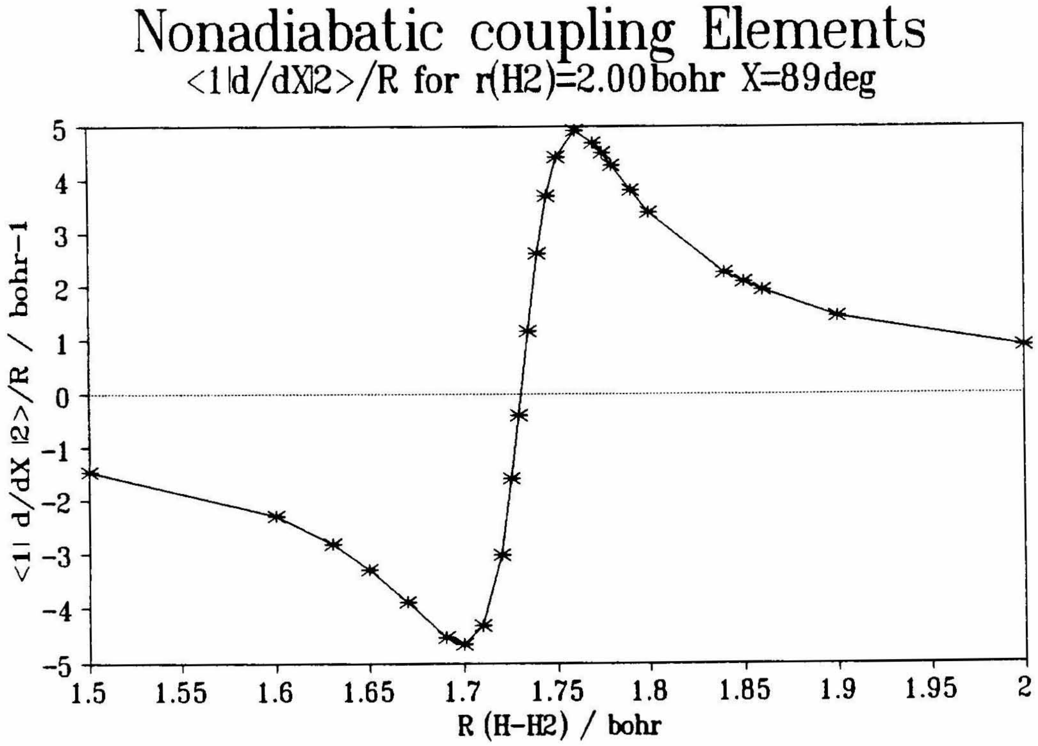

Figure 12a.

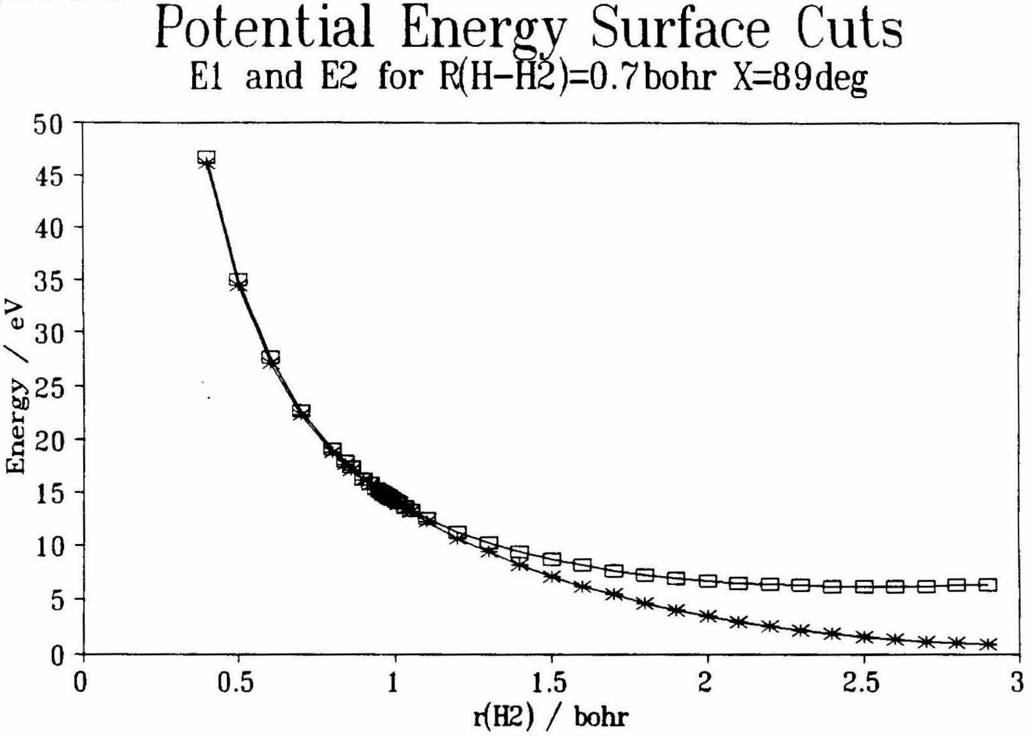

Figure 12b.

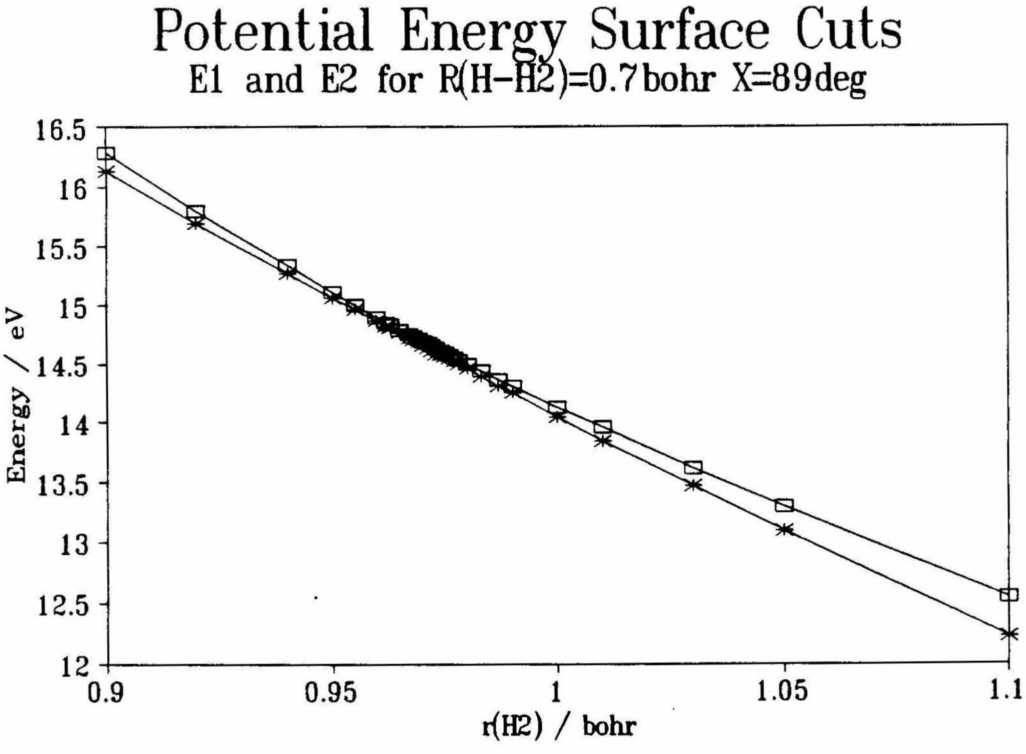

Figure 13a.

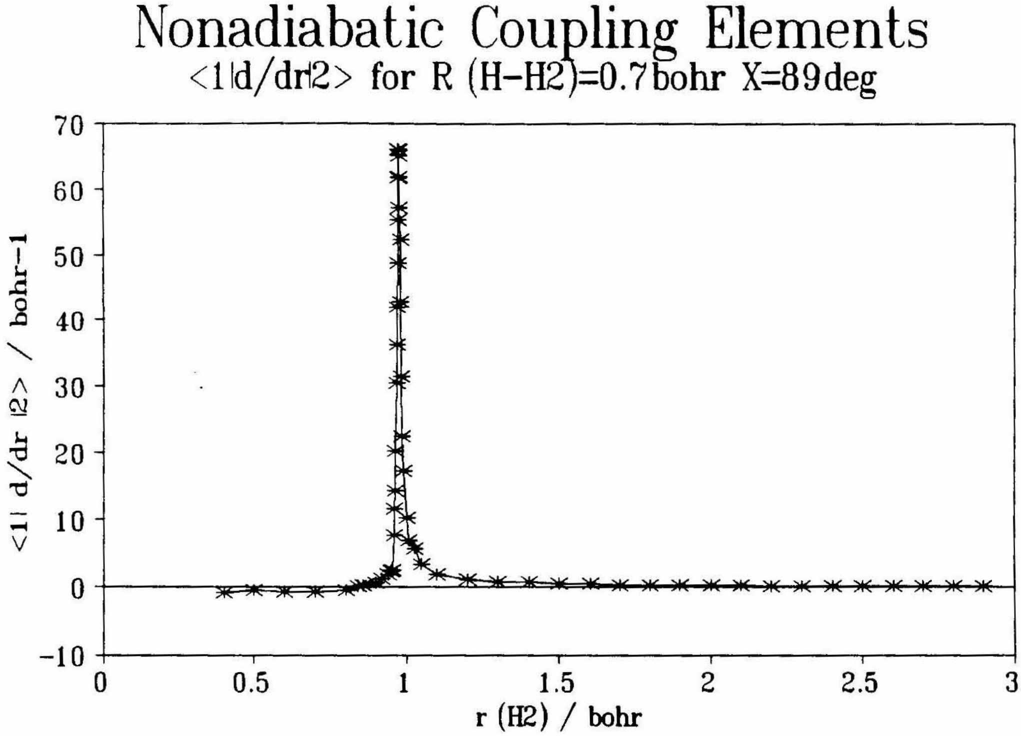

Figure 13b.

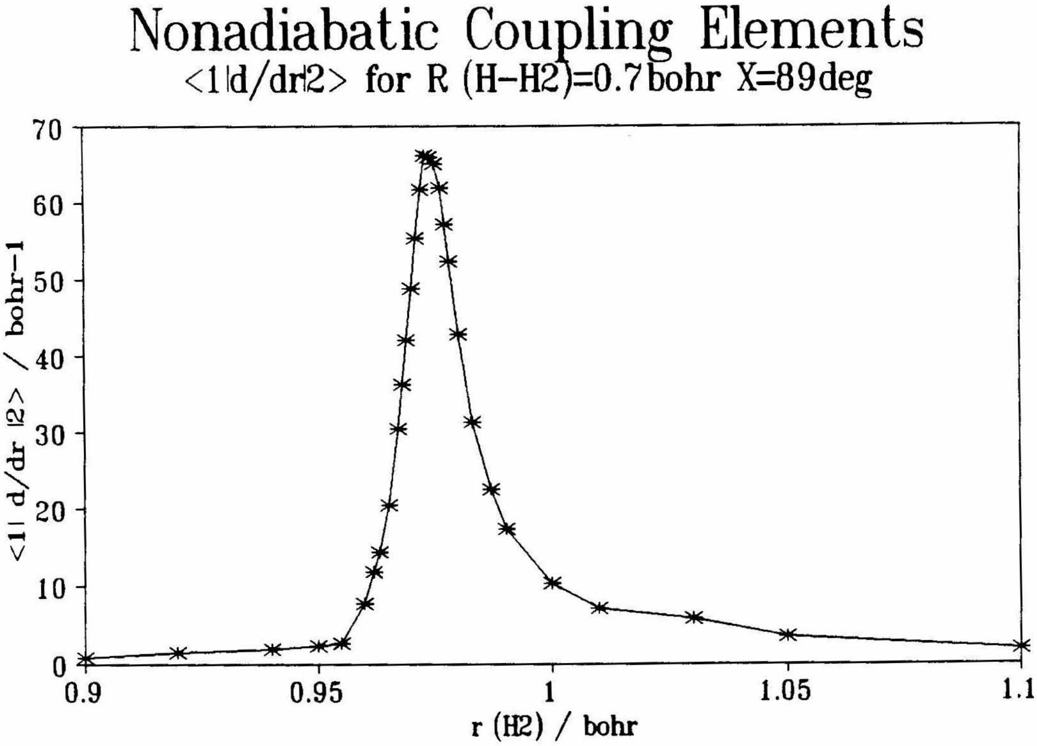

Figure 14a.

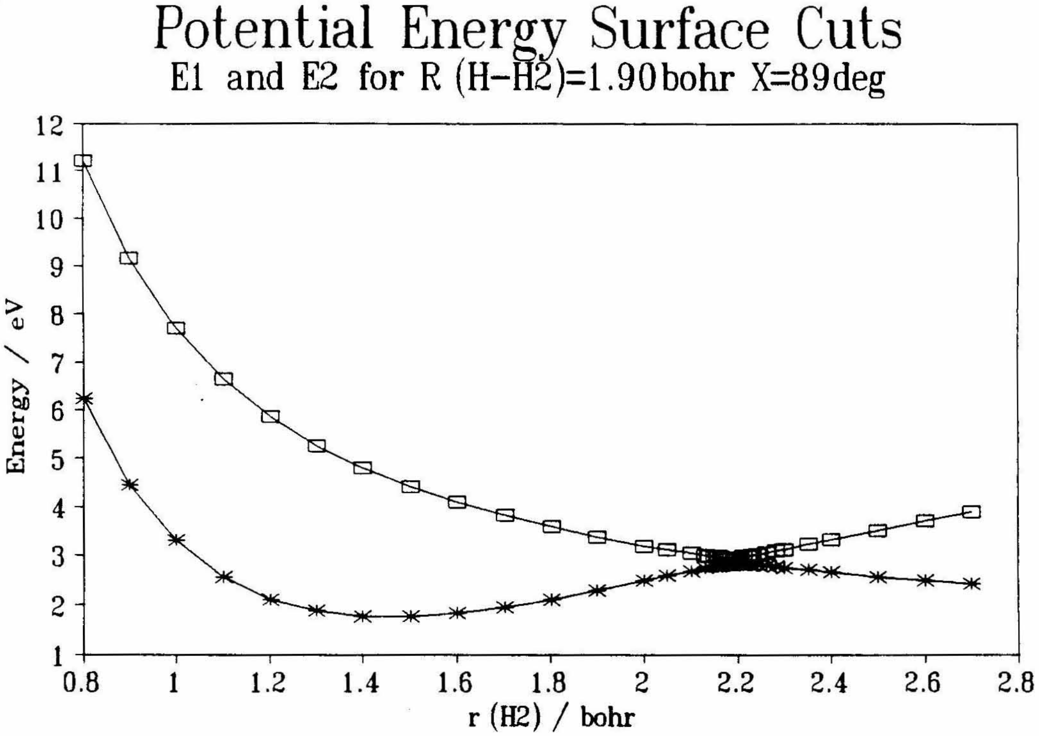

Figure 14b.

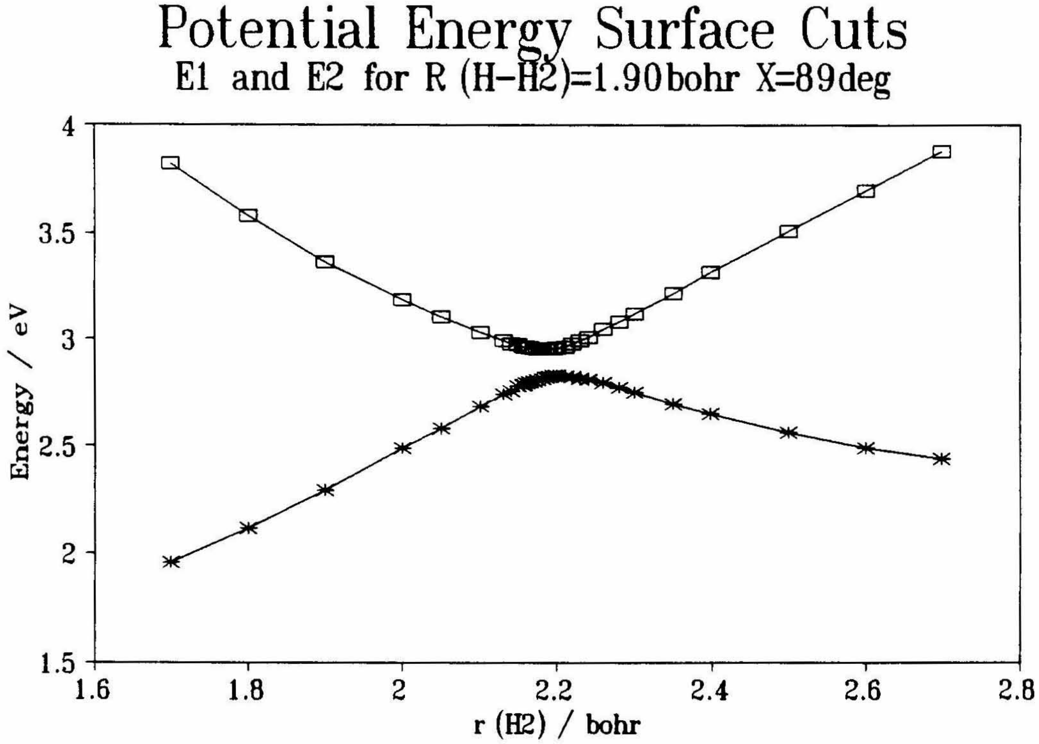

Figure 15.

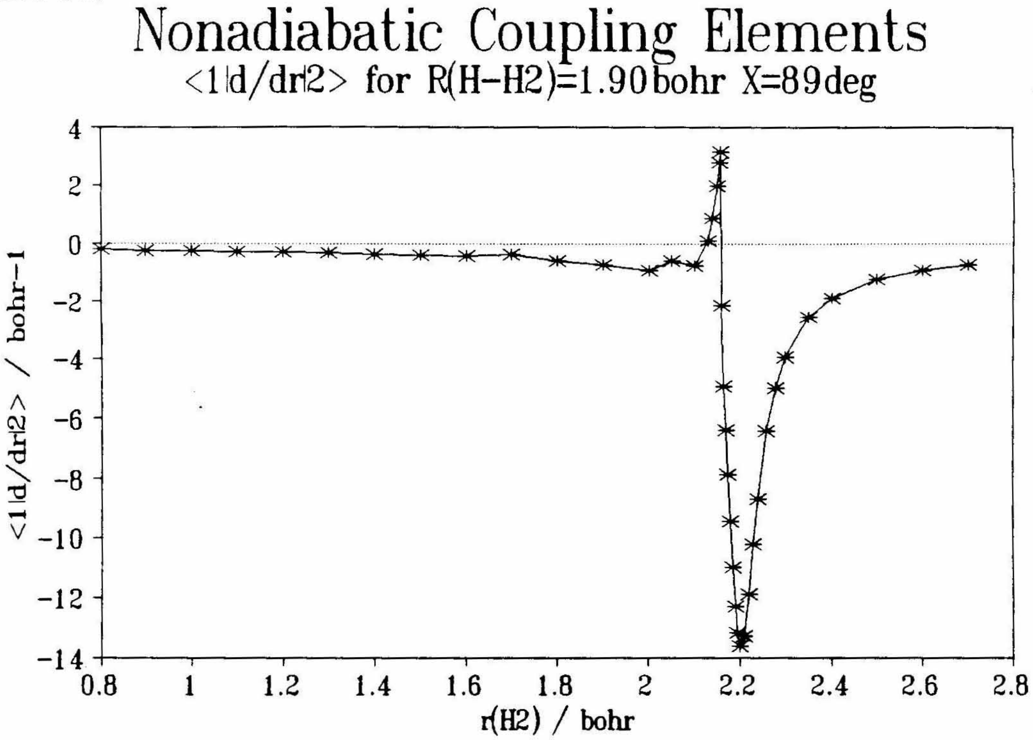

Figure 16a.

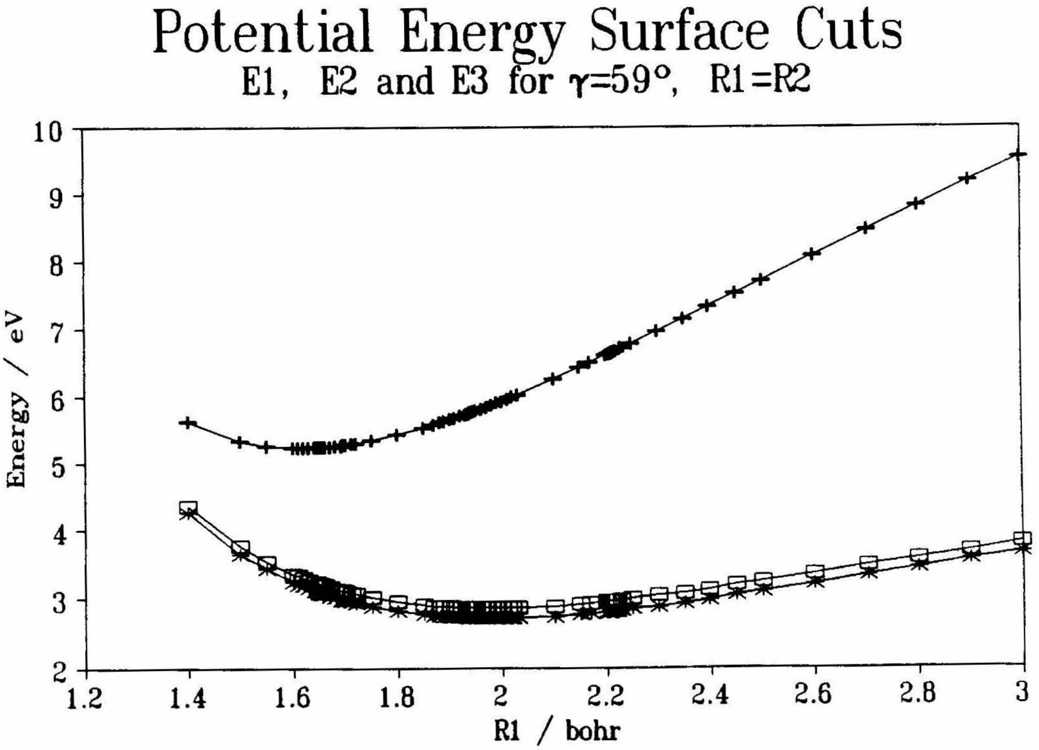

Figure 16b.

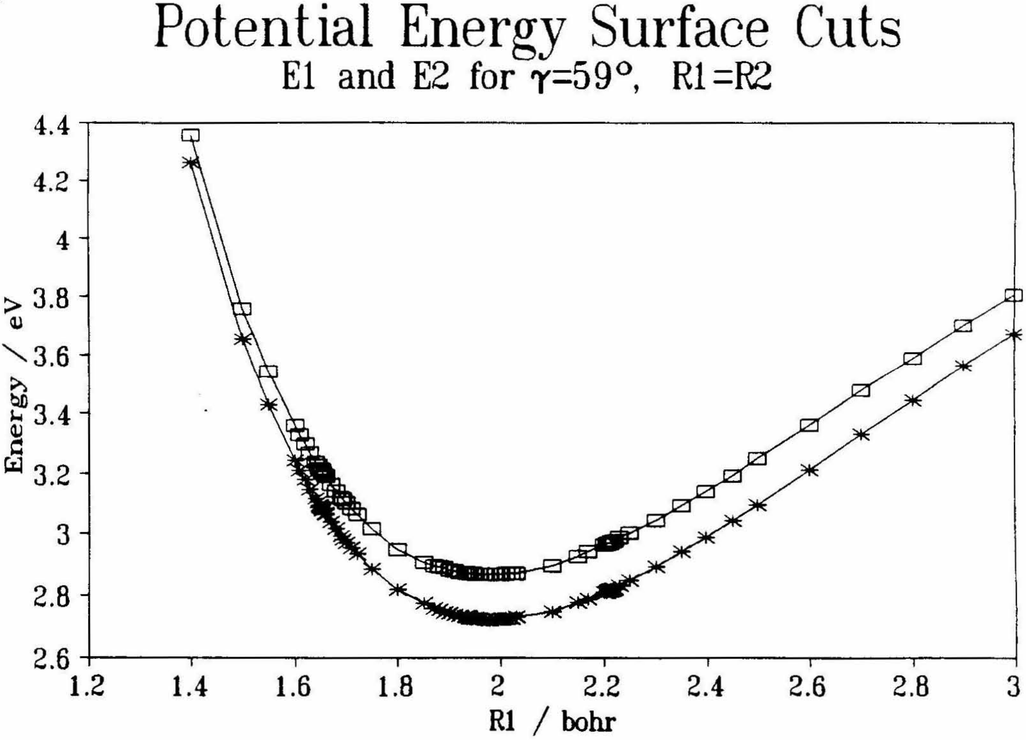

Figure 17a.

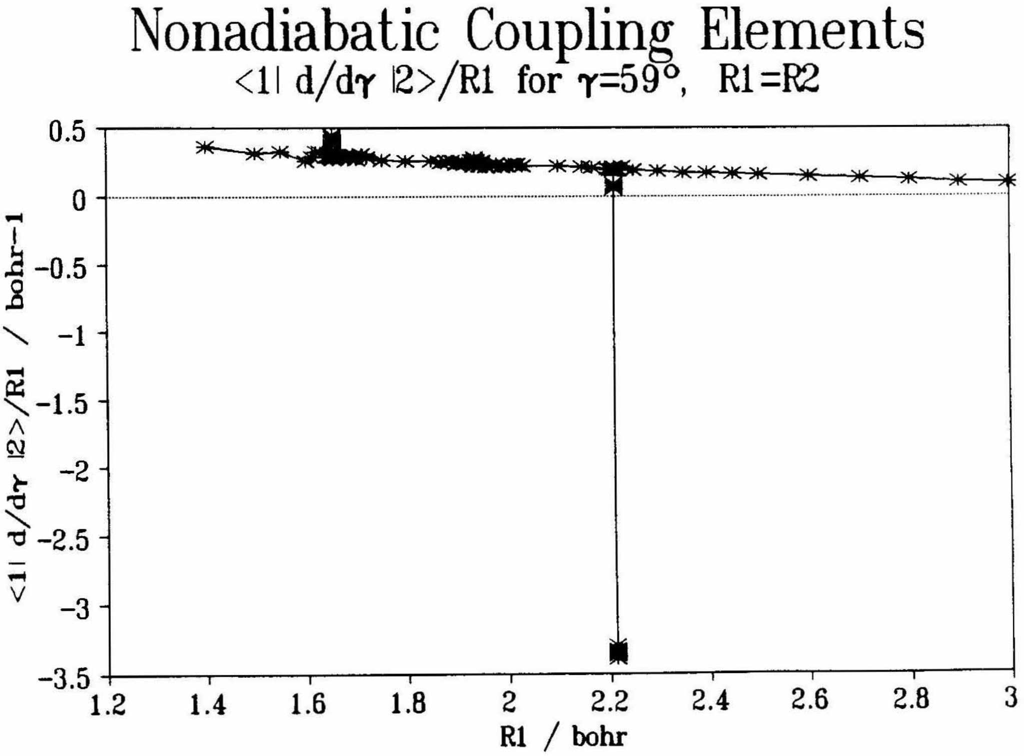

Figure 17b.

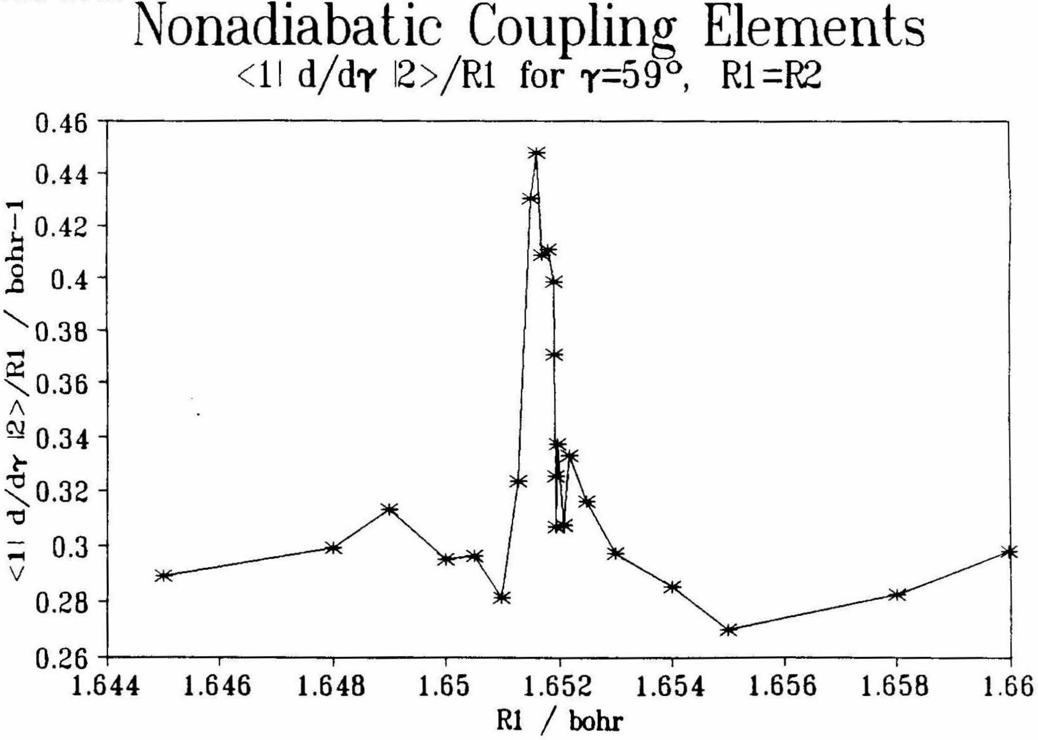

Figure 17c.

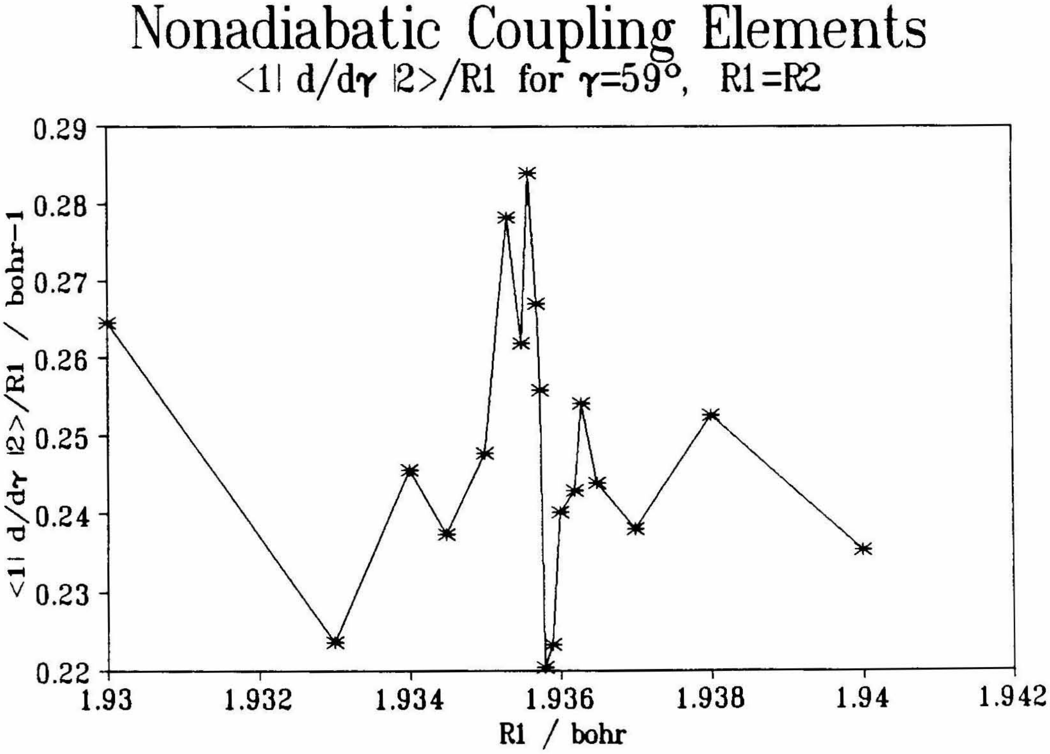

Figure 17d.

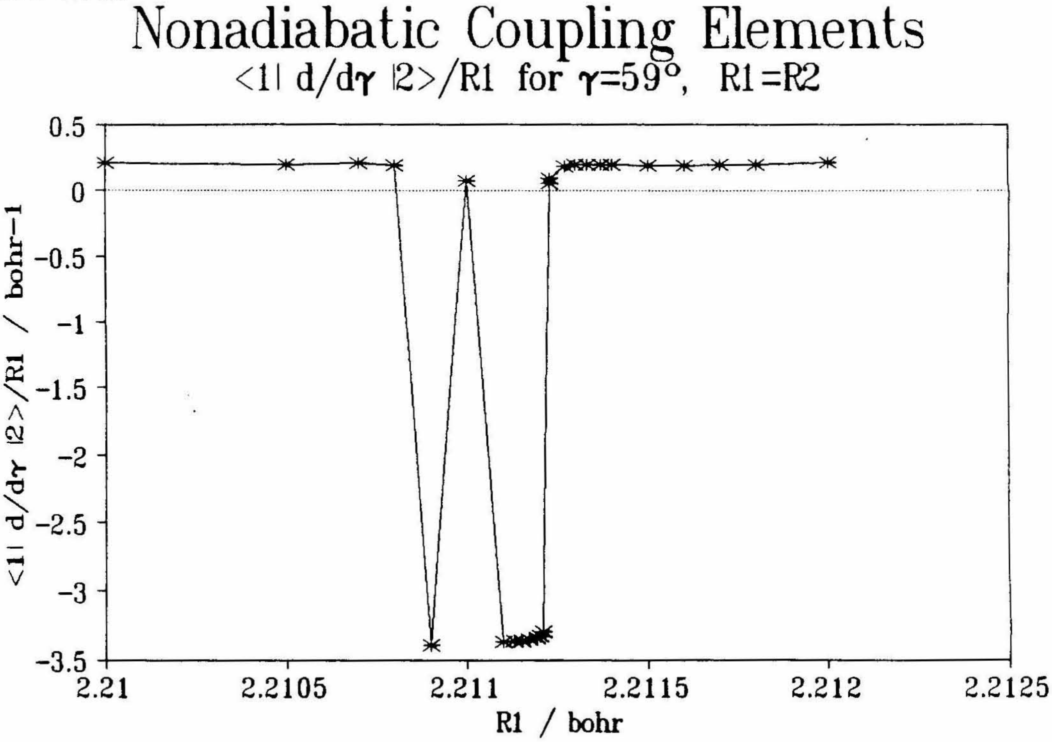

Figure 18a.

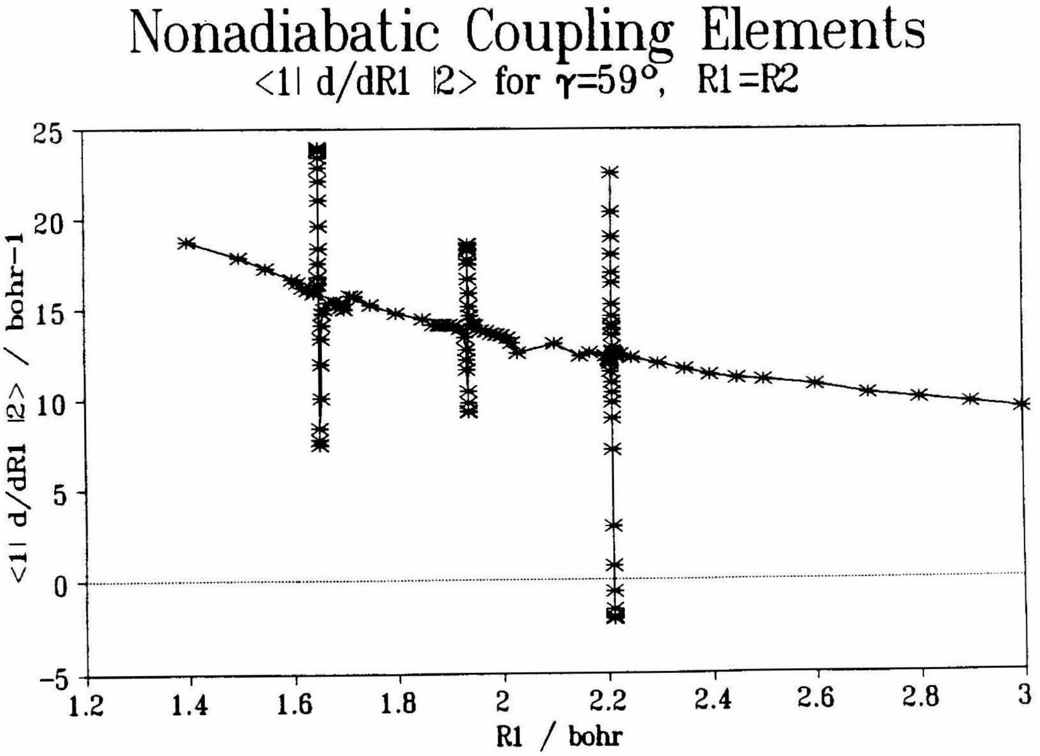

Figure 18b.

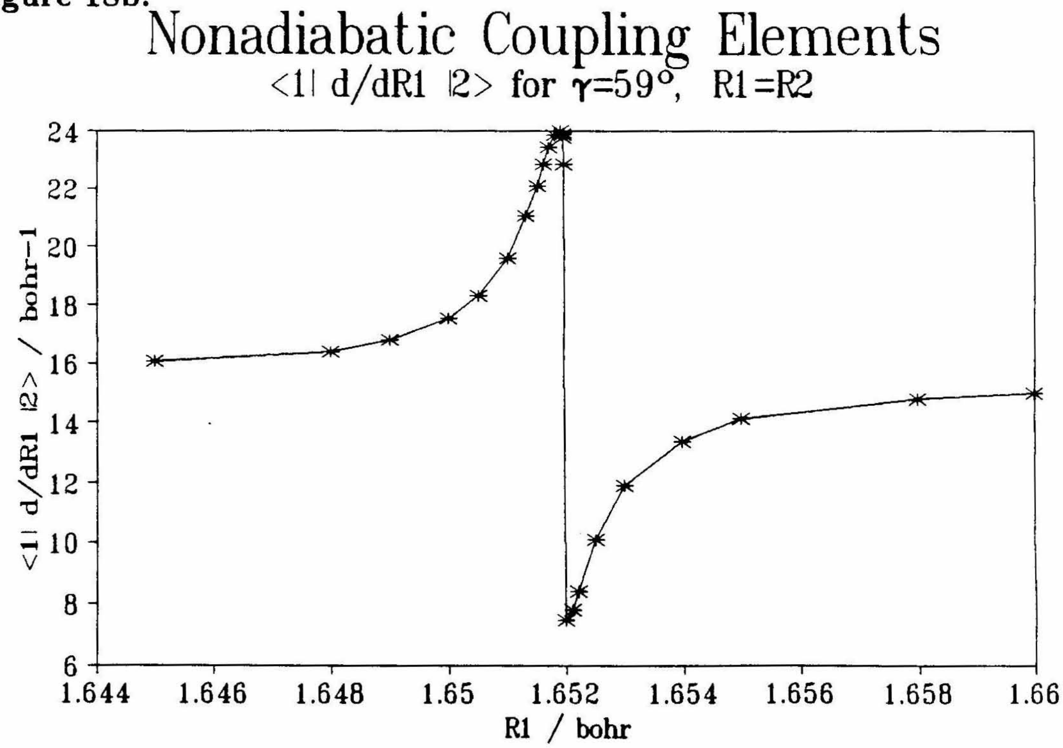

Figure 18c.

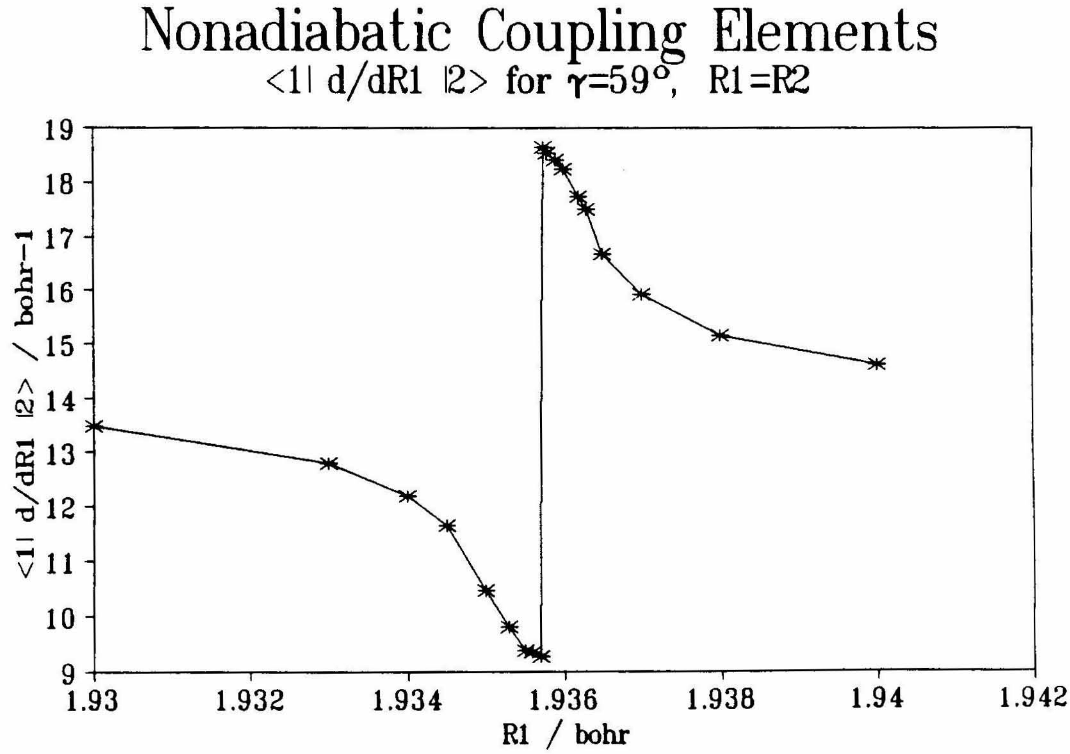

Figure 18d.

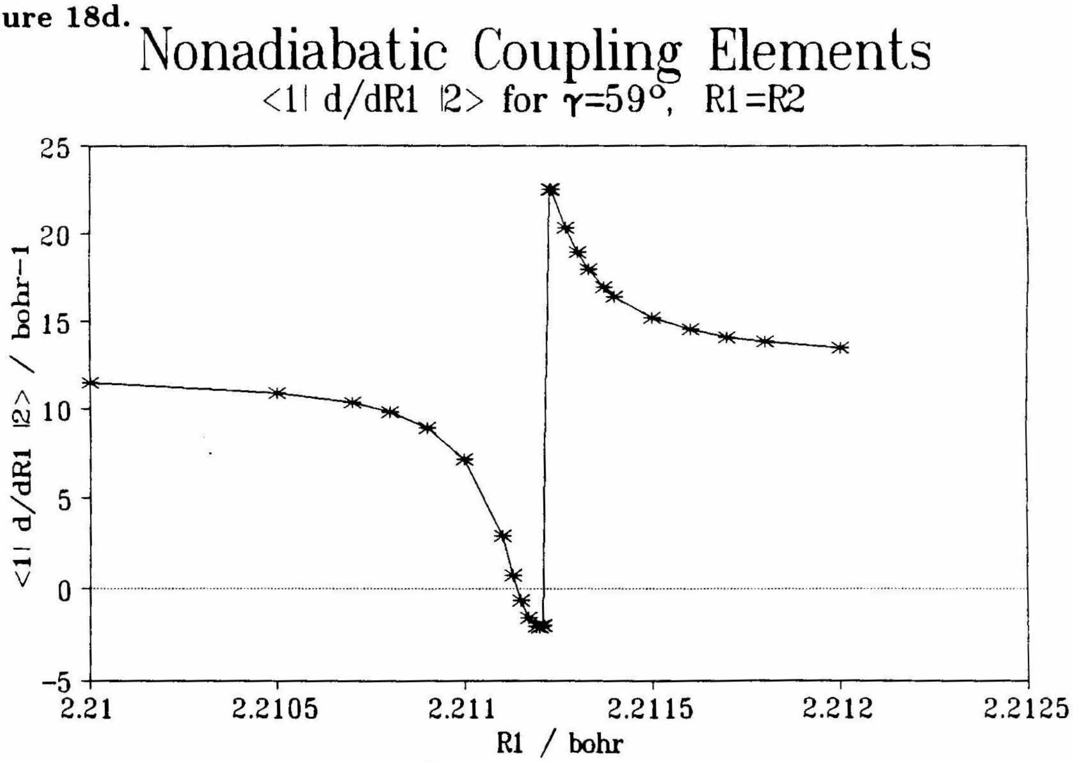

Figure 19a.

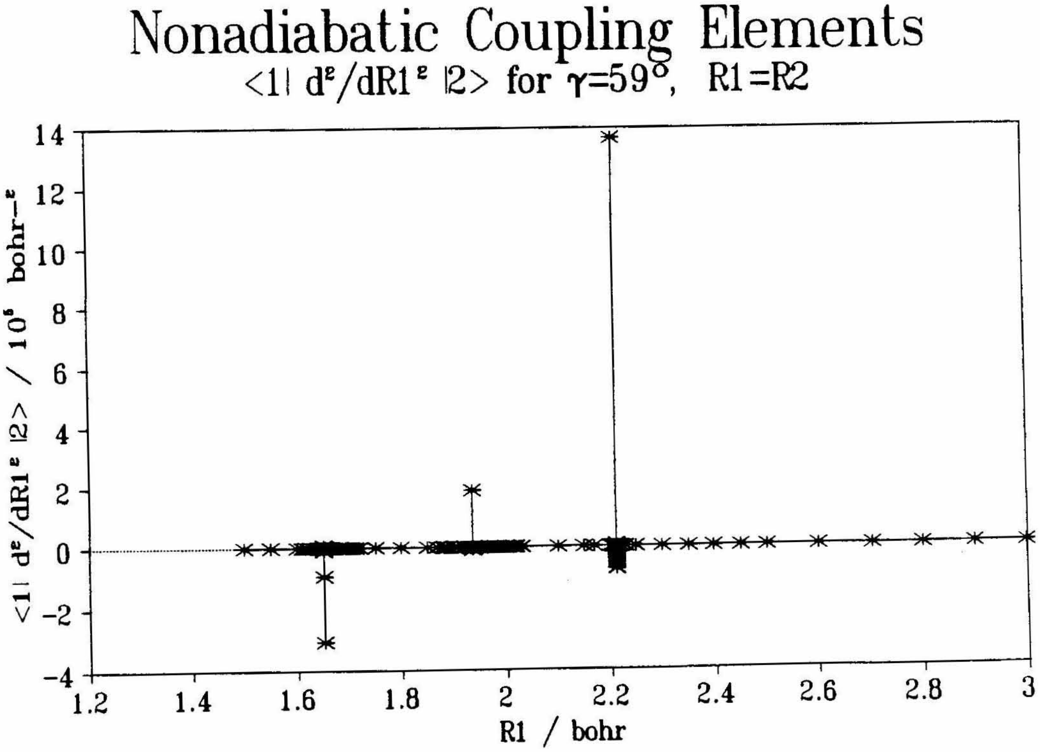

Figure 19b.

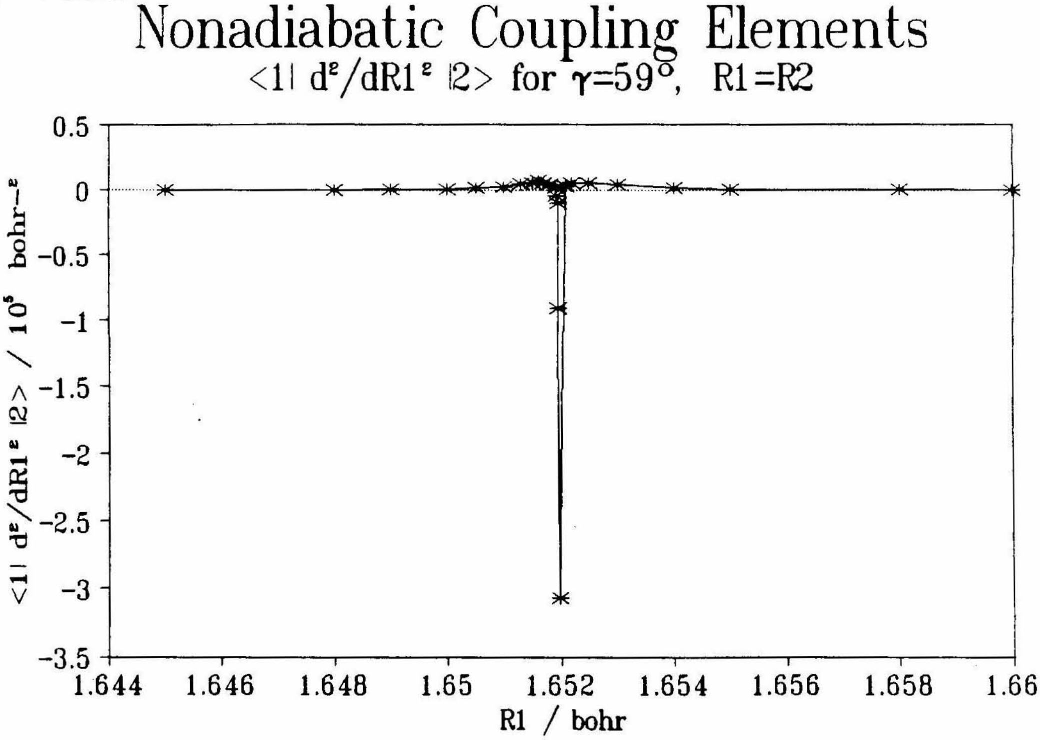

Figure 19c.

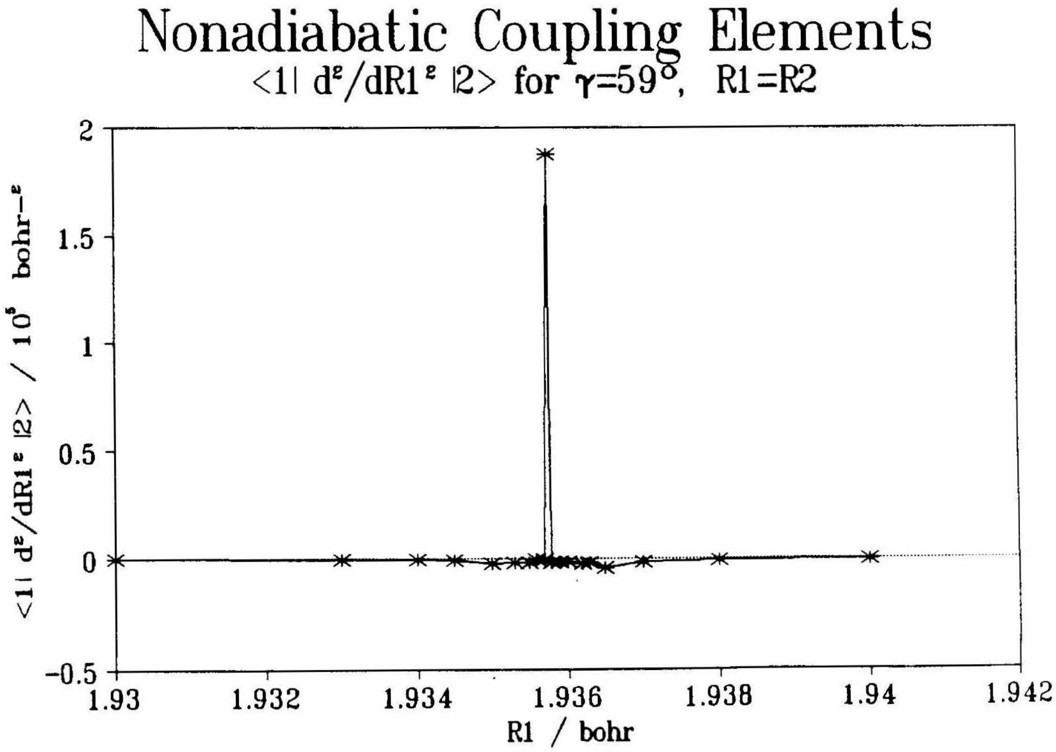

Figure 19d.

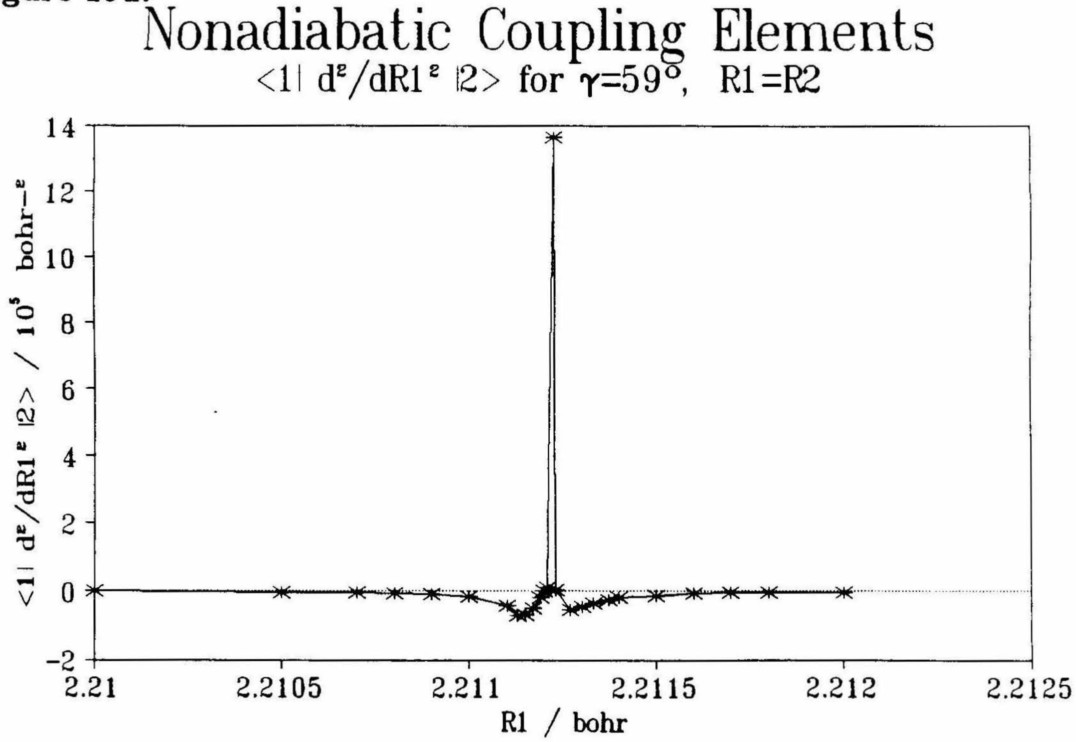

Figure 20a.

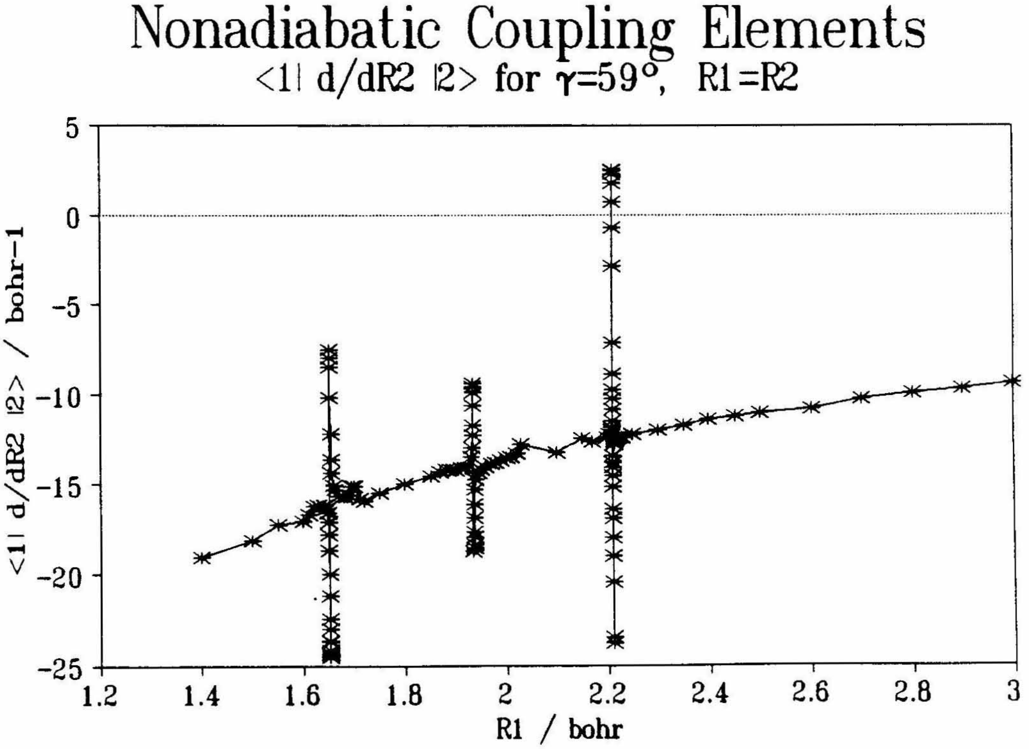

Figure 20b.

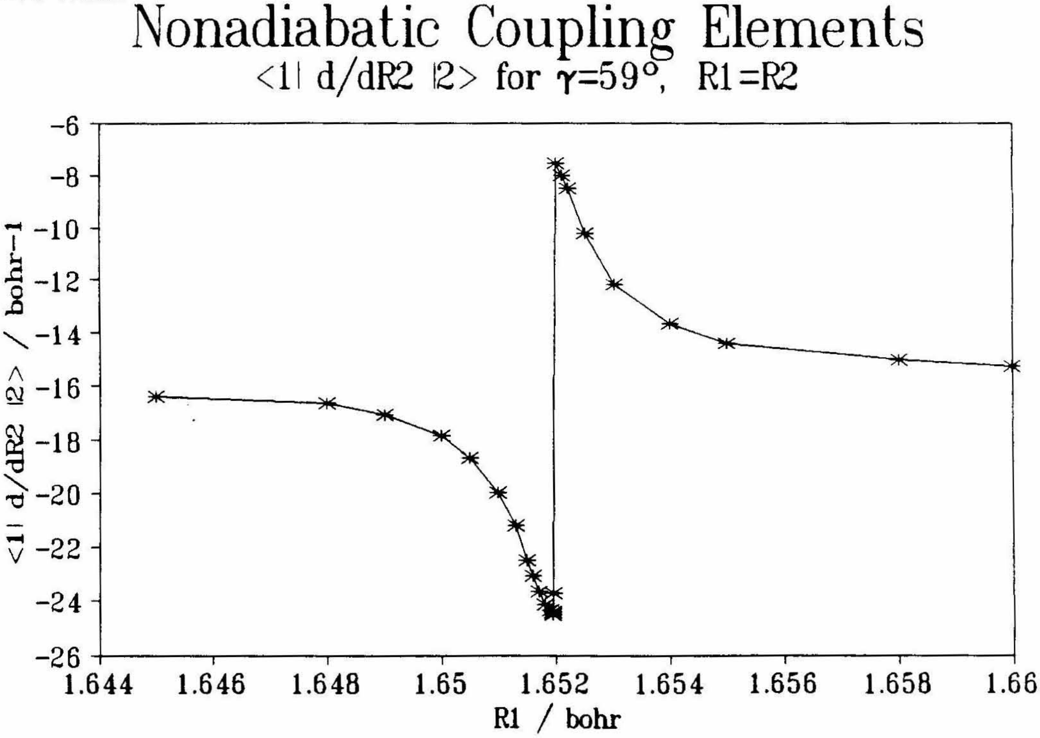

Figure 20c.

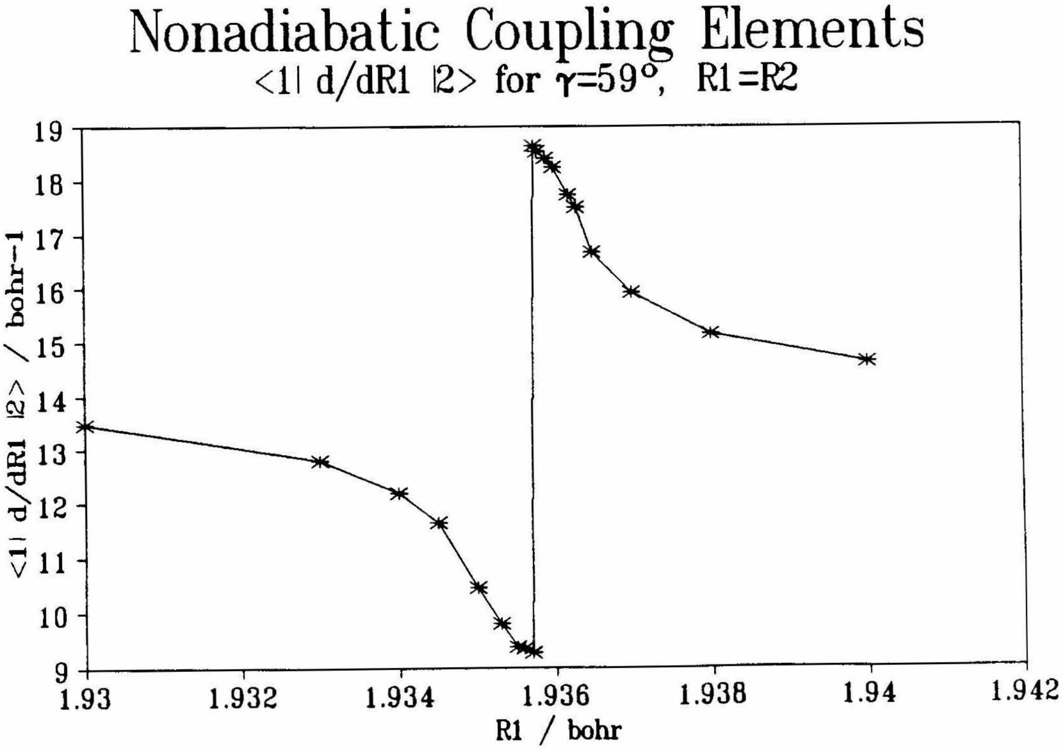

Figure 20d.

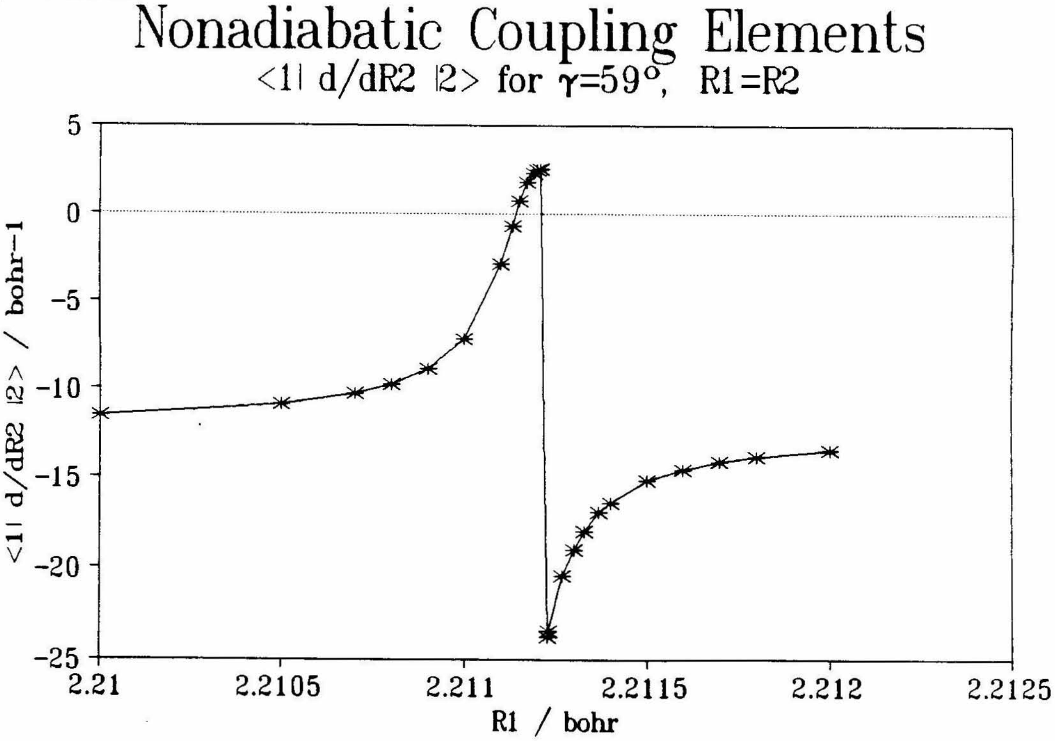

Figure 21a.

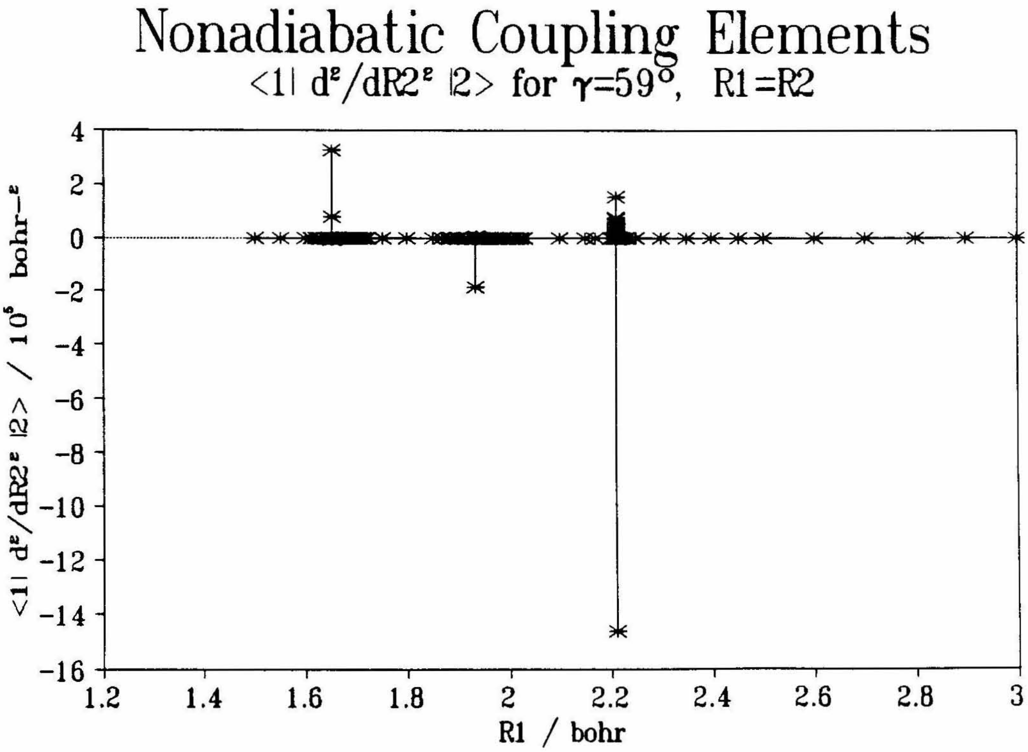

Figure 21b.

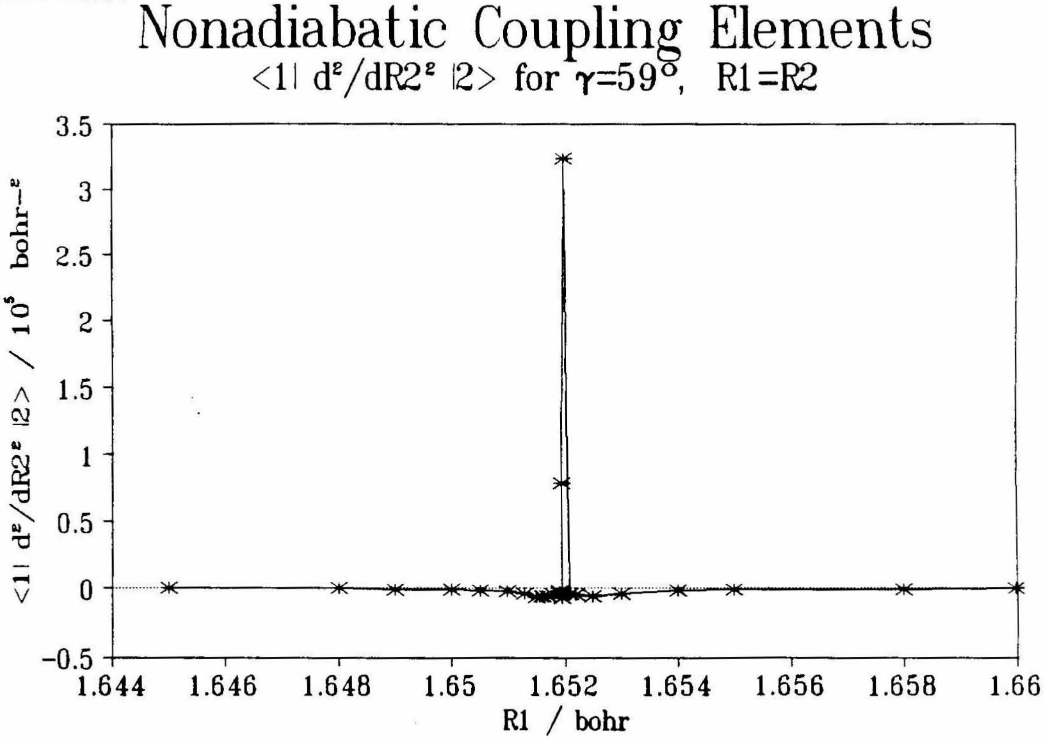

Figure 21c.

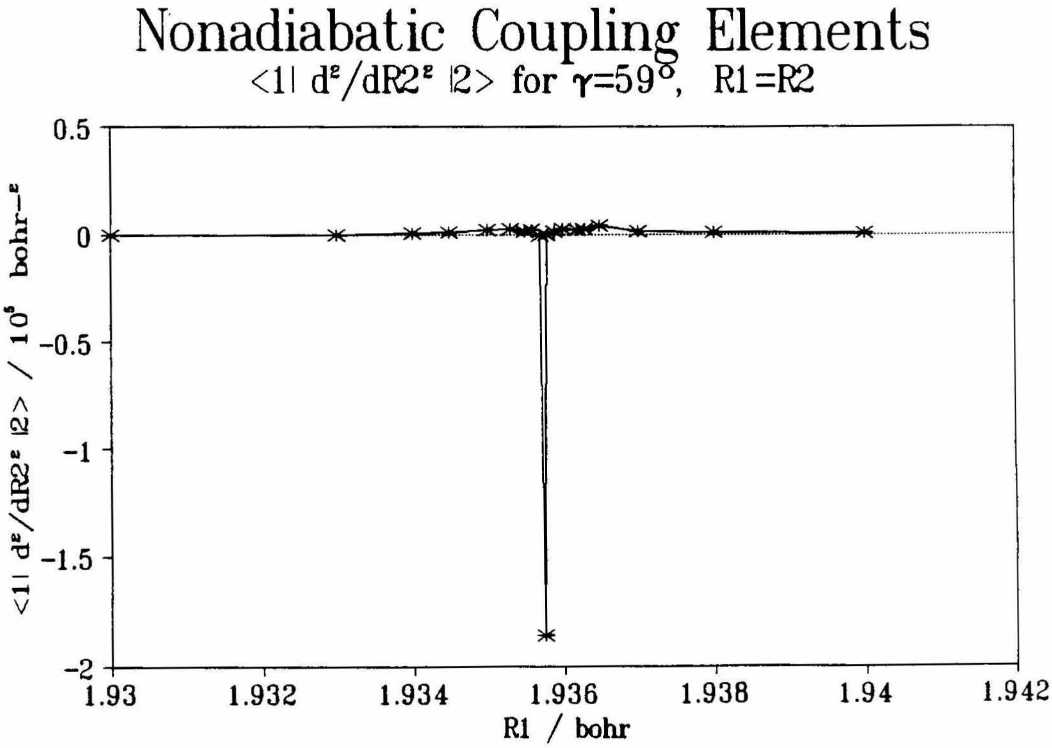

Figure 21d.

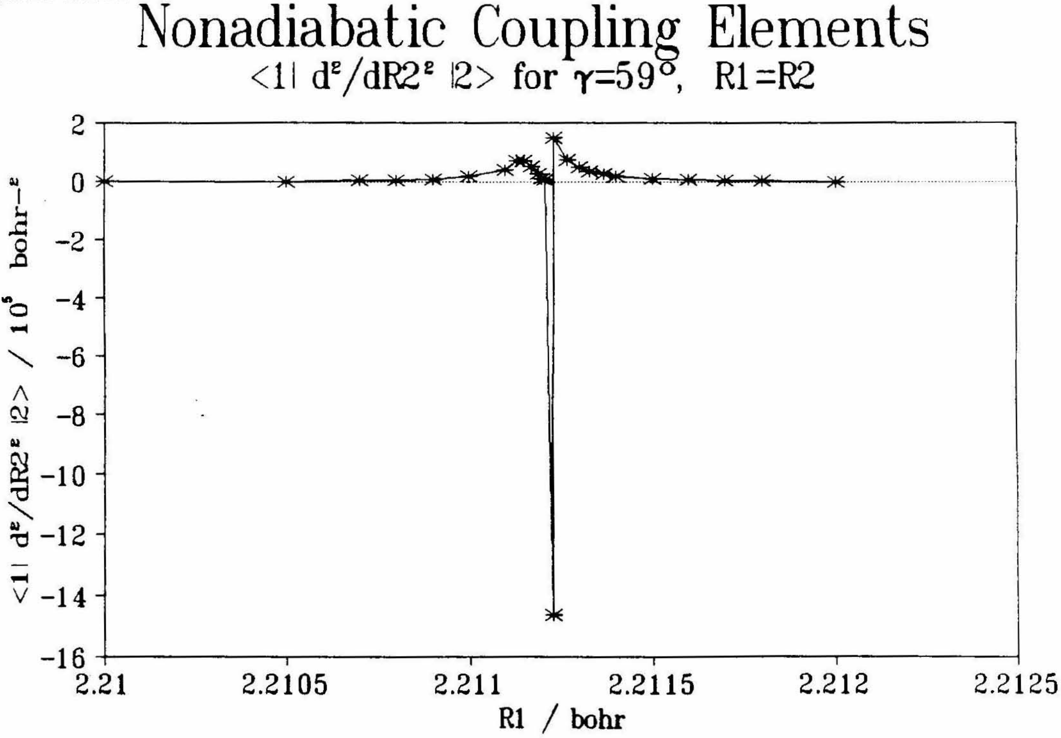

Figure 22a.

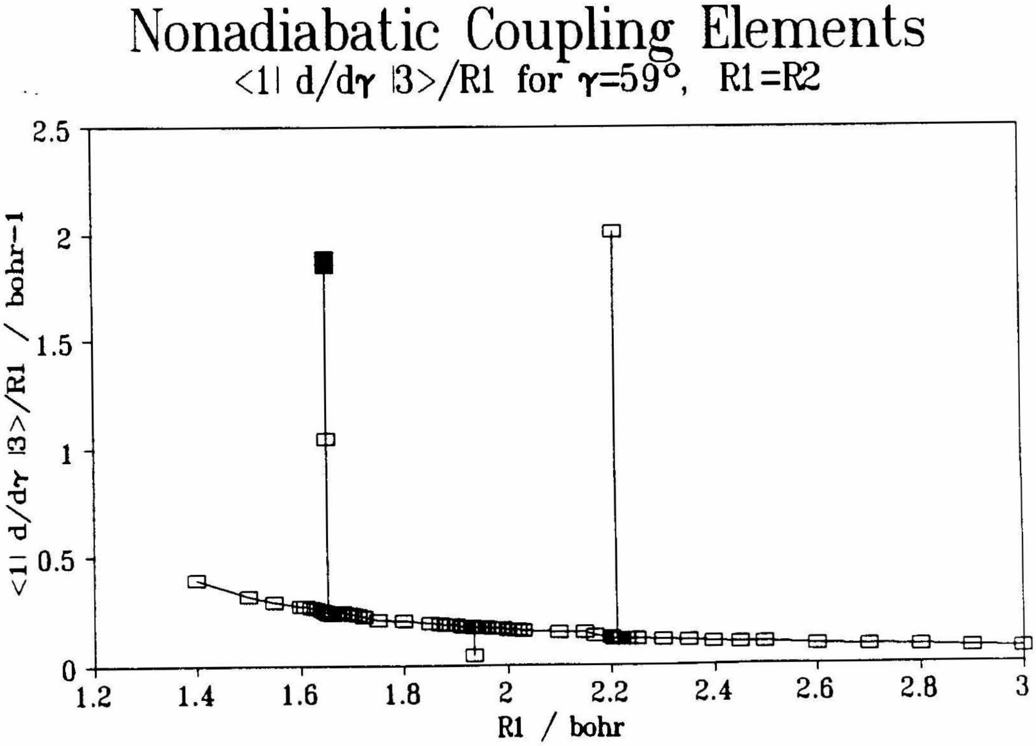

Figure 22b.

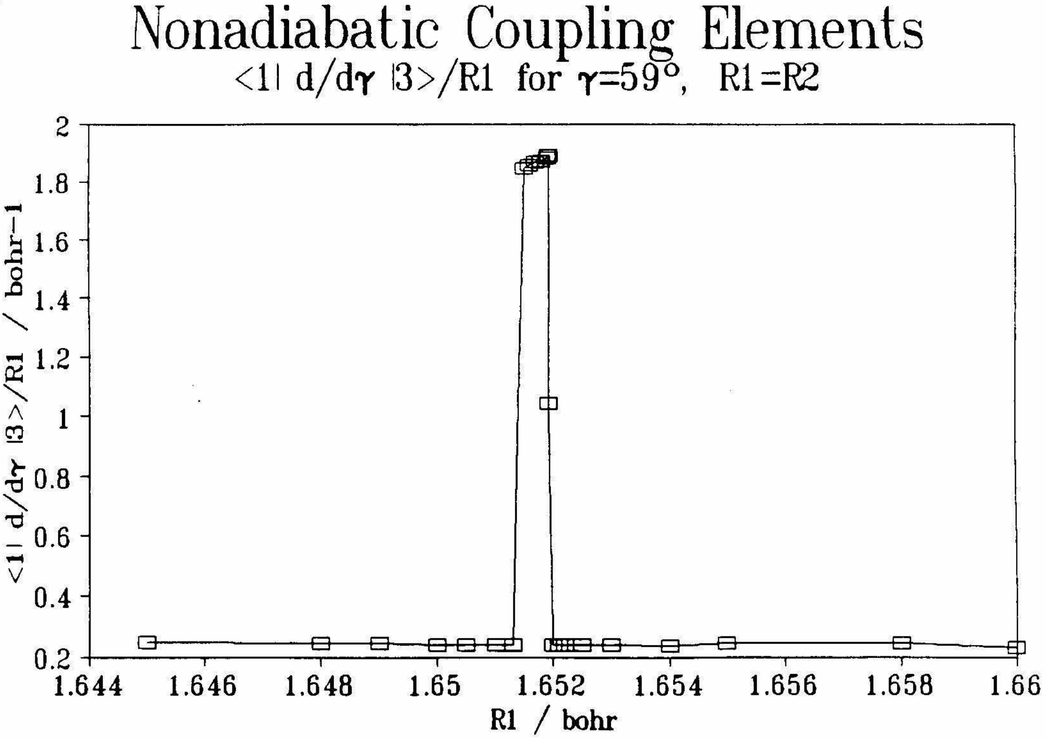

Figure 22c.

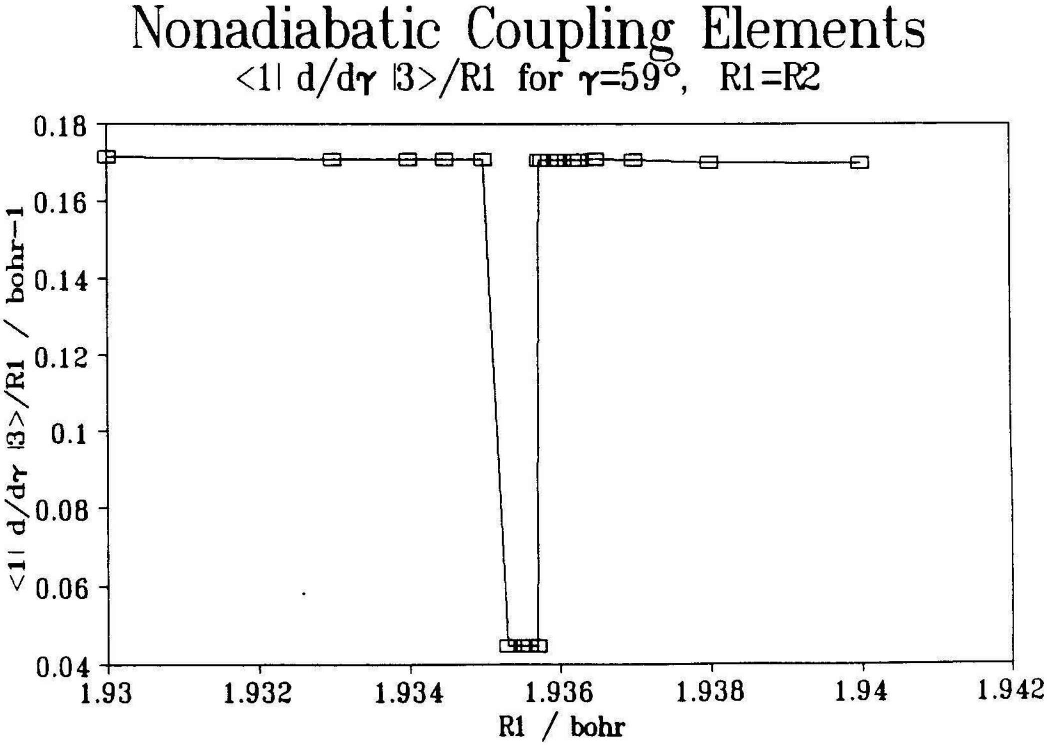

Figure 22d.

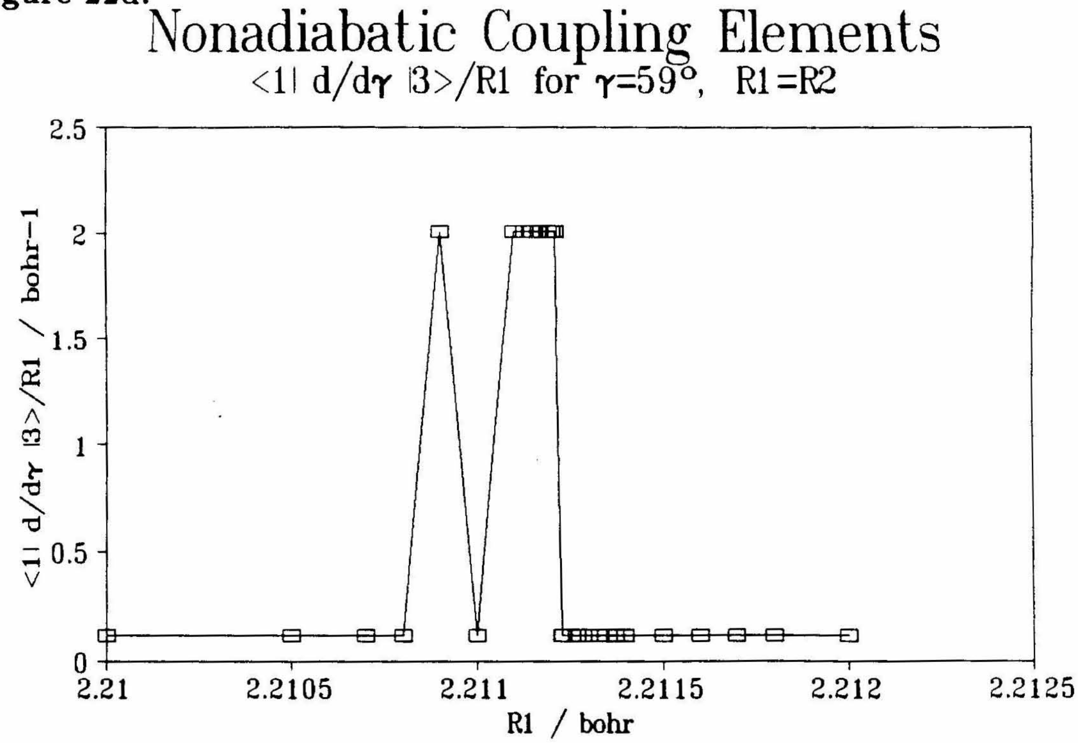

Figure 23a.

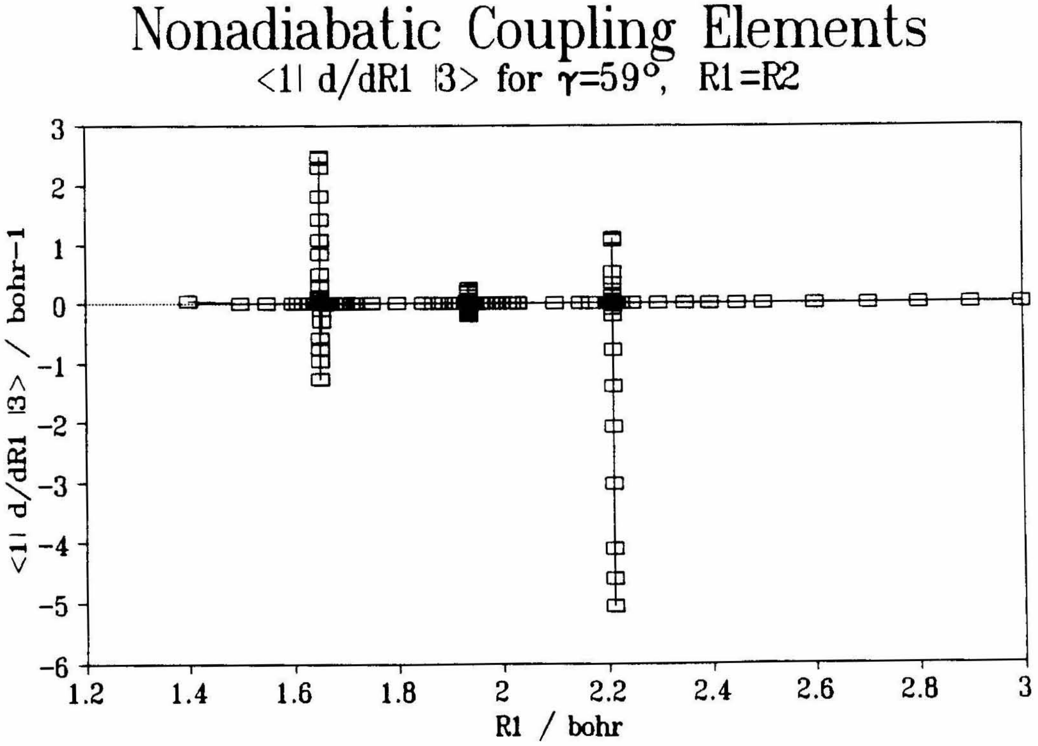

Figure 23b.

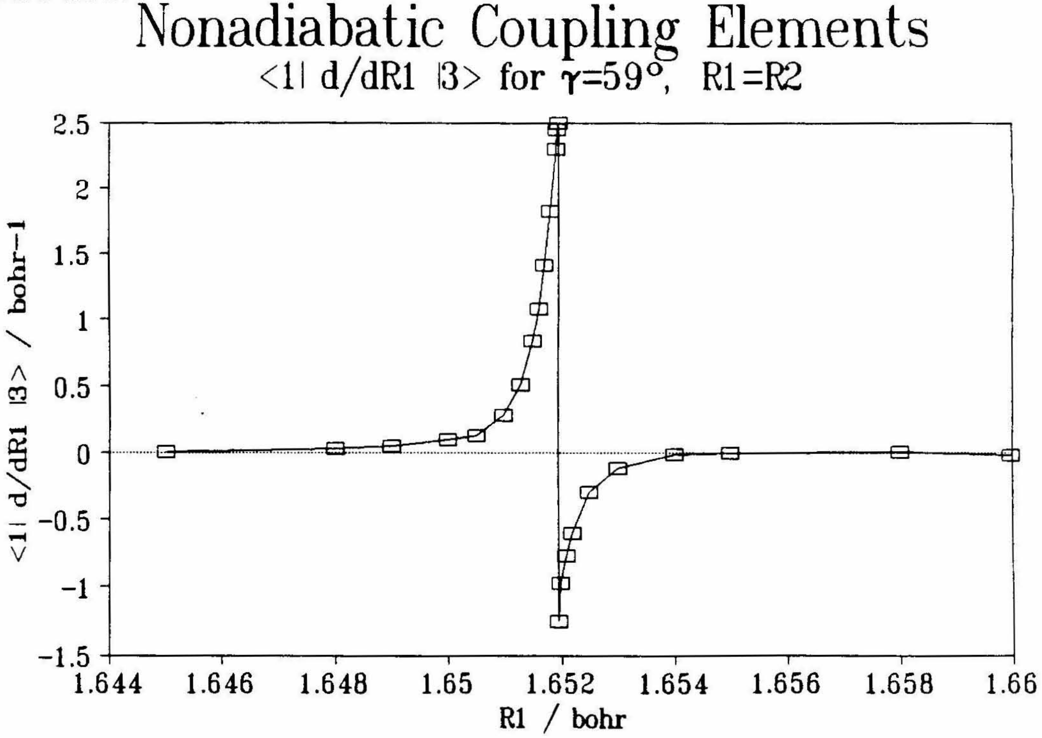

Figure 23c.

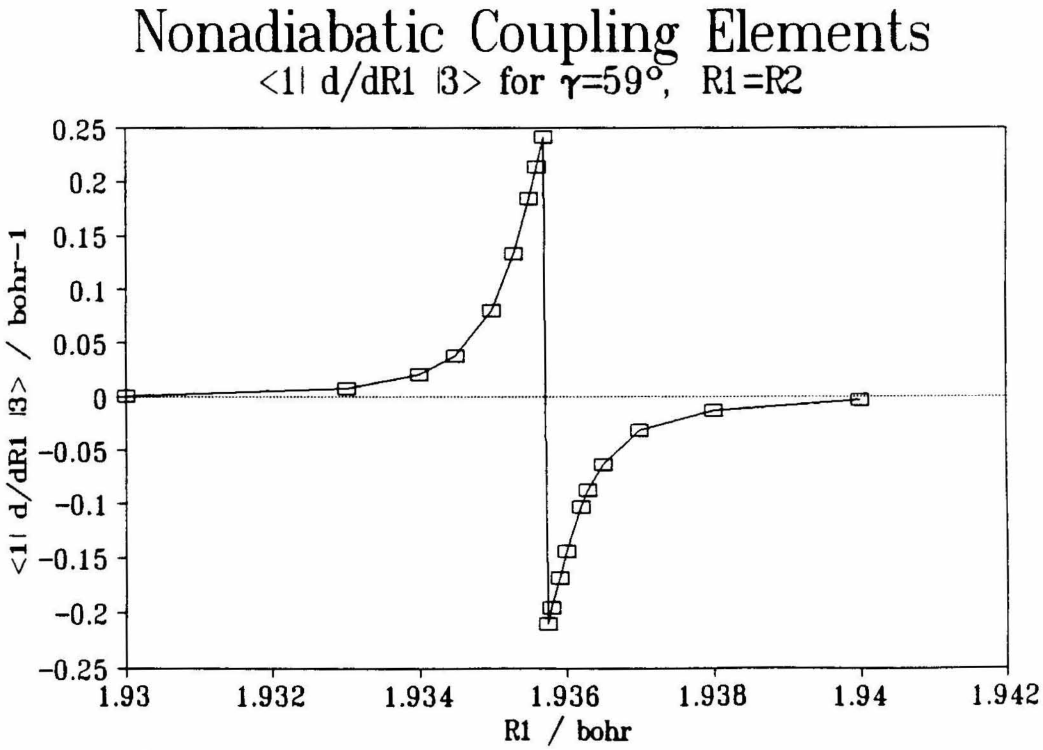

Figure 23d.

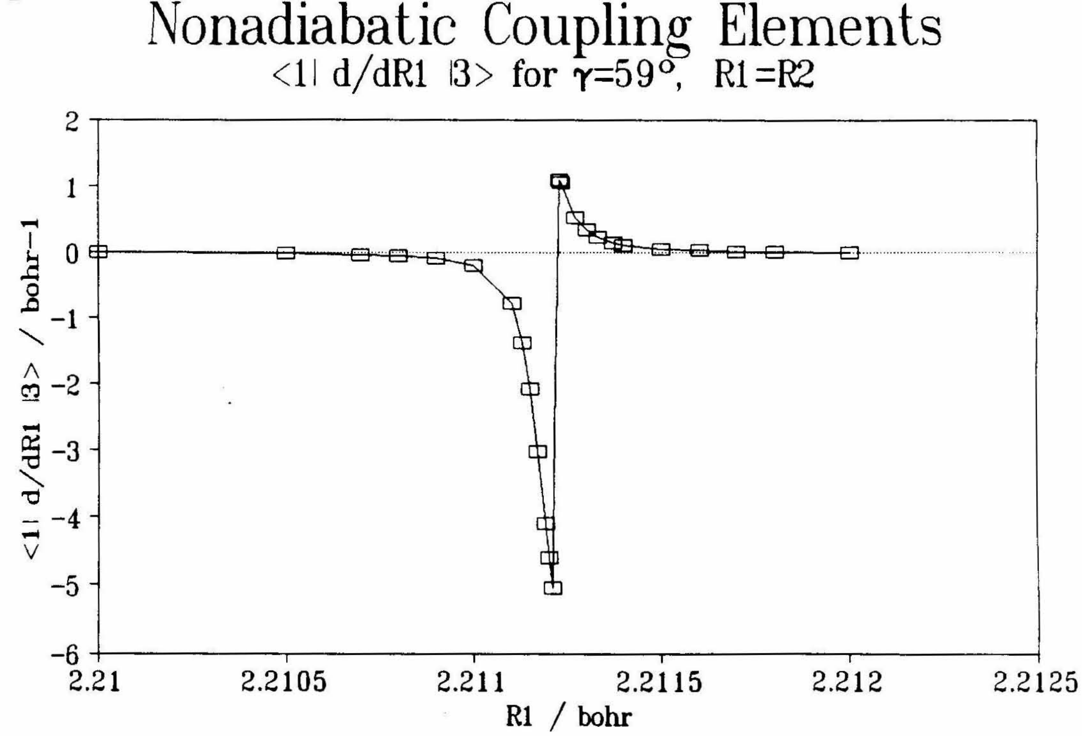

Figure 24a.

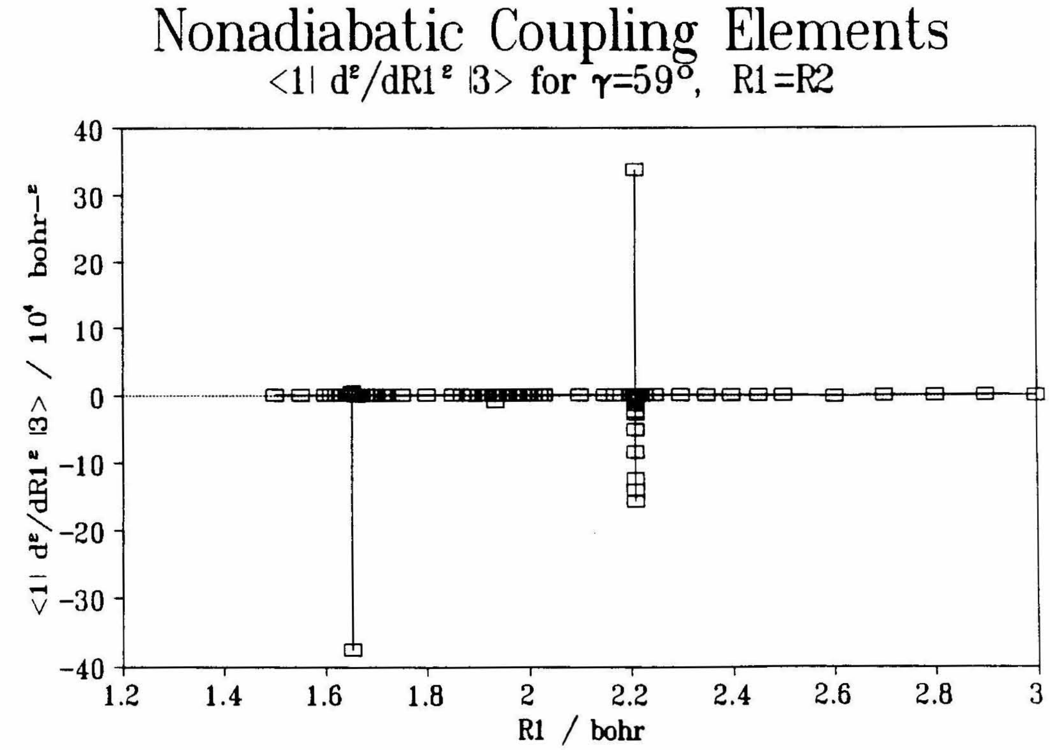

Figure 24b.

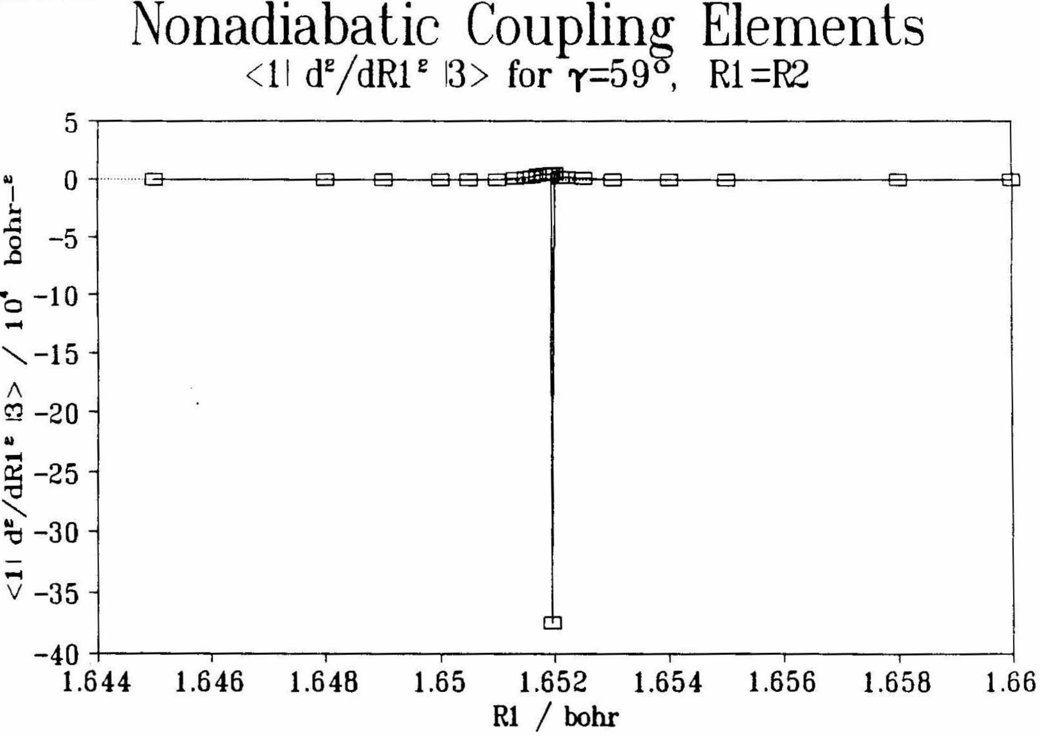

Figure 24c.

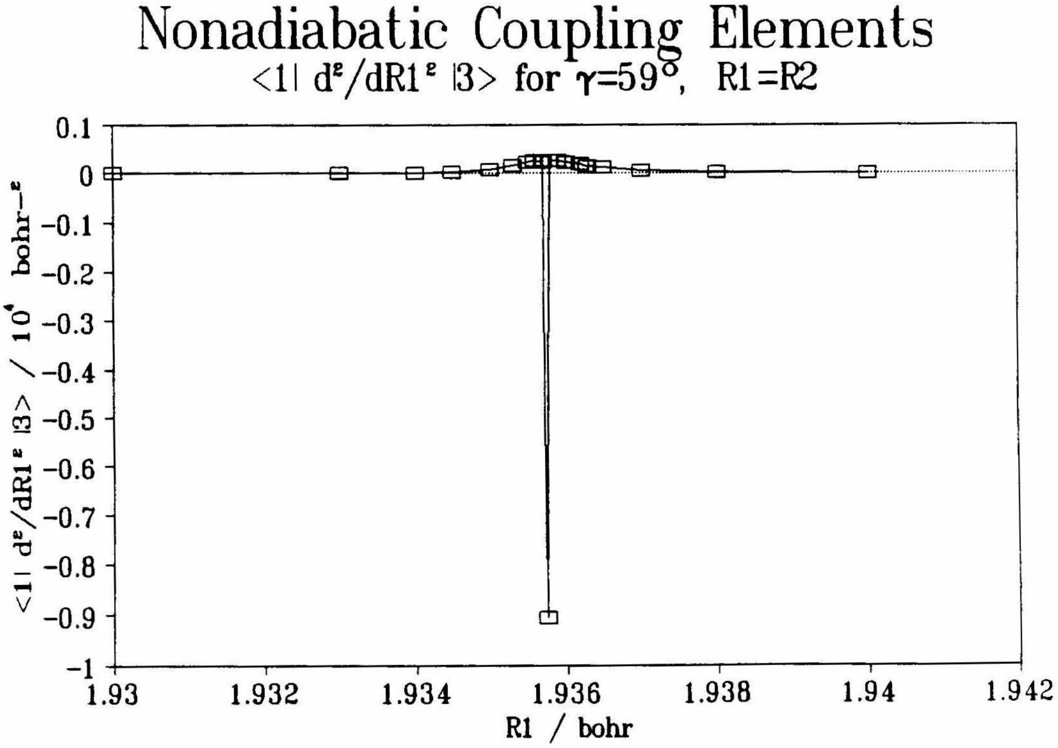

Figure 24d.

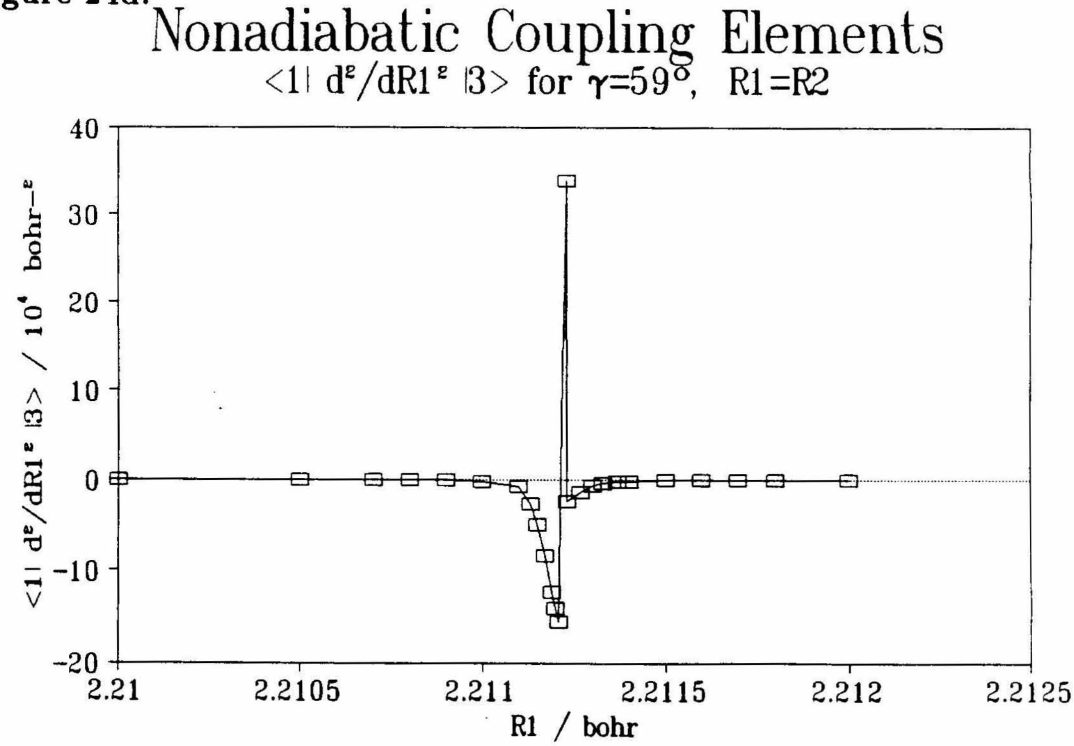

Figure 25a.

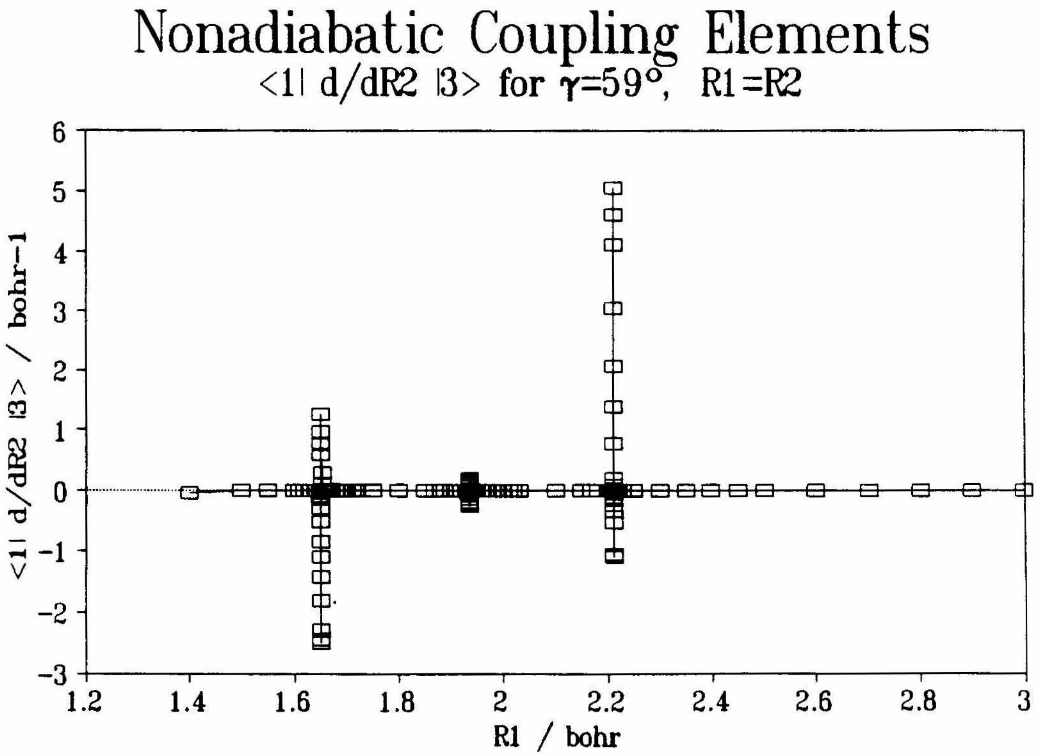

Figure 25b.

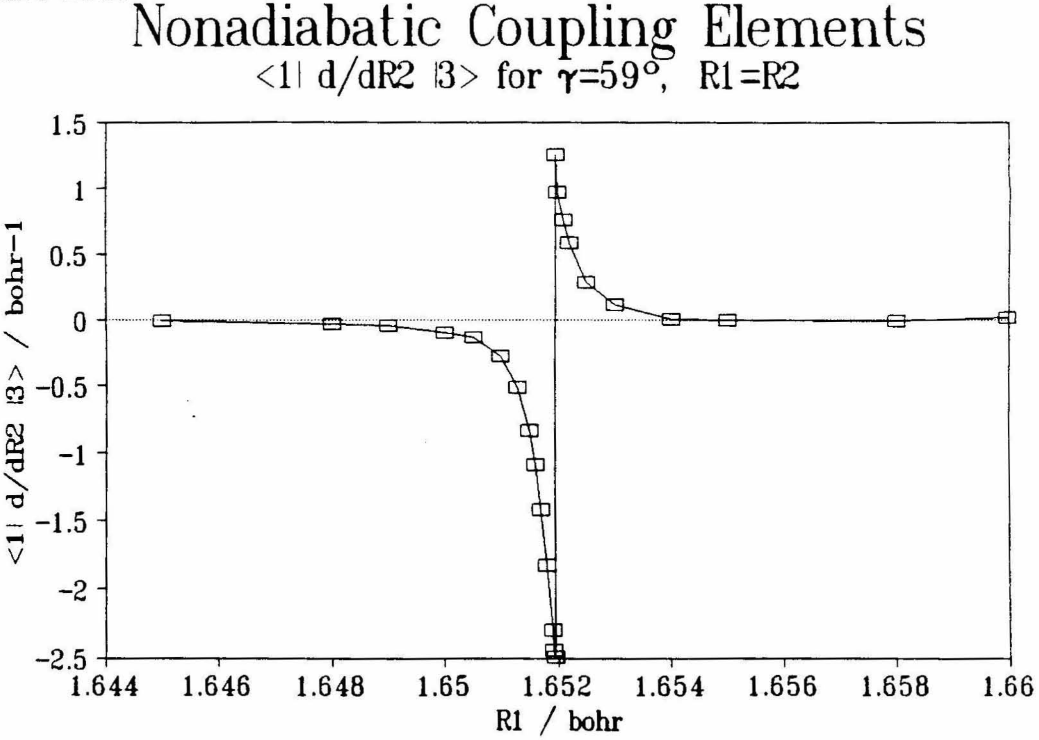

Figure 25c.

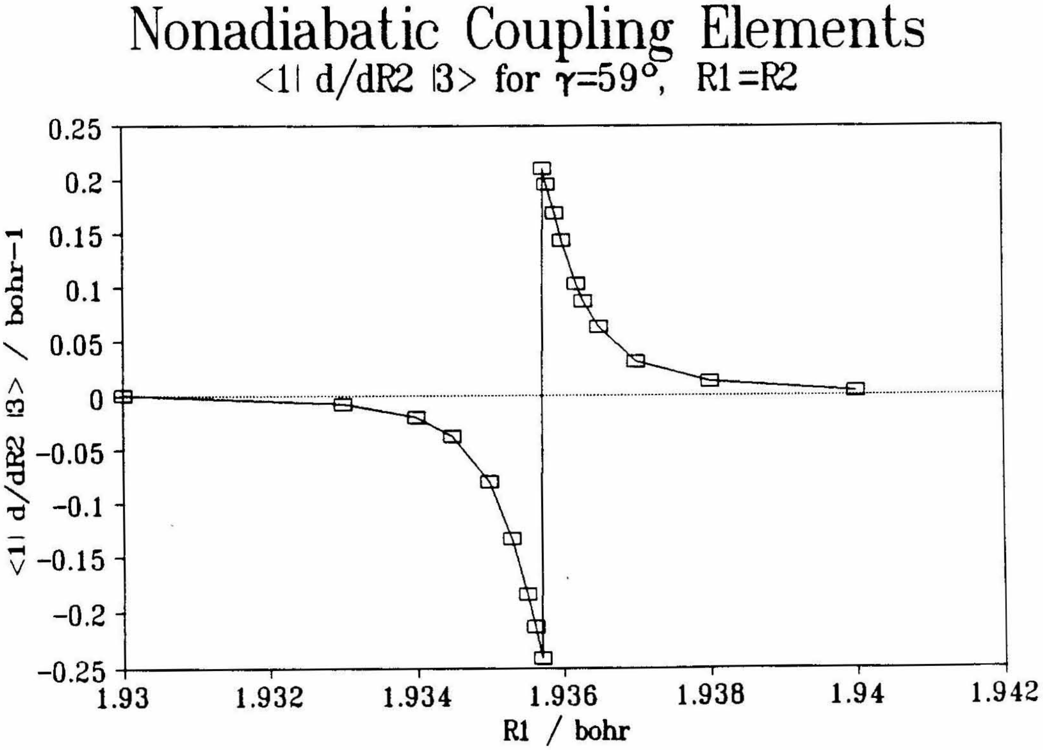

Figure 25d.

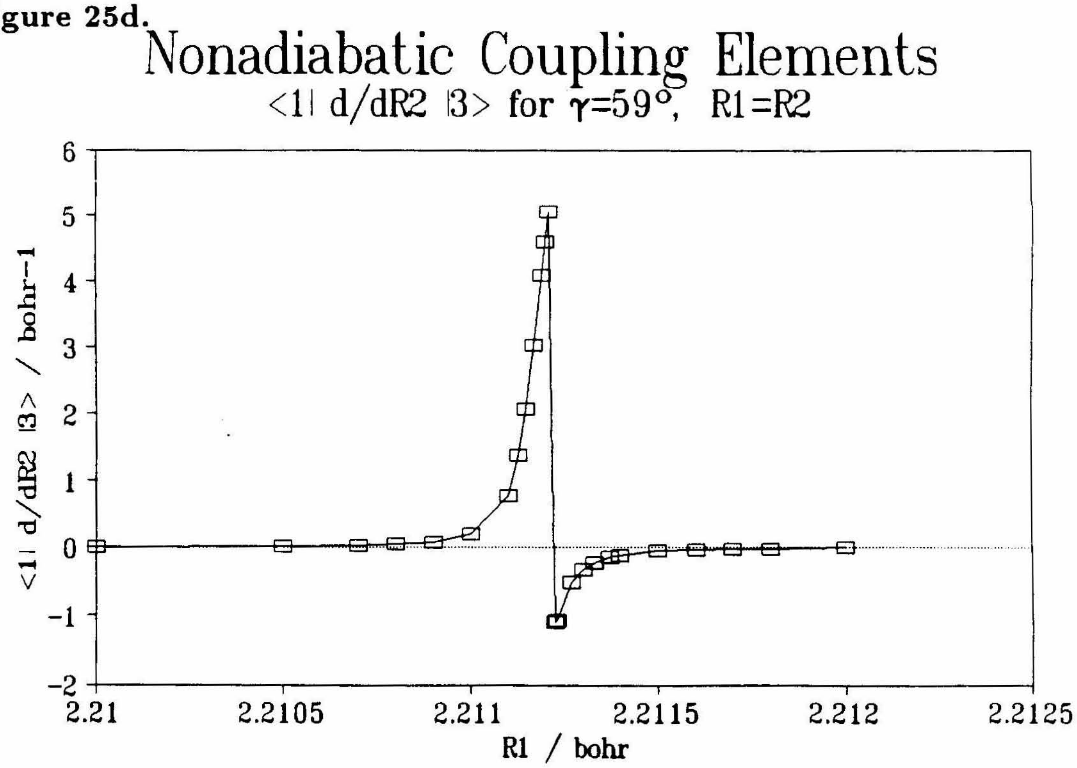

Figure 26a.

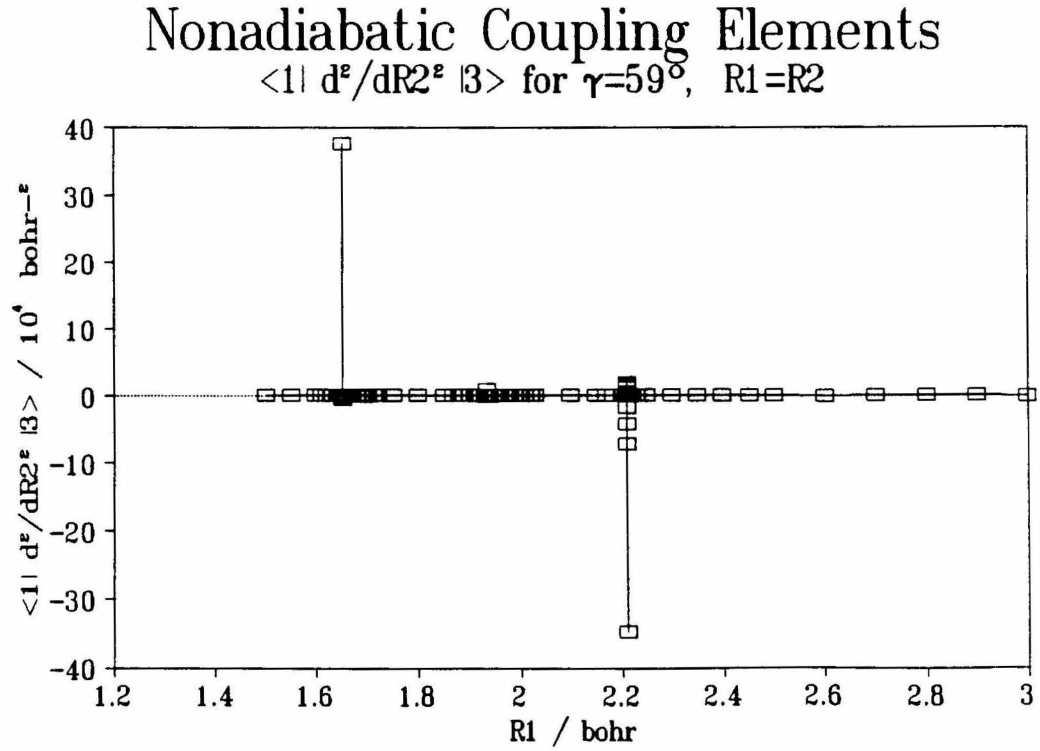

Figure 26b.

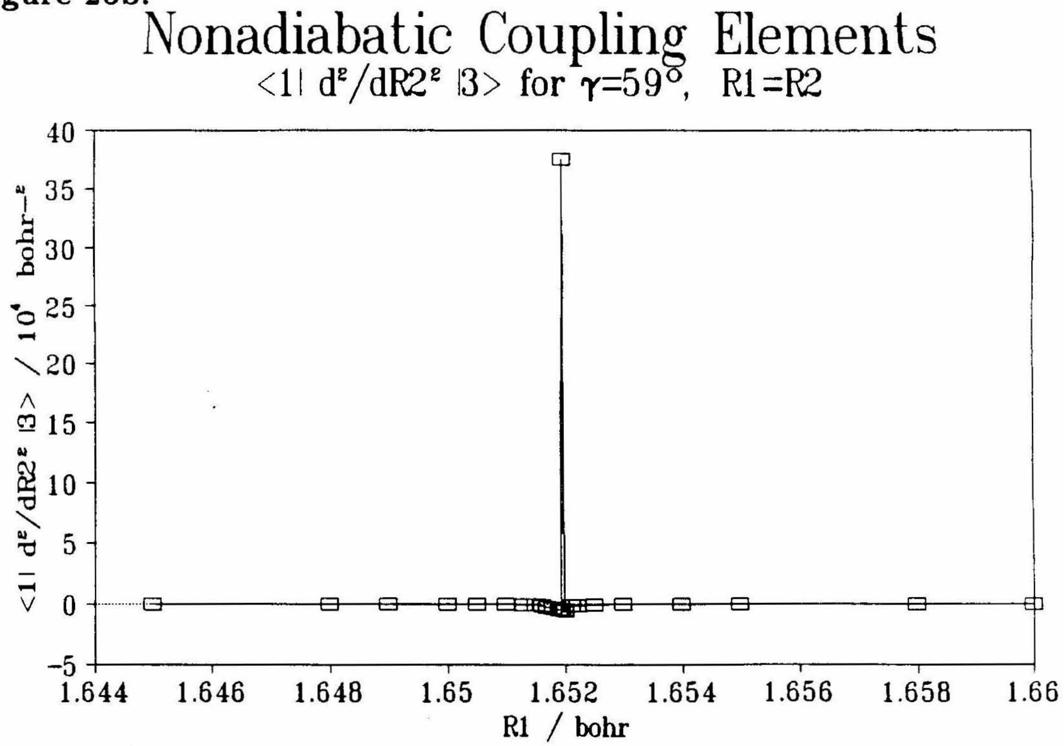

Figure 26c.

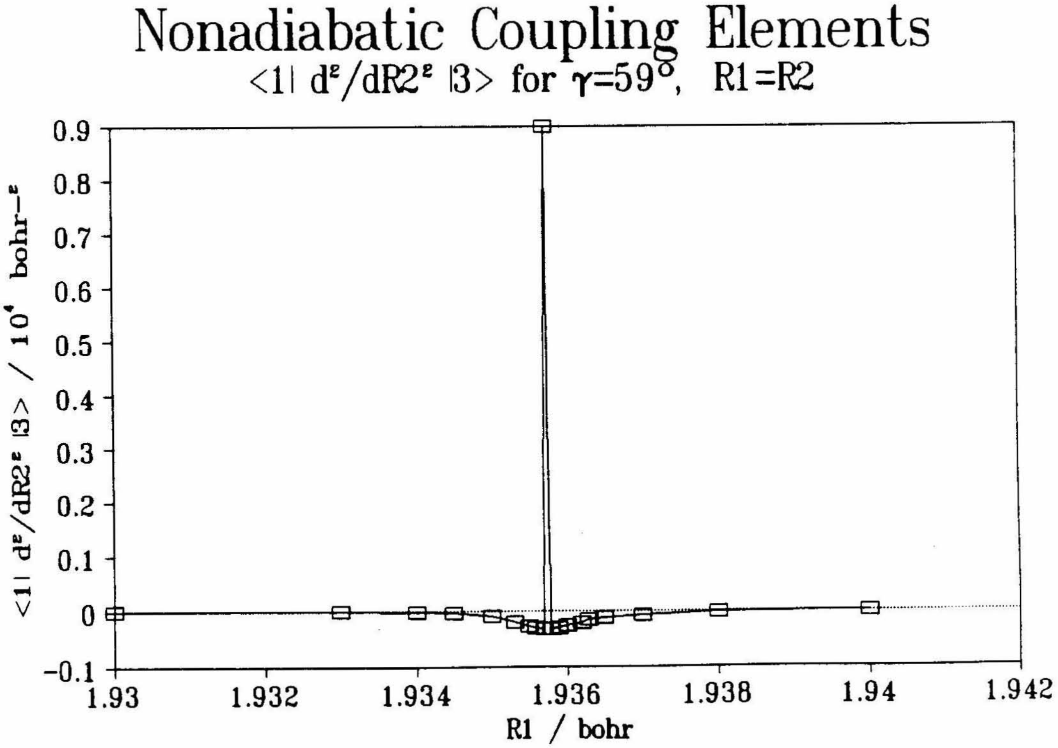

Figure 26d.

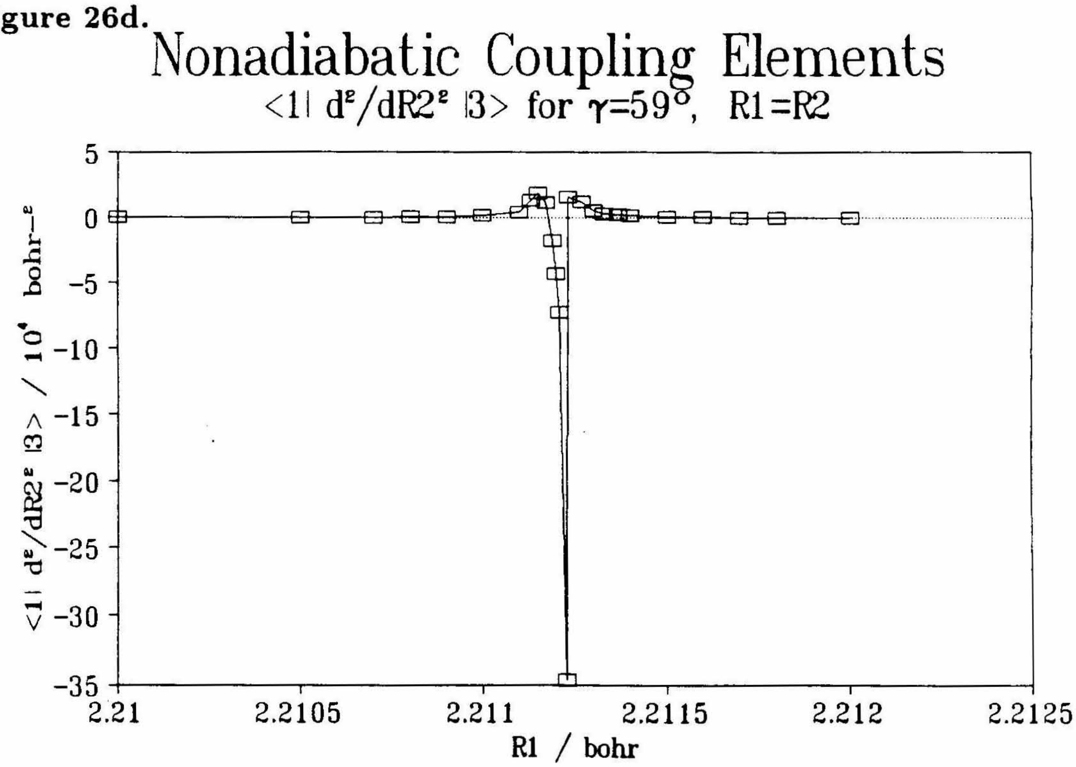

Figure 27a.

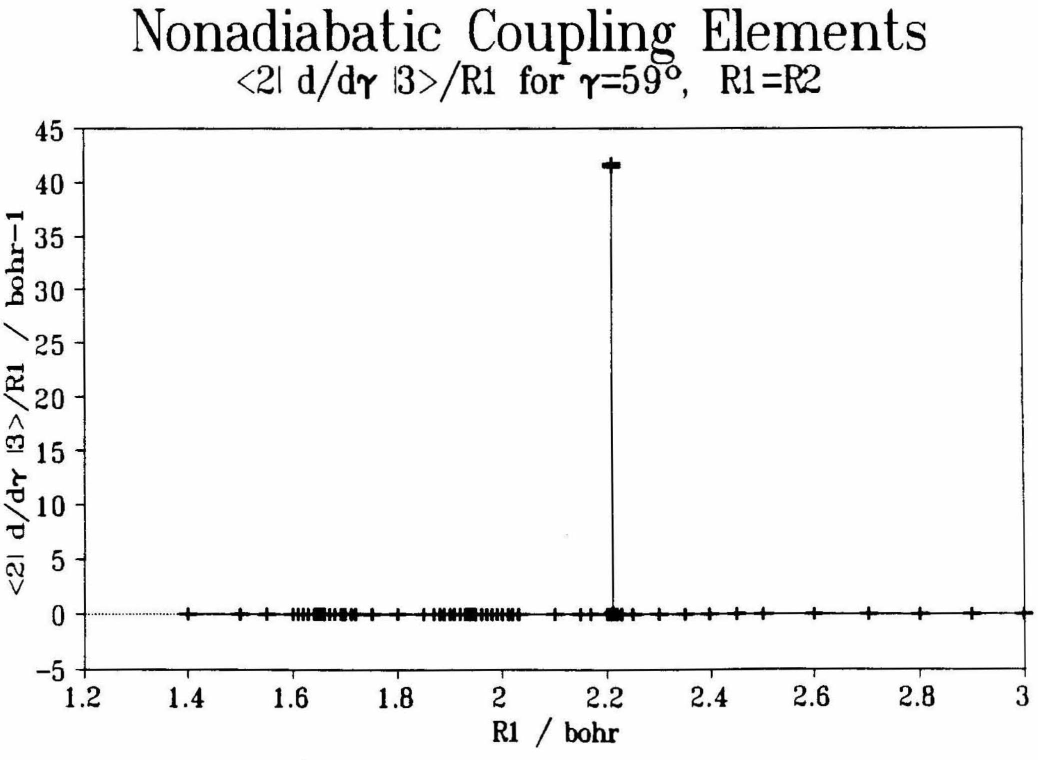

Figure 27b.

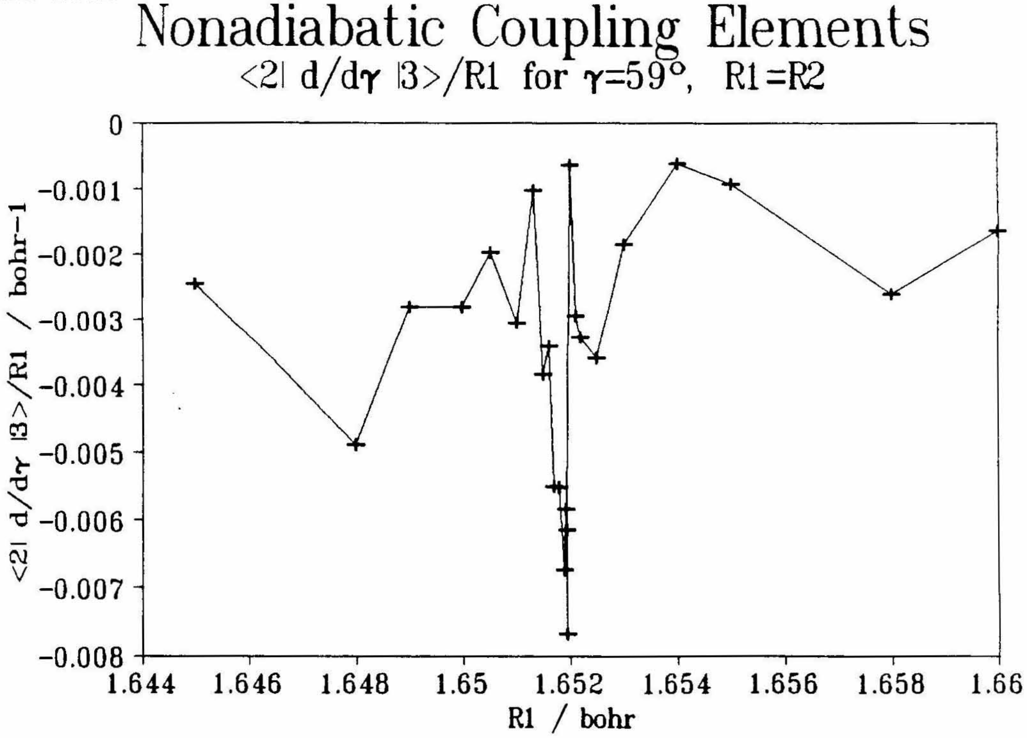

Figure 27c.

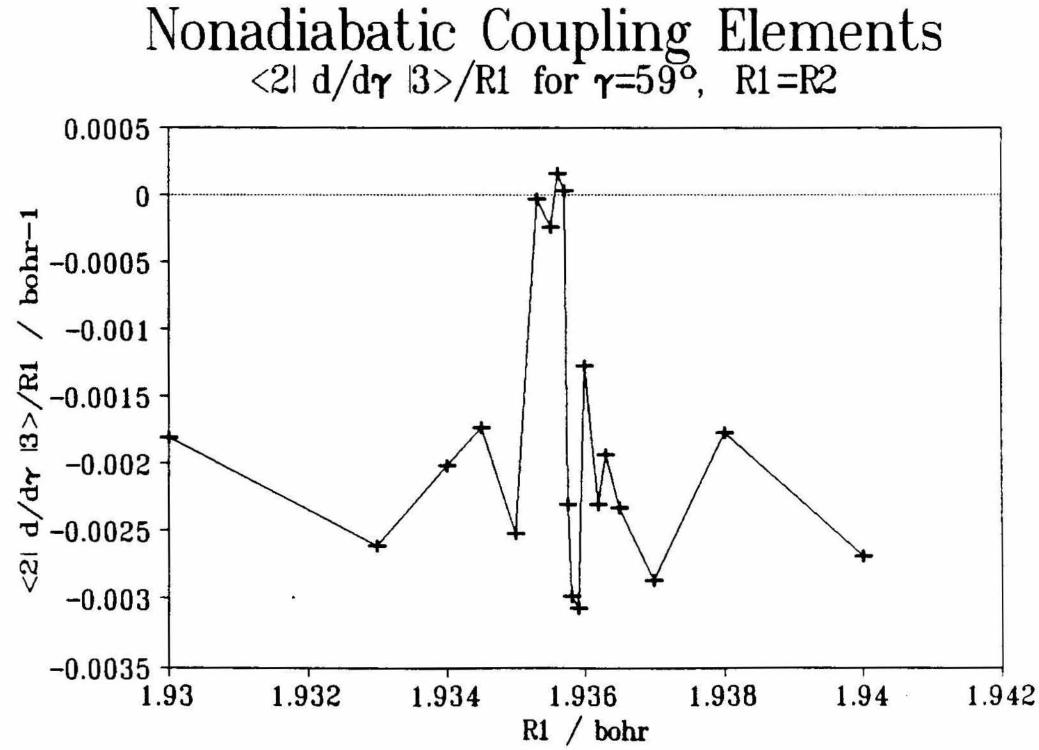

Figure 27d.

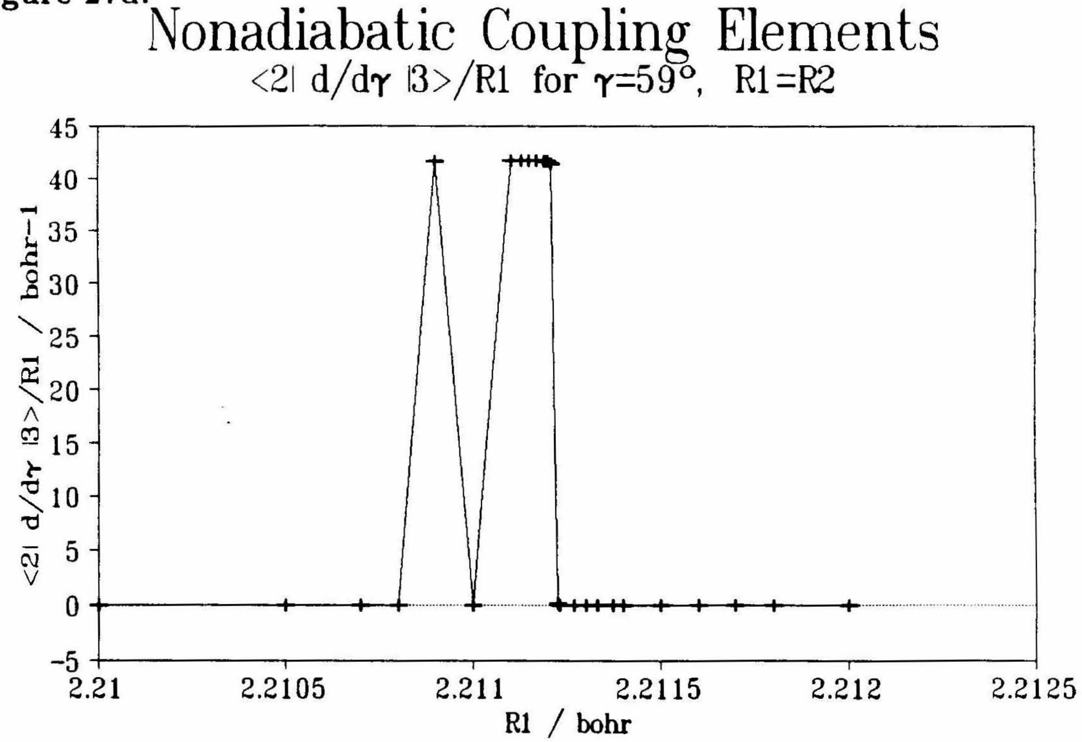

Figure 28a.

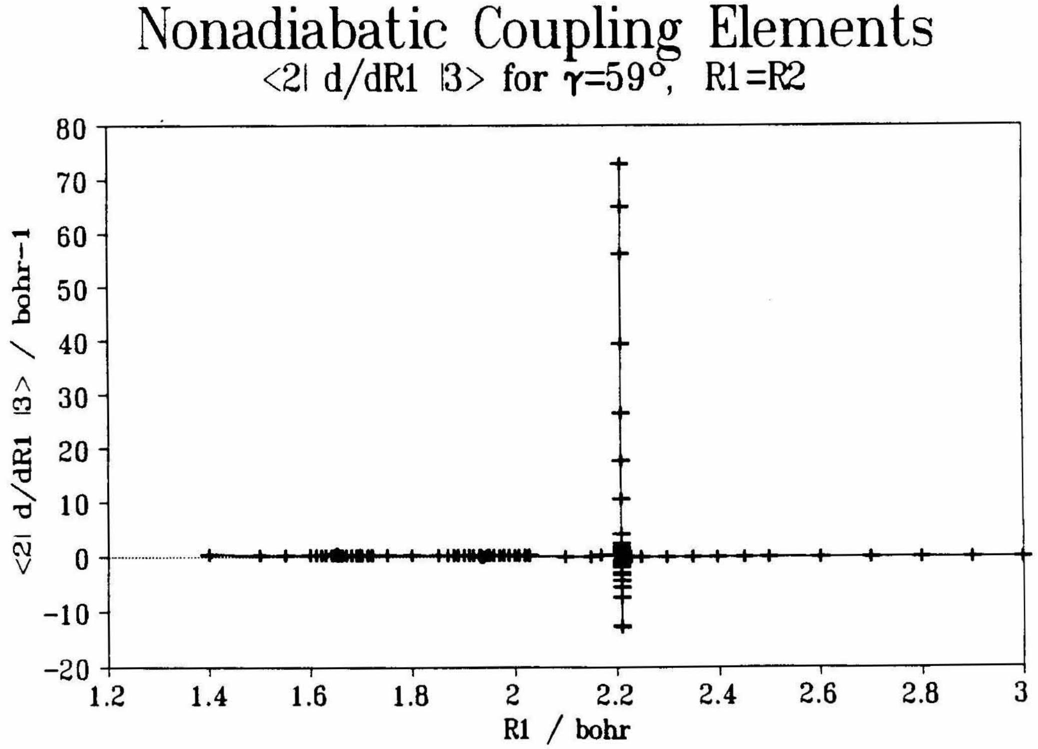

Figure 28b.

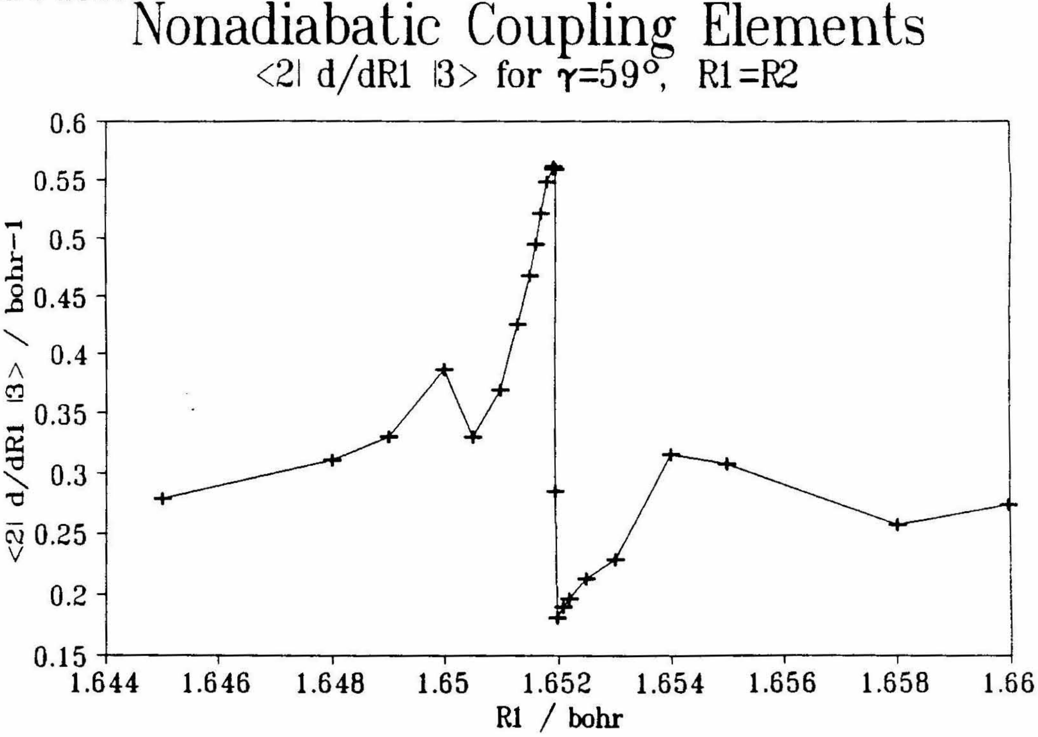

Figure 28c.

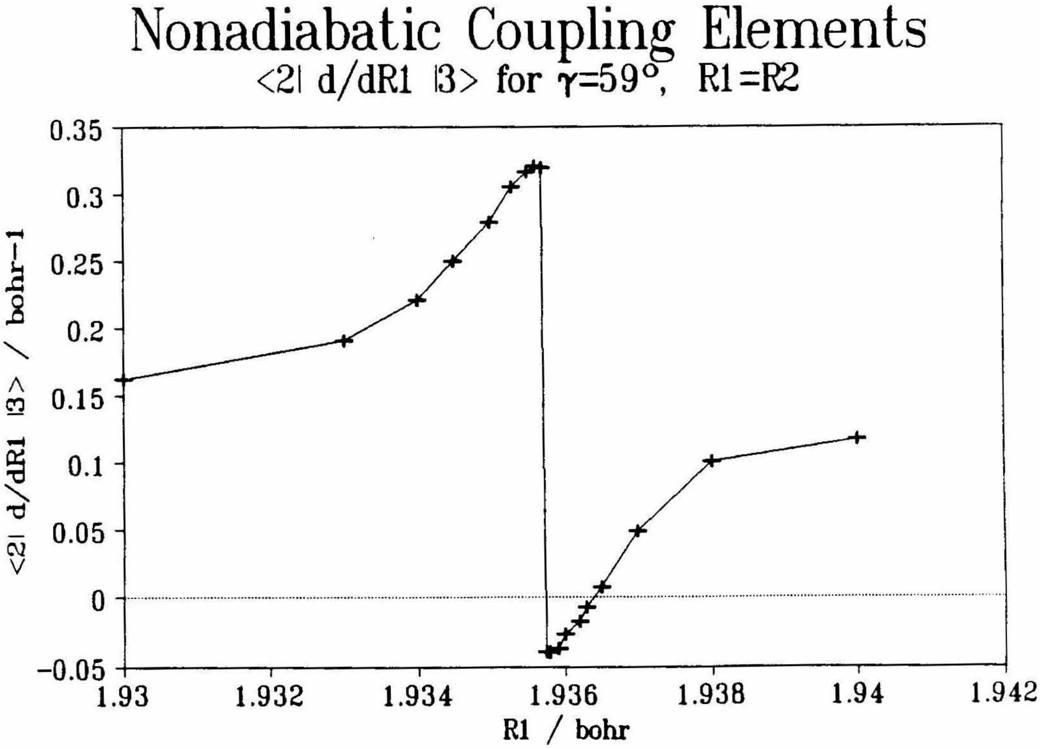

Figure 28d.

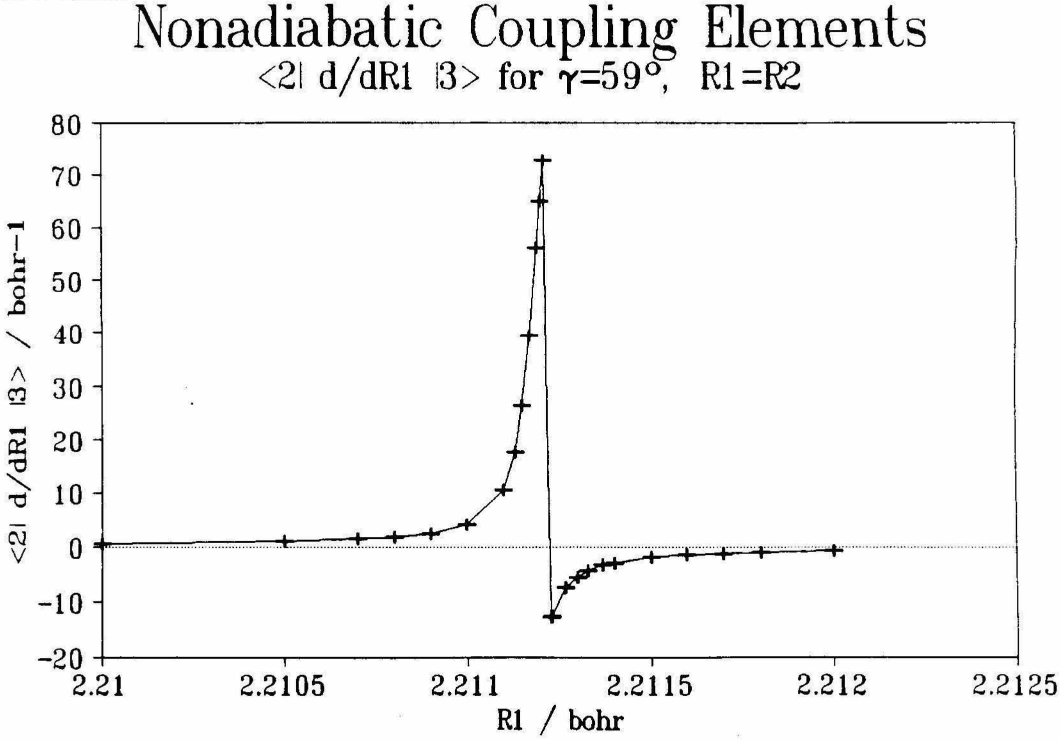

Figure 29a.

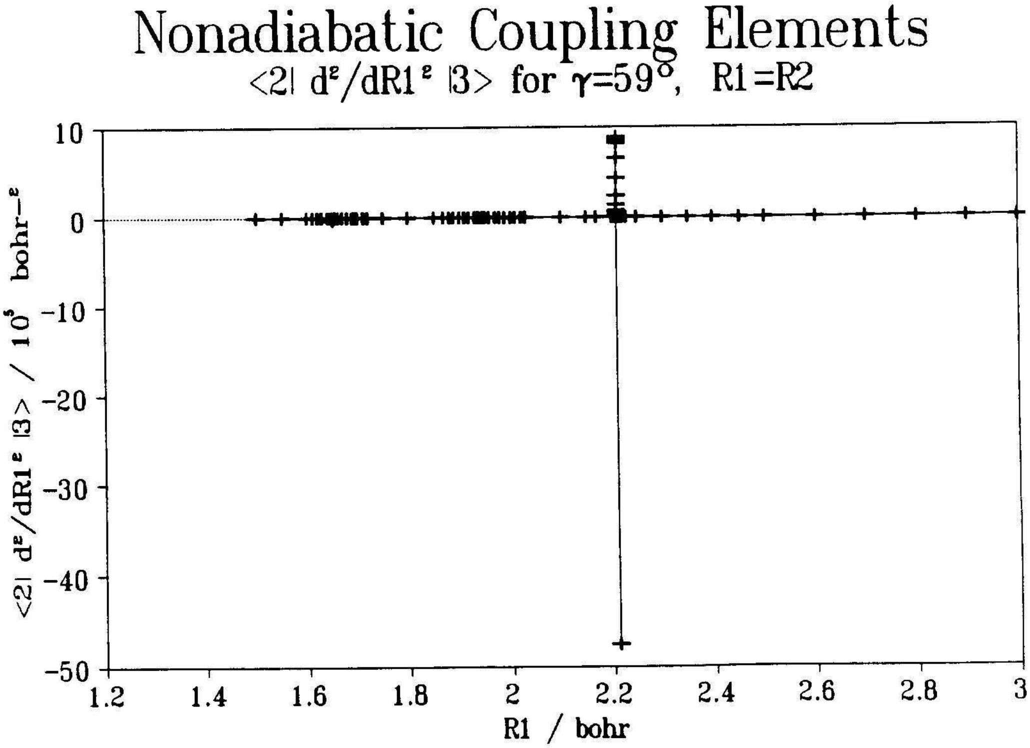

Figure 29b.

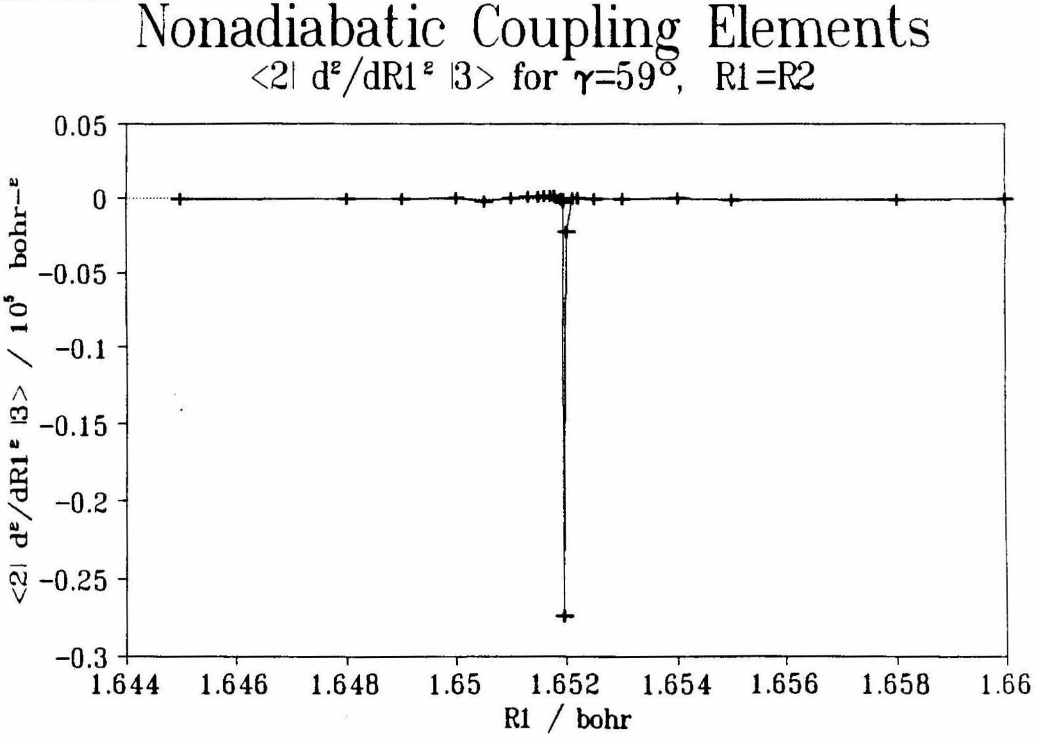

Figure 29c.

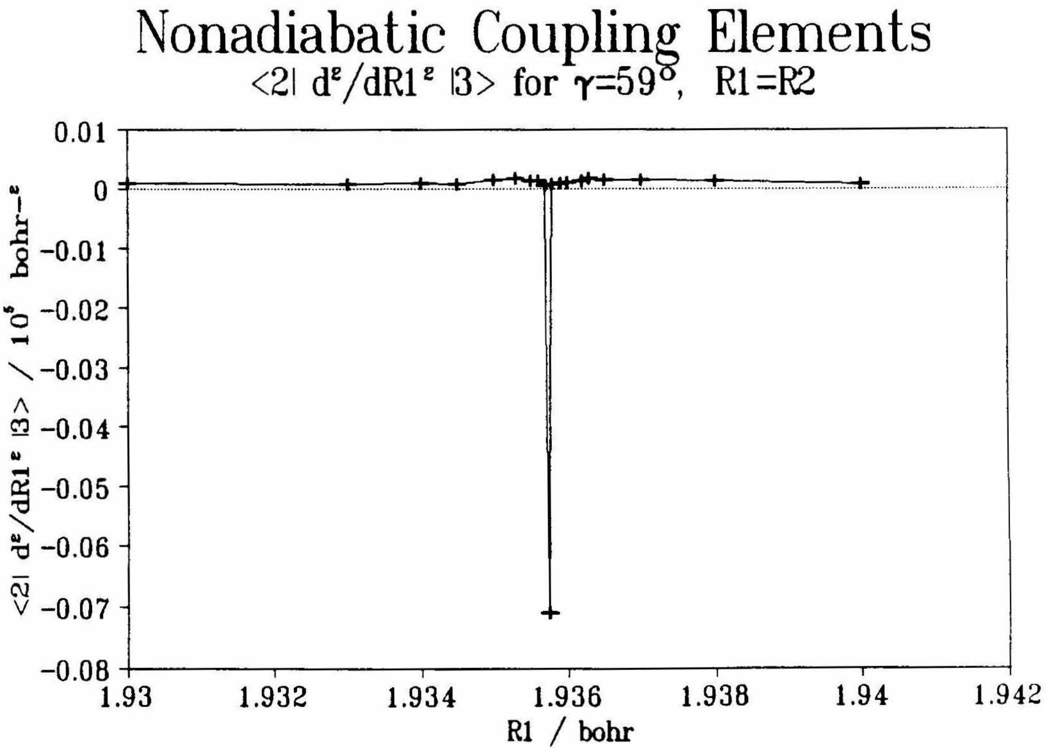

Figure 29d.

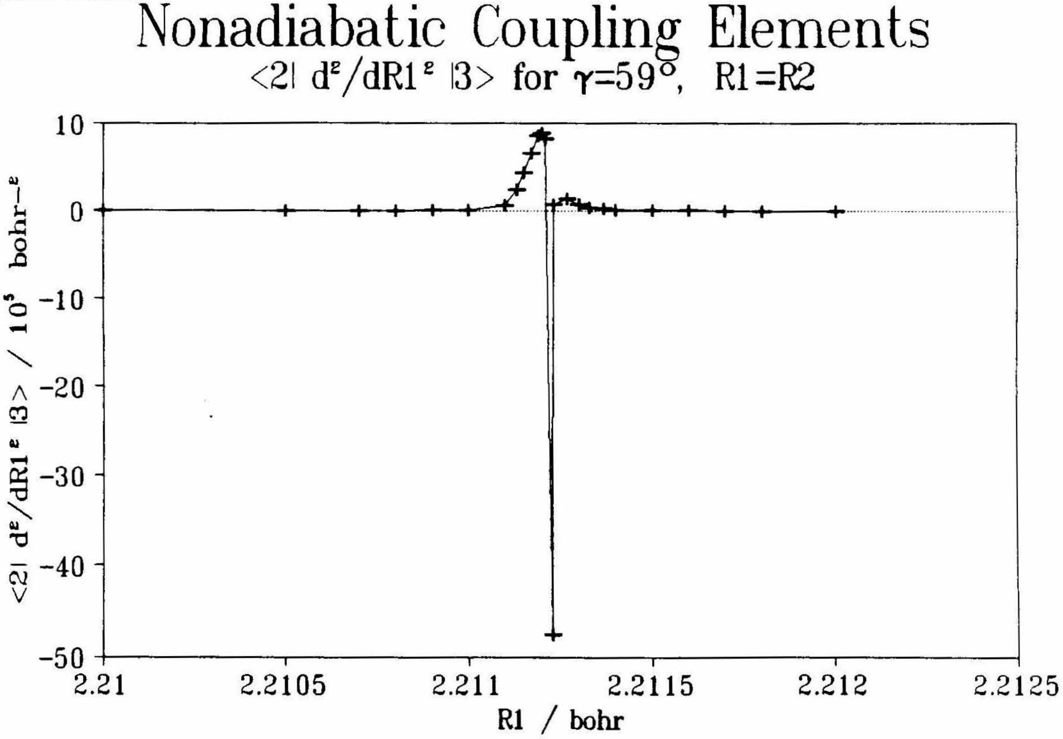

Nonadiabatic Coupling Elements

$<2|\ d^2/dR1^2\ |3>$ for γ=59°, R1=R2

Figure 30a.

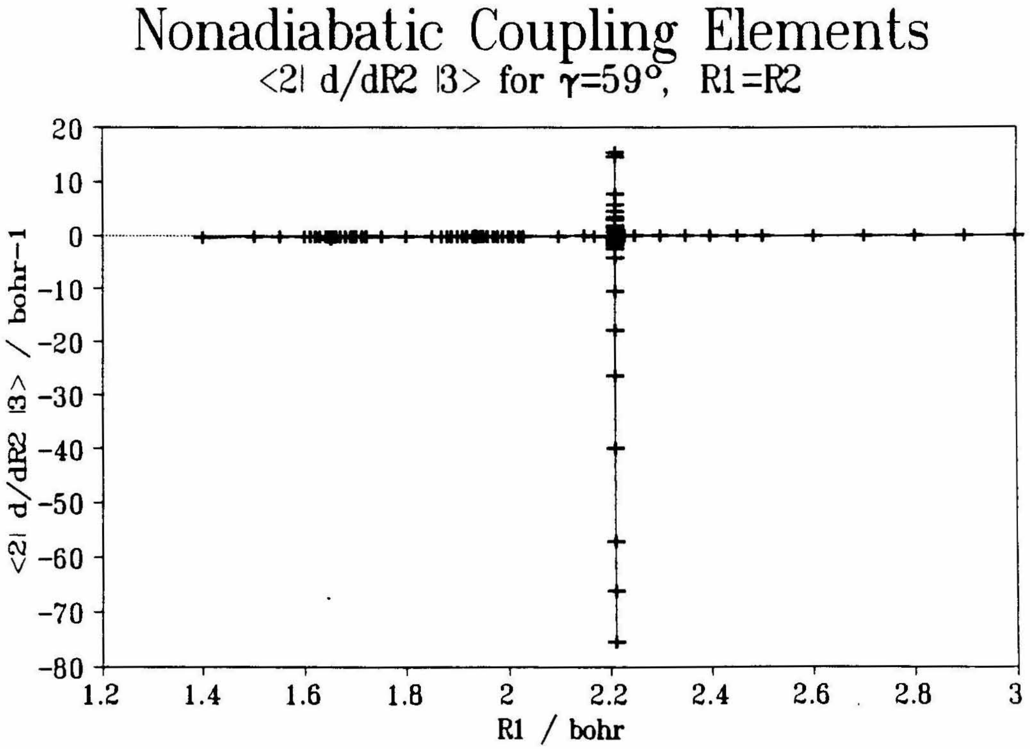

Nonadiabatic Coupling Elements

$<2|\ d/dR2\ |3>$ for γ=59°, R1=R2

Figure 30b.

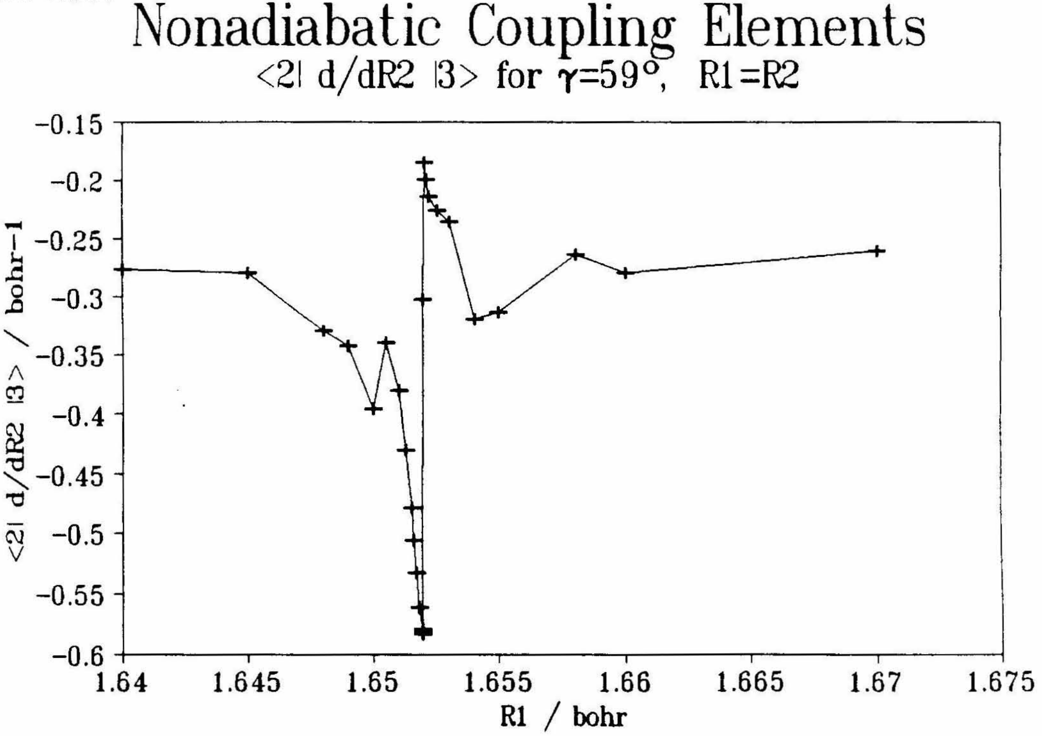

Figure 30c.

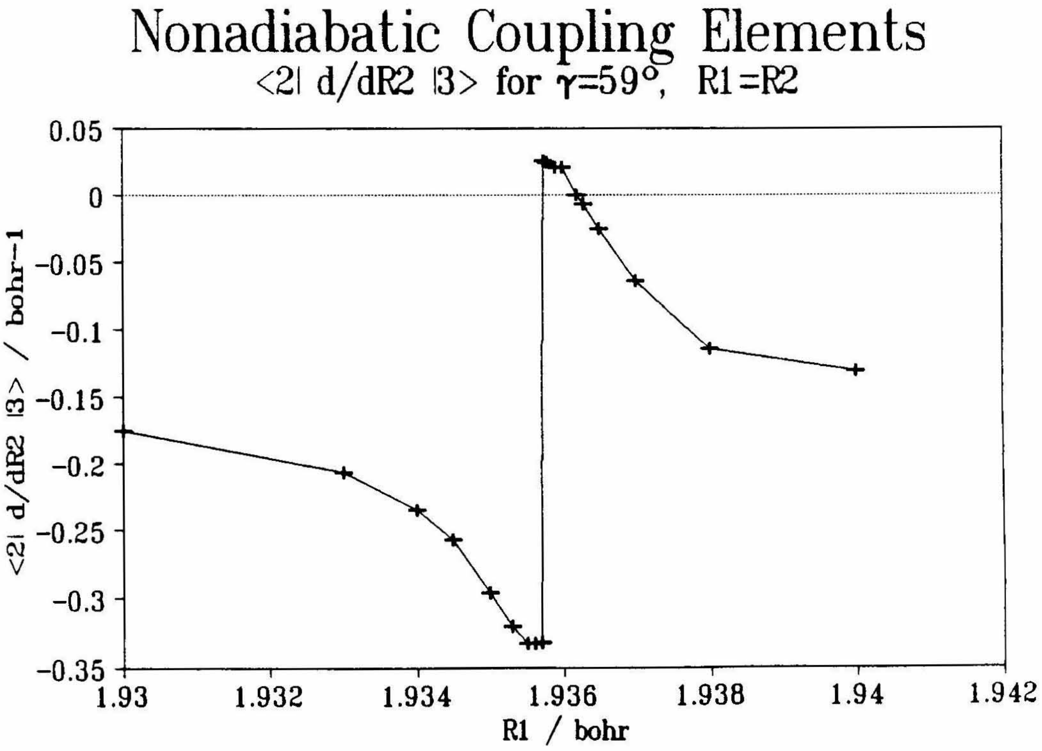

Figure 30d.

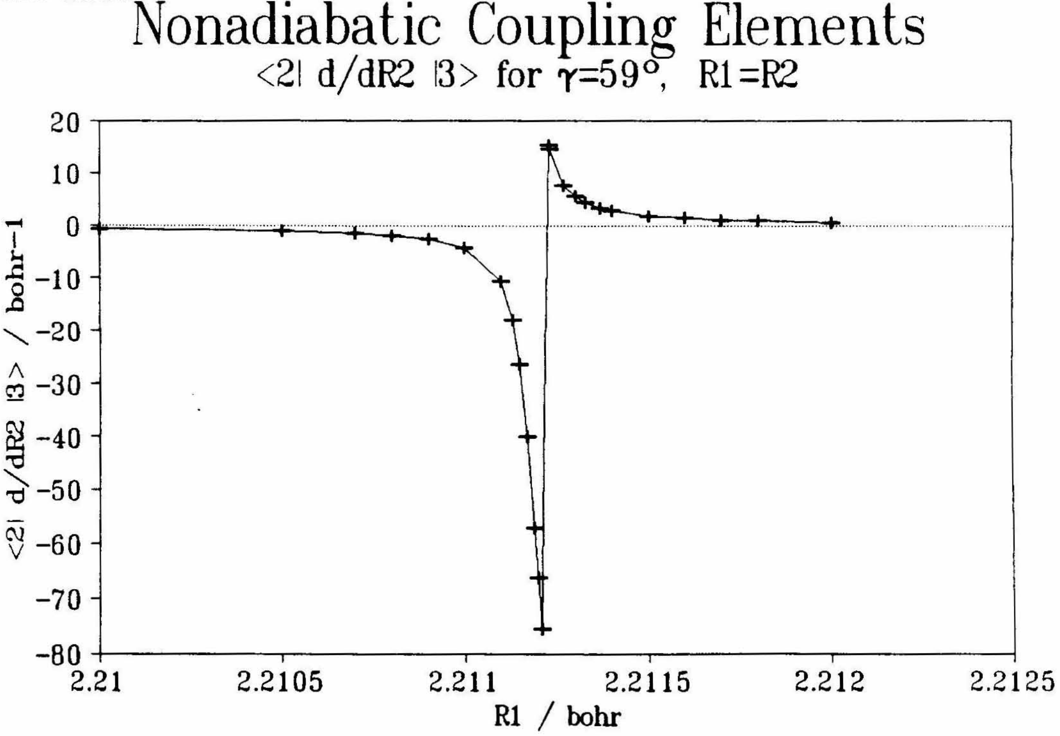

Figure 31a.

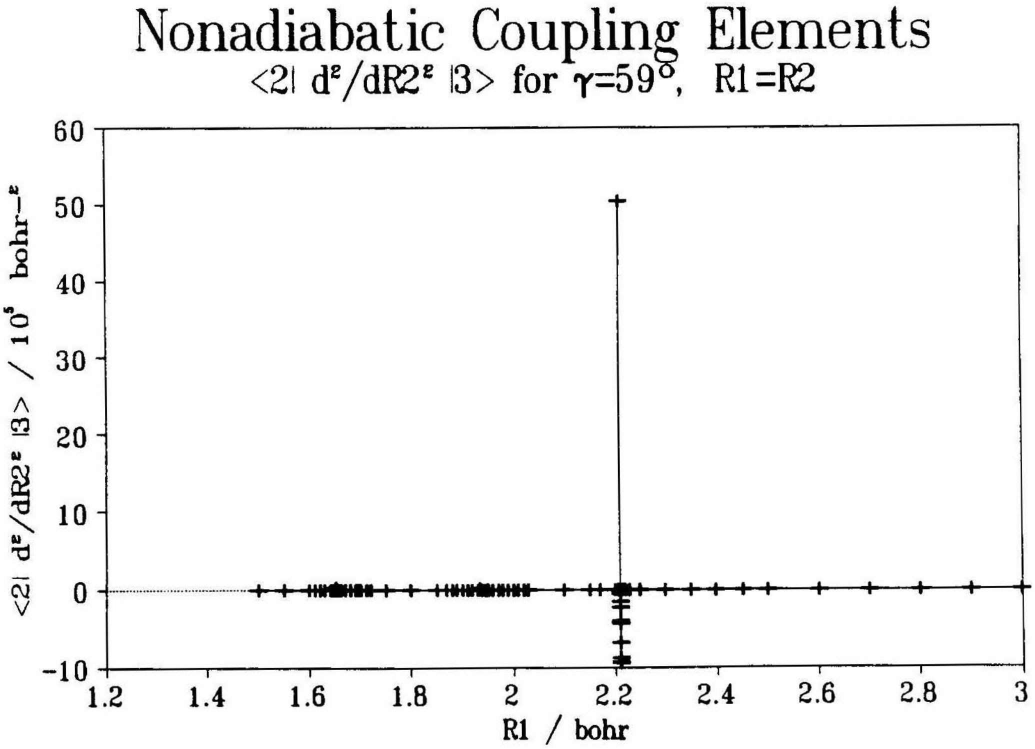

Figure 31b.

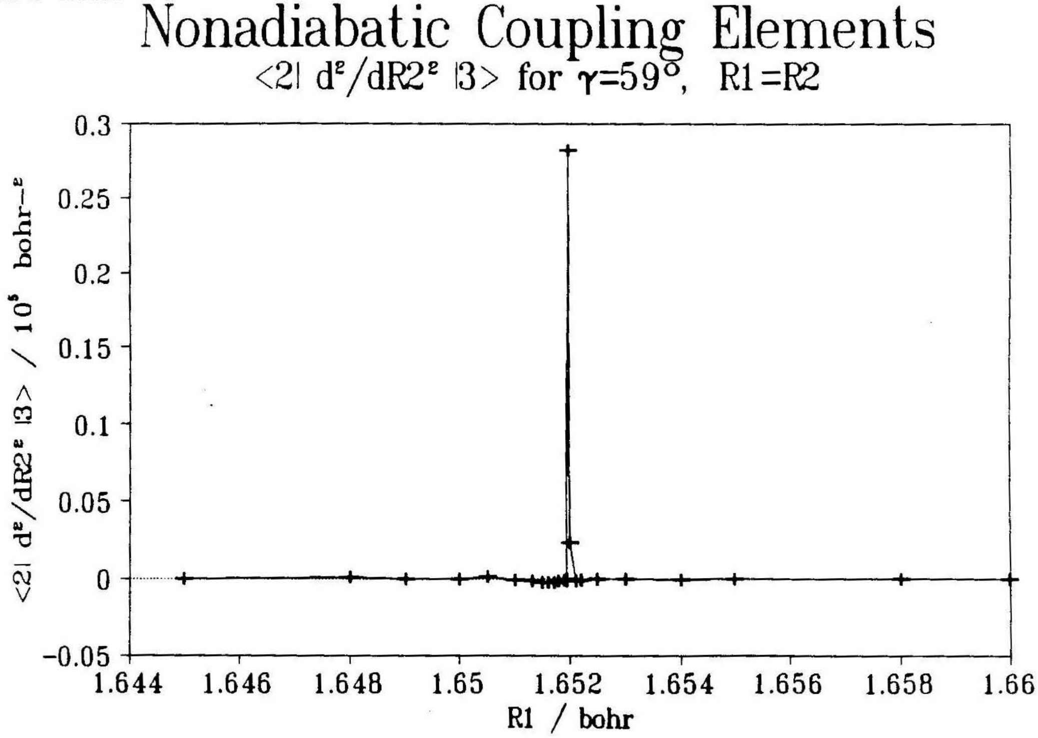

Figure 31c.

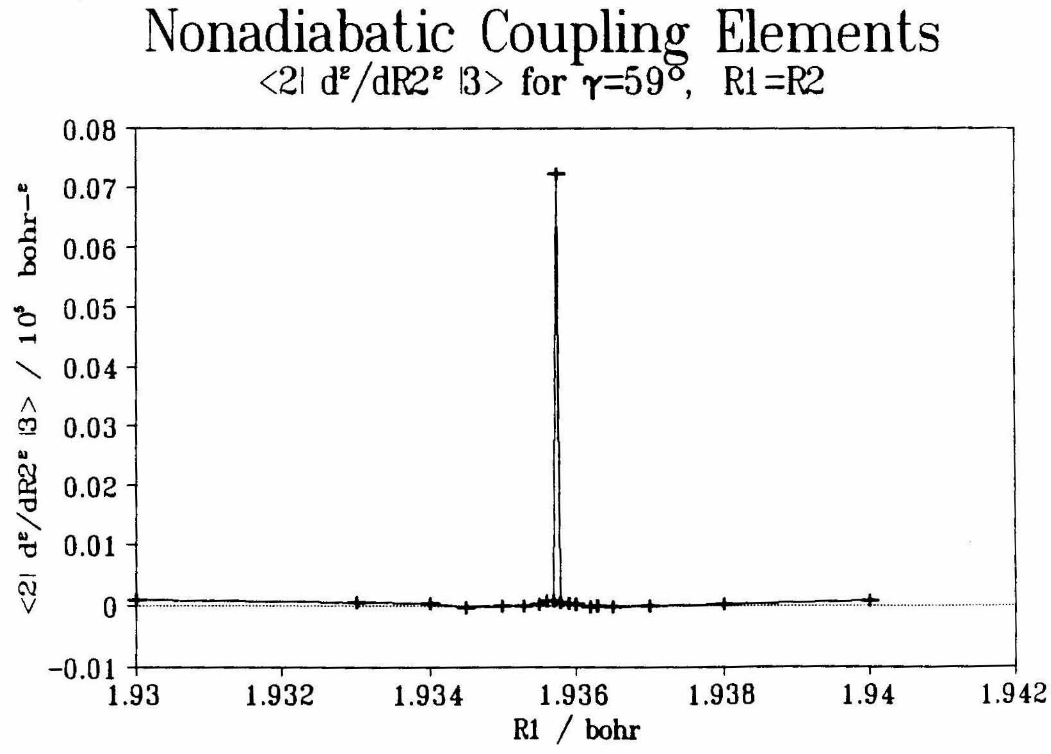

Figure 31d.

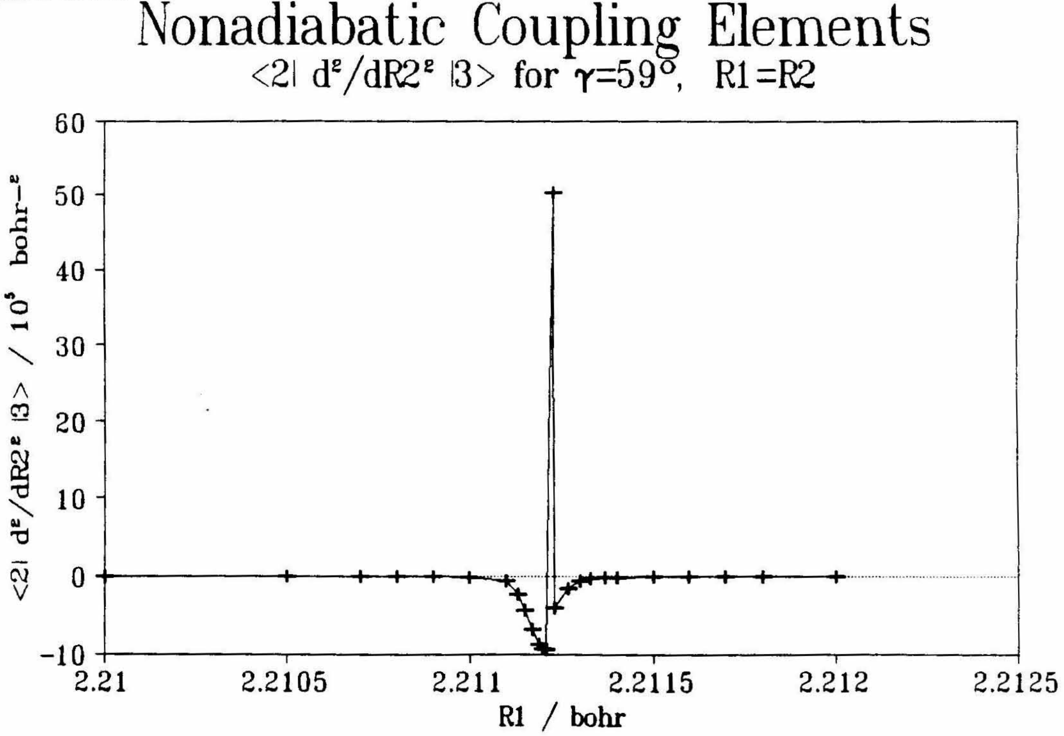

Figure 32a.

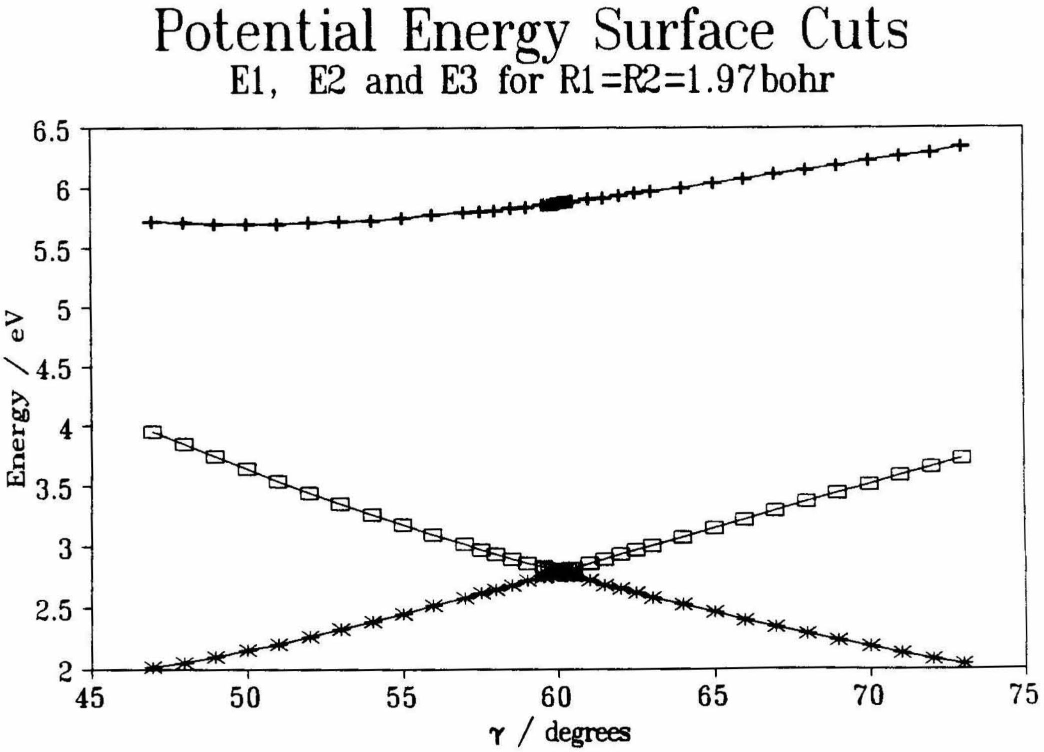

Figure 32b.

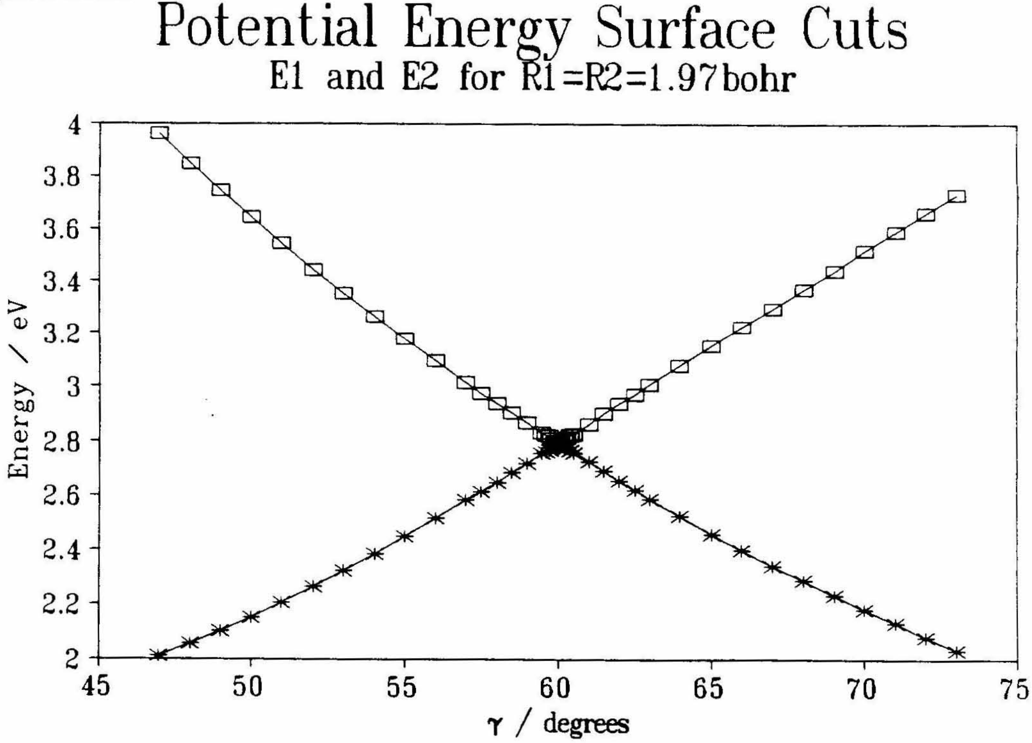

Figure 33a.

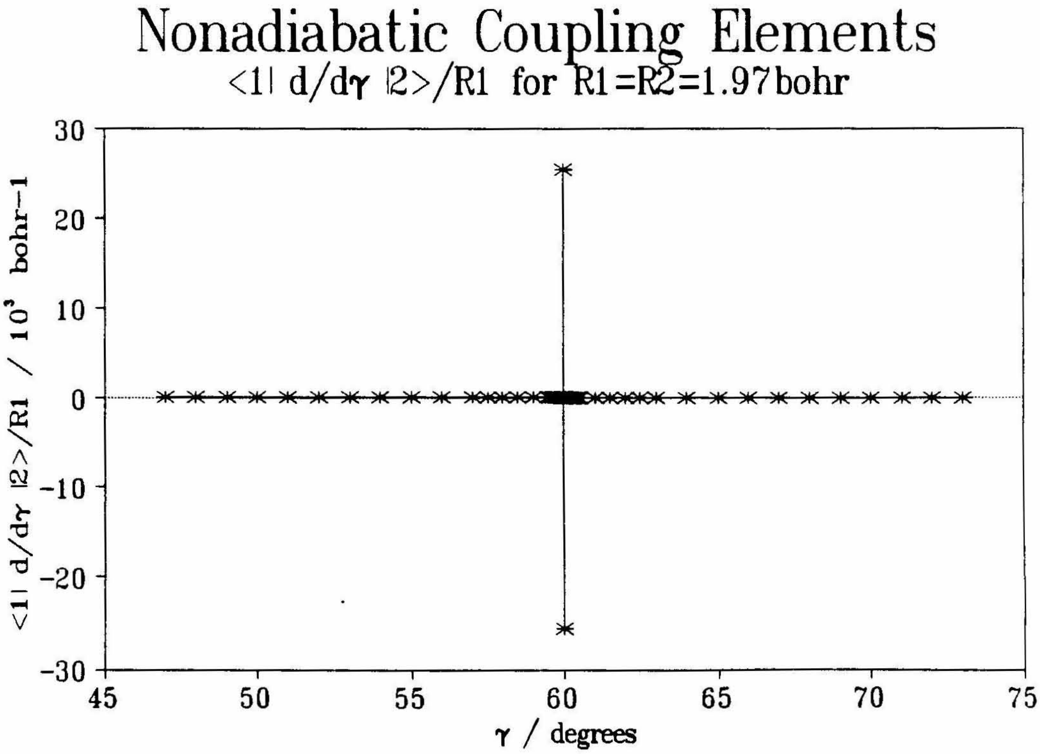

Figure 33b.

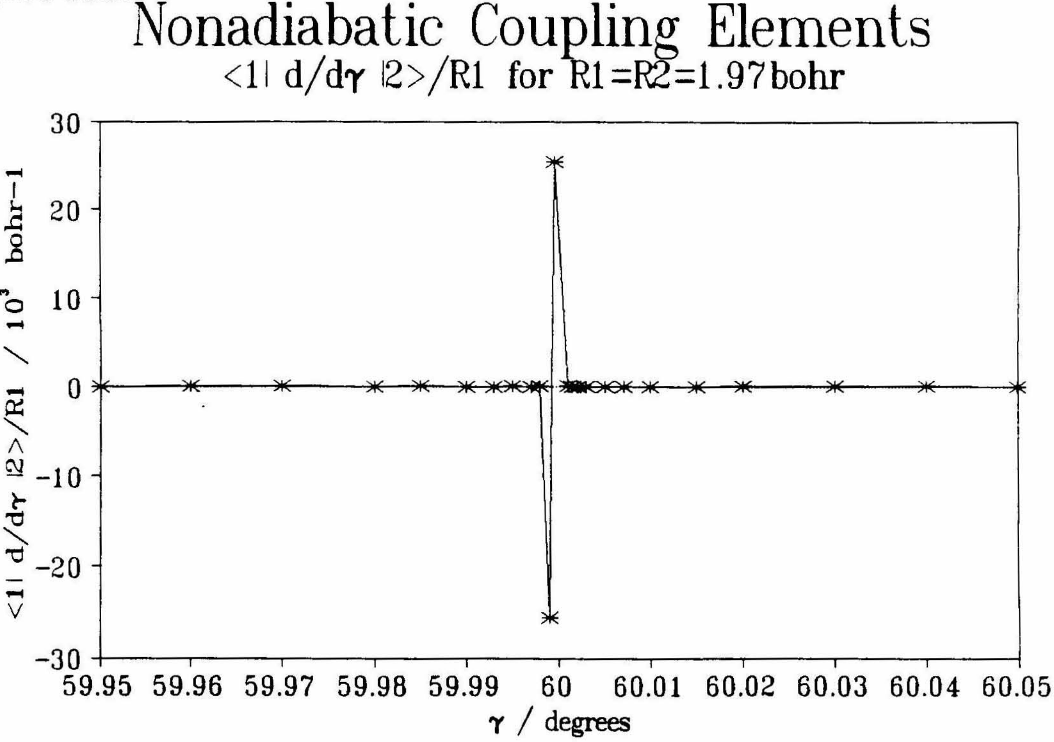

Figure 34a.

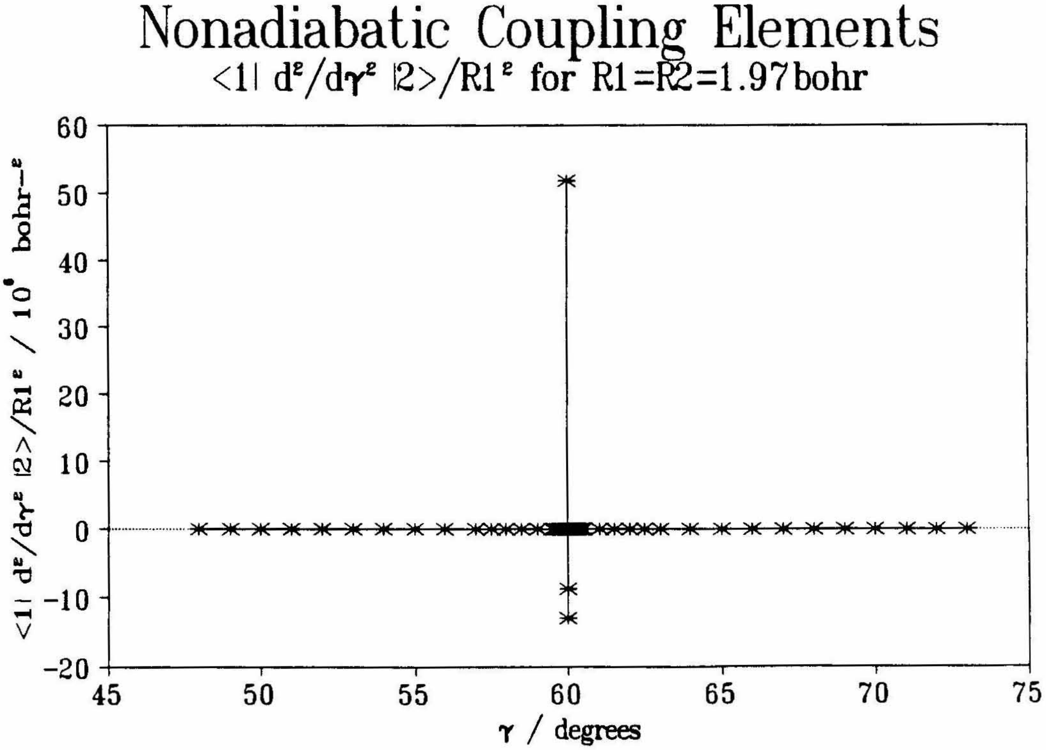

Figure 34b.

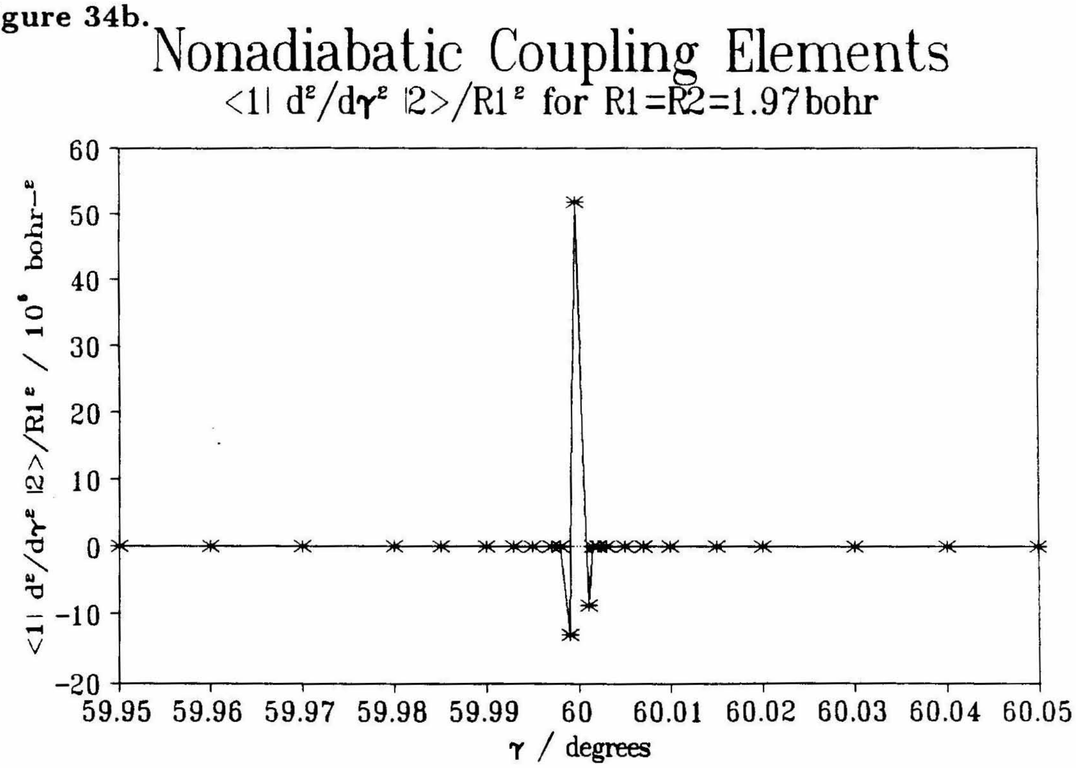

Figure 35a.

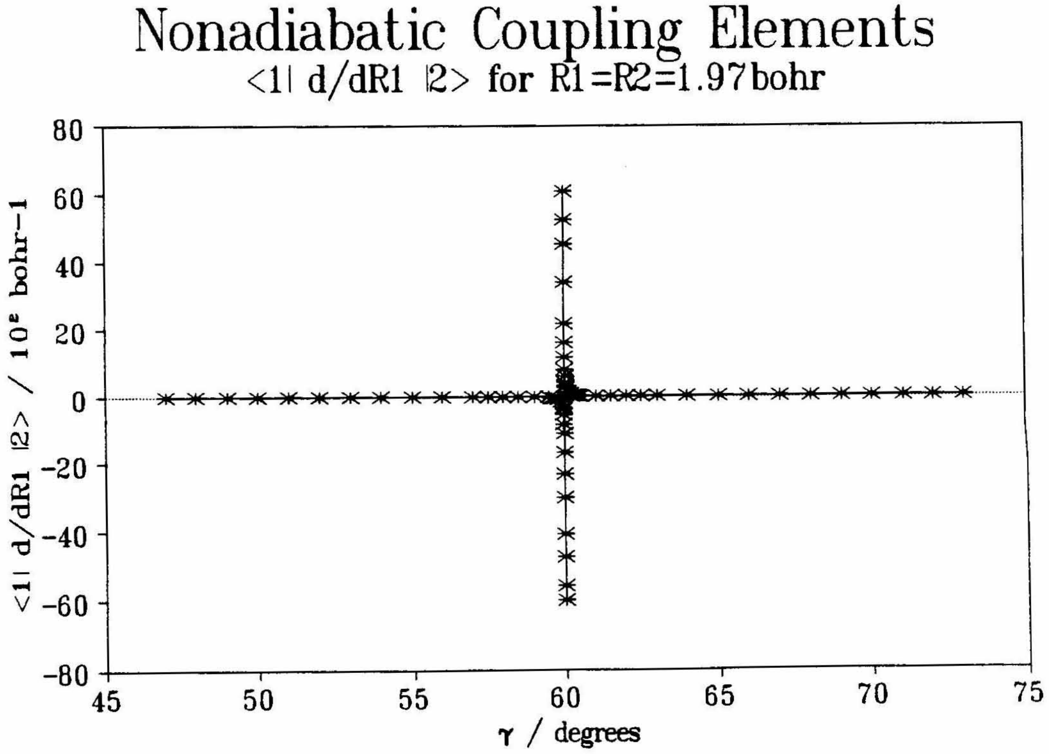

Figure 35b.

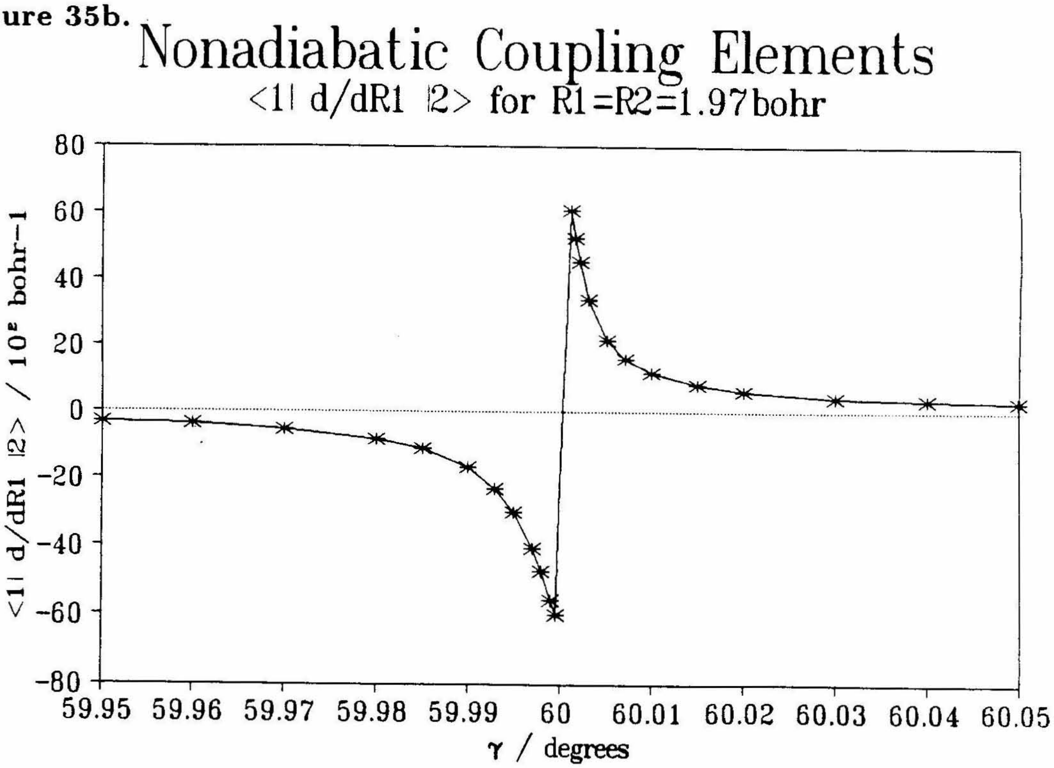

Figure 36a.

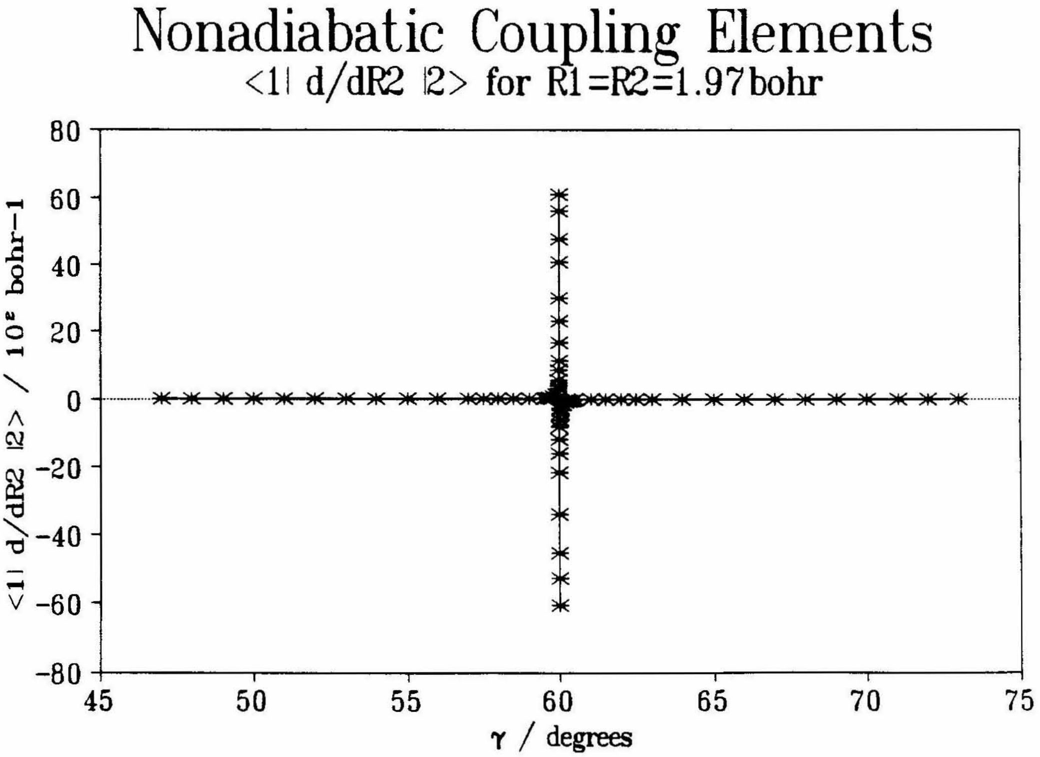

Figure 36b.

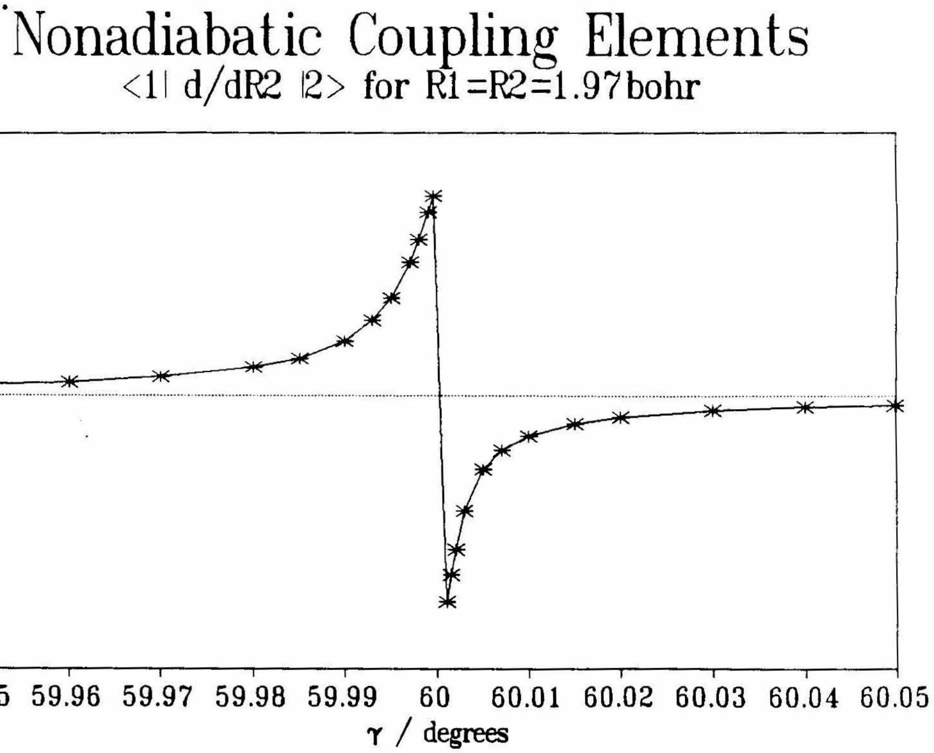

Figure 37a.

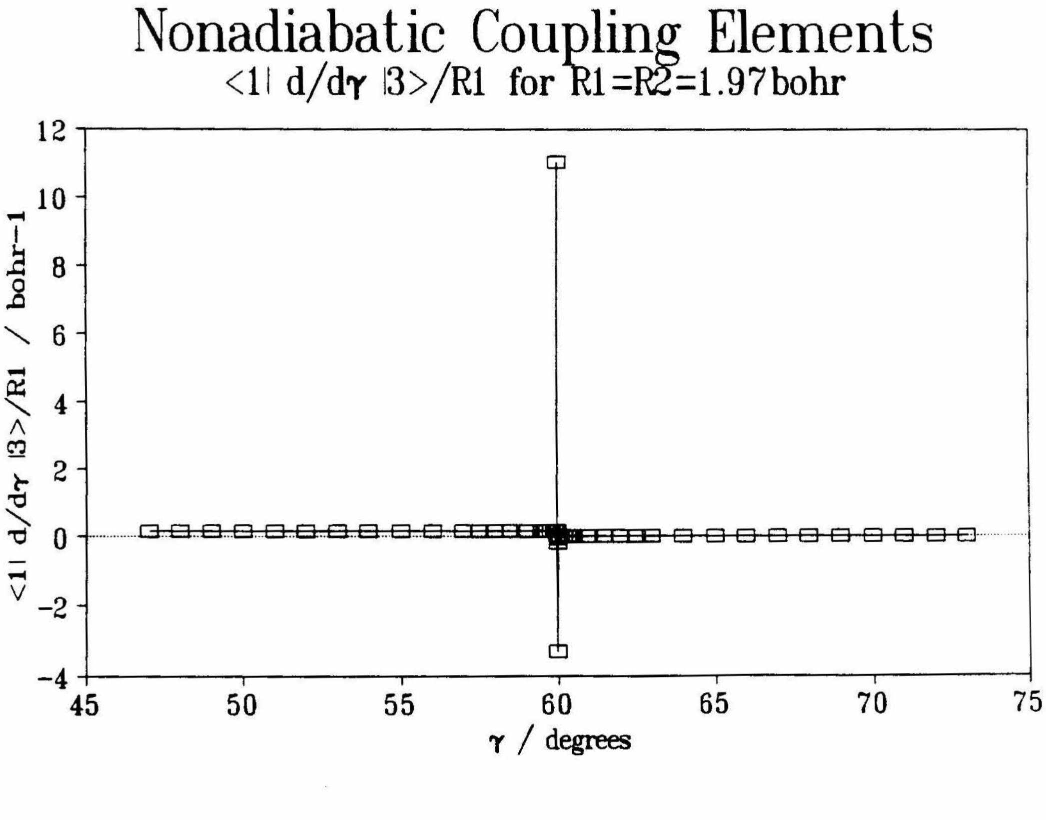

Figure 37b.

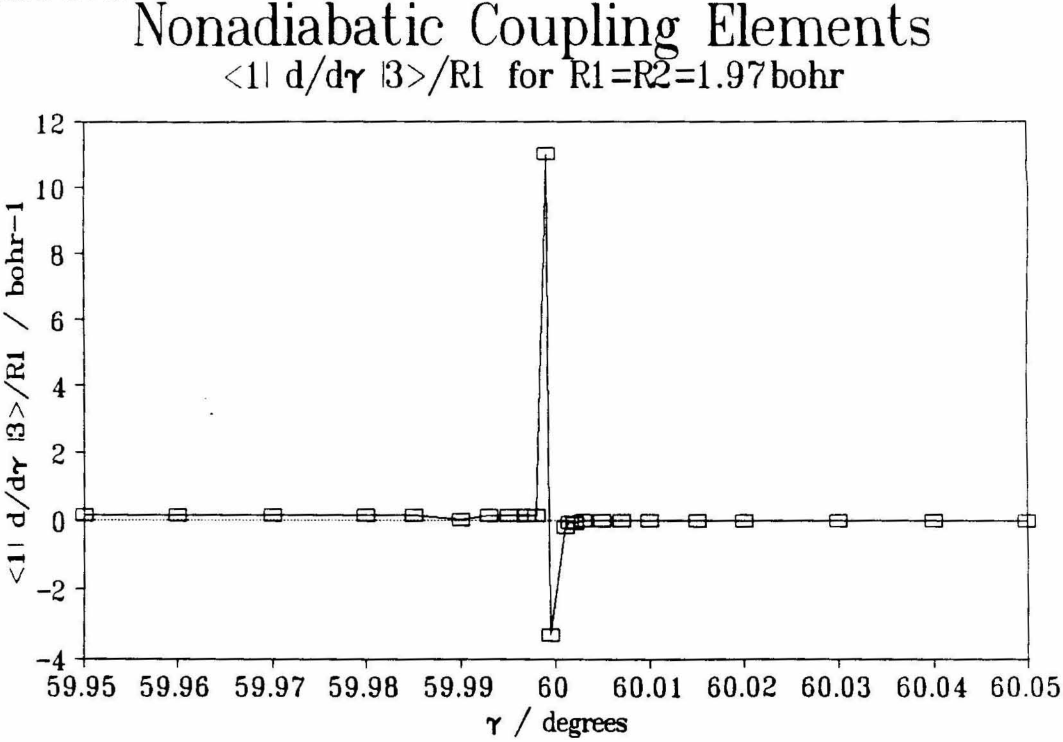

Figure 38a.

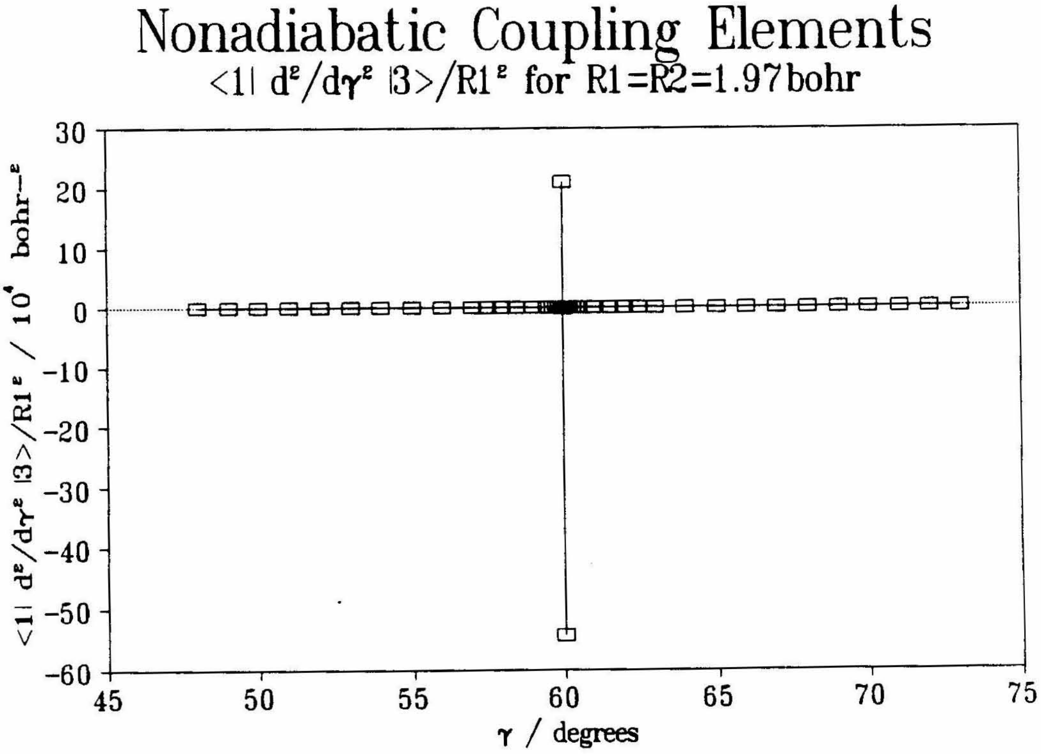

Figure 38b.

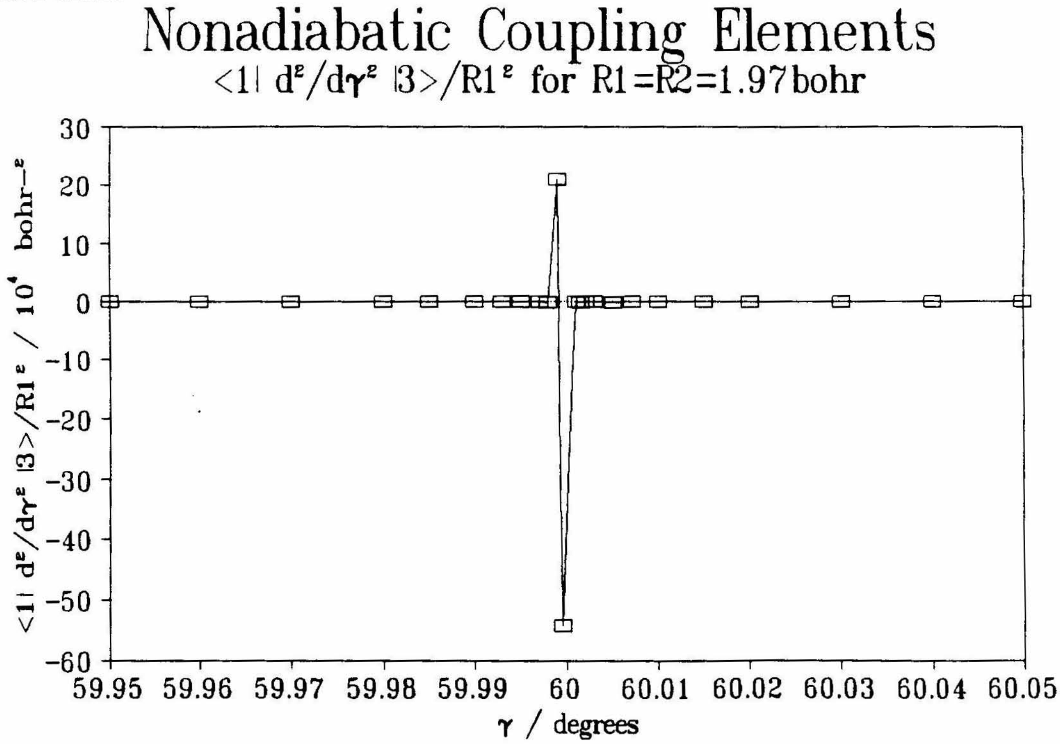

Figure 39a.

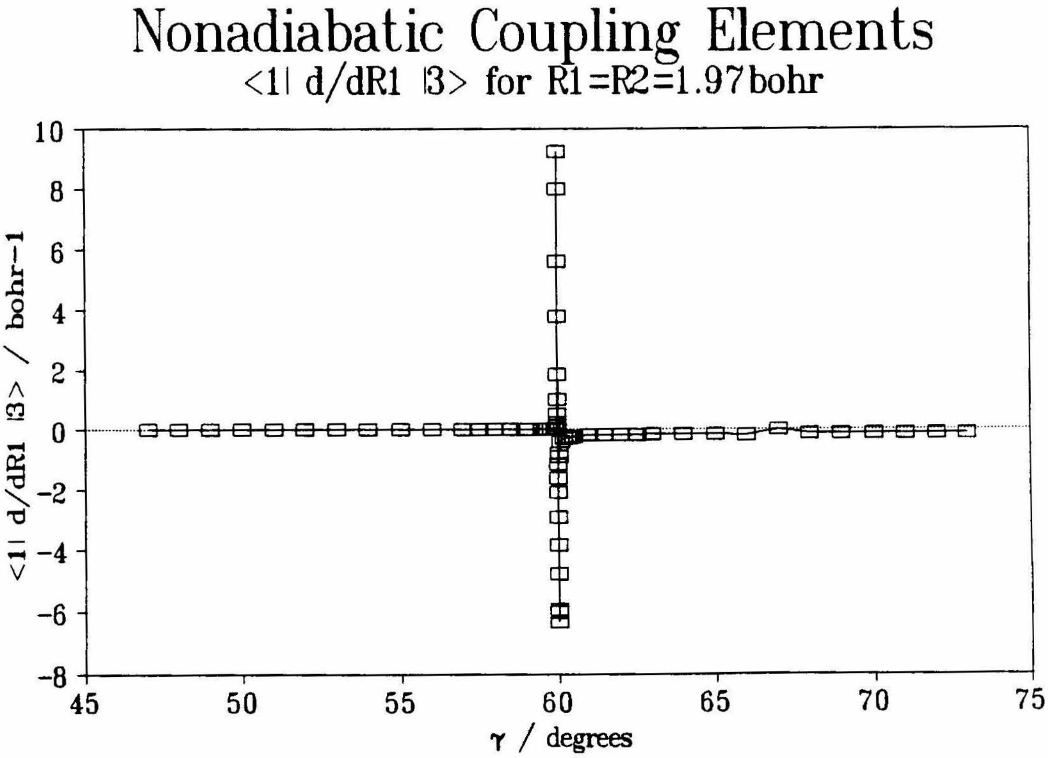

Figure 39b.

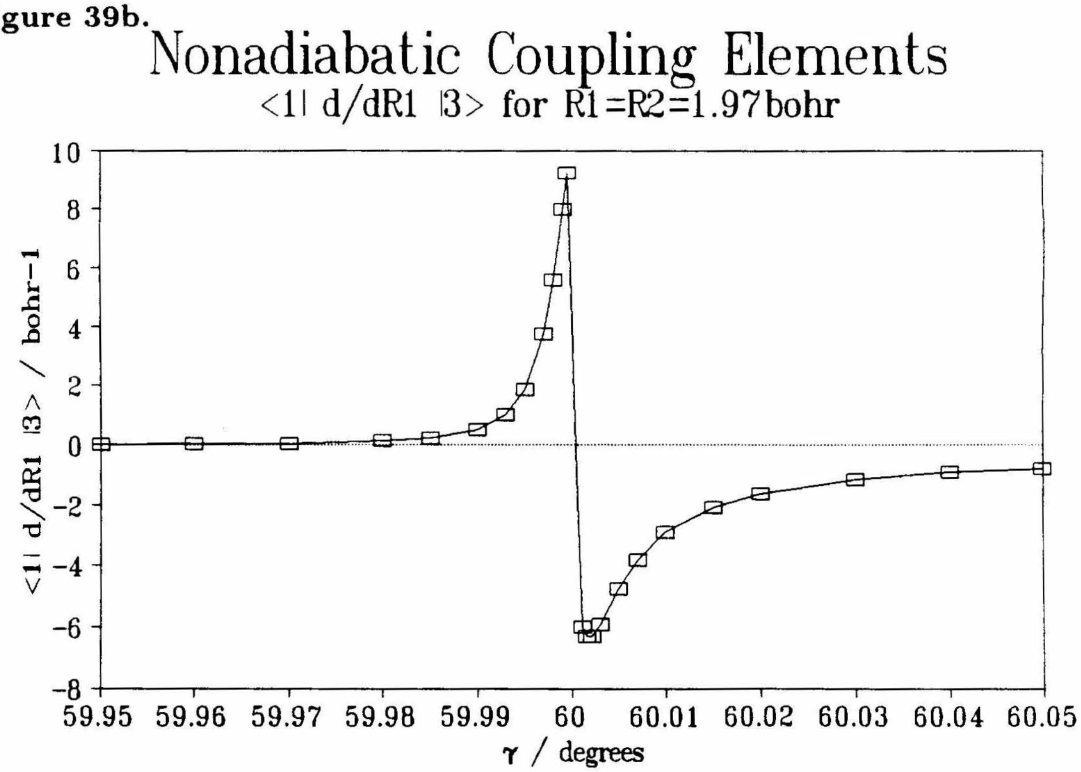

Figure 40a.

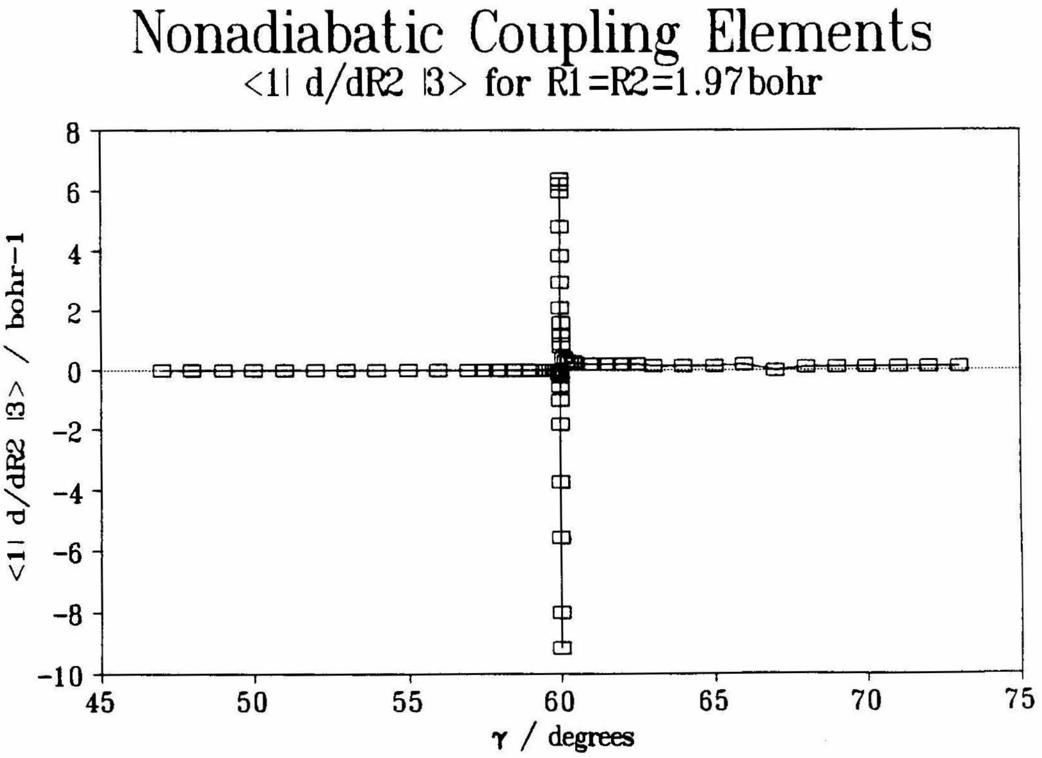

Figure 40b.

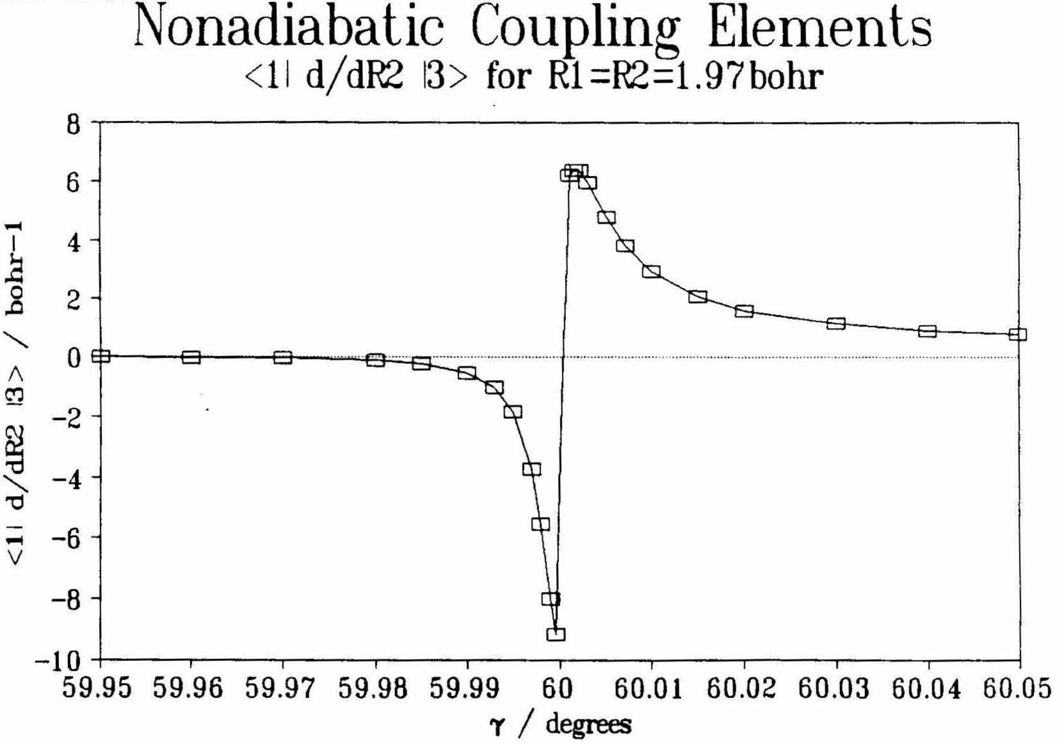

Figure 41a.

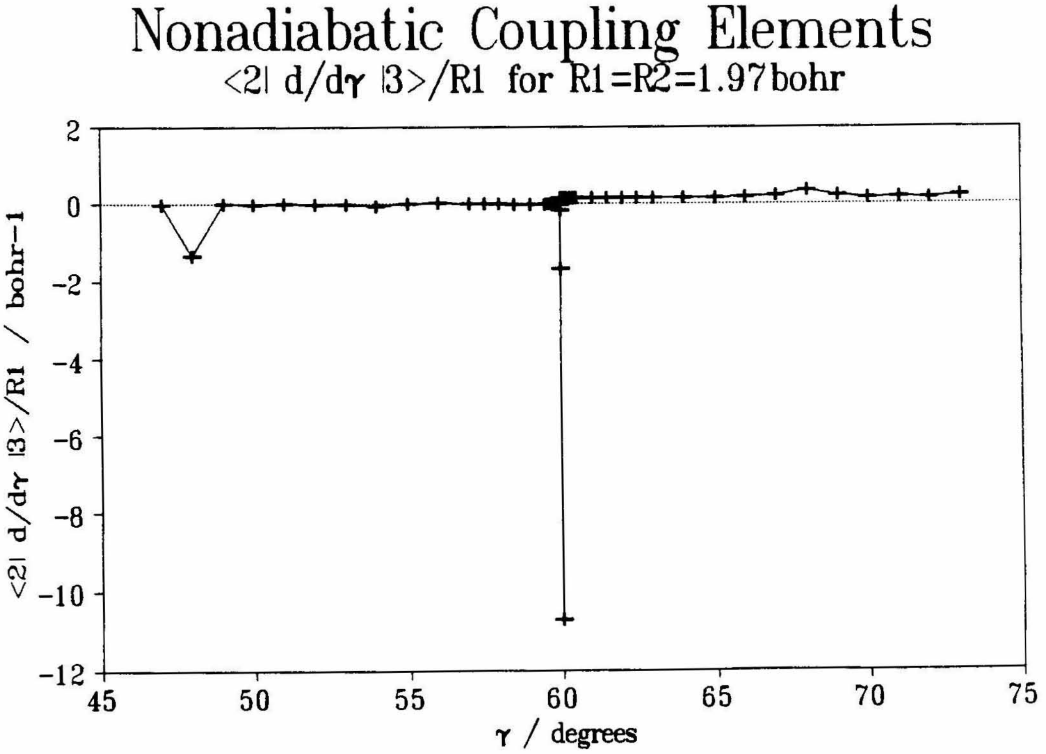

Figure 41b.

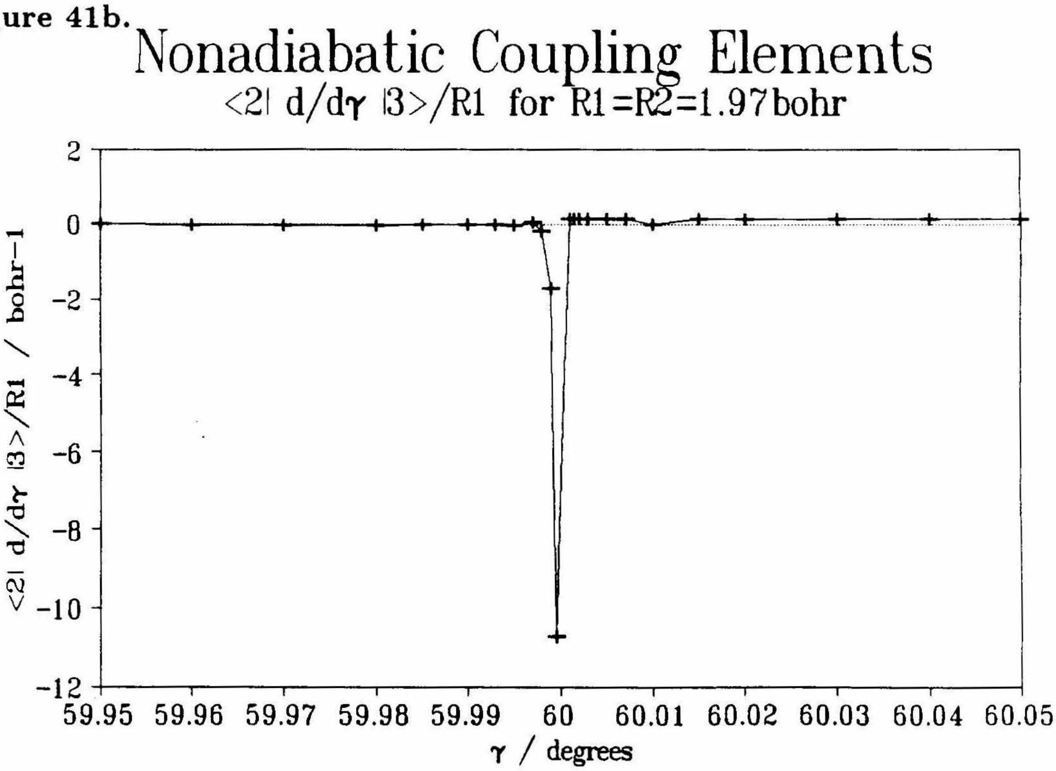

Figure 42a.

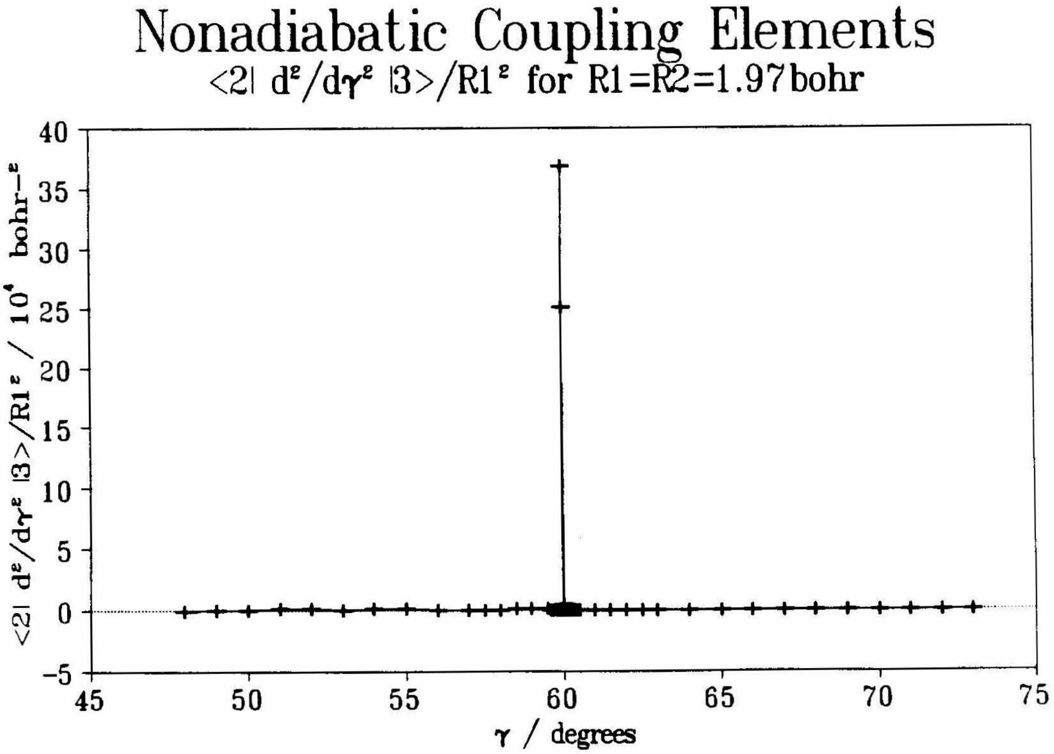

Figure 42b.

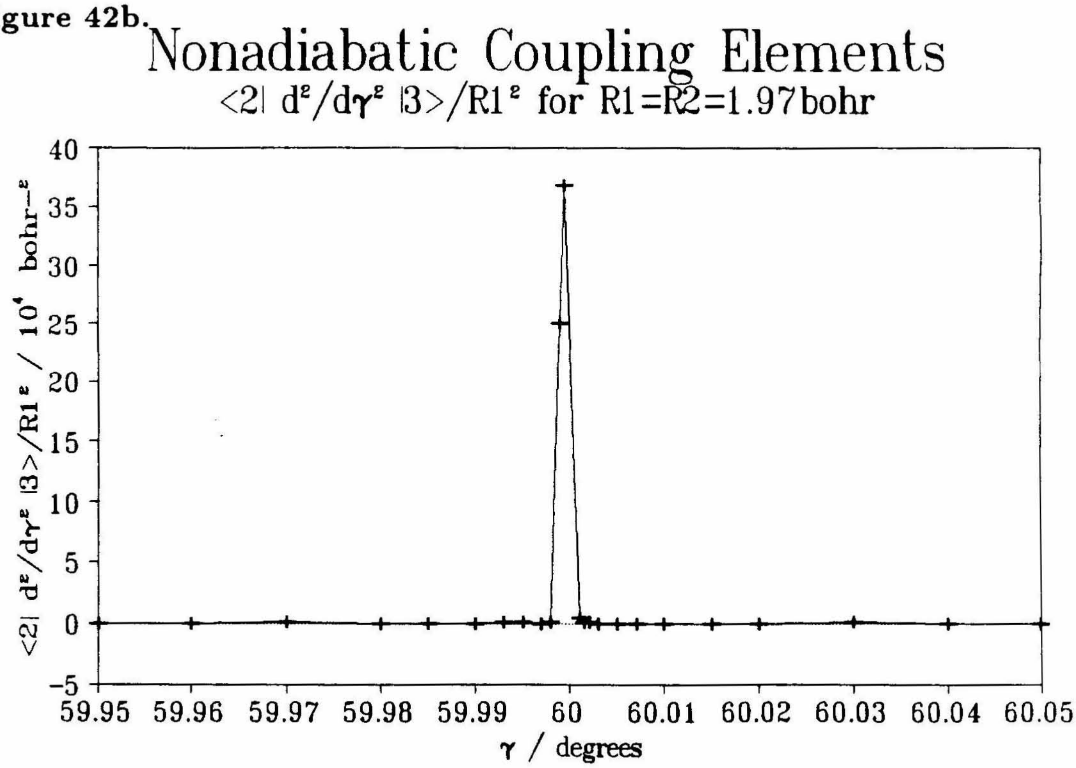

Figure 43a.

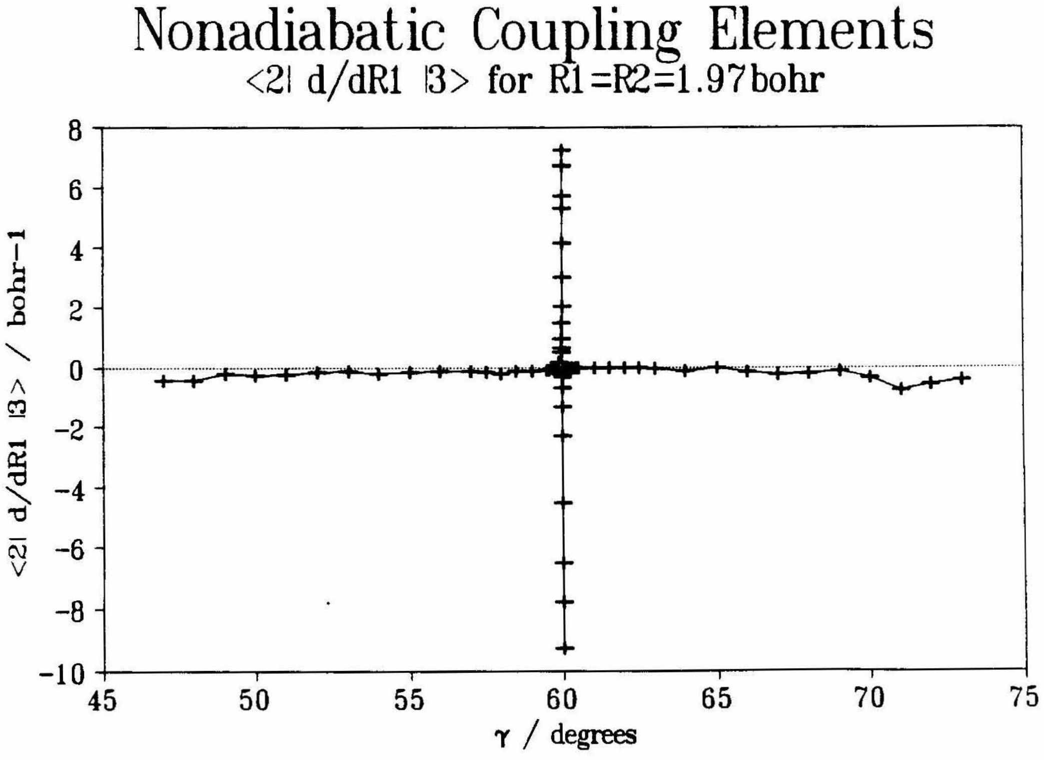

Figure 43b.

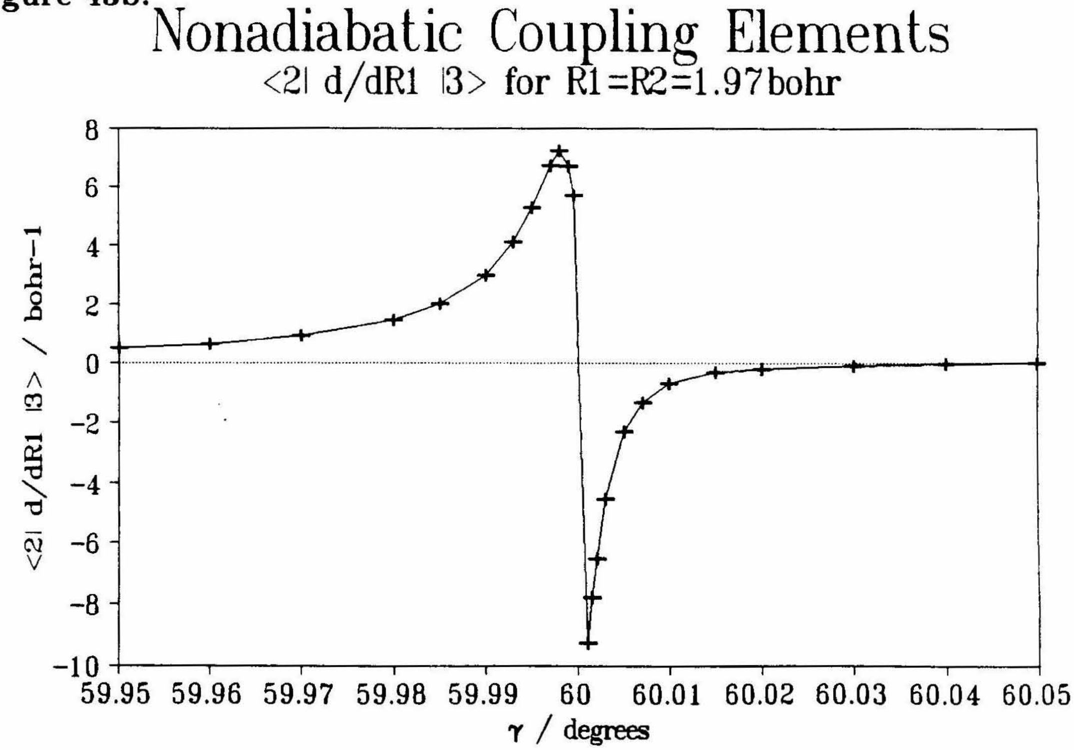

Figure 44a.

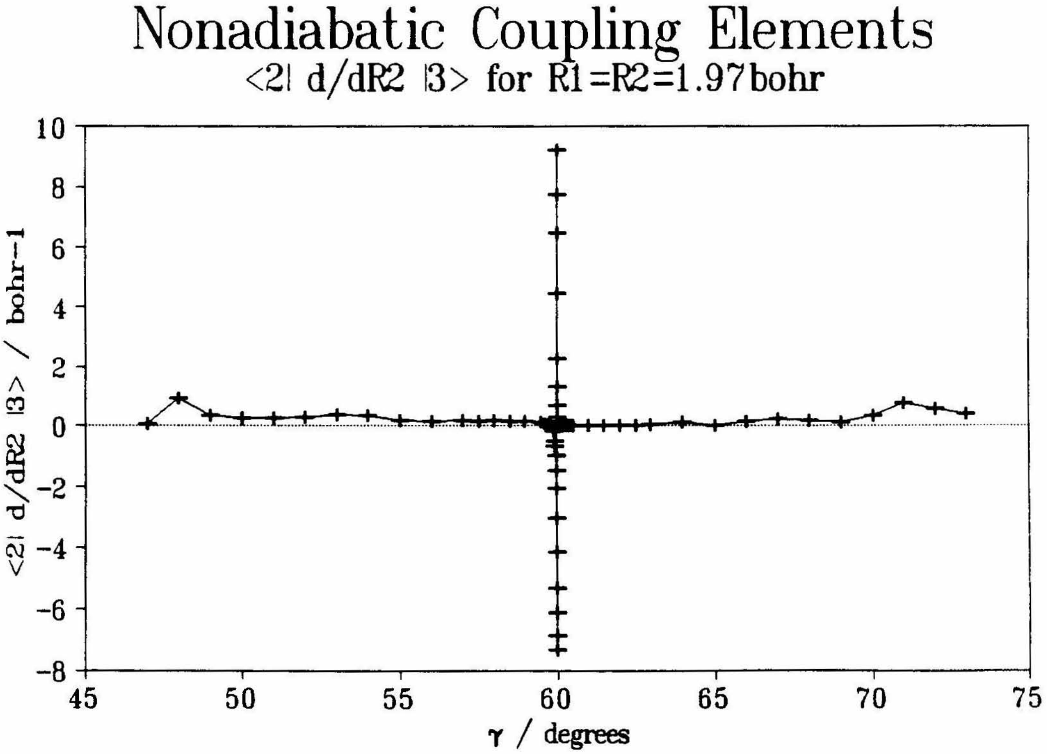

Figure 44b.

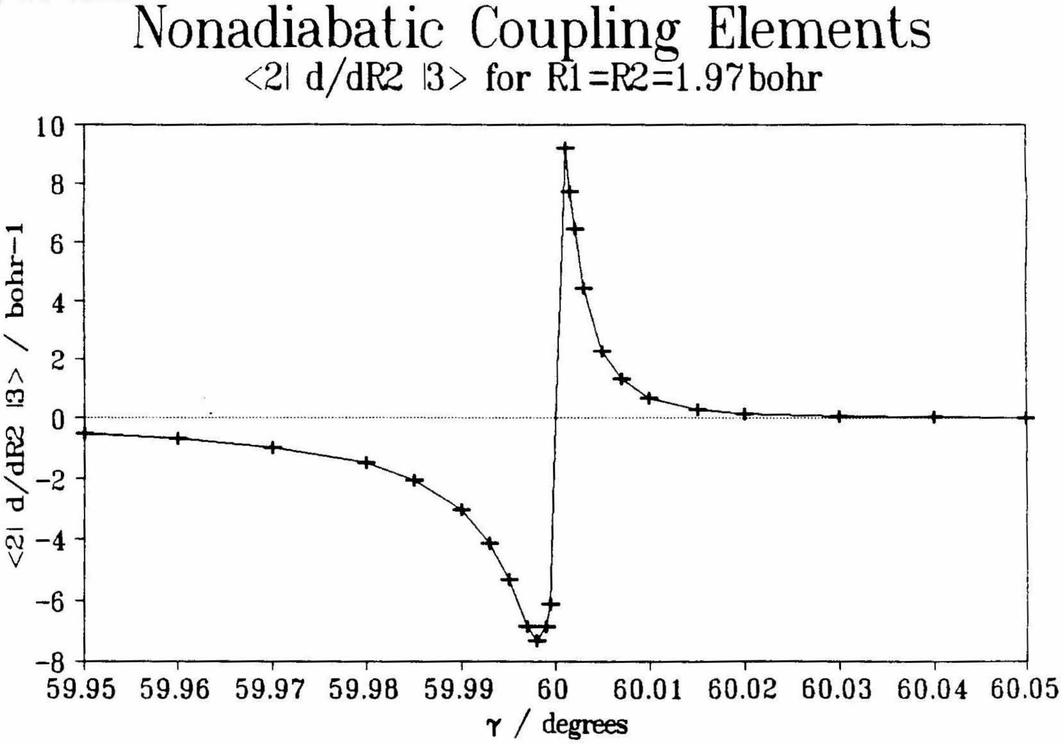

Figure 45a.

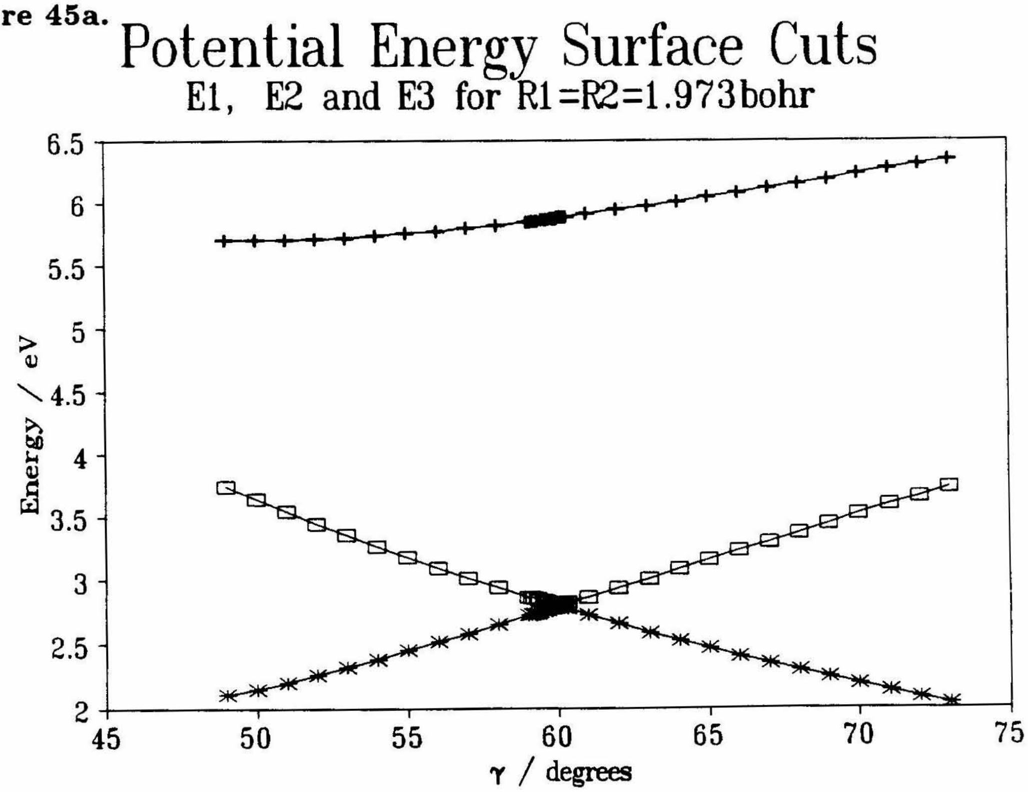

Figure 45b.

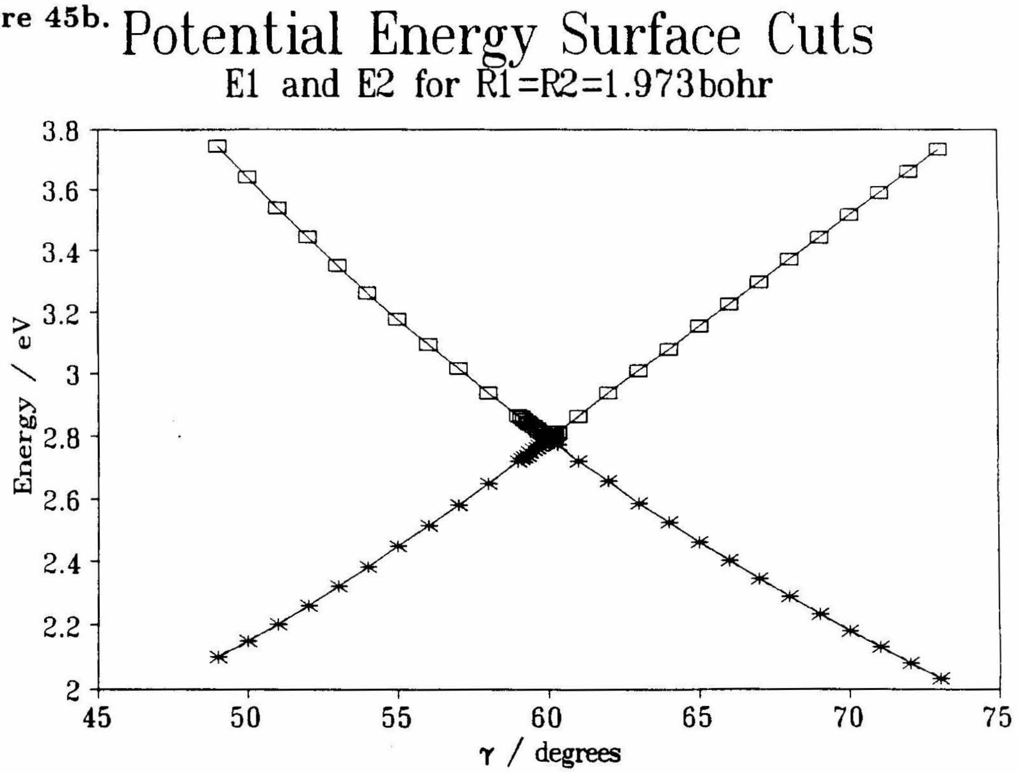

Figure 46a.

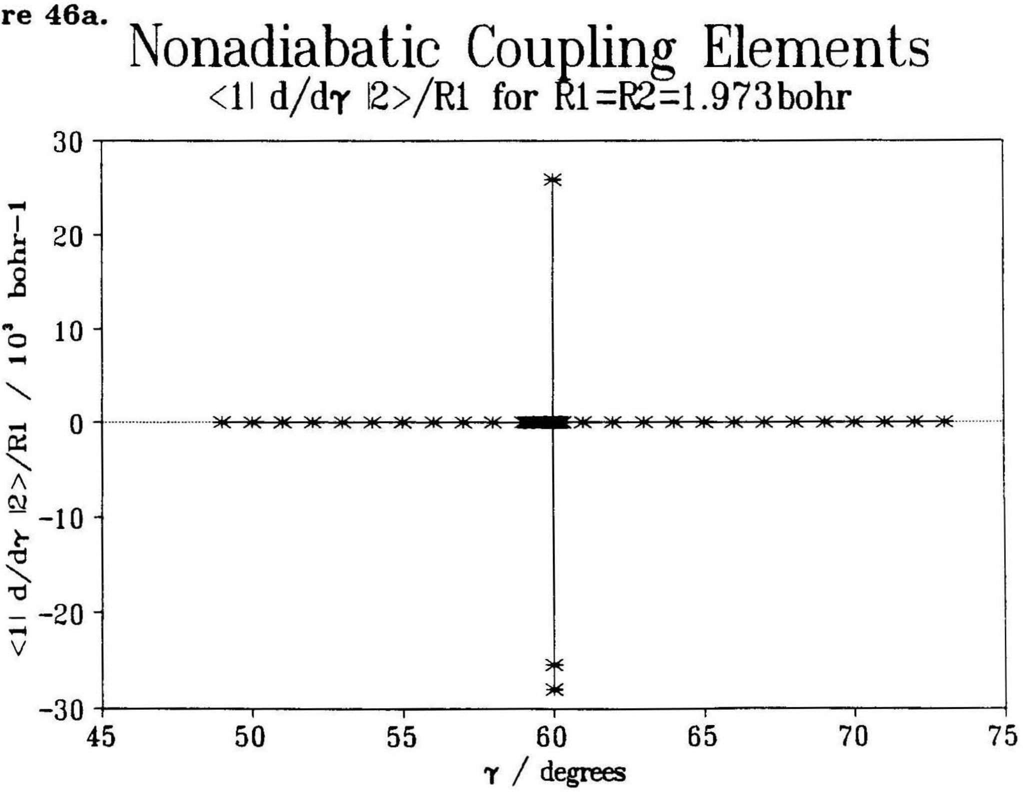

Figure 46b.

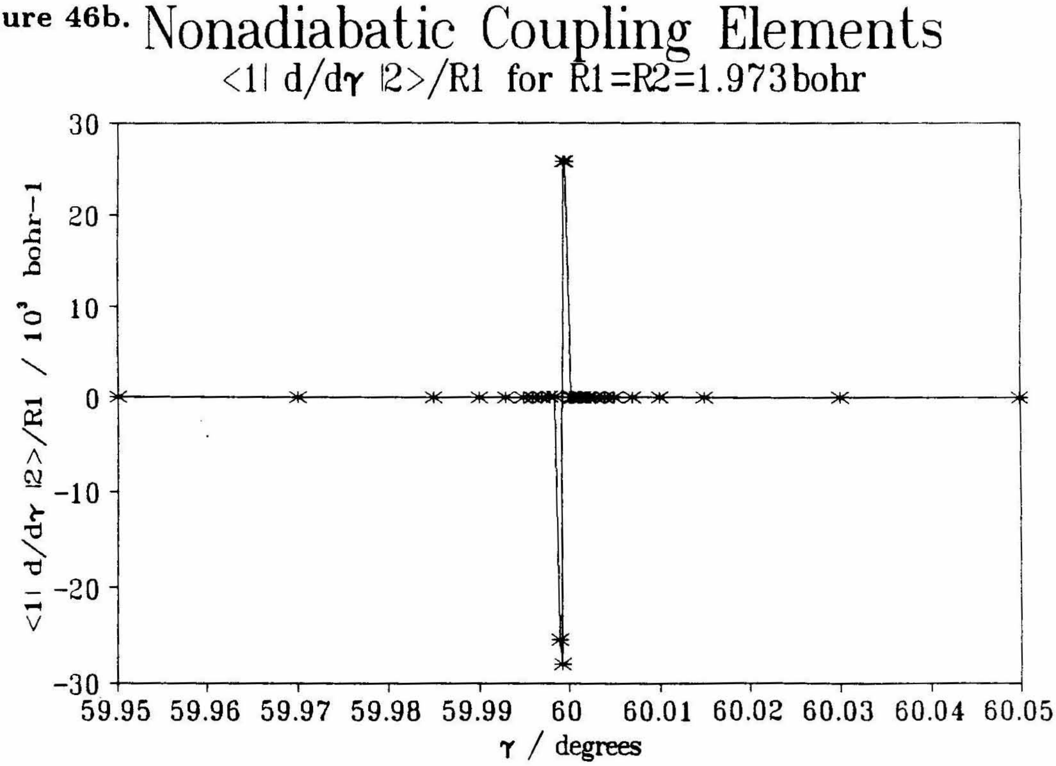

Figure 47a.

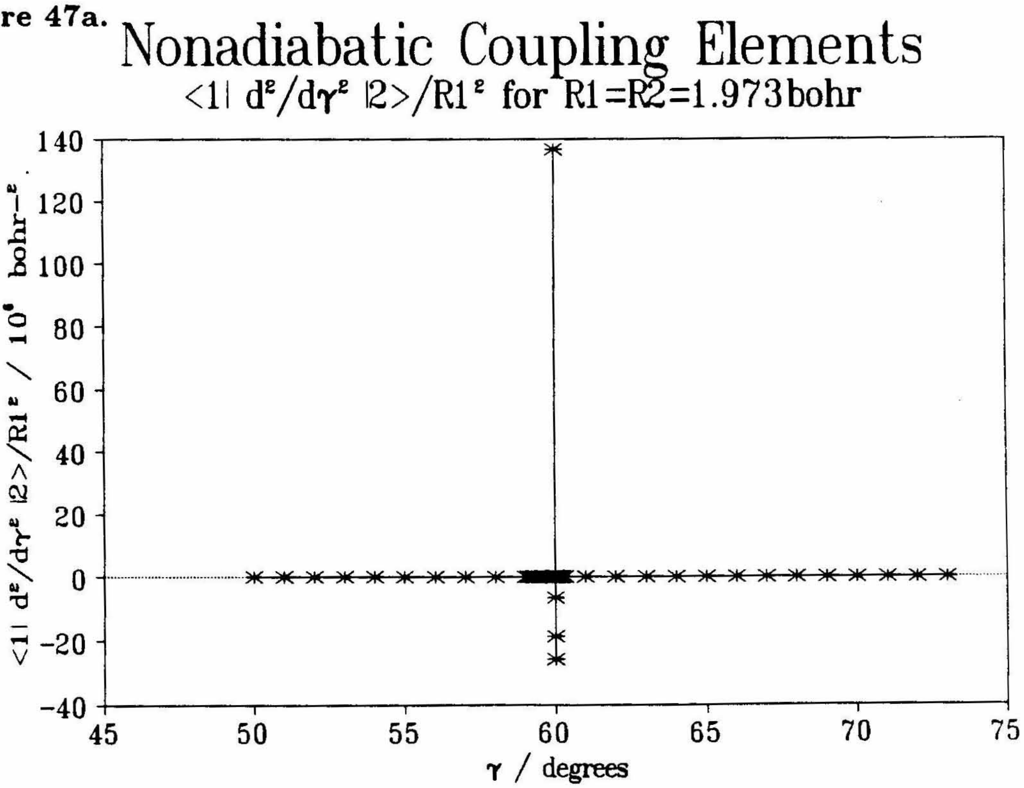

Figure 47b.

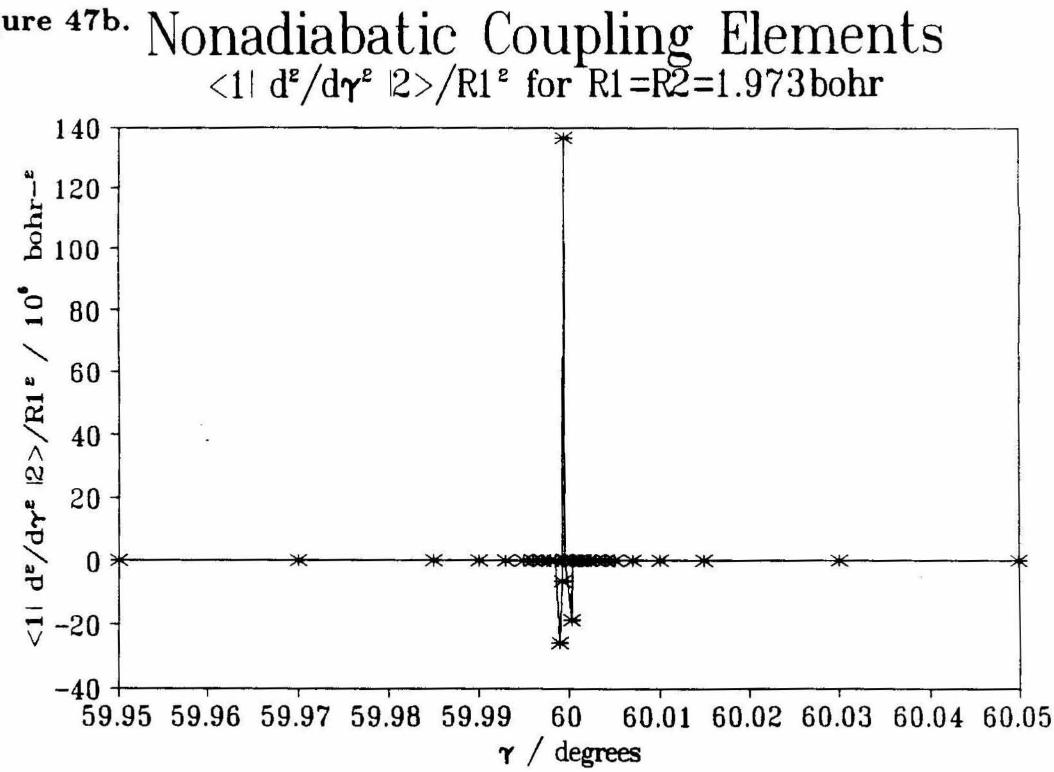

Figure 48a.

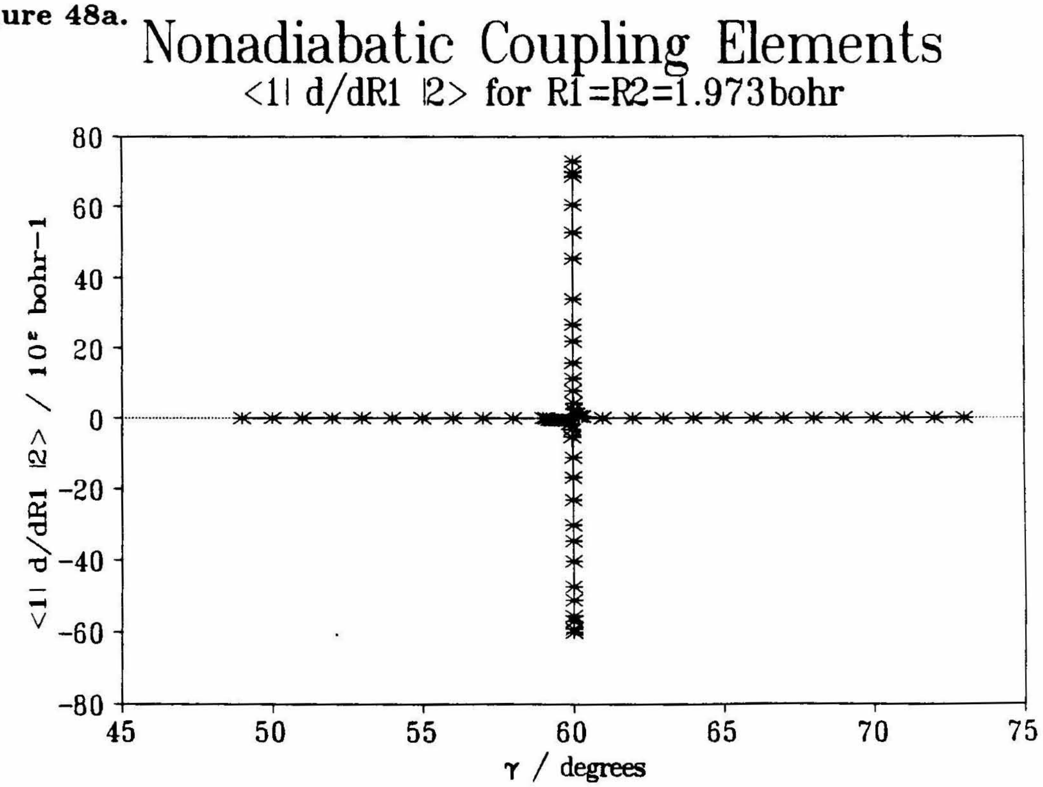

Figure 48b.

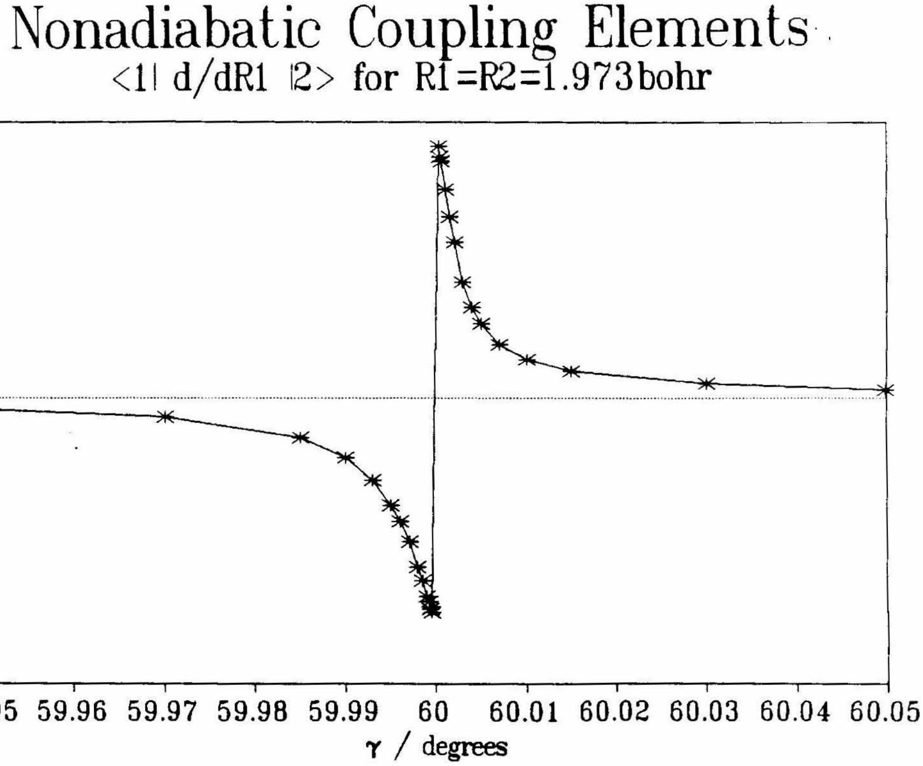

Figure 49a.

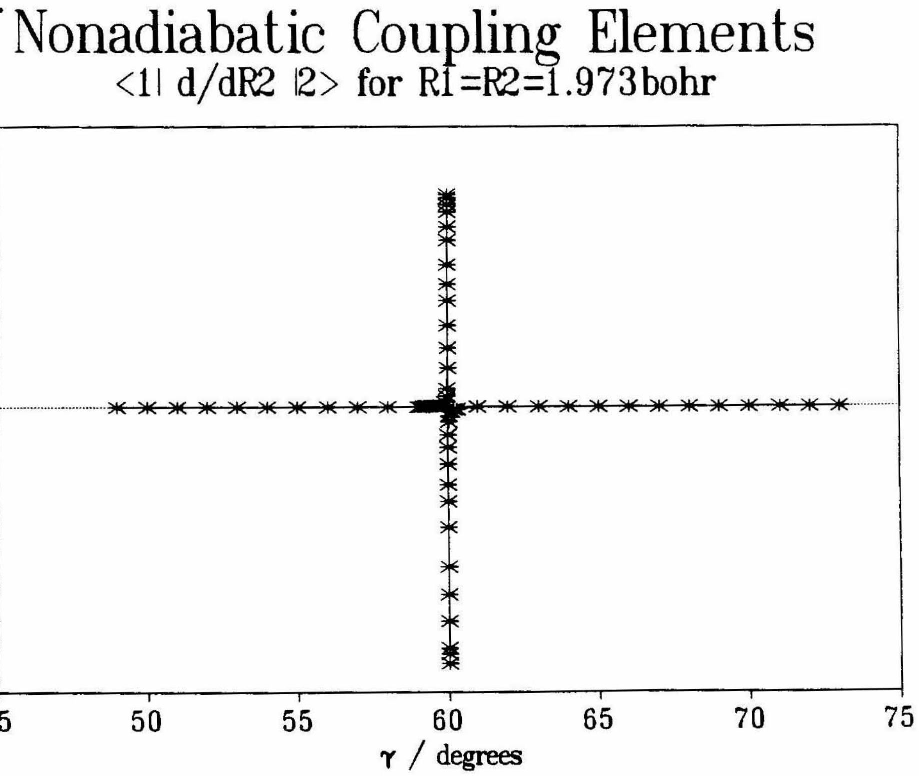

Figure 49b.

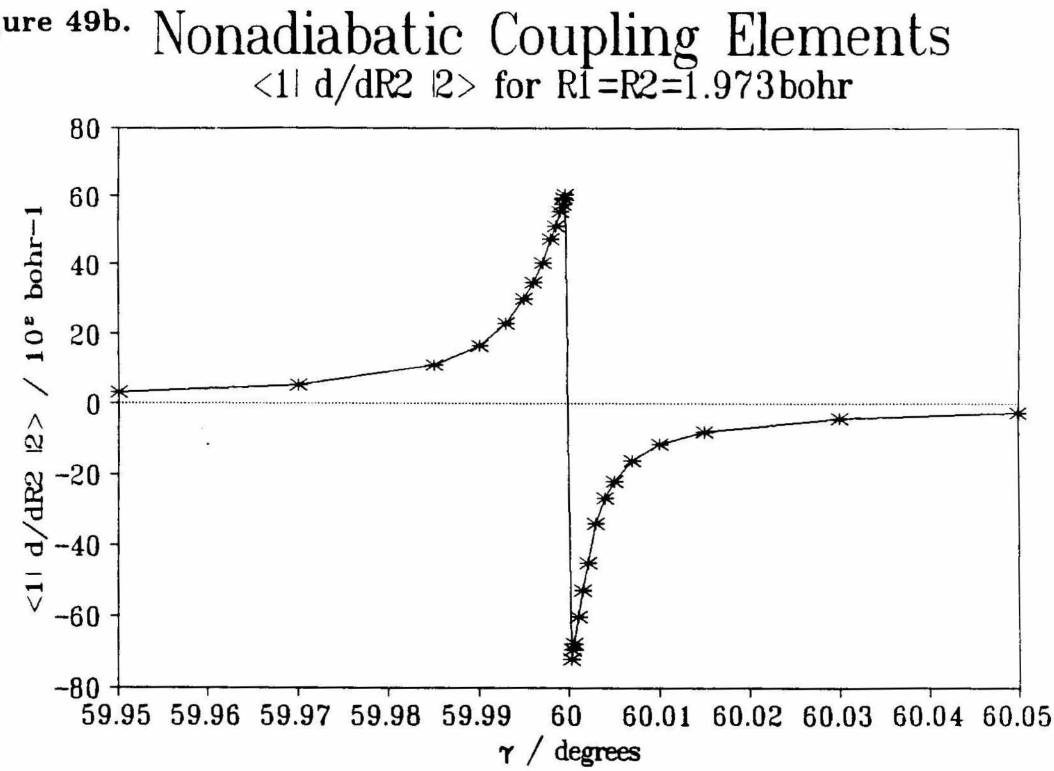

Figure 50a.

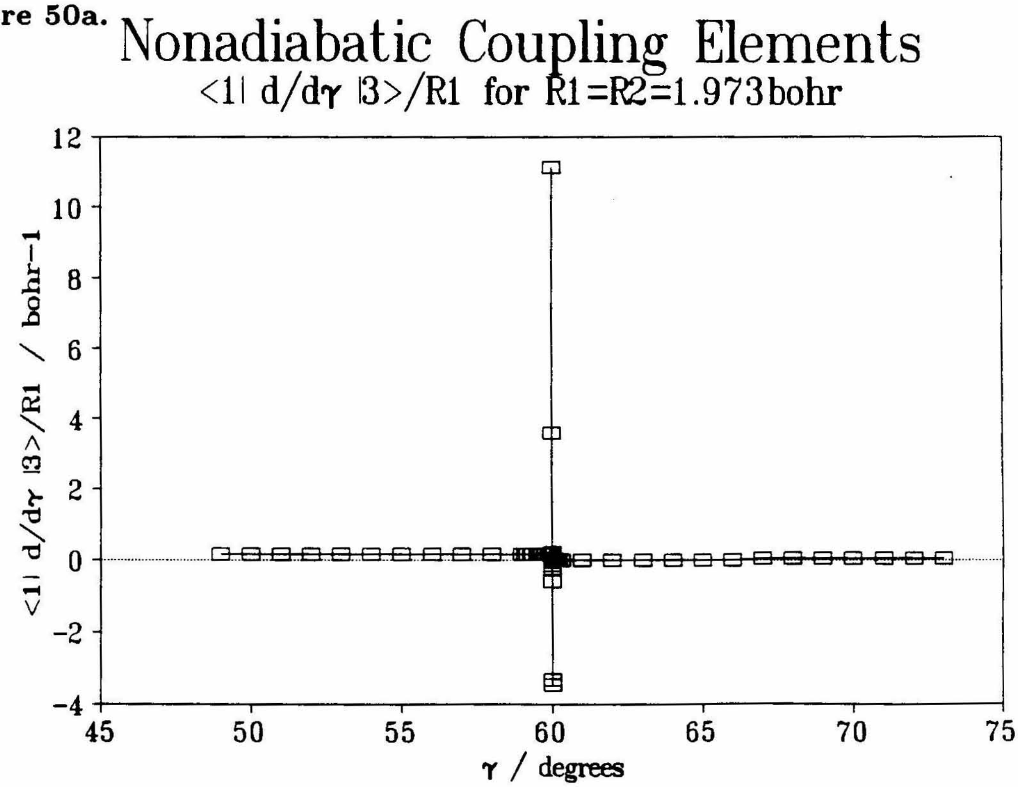

Figure 50b.

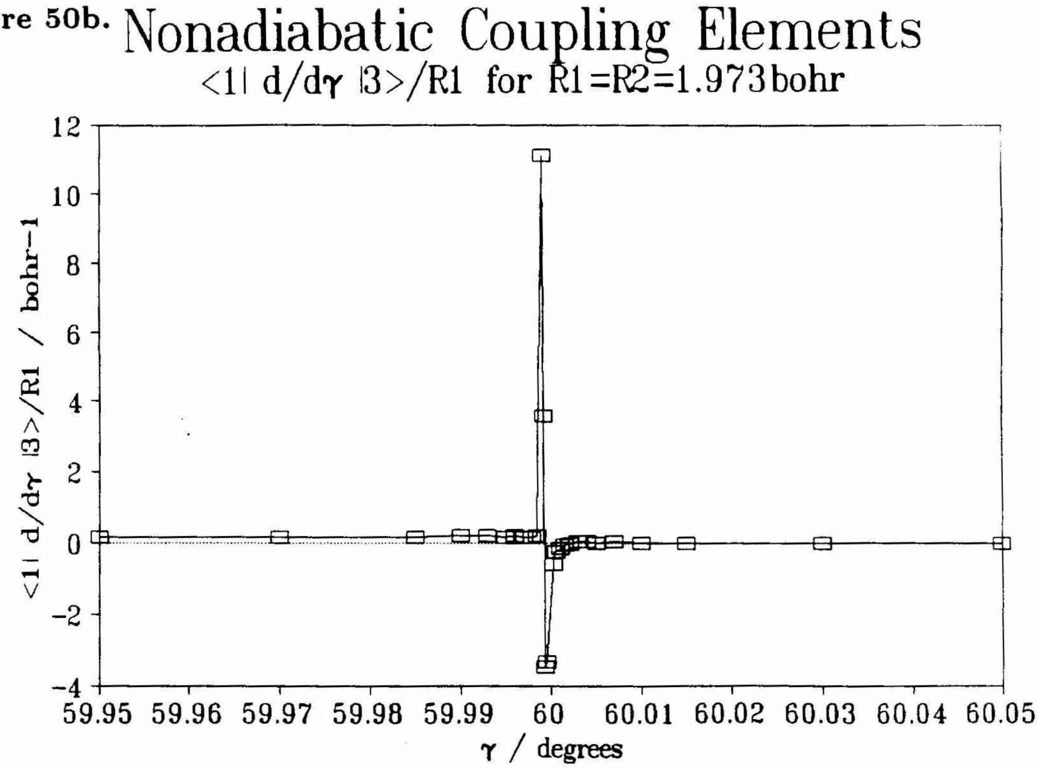

Figure 51a.

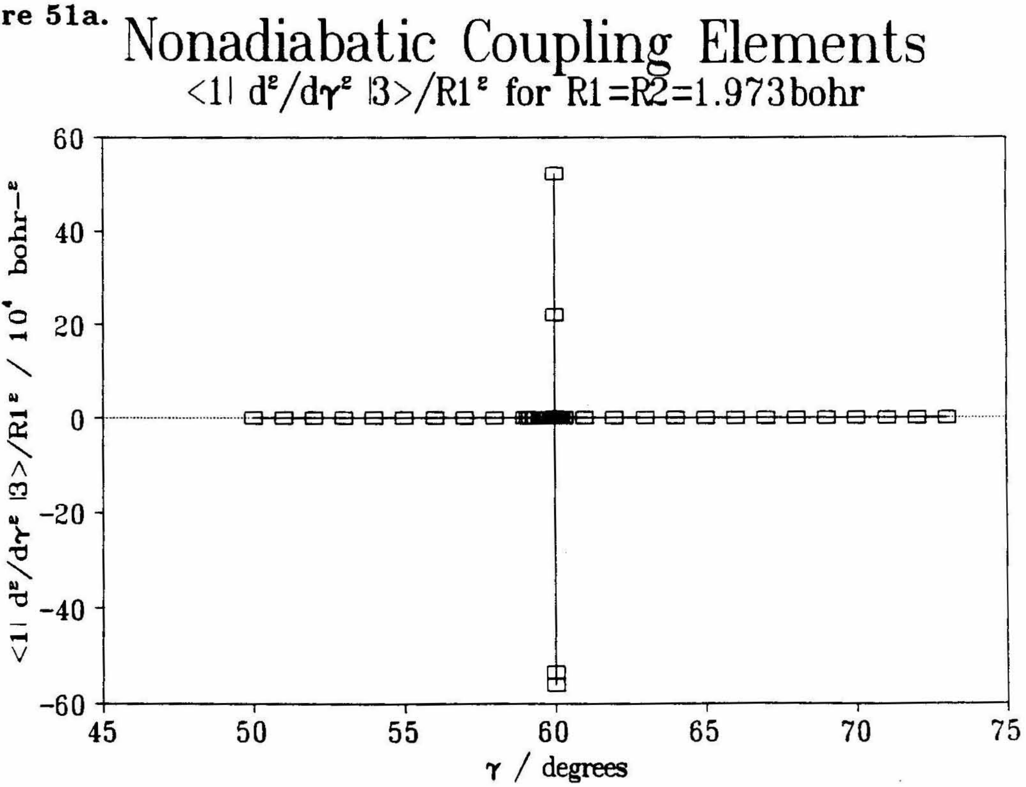

Figure 51b.

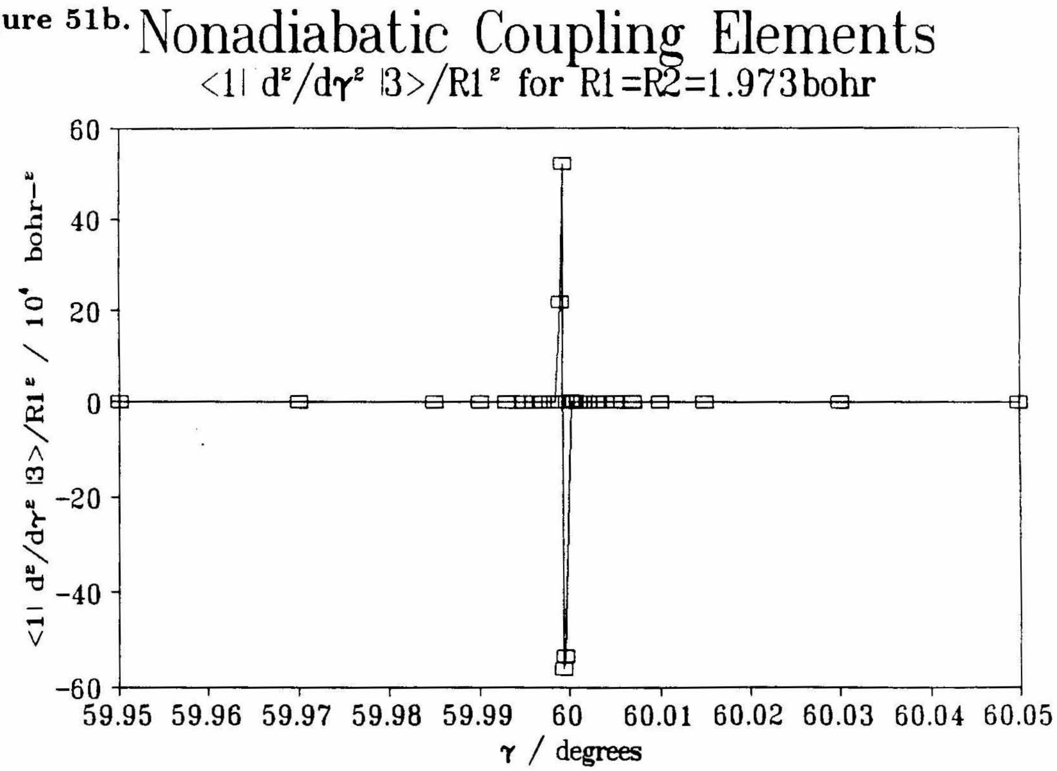

Figure 52a.

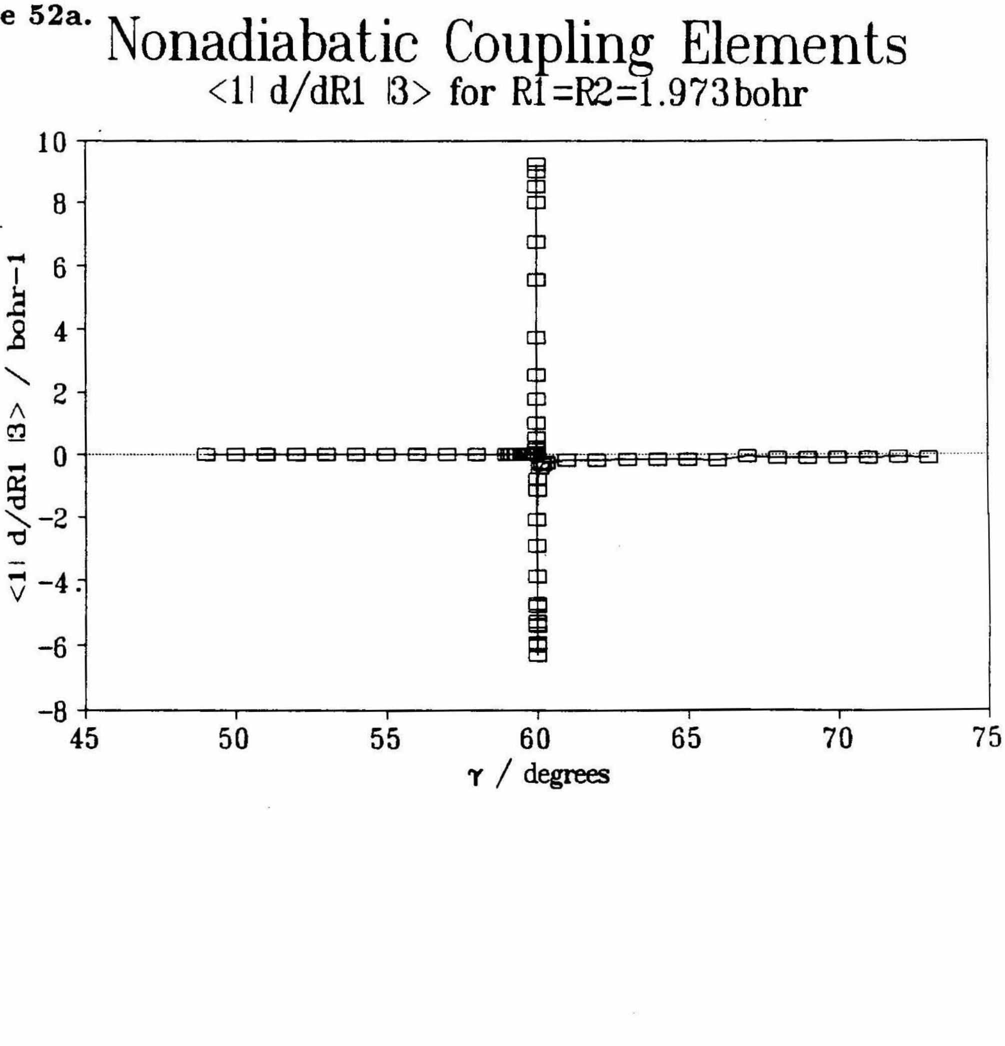

Figure 52b.

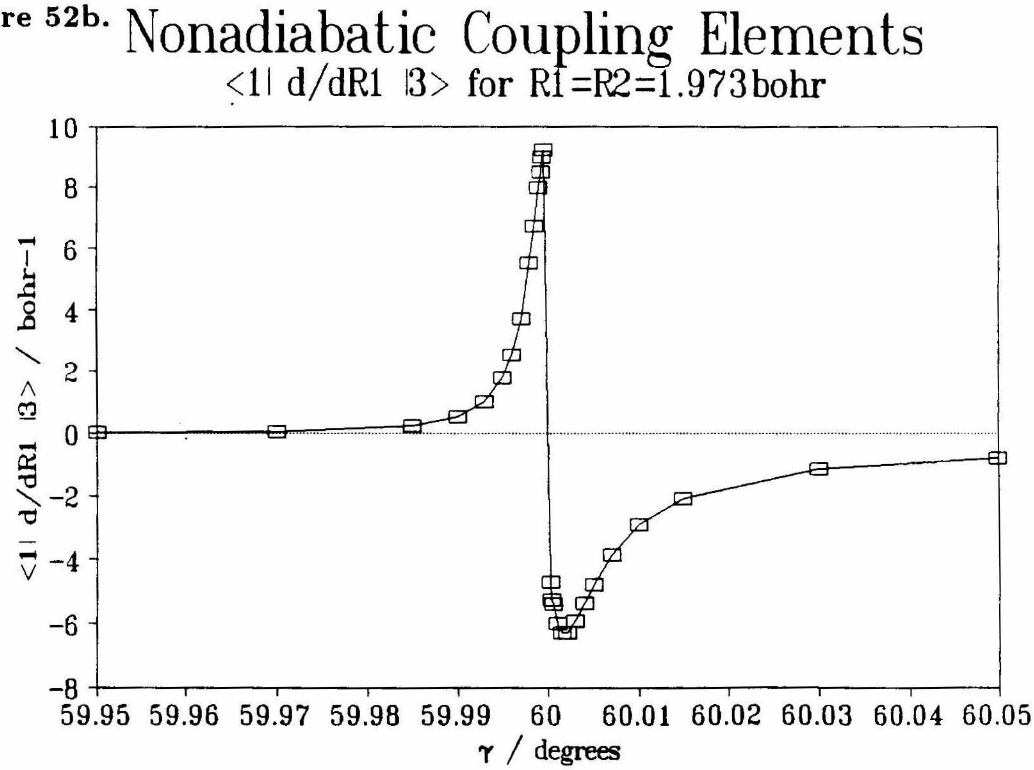

Figure 53a.

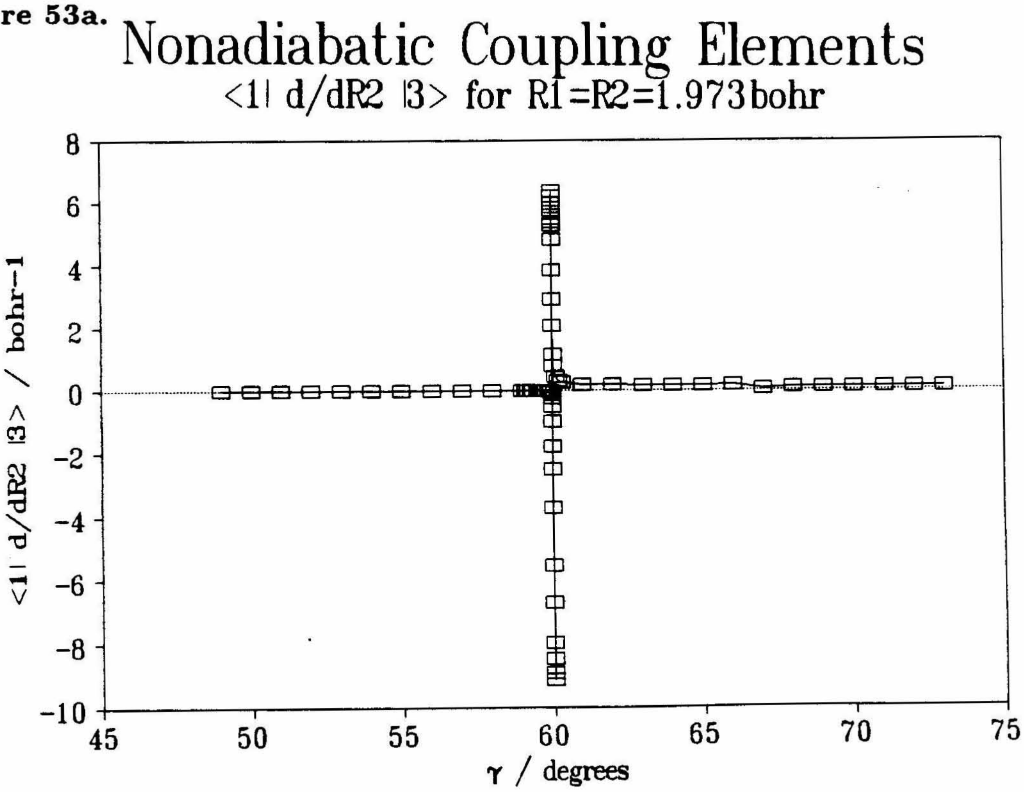

Figure 53b.

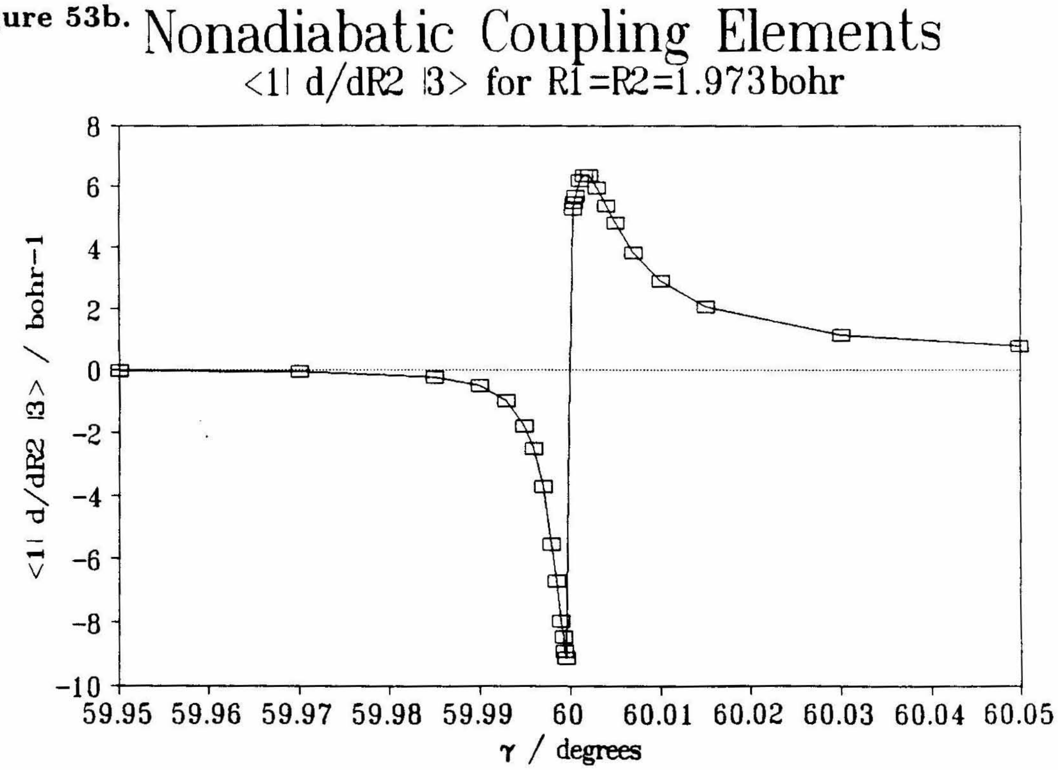

Figure 54a.

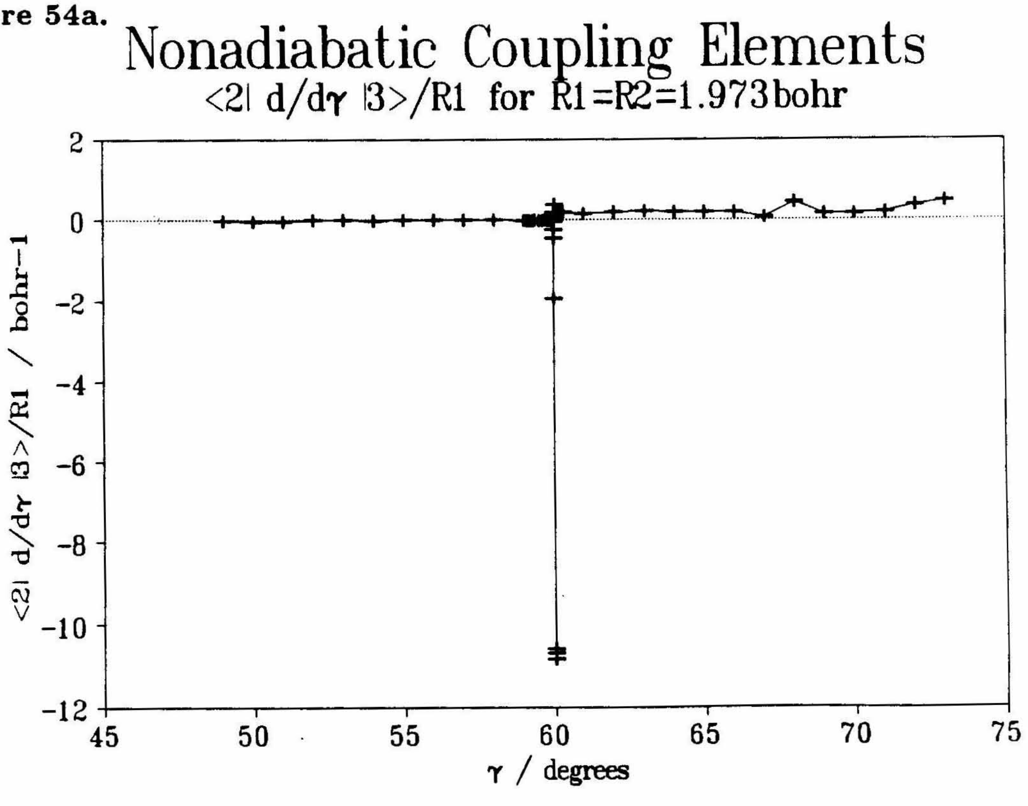

Figure 54b.

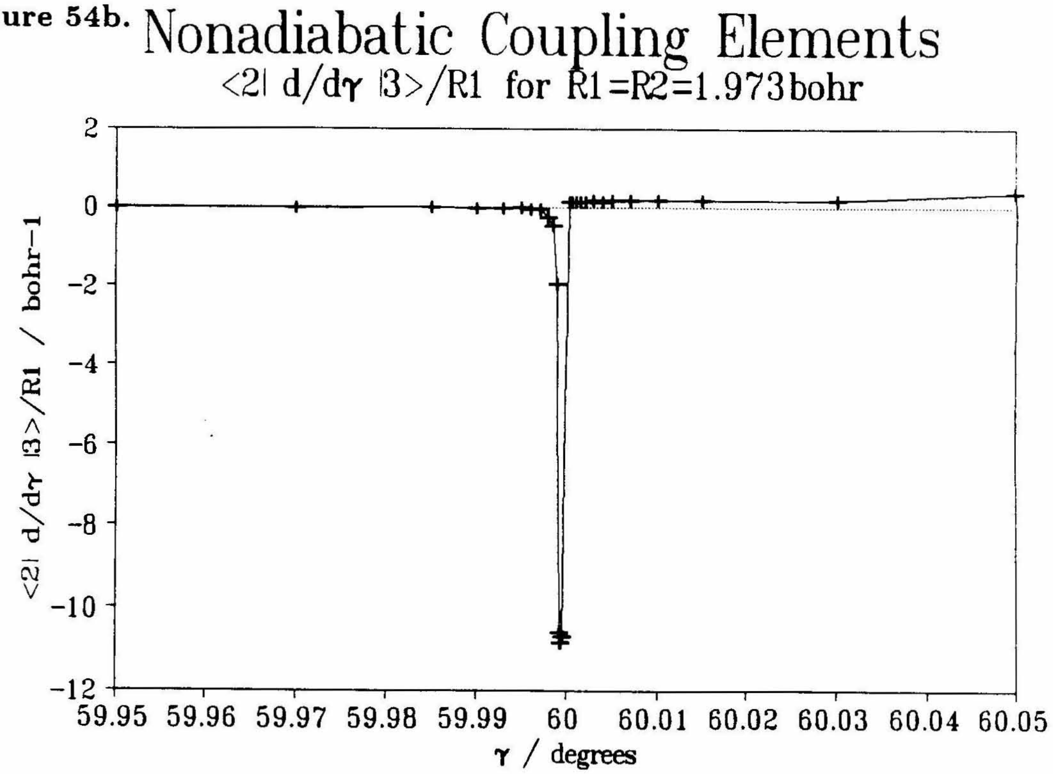

Figure 55a.

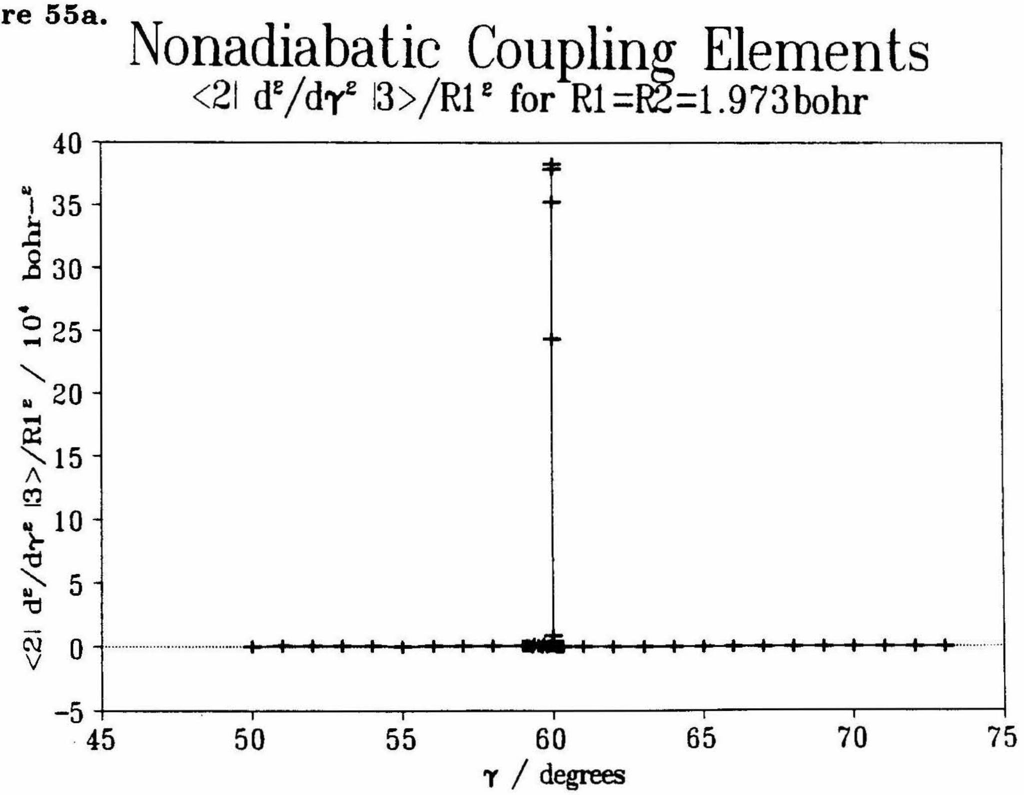

Figure 55b.

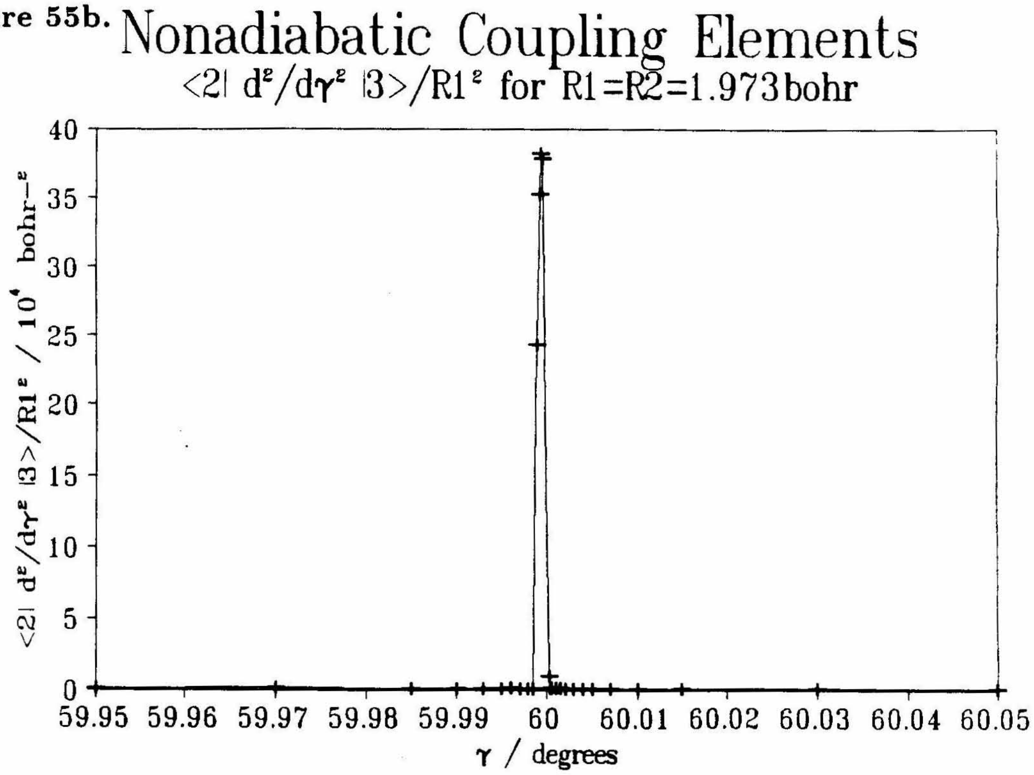

Figure 56a.

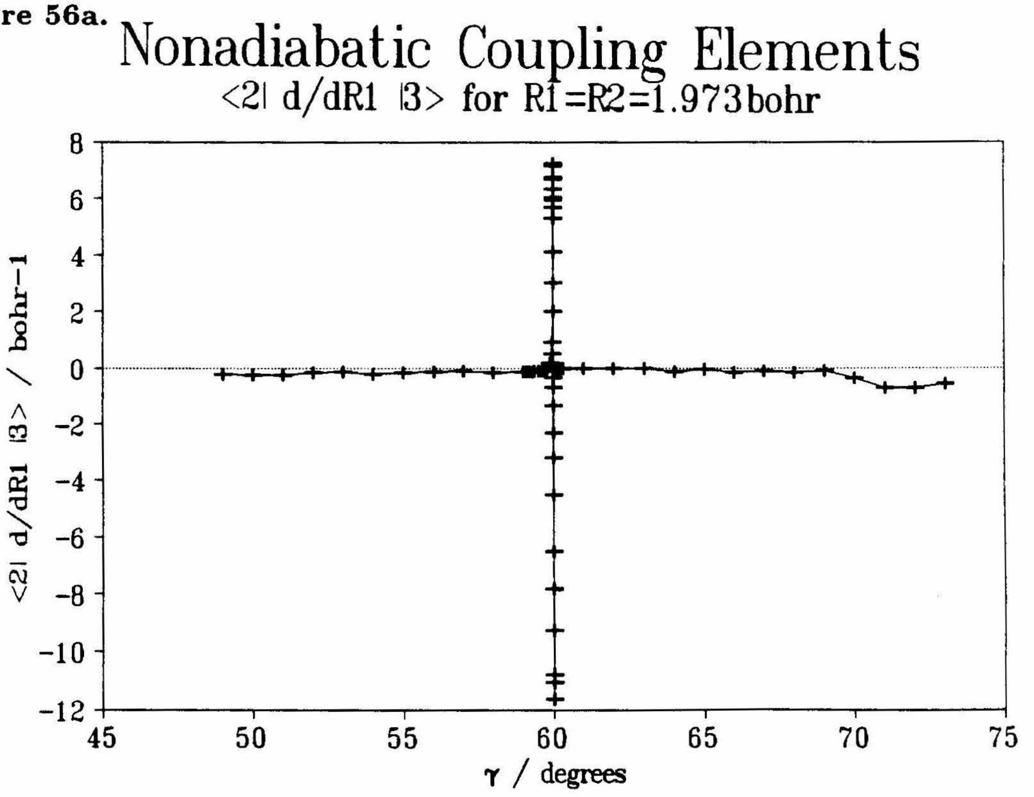

Figure 56b.

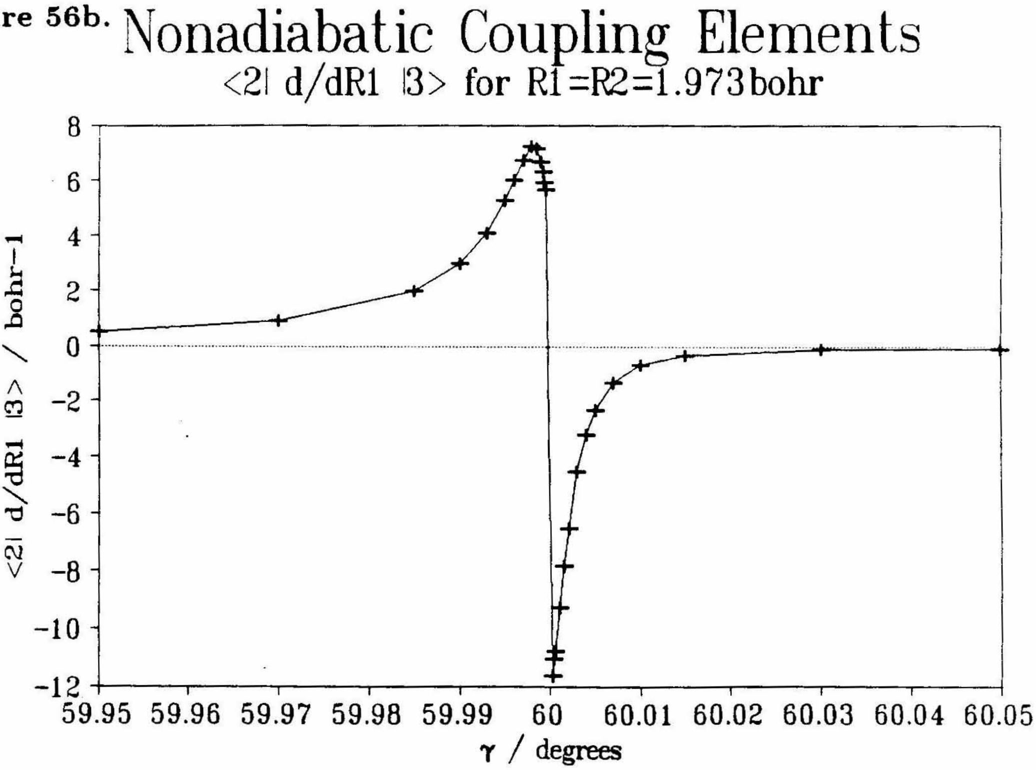

Figure 57a.

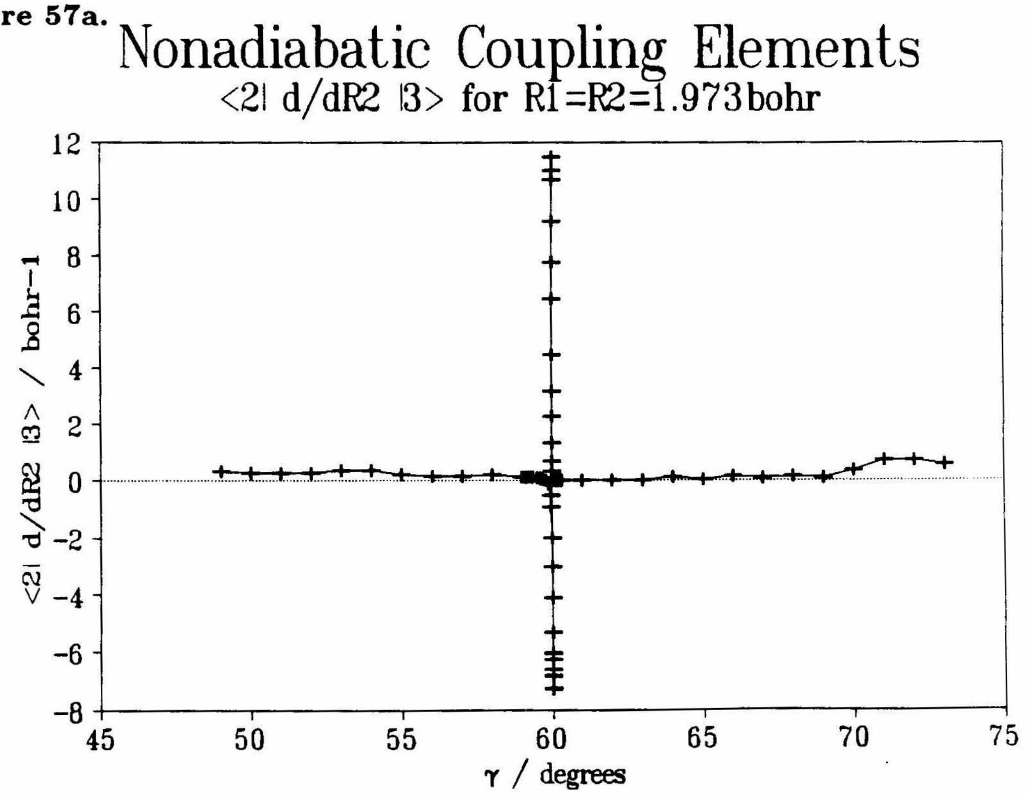

Figure 57b.

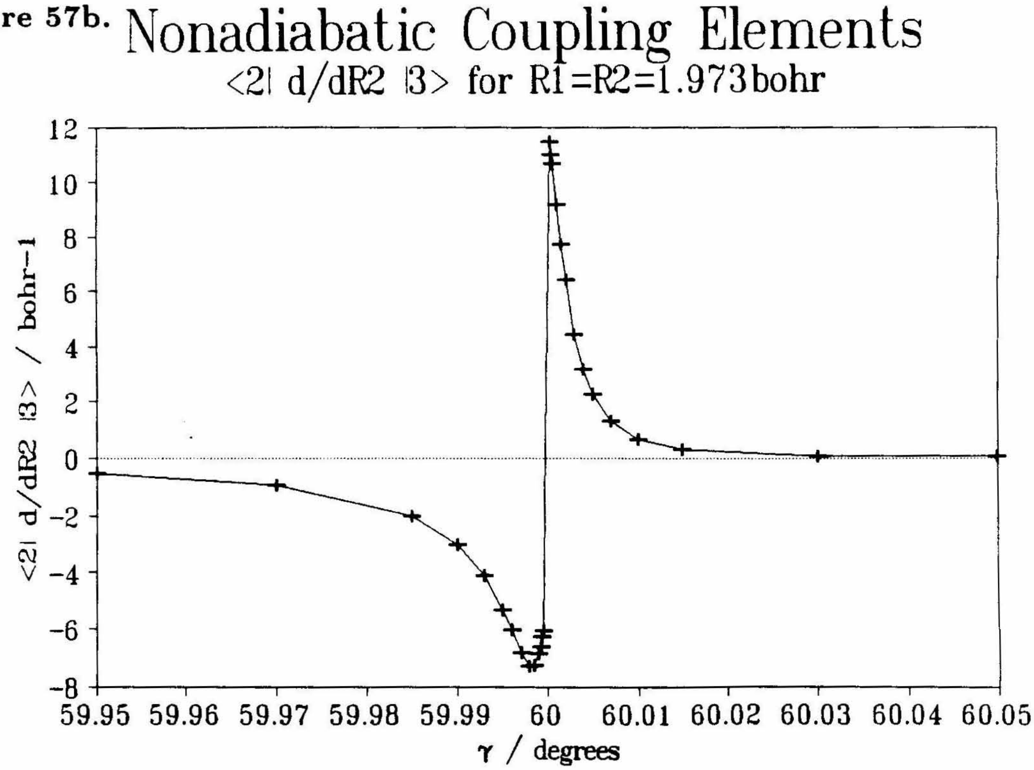

Figure 58a.

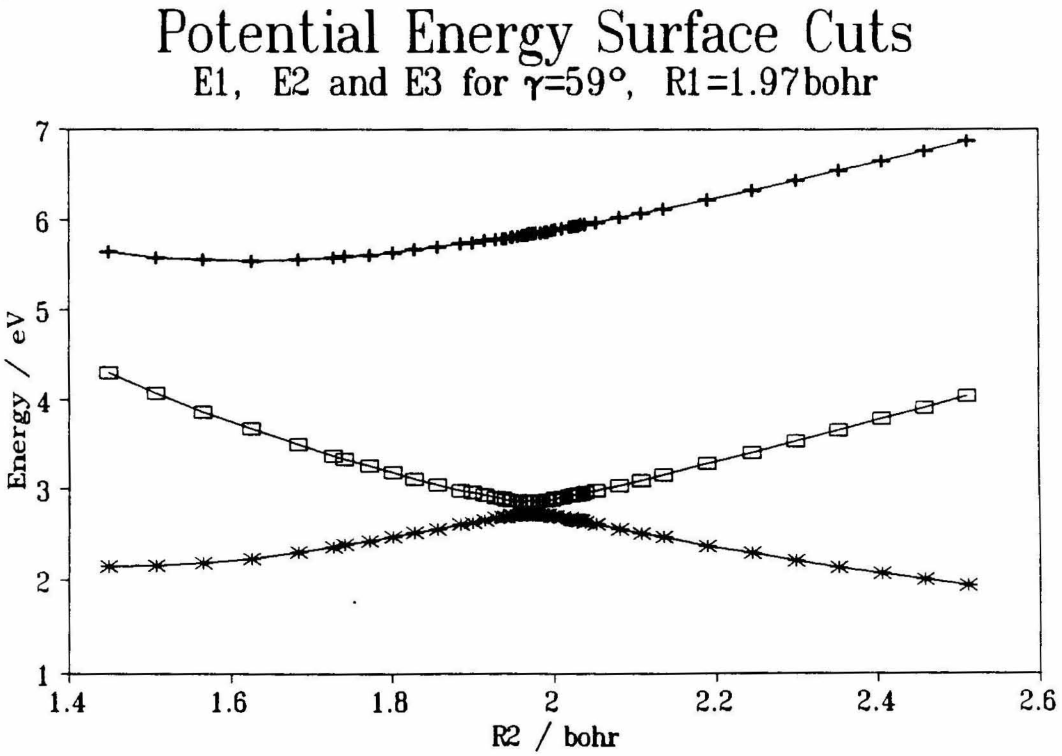

Figure 58b.

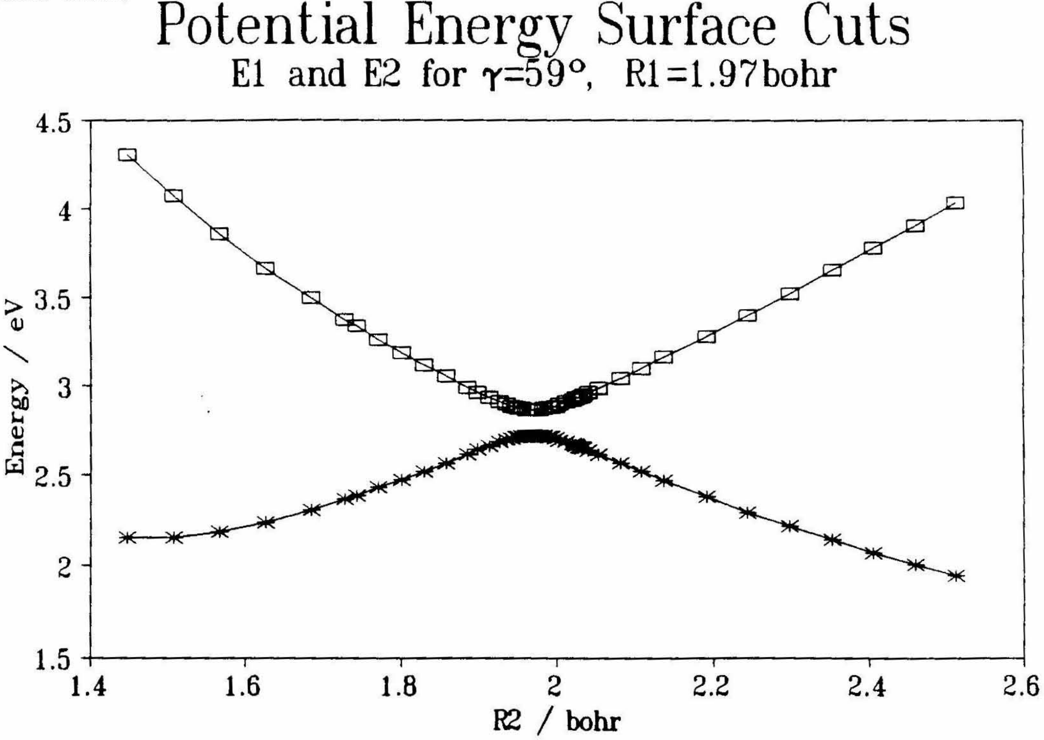

Figure 59.

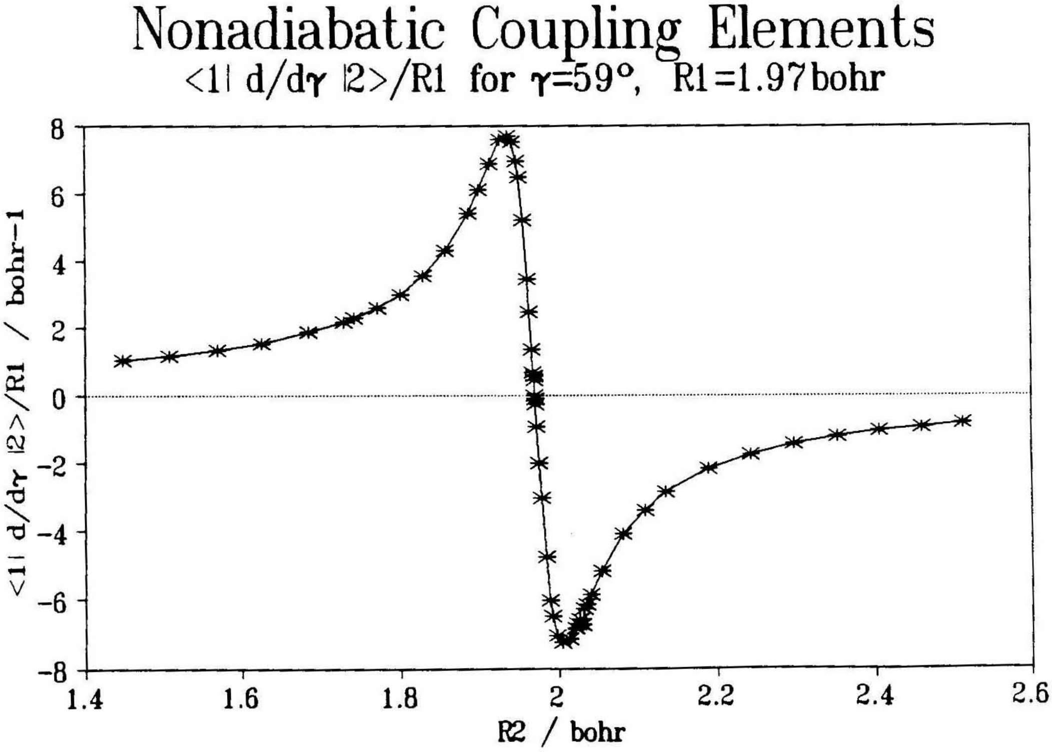

Figure 60.

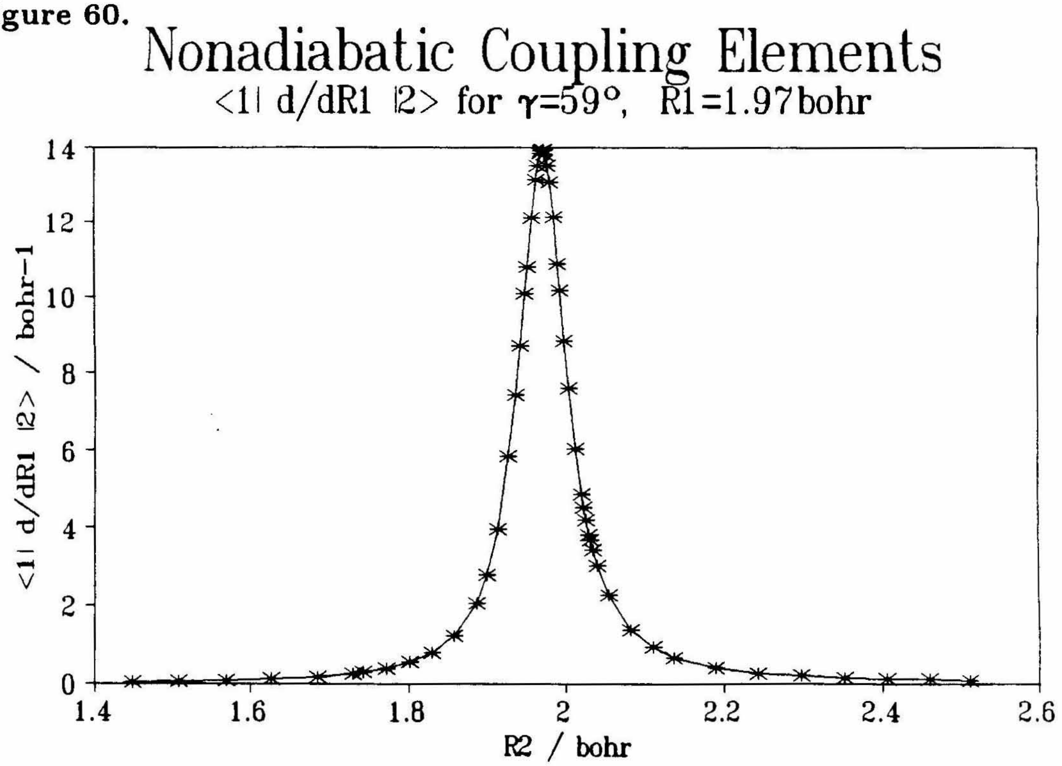

Figure 61.

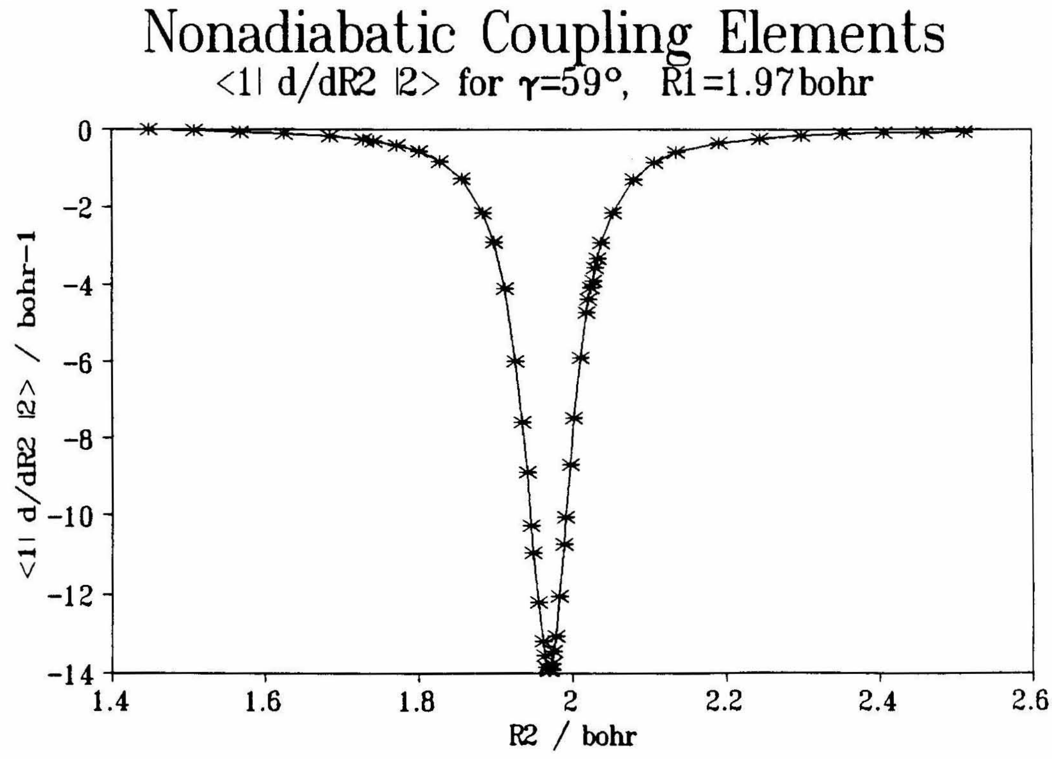

Figure 62.

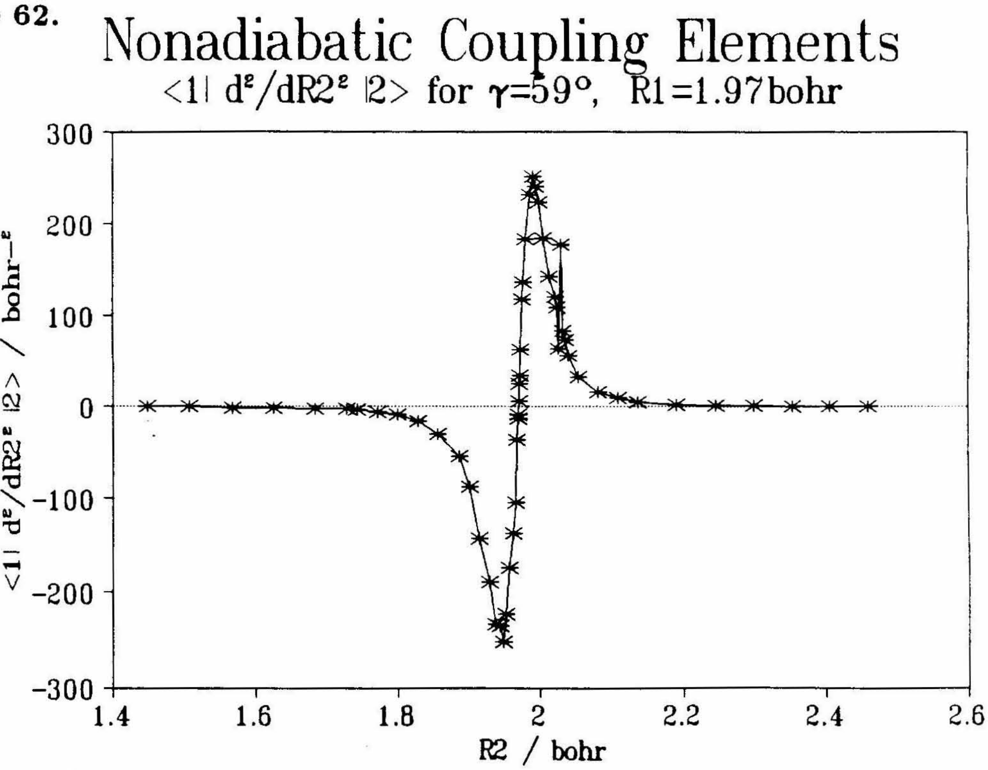

Figure 63.

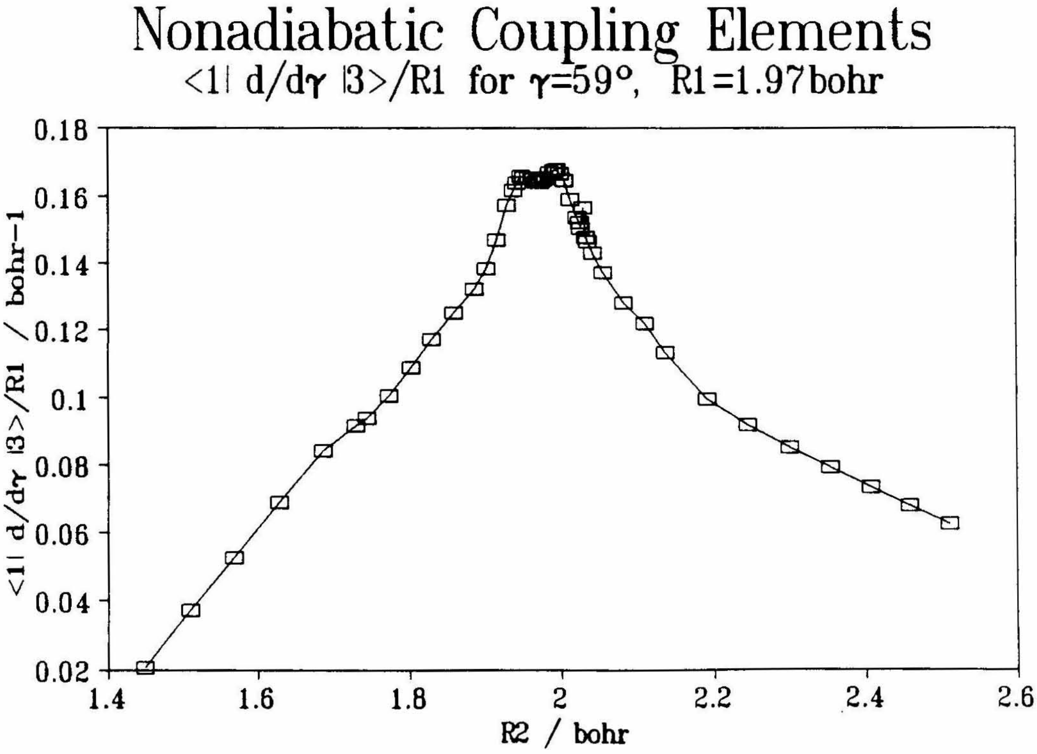

Figure 64.

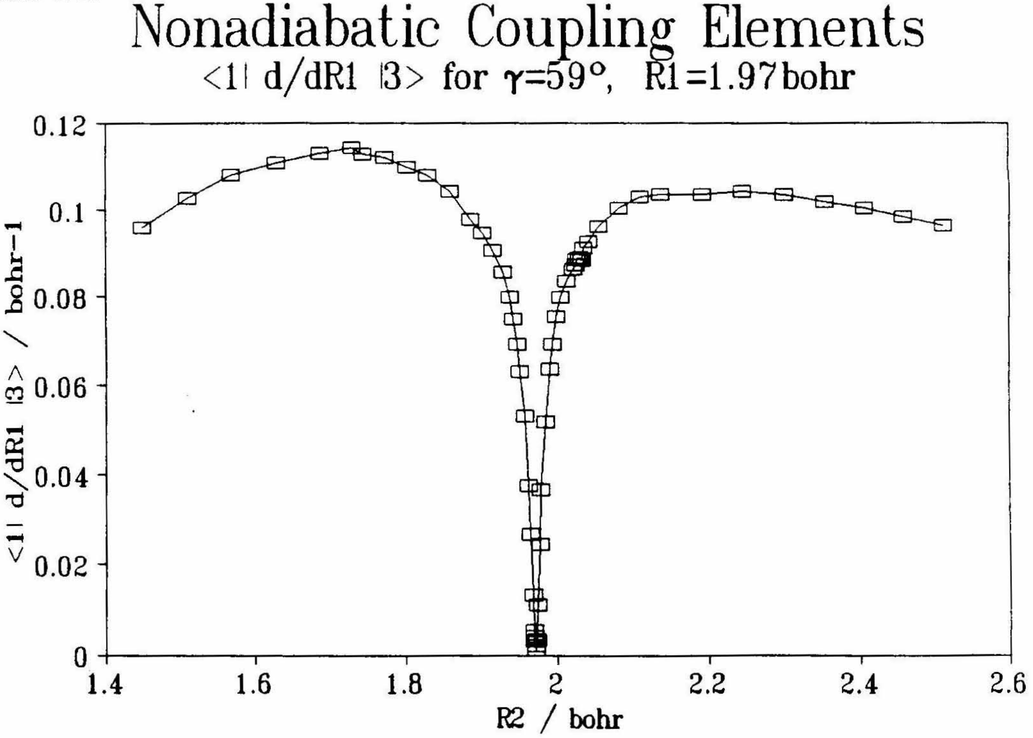

Figure 65.

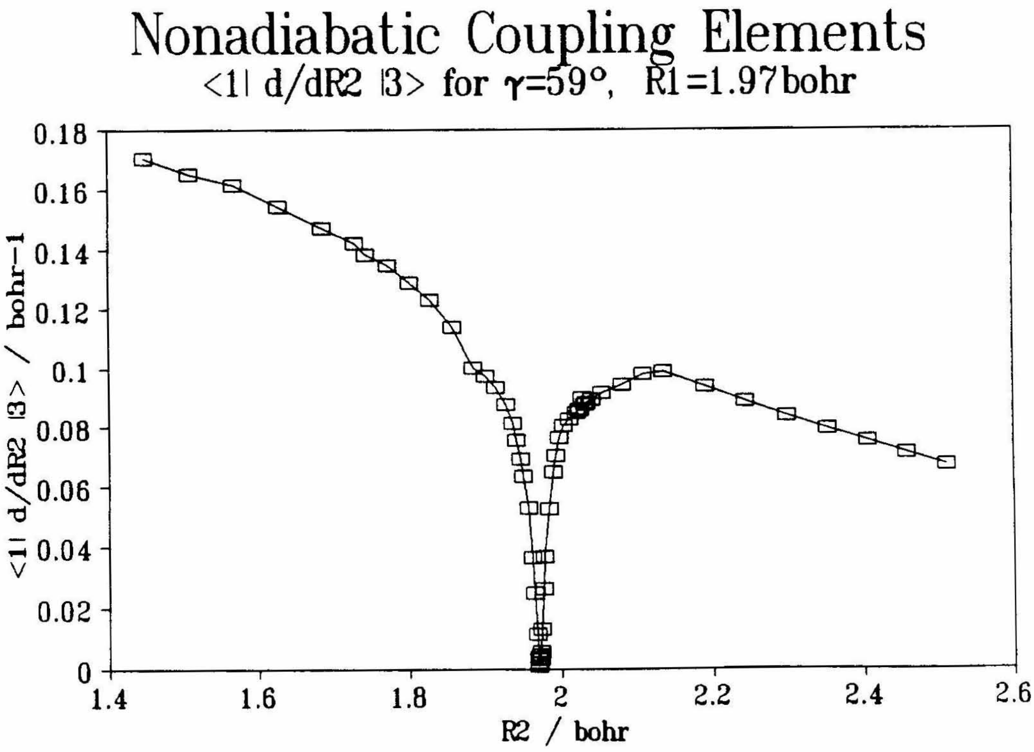

Figure 66.

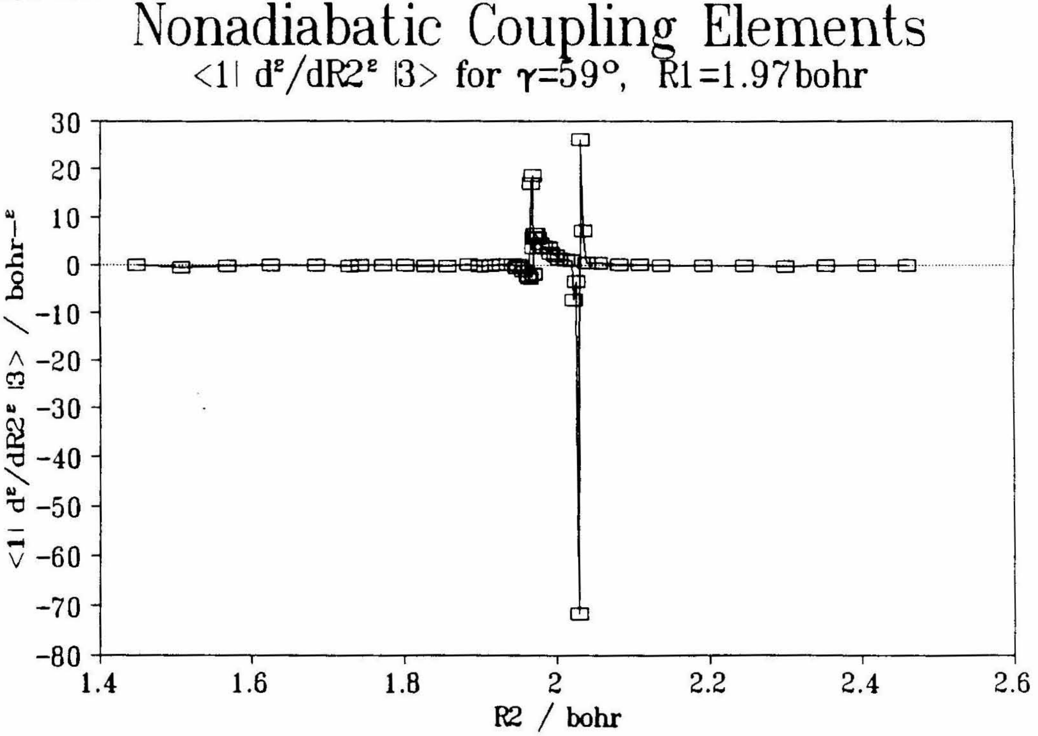

Figure 67.

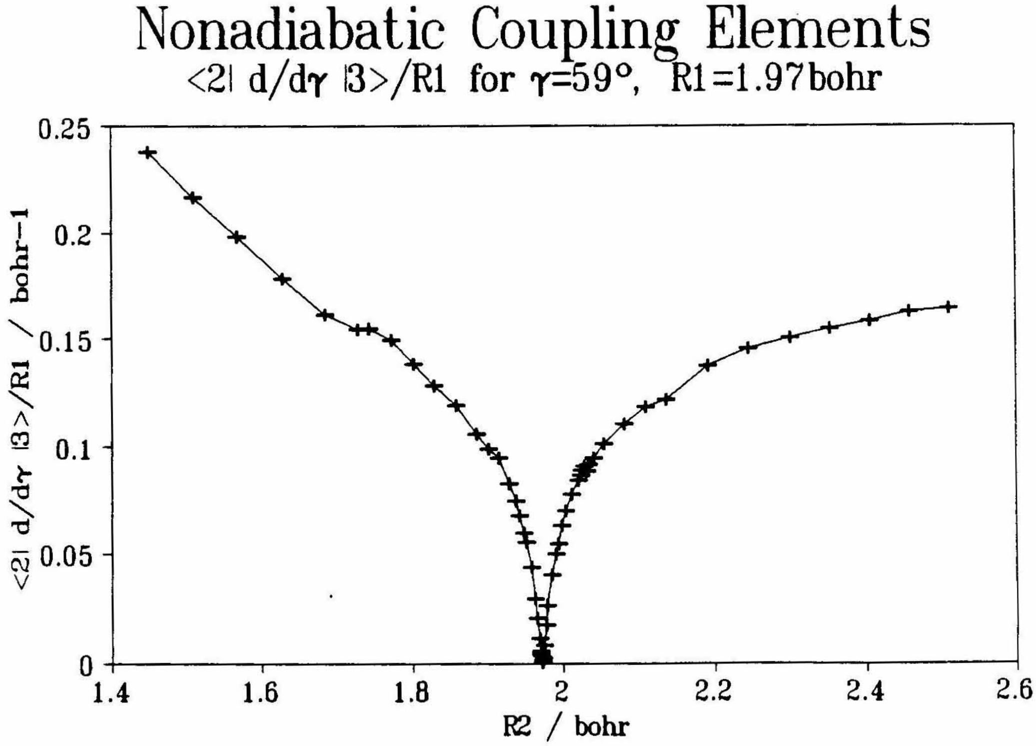

Figure 68.

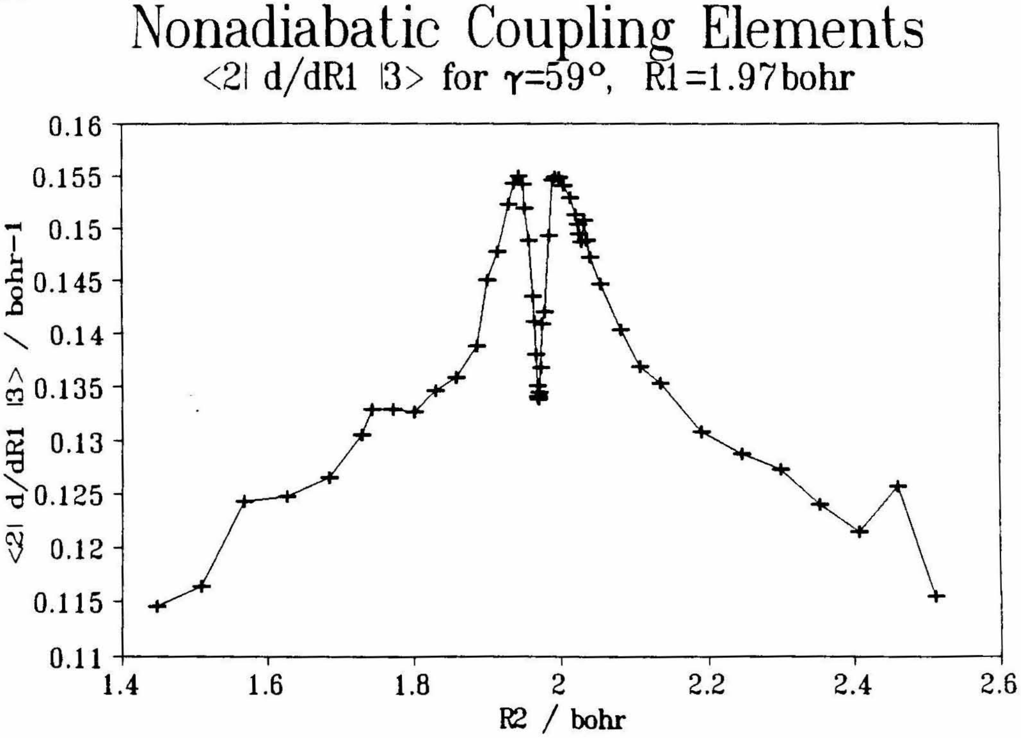

Figure 69.

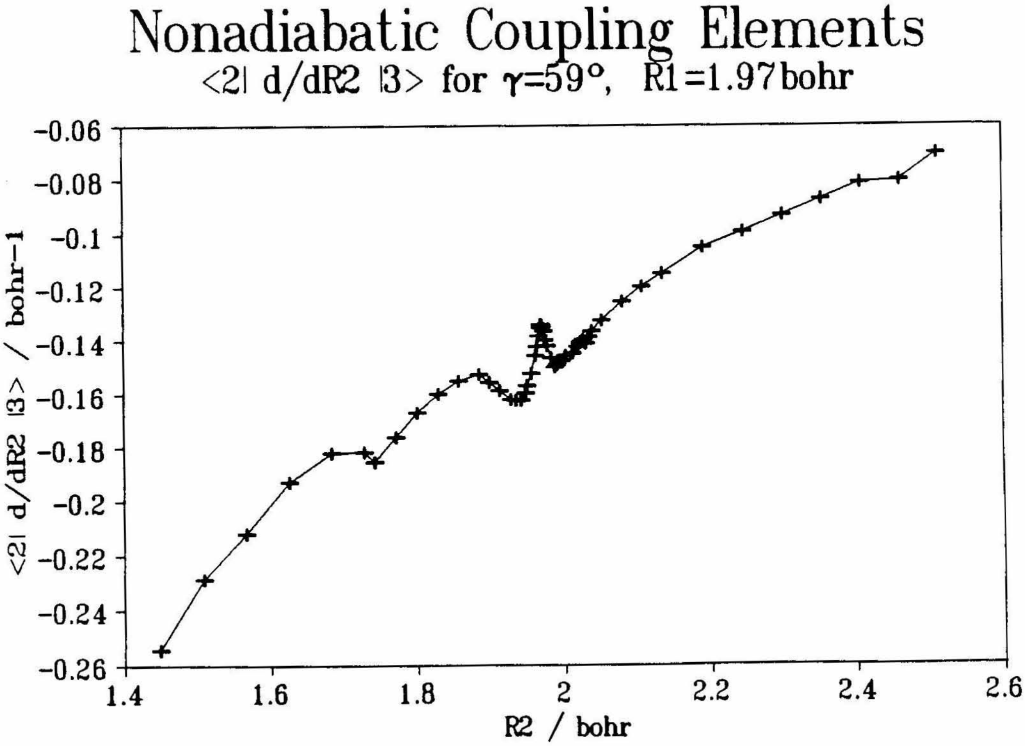

Figure 70.

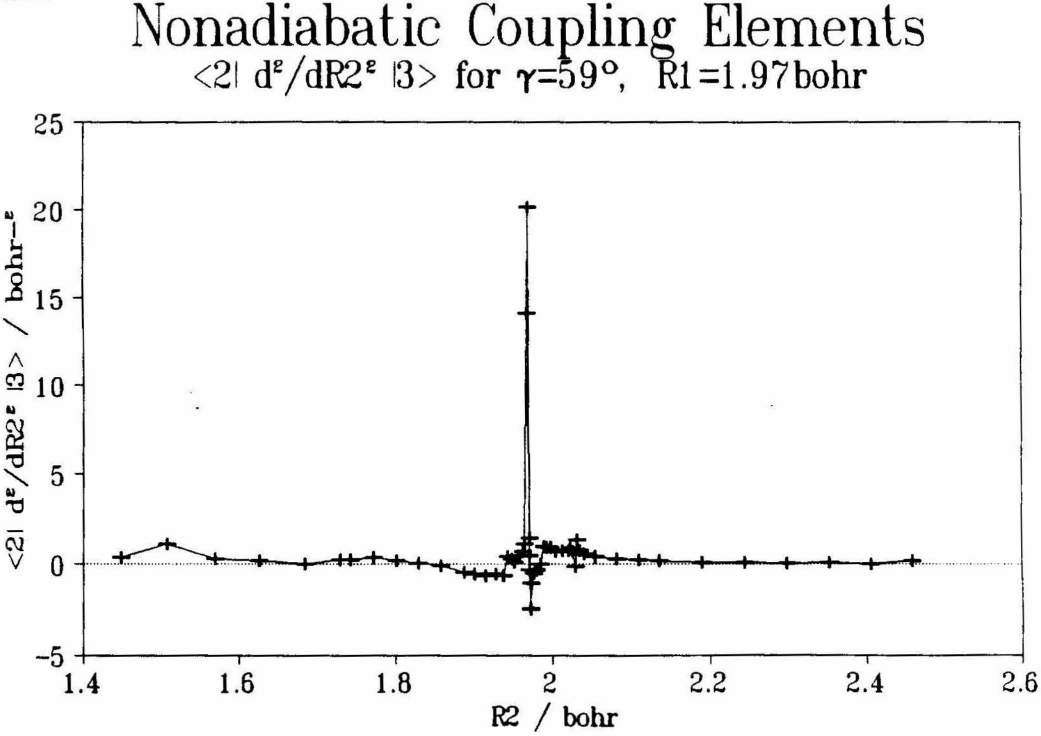

Figure 71a.

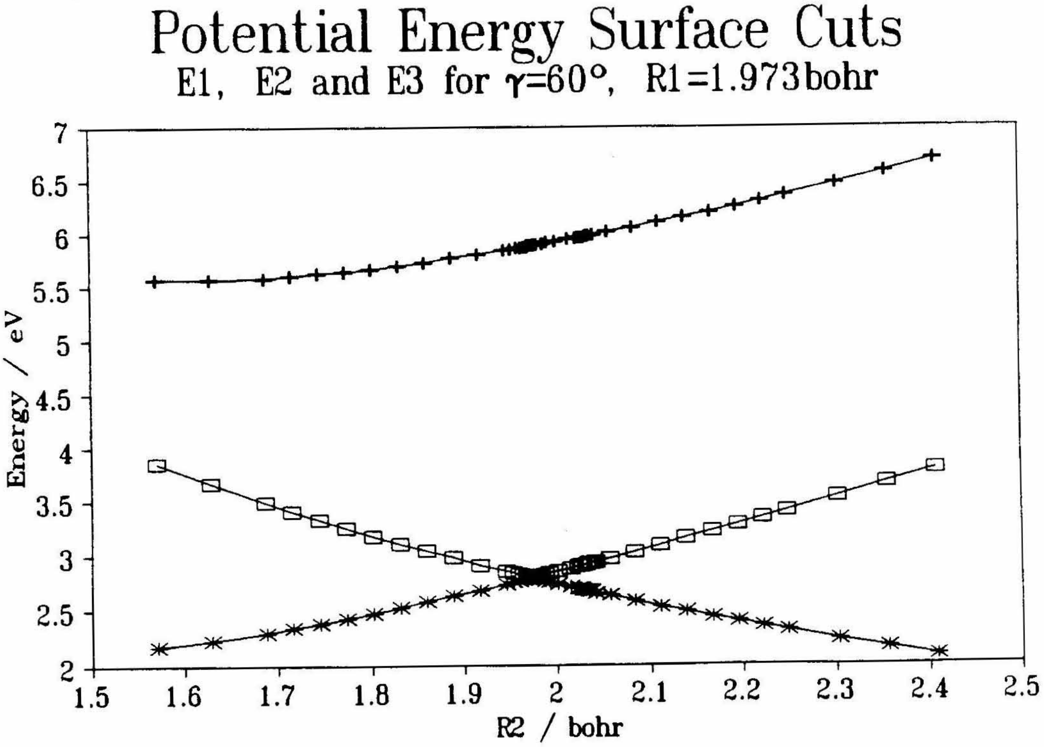

Figure 71b.

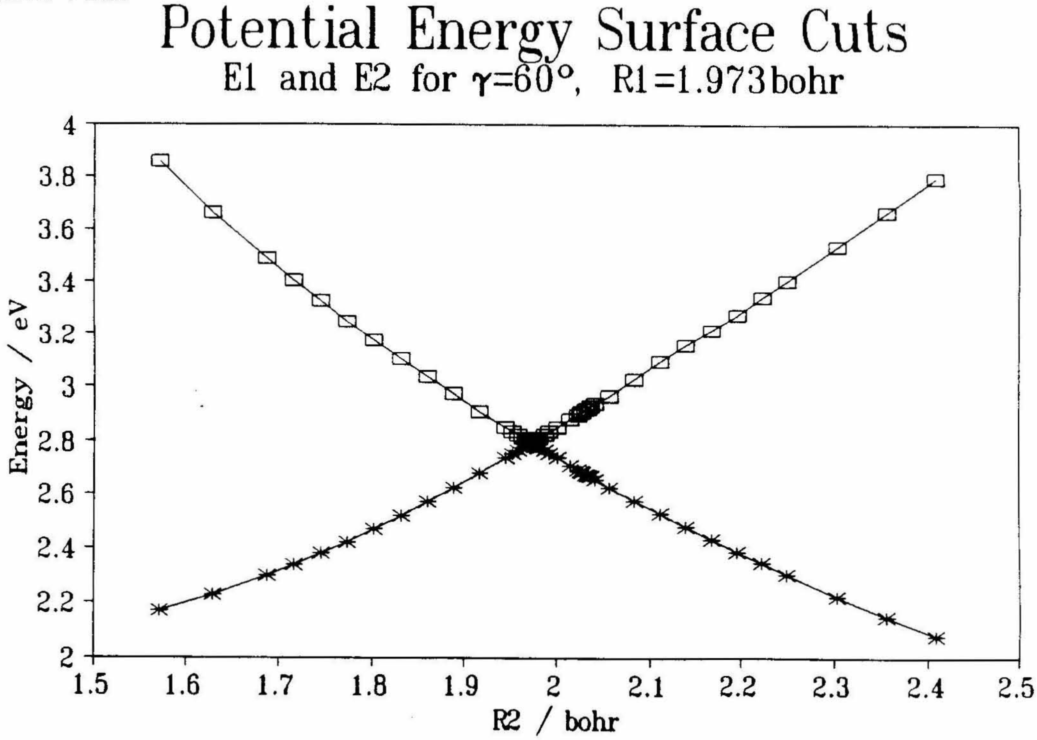

Potential Energy Surface Cuts

E1 and E2 for γ=60°, R1=1.973bohr

Figure 72a.

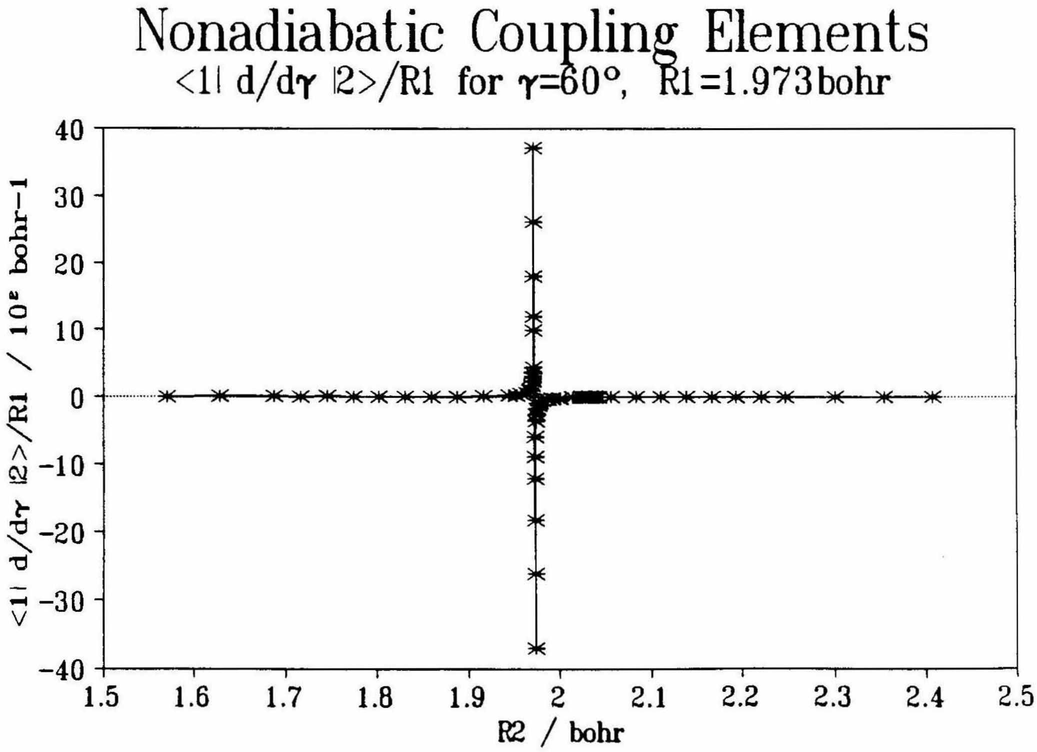

Nonadiabatic Coupling Elements

<1| d/dγ |2>/R1 for γ=60°, R1=1.973bohr

Figure 72b.

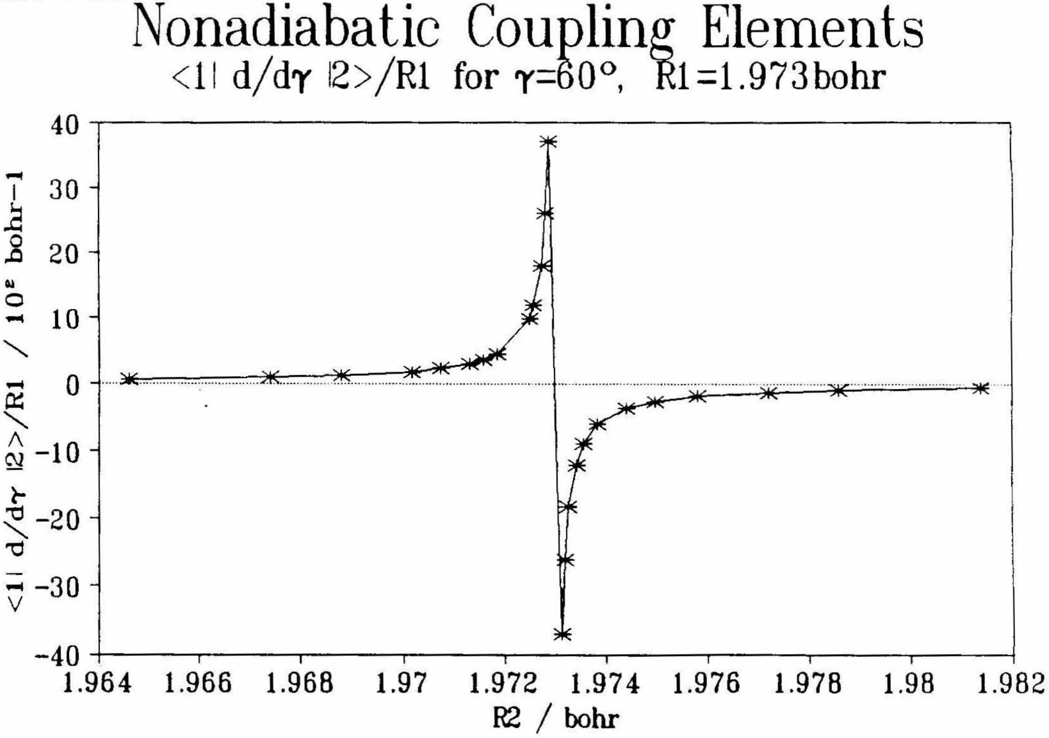

Figure 73a.

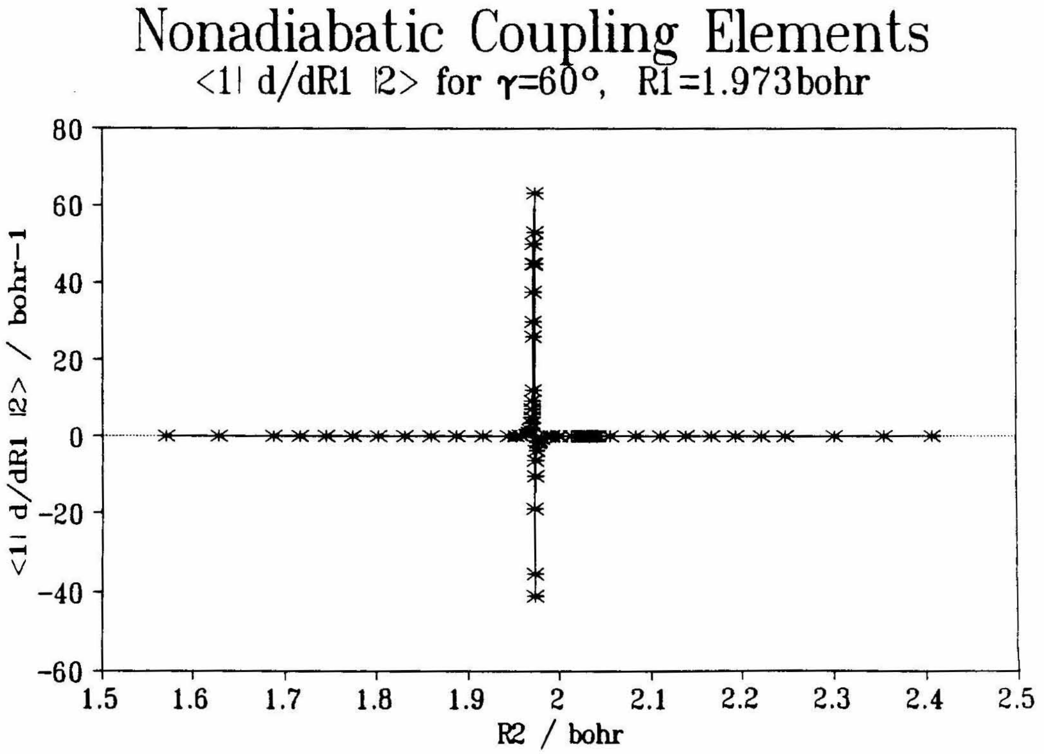

Figure 73b.

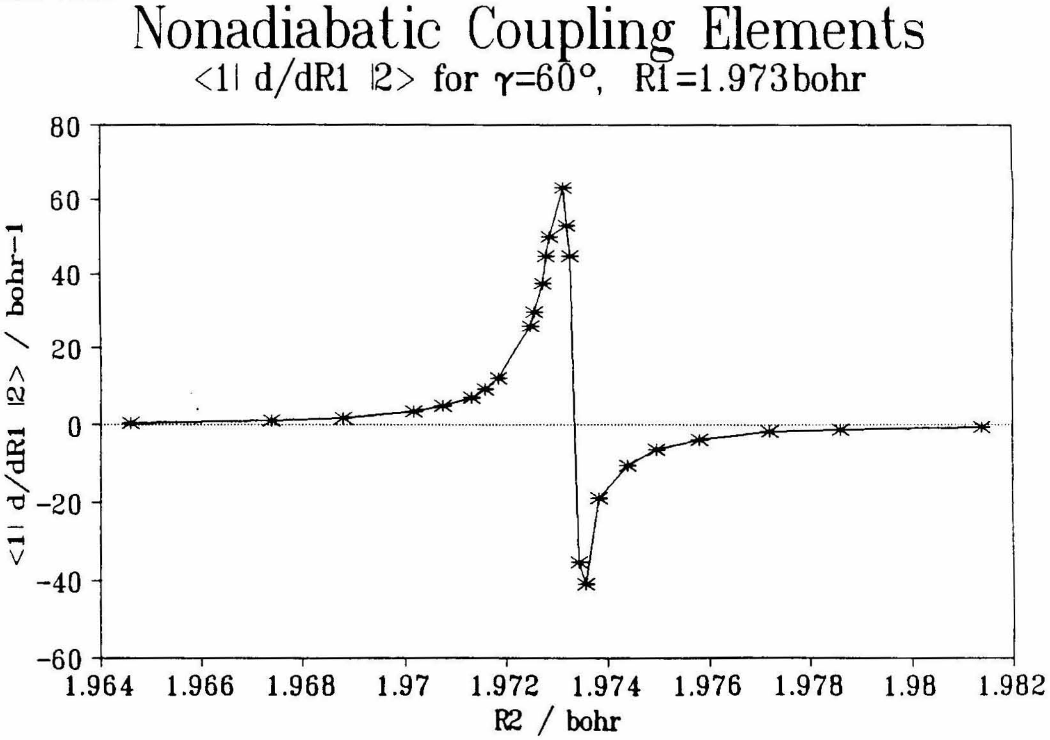

Figure 74a.

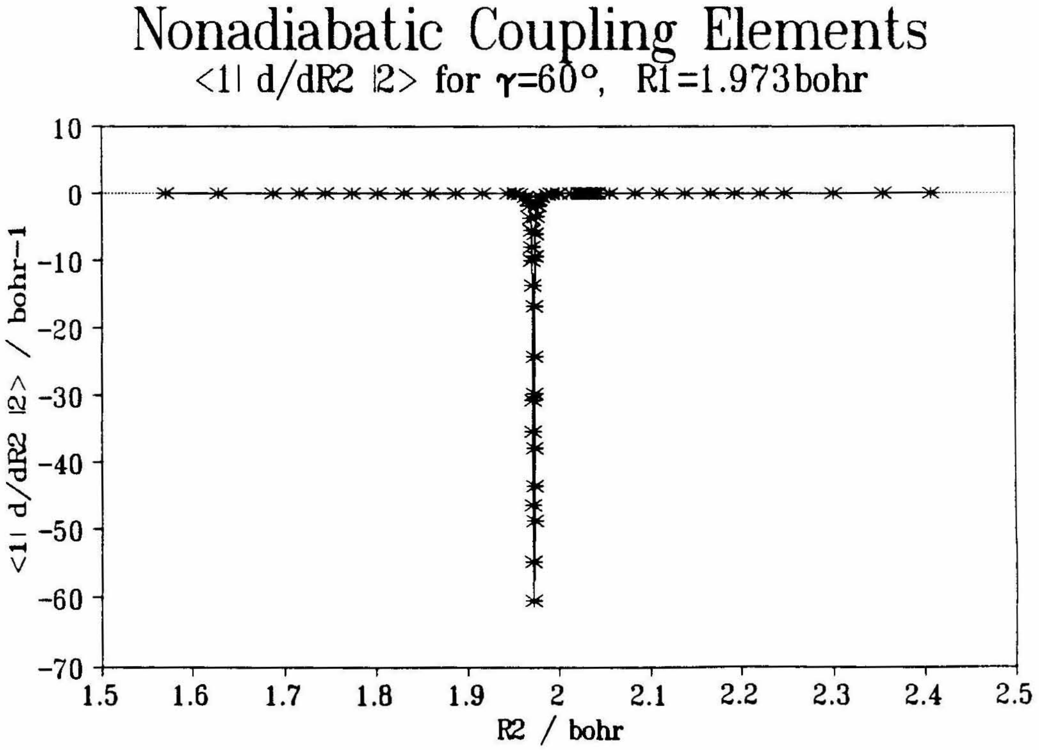

Figure 74b.

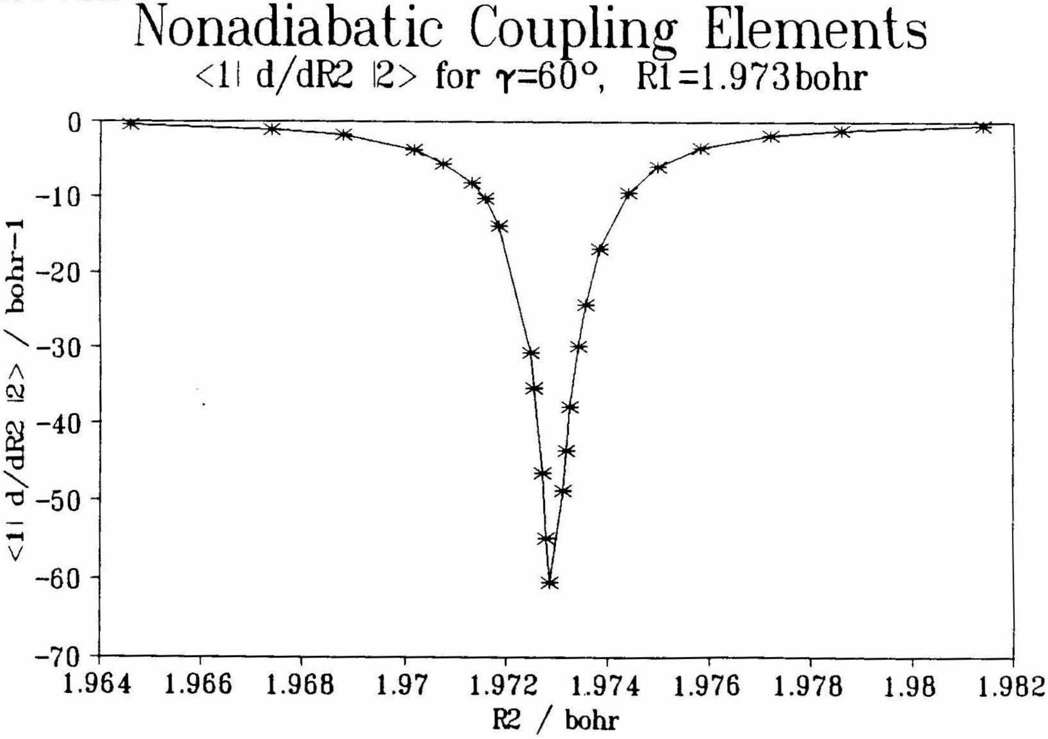

Figure 75a.

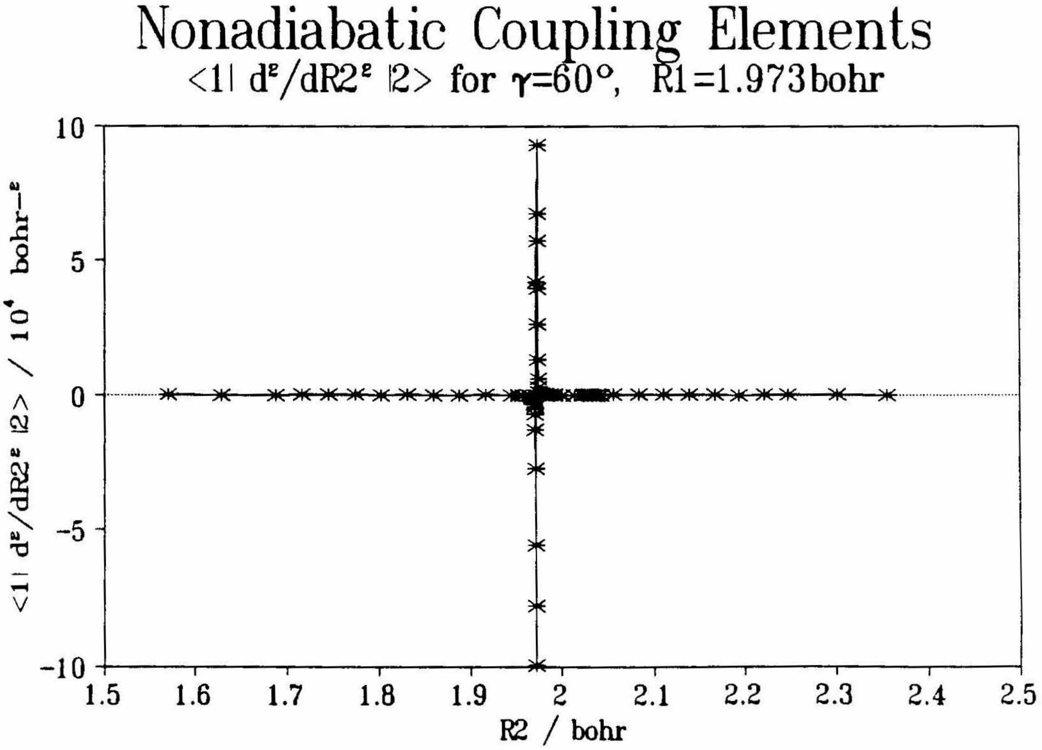

Figure 75b.

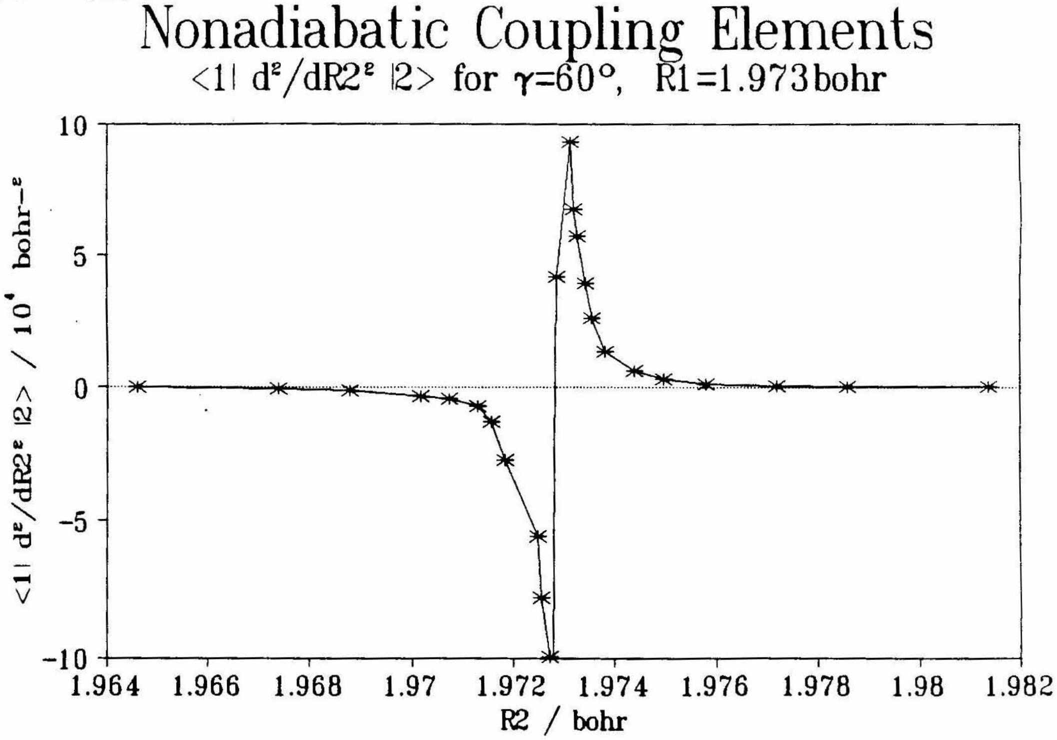

Figure 76a.

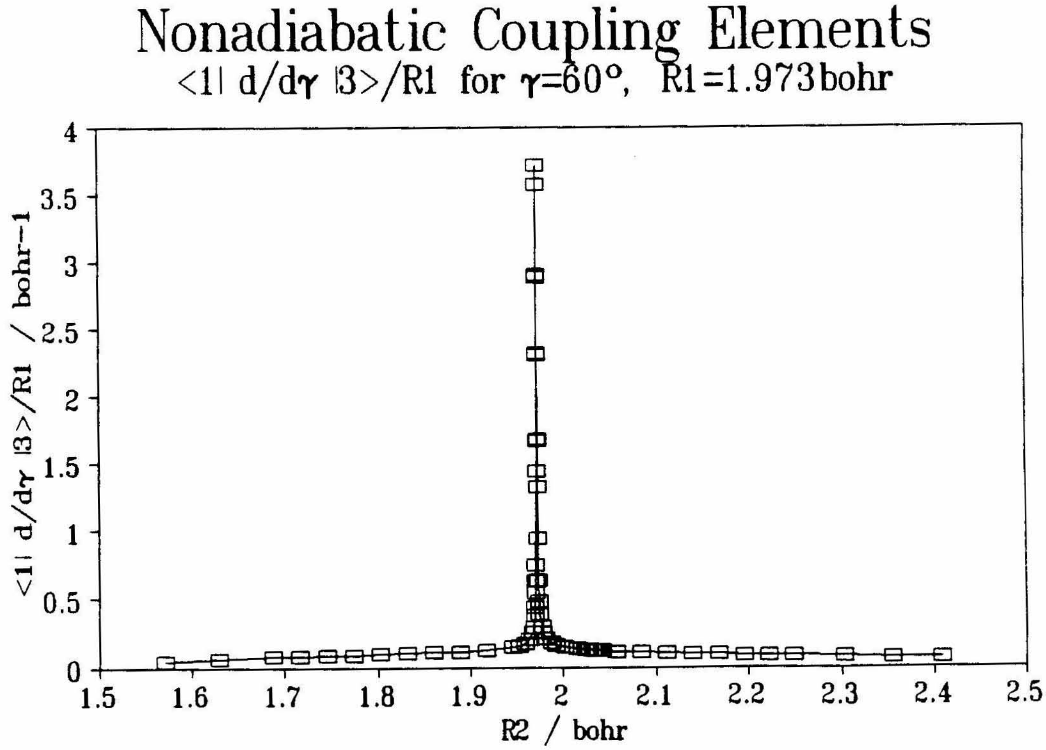

Figure 76b.

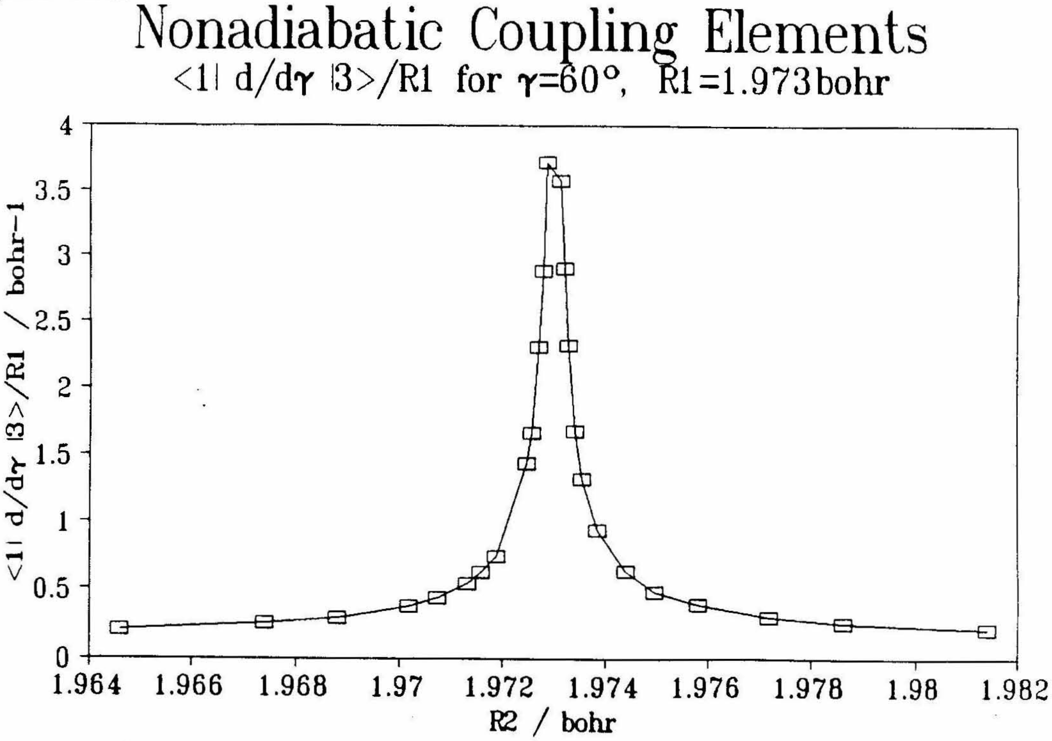

Figure 77a.

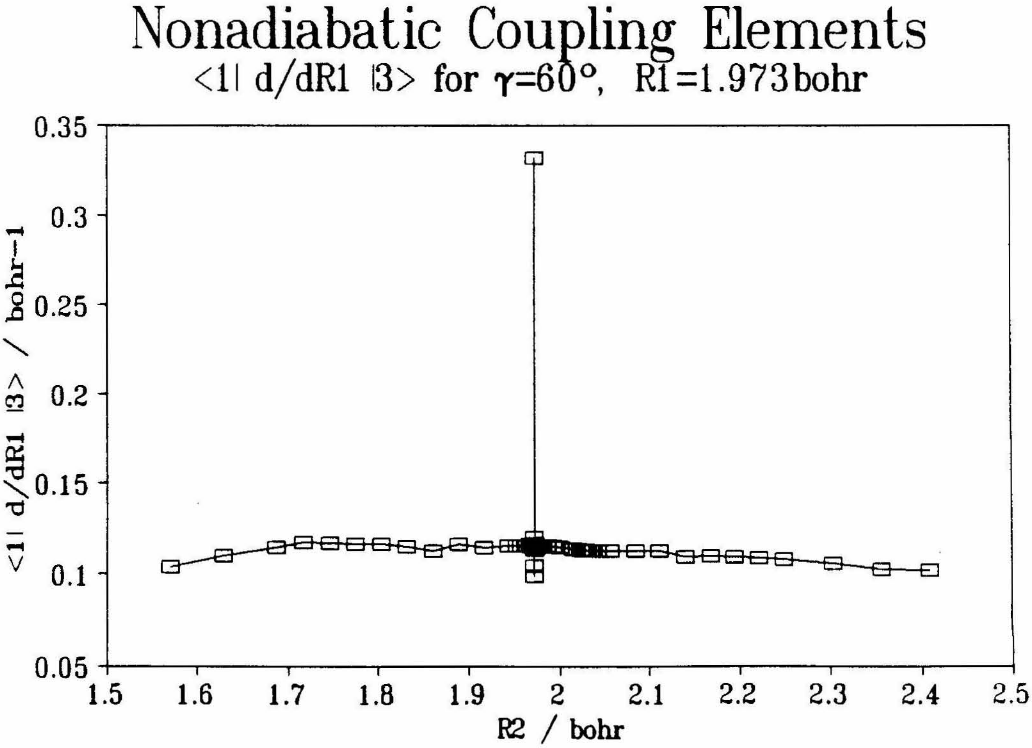

Figure 77b.

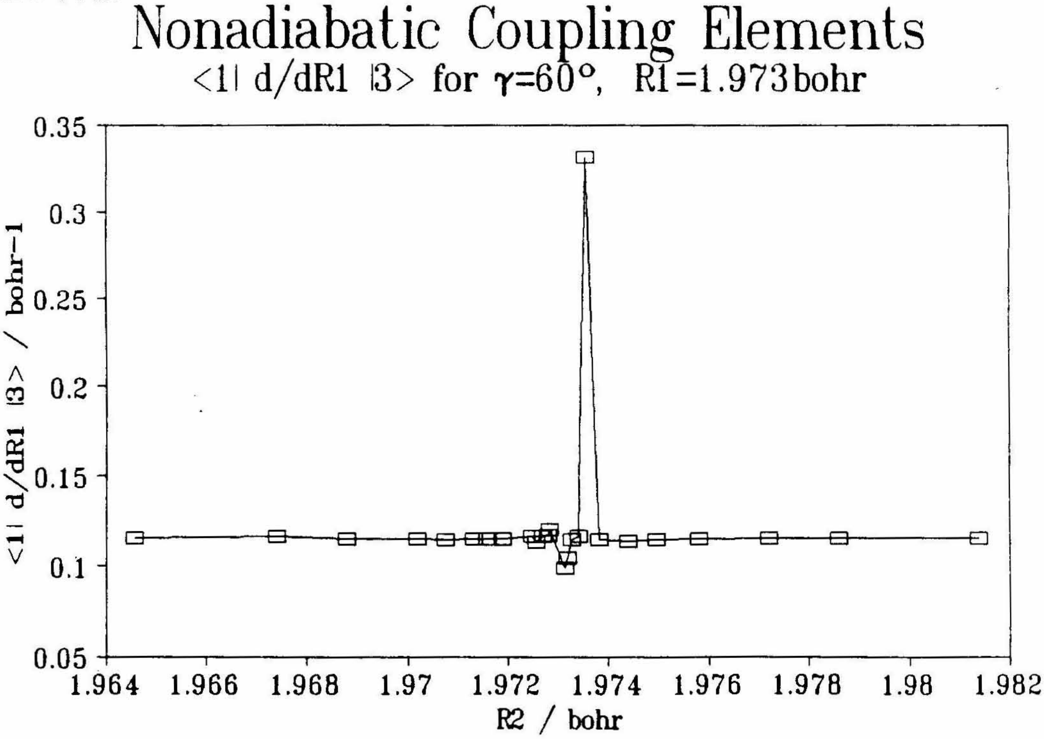

Figure 78a.

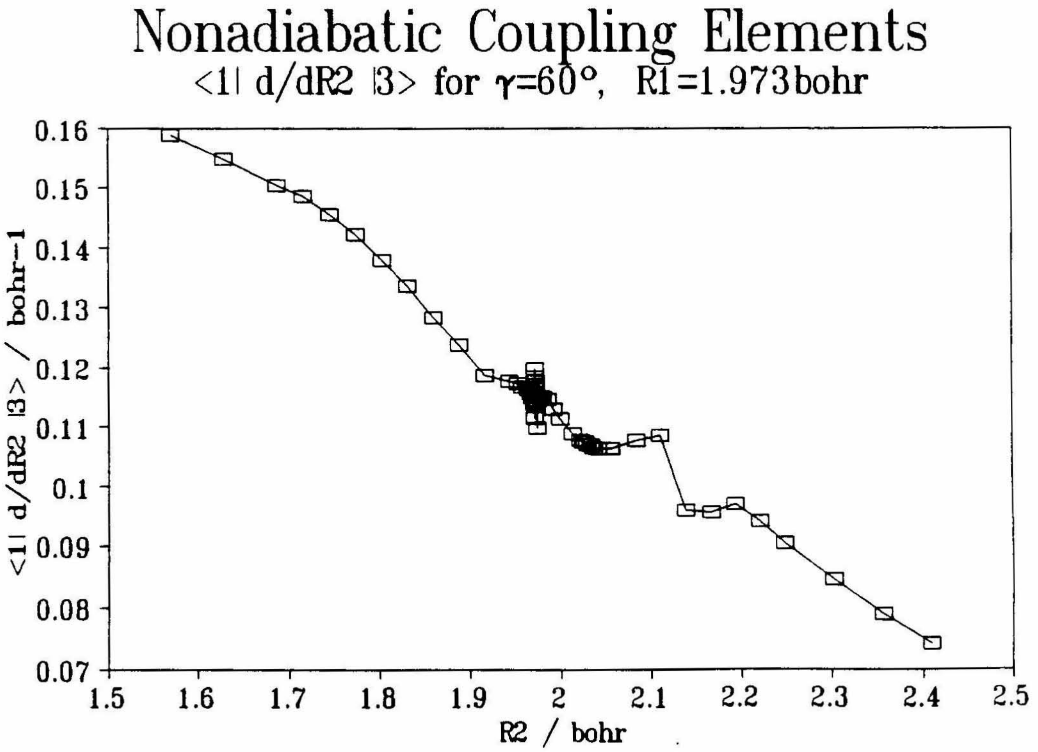

Figure 78b.

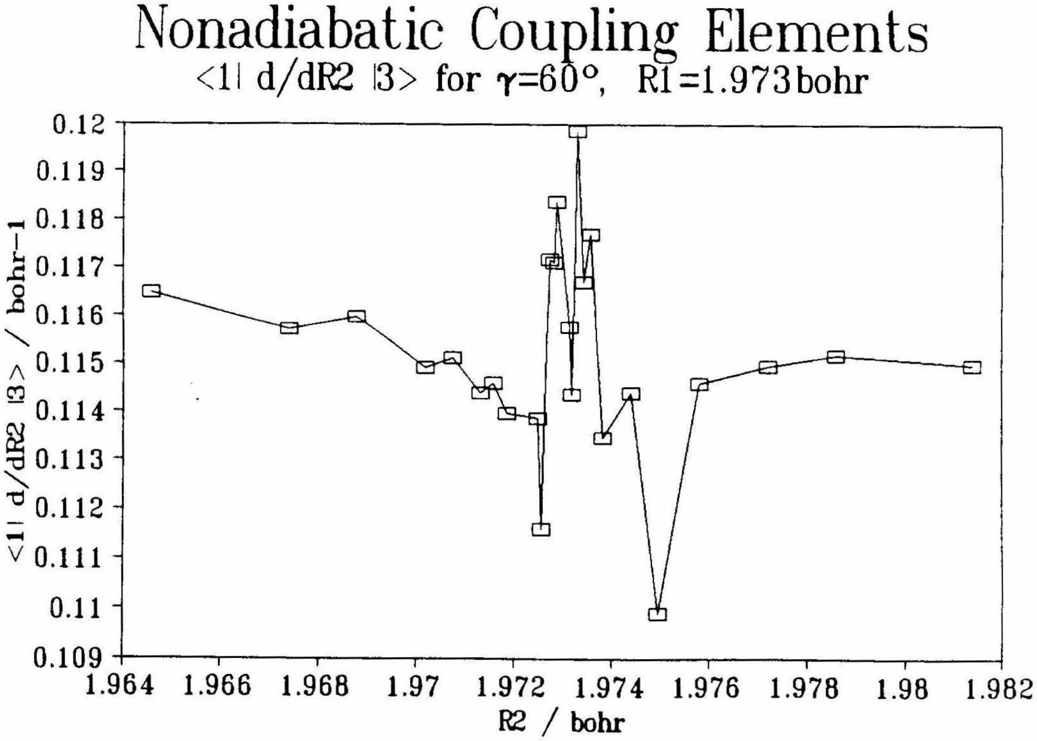

Figure 79a.

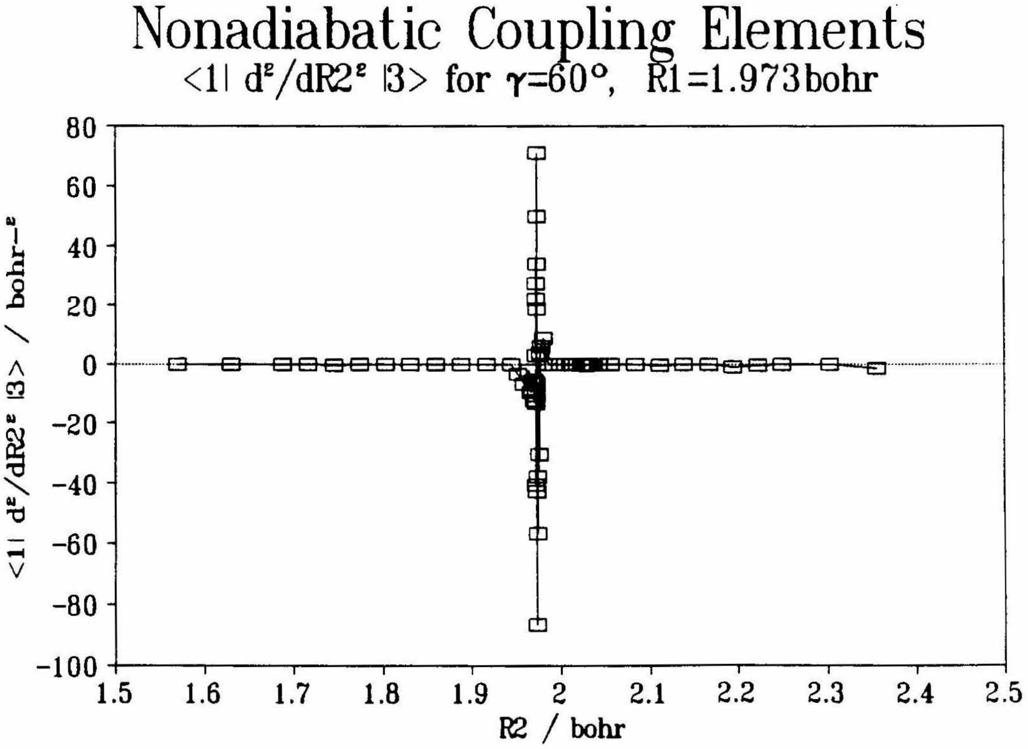

Figure 79b.

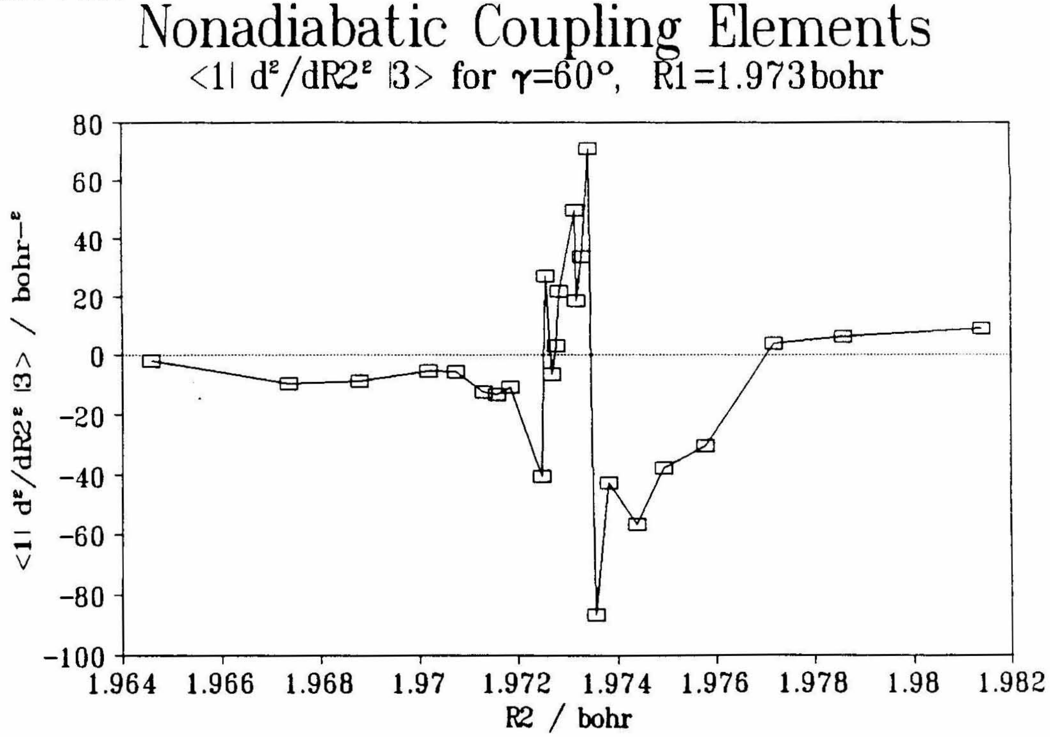

Figure 80a.

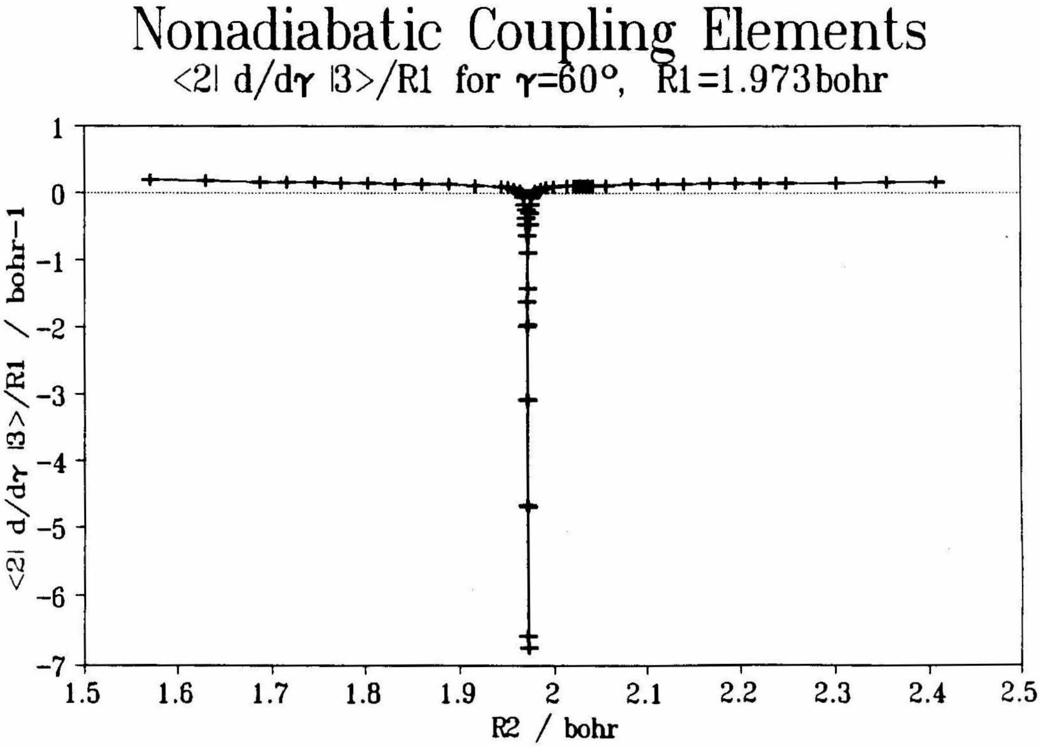

Figure 80b.

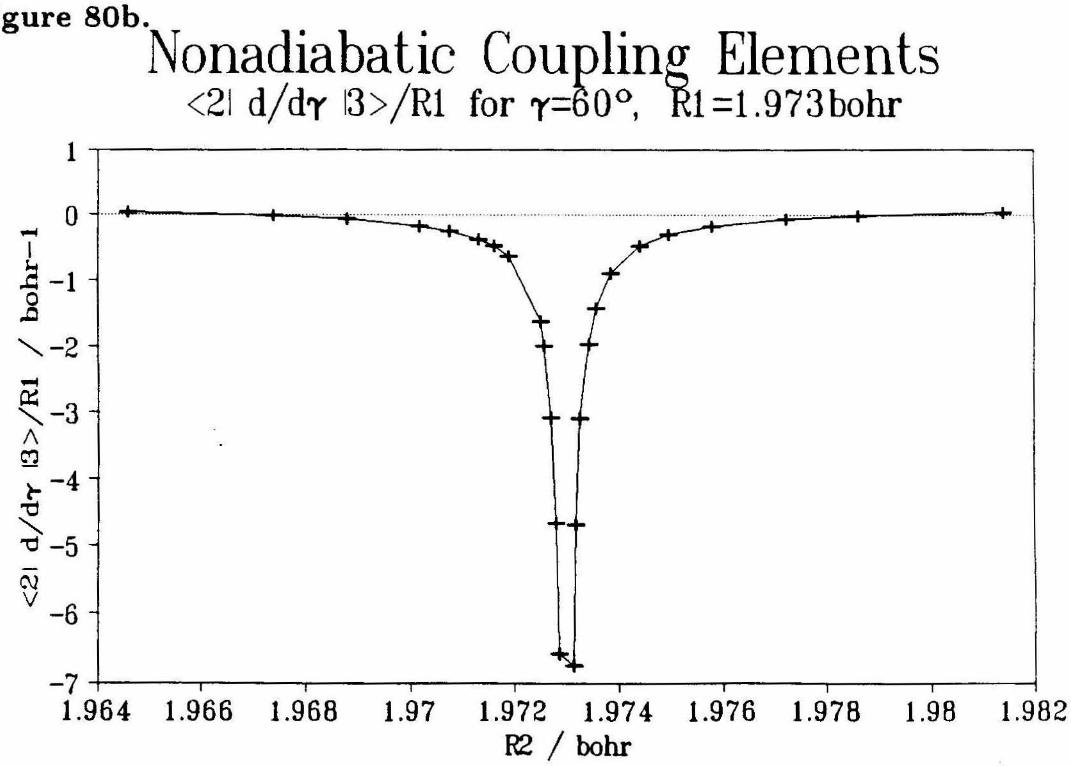

Figure 81a.

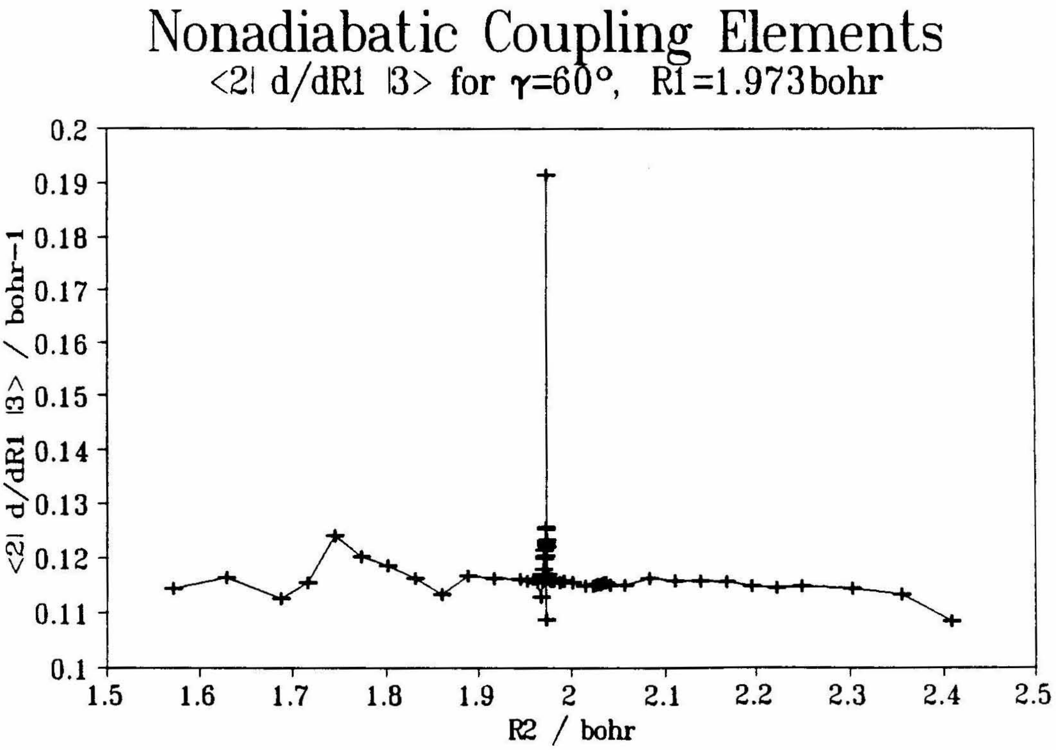

Figure 81b.

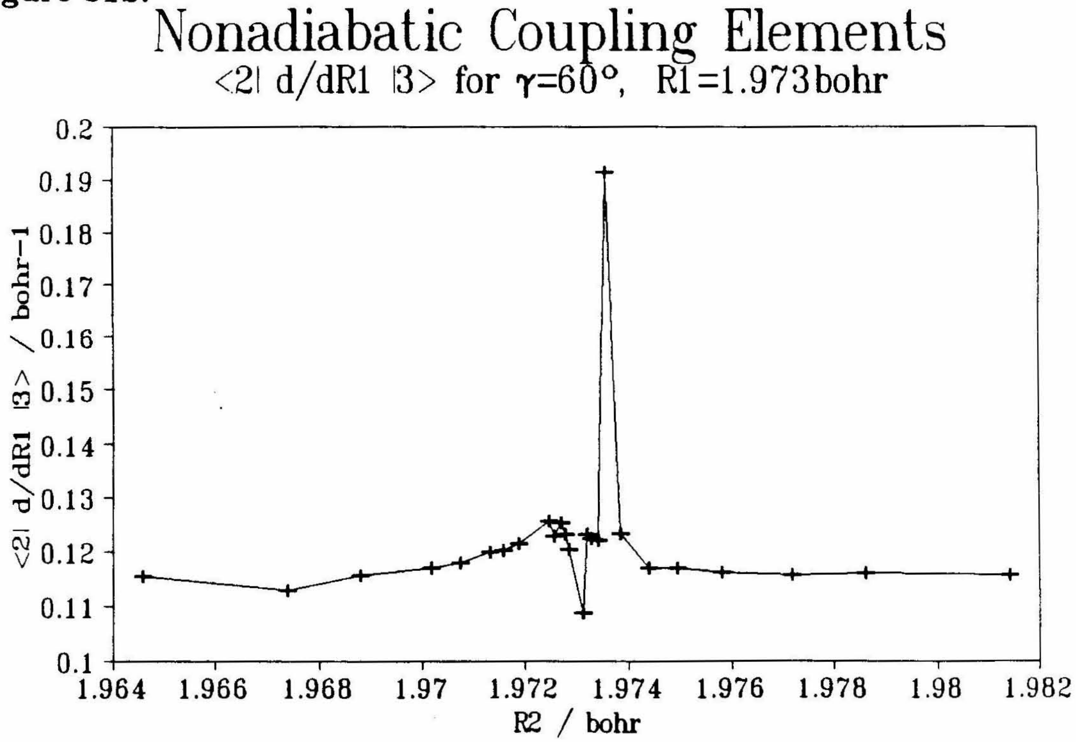

Figure 82a.

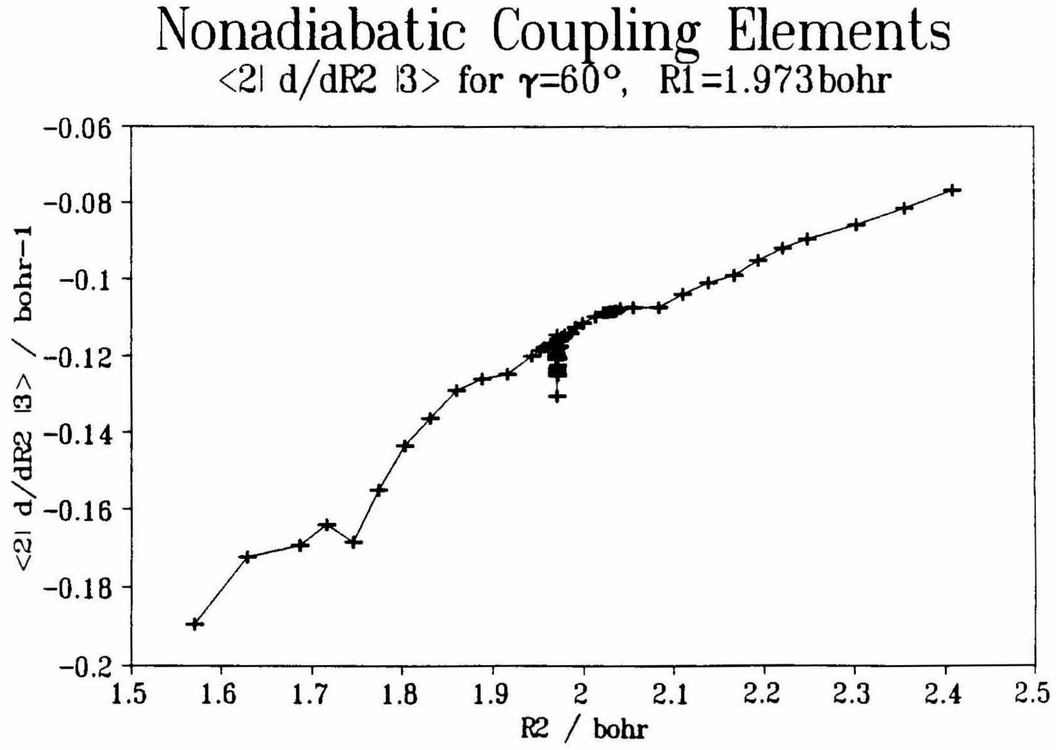

Figure 82b.

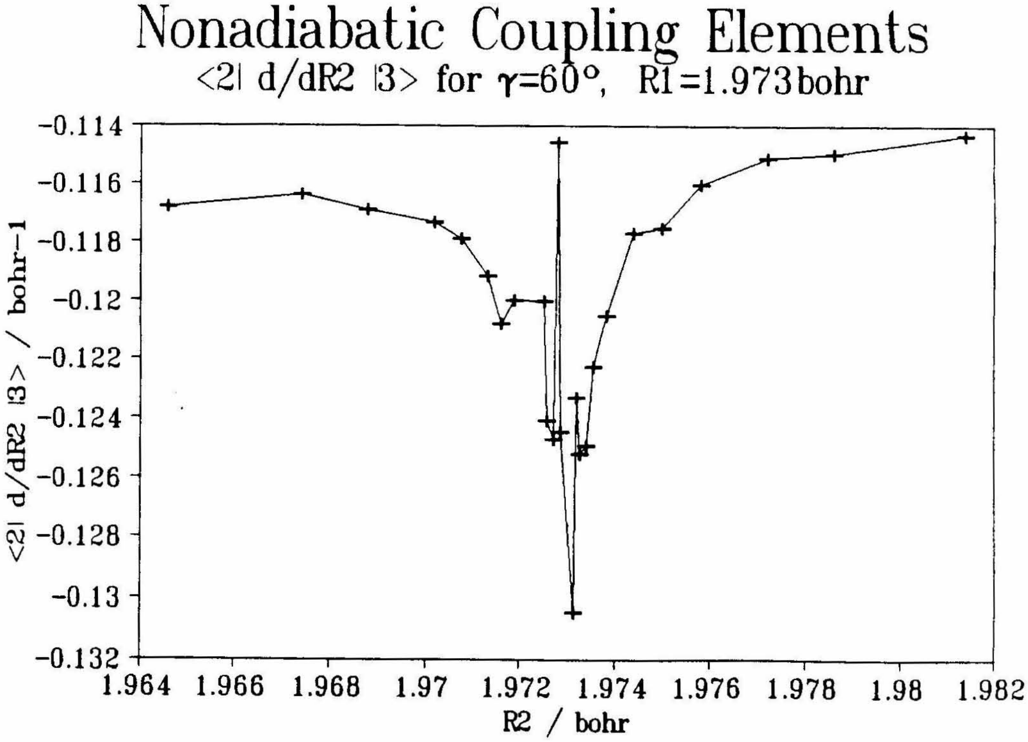

Figure 83a.

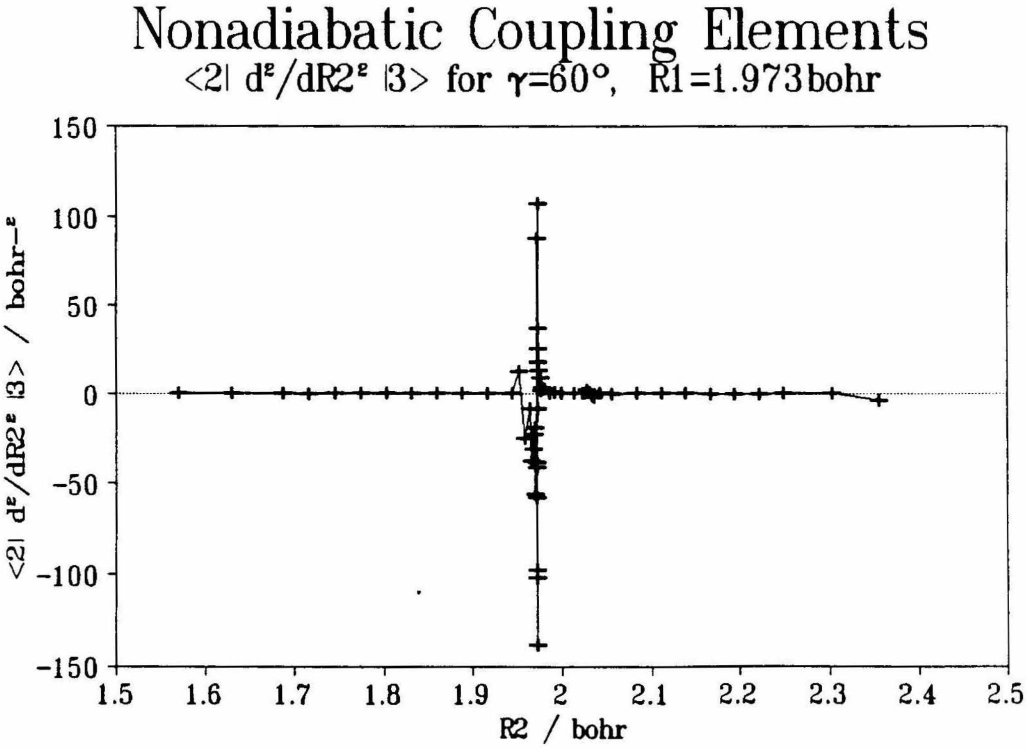

Figure 83b.

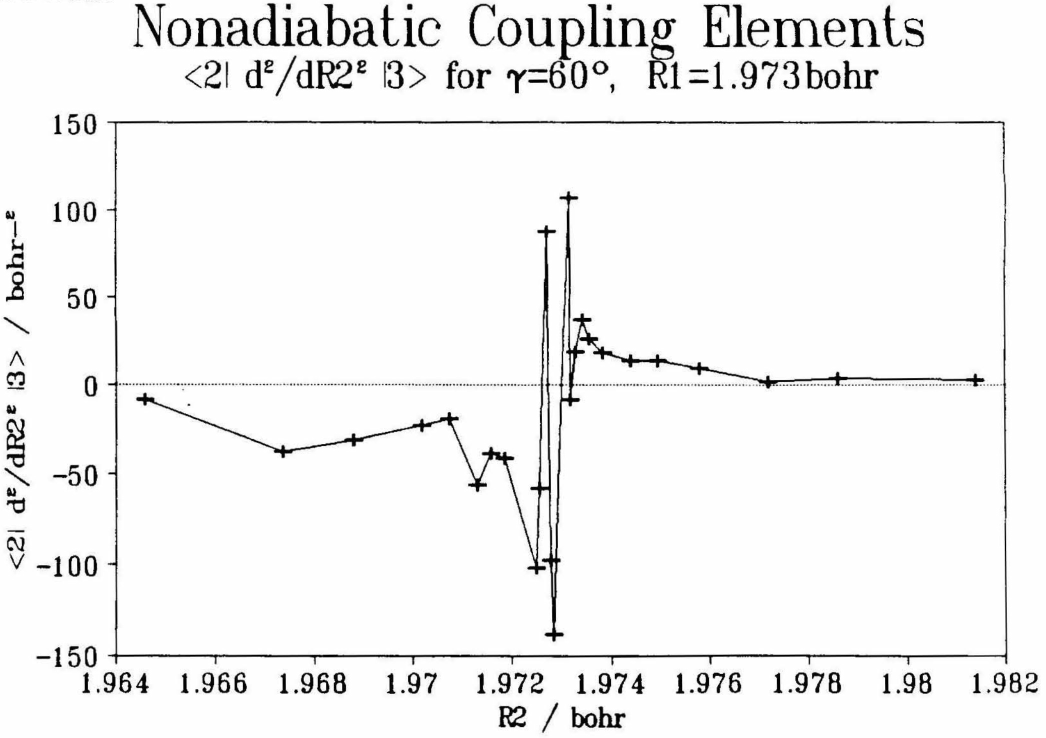
Nonadiabatic Coupling Elements
<2| d²/dR2² |3> for γ=60°, R1=1.973bohr
<2| d²/dR2² |3> / bohr⁻²
150
100
50
0
-50
-100
-150
1.964
1.966
1.968
1.97
1.972
1.974
1.976
1.978
1.98
1.982
R2 / bohr

Chapter 6.

Experimental

I. Apparatus

A. Vacuum System

The entire vacuum system is shown in Figures 1 and 2. The source chamber (VC1) is pumped by a Leybold-Heraeus single stage Roots pump model RUVAC WAU1000. It is a positive displacement vacuum pump with a volumetric displacement of 685 ft^3/min. Its normal operating range is 30 to 10^{-3} torr. However, it can be turned on with the roughing pump at atmospheric pressure for rapid pumpdown. This pump is roughed using a Leybold-Heraeus rotary piston pump model E250 with a volumetric displacement of 171 ft^3/min. It employs three pistons rotating on a common, dynamically balanced shaft. The E250 piston pump is equipped with a gas ballast valve, which permits limited amounts of air to enter the compression chamber and thus ensures the early opening of the exhaust valve. With no load applied to the system, an ultimate pressure of $< 10^{-3}$ torr is achievable. However, while the beam is operating the pressure in VC1 rises to about 5 millitorr. The pumps are mounted in a Leybold-Heraeus RV10000 frame with manual electricals.

The arc source chamber is rectangular in shape and built from stainless steel plates. The back wall of the source chamber equipped with a $9''$ ASA flange which is attached to the Roots pump via $4\frac{1}{2}'$ of $5''$ flexible bellows tubing equipped with an O-ring seal. The chamber is equipped with a $26''$ by $20.5''$ rectangular flange which is used to service the source, and two $6''$ conflat flanges (P1 and P2) each of which is fitted with a quartz window and are used to view the source during operation. Electrical power (for the arc, magnet and translation-rotation assembly), cooling water and gas into the source, and temperature and pressure measurement are provided by seven $2\frac{3}{4}''$ conflat feedthroughs located at the top and back of the source chamber. The front of the source chamber is equipped with a 6″ diameter exit port with a Varian conflat flange. Inside of the source chamber, the aluminum water-cooled skimmer base (S) is mounted to the front via an O-ring seal. A three stage skimmer system is used. It is mounted so that the nozzle of the source and skimmer are in alignment with the center of the 6″ exit port. Pins have been used to insure alignment reproducibility. An interlock-control system is used to protect the system from damage or misuse. It is designed to shut off the arc power or any of the pumps if failures occur in the system.

The source chamber is mated with the differential stage chamber (VC2) through the exit port via 6.25″ of 6″ flexible bellows tubing and a 6″ Varian electropneumatic swing gate valve. The differential stage chamber is pumped by a Leybold-Heraeus TMP360 Turbovac turbomolecular pump. This turbopump is equipped with a model NT360 frequency converter. Its required fore-vacuum pressure is 7.5×10^{-3} to 7.5×10^{-4} torr and has a volumetric displacement of 390 l/sec. It is capable of achieving an ultimate pressure of $< 7.5 \times 10^{-10}$ torr. However, in our system we have only been able to achieve a vacuum of 4.1×10^{-8} torr with no load upon the system. The turbomolecular pump is backed by a Sargeant Welch Duo Seal mechanical vacuum pump model 1402. Its pumping speed is 400 l/min and is capable of an ultimate pressure of 1.0×10^{-4} torr.

Originally, the present differential stage chamber was not used. Instead a larger chamber was used. The original vacuum system is shown in Figures 3 and 4. It was designed to house a Stern-Gerlach magnetic velocity selector to provide a means to perform translational energy selected experiments. This chamber was pumped by a mercury diffusion pump that was trapped by a freon baffle and a liquid nitrogen trap. The pump may be isolated via a 6″ gate valve. The pumping speed of the overall system is 125 l/sec and is capable of giving an ultimate vacuum of $< 1 \times 10^{-7}$ torr. The differential stage chamber is attached to the mercury diffusion pump via a 6″ conflat flange located on one side of the chamber which is mated to a U-shaped flexible stainless steel line composed of a 90° elbow welded to 3′ of 5″ flexible bellows that is in turn mated to the 6″ gate valve via a 9″ flange with an o-ring seal. The differential stage chamber is also rectangular in shape and built from stainless steel plates. It is equipped with a 19.375″ by 19.875″ flange which is used to service the Stern-Gerlach magnetic velocity selector that it houses. Electrical power, cooling water, a viewport, and gas for the magnetic velocity selector are provided by ten $2\frac{3}{4}''$ conflat flanges mounted on the sides of the chamber. With this design we were unable to achieve a low enough vacuum during operation of the source to perform the desired experiments. To combat these difficulties, the mercury diffusion pump was replaced by the turbomolecular pump described above. Although this improved the vacuum obtainable during source operation, the improvement was not enough to allow the planned experiments to be performed. Unsure of whether the problems were caused by the higher pressures during operation or the larger source to detector distance, we replaced the original differential stage chamber with the present one. In addition to improving the ultimate pressure obtainable, this shortened the source to detector distance by 15.8″. However, as will be discussed later this was still not enough to allow the experiments to be performed.

The differential stage chamber is mated with the 20″ bell jar (VC3) through the exit port via 6.5″ of 5″ flexible tubing and a 6″ Varian electropneumatic swing gate valve. It is pumped by a Leybold-Heraeus TMP360CSV Turbovac turbomolecular pump. This turbopump is equipped with a model NT360 frequency converter. Its required fore-vacuum pressure is 7.5×10^{-3} to 7.5×10^{-4} torr and has a volumetric displacement of 390 l/sec. It is capable of achieving an ultimate vacuum pressure of $< 7.5 \times 10^{-10}$ torr. The turbomolecular pump is backed by a Sargeant Welch Duo Seal mechanical vacuum pump model 1397. Its pumping speed is 500 l/min and is capable of an ultimate pressure of 1.0×10^{-4} torr.

The bell jar rests on a base of twenty $2\frac{3}{4}''$ flanges which are used to allow electrical, gas and water connections inside the bell jar. The seal between the bell jar and the base is made with a Viton O-ring©. The bell jar has four 6″ conflat flanges. The first is mated to the differential stage chamber. The second is located 90° away and houses a quartz window to allow viewing inside the vacuum chamber. The third is located directly in front of the entering beam and houses an EAI Quad 300 mass spectrometer. The fourth is mounted at an 45° angle to the top of the bell jar. Movement of the bell jar with respect to the base is achieved using perpendicular push-pull screws mounted to the base. They are used to align the mass spectrometer with the incoming beam. The bell jar is also equipped with a chopper, beam flag and deflection plates.

B. Detection System

Since the principle method of detection of both neutral and ionic species formed in these experiments is by mass spectroscopy, a description of the mass spectrometer is warranted. As mentioned earlier an EAI Quad 300 residual gas analyzer is being used. Figure 5 shows the quadrupole head assembly (QMS). The QMS is responsible for ionization, mass filtering and ion detection. The electronics assembly (MSE) provides the necessary voltages. The head is placed in the bell jar where the pressure is maintained at 10^{-6} torr or less. Connections to the head are made via the feedthroughs in a 4″ ID flange which connects VC3 to the outside. To minimize noise, the feedthroughs are shielded by a metal shield on the outer part of the flange. The ionizer consists of a tungsten filament .007″ in diameter which is heated by passing a DC current of approximately 1.5 A through it. This causes the filament to emit a stream of electrons as shown in Figure 5. These electrons are accelerated into the ionization region by the field produced by biasing the Faraday cage which surrounds it. The Faraday cage is operated at a voltage V_c between 0 and 40 V DC with respect to ground. The energy of these electrons can be controlled by changing the voltage applied to the filament block. This energy is usually 80-90 eV. When these electrons enter the ionization region they bombard the species present and produce parent and fragmented ions as well as electronically excited species. The ionization efficiency of this system is relatively low and of the order of 10^{-6}.

Most of the ions produced in the ionizer are collected, accelerated and focused into the quadrupole rod assembly by the lens system as shown in Figure 5. The lens system consists of a focusing lens and an exit lens. The focusing lens is mounted next to the Faraday cage and is electrically insulated from it. Its potential, V_f may be varied from 0 to -100 V with respect to ground. The exit lens is mounted next to the focusing lens and is at ground potential. As ions pass through the exit lens they lose E_F. Thus the Faraday cage and lens system extract the positive ions from the cage, increase their kinetic energy by $E_c = eV_c$ and focus them onto the axis of the quadrupole rod system. A high transmission efficiency is obtained since all ions whose direction makes an angle of 30° or less with the axis are properly mass analyzed. For most measurements the mass spectrometer will be operated with the potentials to the focus lens and the Faraday cage at 0 V with respect to ground. This is due to the fact that the beam enters the mass spectrometer axially with a high forward translational energy and thus does not require acceleration into the quadrupole rod assembly.

The quadrupole rod assembly as shown in Figure 5, consists of the quadrupole rods and the ceramic supports which separate and define the space between the rods. A DC voltage, V_1 and a superimposed RF voltage, V_0 are applied to the rods. This generates an electrostatic field between them which is given by

$$\Phi = \frac{(V_1 + V_0 \cos\omega t)(x^2 - y^2)}{r_0{}^2} \qquad (6.1)$$

where r_0 is the distance form the pole system axis to the axis of each pole. And x and y are the Cartesian coordinates of a point with respect to axes defined to be parallel to the lines connecting the centers of adjacent poles. When ions pass through the quadrupole rod assembly the field produced by the rods causes them to undergo spiralling trajectories. The trajectory that the ion takes is defined by the appropriate Mathieu equations. Only ions with the appropriate mass to charge ratio will undergo trajectories with constant radii and be able to traverse the pole region and emerge. All other ions will follow trajectories with increasing radii until it collides with a metal surface and is removed from the system. By changing the applied voltages, different mass to charge ratios will emerge.

The mass spectrometer may be operated in an auto or manual mode. In the auto mode a series of masses are scanned by applying a DC sawtooth potential to the rods. The starting position and the width of the spectrum are controlled by the RF voltage applied to the rods. In the manual mode, a single peak is monitored continuously by keeping the applied voltages to the rods constant. The measured DC ion signal is proportional to the intensity of the species being observed.

The ion detector that was used is an AEM 2000 electron multiplier. It has been designed so that its first dynode is off axis rendering it insensitive to line of sight radiation and neutrals. It requires 150 ± 50 V to be applied to its shield to achieve efficient collection of ions. It can be used in either pulsed counting or analog modes. Positive ions emerging from the mass analyzer are curved off axis by the shield voltage and strike the first dynode. If these ions have enough energy, electrons will be emitted from the dynode. This process is repeated through 16 stages. This results in the production of a large number of electrons (of the order of 10^6 to 10^7) for each positive ion that strikes the first dynode. The first dynode is usually operated at -2.5 kV with respect to ground. The voltage drop between successive dynodes is approximately 156 V. The multiplier acts as a high gain amplifier. The current produced is measured using an ESA 75 electrometer amplifier attached to the anode. It is capable of measuring current from 10^{-4} to 10^{-12} A (Figure 2, PA).

A Princeton Applied Research precision lock-in amplifier model HR-8 is attached to the exit of the electrometer. It was used to make AC measurements. A Varian Associates C-1024 Time Averaging Computer was also used to make AC measurements when operating the mass spectrometer in the auto mode. An Everex 286 PC equipped with Unkelskope data acquistition software was also used.

C. Source

A modified version of an arc heated source developed by Garvey and Kuppermann[2-4] following the design of Knuth[5-7] was used. A cut away view of the original and modified design are shown in Figure 6. The principle of operation of the source is quite basic. Gas is introduced between a fixed anode (2) and a cathode tip (10). Operating the source under vacuum conditions causes the gas to flow through the nozzle (1) into the chamber due to the great pressure differential. A plasma flame is created by striking a high voltage pulse between the anode (2) and the cathode tip (10). The plasma jet extends beyond the nozzle due to the expansion of the gas through it. This arc produces very high temperatures and thus requires efficient cooling of metal surfaces to avoid damage to or failure of the source.

The cathode portion of the original and modified source are shown in Figure 7. It is made up of a hollow stainless steel tube (A) with a $\frac{1}{8}''$ diameter tip cathode rod (B) attached to the front. The rod is made of 2% thoriated tungsten and is capable of withstanding temperatures greater than 3000 K. The tip of the tungsted rod is filed such that it resembles a very dull pencil. During operation of the source it tends to erode. The tungsten rod is attached to the base (D) using two set screws located 90° apart. The cathode was originally equipped with a brass bellows (E) which allowed the cathode tip to move $\frac{3}{4}''$ with respect to the base. The cathode is also water-cooled to avoid damage. Two gas inlets are drilled at sharp angles through the base (D) on opposite sides. This tends to create a more stable flow through the nozzle by causing the gas to swirl around inside the source.

The bellows was originally included in the design so that the cathode tip-anode disk distance could be varied from experiment to experiment so as to determine the optimum distance of separation. However, we have found that the presence of the bellows made the source much less stable. It was found that tension in the cooling water lines connected to the cathode or a change in the water pressure to these lines caused the cathode to move. This produced a change in the discharge which in general decreased the intensity of the beam. In addition, the presence of the bellows also made the beam less reproducible. To eliminate this problem the bellows was removed and the cathode tube was welded to the base.

The original and modified anode assembly are shown in Figure 8. It is made up of a large cylindrical brass piece (D1 and D2) which has 6 water cooling channels bored into it. The nozzle assembly fits into the front of it. To avoid striking the arc in the anode housing, it is electrically insulated from the cathode everywhere except at the tungsten rod. This was achieved with a Macor© cylinder cut to cover the entire cathode tube except the rod as shown in Figure 6. The other parts of the anode assembly are also shown in a disassembled configuration. The anode disk (B) is made of a $\frac{1}{8}''$ disk of tungsten which was cut from a .375″ welders rod. The disk has a 1.8 mm hole drilled into it. In the past a 1.2 mm hole was used however, when this was tried it was found to melt and close up during operation. The disk was originally held in place by two copper pieces (C and D) which are threaded into the anode. However, the threads tended to cause the center opening to be off slightly thus making alignment more difficult. To produce a more accurate centering of these pieces the threads were removed and the pieces were machined to fit snugly in place and thus provide a more reproducible centering of the opening in the nozzle.

When assembled, the anode and cathode are joined by six teflon screws. They are electrically isolated by a teflon spacer and a Viton O- ring© which also provides a vacuum seal between them. In addition, we have also placed a ceramic spacer in the center with shoulders on it. This was done to ensure that the cathode and anode were positioned very accurately. This helps to accurately center the cathode rod with respect to the anode disk and thus minimizes damage to the rod and disk during operation. Since these changes have been implemented, we have been able to run the discharge up to 8 times before replacing the cathode rod and anode disk. In the past erosion of these pieces was significant enough to force us to change these after each run. Once assembled, the space between the tungsten rod and anode nozzle forms a small chamber (Figure 6 (4)) into which the gas may flow from the inlet lines (Figure 6 (3)). To prevent shorts, the cathode is insulated from the rest of the chamber by making all water lines from $\frac{1}{4}''$ polyethylene tubing, and by placing a glass spacer in the metal gas inlet line. The 'cathode tip-anode nozzle' distance was originally adjusted when assembled by compressing the cathode bellows (Figure 6 (7)). However, since the optimum gap between the tip of the cathode and the surface of the anode disk was found to be 0.5 mm, this distance is now always used. If in the future we wish to change this distance, it can be easily done by changing the length of the cathode rod. An exploded view of the entire source assembly is shown in Figure 9.

Power for the arc source is provided by a Westinghouse type WS variable current arc welder supply which runs on 440 voltage. Since only a 220 V line is available in our lab, a step-up transformer is used to provide the necessary power.

The level of the regulated output current from the welder can be remotely adjusted by means of a servo motor built into the power supply. The electrical control of the source is accomplished via a panel which provides interlocks to shut down the arc power and pumps in the event of a failure. A picture of the front of the panel and relevant wiring diagrams are shown in Figures 10 through 13. A Westinghouse 0-150 VDC meter is used to measure the output voltage and a 0-250 ADC ammeter is used to measure the current. The arc is started with a 200 amp lamp starter (Hanovia model 29912) which produces a high voltage pulse.

Control and measurement of the inlet gas flow is provided by a gas flow panel equipped with shut off and metering valves, flow meters and a Wallace and Tiernan 0-800 torr pressure gauge. A picture of the front panel and the gas flow diagram are shown in Figures 14 and 15.

A schematic top view of the entire machine with the arc source (AS) in place is shown in Figure 2. The source is mounted into the center of a 6″ diameter by 1.4″ thick electromagnet (M). The magnet is made by wrapping approximately 450 turns of 14 gauge armored polythermalized antenna wire (Belden, 8009-500) around the aluminum magnet support structure. A cross sectional drawing of the magnet is shown in Figure 16. The magnet is water cooled by 2 layers of $\frac{3}{16}''$ copper tubing wound within the windings of the magnet. The center is also cooled by the channel in the center of the support structure. The magnet is usually operated at 18 volts and 16 amperes. Power for the magnet is supplied by an HP Harrison 6269A DC power supply. The field created by the magnet stabilizes the plasma by exerting a perpendicular force on any ions which try to leave the beam. The source fits into the magnet such that the front of it is located in the middle of the magnet. Such positioning causes the magnetic field to have a greater influence on the plasma.

To be able to perform the proposed experiments, as well as, crossed beam experiments with this source very nearly perfect mechanical alignment is necessary. However, since the beam does not seem to follow the optical path, some means of adjusting the direction of the beam during operation is necessary. To achieve such movement during operation, the original translation assembly was redesigned to add the two other translations and two angular degrees of freedom to the source. These movements are motor controlled so that changes can be made during operation. The angular degrees of freedom allow the source to rotate about the point located at the center of the anode disk. The rotation about this point must be very fine. This is illustrated below. In order for the beam to enter the mass spectrometer, the beam axis must be off the optical axis by no more than an angle α shown below.

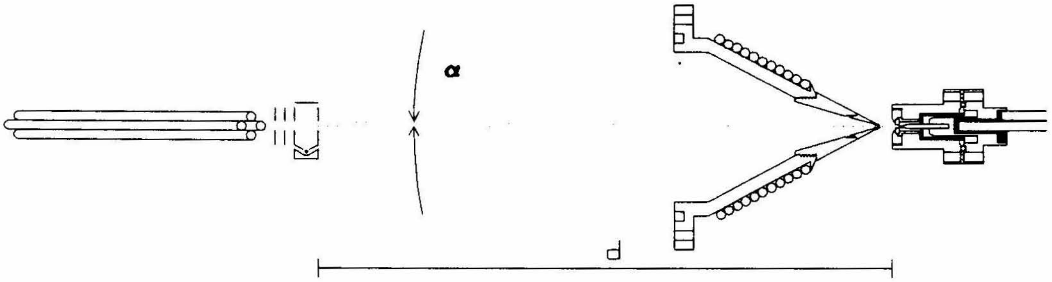

By examining the above diagram, we see that α is given by

$$\alpha = \tan^{-1}\left(\frac{\mathrm{r_{ms}}}{\mathrm{d}}\right)$$

where $\mathrm{r_{ms}}$ is the radius of the opening at the entrance of the mass spectrometer and d is the distance between the nozzle of the source and the entrance to the mass spectrometer. For our conditions, this results in

$$\alpha = 0.092^\circ.$$

For the crossed beam experiments the corresponding requirement is even more stringent due to the longer source to mass spectrometer distance and to the smaller aperatures required. Therefore, the movements produced need to be smaller than this. The design developed provides angular motions of the order of 0.001° accurately. With such movements available, we are able to optimize the alignment of the beam during operation. This has made it possible to perform these experiments, as well as, the crossed beam experiments reproducibly and under optimum conditions.

Figure 17. shows the magnet (M) mounted on a moveable rail track . This translation rotation assembly (TRA) allows movement of the arc source and magnet during operation. Thus the nozzle to skimmer distance can be varied. In addition, this assembly provides four other degrees of freedom to the source (two translations and two rotations). In the original design, the direction of the beam changed during operation. This was attributed to instabilities in the support structure and translation assembly for the source created by the excessive heating of these elements during operation. The original design was modified to eliminate these problems as well as to provide the new degees of freedom. Therefore, when the direction of the beam changes during operation, it can be compensated for by the use of these motions.

As stated earlier, the motions of the source provided by the translation-rotation assembly are motor controlled. Anaheim Automation size 23 stepper motors and MBU3128 bipolar drivers have been used for this purpose. They provide 200 steps per revolution with half step capability. With this design a resolution of:

$1.25 \times 10^{-3}{}''$/step for the x-translation (nozzle to skimmer distance)

$6.25 \times 10^{-5}{}''$/step for the y-translation (side to side motion)

$6.25 \times 10^{-5}{}''$/step for the z-translation (vertical motion)

$1.25 \times 10^{-3}{}^{\circ}$/step for the θ rotation (horizontal rotation)

and

$1.25 \times 10^{-3\circ}$/step for the ϕ rotation (vertical rotation)

can be achieved. To provide control of these motions an electrical control box was designed and built. The front panel and wiring diagrams for this box are shown in Figures 18-22.

The skimmer (S) is shown in Figure 23. It is made up of a two-piece copper assembly which is threaded into a conical water-cooled aluminum base. The skimmer has an exterior angle of 28°30′ and an interior angle of 16°30′ with an orifice diameter of 1.0 mm. Using copper for the skimmer allows the source to get as close as 1 cm without damaging the skimmer.

D. Operation of the Source

It has been found that a safe reliable means of generating the H_3 molecular beam is by first starting the plasma with argon and then gradually switching over to hydrogen.[8] Any attempt to start the discharge with pure hydrogen will result in destruction of the source.[6] To operate the source the vacuum chamber must be pumped down. The water lines for the source, skimmer and chamber are turned on. Next a flow of argon corresponding to 7 SCFH air is established. This corresponds to a stagnation pressure of 400 torr as measured by a 0-800 torr Wallace and Tiernan gauge on the inlet line. At this point the pressure in VC1 rises to 80 mtorr. Next the current to the magnet and to the arc welder are turned on. The argon arc is initiated by throwing the switch on the Hanovia lamp starter thus providing a voltage pulse between the anode and the cathode. At this point the welder supplies 15 volts and 100 amperes. Once the argon discharge is ignited an intense light blue plume is observed. After allowing the discharge to stabilize hydrogen gas is slowly mixed into the argon flow using a Granville-Phillips variable leak valve (series 203). After approximately 24 torr partial pressure of hydrogen has been introduced the appearance of the plume changes dramatically. It becomes reduced in size and turns crimson red. The hydrogen flow is slowly increased until the hydrogen partial pressure reaches 150 torr. As the hydrogen flow is increased the plasma emission decreases.

Once this hydrogen partial pressure has been attained, the argon flow is slowly turned off. This causes the arc current to decrease and the arc voltage to increase. However, it is critical that the arc current be kept constant at 100 amps. The changes in the current are compensated for using the servo motor of the arc welder. If the current is kept constant at 100 amps, the voltage will rise to 30 volts when the argon is fully turned off. At this time the stagnation pressure is about 150 torr and the plume is a brilliant diffuse crimson red. By slowly lowering the H_2 pressure the plasma is observed to go into the 'pencil' mode. At this point the plasma is a very intense white beam surrounded by a diffuse red plume.

Once in the pencil mode, the flux of H_3 molecules is the greatest. At this point the pressure in VC2 (Figure 1.) is $\sim 1.5 \times 10^{-5}$ torr and between 1 and 10 mtorr in VC1. Under these conditions the beam is relatively stable and may be operated for 5 or more hours. After running for about 25 minutes the voltage drops to a value of 25-28 volts and remains there for the entire run. At this time the source can be brought closer to the skimmer. As the distance between the source and skimmer is decreased, the H_3 molecule intensity at the mass spectrometer increases.

E. Laser System

The laser system used in the rovibrational population measurements is shown in Figure 24. It consists of a Quanta Ray model DCR-2A 20 Hz Nd:Yag Laboratory Laser System, a Quanta Ray model PDL-2 Pulsed Dye Laser and a Quanta Ray model WEX-1 Wavelength Extender. The DCR-2A(20) Nd:Yag laser system uses an unstable resonator cavity with diffraction coupled output followed by an amplifier. this design results in an output beam having a "donut" spatial intensity in both the near and far fields. The second harmonic at 532 nm is produced by frequency doubling in a type II KD P crystal contained within a temperature controlled oven. The crystal is rotated around a vertical axis to provide optimum phase matching. If desired, additional crystals are used to generate the third and fourth harmonics. These crystals are rotated around a horizontal axis to provide optimum phase matching. A prism separation system, PHS, consisting of a Pellin-Broca prism, a Porro prism, and two right angle pickoff prisms is used to separate the various harmonics. Losses through the PHS are are typically on the order of 15% . The PHS also includes a $\lambda/2$ plate to rotate the polarization of the 532 nm beam to vertical.

This laser operates at an optimum repitition rate of 20 Hz. The initial output pulse energy after the PHS was approximately 290 mJ. However, severe birefringence within the Nd:YAG rods, caused the spatial intensity profile to appear as a "daisy" rather than a clean "donut". This degradation of the beam quality greatly degraded the performance of the remainder of the laser system. A second polarizer assembly which suppresses the birefringence was installed to cure this problem. The intensity profile was greatly improved, as was the performance of the remainder of the laser system. Currently, the output pulse energy at 532 nm after the PHS is 360 mJ.

A Pockels cell for Q-switching is used. The Q-switch high voltage supply is turned on approximately 3 msec before the flashlamps are fired. The Q-switch is triggered approximately 215 μsec later, with the laser pulse following 50 nsec later.

A schematic of the Quanta Ray PDL-2 dye laser is shown in Figure 24. This dye laser is pumped by the second or third harmonic of a ND:YAG laser. All of the work in this dissertation used the second harmonic. The incident pump laser beam is vertically polarized. A beam splitter diverts approximately 10% of the incident energy into a flowing dye cell located within the oscillator cavity. This cavity is of the Hänsch design. The oscillator output passes through an optional preamplifier, a beam expanding telescope, and then the final amplifier. A second beamsplitter is used to transversely pump the preamplifier when it is used. The remaining radiation is used to pump the amplifier stage which can be either transversely or longitudinally pumped. An additional delay of 2.7 nsec between when the oscillator and the amplifiers are pumped can be introduced by an optional optical delay line consisting of two Porro prisms. This delay reduces the amount of ASE produced, especially when the preamplifier is used.

The normal configuration of this dye laser is to use only the longitudinally pumped final amplifier. In this configuration, the specified dye laser efficiency at 560 nm using Rhodamine 590 Tetrafluoroborate is 28% , while the observed efficiency is 29% . Wavelength scanning is accomplished using a stepping motor that has a step size of 0.12 counter units. It is controlled by a model MCI-1 parallel I/O interface. It requires 12 bits of information: "direction" bit, two "motor address" bits, a "new data ready" bit, and an 8 bit word giving the number of steps to take. This system does not step continuously, but instead jumps immediately to the next wavelength and then waits.

Laser radiation at wavelengths outside of that covered by the dye laser is provided by the Quanta Ray model WEX-1 wavelength extension unit. The complete ultraviolet WEX-1 unit can cover the wavelength interval 217-432 nm using three frequency conversion techniques: doubled dye, dye + Nd:YAG fundamental, and doubled dye + Nd:YAG fundamental. This is accomplished by using 7 KD*P crystals: 4 crystals in one module for the first two processes and 3 crystals in a second module for the latter process. The appropriate crystal depends on the wavelength and conversion process chosen. More complete information is provided in the product literature.

The crystals in the first module are rotated around a vertical axis, while those in the second are rotated around a horizontal axis, to maintain phase-matching. In both modules the correct phase-matching angle is maintained automatically. A small portion of the output from each crystal module is fed to a pair of photodiodes. If the phase-matching is correct, then each photodiode will receive equal levels of UV radiation; however, if the phase-matching angle is incorrect then the output will "walk" to one one side or the other of the desired direction, the photodiodes will receive unequal levels of UV radiation, and a servo-mechanism will rotate the crystal back to the correct position. The success of this technique requires a very good beam quality, but when correctly aligned, scan rates of sereral nm/min are possible.

The various wavelengths are normally separated using a Pellin-Broca prism. The prism is oriented in a manner to minimize reflective losses for the desired wavelength. For example, the doubled dye output is polarized horizontally, hence the prism lies on its side with all optical faces in the vertical plane. In this configuration the prism faces are at approximately Brewster's angle with respect to the UV laser radiation and reflective losses are minimized. The prism is very efficient at separating the visible and UV laser beams; however, it does have one major drawback. the dispersive power of the prism causes the output beam to shift in position and direction during scans in wavelength. This problem is worse the further one works from the WEX and the longer the scan. In some cases the shift in position was unacceptable, and the Pellin-Broca prism was replaced with a right-angle prism and a filter.

To perform the rovibrational measurements an intense source of light having a wavelength which lies in the range from 335-370 nm is required. This light will be generated using the laser system described above. The second harmonic of the YAG output will be used to pump the dye laser. The wavelength of this light is 532 nm. Using the second harmonic of the YAG laser the dye laser is capable of producing light with a wavelength which lies in the range from $\sim$ 540 to 1000 nm. The dye that will be used for these experiments will be LDS698. Using this dye, the dye laser is capable of producing light in the range from 660 to 735 nm. The output energy of the dye laser using this dye is shown in Figure 25. The output of the dye laser is then run through the WEX wavelength extender where it is frequency doubled to produce light in the range from 330 to 368 nm. The tuning curve from the WEX-1 wavelength extender over this range is shown in Figure 25.

II. References

1. J. F. Garvey, Ph. D. Thesis, California Institute of Technology, 1985.
2. J. F. Garvey and A. Kuppermann, *Chem. Phys. Lett.* **107**, 491 (1984).
3. J. F. Garvey and A. Kuppermann, *Rev. Sci. Instrum.*, **57**, 1061 (1986).
4. J. F. Garvey and A. Kuppermann, *J. Chem. Phys.* **85**, (1986).
5. E. L. Knuth, UCLA Department of Engineering Report # 66-19, April, 1966.
6. W. S. Young, W. E. Rodgers, and E. L. Knuth, *Rev. Sci. Instrum.*, **40**, 1346 (1969).
7. W. S. Young, UCLA Department of Engineering Report # 69-39 July 1969.
8. K. R. Way, S. C. Yang, and W. C. Stwalley, Operation of a Superthermal Arc-Heated Hydrogen Atom Source. This film may be rented from Media Library Audio Visual Center, University of Iowa, Iowa City IA. 52242, Catalog No. U-30354.

III. Figure Captions

Figure 1. A side view of the current vacuum system: VC1, vacuum chamber one, the source chamber; P1, P2, viewports; WAU1000, Roots blower vacuum pump; E250, rotary piston pump; VC2, vacuum chamber 2, the differential stage chamber; TMP turbomolecular pump; VC3, vacuum chamber 3, the diagnostics chamber; P3, viewport; QMS, quadrupole mass spectrometer; TMP, turbomolecular pump.

Figure 2. A schematic view of the top of the machine: VC1, vacuum chamber one; AS, anode assembly; A, anode; C, cathode; M, magnet; S, water cooled copper skimmer; TA1, TA2 and TA3, translation assemblies; RA, rotation assembly; P1, viewport; P2, viewport; GV1, gate valve 1; B1, bellows 1; VC2, vacuum chamber two; GV2, gate valve 2; B2, bellows 2; VC3, vacuum chamber 3; C2, 160 Hz chopper; D2, electric field defectors; F2, mechanical flag; QMS, quadrupole mass spectrometer; P4, viewport; PA, EAI preamplifier (ESA-75); LI1, lock-in amplifier; MSE, mass spectrometer electronics; SCR1, strip chart recorder.

Figure 3. A side view of the original vacuum system: VC1, vacuum chamber one, the source chamber; P1, P2, viewports; WAU1000, Roots blower vacuum pump; E250, rotary piston pump; VC2, vacuum chamber 2, the differential stage chamber; DP mercury diffusion pump; VC3, vacuum chamber 3, the diagnostics chamber; P3, viewport; QMS, quadrupole mass spectrometer; TMP, turbomolecular pump.

Figure 4. A schematic view of the top of the machine: VC1, vacuum chamber one; AS, anode assembly; A, anode; C, cathode; M, magnet; S, water cooled copper skimmer; TA1, TA2 and TA3, translation assemblies; RA, rotation assembly; P1, viewport; P2, viewport; GV1, gate valve 1; B1, bellows 1; VC2, vacuum chamber two; C1, 10 Hz chopper; D1, electric

field deflectors; F1, mechanical flag; MVS, magnetic velocity selector, P3, viewport; FT, electrical and water feedthroughs; GV2, gate valve 2; B2, bellows 2; VC3, vacuum chamber 3; C2, 160 Hz chopper; D2, electric field defectors; F2, mechanical flag; QMS, quadrupole mass spectrometer; P4, viewport; PA, EAI preamplifier (ESA-75); LI1, lock-in amplifier; MSE, mass spectrometer electronics; SCR1, strip chart recorder.

Figure 5. a) Combined semi-schematic and pictoral diagram showing the axial beam ionizer and the filter rods of the Quad 250A Analyzer. b) Schematic of ionizer assembly showing gas molecules entering the Faraday cage.

Figure 6. a) Cutaway view of arc-heated source before changes were made: 1, exit aperature; 2, anode housing; 3, water cooling inlet/outlet ports; 4, source gas chamber; 5, O-ring insulator and vacuum seal; 6, cathode support; 7, flexible bellows; 8, cathode; 9, cathode water cooling channel; 10, cathode tip; 11, macor© cylinder; 12, macor© positioning shoulder. b) Cutaway view of arc heated source as it exists now.

Figure 7. a) Scale drawing of cathode assembly before changes were made: A, hollow tube; B, tungensten cathode rod; C, set screw; D, support structure; E, bellows; F, outside casing.The view of the cathode is a cross-sectional cut permitting a view of both sets of teflon screw holes in the support structure. The assembly is made out of stainless steel. b) Scale drawing of cathode assembly as it exists now.

Figure 8. a) Exploded view of anode assembly before changes were made: A, threaded copper top; B, tungsten anode; C, threaded copper bottom; D (1 and 2) brass anode housing; E, macor© cylinder. b) Exploded view of anode assembly as it exists now: C, copper bottom.

Figure 9. Exploded view of the arc heated source: 1, threaded copper top; 2, tungsten anode; 3, copper bottom; 4, brass anode housing; 5, macor©

cylinder; 6, tungsten cathode rod; 7, cathode support structure; 8, viton© o-ring; 9, delrin gasket; 10, macor© positioning shoulder; 11, macor© insulator; 12, bakelight insulator; 13, washer.

Figure 10. Electrical interlock and control panel for the arc discharge source.

Figure 11. Wiring diagram for the electric interlock and control panel for the arc discharge source.

Figure 12. Wiring diagram for the electric interlock and control panel for the arc discharge source.

Figure 13. Wiring diagram for the electric interlock and control panel for the arc discharge source.

Figure 14. Front panel of the inlet gas flow system.

Figure 15. Inlet gas flow diagram for the arc discharge source.

Figure 16. Cross section of electromagnet showing cooling coils. The anode (nozzle) sits snugly in the center of the magnet with the nozzle positioned roughly in the middle.

Figure 17. Pictures of the source and magnet mounted in the translation-rotation assembly.

Figure 18. Front panel of the box for electrical control of the translation rotation assembly.

Figure 19. Vector card wiring diagram for the box which provides electrical control of the translation-rotation assembly.

Figure 20. Limit switch wiring for the stepper motors which provide motion to the translation-rotation assembly.

Figure 21. LED wiring for the front panel of the box which provides electrical control of the translation-rotation assembly.

Figure 22. Connector, feedthrough and motor wiring diagram for the translation-rotation assembly.

Figure 23. Three stage skimmer system. The base is a water-cooled aluminum mount for the two smaller copper skimmers.

Figure 24. A schematic top view of the laser system: DCR2-A, Quanta Ray model DCR-2A 20 Hz Nd:Yag Laboratory Laser System; PDL-2, Quanta Ray model PDL-2 Pulsed Dye Laser; WEX-1, Quanta Ray model WEX-1 Wavelength Extender

Figure 25. a) Tuning curve for the output of the PDL-2 dye laser over the range of wavelengths that will be studied (using LDS 698 as the dye); Tuning curves for the output of the WEX-1 Wavelength Extender: Plot is of output energy (mJ) versus wavelength (nm).

Figure 1.

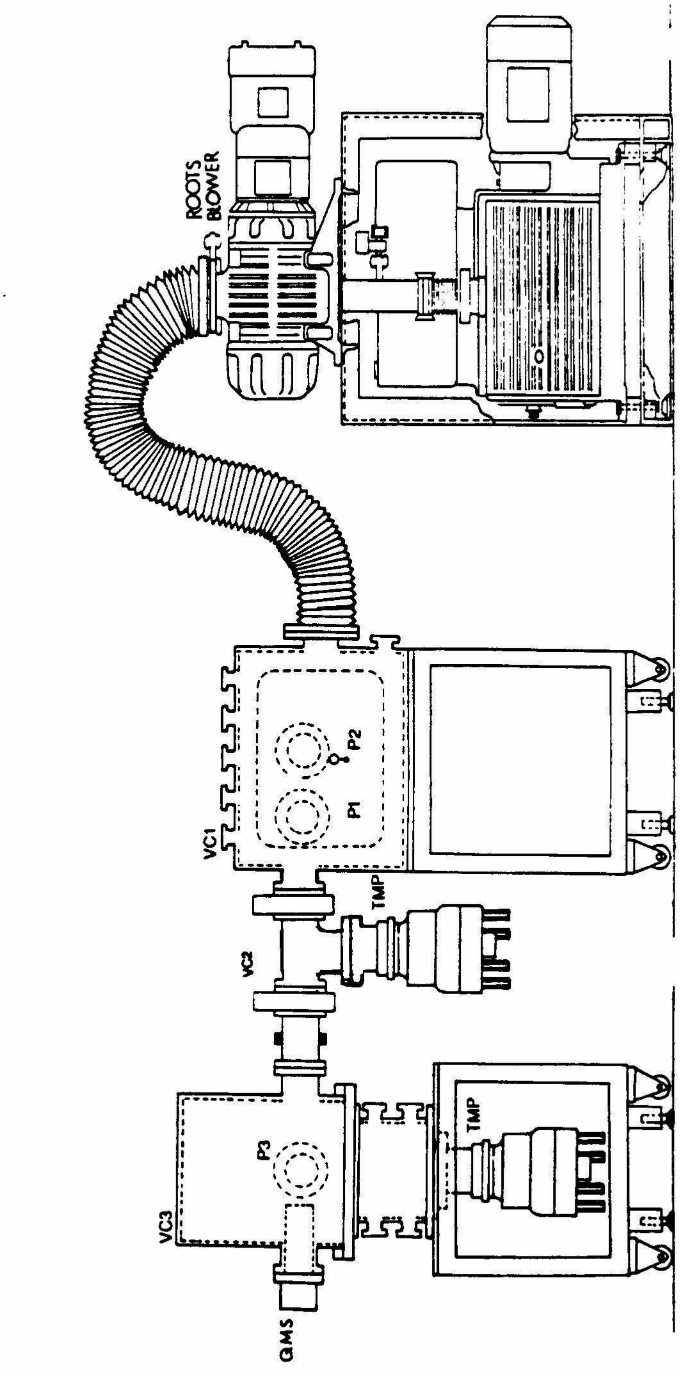

Figure 2.

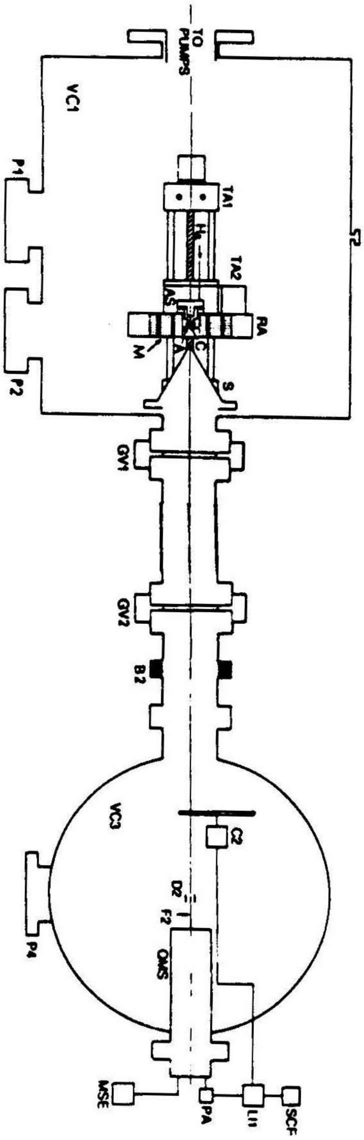
TO PUMPS
VC1
P1
P2
TA1
He
TA2
S2
AS
RA
M
C
S
GV1
GV2
B2
VC3
C2
D2
F2
QMS
P4
MSE
PA
LI1
SCF

Figure 3.

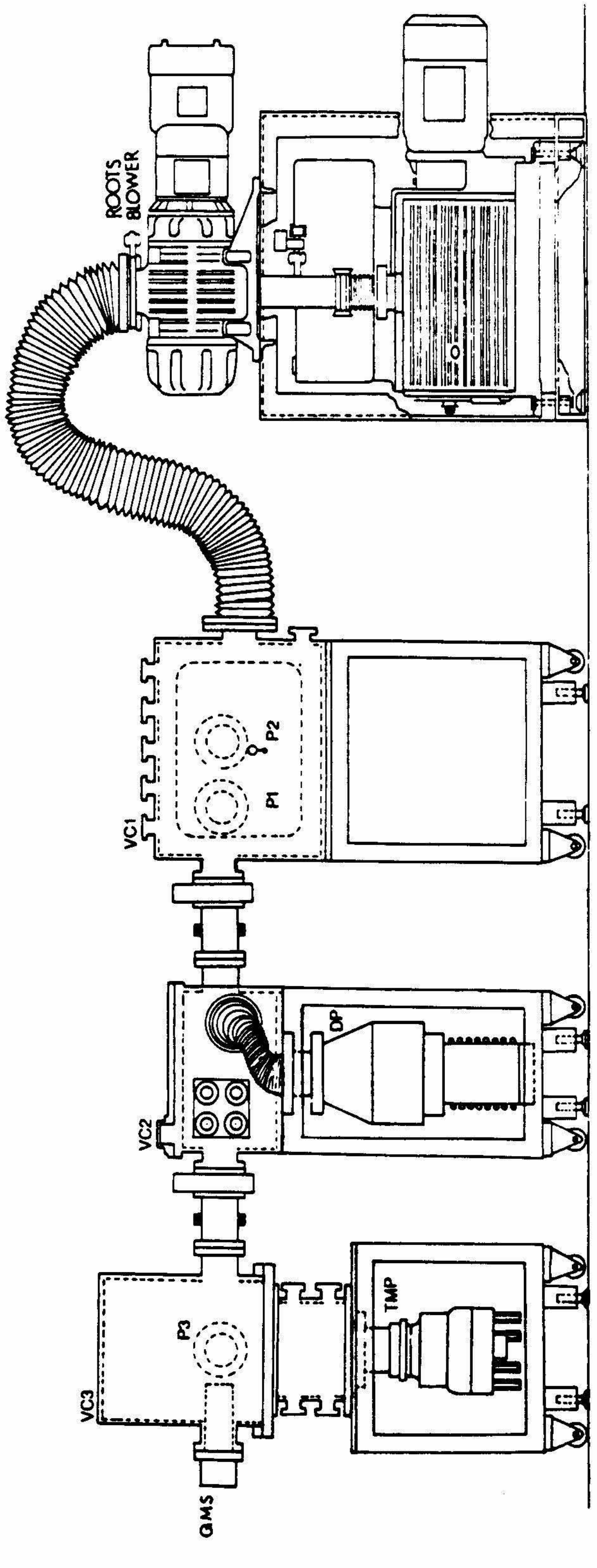

Figure 4.

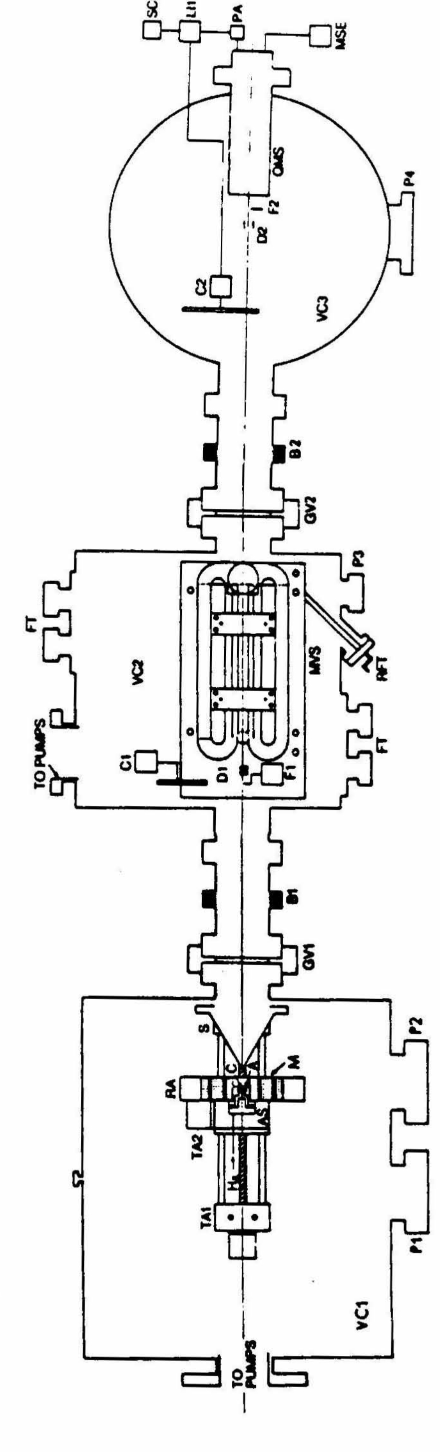
SCF
LI1
PA
MSE
QMS
F2
D2
P4
C2
VC3
B2
GV2
P3
FT
VC2
MVS
RFT
FT
TO PUMPS
C1
D1
F1
B1
GV1
S
C
A
M
FA
TA2
AS
TA1
S2
P2
P1
VC1
TO PUMPS

Figure 5.

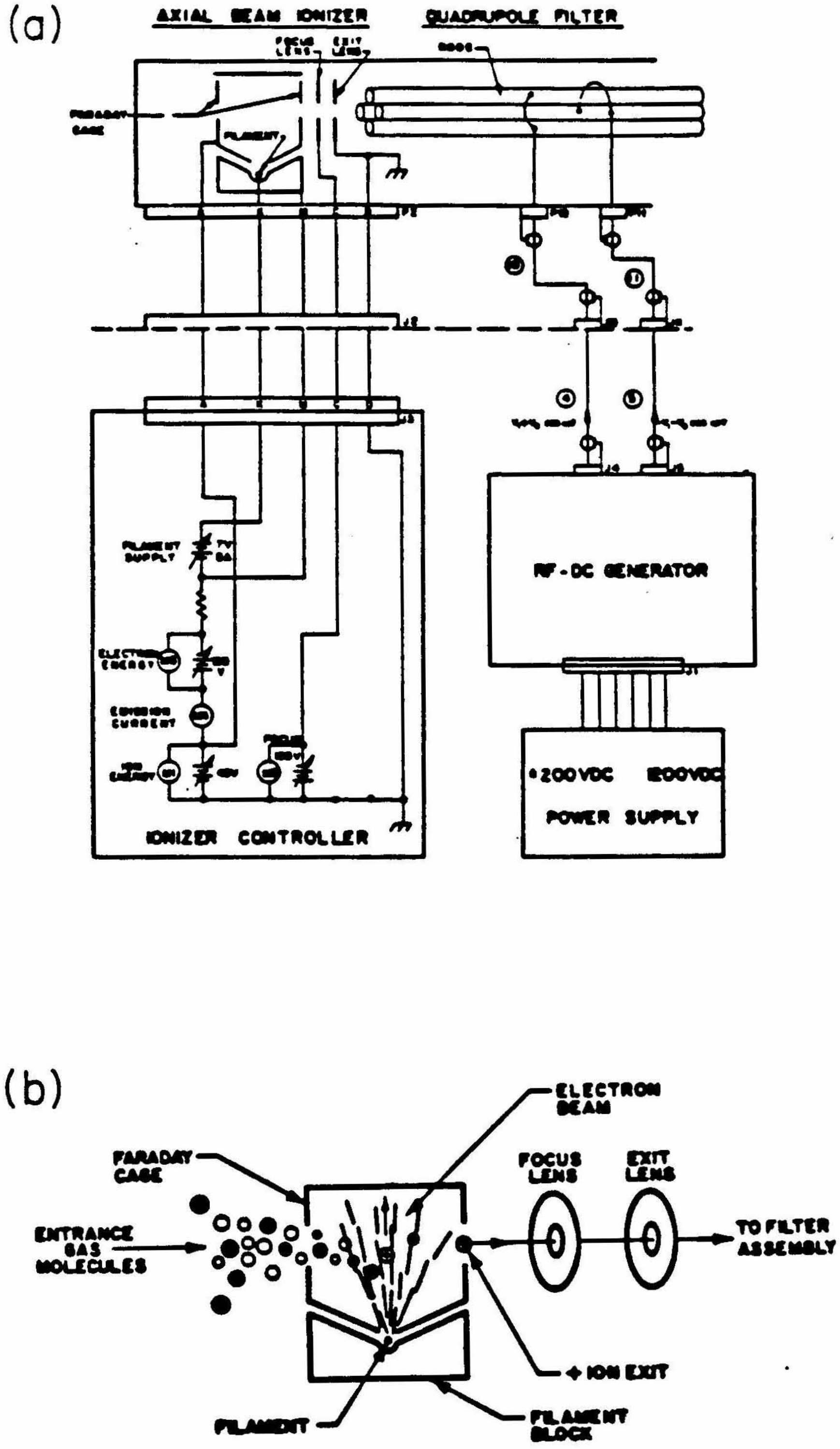
(a)
AXIAL BEAM IONIZER
QUADRUPOLE FILTER
FOCUS LENS
EXIT LENS
RODS
FARADAY CAGE
FILAMENT
FILAMENT SUPPLY
7V
5A
ELECTRON ENERGY
V
EMISSION CURRENT
ION ENERGY
FOCUS
IONIZER CONTROLLER
RF - DC GENERATOR
+200VDC
1200VDC
POWER SUPPLY
(b)
ELECTRON BEAM
FARADAY CAGE
FOCUS LENS
EXIT LENS
ENTRANCE GAS MOLECULES
TO FILTER ASSEMBLY
+ ION EXIT
FILAMENT
FILAMENT BLOCK

Figure 6.

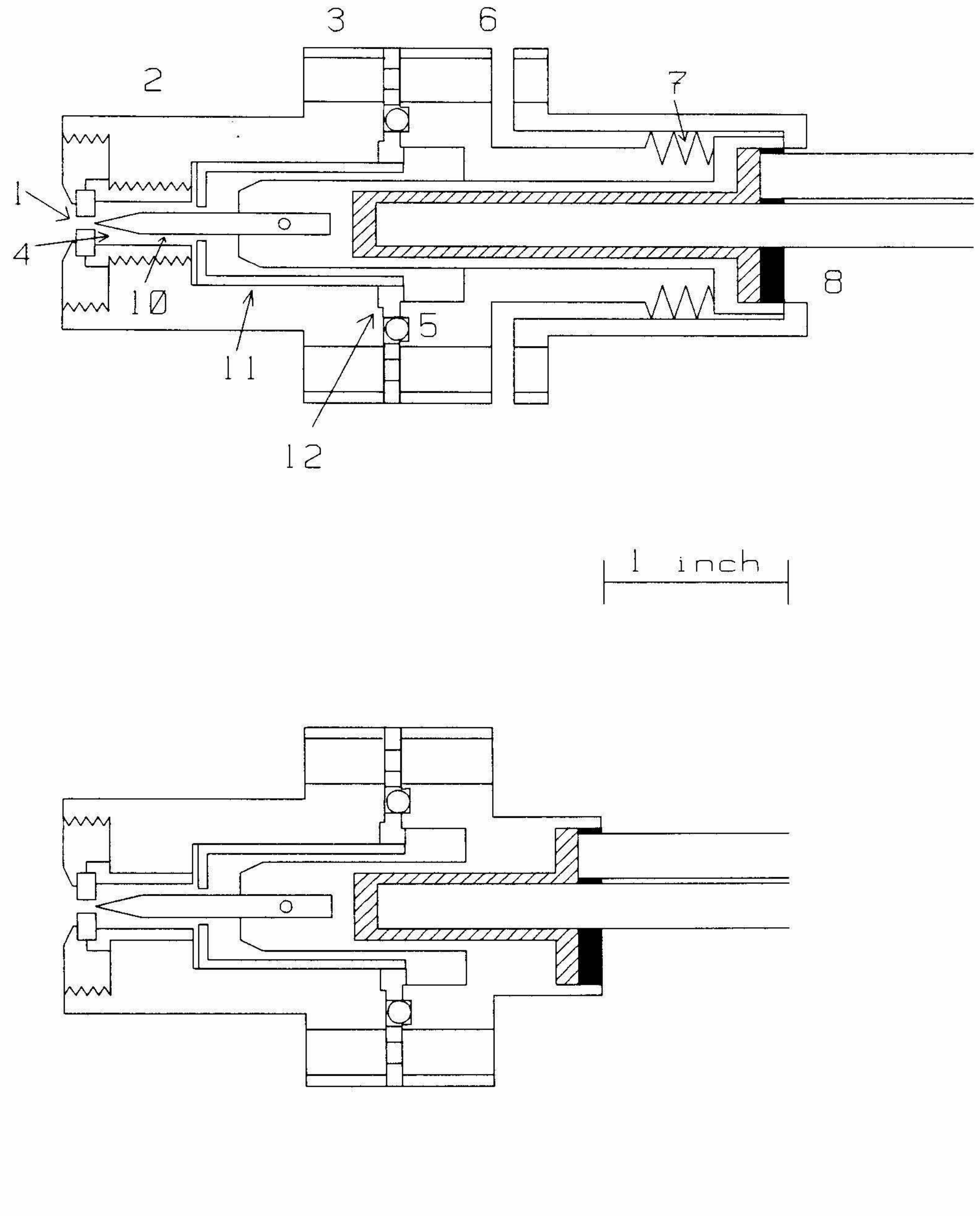

Figure 7.

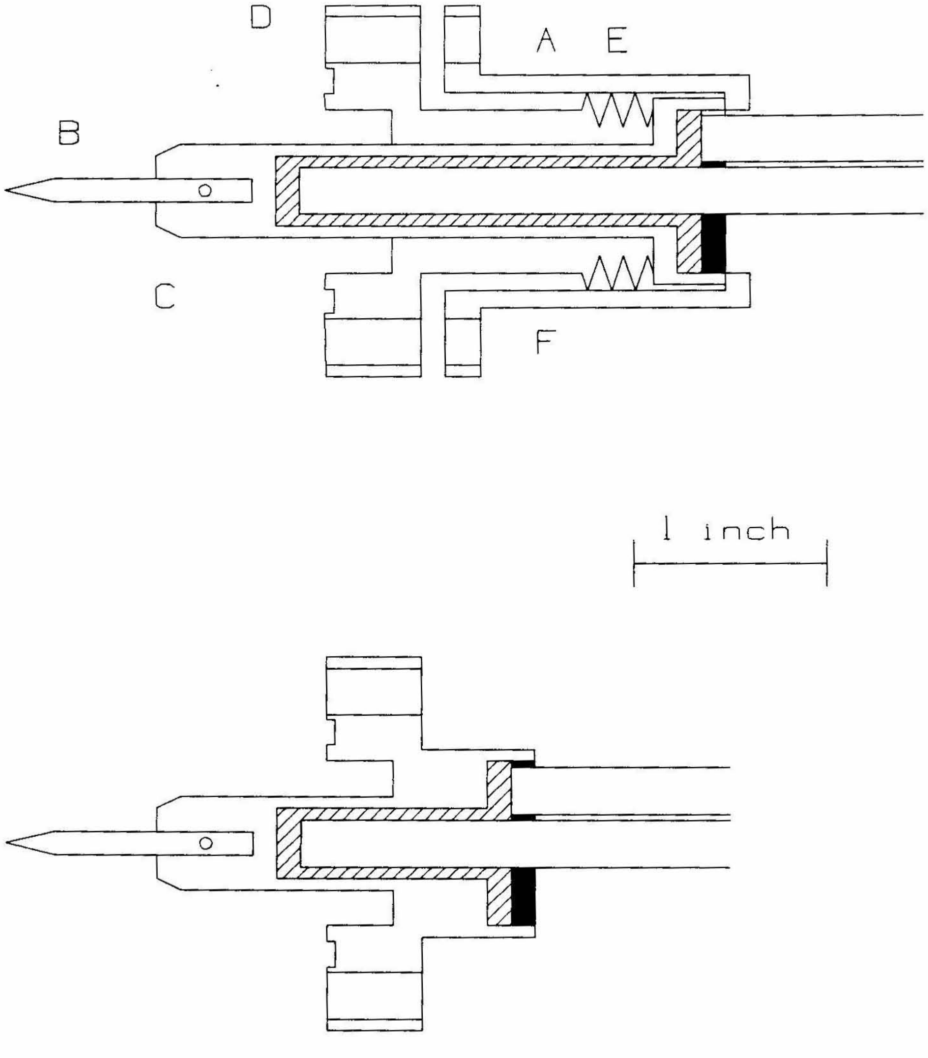

Figure 8.

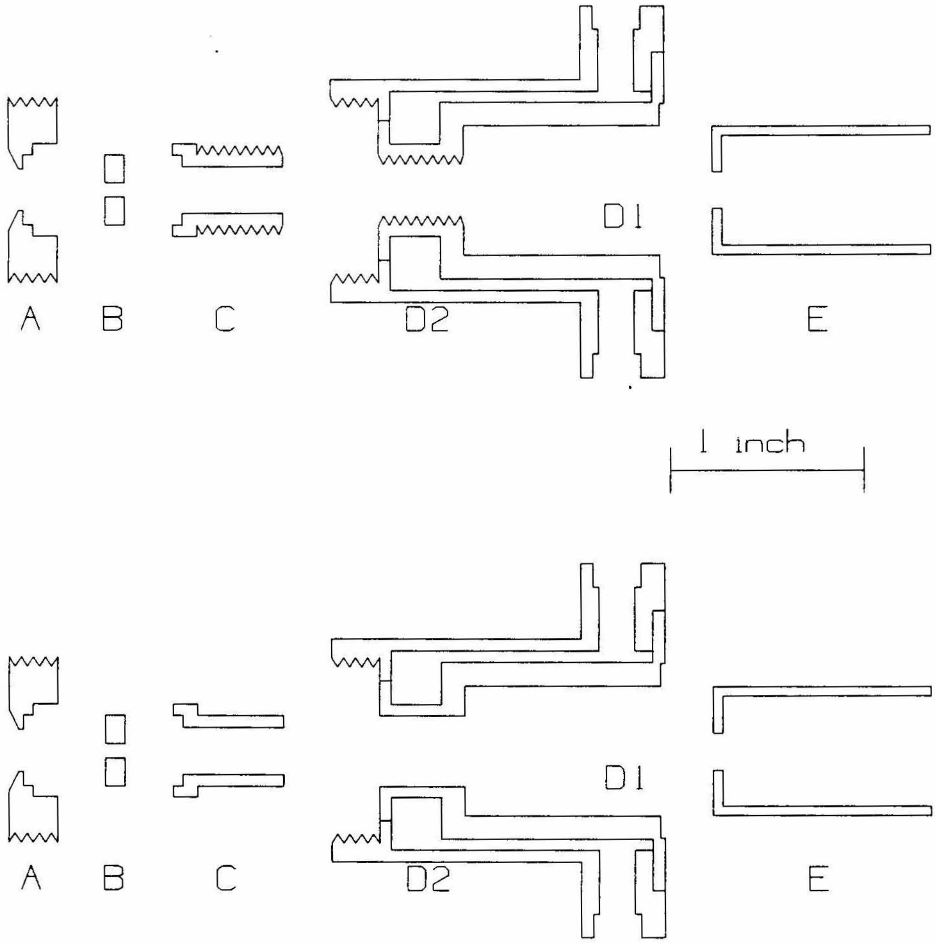

Figure 9.

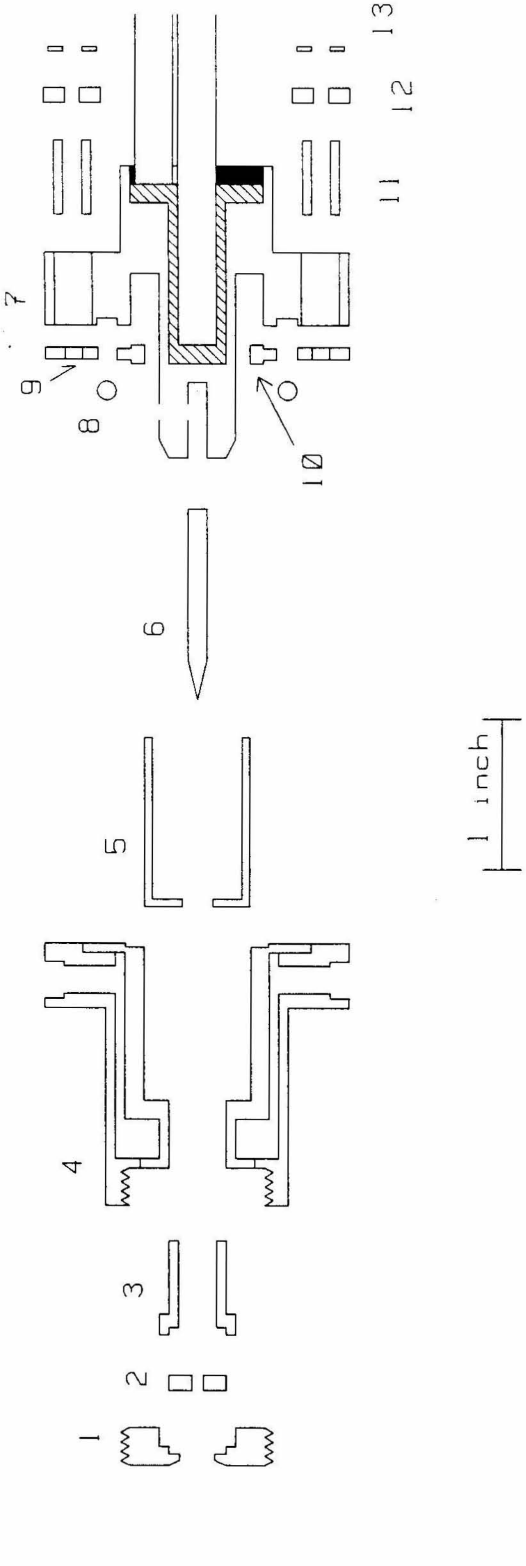

Figure 10.

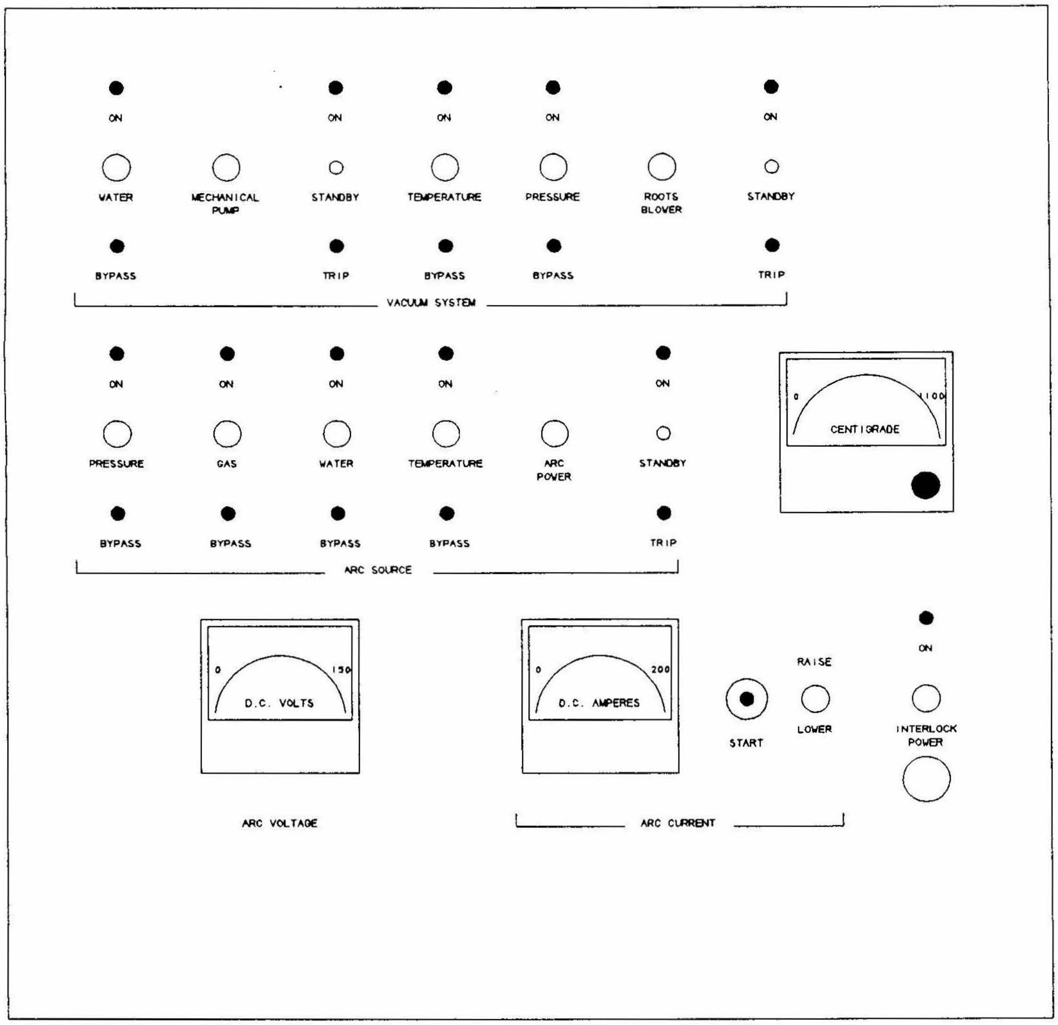
ON
WATER
BYPASS
MECHANICAL PUMP
STANDBY
TRIP
TEMPERATURE
PRESSURE
ROOTS BLOWER
VACUUM SYSTEM
PRESSURE
GAS
WATER
TEMPERATURE
ARC POWER
ARC SOURCE
0
1100
CENTIGRADE
150
D.C. VOLTS
ARC VOLTAGE
200
D.C. AMPERES
START
RAISE
LOWER
ARC CURRENT
INTERLOCK POWER

Figure 11.

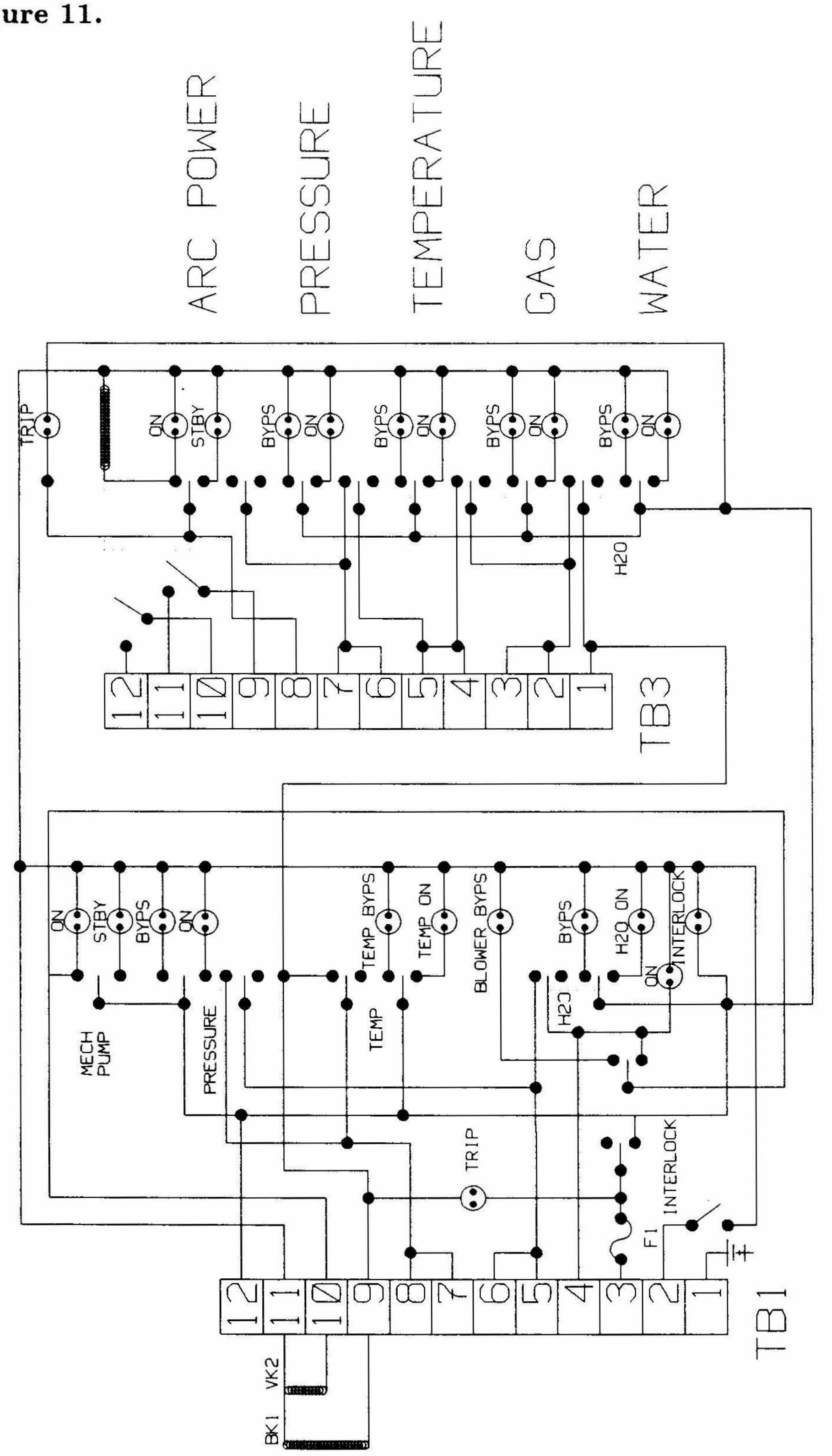
ARC POWER
PRESSURE
TEMPERATURE
GAS
WATER
TRIP
ON
STBY
BYPS
ON
BYPS
ON
BYPS
ON
BYPS
ON
H20
12
11
10
9
8
7
6
5
4
3
2
1
TB3
ON
STBY
BYPS
ON
TEMP BYPS
TEMP ON
BLOWER BYPS
BYPS
H2O ON
INTERLOCK
ON
MECH PUMP
PRESSURE
TEMP
H2O
TRIP
INTERLOCK
F1
12
11
10
9
8
7
6
5
4
3
2
1
TB1
BK1
VK2

Figure 12.

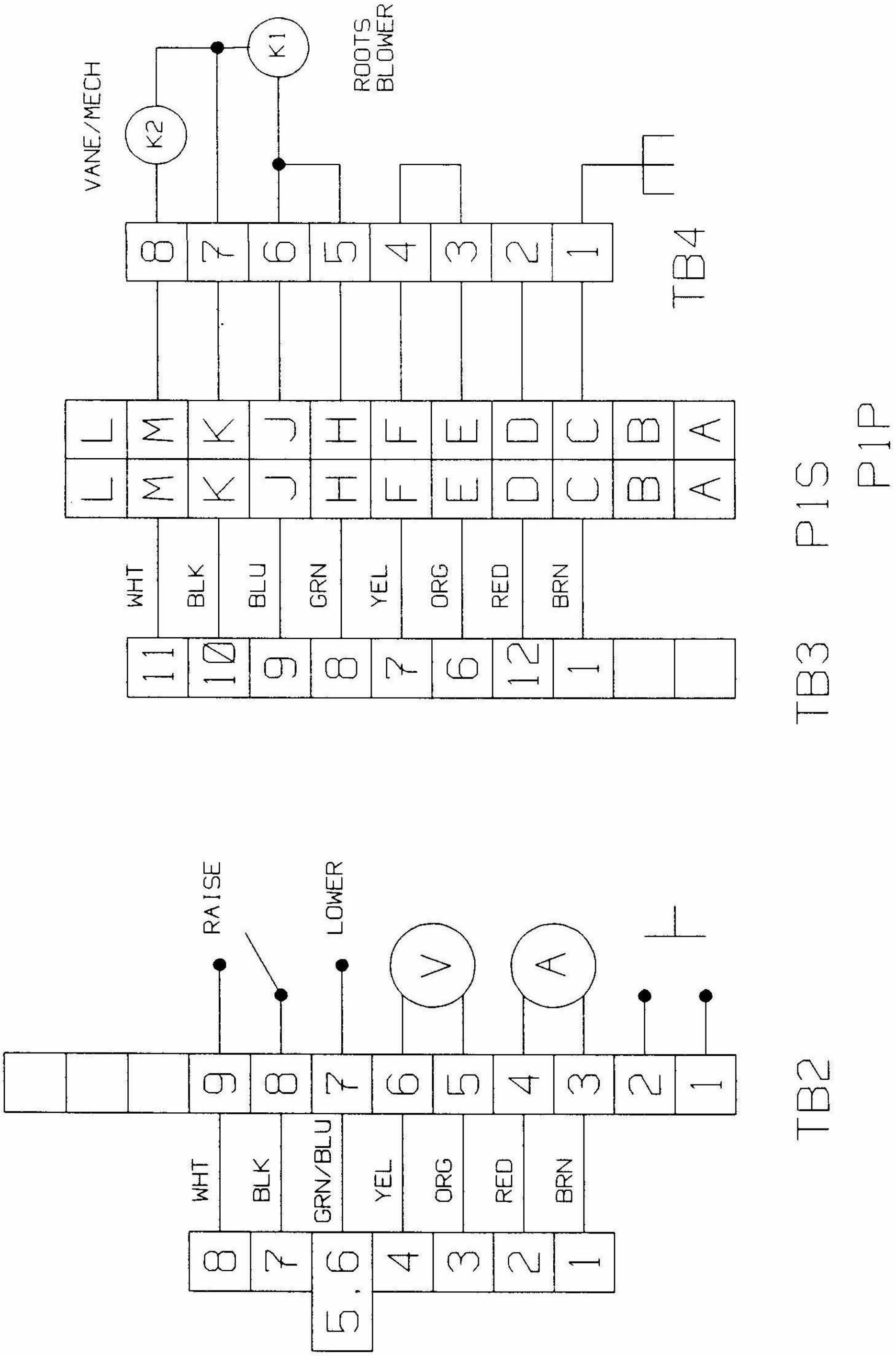
VANE/MECH
K2
K1
ROOTS BLOWER
TB4
P1S
P1P
TB3
WHT
BLK
BLU
GRN
YEL
ORG
RED
BRN
RAISE
LOWER
V
A
GRN/BLU
5,6
TB2

Figure 13.

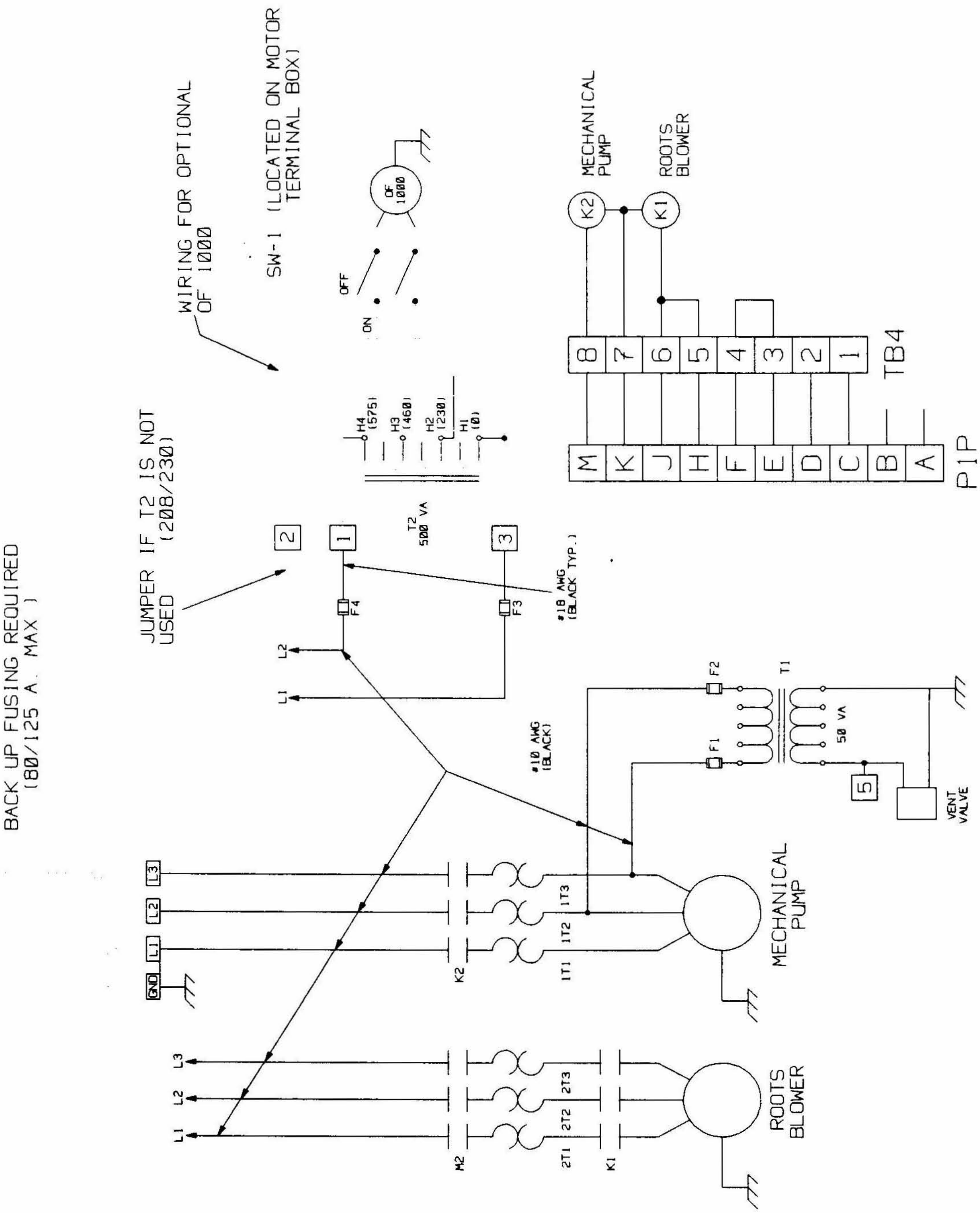
BACK UP FUSING REQUIRED
(80/125 A. MAX)
JUMPER IF T2 IS NOT
USED (208/230)
WIRING FOR OPTIONAL
OF 1000
SW-1 (LOCATED ON MOTOR
TERMINAL BOX)
OFF
ON
OF
1000
MECHANICAL
PUMP
ROOTS
BLOWER
K2
K1
8
7
6
5
4
3
2
1
TB4
M
K
J
H
F
E
D
C
B
A
P1P
H4
(575)
H3
(460)
H2
(230)
H1
(0)
T2
500 VA
2
1
3
F4
F3
#18 AWG
(BLACK TYP.)
L2
L1
#10 AWG
(BLACK)
F2
F1
T1
50 VA
5
VENT
VALVE
L3
L2
L1
GND
K2
1T1
1T2
1T3
MECHANICAL
PUMP
L3
L2
L1
M2
2T1
2T2
2T3
K1
ROOTS
BLOWER

Figure 14.

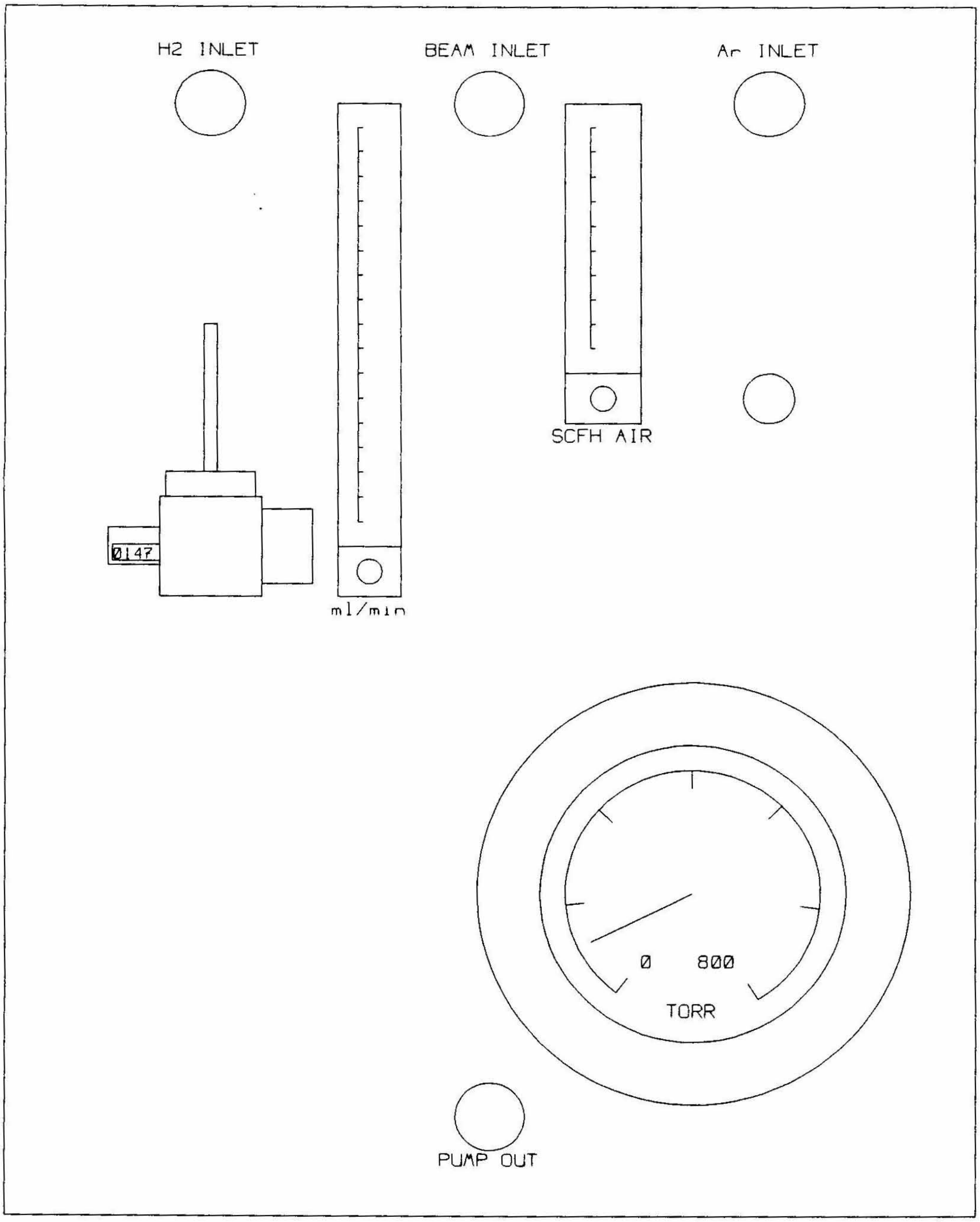
H2 INLET
BEAM INLET
Ar INLET
0147
ml/min
SCFH AIR
0
800
TORR
PUMP OUT

Figure 15.

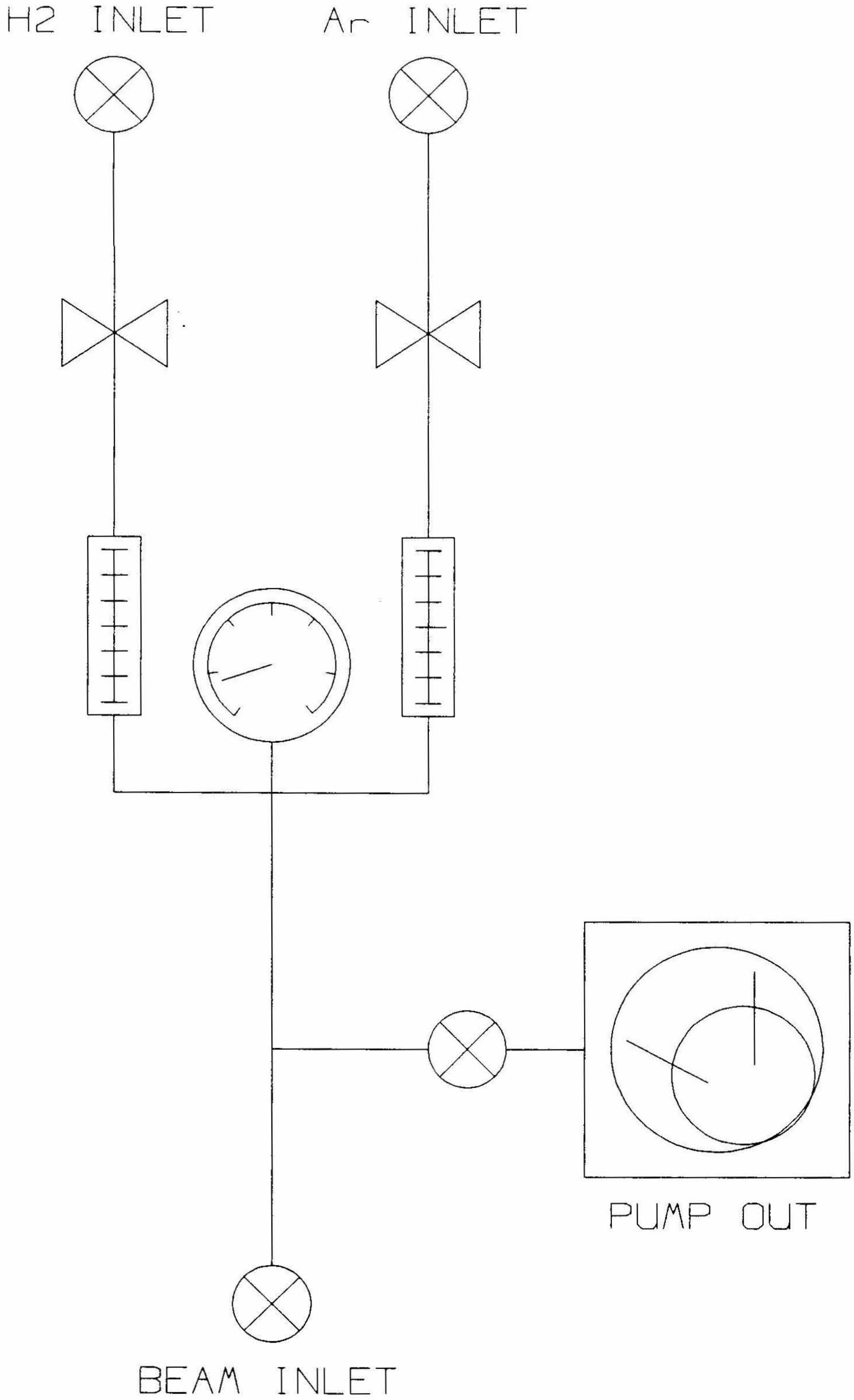

Figure 16.

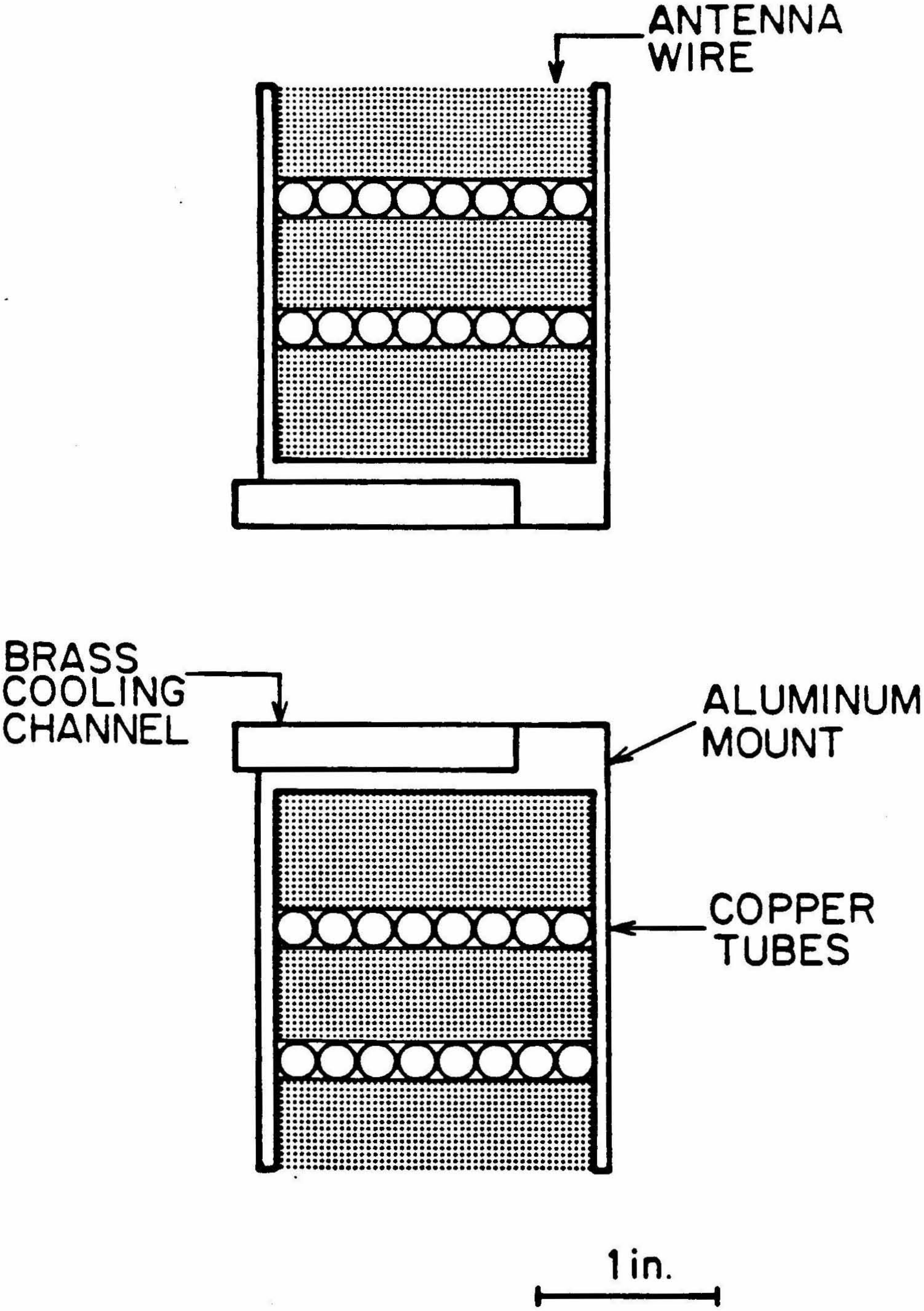
ANTENNA WIRE
BRASS COOLING CHANNEL
ALUMINUM MOUNT
COPPER TUBES
1 in.

Figure 17.

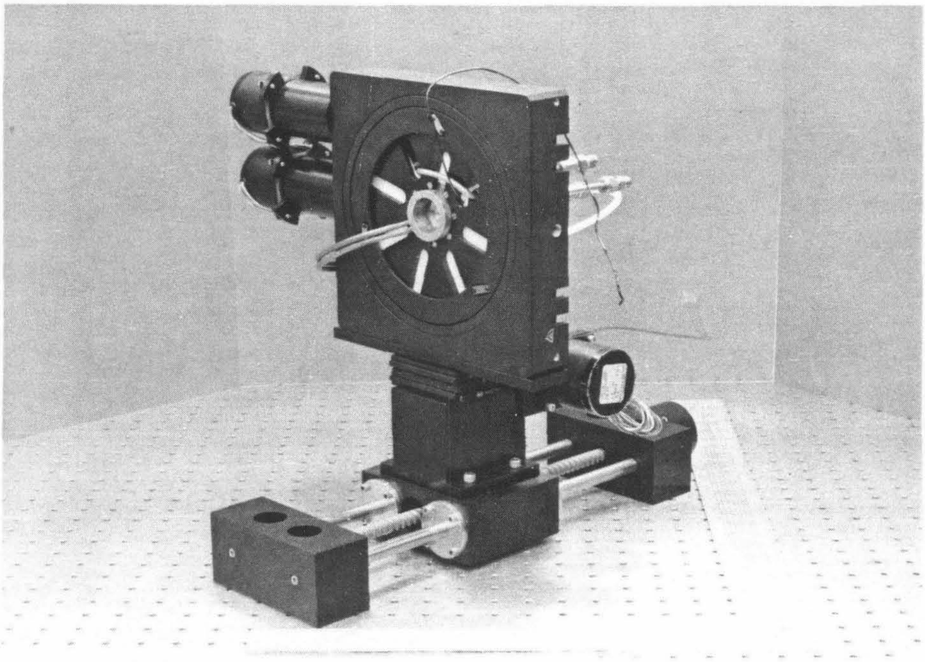

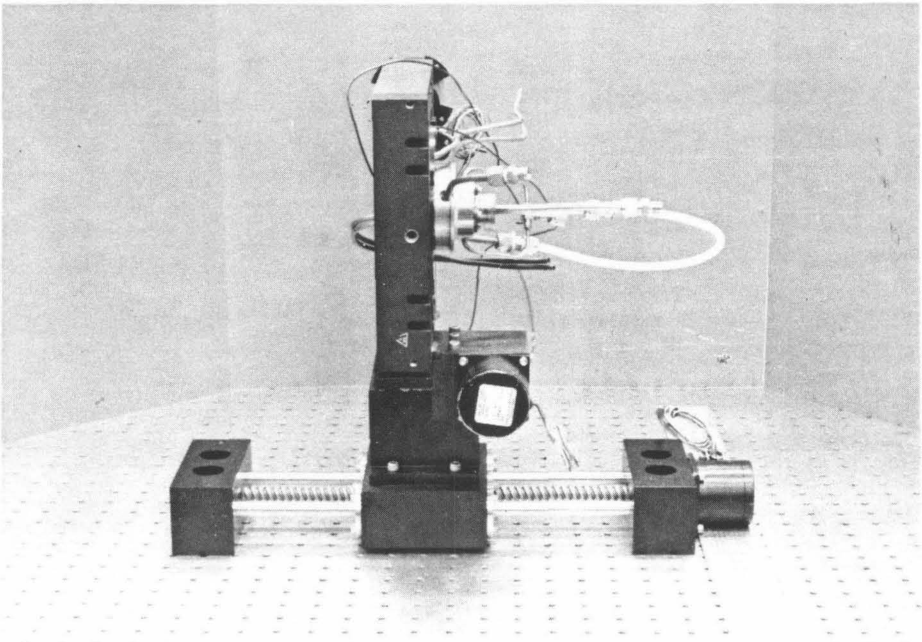

Figure 18.

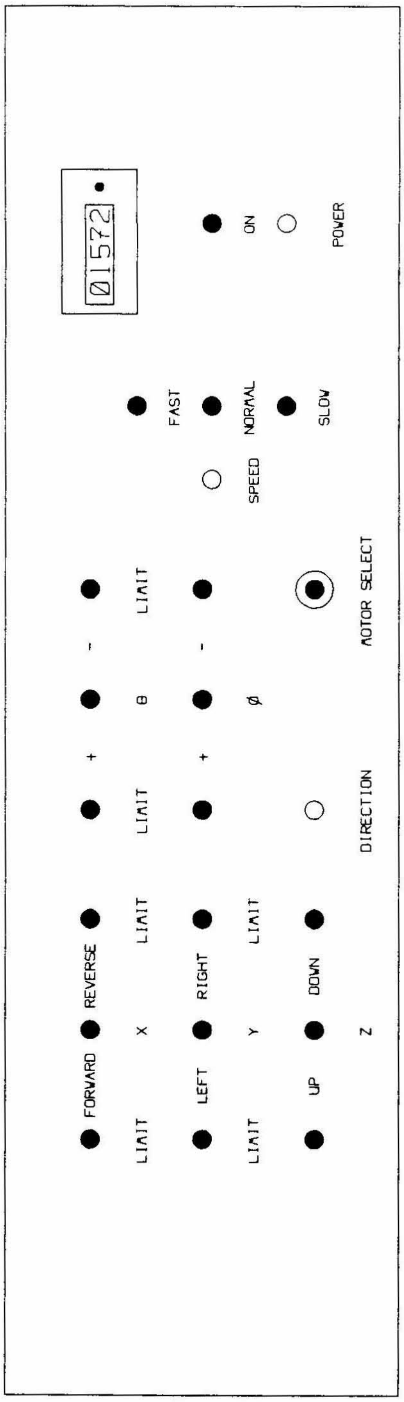
01572
ON
POWER
FAST
NORMAL
SLOW
SPEED
LIMIT
+
θ
-
LIMIT
LIMIT
+
Ø
-
LIMIT
MOTOR SELECT
DIRECTION
LIMIT
FORWARD
X
REVERSE
LIMIT
LIMIT
LEFT
Y
RIGHT
LIMIT
UP
Z
DOWN

Figure 19.

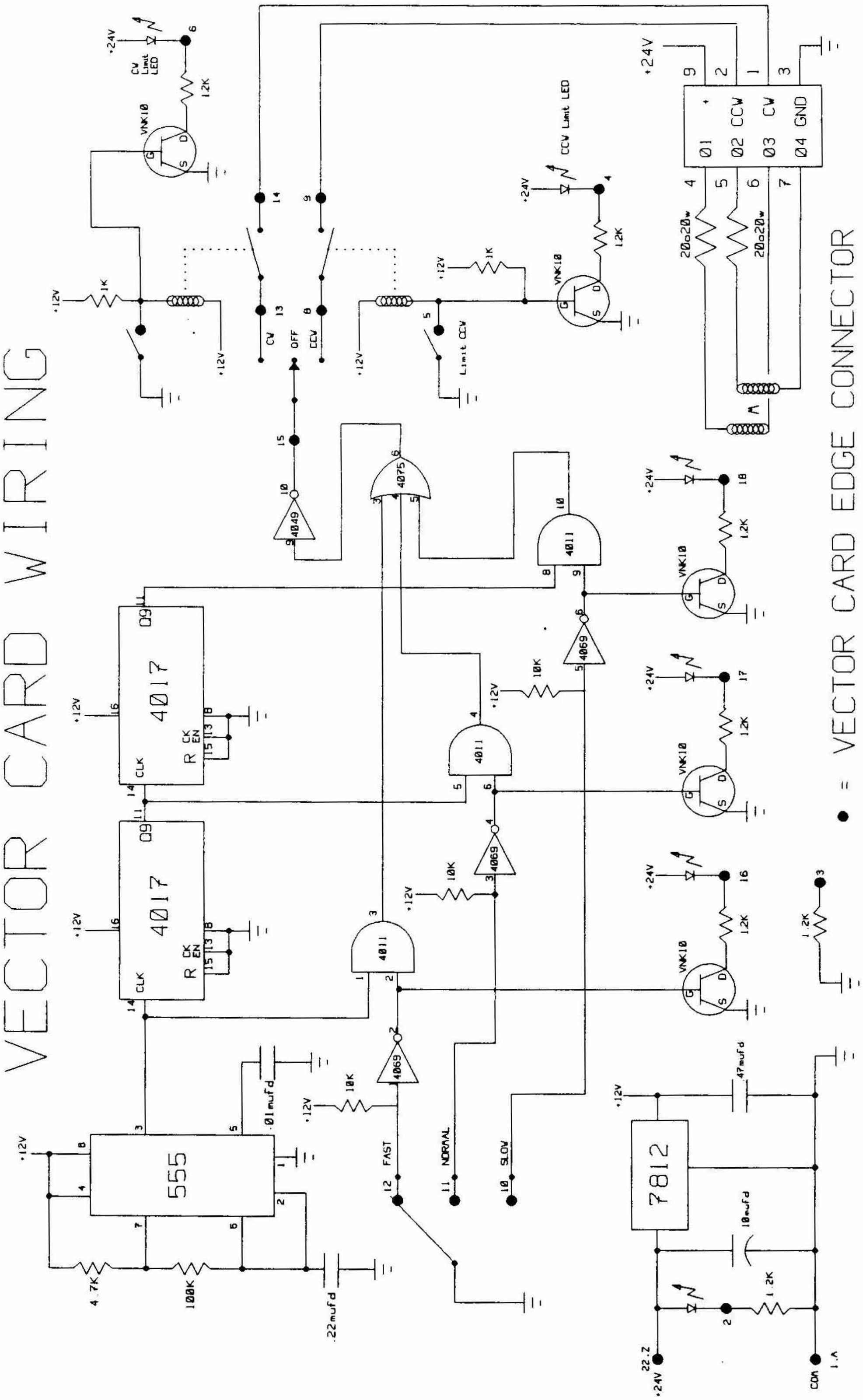
VECTOR CARD WIRING
● = VECTOR CARD EDGE CONNECTOR
555
4017
4017
4011
4011
4011
4069
4069
4069
4049
4075
7812
VNK10
CLK
R
CK EN
Q9
+12V
+24V
1K
12K
10K
4.7K
100K
.22mufd
.01mufd
47mufd
10mufd
1.2K
FAST
NORMAL
SLOW
CW
OFF
CCW
Limit CCW
CW Limit LED
CCW Limit LED
20Ω20w
01
02 CCW
03 CW
04 GND
22.2
COM
1.A

Figure 20.

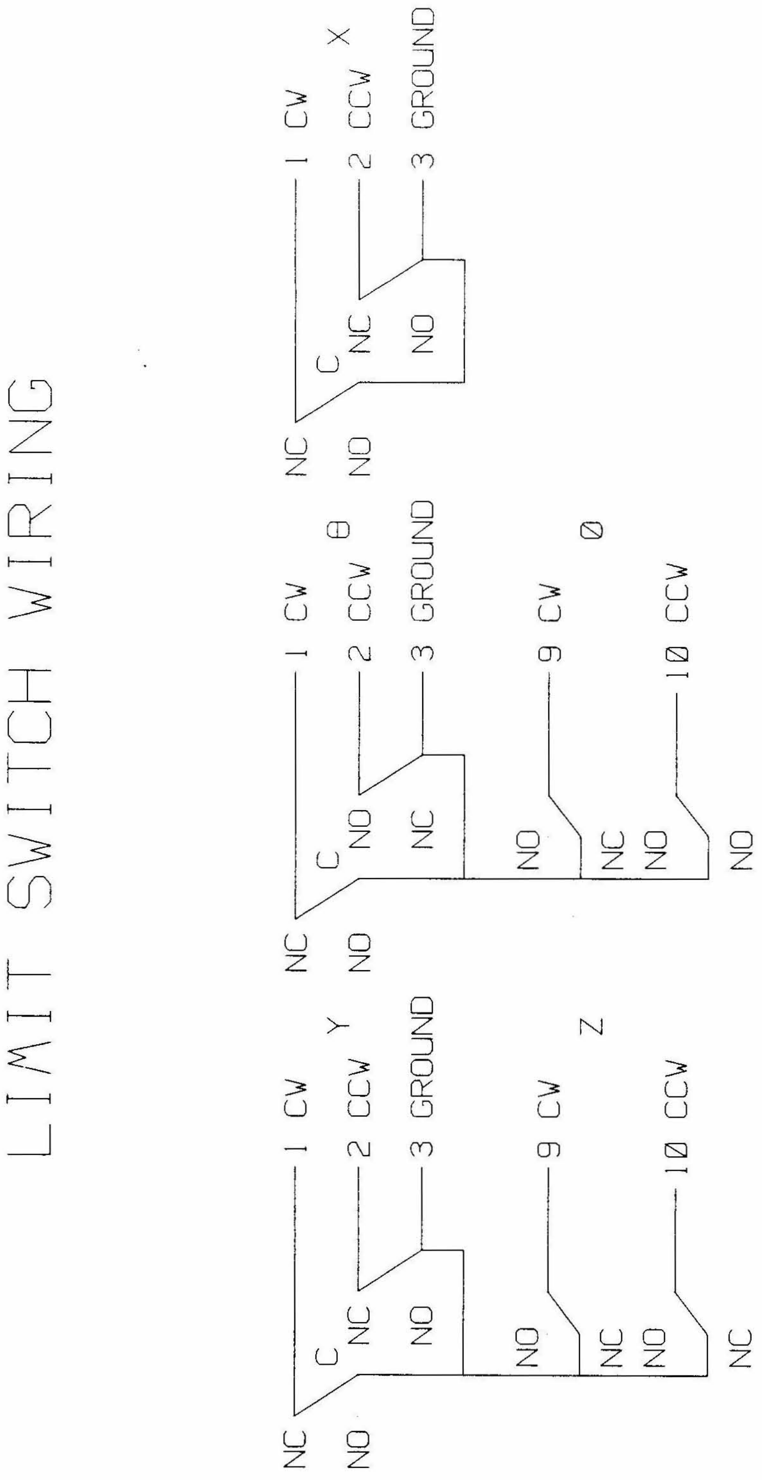
LIMIT SWITCH WIRING
NC
NO
C
NC
NO
1 CW
2 CCW
3 GROUND
X
NC
NO
C
NO
NC
1 CW
2 CCW
3 GROUND
Θ
NO
9 CW
NC
NO
10 CCW
NO
Ø
NC
NO
C
NC
NO
1 CW
2 CCW
3 GROUND
Y
NO
9 CW
NC
NO
10 CCW
NC
Z

Figure 21.

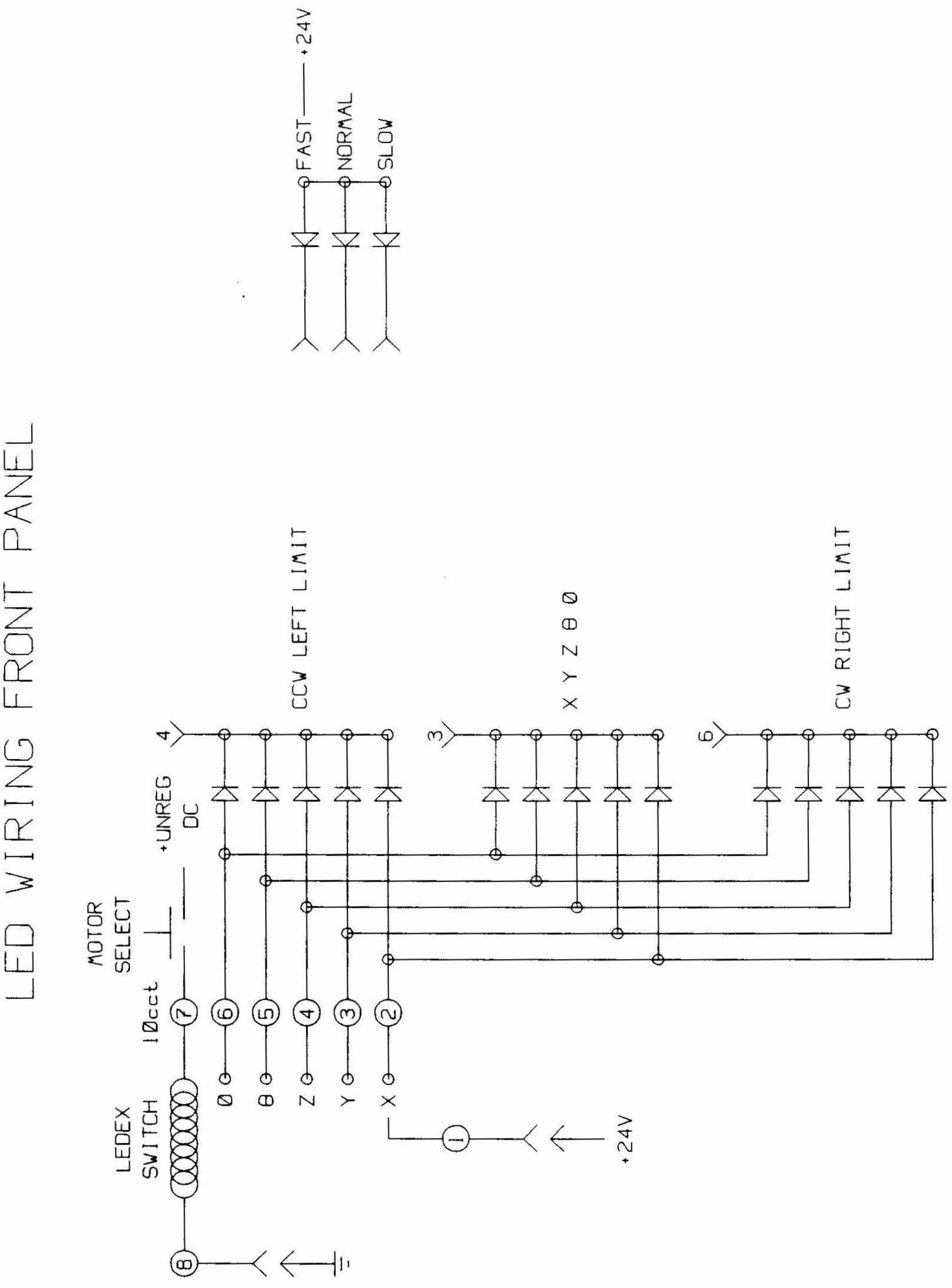
LED WIRING FRONT PANEL
FAST
NORMAL
SLOW
+24V
CCW LEFT LIMIT
X Y Z θ Ø
CW RIGHT LIMIT
4
3
6
MOTOR SELECT
+UNREG DC
10cct
LEDEX SWITCH
7
6
5
4
3
2
1
8
Ø
θ
Z
Y
X
+24V

Figure 22.

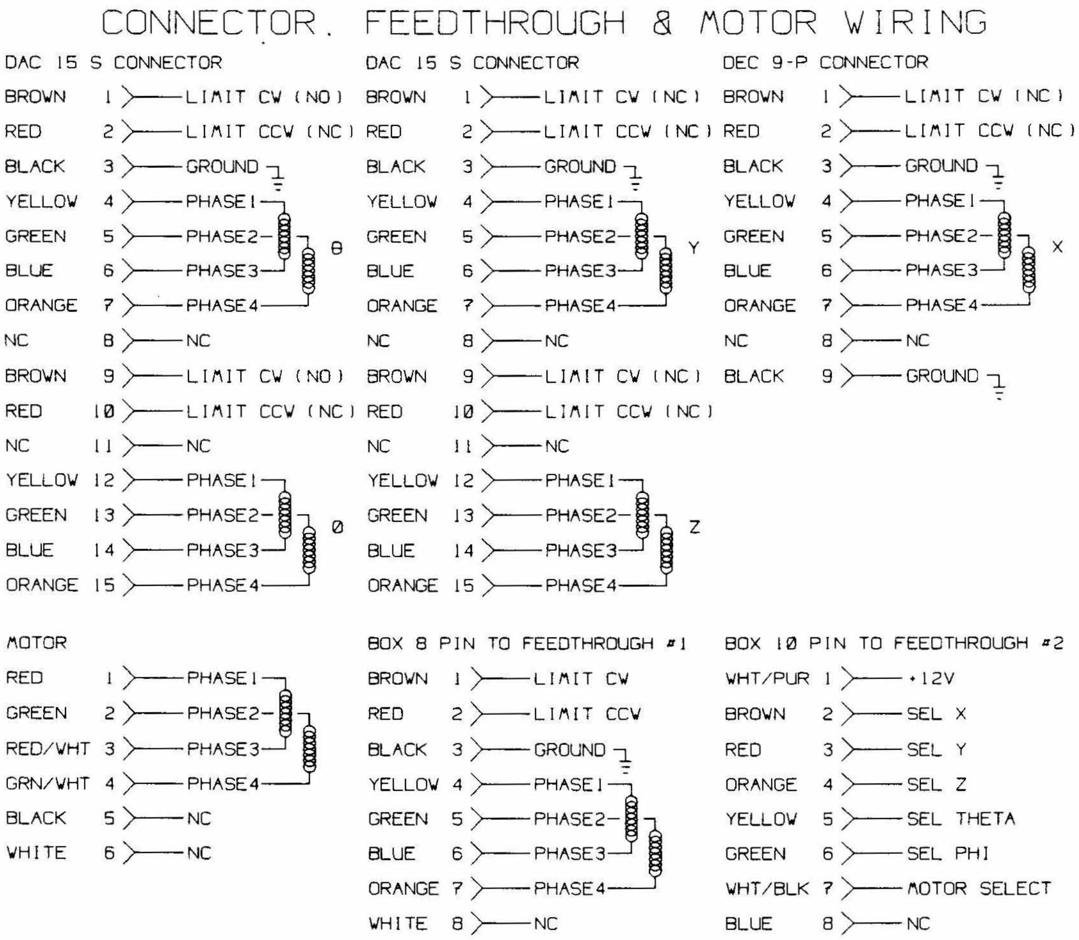
CONNECTOR, FEEDTHROUGH & MOTOR WIRING
DAC 15 S CONNECTOR
BROWN 1 LIMIT CW (NO)
RED 2 LIMIT CCW (NC)
BLACK 3 GROUND
YELLOW 4 PHASE1
GREEN 5 PHASE2
BLUE 6 PHASE3
ORANGE 7 PHASE4
θ
NC 8 NC
BROWN 9 LIMIT CW (NO)
RED 10 LIMIT CCW (NC)
NC 11 NC
YELLOW 12 PHASE1
GREEN 13 PHASE2
BLUE 14 PHASE3
ORANGE 15 PHASE4
Ø
DAC 15 S CONNECTOR
BROWN 1 LIMIT CW (NC)
RED 2 LIMIT CCW (NC)
BLACK 3 GROUND
YELLOW 4 PHASE1
GREEN 5 PHASE2
BLUE 6 PHASE3
ORANGE 7 PHASE4
Y
NC 8 NC
BROWN 9 LIMIT CW (NC)
RED 10 LIMIT CCW (NC)
NC 11 NC
YELLOW 12 PHASE1
GREEN 13 PHASE2
BLUE 14 PHASE3
ORANGE 15 PHASE4
Z
DEC 9-P CONNECTOR
BROWN 1 LIMIT CW (NC)
RED 2 LIMIT CCW (NC)
BLACK 3 GROUND
YELLOW 4 PHASE1
GREEN 5 PHASE2
BLUE 6 PHASE3
ORANGE 7 PHASE4
X
NC 8 NC
BLACK 9 GROUND
MOTOR
RED 1 PHASE1
GREEN 2 PHASE2
RED/WHT 3 PHASE3
GRN/WHT 4 PHASE4
BLACK 5 NC
WHITE 6 NC
BOX 8 PIN TO FEEDTHROUGH #1
BROWN 1 LIMIT CW
RED 2 LIMIT CCW
BLACK 3 GROUND
YELLOW 4 PHASE1
GREEN 5 PHASE2
BLUE 6 PHASE3
ORANGE 7 PHASE4
WHITE 8 NC
BOX 10 PIN TO FEEDTHROUGH #2
WHT/PUR 1 +12V
BROWN 2 SEL X
RED 3 SEL Y
ORANGE 4 SEL Z
YELLOW 5 SEL THETA
GREEN 6 SEL PHI
WHT/BLK 7 MOTOR SELECT
BLUE 8 NC

Figure 23.

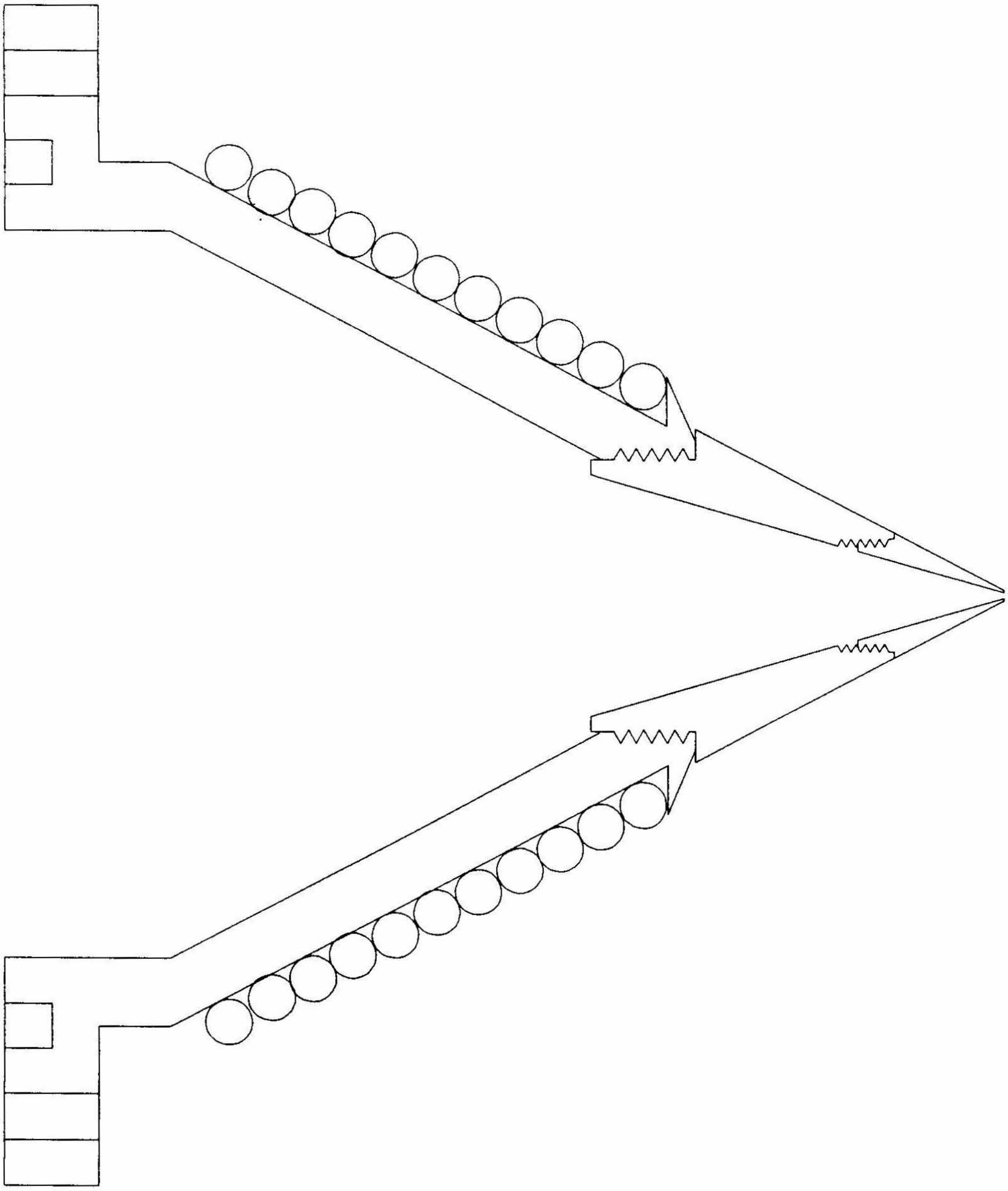

Figure 24.

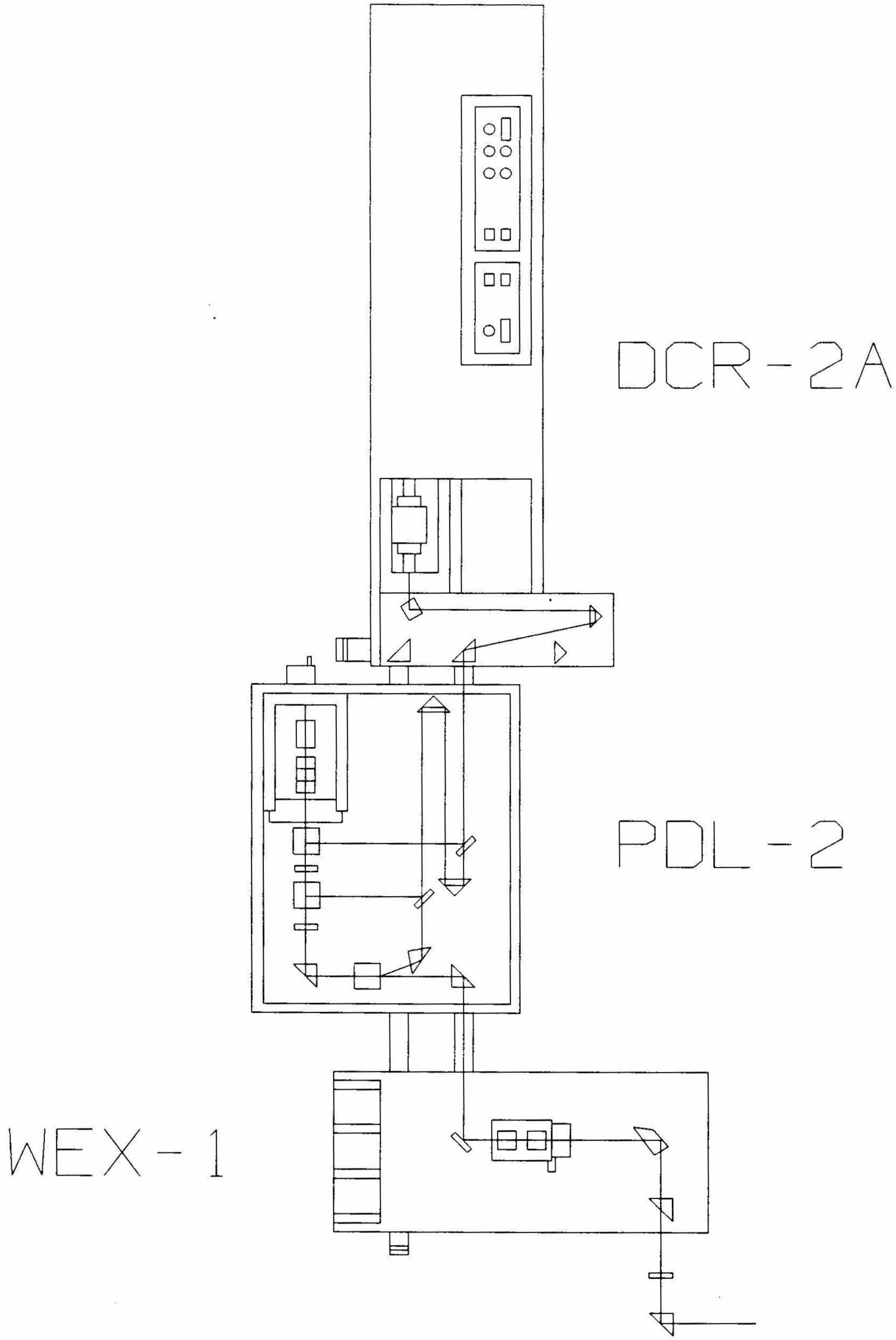

Figure 25.

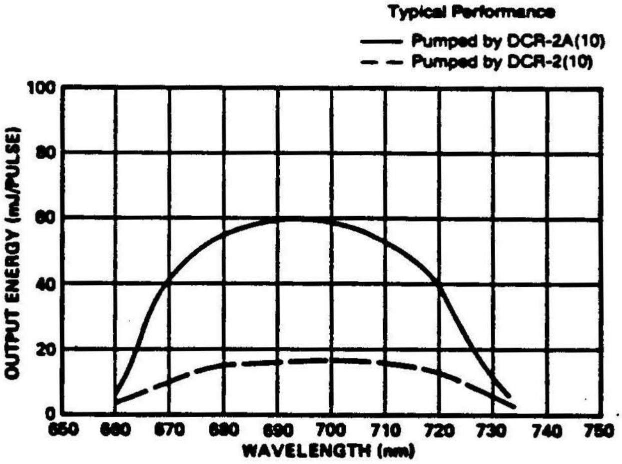
Typical Performance
Pumped by DCR-2A(10)
Pumped by DCR-2(10)
OUTPUT ENERGY (mJ/PULSE)
100
80
60
40
20
0
650
660
670
680
690
700
710
720
730
740
750
WAVELENGTH (nm)

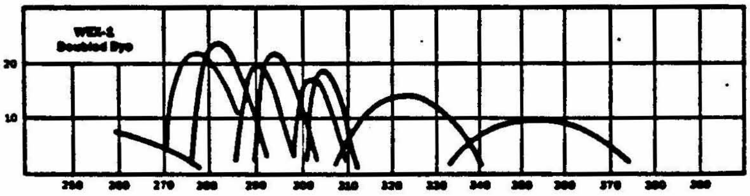
WEX-1
Doubled Dye
20
10
250
260
270
280
290
300
310
320
330
340
350
360
370
380
390

Chapter 7.

Rovibrational Population Measurements

I. Introduction

In order to understand the reason behind the long lifetime ($> 40\mu$sec) of metastable H_3 molecules in our beam, it would be useful to determine the rovibrational population distribution of the beam. The longest lived rovibrational states of ${}^2A_2''$ electronic state of the H_3 molecule are those in the ground rotational state, due to the fact that predissociation to the ground state occurs through rotational coupling. Thus, it is expected that the H_3 molecules in the beam are in those states with no rotational energy.

As shown by Helm,[1] the rovibrational population can be measured with the help of a dye laser aligned coaxially with the H_3 molecular beam. The laser is tuned so as to excite transitions to high Rydberg states of H_3. The excited molecules are then electric field ionized and mass analyzed.

II. Proposed Experiment

The Experimental apparatus used for the rovibrational population measurements is depicted in Figure 1. An arc discharge source used to produce an intense stable beam of H_3 molecules in their $2p^2A_2''$ electronic state. This source is discussed in Chapter 6 section I.C. and its operation is described in Chapter 6 section I.D. Ions are swept out of the beam path by the electric field produced by the deflection plates (D), therefore, beyond this point the beam consists of only neutral species. This beam of H_3 molecules is then crossed with a 20 Hz dye laser aligned coaxially with the beam. The laser is tuned over the range from $\sim 335 - 370$ nm to excite transitions to high-n Rydberg states ($7 < n < 40$) of the H_3 molecule. Over this range the dye laser provides 10 ns pulses having energies of typically 8-10 mJ and a spectral width of ~ 0.5 cm^{-1}.

Detectable excitation takes place after the first set of deflection plates (D) and up to the the field ionization plates (IL). H_3 molecules which initially have at least one quanta of vibrational excitation are excited into the autoionization continuum and therefore do not require an electric field for ionization. H_3 molecules initially in their ground vibrational state are excited to high-n Rydberg states and are easily and efficiently ionized by a DC electric field of the appropriate field strength. The ions produced are accelerated into the mass spectrometer by the field ionization plates (three plates with a voltage drop between successive plates) which act as an 'ion lens'. The ions produced are then mass analyzed. During these measurements, the mass spectrometer is operated with the ionizer off since the species we are interested in analyzing are ions produced by laser induced auto- or field ionization. The electron multiplier output signal is counted over a time window beginning about 200 ns following the laser pulse and ending after 2.5 μs (corresponding to the time of flight for 8 eV H_3 molecules between (D) and (IL)).

Background noise is eliminated by taking measurements in three different modes. In the first, measurements are taken as described above. In the second mode, measurements are taken as described above except that the H_3 beam is blocked by a mechanical flag placed in its path. In the third mode, measurements are taken as described above except that the laser beam is blocked by a mechanical flag placed in its path instead of in the H_3 beam path. By subtracting the signal measured in the second and third modes from that measured in the first mode, background noise produced by the source and the laser is eliminated.

Some of the vibrational bands in these electronic transitions have already been tentatively assigned by Helm.[1] He was able to assign transitions belonging to five Rydberg series which he labelled A, B, B′, C and D. Helm observed longlived metastable H_3 produced by means other than ours. The initial electronic state of the molecules he observed was $2p^2A_2''$ and they were all in the ground rotational state (no rotational energy) with varying amounts of vibrational energy. This is what was expected to exist in our beam. However, it is likely that there exists a greater number of vibrational states in our beam due to the manner in which it is produced.

Helm found that the line positions in these series could be represented with a precision of better than 0.5 cm^{-1} using the following expression

$$E_n = T_\infty - \frac{R}{(n - \delta_{eff})^2} \tag{7.1}$$

where $R = 109717.39\ cm^{-1}$. A fit of this equation to the spectra he observed yielded the series limits T_∞ and effective quantum defects δ_{eff} listed in Table 1 of Figure 2. Also shown in Figure 2 are the spectra he observed and tentative assignments made. This information should facilitate the interpretation of results.

III. Laser Induced Field Ionization

The method of ionization spectroscopy can be used to monitor the absorption of photons on a molecular transition $E_k \rightarrow E_{k'}$. The number of photons absorbed per second when the laser is tuned to the corresponding wavelength ($\lambda_L = \frac{hc}{E_{k'} - E_k}$) is given by

$$n_{abs} = N_k \sigma_{kk'} n_L \Delta x \tag{7.2}$$

where N_{mitk} is the density of molecules in the absorbing state E_k, $\sigma_{kk'}$ is the absorption cross section per molecule, n_L is the number of incident photons per second, and Δx is the absorbing pathlength.[2]

The absorption of photons is monitored by detecting ions or electrons that are produced by some means while the molecule is in its excited state E_k. The ionization of the excited molecule can be brought about in various ways. One commonly used method is field ionization. If the excited level E_k lies close in energy to the ionization limit, the molecule $M^*(E_k)$ can be ionized by an external electric dc field. This method is very efficient when the excited level is a longlived highly excited Rydberg state. An estimation of the minimum electric field required to bring about ionization can be made using Bohr's atomic model. This model gives a good approximation for atomic levels that have a large principle quantum number n. The ionization potential for the outer electron at a mean radius r from the nucleus is determined by the coulomb field of the nucleus screened by the inner electron core. Using this approximation the ionization potential is given by

$$IP = \int_r^\infty \frac{Z_{eff} e^2}{4\pi\varepsilon_0 r^2} dr = \int_r^\infty E_{eff} dr \tag{7.3}$$

where the ionization potential is in electron volts and $Z_{eff}e$ is the effective nuclear charge (the nuclear charge Ze partly screened by the inner electron core). If an external field $E_{ext}(r) > E_{eff}(r)$ is applied, field ionization occurs. A schematic energy level diagram for field ionization of atoms is shown in Figure 3. The actual field required for complete ionization is somewhat lower due to quantum mechanical tunnelling.[2]

Evaluation of the sensitivity of ionization spectroscopy for detecting the absorption of photons on a molecular transition $E_k \rightarrow E_{k'}$ follows. Let $N_{k'}$ be the density of excited molecules in level $E_{k'}$, $P_{k'I}$ be the probability per second that a molecule in level $E_{k'}$ is ionized and n_{abs} be the number of photons absorbed per second on the molecular transition $E_k \rightarrow E_{k'}$. If $R_{k'}$ is the total relaxation rate of level $E_{k'}$, excluding the ionization rate (spontaneous transitions plus collision-induced deactivation) then the signal rate in counts per second is given by

$$S = N_{k'} P_{k'I} \delta\eta = n_{abs} \frac{P_{k'I}}{P_{k'I} + R_{k'}} \delta\eta \tag{7.4}$$

where δ is the ion collection efficiency, and η is the detection efficiency. With the proper set up, a collection efficiency δ of 100% for the electrons or ions can be achieved. In addition, if the electrons or ions are accelerated to several keV and detected using an electron multiplier or channeltron, a detection efficiency η of 100% can also be achieved. For the ideal case, $\delta = \eta = 1$ and $P_{k'I} \gg R_{k'}$ Equation 7.4 reduces to

$$S = n_{abs} \tag{7.5}$$

and the signal rate is equal to the rate of photon absorption n_{abs}. In practice there are other losses and sources of noise which result in a somewhat lower efficiency. However, for all absorbing transitions $E_k \rightarrow E_{k'}$, where the excited level $E_{k'}$ can be readily ionized, ionization spectroscopy is the most sensitive detection technique.[2]

IV. The Spectroscopy of H_3

As stated earlier, the equilibrium geometry of the H_3 molecule is that of an equilateral triangle and possesses D_{3h} symmetry. The character table for this point group is shown in Figure 4. A molecule containing N atoms possesses 3N degrees of freedom. Since the H_3 molecule is nonlinear it has 3 translational degrees of freedom, 3 rotational degrees of freedom and 3 vibrational degrees of freedom. Under D_{3h} symmetry the 3 normal modes of vibration transform like a_1' and e'. Therefore, there are two fundamental vibrational modes ν_1 and ν_2, the second of which is doubly degenerate. The vibrational modes of the H_3 molecule are shown in Figure 5. The other important quantum numbers that we will be interested in are N and K. Where N is the total angular momentum quantum number apart from spin and K is its projection on the z-axis.[3]

In examining the spectroscopy of the H_3 molecules produced in the beam we will assume that they are all in the $2p^2A_2''$ electronic state with no rotational energy. With this information, we can determine which transitions these molecules will undergo. In considering these transitions we will only be interested in transitions between nondegenerate electronic states. To obtain the selection rules for these transitions we will make the Born-Oppenheimer approximation. Using this approximation, the electronic and nuclear motions can be separated and the wavefunction can be expressed as

$$\Psi_{evs} = \Psi_e(\mathbf{q};\mathbf{Q})\Psi_v(\mathbf{Q})\Psi_s \tag{7.6}$$

where Ψ_e is the electronic wavefunction and depends upon the electronic coordinates and parametrically on the nuclear coordinates, Ψ_v is the nuclear wavefunction and depends upon the nuclear coordinates, and Ψ_s is the spin wavefunction.The electric-dipole moment operator **M** can be separated into a sum over electrons and a sum over nuclei.

$$\mathbf{M} = \sum_{\mathrm{i}} \mathrm{e}\mathbf{q}_{\mathrm{i}} + \sum_{\mathrm{j}} \mathrm{Z}_{\mathrm{j}}\mathrm{e}\mathbf{Q}_{\mathrm{j}} \tag{7.7}$$

$$= (\mathbf{M}_{\mathrm{e}} + \mathbf{M}_{\mathrm{v}}) \tag{7.8}$$

Thus the electric dipole transition moment is given by

$$\mathrm{R}_{\mathrm{e'v'e''v''}} = \int \Psi'^{*}_{\mathrm{evs}} \mathbf{M} \Psi''_{\mathrm{evs}} \mathrm{d}\tau_{\mathrm{evs}} \tag{7.9}$$

$$= \int\int\int \Psi'^{*}_{\mathrm{e}} \Psi'^{*}_{\mathrm{v}} \Psi'^{*}_{\mathrm{s}} (\mathbf{M}_{\mathrm{e}} + \mathbf{M}_{\mathrm{v}}) \Psi''_{\mathrm{e}} \Psi''_{\mathrm{v}} \Psi''_{\mathrm{s}} \mathrm{d}\tau_{\mathrm{e}} \mathrm{d}\tau_{\mathrm{v}} \mathrm{d}\tau_{\mathrm{s}} \tag{7.10}$$

$$= \int \Psi'^{*}_{\mathrm{v}} \Psi''_{\mathrm{v}} \int \Psi'^{*}_{\mathrm{e}} \mathbf{M}_{\mathrm{e}} \Psi''_{\mathrm{e}} \mathrm{d}\tau_{\mathrm{e}} \mathrm{d}\tau_{\mathrm{v}} \int \Psi'^{*}_{\mathrm{s}} \Psi''_{\mathrm{s}} \mathrm{d}\tau_{\mathrm{s}}$$

$$+ \int \Psi'^{*}_{\mathrm{v}} \mathbf{M}_{\mathrm{v}} \Psi''_{\mathrm{v}} \int \Psi'^{*}_{\mathrm{e}} \Psi''_{\mathrm{e}} \mathrm{d}\tau_{\mathrm{e}} \mathrm{d}\tau_{\mathrm{v}} \int \Psi'^{*}_{\mathrm{s}} \Psi''_{\mathrm{s}} \mathrm{d}\tau_{\mathrm{s}} \tag{7.11}$$

The electronic wavefunctions Ψ'_{e} and Ψ''_{e} are eigenfunctions of the Hermitian operator $\mathbf{H}_{\mathrm{e}}$ with different eigenvalues; and hence they are orthogonal. Thus Equation 7.11 reduces to

$$\mathrm{R}_{\mathrm{e'v'e''v''}} = \int \Psi'^{*}_{\mathrm{v}} \Psi''_{\mathrm{v}} \int \Psi'^{*}_{\mathrm{e}} \mathbf{M}_{\mathrm{e}} \Psi''_{\mathrm{e}} \mathrm{d}\tau_{\mathrm{e}} \mathrm{d}\tau_{\mathrm{v}} \int \Psi'^{*}_{\mathrm{s}} \Psi''_{\mathrm{s}}. \tag{7.12}$$

For an allowed electronic transition the electric-dipole transition moment must be nonzero

$$\mathrm{R}_{\mathrm{e'v'e''v''}} \neq 0. \tag{7.13}$$

Therefore the following three conditions must be satisfied simultaneously;[3−5]

$$\int \Psi'^{*}_{\mathrm{e}} \mathbf{M}_{\mathrm{e}} \Psi''_{\mathrm{e}} \mathrm{d}\tau_{\mathrm{e}} \neq 0 \tag{7.14}$$

$$\int \Psi'^{*}_{\mathrm{v}} \Psi''_{\mathrm{v}} \mathrm{d}\tau_{\mathrm{v}} \neq 0 \tag{7.15}$$

and

$$\int \Psi'^{*}_{\mathrm{s}} \Psi''_{\mathrm{s}} \mathrm{d}\tau_{\mathrm{s}} \neq 0 \tag{7.16}$$

To satisfy the first condition requires that

$$\Psi_e'^{*}\mathbf{M}_e\Psi_e'' \tag{7.17}$$

is totally symmetric for at least one orientation of **M**, *i.e.*, the product

$$\Psi_e'^{*}\Psi_e'' \tag{7.18}$$

must belong to the same species as one of the components of **M**. Since the initial electronic state has $^2A_2''$ symmetry, the D_{3h} character table can be used to determine which final state symmetries lead to an allowed transition. The allowed final state symmetries are $^2A_1'$ and E'', or more explicitly ns^2A_1', nd^2A_1' and nd^2E''.[3–5]

To satisfy the second condition requires that

$$\Psi_v'^{*}\Psi_v'' \tag{7.19}$$

is totally symmetric. There are two fundamental vibrational modes under D_{3h} symmetry and both must satisfy the above condition. The ν_1 vibrational mode is symmetric for all values of ν_1. Therefore,

$$\Delta\nu_1 = 0, \pm1, \pm2, \pm3, ... \tag{7.20}$$

The ν_2 vibrational mode is antisymmetric. This mode is symmetric for even ν_2 and antisymmetric for odd ν_2. The product of the initial and final wavefunctions is totally symmetric when ν_2 is even in both states or odd in both states.[3–5] Thus we get that

$$\Delta\nu_2 = 0, \pm2, \pm4, \pm6, ... \tag{7.21}$$

To satisfy the third condition we must have that

$$\Psi_s'^{*}\Psi_s'' \tag{7.22}$$

is totally symmetric. Therefore, we get the selection rule for spin

$$\Delta S = 0 \ , \tag{7.23}$$

implying that only states with the same multiplicity combine with each other.[3−5]

If the rotational structure of the transitions is also considered, we must include a rotational eigenfunction in the total wavefunction

$$\Psi_{\mathrm{evsr}} = \Psi_{\mathrm{e}}(\mathbf{q};\mathbf{Q})\Psi_{\mathrm{v}}(\mathbf{Q})\Psi_{\mathrm{s}}\Psi_{\mathrm{r}}(\cos\alpha_{\mathrm{x_i x_j}}). \tag{7.24}$$

The form of the electric-dipole moment operator becomes much more complex

$$\mathbf{M} = \sum_{j=1}^{3}(M_x\cos\alpha_{xj} + M_y\cos\alpha_{yj} + M_z\cos\alpha_{zj}) \tag{7.25}$$

where M_x, M_y and M_z are the x, y and z components of the electric-dipole moment operator discussed above. The angles α_{ij} are the Euler angles between the molecule fixed j-axis and the space fixed i-axis.[3−5]

The condition for an allowed transition now also requires that

$$\int \Psi'_{\mathrm{r}}\cos\alpha_{ij}\Psi''_{\mathrm{r}}d\tau_{\mathrm{r}} \neq 0 \tag{7.26}$$

for at least one of the α_{ij}. This condition is satisfied for

$$\Delta N = 0, \pm 1 \quad \text{and} \quad \Delta K = 0 \quad \text{if} \quad K \neq 0 \tag{7.27}$$

or

$$\Delta N = \pm 1 \quad \text{and} \quad \Delta K = 0 \quad \text{if} \quad K = 0 \tag{7.28}$$

when the transition moment is parallel to the z-axis. When the transition moment is perpendicular to the z-axis, we get the selection rule,

$$\Delta N = 0, \pm 1 \quad \text{and}\Delta K = \pm 1 \ . \tag{7.29}$$

The relative intensities of these transitions are determined by the Franck-Condon principle. This principle is based on the idea that the electron jump takes places so rapidly compared to the vibrational motion that immediately after the transition the nuclei still occupy nearly the same position and have the same velocity as before the jump. Therefore, states with the greatest overlap will be the most populated.[3−5]

For cold absorption, it has been found that the most populated final vibrational state of a symmetric vibration is $\nu_1 = 0$. In hot absorption the most populated final vibrational state of a symmetric vibration corresponds to the state with $\Delta\nu_1 = 0$. In addition, the most populated final vibrational state of an antisymmetric vibration corresponds to the state with $\Delta\nu_2 = 0$. These statements are valid as long as the symmetry in the upper and lower state is the same. The potential minimum occurs at the same value of the antisymmetric coordinate for both states irrespective of any contraction or expansion of the molecule which conserves the symmetry.[3]

To determine the relative intensities explicitly requires a great deal of information about the potential energy surfaces of these states. Conversely, by measuring the relative intensities of these transitions one can obtain information pertaining to the shapes of the initial and final potential energy surfaces.

Using time-dependent perturbation theory, the absorption cross section can be written as

$$\sigma_{kk'} = \frac{4\pi^2\alpha}{\mu^2\omega_{k'k}}\left|\left\langle k'\middle|e^{i\omega_{k'k}(\hat{\mathbf{n}}\cdot\mathbf{r})/c}(\mathbf{p}\cdot\hat{\mathbf{e}})\middle|k\right\rangle\right|^2 \tag{7.30}$$

where $\sigma_{kk'}$ is the absorption cross section, α is the fine structure constant, μ is the reduced mass, k is the initial state, k' is the final state, $\hat{\mathbf{n}}$ is a unit vector pointing in the direction of propagation, c is the speed of light, $\mathbf{r}$ is the radius vector, $\mathbf{p}$ is the momentum operator, $\hat{\mathbf{e}}$ is a unit vector in the direction of the linear polarization, and $\omega_{kk'}$ is the frequency of the absorbed light given by

$$\omega_{k'k} = \frac{(\mathrm{E}_{k'} - \mathrm{E}_k)}{\hbar}. \tag{7.31}$$

If the wavelength of the incident light $\lambda_\mathrm{L} = \frac{2\pi c}{\omega_{k'k}}$ is large compared with the linear dimensions of the absorbing system, the exponential operator can be expanded in a power series

$$\mathrm{e}^{i\omega_{k'k}(\hat{\mathbf{n}}\cdot\mathbf{r})/c} = 1 + i\omega_{k'k}(\hat{\mathbf{n}}\cdot\mathbf{r})/c + ... \tag{7.32}$$

Only the first nonvanishing term in the corresponding matrix elements is retained. For allowed electric dipole transitions the first term is nonzero. Thus the absorption cross section becomes

$$\sigma_{kk'} = \frac{4\pi^2\alpha}{\mu^2\omega_{k'k}}\left|\langle k'|\mathbf{p}\cdot\hat{\mathbf{e}}|k\rangle\right|^2. \tag{7.33}$$

If the Hamiltonian has the form

$$\mathrm{H}_\mathrm{o} = \frac{\mathbf{p}^2}{2\mu} + \mathrm{V}_\mathrm{o} \tag{7.34}$$

and if V_o commutes with $\mathbf{r}$, then

$$\mathbf{r}\mathrm{H}_\mathrm{o} - \mathrm{H}_\mathrm{o}\mathbf{r} = \frac{i\hbar\mathbf{p}}{\mu}. \tag{7.35}$$

By taking the matrix element of both sides of Equation 7.35, we get

$$\langle k'|\mathbf{p}|k\rangle = \frac{\mu}{i\hbar}(\mathrm{E}_k - \mathrm{E}_{k'})\langle k'|\mathbf{r}|k\rangle. \tag{7.36}$$

However, this can be rewritten as

$$\langle k'|\mathbf{p}|k\rangle = i\mu\omega_{k'k}\langle k'|\mathbf{r}|k\rangle. \tag{7.37}$$

The absorption cross section can then be written as

$$\sigma_{kk'} = 4\pi^2\alpha\omega_{k'k}\left|\langle k'|\mathbf{r}\cdot\hat{\mathbf{e}}|k\rangle\right|^2 \tag{7.38}$$

and if the eigenfunctions for the initial and final states are approximately known, the absorption cross section can be calculated.[6]

V. Estimate of Expected Signal

To estimate the expected signal, several assumptions must be made. The first is that all of the H_3 molecules produced in the beam which live long enough to pass through the deflection plates are in the $2p^2A_2''$ electronic state. This is reasonable to assume since:

(i) the highly excited Rydberg states of H_3 ($n \geq 25$) are field ionized and therefore swept out of the beam path by the 1 kV/cm field produced by the deflection plates[7,8]

and

(ii) radiative lifetimes of states with $n \leq 25$ are expected to be less than 10 μsec[9−11] and therefore would not live long enough to make it to the deflection plates. However, the $2p^2A_2''$ state is excluded from this generalization since transitions to the ground state are electronically and vibronically forbidden.

Since rovibronic coupling of the $2p^2A_2''$ state to the ground state can result in rovibronic predissociation of the H_3 molecule, it will be assumed that all of the H_3 molecules that live long enough to pass the deflection plates are in their ground rotational state. This is also reasonable since the $2p^2A_2''$ electronic state of H_3 can rovibronically couple with the ground state if the molecule possess any rotational energy and result in rovibronic predissociation. If the H_3 molecules possesses no rotational energy this process is forbidden and therefore such molecules would be expected to live longer.

It is expected that these H_3 molecules have varying amounts of vibrational energy. As stated earlier, there are two fundamental modes ν_1 and ν_2 for H_3 molecule having D_{3h} symmetry.[3] The second fundamental vibrational mode is doubly degenerate. If we assume that the only states present in the beam are those with

$$\nu_1 = 0,\ 1,\ 2,\ \text{or } 3 \tag{7.39}$$

and

$$\nu_2 = 0,\ 1,\ 2,\ \text{or } 3 \tag{7.40}$$

then there exists 16 possible vibrational states of these molecules. In addition, let us assume that each of these states represent between 1 and 10 % of the total H_3 molecule intensity.

Since the absorption cross sections for H_3 are not known, the last assumption is that the cross section for absorption of a photon by H_3 is of the order of 1 $Å^2$ (10^{-16} cm^2). The cross sections for allowed electric dipole transitions are typically of this order.

To estimate the expected signal the number density of the H_3 beam must be known. The number density of the H_3 molecules at the mass spectrometer is $\sim 6.9 \times 10^9$ molecules cm^{-3}. Since the beam expands as it traverses the path to the mass spectrometer, its number density along the entire path will be at least this large.

In addition, we need to know the energy output of the dye laser at the appropriate wavelength. Over the range of wavelengths to be examined $\sim$ 335 – 370 nm, the output of the dye laser varies between 8 to 10 mJ. For a 20 Hz laser this corresponds to an incident intensity of 2.82×10^{17} photons/s.

The maximum path length must also be known. The distance between the first set of deflection plates and the field ionization plates is 5 cm. This corresponds to the maximum pathlength since any molecules excited to high Rydberg states before the first set of deflection plates will be swept out of the beam path by the field produced by them. Also any molecules excited to high Rydberg states after the field ionization plates will not be field ionized and therefore not detected.

If we assume that the absorbing species represent 10% of the total H_3 molecule intensity and that the rate of ionization is much larger than the total relaxation rate of the excited molecules, then we can use Equation 7.4 to calculate the expected signal. Doing so, we obtain

$$S = 9.7 \times 10^{10} \text{ Hz} . \qquad (7.41)$$

This assumes an ion collection and detection efficiencies of unity. Even if the absorbing species only represent 1 % of the total H_3 intensity and the cross section is only of the order of .01 Å^2 (10^{-18} cm^2) and the ion collection and detection efficiencies are only 10 %, this would still result in an expected signal of

$$S = 9.7 \times 10^{5} \text{ Hz} \qquad (7.42)$$

which can be easily measured.

VI. Estimate of Background Noise

For an estimate of expected signal to be useful, an estimate of expected background noise is also needed. In this proposed experiment most of the background noise will arise from one of four sources; ions present in the beam before laser induced field ionization, light emanating from the source, scattered laser light, and electrical noise produced by the firing of the laser.

The elimination of background noise due to the presence of any ions in the beam is very important due to the fact we are only interested in detecting ions produced by the laser induced field ionization. In order to effectively eliminate the ions from the beam before they reach the mass spectrometer, an electrostatic field perpendicular to the beam direction is placed in the path of the beam. This field is produced by a pair of deflection plates whose position is indicated in Figure 1 (the size of the plates is exaggerated for clarity). They consist of two .005" thick pieces of copper having dimensions of .450" by 1", and are separated by a 0.5 cm gap through which the beam passes.

Any species having a charge e passing through a field Φ experiences a force in the direction of the field given by

$$F = e\Phi. \tag{7.43}$$

This results in a deflection of ions in the beam equal to

$$x = \frac{eV}{2md} \frac{\ell^2}{{v_t}^2} \tag{7.44}$$

where V is the potential difference between the plates , ℓ is the length, d is the gap between them, v_t is the translational velocity of the ions and m the mass of the ions. For the experimental conditions being used, this results in

$$x = .1249 \frac{m\Phi}{E} \tag{7.45}$$

where m is the mass of the species in atomic units, E is the energy of the ion in eV, Φ is the deflection field in volts/cm and x is the deflection in cm. For example, for an H_3^+ ion with an energy of 15 eV passing through a field of 800 volts/cm will have undergone a deflection of 20 cm away from the beam axis by the time it emerges from the deflection plates, indicating that nearly all of the ions should be eliminated from the beam.

The effectiveness of these deflection plates in cleaning ions out of the beam was measured. The DC ion intensity at m/e = 3 was monitored as a function of applied field. The mass spectrometer was operated in the manual mode and tuned to the m/e =3 peak with the ion energy lens and the focus lens turned off to discriminate against the thermal background signal. The intensity of the peak was recorded as a function of deflection field and is shown in Figure 6. A rapid drop-off in intensity was observed until a field of approximately 500 volts/cm was reached, after which the intensity decreased much more slowly with increasing fields. Apparently after this point a majority of the ions have been swept out of the beam path leaving the signal due mainly to neutral species. Thus background noise resulting from ions present in the beam before laser induced field ionization should play a negligible role in these experiments.

The elimination of background noise due to light emanating from the source or from scattered laser light was accomplished by replacing the existing electron multiplier with an AEM-2000 solar blind multiplier. Its has been designed so that its first dynode is off axis rendering it insensitive to line of sight radiation and neutrals. Thus background noise resulting from light emanating from the source or from scattered laser light plays only a negligible role in these experiments.

The elimination of electrical noise produced by the firing of the laser system is essentially impossible, however, due to its magnitude some means must be found to subtract out such noise. This is done by measuring the signal produced when the laser is fired and the light is allowed to interact with the H_3 beam and then measuring the signal produced when the laser is fired and the light is kept from interacting with the H_3 beam by placing a mechanical flag in the H_3 beam path. The signal measured in the first case will correspond to the true signal plus background, in the second case, only to the background noise produced by the laser. Thus noise produced by the laser is subtracted out and therefore plays a negligible role in these experiments.

VII. References

1. H. Helm, *Phys. Rev. Lett.* **56**, 42 (1986).
2. W. Demtröder, *Laser Spectroscopy: Basic Concepts and Instrumentation*, (Springer-Verlag, New York, 1982) p.398ff.
3. G. Herzberg, *Molecular Spectra and Molecular Structure III: Electronic Spectra and Electronic Structure of Polyatomic Molecules*, (Van Nostrand Reinhold Co., New York, 1966). p. 45, 128ff., 298.
4. I. N. Levine, *Molecular Spectroscopy*, (John Wiley & Sons, New York, 1975) p. 195ff., 235ff., 296ff.
5. J. I. Steinfield, *Molecules and Radiation: An Introduction to Modern Molecular Spectroscopy*, (MIT Press, Cambridge, 1974) p. 214ff., 230ff., 262ff.
6. E. Merzbacher, *Quantum Mechanics*, (John Wiley & Sons, New York, 1970) p.450ff.
7. J. F. Garvey, Ph. D. Thesis, California Institute of Technology, 1985.
8. J. F. Garvey and A. Kuppermann, *Chem. Phys. Lett.* **107**, 491 (1984).
9. H. A. Bethe and E. E. Salpeter, *Quantum Mechanics of One- and Two-Electron Atoms*, (Springer-Verlag, Berlin, 1957).
10. R. F. Stebbings, C. J. Latimer, W. P. West, F. B. Dunning and T. B. Cook, *Phys. Rev.* **A12**, 1453 (1975).
11. L. Allen, D. G. C. Jones, and D. G. Schofield, *J. Opt. Soc. Amer.* **59**, 842 (1969).

VIII. Figure Captions

Figure 1. A schematic view of the top of the machine: VC1, vacuum chamber one; AS, anode assembly; A, anode; C, cathode; M, magnet; S, water cooled skimmer; TA1, TA2, TA3, translation assemblies; RA, rotation assembly; P1,P2, viewports; GV1, gate valve; B1, bellows; VC2, vacuum chamber two; C1, 10 Hz chopper; D1, electric field deflectors; F1, mechanical flag; MVS, magnetic velocity selector; RFT, rotary feedthrough, FT, electrical and cooling water feedthroughs; P3, viewport; GV2, gate valve; B2, bellows; VC3, vacuum chamber 3; C2, 160 Hz chopper; D2, electric field deflectors; F2, mechanical flag; FIP, field ionization plates; QMS, quadrupole mass spectrometer; P4, viewport; PA, EAI preamplifier (ESA-75); LI1, lock-in amplifier; MSE, mass spectrometer electronics; SCR1, strip chart recorder.

Figure 2. Summary of Helm's results: a) Table 1; the observed Rydberg series of the H_3 molecule. The state designation is (ν_1, ν_2, N, K) for the lower state and (ν_1, ν_2, N^+, G) for the H_3^+ core. b) Excitation spectrum of n = 7 states of H_3 . c) Excitation spectrum of high-n Rydberg states of H_3 . Four series are marked in the top of the figure. The series B′ is indicated by the small tick marks along with series B.

Figure 3. Schematic energy level scheme for field ionization of atoms.

Figure 4. The character table for the D_{3h} point group.

Figure 5. The fundamental vibrational modes of H_3 molecule; ν_1 *and* ν_2.

Figure 6. DC ion intensity of the m/e = 3 peak as a function of electric field of the deflector plates. The electron impact ionizer is on with a current of 150 μA.

Figure 1.

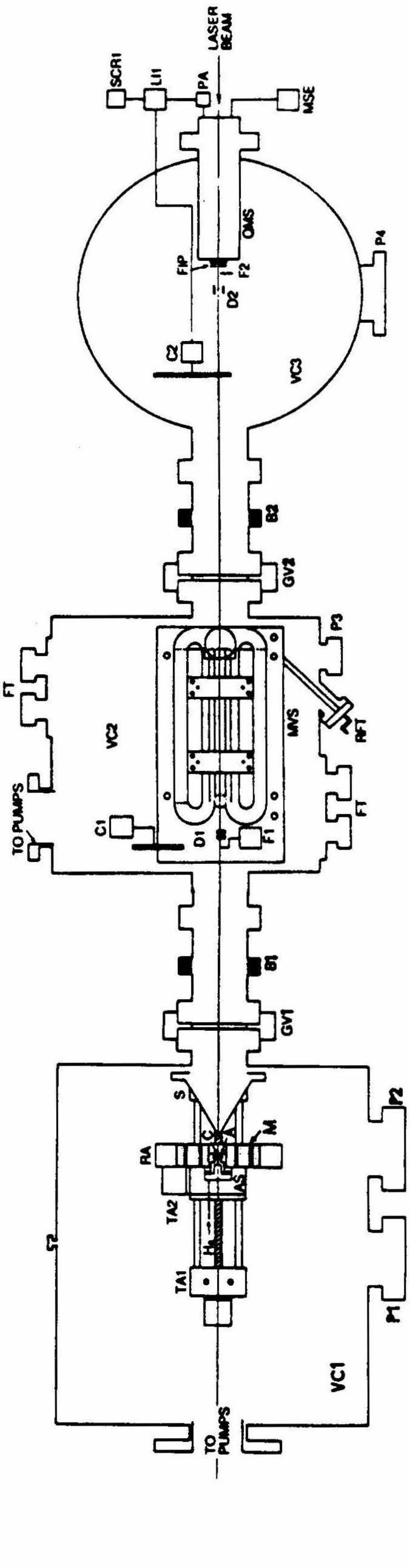
LASER BEAM
SCR1
LI1
PA
MSE
OMS
FIP
F2
D2
C2
VC3
P4
B2
GV2
P3
FT
VC2
MVS
RFT
TO PUMPS
C1
D1
F1
FT
B1
GV1
S
RA
C
A
M
TA2
AS
H
TA1
P2
P1
VC1
TO PUMPS

Figure 2.

TABLE I. Observed Rydberg series of H_3 molecule. The state designation is (ν_1, ν_2, N, K) for the lower state and (ν_1, ν_2, N^+, G) for the H_3^+ core.

Series	$\tilde{B}\, 2p\, {}^2A_2''$	Upper state H_3^+ core		T_∞ (cm^{-1})	δ_{eff}	Observed n range
A	(0,0,0,0)	(0,0,1,0)	· · ·	29 566.0	[a]	33–40
B	(0,1,0,0)	(0,1,1,1)	*nd*	29 485.5	0.022	7,8,12–40
B'	(0,1,0,0)	(0,1,1,1)	*ns*	29 485.5	0.073	7,12–32
C	(· · · ·)	(· · · ·)	*nd*	29 402.0	0.02	13–36
D	(1,0,0,0)	(1,0,1,0)	*nd*	29 469.5	0.02	7,12–32

[a] When series *A* is fitted together with the *R*0 ($3s - 2p$) transition (Ref. 2) a value $\delta_{eff} = 0.0803$ is obtained. When fitted together with the *R*0 ($3d - 2p$) transition (Ref. 5) $\delta_{eff} = 0.0095$ is obtained.

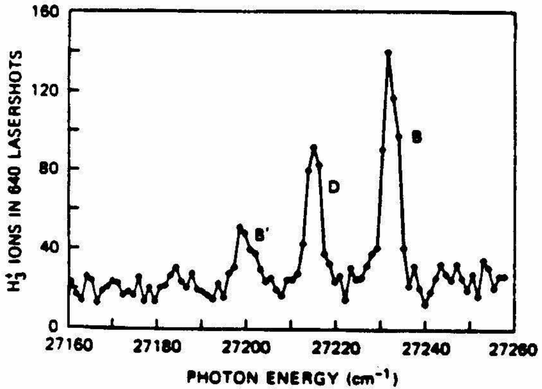

FIG. 2. Excitation spectrum of $n = 7$ states of H_3.

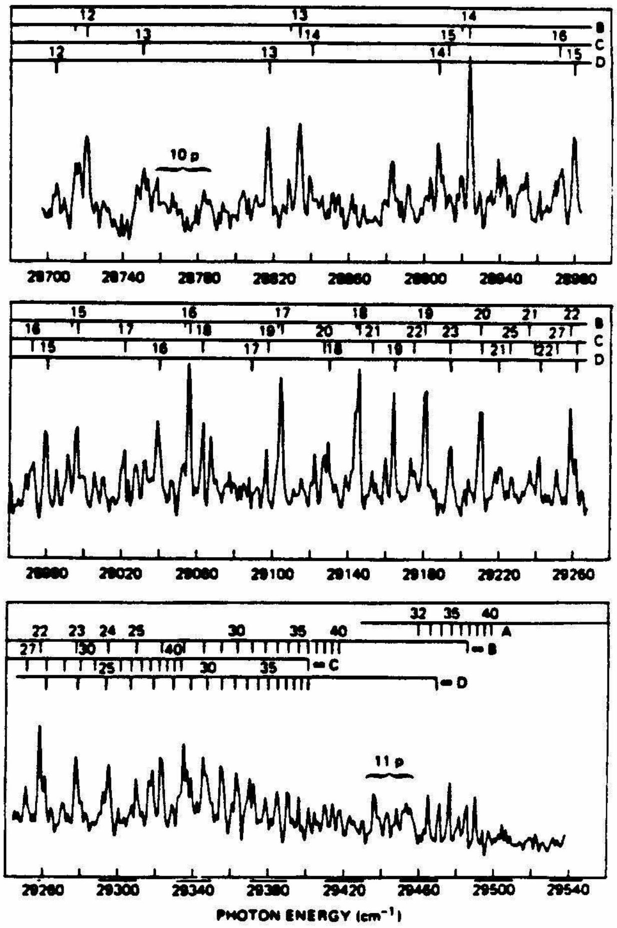

FIG. 3. Excitation spectrum of high-n states of H_3. Four series are marked in the top of the figure. The series *B'* is indicated by the small tick marks along with series *B*.

Figure 3.

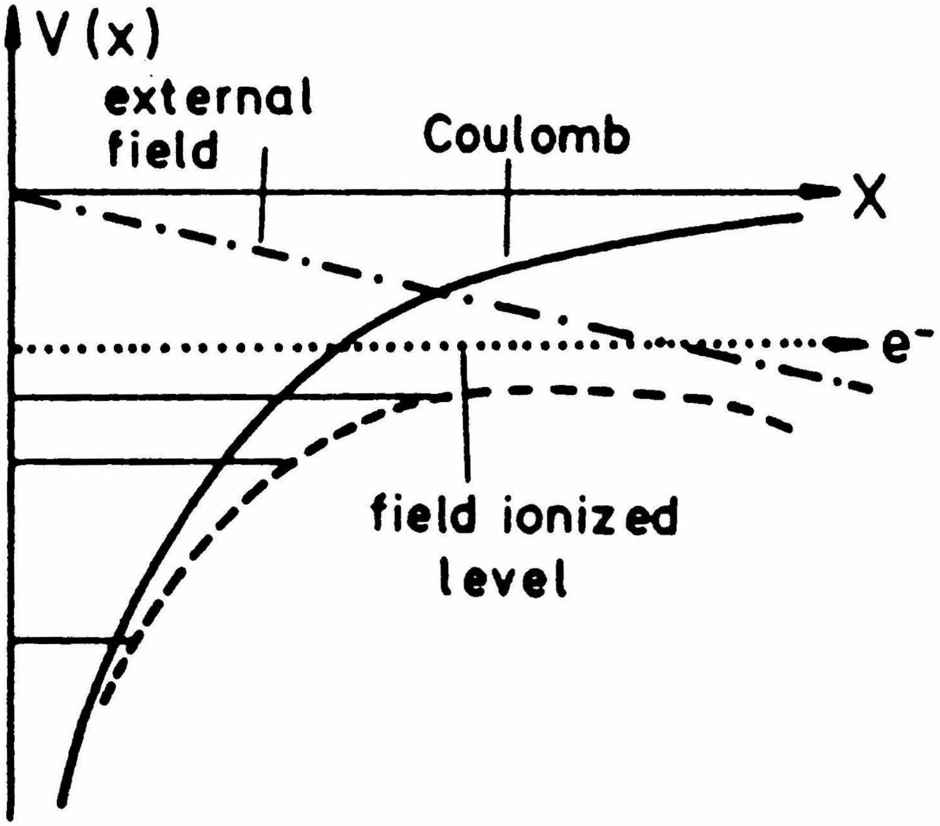

Figure 4.

D_{3h}	E	$2C_3$	$3C_2$	σ_h	$2S_3$	$3\sigma_v$		
A_1'	1	1	1	1	1	1		$x^2 + y^2, z^2$
A_2'	1	1	-1	1	1	-1	R_z	
E'	2	-1	0	2	-1	0	(x, y)	$(x^2 - y^2, xy)$
A_1''	1	1	1	-1	-1	-1		
A_2''	1	1	-1	-1	-1	1	z	
E''	2	-1	0	-2	1	0	(R_x, R_y)	(xz, yz)

D_{3h}	A_1'	A_2'	A_1''	A_2''	E'	E''
A_1'	A_1'	A_2'	A_1''	A_2''	E'	E''
A_2'		A_1'	A_2''	A_1''	E'	E''
A_1''			A_1'	A_2'	E''	E'
A_2''				A_1'	E''	E'
E'					$A_1', [A_2'], E'$	A_1'', A_2'', E''
E''						$A_1', [A_2'], E'$

Figure 5.

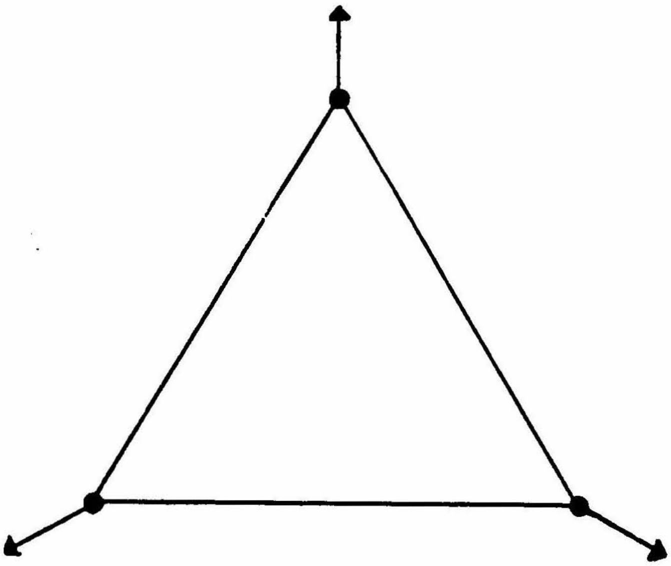

$\nu_1\ (a_1')$

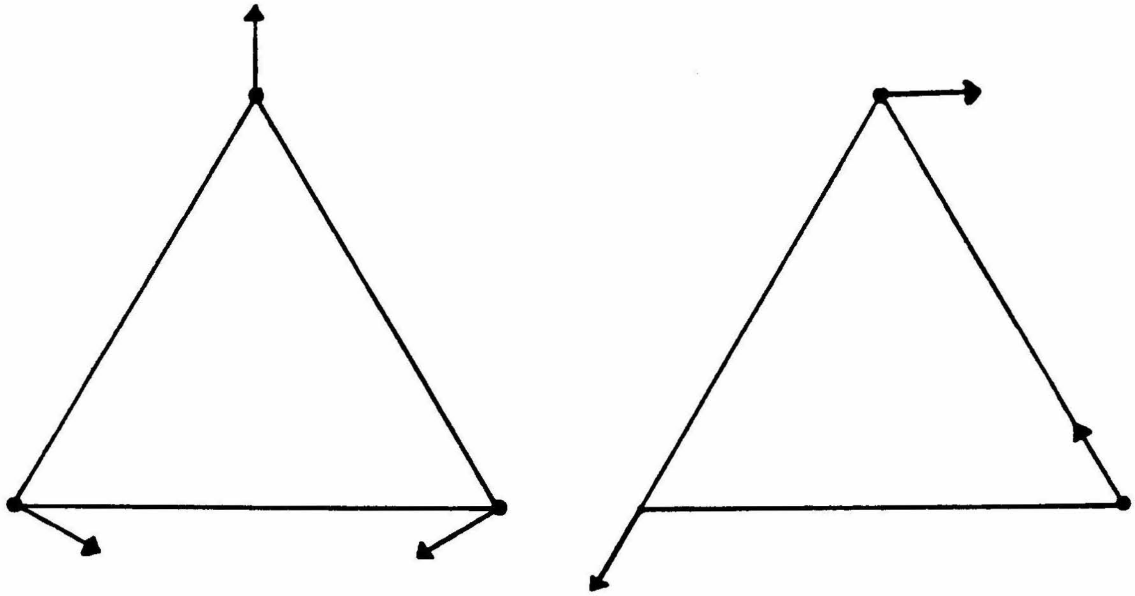

$\nu_2\ (e')$

Figure 6.

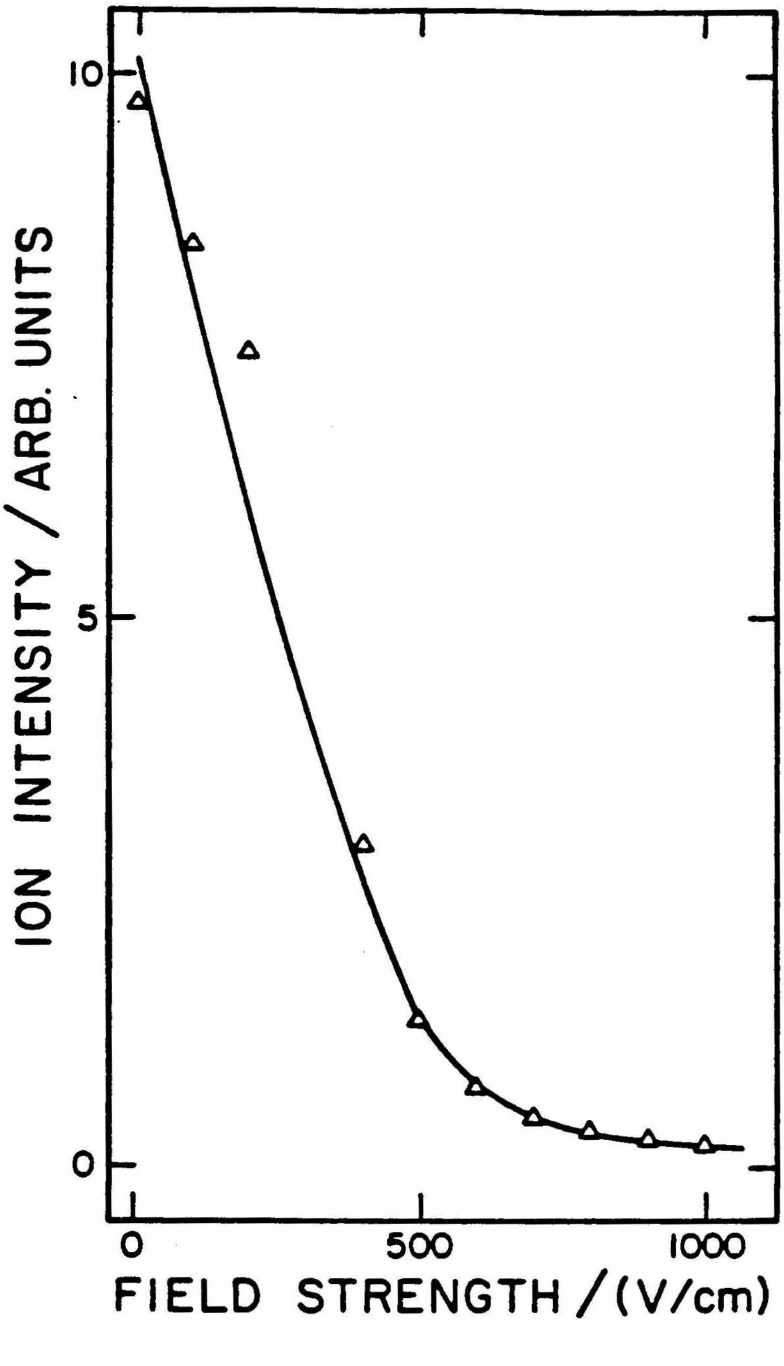

Chapter 8.

Lifetime Measurements

I. Introduction

In order to understand the reason behind the long lifetime ($> 40\ \mu$sec) of the metastable H_3 molecules in our beam, and whether or not this beam could be used in various applications, a better estimate of its lifetime is needed. Although radiative transitions from the $2p\,^2A_2''$ electronic state to the ground $^2E'$ electronic state are electric dipole forbidden, they are magnetic dipole and electric quadrupole allowed. The corresponding lifetimes are expected to be of the order of 10^{-3} and 1 s respectively.[1] However, these lifetimes have not been measured. Therefore, it would be useful to determine the radiative lifetimes of the magnetic-dipole transition and electric-quadrupole transition from the $^2A_2''$ electronic state to the ground $^2E'$ electronic state, and the lifetime of the electric-dipole transition from the $^2A_2''$ electronic state to the first excited $^2A_1'$ electronic state. The longest lived states of the $^2A_2''$ electronic state of the H_3 molecule are those with no rotational energy because predissociation to the ground state must occur through rovibronic coupling to the ground state, or by one of the above processes. Therefore, determination of the above lifetimes should explain the reason behind the long lifetime of the metastable H_3 molecules in our beam.

II. Proposed Experiment

The experimental set-up for the lifetime measurements is depicted in Figure 1. An arc discharge source is used to produce an intense stable beam of H_3 molecules in their $^2A_2''$ electronic state. The arc discharge source and its operation are discussed in Chapter 6 section I.C and I.D. Ions as well as highly excited Rydberg states of the H_3 molecules are swept out of the beam path by the electric field produced by the deflection plates (DP), therefore, beyond this point the beam consists of only neutral H_3 molecules in their $2p^2A_2''$ electronic state. Other low lying Rydberg states of H_3 are expected to have lifetimes less than 10 μsec,[2−4] and will have already decayed to the $2p^2A_2''$ electronic state or to the ground $2p^2E'$ electronic state and predissociated. Therefore, any emission which occurs beyond the deflection plates is the result of the decay of the $2p^2A_2''$ electronic state of H_3. This intense beam is then passed through a cell similar to the design shown in Figures 2 and 3. By viewing the light emitted from the H_3 beam as it traverses the cell a better estimate of the radiative lifetime can be made.

Attempts to use this cell in the past to observe the spontaneous emission from the $2p^2A_2''$ electronic state have failed due to the large photon background in the chamber. To eliminate this problem, the design of the cell was modified. The entrance and exit of the cell were baffled to eliminate background light emanating from the source and chamber as much as possible. The emitted photons are focused into a monochromator. This allows only those photons having an energy which corresponds to the energy difference between these two states to be detected. These changes eliminate the large photon background which led to the failure of the early attempts to carry out this experiment. The results of this investigation furnish an upper limit to the lifetime of these metastable H_3 molecules.

III. Predissociation Analysis

The equilibrium geometry of the H_3 molecule is that of an equilateral triangle. In this configuration, the H_3 molecule possesses D_{3h} symmetry. The character table for this point group is shown in Figure 4.

To examine the lifetime of the H_3 molecules produced in the beam, it is assumed that they are in the $2p^2A_2''$ electronic state. Reasons for this assumption have been stated previously. Transitions from this state to states with E' symmetry are electric dipole forbidden.[1] However, it has been stated that it can rovibronically couple with the $2p^2E'$ ground state, and result in predissociation. What follows is a brief discussion of predissociation and the validity of this statement.

Predissociation can occur when a discrete state of a system overlaps a continuous range of levels which correspond to a dissociation into atoms, radicals, or ions. The overlapping of the discrete state with the dissociation continuum causes the state to become more diffuse and produces mixing of the eigenfunctions. Therefore, when the system is in the discrete state it will after a period of time end up in the continuous range and fly apart.[1]

The selection rules for predissociation of this state can be obtained by invoking the Born-Oppenheimer approximation

$$\Psi_{\mathrm{evrs}} = \Psi_{\mathrm{e}}\Psi_{\mathrm{v}}\Psi_{\mathrm{r}}\Psi_{\mathrm{s}} \tag{8.1}$$

where these quantities are defined in Chapter 7. The 'predissociation operator', W corresponds to certain neglected terms in the Hamiltonian, and is treated as a perturbation of the system. The matrix element corresponding to this process is given by

$$\mathrm{W} = \int \Psi'^{*}_{\mathrm{evrs}} \hat{\mathrm{W}} \Psi''_{\mathrm{evrs}} d\tau_{\mathrm{evrs}} \tag{8.2}$$

where Ψ'_{evrs} corresponds to the $2p^2A''_2$ electronic state and Ψ''_{evrs} corresponds to the continuum state. Thus the predissociation matrix element is given by

$$W = \int\int\int \Psi_e'^{*}\Psi_v'^{*}\Psi_r'^{*}\Psi_s'^{*}\hat{W}\Psi_e''\Psi_v''\Psi_r''\Psi_s''d\tau_e d\tau_v d\tau_r d\tau_s \tag{8.3}$$

Since $\hat{W}$ is symmetric, W is zero unless

$$\Psi_v'^{*}\Psi_v'' \tag{8.4}$$

and

$$\Psi_s'^{*}\Psi_s'' \tag{8.5}$$

are totally symmetric. These conditions lead to the same selection rules for vibration and spin as in Chapter 7. In addition, one of the two following conditions must also be satisfied;

$$\Psi_e'^{*}\Psi_e'' \tag{8.6}$$

or

$$\Psi_e'^{*}\Psi_r'^{*}\Psi_e'' \tag{8.7}$$

must be totally symetric. Therefore, predissociation to a nondegenerate electronic state can occur only through coupling of rotation and electronic motion, and only when the species of the two electronic states differ by a rotation. Therefore unless the initial state possesses at least one quanta of rotational excitation predissociation is forbidden. For states possessing rotational energy, the probability of transition increases as $J(J+1)$.[1,5,6]

For the $2p^2A''_2$ electronic state predissociation to the ground $2p^2E'$ ground state not is allowed. Predissociation to this state requires a rotation of E'' symmetry (rotation about an axis perpendicular to the z-axis of the molecule).

Since predissociation lifetimes are typically of the order of 10^{-12} s, the H_3 molecules in our beam which live long enough to be detected must be in their ground rotational state.

IV. Radiative Lifetime Analysis

In examining the spontaneous emission of the H_3 molecules produced in the beam we will assume that they are all in the $2p^2A_2''$ electronic state with no rotational energy. Transitions from this state to states with E' symmetry are electric dipole forbidden.[1] However, this transition is magnetic dipole and electric quadrupole allowed. A derivation of the validity of this statement follows. We are interested in the lifetimes of these transitions and not concerned with the rotational and vibrational states of the products therefore, only the electronic transition will be considered.

Let Ψ_e'andΨ_e'' be the electronic eigenfunctions of the upper and lower nondegenerate states respectively of an electronic transition. The magnetic dipole or electric quadrupole transition between these two states is allowed if and only if the matrix element

$$R_{e'e''} = \int \Psi_e'^{*} \mathbf{M} \Psi_e'' d\tau_e \neq 0 \tag{8.8}$$

where **M** is the magnetic dipole moment or electric quadrupole moment operator. For a magnetic dipole transition **M** is an axial vector, its components behave like the three rotations R_x, R_y and R_z. For an electric quadrupole transition **M** is a tensor whose components behave like the components of the polarizibility or like the product of two translations.[1,5,6]

For an allowed transition,

$$\Psi_e'^{*} \mathbf{M} \Psi_e'' \tag{8.9}$$

is totally symmetric for at least one orientation of **M**. Therefore, the product

$$\Psi_e' \Psi_e'' \tag{8.10}$$

must belong to the same symmetry species as one of the components of **M**. Since the initial electronic state has $^2A_2''$ symmetry, the D_{3h} character table can be used to determine which final state symmetries lead to an allowed transition. The allowed final state symmetries for magnetic dipole transitions are $^2A_1'$ and $^2E'$, and for electric quadrupole transitions they are $^2A_2''$, $^2E'$ and $^2E''$. Therefore, radiative transitions from the $2p\,^2A_2''$ electronic state to the $2p_{xy}\,^2E'$ electronic state are both magnetic dipole and electric quadrupole allowed.

The average lifetime τ of these transitions is given by

$$\tau = \frac{1}{A_{k \rightarrow k'}} \tag{8.11}$$

where $A_{k \rightarrow k'}$ is the Einstein coefficient for the spontaneous emission from the state k resulting in state k'. Here k is the $2p\,^2A_2''$ electronic state and k' is the ground $2p\,^2E'$ electronic state.

The Einstein coefficient is given by

$$A_{k \rightarrow k'} = \frac{64\pi^4 \nu_{kk'}^3}{3hc^2} \Big(\int \Psi_e'^{*} M \Psi_e'' d\tau_2 \Big)^2 \tag{8.12}$$

where $\nu_{kk'} = \frac{(E_k - E_{k'})}{h}$. From this expression it is obvious that a different Einstein coefficient exists depending upon whether we are examining magnetic dipole or electric quadrupole transitions. Using the above expression, the lifetime for these transitions can be obtained if the electronic eigenfunctions are known. Conversely, measurement of these lifetimes will provide information pertaining to the shapes of the $^2A_2''$ and $^2E'$ potential energy surfaces.

V. Estimate of Expected Signal

To estimate the expected signal, several assumptions must be made. All of the H_3 molecules that are produced in the beam and that live long enough to make it through the deflection plates are assumed to be in the $2p^2A_2''$ electronic state. This assumption is valid since:

(i) highly excited Rydberg states of H_3 ($n \geq 25$) are field ionized and therefore swept out of the beam path by the 1 kV/cm field produced by the deflection plates

and

(ii) that the radiative lifetimes of states with $n \leq 25$ are expected to be less than 10 μsec and therefore would not live long enough to make it to the deflection plates. However, the $2p^2A_2''$ state is excluded from this estimate since transitions to the ground state are electronically and vibronically forbidden.

The second assumption is that the H_3 molecules have a translational energy of 8 eV. When the translational energy distribution of the H_3 molecules in the beam was measured, it was found to span the range from 0.1 to 15 eV with a maximum at 8 eV. Therefore, it is assumed that the average translational energy of the H_3 beam is ~ 8 eV. This corresponds to a velocity of

$$v = 1.6 \times 10^6 \text{ cm/s}. \tag{8.13}$$

The pathlength, d of detectable emission is ~ 2 cm, this corresponds to a traversal time of

$$t = \frac{d}{v} = 1.3 \times 10^{-6} \text{ s}. \tag{8.14}$$

If the radiative lifetime for the emission of visible photons corresponding to decay to the ground state is assumed to be 10^{-3} s then the Einstein coefficient for this process is estimeated as

$$A_{k \rightarrow k'} = \frac{1}{\tau} = 10^{3}\ \mathrm{s}^{-1} \tag{8.15}$$

where k corresponds to the $2p^2A_2''$ electronic state and k' to the ground $2p^2E'$ electronic state. Using this value, the rate of spontaneous emission to the ground state is given by

$$\frac{dN_{k'}}{dt} = A_{k \rightarrow k'}N_k = A_{k \rightarrow k'}I_k t = 1.2 \times 10^{12}\ \text{photons/s} \tag{8.16}$$

which can easily be measured. A flux of $I_k = 9.0 \times 10^{14}$ molecules/s corresponding to the minimum flux of our H_3 beam was used in this calculation. Even if the lifetime is as large as 1 s, the corresponding emission rate would be 1.2×10^{9} photons/s which can also be easily measured.

VI. Estimate of Background Noise

For an estimate of expected signal to be useful, an estimate of expected background noise is also needed. In this proposed experiment, most of the background noise arises from one of two sources; light emanating from the source and scattered light inside the chamber.

The elimination of background noise due to light emanating from the source and scattered light inside the chamber will be accomplished by baffling the cell used to make these measurements at both the entrance and the exit of the cell. In addition, a monochromator will be used to eliminate any light which does not have a wavelength which corresponds to that emitted by the H_3 molecules in the $2p^2A_2''$ state when they decay to the ground $2p^2E'$ electronic state. Therefore, the background light emanating from the source or from scattered light inside the chamber should play a negligible role in these experiments.

VII. References

1. G. Herzberg, *Molecular Spectra and Molecular Structure III: Electronic Spectra and Electronic Structure of Polyatomic Molecules*, (Van Nostrand Reinhold Co., New York, 1966). p. 45, 128ff., 298.
2. H. A. Bethe and E. E. Salpeter, *Quantum Mechanics of One- and Two-Electron Atoms*, (Springer-Verlag, Berlin, 1957).
3. R. F. Stebbings, C. J. Latimer, W. P. West, F. B. Dunning and T. B. Cook, *Phys. Rev.* **A12**, 1453 (1975).
4. L. Allen, D. G. C. Jones, and D. G. Schofield, *J. Opt. Soc. Amer.* **59**, 842 (1969).
5. I. N. Levine, *Molecular Spectroscopy*, (John Wiley & Sons, New York, 1975) p. 195ff., 235ff., 296ff.
6. J. I. Steinfield, *Molecules and Radiation: An Introduction to Modern Molecular Spectroscopy*, (MIT Press, Cambridge, 1974) p. 214ff., 230ff., 262ff.
7. J. F. Garvey, Ph. D. Thesis, California Institute of Technology, 1985.
8. J. F. Garvey and A. Kuppermann, *Chem. Phys. Lett.* **107**, 491 (1984).

VIII. Figure Captions

Figure 1. A schematic view of the top of the machine: VC1, vacuum chamber one; AS, anode assembly; A, anode; C, cathode; M, axial magnet; TA1, TA2, TA3, translation assemblies; RA, rotation assembly; S, water-cooled skimmer; P1, P2, viewports; GV1, gate valve; B1, bellows; VC2, vacuum chamber two; C1, 10 Hz chopper; D1, electric field deflectors; F1, mechanical flag; MVS, magnetic velocity selector; RFT, rotary feedthrough; FT, electrical and water feedthroughs; P3, viewport; GV2, gate valve; B2, bellows; VC3, vacuum chamber three; C2, 160 Hz chopper, D2, electric field defectors; F2, mechanical flag; SM spherical mirror P4, mounting port for photoionization cell; IG, ion gauge; QMS, quadrupole mass spectrometer; PA, EAI preamplifier (ESA-75); MSE, mass spectrometer electronics; LI1, lock-in amplifier; SCR1, strip chart recorder

Figure 2. Top cross sectional view of the photoionization cell with mounting flange. Hatched area of drawing indicates the pipe walls.

Figure 3. a) Side view of photoionization cell sighting through entrance aperature looking toward the mass spectrometer. The hatched areas indicate the cell walls. b) Front view of photoionization cell looking at it mounted on P2 (Figure 2).

Figure 4. The character table for the D_{3h} point group.

Figure 1.

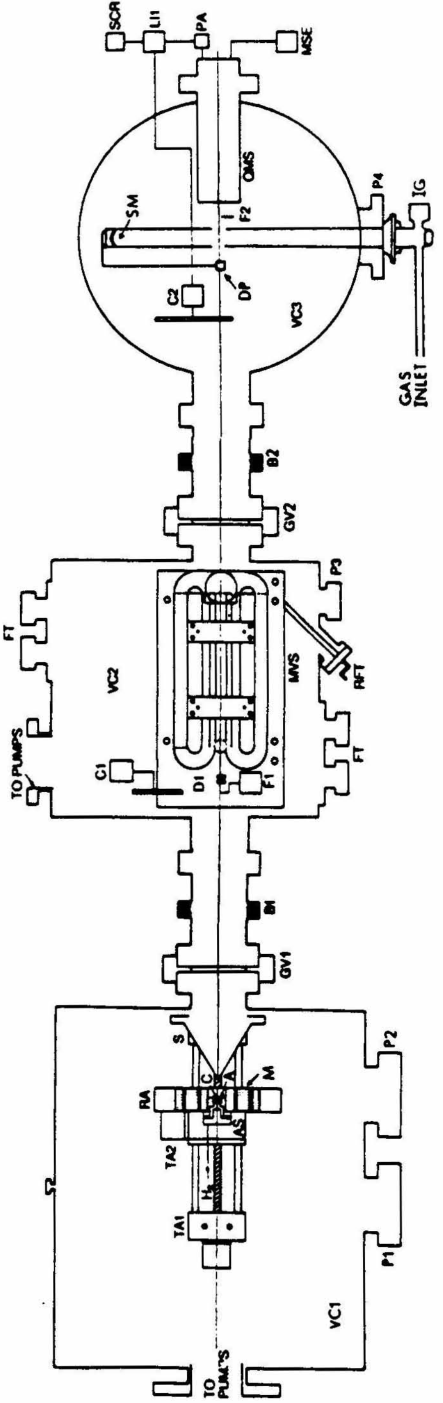
SCR1
LI1
PA
MSE
QMS
SM
F2
P4
IG
DP
C2
VC3
GAS INLET
B2
GV2
P3
FT
VC2
MVS
RFT
TO PUMPS
C1
D1
F1
FT
B1
GV1
S
P2
C
A
M
RA
AS
TA2
H_2
TA1
P1
VC1
TO PUMPS

Figure 2.

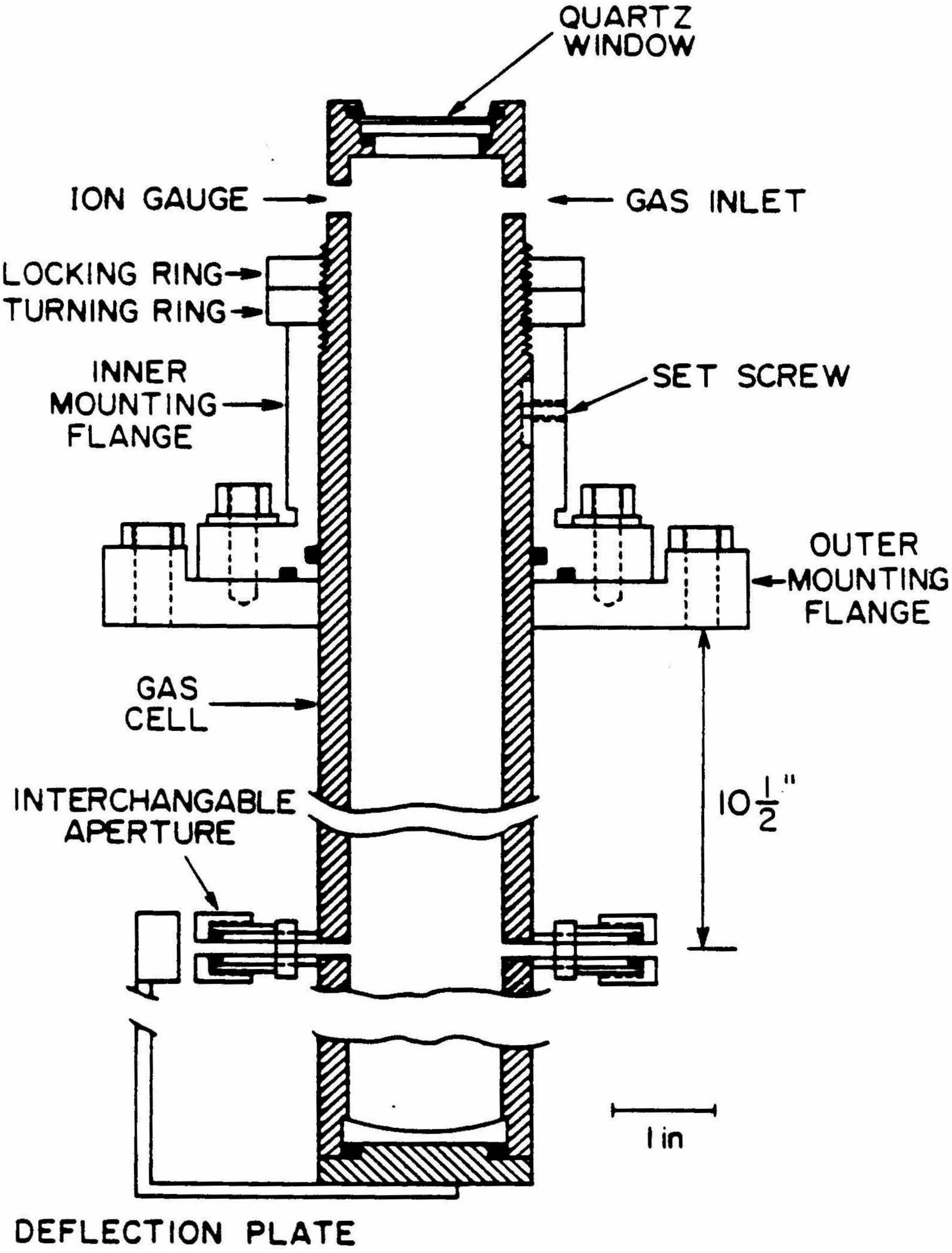
QUARTZ WINDOW
ION GAUGE
GAS INLET
LOCKING RING
TURNING RING
INNER MOUNTING FLANGE
SET SCREW
OUTER MOUNTING FLANGE
GAS CELL
INTERCHANGABLE APERTURE
$10\frac{1}{2}''$
1 in
DEFLECTION PLATE

Figure 3.

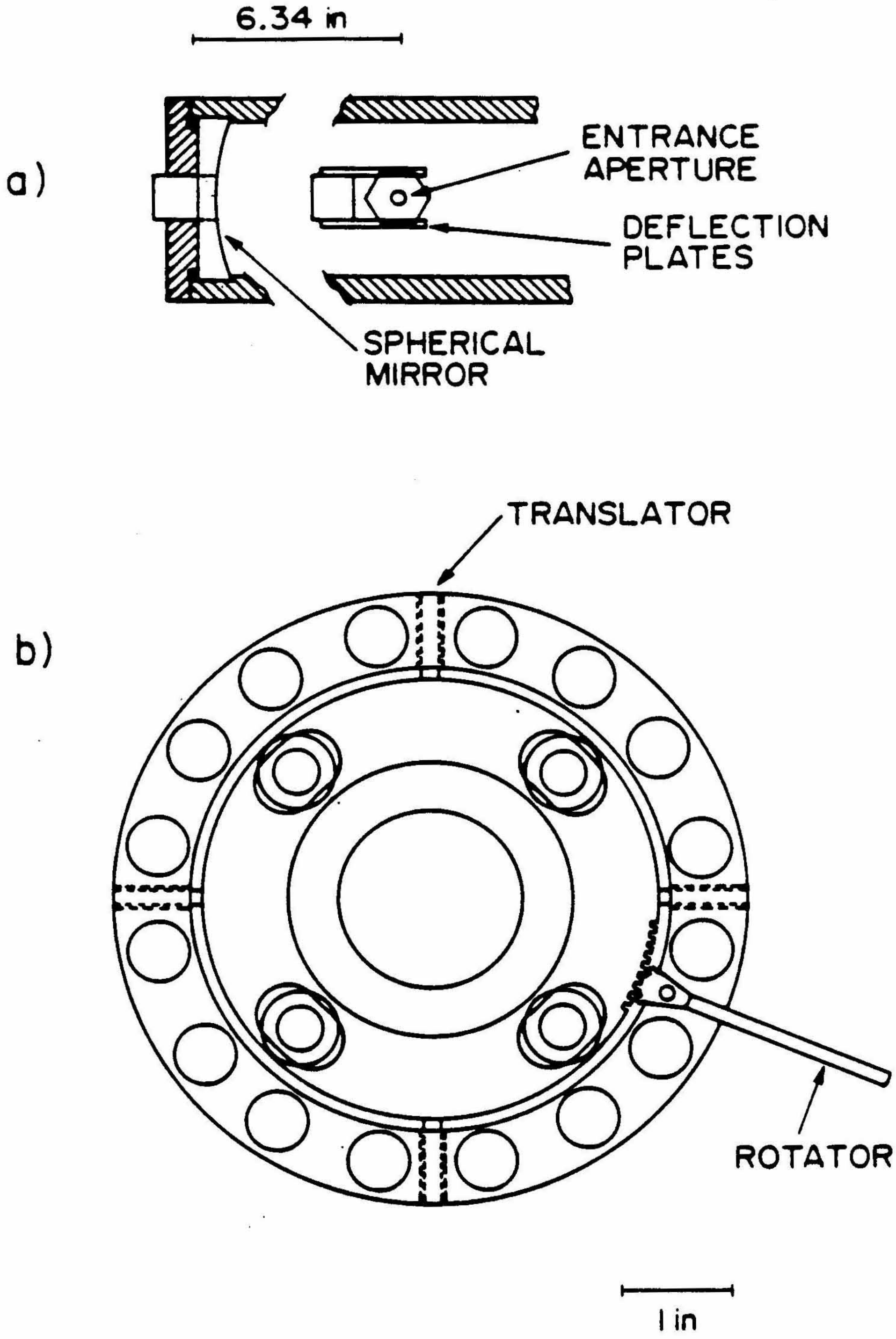
a)
6.34 in
ENTRANCE APERTURE
DEFLECTION PLATES
SPHERICAL MIRROR
b)
TRANSLATOR
ROTATOR
1 in

Figure 4.

D_{3h}	E	$2C_3$	$3C_2$	σ_h	$2S_3$	$3\sigma_v$		
A_1'	1	1	1	1	1	1		x^2+y^2, z^2
A_2'	1	1	-1	1	1	-1	R_z	
E'	2	-1	0	2	-1	0	(x, y)	(x^2-y^2, xy)
A_1''	1	1	1	-1	-1	-1		
A_2''	1	1	-1	-1	-1	1	z	
E''	2	-1	0	-2	1	0	(R_x, R_y)	(xz, yz)

D_{3h}	A_1'	A_2'	A_1''	A_2''	E'	E''
A_1'	A_1'	A_2'	A_1''	A_2''	E'	E''
A_2'		A_1'	A_2''	A_1''	E'	E''
A_1''			A_1'	A_2'	E''	E'
A_2''				A_1'	E''	E'
E'					$A_1', [A_2'], E'$	A_1'', A_2'', E''
E''						$A_1', [A_2'], E'$

Chapter 9.

Preliminary Experiments and Results

I. Experimental Results and Discussion

The initial experiments performed were conducted using the apparatus shown in Figure 1. This system was being used to perform crossed beam experiments with the H_3 molecules produced in the beam. Efforts were made to examine the scattering of H_3 with Ar and HI. The crossed beam experiments with HI were of particular interest since at that time it was believed that H_4 might exist is some metastable state. Calculations by Nicolaides *et al.*[1] using the maximum ionicity excited state (MIES) approach had found a relatively deep well in the lowest potential energy surface of H_4. It metastability was thought to be caused by the presence of avoided crossings in the excited state potential energy surfaces. A summary of their results follows. Its equilibrium geometry is that of a trigonal pyramid whose base is an equilateral triangle with side of 1.7 a_o and a height of 4.0 a_o. Its base is only slightly larger than the equilateral triangle of H_3, and its height is comparable in dimension to that of the $2p_z$ orbital in which the Rydberg electron of H_3 occupies. In addition, in the equilibrium geometry of this state, its energy is lower that that of any other state. Later it was shown that the results of Nicholaides were in error.

Due to severe alignment problems of the source, the results obtained in the crossed beam experiments were unreliable. In an effort to improve conditions, it was decided that a steerable arc source was necessary. However, the source chamber being used was already very cramped and could not accomodate additional equipment. These restrictions forced us to build an entirely new arc source, motion assembly and chamber for the planned experiments. While under design and construction, other efforts were made to improve alignment conditions as much as possible. Several of these changes were in the design of the source itself and are discussed in Chapter 6 section I.C. A typical mass spectrum obtained using this modified source is compared to results obtained previously in Figure 2. The apparatus used for the previous measurements is shown in Figure 3.[2] Although the overall intensity of the beam is lower (as expected since these measurement were made in the crossed molecular beam system which has a longer source to detector distance than the test system which was used in previous measurements), the changes we have made in the source have optimized the intensity of H_3 with respect to H and H_2. In addition, these changes have improved the life cycle of the internal parts. Previously, it was necessary to change the tungsten rod and disk after each run and to change the copper inserts after several runs. With the changes made, the tungsten rod and disk can be used 8 to 10 times before replacement is necessary and the copper inserts last indefinitely under normal operating conditions.

In addition to the changes in the arc source, other components of the apparatus were changed to improve alignment problems and steerability of the arc source. Several parts of the arc source translational assembly were replaced by more carefully machined parts to tighten the fit of the arc source in its support structure. The back of the translation assembly was bolted down to the source chamber to make it less susceptible to changes produced by vibrations of the pumps in the lab. A pivot system was added to the source chamber support structure to allow the chamber to be rotated during operation, and the entire structure was bolted down to the lab floor. These changes helped to make the direction of the beam more reproducible but did not eliminate the problem. Since it seemed that the reliability could not be further improved in this system all efforts were directed towards building the new system.

A new arc source chamber was built which eliminated many of the problems existing in the original system. For a description of this chamber see Chapter 6 section I.A. The source chamber as it existed was awkward to work with, the difficulty being its cylindrical shape. The bottom of the chamber interior was curved making alignment of the source and translation assembly difficult. The horizontal and vertical motions along the base were coupled so that, a movement of the translational assembly to one side also caused movement in the vertical direction. Therefore, alignment of the source and translational assembly was a very time consuming process requiring optimization in one direction and then the other, repeating this process until the system was aligned as accurately as possible. In addition, since the bottom of the source chamber was not flat, alignment of the source and translation assembly was more susceptible to vibrations of the pumps.

A second problem with the design of the source chamber was difficulty in getting at parts of the source. A 10″ flange located at the side of the chamber provided the only access to the source, magnet and attached cooling water and electrical lines. Removal or adjustment of various parts often required other parts also to be removed. For example, if there was a leak in the cooling water line for the magnet, we had to remove the source, disassemble the translation assembly, remove the magnet, tighten the connection for the water line and then replace everything. However, the work did not end there since removal of these parts destroyed the alignment of the source and translation assembly and therefore had to be repeated.

A third problem with the design of the source chamber is the view of the source which was available, the discharge was only in view when the source was as far away from the skimmer as the translation assembly allowed. This was adequate for ignition of the source, but did not allow observation of the discharge when the source was close to the skimmer, as when experiments were performed. Therefore, we desired the ability to observe the discharge in this geometry.

A fourth problem was that the translation assembly movement of the source was very coarse. The source was moved by turning a knob on the outside of the chamber. This knob was marked so that small movements could be made, but slack in the mechanism was large enough to make such movements inaccurate. Therefore, the source to skimmer distance was not reproducible.

The last major flaw in the design of the source chamber was that the structure used to support it was not stable. The stand rested upon four large bolts which aligned the source chamber by providing vertical motion. These bolts were not very stable, and vibrations produced by the pumps in the lab were able to move these bolts slightly and over time destroy the alignment.

To improve the duty cycle of these experiments, a new source chamber was designed and constructed. The new chamber minimized the problems present in the previous system without creating new ones. In addition, it was designed to make sufficient room for the new translation-rotation assembly being constructed. The new source chamber is rectangular in shape. Providing a flat surface in the interior which makes alignment of the source and translation assembly much easier. In addition, the flange for access to the source was made the entire side of the new chamber to provide easier servicing of the source, magnet, cooling water lines and electrical lines. To allow viewing of the discharge during ignition as well as in the operational mode, two view ports were included on the chamber wall. A support structure for the source chamber was also constructed, which was bolted to the floor to make the chamber less susceptible to vibrations. With this set up, alignment was much less time consuming and did not have to be performed nearly as often.

The source chamber pumping system was also replaced. An analysis was performed to determine the needs of our system based upon measurements of the flow rate and pressure during experiments. The results of this analysis led us to choose a Leybold-Heraeus RV-10000 frame mounted Roots pumping system. This system consists of a WAU-1000 Roots blower coupled with an E250 rotary piston pump. For a more detailed description of this system see Chapter 6 section I.A.

A new translation-rotation assembly for the source and magnet was designed and constructed. It provides three translations and two rotations to the source and magnet during operation. The motions of these assemblies are very fine and motor controlled. For a detailed description of this system see Chapter 6 section I.C. This new assembly has allowed us to correct for the most crippling of all problems in the previous system, differences in the optical and beam paths during operation.

Since it was our original intention to allow experiments to be carried out at both ends of the lab (spectroscopic and crossed beam experiments), all of the associated electonics were also duplicated. As in the design of the source, translation-rotation assembly and chamber, changes were made to eliminate problems in the previous design.

A second chamber was designed to house a Stern-Gerlach magnetic velocity selector and built to provide a differential stage of pumping between the source chamber and the detection chamber. For a detailed description of this chamber see Chapter 6 section I.A. Stands for this chamber and for the existing detection chamber were designed and built. Many other small components were also constructed to improve the experimental set-up.

After building the new equipment, the system was assembled and tested. As with any new project, there were many bugs to be worked out, after which attempts were made to perform the planned experiments. However, as each problem was worked out, new ones appeared. The quadrupole mass spectrometer, initially planned for replacement was the source of much trouble and a great deal of time was spent repairing the associated electronics.

During the periods of time when the system was working properly, attempts to measure the mass spectrum of the beam were made. In all cases, the background pressure was high enough to swamp the beam signal. To combat this, measurements were made with no voltage applied to the focus lens which should have drastically reduced the background signal. Beam molecules have a high enough translation energy to pass through the mass spectrometer ionizer region and into the quadrupole rod assembly whereas background molecules require the acceleration provided by the focus lens to reach the detector. Although this reduced the background signal significantly, it did not eliminate enough of the background to make beam intensity measurements possible on a regular basis and it became obvious that the pumping capabilities of the system needed improvement. At first small changes in the system were tried, when these failed a turbomolecular pump available in the lab was installed in the system to replace the less efficient mercury diffusion pump. This change also reduced the background signal, but not sufficiently. At this point we decided to replace the differential stage chamber with a small tube. This not only reduced the volume of the chamber which reduced operational pressures, it also shortened the source to detector distance which could be expected to strengthen the beam signal. But the changes were still not enough to eliminate the background signal problems.

It is still not entirely clear what caused these problems. According to the calculations performed, and the rated pumping speeds of the pumps used, the background pressure should have been lower than observed. Either the assumptions made in the calculations were in error, or the rated pumping speeds were overly optimistic. After careful analysis we have decided that both have contributed to our problems. The anlaysis performed was based upon an equilibrium pressure measurement in the source chamber rather than an actual pressure measurement directly in front of the source. Therefore, our estimate of pressures down field was probably optimistic. In addition, after speaking with engineers from Leybold-Heraeus, we learned that the pumping efficiency of hot hydrogen is much lower than for many other atoms and molecules due to its low mass and high velocity. Therefore, the rated pumping speeds were also optimistic.

Since the monies were not available to buy higher capacity pumping systems, the experiments were abandoned, and efforts were directed towards *ab initio* quantum mechanical calculations of the nonadiabatic coupling in the H_3 system.

II. Future Work

Due to financial limitations some of the goals of the experimental portion of this thesis were not achieved. New pumping systems are necessary for the differential stage and detection chambers with which complete characterization of the beam of H_3 moleclues would be possible. In addition, H_3 can be thought of as an excited state of the H + H_2 reaction and as such makes an interesting species for study. The electronic energy of the H_3 molecule in its $2p_z^2A_2''$ electronic state is 5.85 eV higher and the $2p_{x,y}^2E'$ repulsive ground state is 2.65 eV higher in energy than H + H_2.[3-6] Therefore, upon a vertical transition to the ground state, the $2p_z^2A_2''$ state of H_3 will liberate about 3 eV of electronic energy with the remaining energy being channeled into vibration and rotation of the H + H_2 dissociated system. In a collision with another molecule, this energy could become available for reaction. In addition, the translational energy of this beam spans the range from 1 to 12 eV, providing an additional source of energy for reaction. This species can be expected to exhibit unusual dynamics, in that it may undergo novel chemical reactions as well as unique partitioning of the available energy into electronic, vibrational, rotational and translational energy of the products. Chemiluminescent processes are possible and population inversions may be possible as well. Since the intensity of H_3 with respect to H in the beam has improved and can be controlled to an extent by varying the stagnation pressure, it should be possible to deconvolve the dynamical properties of H from those of H_3.

Future experiments of interest include:

1. Collisionally induced chemiluminescence: A gas cell and a series of rare gas targets could be utilized to detect the $2p^2A_2'' \longrightarrow 2p^2E'$ emission induced by collision between the rare gas targets and H_3.

2. Laser spectroscopy: Electronically excited states of H_3 lying above the $2p_z^2A_2''$ state can be probed using lasers. If, after excitation, the resulting state cascades down to the repulsive $2p_{x,y}^2E'$ ground state and dissociates to form H + H_2, a decrease in the $m/e^- = 3$ peak intensity will be observed. By examining this change in intensity as a function of laser wavelength, information pertaining to the spectroscopy in a collision-free environment of a molecular beam can be obtained. Furthmore, if emission to states above the ground state occur in that time interval, laser induced fluorescence could be detected to obtain complementary information about the excitation event.

3. Reactive collision dynamics: Studies of the reaction dynamics of metastable H_3 should be particularly interesting. In many respects, the dynamics may resemble those of H atoms since H atoms are produced upon photon emission or internal conversion to the $2p_{x,y}^2E'$ repulsive ground state. In addition, H_3's high internal energy of 5.85 eV makes it a highly reactive species. The translational energy available of between 1 and 12 eV further enhances the range of chemical reactions that are energetically possible. Several examples follow:

$$H_3 + X \longrightarrow H_2 + HX \tag{9.1}$$

$$H_3 + O \longrightarrow H_2 + OH \tag{9.2}$$

$$H_3 + X_2 \longrightarrow H_2 + HX + X \tag{9.3}$$

$$H_3 + DX \longrightarrow H_2 + HD + X^\star \tag{9.4}$$

$$\longrightarrow H_2 + HD + X \tag{9.5}$$

$$\longrightarrow H_2 + HX + D \tag{9.6}$$

$$H_3 + CO \longrightarrow H_2 + COH \tag{9.7}$$

$$H_3 + NO \longrightarrow H_2 + NOH \tag{9.8}$$

Reactions 9.1 and 9.2 are not possible with hydrogen atoms unless a third body is involved, but may be possible with H_3. Reaction 9.3 in analogous to an abstraction reaction and occur via a harpooning mechanism. Reactions 9.4, 9.5 and 9.6 are analogous to the hydrogen atom exchange and abstraction, with H_2 acting as a chaperone. Reactions 9.8 and 9.9 would also not be possible for H atoms but may be possible for H_3 molecules.

The H_3 molecule can be thought of as a H atom carrying its own third body. As a result many new reactions become possible, some of which may be chemiluminescent or may be suited for study by laser induced fluorescence detection techniques. These reactions may provide a unique opportunity to observe new reaction dynamics.

III. References

1. C.A. Nicholaides, G. Theodorakopoulos and I.D. Petsalakis, *J. Chem. Phys.* **80**, 1705 (1984).
2. J.F. Garvey, *Ph.D. Thesis*, California Institute of Technology, 1985.
3. M. Baer, in *Theory of Chemical Reaction Dynamics*, edited by M. Baer, **Vol. II**, (CRC Press, 1985), pp. 219-280.
4. J.C. Tulley and R.K. Preston, *J. Chem. Phys.* **55**, 562 (1971).
5. J.P. Braga, H. Guo, J.N. Murrell and L.J. Dunne, *Molec. Phys.* **65**, 909 (1988).
6. B. Lepetit, J.M. Launay and M. Le Dourneuf, *Chem. Phys.* **117**, 17 (1987).

IV. Figures and Captions

Figure 1. Side view of the crossed beam apparatus using the H_3 molecule beam as the primary beam: VC1, vacuum chamber one; S, water cooled copper skimmer; GV, pneumatic gate valve; F, flexible bellows; BJ, 50″ bell jar. Dashed lines indicate box within the bell jar which houses the magnetic velocity selector.

Figure 2. a) Ion intensity as a function of m/e^-. The lower curve is the ion background obtained with the electron beam turned off, and the upper curve is the ion signal shifted upwards by 0.2×10^{10} A. Electron impact current, 100 μA; electron accelerating voltage, 60 V. ion source pressure, 2.1×10^{-5} torr. The stagntion pressure of H_2 in the molecular beam source was 60 torr. b) Same as a) except the electron impact current was 0.4 mA, the ion source pressure was 2.3×10^{-7} torr and the stagnation pressure of H_2 in the source was 55 torr.

Figure 3. Side view of the vacuum system: VC1, vacuum chamber one, the source chamber; P1, P2 viewports, unistrut mechanical coupler; VC2, vacuum chamber two, the diagnostic chamber.

Figure 1

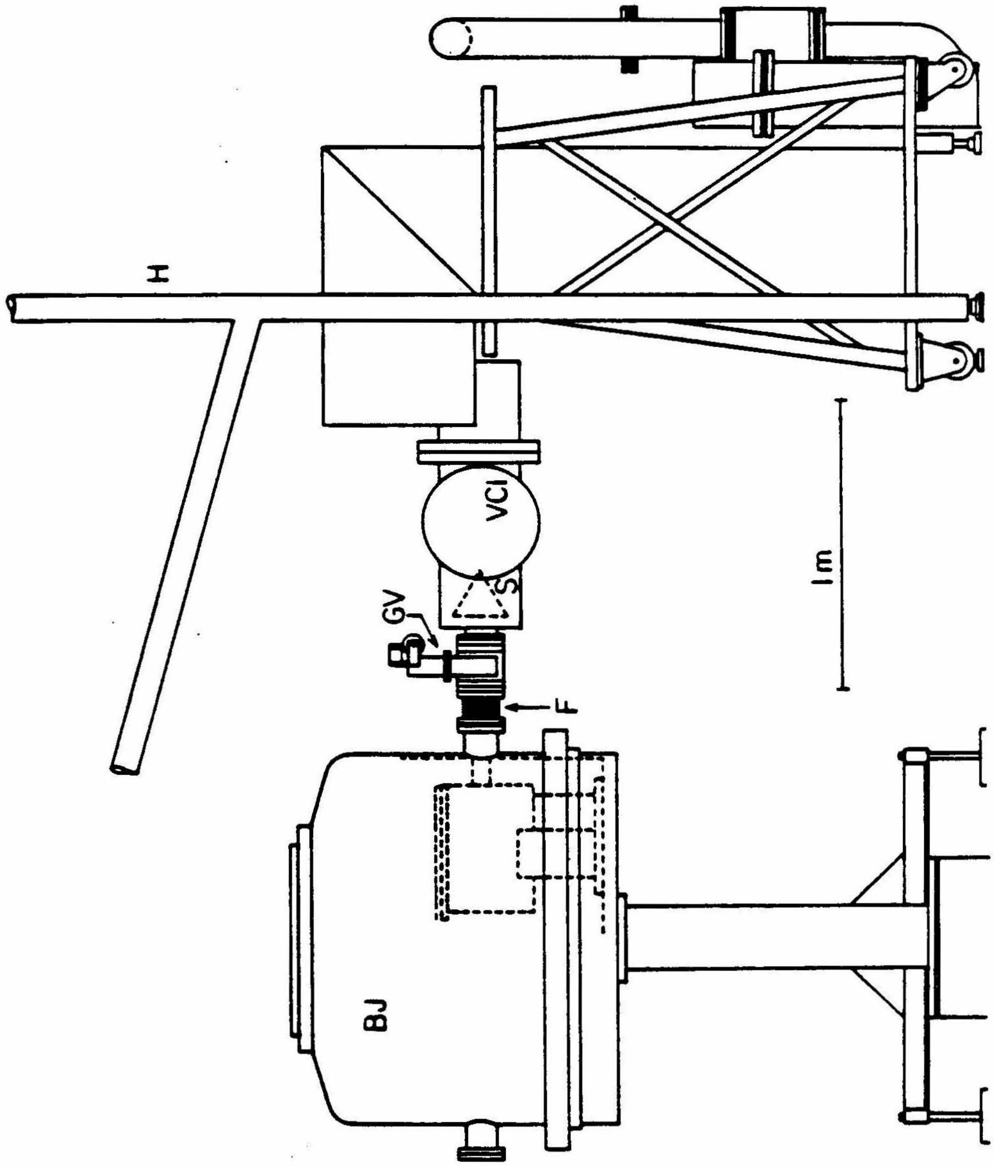

Figure 2

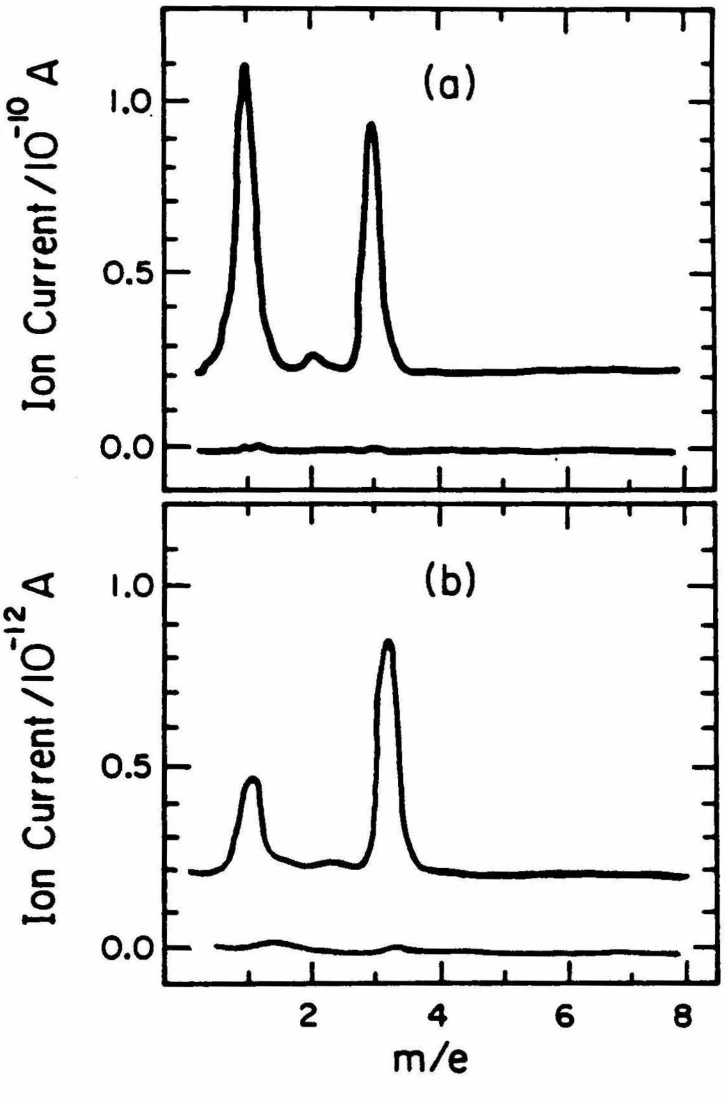
(a)
(b)
Ion Current /10^{-10} A
Ion Current /10^{-12} A
1.0
0.5
0.0
1.0
0.5
0.0
2
4
6
8
m/e

Figure 3

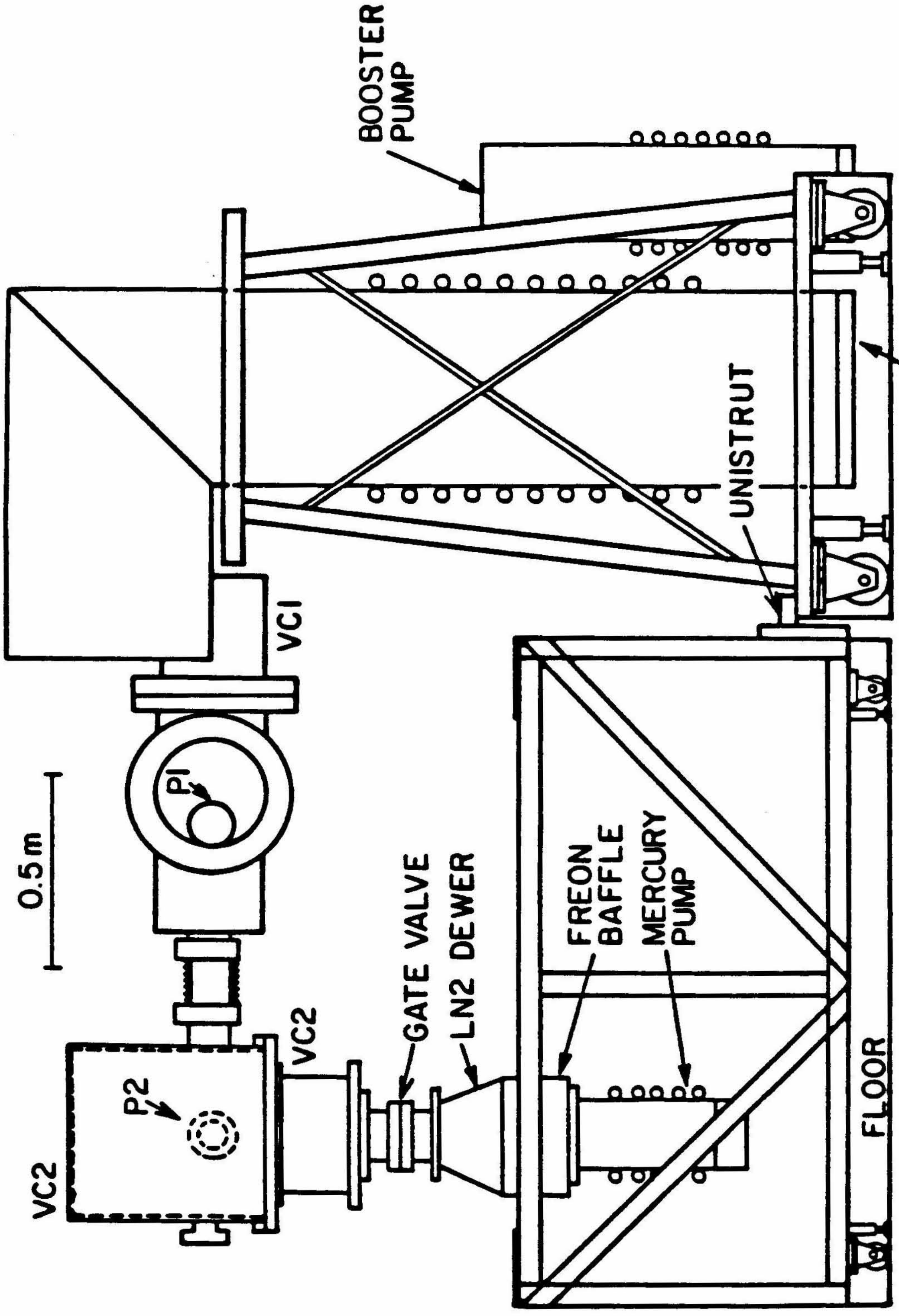
BOOSTER PUMP
MAIN DIFFUSION PUMP
UNISTRUT
VC1
P1
0.5 m
VC2
VC2
P2
GATE VALVE
LN2 DEWER
FREON BAFFLE
MERCURY PUMP
FLOOR

Chapter 10.

Summary and Future Work

I. Summary

We have conducted an *ab initio* quantum study of the first three electronic states of the H_3 system. The electronically nonadiabatic coupling elements between the lowest three states have also been calculated. The calculated nonadiabatic coupling elements compare well in some regions of configuration space with previous calculations performed on this system. Discrepancies in other regions can be attributed to the method of calculation. In our study these coupling elements were calculated by an *ab initio* method whereas analytic continuation was used in previous work. Calculation of the electronically nonadiabatic coupling surfaces represents notable progress. All 3-D quantum mechanical theoretical investigations to date invoke the Born-Oppenheimer approximation and neglect nonadiabatic coupling of nearby states. Although this is justified in many cases, the H_3 system exhibits a conical intersection near which this approximation breaks down. Inclusion of these coupling terms in the Hamiltonian will improve the quality and accuracy of dynamics calculations of the H_3 system. In recent scattering calculations, inclusion of the geometical phase effect which is a result of the conical intersection begins to significantly change the differential and integral cross sections at energies above 1.8 eV. Therefore, it is likely that the electronically nonadiabatic coupling also plays a role at energies lower that the conical intersection (2.72 eV). To obtain theoretical estimates of the predissociative lifetimes of the excited states of the H_3 system, accurate bound state wavefunctions and energies of the excited states of H_3 and accurate differential and integral cross sections in quantum mechanical scattering studies of the $H + H_2$ system (near 2.72 eV) these nonadiabatic terms must be included.

We have also conducted an experimental study of metastable H_3 molecules. Most of the experimental effort was spent designing, building and debugging an apparatus for performing spectroscopic and scattering experiments of the H_3 beam. The new design of the arc discharge source improved its reliability, as well as the life cycle of the electrodes. A translation-rotation assembly was designed and built which provided 5 degrees of freedom to the arc source and magnet during operation (3 translations and 2 rotations). These fine motions greatly simplified operation of the source as they provided a means of interactive alignment of the beam during experiments. The source chamber design has improved the duty cycle of these experiments by improving access to and providing room for the source and its assemblies. The differential stage chamber provides a differential stage of pumping before the detection chamber. In addition, it was designed to house a Stern-Gerlach magnetic velocity selector and therefore provides a means of performing translationally selected experiments. Continued progress in the development of this apparatus hinged upon the purchase of new pumping systems. Since the monies were not available for these purchases, only preliminary experiments were performed.

II. Future Work

The calculations performed to date have only scratched the surface of what is possible to learn about the electronically nonadiabatic dynamics of the H_3 system. As discussed in Chapter 5, the potential energy surfaces and nonadiabatic coupling elements were calculated along 5 cuts in nuclear configuration space near the conical intersection. To map out the nonadiabatic coupling surfaces this must be extended to a 3-D grid in nuclear configuration space in the vicinity of the conical intersection. Once calculated, a functional form can be fitted to the coupling surfaces. With this information, a diabatic representation can be constructed for use in 3-D quantum mechanical dynamics studies.

The experiments performed to date have only partially characterized the metastable H_3 molecules in our beam. The ultimate goal of this work was to fully characterize the metastable H_3 molecules formed in our beam and to create a source of monoenergetic H_3 molecules whose translational energy would be continuously tunable from $\sim 1 - 12$ eV. This source could be utilized in crossed beam experiments and would enable study of many reactions that might not otherwise take place due to very low reaction probability. The H_3 molecule in its $2p_z^2A_2''$ electronic state is approximately 5.85 eV and the $2p_{x,y}^2E'$ repulsive ground state is approximately 2.65 eV higher in energy than $H + H_2$. Therefore, upon a vertical transition to the ground state, the $2p_z^2A_2''$ state of H_3 will liberate about 3 eV of electronic energy with the remaining energy being channelled into vibration and rotation of the $H + H_2$ dissociated system. In a collision with another molecule, this energy could become available for reaction. The translational energy of these molecules (1-12 eV) could provide an additional source of energy. Therefore, this species can be expected to exhibit unusual dynamics in that it may undergo novel chemical reactions as well as unique partitioning of the available energy into electronic, vibrational, rotational and translational energy of the products.

Appendix 1.

Results of Ab initio calculations of energies and nonadiabatic coupling elements of H_3 for geometries near the conical intersection

I. Introduction

The energies of the lowest three electronic states of H_3 and the nonadiabatic coupling elements between these states for geometries near the conical intersection are given in the series of tables which follow. The energies are denoted by E_1, E_2 and E_3 and correspond to the lowest three states in order of increasing energy. The nonadiabatic coupling elements are denoted by $\langle k|\frac{d}{dR_a}|k'\rangle$ and $\langle k|\frac{d^2}{dR_a^2}|k'\rangle$ where R_a corresponds to one of the coordinate geometry variables R_1, R_2 and γ and k and k' correspond to the electronic states for which the nonadiabatic coupling elements are being calculated. For a detailed description of the calculations see Chapters 4 and 5.

Table 1: Energies in eV and nonadiabatic coupling elements in bohr^{-1} at r = 1.4 bohr and $\chi = 89°$

R (bohr)	E_1	E_2	$\langle 1 \vert \frac{d}{dR} \vert 2 \rangle$
1	5.120562	5.815146	-0.63979915
1.05	4.838371	5.390176	-0.86117344
1.11	4.567584	4.933967	-2.3980636
1.13	4.493236	4.79299	-3.1300646
1.15	4.422893	4.658209	-4.4912563
1.17	4.359326	4.530456	-7.3044792
1.18	4.327743	4.470187	-9.815929
1.19	4.297413	4.411758	-13.7252632
1.2	4.266579	4.35769	-19.1022429
1.205	4.249721	4.333243	-22.096771
1.208	4.238238	4.318355	-22.9808856
1.211	4.22719	4.305751	23.515627
1.212	4.222751	4.300945	23.5292538
1.215	4.210707	4.288648	23.0451376
1.22	4.189128	4.27158	19.6419196
1.225	4.165446	4.25521	15.3835994
1.23	4.140383	4.241272	11.4620068
1.24	4.087146	4.216275	6.1186533
1.25	4.03372	4.194217	3.3499294
1.27	3.928429	4.161146	1.029839
1.3	3.772412	4.120056	0.1119638
1.4	3.303195	4.065877	-0.19936552

Table 2: Energies in eV and nonadiabatic coupling elements in bohr^{-1} at $r = 2.0$ bohr and $\chi = 89°$

R (bohr)	E_1	E_2	$\langle 1 \vert \frac{d}{dR} \vert 2 \rangle$
1.5	2.373723	3.326227	0.987362
1.6	2.527419	3.082098	1.887319
1.63	2.581136	3.017556	2.588536
1.65	2.615953	2.974692	3.493631
1.67	2.653408	2.936149	4.931673
1.69	2.686149	2.901606	7.569463
1.7	2.701073	2.883793	9.641041
1.71	2.716698	2.872916	12.31485
1.72	2.727041	2.861095	15.14447
1.726	2.730369	2.858184	16.31221
1.73	2.731471	2.857147	16.57456
1.735	2.734717	2.858535	16.12828
1.74	2.732271	2.860521	14.73106
1.745	2.731324	2.864802	12.78073
1.75	2.726902	2.870377	10.73217
1.76	2.713421	2.883181	7.104058
1.77	2.699511	2.897701	4.566259
1.775	2.693578	2.90894	3.660919
1.78	2.682884	2.917013	2.934563
1.79	2.66616	2.936873	1.912304
1.8	2.650921	2.957567	1.269467
1.84	2.583013	3.044638	0.221369
1.85	2.566697	3.068971	0.127912
1.86	2.549787	3.091687	0.05315
1.9	2.486136	3.185843	-0.08789
2	2.32961	3.43528	-0.13471

Table 3a: Energies (in eV) and Nonadiabatic coupling elements (in bohr^{-1}) at R = 0.70 bohr and $\chi = 89°$

r (bohr)	E_1	E_2	$\langle 1 \| \frac{d}{dr} \| 2 \rangle$
0.4	46.08396	46.71801	-0.77991
0.5	34.45757	35.00522	-0.44675
0.6	27.16199	27.63239	-0.54004
0.7	22.24283	22.64344	-0.64772
0.8	18.738	19.07671	-0.48531
0.84	17.60786	17.88343	0.276087
0.86	17.08878	17.32426	0.436877
0.9	16.13234	16.28444	0.766194
0.92	15.69004	15.79918	1.326272
0.94	15.27031	15.33553	1.857227
0.95	15.06753	15.11145	2.282769
0.955	14.96657	15.00216	2.569301
0.96	14.8669	14.89468	7.687067
0.962	14.8267	14.85231	11.68127
0.963	14.80651	14.83143	14.27867
0.965	14.7661	14.7901	20.34784
0.967	14.72438	14.74999	30.49784
0.968	14.7028	14.7301	36.2762
0.969	14.6812	14.71075	42.00386
0.97	14.65874	14.69191	48.90741
0.971	14.63553	14.67366	55.42277
0.972	14.61132	14.656	61.7859
0.973	14.5856	14.6388	66.14621
0.974	14.58544	14.60998	66.00922
0.975	14.56443	14.59091	65.12873
0.976	14.54348	14.57194	61.99956
0.977	14.52212	14.55319	57.32756

Table 3b: Energies (in eV) and Nonadiabatic coupling elements (in bohr^{-1}) at R = 0.70 bohr and $\chi = 89°$

r (bohr)	E_1	E_2	$\langle 1 \vert \frac{d}{dr} \vert 2 \rangle$
0.978	14.50119	14.53428	52.41674
0.98	14.45935	14.49725	42.84182
0.983	14.39642	14.44116	31.35705
0.987	14.31386	14.3682	22.43295
0.99	14.25179	14.3136	17.35784
1	14.04852	14.13498	10.25556
1.01	13.84557	13.96482	7.022872
1.03	13.47415	13.61833	5.672743
1.05	13.09476	13.29792	3.400958
1.1	12.22343	12.5477	1.812156
1.2	10.67452	11.27323	1.222123
1.3	9.339897	10.23756	0.870144
1.4	8.171406	9.384476	0.854699
1.5	7.137401	8.681274	0.581661
1.6	6.217361	8.101631	0.532824
1.7	5.399243	7.62873	0.436175
1.8	4.667695	7.244004	0.385701
1.9	4.020327	6.938852	0.346471
2	3.44679	6.699128	0.314743
2.1	2.944625	6.510665	0.291079
2.2	2.506333	6.372565	0.276497
2.3	2.126627	6.274618	0.261314
2.4	1.803425	6.214215	0.245212
2.5	1.531874	6.18349	0.2391
2.6	1.302207	6.179841	0.232461
2.7	1.113794	6.194152	0.227411
2.8	0.965478	6.227625	0.228535
2.9	0.847214	6.27062	0.227505

Table 4a: Energies (in eV) and Nonadiabatic coupling elements (in bohr^{-1}) at R = 1.9 bohr and $\chi = 89°$

r (bohr)	E_1	E_2	$\langle 1 \vert \frac{d}{dr} \vert 2 \rangle$
0.8	6.236524	11.20252	-0.21181
0.9	4.460886	9.150412	-0.22557
1	3.304757	7.69789	-0.22783
1.1	2.567938	6.648785	-0.26248
1.2	2.1166	5.862984	-0.28377
1.3	1.870304	5.267368	-0.3058
1.4	1.767524	4.797063	-0.33629
1.5	1.767116	4.410598	-0.37743
1.6	1.835527	4.090966	-0.42726
1.7	1.957845	3.819799	-0.33629
1.8	2.112844	3.579136	-0.58338
1.9	2.289502	3.364553	-0.72048
2	2.486136	3.185843	-0.91378
2.05	2.582709	3.105252	-0.56683
2.1	2.684215	3.034496	-0.7446
2.13	2.740908	2.995134	0.086214
2.14	2.757714	2.983247	0.865508
2.15	2.776091	2.973625	2.006064
2.155	2.784409	2.967764	2.796826

Table 4b: Energies (in eV) and Nonadiabatic coupling elements (in bohr^{-1}) at R = 1.9 bohr and $\chi = 89°$

r (bohr)	E_1	E_2	$\langle 1 \vert \frac{d}{dr} \vert 2 \rangle$
2.157	2.78762	2.965968	3.159722
2.16	2.79195	2.964588	-2.15227
2.165	2.798804	2.960553	-4.92238
2.17	2.805197	2.956588	-6.37762
2.175	2.811485	2.955001	-7.86885
2.18	2.816392	2.953543	-9.40856
2.185	2.821173	2.952824	-10.9768
2.19	2.825861	2.956242	-12.3046
2.195	2.827826	2.956708	-13.2021
2.2	2.83067	2.960332	-13.6482
2.21	2.823839	2.967429	-13.3111
2.22	2.819007	2.980447	-11.8949
2.23	2.813717	2.994108	-10.2208
2.24	2.808076	3.01231	-8.68131
2.26	2.791947	3.046779	-6.40579
2.28	2.771927	3.084917	-4.93621
2.3	2.749975	3.120426	-3.94555
2.35	2.696819	3.217896	-2.55027
2.4	2.648975	3.31706	-1.86491
2.5	2.55834	3.508991	-1.2136
2.6	2.489812	3.697181	-0.90863
2.7	2.434708	3.879883	-0.74125

Table 5a: Energies in eV at $\gamma = 59^\circ$ and $R_1 = R_2$

R_1 (bohr)	E_1	E_2	E_3
1.4	4.265558	4.356882	5.620498
1.5	3.655493	3.75947	5.331561
1.55	3.429878	3.542971	5.263776
1.6	3.243367	3.360977	5.23504
1.61	3.209706	3.328894	5.234006
1.62	3.179473	3.298634	5.234578
1.63	3.148941	3.269218	5.235285
1.64	3.118464	3.241925	5.236809
1.645	3.104695	3.228455	5.23866
1.648	3.09634	3.219801	5.240374
1.649	3.093728	3.217652	5.240129
1.65	3.091497	3.216237	5.240728
1.6505	3.090054	3.215012	5.24051
1.651	3.088694	3.212808	5.240564
1.6513	3.087986	3.211257	5.240864
1.6515	3.087578	3.210712	5.240864
1.6516	3.087306	3.210767	5.240918
1.6517	3.087796	3.210413	5.240945
1.6518	3.087605	3.210658	5.241517
1.6519	3.08736	3.210876	5.241544
1.65193	3.087252	3.211039	5.241598
1.65194	3.087224	3.211012	5.241598
1.65195	3.087197	3.210849	5.241598
1.652	3.087088	3.210712	5.241925
1.6521	3.086898	3.210332	5.241979
1.6522	3.086462	3.210087	5.242034
1.6525	3.085619	3.209107	5.241653
1.653	3.084177	3.208209	5.242224
1.654	3.081047	3.204508	5.243122
1.655	3.07819	3.201977	5.244102
1.658	3.070516	3.195719	5.245136
1.66	3.065999	3.191229	5.24549

Table 5b: Energies in eV at $\gamma = 59°$ and $R_1 = R_2$

R_1 (bohr)	E_1	E_2	E_3
1.67	3.040637	3.166656	5.252211
1.68	3.017262	3.142438	5.260783
1.69	2.994949	3.12192	5.268157
1.695	2.984554	3.112232	5.273219
1.7	2.973016	3.101919	5.277981
1.71	2.953042	3.082816	5.28824
1.72	2.934837	3.064502	5.301492
1.75	2.884114	3.014596	5.339344
1.8	2.81788	2.950266	5.427157
1.85	2.772001	2.906319	5.533284
1.87	2.758531	2.896169	5.579626
1.88	2.752707	2.892087	5.60428
1.89	2.74536	2.88776	5.629886
1.9	2.741469	2.882645	5.655493
1.91	2.736707	2.87927	5.681263
1.92	2.732897	2.876059	5.705699
1.93	2.730393	2.873746	5.732095
1.933	2.729632	2.872957	5.739932
1.934	2.72974	2.872712	5.742626
1.9345	2.729305	2.87244	5.744122
1.935	2.729468	2.872467	5.745048
1.9353	2.729359	2.872386	5.746191
1.9355	2.729359	2.872141	5.746762
1.9356	2.729332	2.872141	5.747034
1.9357	2.729305	2.872114	5.747306
1.93575	2.729142	2.872086	5.74747
1.9358	2.729142	2.871651	5.747606
1.9359	2.729115	2.871624	5.748041
1.936	2.72906	2.871597	5.748313
1.9362	2.728815	2.871324	5.748885
1.9363	2.728679	2.871488	5.749157
1.9365	2.728353	2.871433	5.749783

Table 5c: Energies in eV at $\gamma = 59°$ and $R_1 = R_2$

R_1 (bohr)	E_1	E_2	E_3
1.937	2.728217	2.871406	5.751252
1.938	2.727672	2.871134	5.753619
1.94	2.726203	2.870943	5.758953
1.945	2.72457	2.869773	5.772396
1.95	2.723536	2.868658	5.786736
1.96	2.720924	2.867705	5.814901
1.97	2.719618	2.867297	5.843909
1.98	2.719237	2.868168	5.872781
1.99	2.719563	2.867977	5.902333
2	2.721033	2.867814	5.93194
2.01	2.723999	2.869583	5.963451
2.02	2.725223	2.869637	5.994146
2.03	2.727509	2.870073	6.025658
2.1	2.745932	2.895434	6.256824
2.15	2.777307	2.927109	6.429484
2.17	2.789144	2.942974	6.49999
2.2	2.809853	2.965478	6.608893
2.205	2.812764	2.967519	6.626472
2.208	2.81437	2.970322	6.637302
2.209	2.814996	2.971084	6.640622
2.21	2.815975	2.971818	6.644568
2.2105	2.816329	2.972335	6.646282
2.2107	2.816492	2.972254	6.646989
2.2108	2.816547	2.972254	6.647343
2.2109	2.816601	2.972335	6.647697
2.211	2.816519	2.972417	6.648051
2.2111	2.816574	2.972471	6.648404
2.21113	2.816601	2.972499	6.648513
2.21115	2.816628	2.972526	6.648568
2.21117	2.816628	2.972526	6.648649
2.21119	2.816656	2.972553	6.648731

Table 5d: Energies in eV at $\gamma = 59^\circ$ and $R_1 = R_2$

R_1 (bohr)	E_1	E_2	E_3
2.2112	2.816656	2.972553	6.648758
2.21121	2.816656	2.97258	6.648785
2.211228	2.816683	2.97258	6.648867
2.21123	2.816683	2.97258	6.648867
2.21127	2.81671	2.972607	6.649003
2.2113	2.816737	2.972635	6.649112
2.21133	2.816737	2.972662	6.649221
2.21137	2.816792	2.972689	6.649357
2.2114	2.816792	2.972716	6.649874
2.2115	2.816873	2.972798	6.650228
2.2116	2.816737	2.97288	6.650581
2.2117	2.816792	2.972716	6.650935
2.2118	2.816873	2.972798	6.651289
2.212	2.817009	2.972934	6.651996
2.213	2.817662	2.973614	6.655561
2.214	2.818397	2.974893	6.659126
2.215	2.819431	2.975682	6.6625
2.217	2.821499	2.976172	6.669575
2.22	2.823731	2.978757	6.680433
2.23	2.832901	2.988472	6.715509
2.25	2.848276	3.004173	6.78656
2.3	2.891869	3.047658	6.971003
2.35	2.940715	3.094762	7.15531
2.4	2.988989	3.144451	7.341467
2.45	3.046189	3.195964	7.527352
2.5	3.099987	3.250823	7.717918
2.6	3.213434	3.362338	8.088708
2.7	3.332622	3.479186	8.463989
2.8	3.44762	3.592306	8.829963
2.9	3.563815	3.704855	9.190822
3	3.675221	3.809594	9.539435

Table 6a: Nonadiabatic coupling elements in bohr^{-1} at $\gamma = 59^\circ$ and $R_1 = R_2$

R_1 (bohr)	$\langle 1\vert\frac{d}{d\gamma}\vert 2\rangle/R_1$	$\langle 1\vert\frac{d}{d\gamma}\vert 3\rangle/R_1$	$\langle 2\vert\frac{d}{d\gamma}\vert 3\rangle/R_1$
1.4	0.366071	0.389484	0.001531
1.5	0.315735	0.313844	0.004808
1.55	0.32263	0.28789	-0.00213
1.6	0.255154	0.268899	-0.00022
1.61	0.291989	0.265475	-0.00466
1.62	0.325151	0.263496	-0.00207
1.63	0.321852	0.257865	-0.00116
1.64	0.289835	0.252115	-0.00228
1.645	0.289173	0.248521	-0.00245
1.648	0.299385	0.242853	-0.0049
1.649	0.313367	0.241707	-0.00279
1.65	0.295639	0.240708	-0.0028
1.6505	0.296655	0.239495	-0.00197
1.651	0.281309	0.240128	-0.00304
1.6513	0.323801	0.240796	-0.00101
1.6515	0.43094	1.850279	-0.00384
1.6516	0.447737	1.861257	-0.0034
1.6517	0.40929	1.871643	-0.00551
1.6518	0.411245	1.876457	-0.00551
1.6519	0.398776	1.887341	-0.00673
1.65193	0.371107	1.89257	-0.00583
1.65194	0.325208	1.893577	-0.00767
1.65195	0.307068	1.045019	-0.00615
1.652	0.337548	0.239513	-0.00063
1.6521	0.30734	0.239747	-0.00292
1.6522	0.33309	0.238526	-0.00328
1.6525	0.31619	0.238006	-0.00359
1.653	0.29738	0.240906	-0.00183
1.654	0.285497	0.236594	-0.00061
1.655	0.269833	0.241669	-0.00092
1.658	0.282433	0.241774	-0.0026
1.66	0.298495	0.232557	-0.00163

Table 6b: Nonadiabatic coupling elements in bohr^{-1} at $\gamma = 59^\circ$ and $R_1 = R_2$

R_1 (bohr)	$\langle 1 \vert \frac{d}{d\gamma} \vert 2 \rangle / R_1$	$\langle 1 \vert \frac{d}{d\gamma} \vert 3 \rangle / R_1$	$\langle 2 \vert \frac{d}{d\gamma} \vert 3 \rangle / R_1$
1.67	0.281086	0.241879	-0.00367
1.68	0.295609	0.238668	-0.00178
1.69	0.277979	0.23553	-0.0037
1.695	0.293279	0.2337	-0.00527
1.7	0.274907	0.23081	-9.4E-05
1.71	0.30369	0.225649	-0.00302
1.72	0.280305	0.220375	-0.00366
1.75	0.261351	0.206795	-0.00243
1.8	0.2571	0.19812	-0.00148
1.85	0.252482	0.18795	-0.00038
1.87	0.243879	0.183584	-0.00245
1.88	0.255868	0.18094	-0.00204
1.89	0.254472	0.178912	-0.00266
1.9	0.22899	0.176983	-0.0016
1.91	0.250653	0.17441	-0.00198
1.92	0.241135	0.173558	-0.00243
1.93	0.264569	0.171485	-0.00181
1.933	0.22356	0.170942	-0.00261
1.934	0.245693	0.170894	-0.00202
1.9345	0.237419	0.170817	-0.00174
1.935	0.247794	0.17078	-0.00252
1.9353	0.278283	0.044595	-3.9E-05
1.9355	0.261953	0.044562	-0.00025
1.9356	0.283978	0.04456	0.000155
1.9357	0.266996	0.044553	2.8E-05
1.93575	0.255859	0.170645	-0.00231
1.9358	0.220362	0.170638	-0.00298
1.9359	0.223317	0.17062	-0.00307
1.936	0.240183	0.170603	-0.00127
1.9362	0.242939	0.170567	-0.00231
1.9363	0.254038	0.170532	-0.00193
1.9365	0.243819	0.170725	-0.00233

Table 6c: Nonadiabatic coupling elements in bohr^{-1} at $\gamma = 59^\circ$ and $R_1 = R_2$

R_1 (bohr)	$\langle 1\vert\frac{d}{d\gamma}\vert 2\rangle/R_1$	$\langle 1\vert\frac{d}{d\gamma}\vert 3\rangle/R_1$	$\langle 2\vert\frac{d}{d\gamma}\vert 3\rangle/R_1$
1.937	0.237873	0.170628	-0.00287
1.938	0.252671	0.170108	-0.00177
1.94	0.235316	0.169744	-0.00269
1.945	0.22177	0.169246	-0.00267
1.95	0.257571	0.168727	-0.00152
1.96	0.215709	0.167033	-0.00271
1.97	0.224366	0.164862	-0.00263
1.98	0.236155	0.163339	-0.00214
1.99	0.216817	0.161779	-0.0026
2	0.219444	0.159518	-0.00281
2.01	0.228767	0.15823	-0.00224
2.02	0.230728	0.156617	-0.00185
2.03	0.220776	0.155283	-0.00243
2.1	0.21825	0.146851	-0.00178
2.15	0.210935	0.149863	-0.00165
2.17	0.202364	0.131958	-0.00146
2.2	0.197833	0.119875	-0.00159
2.205	0.187917	0.119216	-0.00184
2.208	0.19844	0.11894	-0.00155
2.209	0.195496	0.118865	-0.00151
2.21	0.205148	0.119002	-0.0009
2.2105	0.193111	0.11896	-0.00083
2.2107	0.202883	0.118942	3.64E-05
2.2108	0.18774	0.11893	0.003885
2.2109	-3.39918	2.008895	41.61744
2.211	0.068764	0.118437	0.007812
2.2111	-3.37246	2.009572	41.74314
2.21113	-3.36689	2.009676	41.73696
2.21115	-3.36674	2.009597	41.72674
2.21117	-3.35697	2.009452	41.69638
2.21119	-3.33641	2.009449	41.65292

Table 6d: Nonadiabatic coupling elements in bohr^{-1} at $\gamma = 59°$ and $R_1 = R_2$

R_1 (bohr)	$\langle 1\|\frac{d}{d\gamma}\|2\rangle/R_1$	$\langle 1\|\frac{d}{d\gamma}\|3\rangle/R_1$	$\langle 2\|\frac{d}{d\gamma}\|3\rangle/R_1$
2.2112	-3.32814	2.009078	41.58134
2.21121	-3.29837	2.00876	41.45762
2.211228	0.054061	0.118326	0.093613
2.21123	0.08814	0.11857	0.070429
2.21127	0.183655	0.118891	0.007747
2.2113	0.19331	0.118894	0.003768
2.21133	0.197082	0.118892	0.001475
2.21137	0.194288	0.118888	0.000381
2.2114	0.199763	0.118891	8.62E-05
2.2115	0.187203	0.118883	-0.001
2.2116	0.190771	0.118874	-0.00132
2.2117	0.193749	0.118867	-0.00139
2.2118	0.198498	0.118857	-0.0011
2.212	0.212441	0.118844	-0.00096
2.213	0.205247	0.118753	-0.00117
2.214	0.193556	0.118662	-0.0017
2.215	0.19741	0.118563	-0.00144
2.217	0.197634	0.118519	-0.00162
2.22	0.189547	0.11823	-0.00165
2.23	0.21022	0.117438	-0.00109
2.25	0.192557	0.116081	-0.00142
2.3	0.181497	0.111154	-0.00106
2.35	0.173386	0.106391	-0.0012
2.4	0.168491	0.101672	-0.00105
2.45	0.163552	0.098136	-0.00106
2.5	0.15813	0.09475	-0.00091
2.6	0.144481	0.087532	0.000785
2.7	0.133822	0.081689	-0.00053
2.8	0.123851	0.075902	-0.00035
2.9	0.108587	0.070261	4.8E-05
3	0.099507	0.065836	-0.00053

Table 7a: Nonadiabatic coupling elements in bohr^{-1} at $\gamma = 59°$ and $R_1 = R_2$

R_1 (bohr)	$\langle 1 \vert \frac{d}{dR_1} \vert 2 \rangle$	$\langle 1 \vert \frac{d}{dR_1} \vert 3 \rangle$	$\langle 2 \vert \frac{d}{dR_1} \vert 3 \rangle$
1.4	18.76616	0.037639	0.428033
1.5	17.87346	0.003288	0.290824
1.55	17.25342	0.002637	0.273336
1.6	16.71509	0.003081	0.249045
1.61	16.50382	0.003387	0.261972
1.62	16.18473	0.00246	0.243009
1.63	16.07269	0.002507	0.257651
1.64	15.91094	0.004855	0.275853
1.645	16.05248	0.008745	0.279495
1.648	16.39971	0.027278	0.311399
1.649	16.81426	0.044908	0.330918
1.65	17.5703	0.100458	0.386322
1.6505	18.35584	0.130912	0.330405
1.651	19.6252	0.281402	0.36941
1.6513	21.05426	0.51404	0.425961
1.6515	22.12141	0.840058	0.467452
1.6516	22.87091	1.08862	0.495009
1.6517	23.42152	1.417665	0.521268
1.6518	23.84523	1.819582	0.54829
1.6519	23.99583	2.294825	0.55938
1.65193	23.8649	2.44526	0.561163
1.65194	23.76061	2.49498	0.559722
1.65195	22.85116	-1.2585	0.285588
1.652	7.493604	-0.97136	0.180779
1.6521	7.814794	-0.76655	0.189861
1.6522	8.400677	-0.59573	0.196349
1.6525	10.11558	-0.29144	0.213404
1.653	11.93334	-0.11528	0.22894
1.654	13.39265	-0.01447	0.315276
1.655	14.15626	-0.00354	0.307826
1.658	14.7791	0.005043	0.25795
1.66	14.99797	-0.01748	0.274363

Table 7b: Nonadiabatic coupling elements in bohr^{-1} at $\gamma = 59°$ and $R_1 = R_2$

R_1 (bohr)	$\langle 1\|\frac{d}{dR_1}\|2\rangle$	$\langle 1\|\frac{d}{dR_1}\|3\rangle$	$\langle 2\|\frac{d}{dR_1}\|3\rangle$
1.67	15.38988	0.007046	0.243583
1.68	15.42007	0.00173	0.243162
1.69	15.32194	0.000997	0.243986
1.695	15.11947	0.00276	0.283823
1.7	15.00197	0.001454	0.125845
1.71	15.74463	-0.00228	0.19832
1.72	15.70515	-0.00113	0.209564
1.75	15.28512	-0.00078	0.179515
1.8	14.75835	0.001679	0.167283
1.85	14.46346	0.001729	0.162211
1.87	14.16117	0.001608	0.147186
1.88	14.16393	0.001649	0.154897
1.89	14.13464	0.001721	0.151818
1.9	14.11057	0.00156	0.156224
1.91	14.09018	0.001191	0.154868
1.92	13.90827	0.005297	0.156411
1.93	13.47235	0.000968	0.16229
1.933	12.78983	0.007616	0.191104
1.934	12.18375	0.020285	0.220689
1.9345	11.64866	0.037631	0.249667
1.935	10.46311	0.080542	0.278885
1.9353	9.794399	0.133799	0.305971
1.9355	9.359721	0.184436	0.316399
1.9356	9.336828	0.212726	0.320517
1.9357	9.264182	0.24127	0.319398
1.93575	18.62744	-0.20993	-0.03931
1.9358	18.53423	-0.19572	-0.03921
1.9359	18.39852	-0.16842	-0.03717
1.936	18.24982	-0.14349	-0.02614
1.9362	17.72933	-0.10281	-0.01705
1.9363	17.50484	-0.08727	-0.00699
1.9365	16.67137	-0.06356	0.00791

Table 7c: Nonadiabatic coupling elements in bohr^{-1} at $\gamma = 59^\circ$ and $R_1 = R_2$

R_1 (bohr)	$\langle 1 \vert \frac{d}{dR_1} \vert 2 \rangle$	$\langle 1 \vert \frac{d}{dR_1} \vert 3 \rangle$	$\langle 2 \vert \frac{d}{dR_1} \vert 3 \rangle$
1.937	15.91253	-0.03169	0.048858
1.938	15.15795	-0.01326	0.100615
1.94	14.61504	-0.00338	0.117075
1.945	14.1889	-8.4E-05	0.126196
1.95	14.09441	0.000685	0.13022
1.96	13.84735	0.00105	0.127481
1.97	13.75736	0.000975	0.126937
1.98	13.65108	0.00091	0.126036
1.99	13.56777	0.000815	0.128228
2	13.50399	0.000772	0.128434
2.01	13.3758	0.00087	0.128525
2.02	13.17245	0.000951	0.128956
2.03	12.60242	0.002889	0.126593
2.1	13.09203	-0.00071	0.120988
2.15	12.37941	-0.00618	0.102673
2.17	12.58318	-0.00468	0.124739
2.2	12.40659	-0.00411	0.167268
2.205	12.19908	-0.00314	0.214562
2.208	12.07621	-0.0023	0.315687
2.209	11.93368	-0.00143	0.410506
2.21	11.53989	-0.00223	0.659381
2.2105	10.91221	-0.01201	1.070707
2.2107	10.32881	-0.02627	1.48376
2.2108	9.799504	-0.04343	1.863392
2.2109	8.925243	-0.08174	2.538063
2.211	7.190238	-0.19588	4.092773
2.2111	2.921079	-0.77999	10.61996
2.21113	0.754814	-1.38816	17.7263
2.21115	-0.64159	-2.07307	26.29274
2.21117	-1.6345	-3.02413	39.40743
2.21119	-2.07113	-4.09885	56.21601

Table 7d: Nonadiabatic coupling elements in bohr^{-1} at $\gamma = 59°$ and $R_1 = R_2$

R_1 (bohr)	$\langle 1\vert\frac{d}{dR_1}\vert 2\rangle$	$\langle 1\vert\frac{d}{dR_1}\vert 3\rangle$	$\langle 2\vert\frac{d}{dR_1}\vert 3\rangle$
2.2112	-2.08776	-4.60532	64.89151
2.21121	-2.00126	-5.04961	72.88485
2.211228	22.54618	1.103627	-12.83
2.21123	22.55502	1.063427	-12.6807
2.21127	20.37031	0.525786	-7.52715
2.2113	19.00138	0.340989	-5.52612
2.21133	17.97729	0.235407	-4.32821
2.21137	16.98645	0.155305	-3.34592
2.2114	16.43157	0.118493	-2.85156
2.2115	15.25476	0.057718	-1.90458
2.2116	14.58265	0.03333	-1.42105
2.2117	14.16927	0.021219	-1.12585
2.2118	13.9148	0.014506	-0.92529
2.212	13.53912	0.0074	-0.6738
2.213	12.86822	-0.00028	-0.24491
2.214	12.61819	-0.0014	-0.12284
2.215	12.53615	-0.00152	-0.06114
2.217	12.44841	-0.00177	-0.00142
2.22	12.33682	-0.00178	0.035456
2.23	12.48684	-0.00171	0.04752
2.25	12.2683	-0.00034	0.078546
2.3	11.9342	0.000142	0.087522
2.35	11.64975	0.000287	0.086297
2.4	11.35505	0.000546	0.084372
2.45	11.17549	0.000213	0.077312
2.5	11.01384	0.000407	0.078629
2.6	10.7842	-0.0006	0.075502
2.7	10.26364	0.000172	0.065718
2.8	9.969437	0.000539	0.063552
2.9	9.72477	0.001223	0.057302
3	9.405447	-0.00223	0.049616

Table 8a: Nonadiabatic coupling elements in bohr^{-2} at $\gamma = 59°$ and $R_1 = R_2$

R_1 (bohr)	$\langle 1 \vert \frac{d^2}{dR_1^2} \vert 2 \rangle$	$\langle 1 \vert \frac{d^2}{dR_1^2} \vert 3 \rangle$	$\langle 2 \vert \frac{d^2}{dR_1^2} \vert 3 \rangle$
1.4			
1.5	-0.00037	0.048443	-0.0094
1.55	-5.4E-06	0.046897	-0.00238
1.6	0.000132	0.042808	-0.00364
1.61	0.0001	0.044005	-0.01562
1.62	-0.00036	0.039184	0.061462
1.63	-0.00027	0.070023	0.00934
1.64	-9.6E-05	0.050803	-0.02193
1.645	0.000307	0.063846	-0.01538
1.648	0.001286	0.155049	0.060828
1.649	0.00435	0.310378	0.018547
1.65	0.007516	0.80683	0.073202
1.6505	0.015806	0.899863	-0.12858
1.651	0.025407	3.590096	0.069993
1.6513	0.047543	8.783683	0.178722
1.6515	0.053372	17.9629	0.169155
1.6516	0.075027	26.95651	0.235233
1.6517	0.055129	35.57839	0.236986
1.6518	0.042296	43.58716	0.254467
1.6519	0.015313	51.70955	0.02863
1.65193	-0.04362	54.5467	0.017007
1.65194	-0.10413	54.18331	-0.22064
1.65195	-0.90922	-3751.28	-27.4336
1.652	-3.07141	59.10628	-2.15435
1.6521	0.032221	21.81609	0.067915
1.6522	0.05863	18.12355	0.106966
1.6525	0.057283	10.58823	0.0532
1.653	0.036365	3.684916	0.015712
1.654	0.01456	1.011009	0.074749
1.655	0.007841	0.128501	-0.05728
1.658	0.002109	-0.04486	-0.03461
1.66	0.00106	-0.07652	-0.00677

Table 8b: Nonadiabatic coupling elements in bohr^{-2} at $\gamma = 59°$ and $R_1 = R_2$

R_1 (bohr)	$\langle 1 \vert \frac{d^2}{dR_1^2} \vert 2 \rangle$	$\langle 1 \vert \frac{d^2}{dR_1^2} \vert 3 \rangle$	$\langle 2 \vert \frac{d^2}{dR_1^2} \vert 3 \rangle$
1.67	0.000795	0.058107	-0.01615
1.68	0.000243	0.029708	-0.02773
1.69	0.000253	0.036686	-0.00485
1.695	1.65E-05	0.024603	0.011773
1.7	4.69E-05	0.027644	-0.02768
1.71	0.001006	0.027717	0.009138
1.72	0.000443	0.022146	0.003482
1.75	2.59E-05	0.028085	0.000834
1.8	0.000111	0.025048	0.00235
1.85	-0.00011	0.023563	0.004176
1.87	-7.8E-05	0.021184	0.056808
1.88	-3.4E-05	0.032457	0.085715
1.89	-4.4E-05	0.029148	0.079726
1.9	7.36E-05	0.028755	0.011623
1.91	-1E-04	0.024207	0.08305
1.92	-7.3E-05	0.260713	0.067217
1.93	-0.00046	0.02086	0.085857
1.933	-0.00215	0.037518	0.080506
1.934	-0.00596	0.127908	0.099791
1.9345	-0.01057	0.32637	0.069555
1.935	-0.0236	0.778112	0.141464
1.9353	-0.02226	1.612028	0.176592
1.9355	-0.02163	2.274947	0.135345
1.9356	-0.00235	2.510777	0.127155
1.9357	-0.00725	2.465127	0.056977
1.93575	1.872734	-90.5869	-7.09068
1.9358	-0.01851	2.52729	0.071773
1.9359	-0.01342	2.471308	0.094705
1.936	-0.01476	2.281242	0.120326
1.9362	-0.02588	1.891399	0.130358
1.9363	-0.02235	1.437227	0.16762
1.9365	-0.04153	1.106265	0.155207

Table 8c: Nonadiabatic coupling elements in bohr^{-2} at $\gamma = 59^{\circ}$ and $R_1 = R_2$

R_1 (bohr)	$\langle 1 \vert \frac{d^2}{dR_1^2} \vert 2 \rangle$	$\langle 1 \vert \frac{d^2}{dR_1^2} \vert 3 \rangle$	$\langle 2 \vert \frac{d^2}{dR_1^2} \vert 3 \rangle$
1.937	-0.01507	0.607148	0.156398
1.938	-0.00747	0.195204	0.124351
1.94	-0.00263	0.067809	0.081503
1.945	-0.00075	0.028933	0.074905
1.95	-0.00016	0.025564	0.08684
1.96	-0.0002	0.024398	0.067717
1.97	-5.7E-05	0.022147	0.071826
1.98	-6.9E-05	0.019576	0.077173
1.99	-3.5E-05	0.017414	0.077321
2	-7.5E-05	0.016236	0.079663
2.01	-5.3E-05	0.016331	0.073341
2.02	-0.00018	0.014816	0.055868
2.03	-0.00048	0.018117	0.064145
2.1	0.000102	0.015849	0.047917
2.15	-0.00016	0.006944	0.038733
2.17	0.000124	0.052771	0.03241
2.2	-9.7E-05	0.018983	0.033981
2.205	-0.00043	0.025128	0.043706
2.208	-0.00057	0.03705	0.064261
2.209	-0.00159	0.054808	0.123252
2.21	-0.0041	0.077817	0.273582
2.2105	-0.01269	-0.00255	0.85139
2.2107	-0.02929	-0.31106	2.087879
2.2108	-0.05301	-1.16535	3.815506
2.2109	-0.0875	-3.06371	6.763565
2.211	-0.17344	-10.8116	15.55274
2.2111	-0.4257	-76.0447	65.41482
2.21113	-0.71931	-269.264	237.7155
2.21115	-0.69342	-500.924	430.8147
2.21117	-0.48855	-830.767	662.464
2.21119	-0.20587	-1230.07	855.3133

Table 8d: Nonadiabatic coupling elements in bohr^{-2} at $\gamma = 59^\circ$ and $R_1 = R_2$

R_1 (bohr)	$\langle 1\|\frac{d^2}{dR_1^2}\|2\rangle$	$\langle 1\|\frac{d^2}{dR_1^2}\|3\rangle$	$\langle 2\|\frac{d^2}{dR_1^2}\|3\rangle$
2.2112	-0.00147	-1409.11	887.8281
2.21121	0.104521	-1562.64	825.3082
2.211228	13.63535	3383.469	-4762.22
2.21123	0.042158	-234.713	74.38948
2.21127	-0.54707	-141.957	128.8766
2.2113	-0.45686	-64.0189	66.76109
2.21133	-0.34175	-35.8985	39.9857
2.21137	-0.24799	-20.0229	24.60661
2.2114	-0.18519	-12.1161	16.526
2.2115	-0.11785	-5.90331	9.511437
2.2116	-0.0673	-2.33104	4.873811
2.2117	-0.04145	-1.14827	2.984747
2.2118	-0.02567	-0.66596	2.036801
2.212	-0.01897	-0.36643	1.28959
2.213	-0.00677	-0.08609	0.453887
2.214	-0.00252	-0.01471	0.15994
2.215	-0.00088	0.0742	0.08958
2.217	-0.00051	0.002633	0.061733
2.22	-0.00038	0.006292	0.047962
2.23	-1.9E-05	0.003843	0.028571
2.25	4.4E-05	0.010924	0.000603
2.3	-0.00014	0.010555	0.020826
2.35	-5.6E-05	0.006465	0.017439
2.4	-2E-05	0.0099	0.01825
2.45	-3.7E-06	0.036071	0.01289
2.5	4.47E-06	0.008795	0.011207
2.6	-6.1E-05	-0.02588	-0.00744
2.7	-9.5E-05	0.007065	0.007413
2.8	-4.9E-05	0.006519	0.00351
2.9	-6.3E-06	0.003005	-0.0016
3	-7.1E-05	-0.0053	0.002989

Table 9a: Nonadiabatic coupling elements in bohr^{-1} at $\gamma = 59°$ and $R_1 = R_2$

R_1 (bohr)	$\langle 1 \vert \frac{d}{dR_2} \vert 2 \rangle$	$\langle 1 \vert \frac{d}{dR_2} \vert 3 \rangle$	$\langle 2 \vert \frac{d}{dR_2} \vert 3 \rangle$
1.4	-19.06	-0.03768	-0.43409
1.5	-18.1024	-0.00324	-0.30957
1.55	-17.2778	-0.00263	-0.27434
1.6	-17.0635	-0.0031	-0.25717
1.61	-16.662	-0.00336	-0.27849
1.62	-16.2778	-0.00245	-0.25068
1.63	-16.2046	-0.00283	-0.25966
1.64	-16.2052	-0.00483	-0.27672
1.645	-16.3773	-0.00872	-0.27913
1.648	-16.6492	-0.02718	-0.32933
1.649	-17.1153	-0.04251	-0.34272
1.65	-17.8344	-0.10003	-0.3955
1.6505	-18.6718	-0.13029	-0.34029
1.651	-19.975	-0.28038	-0.37984
1.6513	-21.1878	-0.51252	-0.42931
1.6515	-22.4885	-0.83482	-0.47809
1.6516	-23.0697	-1.08644	-0.50499
1.6517	-23.6679	-1.41565	-0.53242
1.6518	-24.1436	-1.81955	-0.56116
1.6519	-24.3432	-2.2952	-0.57864
1.65193	-24.4394	-2.44666	-0.58131
1.65194	-24.5166	-2.49594	-0.58397
1.65195	-23.7388	1.258587	-0.30202
1.652	-7.53136	0.971462	-0.18375
1.6521	-7.95399	0.765964	-0.19902
1.6522	-8.46429	0.594849	-0.21312
1.6525	-10.2316	0.290682	-0.22562
1.653	-12.1795	0.114903	-0.23459
1.654	-13.64	0.014421	-0.31939
1.655	-14.4107	0.003496	-0.31285
1.658	-15.0577	-0.00507	-0.26298
1.66	-15.2997	0.017496	-0.27935

Table 9b: Nonadiabatic coupling elements in bohr^{-1} at $\gamma = 59^\circ$ and $R_1 = R_2$

R_1 (bohr)	$\langle 1 \vert \frac{d}{dR_2} \vert 2 \rangle$	$\langle 1 \vert \frac{d}{dR_2} \vert 3 \rangle$	$\langle 2 \vert \frac{d}{dR_2} \vert 3 \rangle$
1.67	-15.7066	0.007088	-0.26095
1.68	-15.7027	0.001741	-0.24998
1.69	-15.6193	0.001024	-0.2553
1.695	-15.1652	0.000772	-0.29611
1.7	-15.1124	0.001432	-0.13525
1.71	-15.8122	-0.00228	-0.20569
1.72	-15.9357	-0.00127	-0.22286
1.75	-15.4941	-0.00077	-0.18957
1.8	-14.9999	0.001688	-0.18563
1.85	-14.5914	0.001735	-0.16774
1.87	-14.3213	0.001627	-0.16406
1.88	-14.2302	0.001697	-0.16997
1.89	-14.1992	0.001642	-0.16645
1.9	-14.2912	0.001485	-0.16367
1.91	-14.1336	0.001162	-0.16612
1.92	-14.1206	0.001282	-0.17664
1.93	-13.5109	0.000956	-0.17508
1.933	-13.0053	-0.00761	-0.20695
1.934	-12.3598	-0.02029	-0.23546
1.9345	-11.756	-0.03764	-0.25754
1.935	-10.6496	-0.08055	-0.29578
1.9353	-9.8889	-0.13381	-0.32035
1.9355	-9.57083	-0.18445	-0.33336
1.9356	-9.39562	-0.21273	-0.3334
1.9357	-9.43127	-0.24128	-0.33219
1.93575	-18.7335	0.209932	0.025223
1.9358	-18.7347	0.195715	0.024411
1.9359	-18.5862	0.168422	0.020567
1.936	-18.3439	0.143492	0.020797
1.9362	-17.9318	0.102814	-0.00026
1.9363	-17.6751	0.087275	-0.00699
1.9365	-16.8588	0.063589	-0.0251

Table 9c: Nonadiabatic coupling elements in bohr^{-1} at $\gamma = 59°$ and $R_1 = R_2$

R_1 (bohr)	$\langle 1\|\frac{d}{dR_2}\|2\rangle$	$\langle 1\|\frac{d}{dR_2}\|3\rangle$	$\langle 2\|\frac{d}{dR_2}\|3\rangle$
1.937	-16.1163	0.031708	-0.06427
1.938	-15.3184	0.013284	-0.11439
1.94	-14.7854	0.003387	-0.13103
1.945	-14.3591	9.23E-05	-0.14038
1.95	-14.1731	0.000671	-0.14409
1.96	-14.0773	0.001036	-0.14396
1.97	-13.9168	0.000963	-0.14197
1.98	-13.8131	0.00092	-0.14255
1.99	-13.7151	0.000813	-0.14342
2	-13.5669	0.000765	-0.14395
2.01	-13.5466	0.000871	-0.14534
2.02	-13.3465	0.000958	-0.14436
2.03	-12.8306	0.002901	-0.1431
2.1	-13.2503	-0.00072	-0.1333
2.15	-12.5022	-0.00612	-0.11365
2.17	-12.7171	-0.00466	-0.1337
2.2	-12.4495	-0.0041	-0.17278
2.205	-12.2807	-0.00313	-0.22002
2.208	-12.0385	-0.00229	-0.31843
2.209	-11.8914	-0.00142	-0.41348
2.21	-11.4951	0.002182	-0.66275
2.2105	-10.9037	0.01187	-1.07546
2.2107	-10.301	0.02599	-1.48883
2.2108	-9.78608	0.043001	-1.86794
2.2109	-8.90001	0.080921	-2.54243
2.211	-7.16234	0.193258	-4.0889
2.2111	-2.88395	0.774435	-10.6527
2.21113	-0.69721	1.379181	-17.774
2.21115	0.729249	2.069695	-26.4912
2.21117	1.80638	3.031732	-39.989
2.21119	2.323483	4.1016	-57.1312

Table 9d: Nonadiabatic coupling elements in bohr^{-1} at $\gamma = 59°$ and $R_1 = R_2$

R_1 (bohr)	$\langle 1 \vert \frac{d}{dR_2} \vert 2 \rangle$	$\langle 1 \vert \frac{d}{dR_2} \vert 3 \rangle$	$\langle 2 \vert \frac{d}{dR_2} \vert 3 \rangle$
2.2112	2.459026	4.604326	-66.2951
2.21121	2.571517	5.059364	-75.504
2.211228	-23.7687	-1.09348	15.37088
2.21123	-23.4667	-1.054	14.54633
2.21127	-20.444	-0.52124	7.66111
2.2113	-19.0174	-0.33747	5.572462
2.21133	-17.9704	-0.23327	4.349664
2.21137	-16.9679	-0.15358	3.350728
2.2114	-16.4138	-0.11745	2.858588
2.2115	-15.2268	-0.05711	1.903509
2.2116	-14.5822	-0.03293	1.416124
2.2117	-14.1534	-0.02095	1.120292
2.2118	-13.8335	-0.01433	0.922944
2.212	-13.4676	-0.0073	0.669223
2.213	-12.8492	-0.00032	0.239099
2.214	-12.6857	-0.00142	0.113063
2.215	-12.5899	-0.00152	0.051738
2.217	-12.508	-0.00178	-0.00818
2.22	-12.4732	-0.00178	-0.04637
2.23	-12.4496	-0.00171	-0.05359
2.25	-12.2937	-0.00035	-0.08426
2.3	-12.0043	0.000144	-0.09082
2.35	-11.743	0.000289	-0.09032
2.4	-11.4568	0.000546	-0.08812
2.45	-11.2718	0.000206	-0.08086
2.5	-11.0909	0.000407	-0.08115
2.6	-10.8145	-0.00059	-0.07679
2.7	-10.2774	0.000171	-0.06678
2.8	-9.9684	0.000538	-0.06445
2.9	-9.7294	0.001216	-0.05807
3	-9.41268	-0.00223	-0.04969

Table 10a: Nonadiabatic coupling elements in bohr^{-2} at $\gamma = 59°$ and $R_1 = R_2$

R_1 (bohr)	$\langle 1 \vert \frac{d^2}{dR_2^2} \vert 2 \rangle$	$\langle 1 \vert \frac{d^2}{dR_2^2} \vert 3 \rangle$	$\langle 2 \vert \frac{d^2}{dR_2^2} \vert 3 \rangle$
1.4			
1.5	4.3E-05	0.059253	-5.12172
1.55	0.000189	0.047432	-2.04363
1.6	0.000384	0.044895	-4.63025
1.61	0.000855	0.046895	-17.692
1.62	0.000532	0.041443	67.97373
1.63	0.000136	0.072814	9.2732
1.64	0.000377	0.048125	-22.3262
1.645	2.95E-05	0.049402	-12.9873
1.648	-0.0004	0.034655	37.6009
1.649	-0.0041	-0.04836	-9.29203
1.65	-0.00683	-0.32137	-27.7618
1.6505	-0.01624	-0.31126	102.7641
1.651	-0.0256	-2.41794	-70.2394
1.6513	-0.04004	-6.70677	-144.387
1.6515	-0.06444	-14.488	-232.687
1.6516	-0.05749	-23.0646	-244.681
1.6517	-0.05922	-30.2348	-215.786
1.6518	-0.04717	-36.9582	-195.863
1.6519	-0.01937	-43.2944	-124.325
1.65193	-0.03179	-45.9333	8.773743
1.65194	-0.07673	-44.6195	-199.577
1.65195	0.778246	3756.869	28242.73
1.652	3.242246	-55.6859	2332.729
1.6521	-0.04162	-19.2	-152.371
1.6522	-0.05051	-16.0622	-78.2795
1.6525	-0.05837	-9.68931	-31.1804
1.653	-0.03853	-3.35035	-25.0573
1.654	-0.01421	-0.99932	-92.2163
1.655	-0.00707	-0.08463	-39.2592
1.658	-0.00259	-0.10637	3.107477
1.66	-0.00075	0.150906	-17.5495

Table 10b: Nonadiabatic coupling elements in bohr^{-2} at $\gamma = 59°$ and $R_1 = R_2$

R_1 (bohr)	$\langle 1 \vert \frac{d^2}{dR_2^2} \vert 2 \rangle$	$\langle 1 \vert \frac{d^2}{dR_2^2} \vert 3 \rangle$	$\langle 2 \vert \frac{d^2}{dR_2^2} \vert 3 \rangle$
1.67	-2E-06	0.031298	-11.0215
1.68	0.000218	0.035913	-26.6146
1.69	0.000437	0.040636	-5.16276
1.695	0.00148	-0.00692	-5.20308
1.7	0.000387	0.032996	36.14285
1.71	-0.00044	0.029013	-5.20633
1.72	7.61E-05	0.018024	-3.69949
1.75	0.000635	0.030237	6.11738
1.8	0.000732	0.028275	7.095984
1.85	0.000462	0.024346	9.075539
1.87	0.000564	0.022982	61.65808
1.88	0.000385	0.01591	88.29366
1.89	0.000331	0.015644	83.49101
1.9	0.000301	0.01578	14.78036
1.91	0.000354	0.019971	85.0205
1.92	0.00038	0.02131	81.90955
1.93	0.000822	0.021563	86.4919
1.933	0.002036	-0.01393	61.23612
1.934	0.006795	-0.12605	42.16192
1.9345	0.012441	-0.36758	-32.45
1.935	0.022485	-0.93906	5.84351
1.9353	0.025649	-1.93947	2.09376
1.9355	0.016308	-2.78938	13.38654
1.9356	0.017791	-3.14764	78.73418
1.9357	-0.00319	-3.24417	70.59509
1.93575	-1.8602	89.89505	7229.95
1.9358	7.18E-05	-3.15793	51.37251
1.9359	0.015211	-2.98799	33.25951
1.936	0.024541	-2.70484	9.74503
1.9362	0.02097	-2.17651	-22.3775
1.9363	0.026002	-1.67103	-1.8544
1.9365	0.041184	-1.26792	-10.8997

Table 10c: Nonadiabatic coupling elements in bohr^{-2} at $\gamma = 59°$ and $R_1 = R_2$

R_1 (bohr)	$\langle 1\vert\frac{d^2}{dR_2^2}\vert 2\rangle$	$\langle 1\vert\frac{d^2}{dR_2^2}\vert 3\rangle$	$\langle 2\vert\frac{d^2}{dR_2^2}\vert 3\rangle$
1.937	0.01519	-0.67156	-4.02196
1.938	0.008282	-0.17668	22.85383
1.94	0.002972	-0.03436	65.24831
1.945	0.001165	0.01409	70.74532
1.95	0.000609	0.024194	84.47643
1.96	0.00041	0.02518	68.30493
1.97	0.00055	0.022882	74.48888
1.98	0.000544	0.020502	81.52786
1.99	0.000483	0.018029	79.71243
2	0.000504	0.016555	83.50334
2.01	0.000466	0.017169	77.13139
2.02	0.000613	0.015516	60.63561
2.03	0.000977	0.018257	69.42981
2.1	0.00033	0.016968	48.71223
2.15	0.000461	0.007911	42.4165
2.17	0.000231	0.053453	33.49282
2.2	0.000347	0.019033	34.55198
2.205	0.000616	0.024957	28.43835
2.208	0.000935	0.036587	2.107713
2.209	0.00159	0.054394	-61.5089
2.21	0.004091	0.121435	-216.226
2.2105	0.01197	0.38538	-786.519
2.2107	0.030275	1.106781	-2028.51
2.2108	0.051645	2.249428	-3752.19
2.2109	0.088702	4.555702	-6699.64
2.211	0.173721	11.83598	-15408.9
2.2111	0.4267	40.38999	-65711.6
2.21113	0.726192	134.8412	-238145
2.21115	0.708532	184.827	-438320
2.21117	0.530619	117.1324	-681735
2.21119	0.246021	-174.942	-872340

Table 10d: Nonadiabatic coupling elements in bohr^{-2} at $\gamma = 59^\circ$ and $R_1 = R_2$

R_1 (bohr)	$\langle 1 \vert \frac{d^2}{dR_2^2} \vert 2 \rangle$	$\langle 1 \vert \frac{d^2}{dR_2^2} \vert 3 \rangle$	$\langle 2 \vert \frac{d^2}{dR_2^2} \vert 3 \rangle$
2.2112	0.120235	-428.944	-937352
2.21121	0.094126	-724.146	-948465
2.211228	-14.6311	-3469.39	5049087
2.21123	1.5122	152.2275	-411863
2.21127	0.756561	125.2227	-172104
2.2113	0.476114	58.74709	-69618.4
2.21133	0.349382	34.0016	-40757.4
2.21137	0.250908	19.92046	-24963
2.2114	0.184933	12.19611	-16388.7
2.2115	0.11889	6.209692	-9526.46
2.2116	0.064678	2.52574	-4847
2.2117	0.043076	1.261619	-2934.53
2.2118	0.032064	0.666354	-1945.17
2.212	0.018405	0.341052	-1239.22
2.213	0.006414	0.06133	-404.668
2.214	0.001902	-0.01292	-86.9202
2.215	0.001179	0.076534	-31.8529
2.217	0.000624	0.00385	3.922578
2.22	0.00039	0.007741	25.06493
2.23	0.000126	0.004263	29.03581
2.25	0.0001	0.011317	53.27119
2.3	0.000216	0.01075	22.78597
2.35	0.000239	0.006418	20.27292
2.4	0.000227	0.010174	18.8692
2.45	0.000176	0.035959	13.96854
2.5	0.000149	0.009028	11.57374
2.6	3.48E-05	-0.02597	-7.0147
2.7	6.54E-05	0.007118	7.471938
2.8	9.9E-05	0.006587	3.375323
2.9	-8.5E-05	0.002466	-1.50333
3	0.000174	-0.00536	3.120676

Table 11a: Energies in eV at $R_1 = R_2 = 1.97$ bohr

γ (degrees)	E_1	E_2	E_3
47	2.012323	3.959532	5.717264
48	2.055400	3.850222	5.707359
49	2.101660	3.746000	5.700638
50	2.150070	3.643193	5.700964
51	2.204467	3.544141	5.701862
52	2.261531	3.447021	5.707305
53	2.321370	3.354827	5.716584
54	2.385073	3.265817	5.732938
55	2.449811	3.181269	5.750164
56	2.514766	3.097429	5.772314
57	2.582660	3.019875	5.795689
57.5	2.616239	2.979030	5.806710
58	2.650417	2.941749	5.818166
58.5	2.685330	2.905122	5.829704
59	2.719618	2.867297	5.843909
59.5	2.755592	2.832030	5.858250
59.6	2.763157	2.824874	5.860563
59.7	2.770477	2.817826	5.863910
59.8	2.777824	2.810424	5.867202
59.9	2.784926	2.803349	5.870468
59.95	2.788790	2.799975	5.871828
59.96	2.789525	2.799267	5.872128
59.97	2.790042	2.798070	5.872509
59.98	2.790777	2.796682	5.872835
59.985	2.791131	2.796219	5.872999
59.99	2.791484	2.795838	5.873135
59.993	2.791702	2.795648	5.873216
59.995	2.791838	2.795485	5.873271
59.997	2.791974	2.795349	5.873352
59.998	2.792056	2.795267	5.873352
59.999	2.792138	2.795212	5.873407
59.9995	2.792165	2.795158	5.873407

Table 11b: Energies in eV at $R_1 = R_2 = 1.97$ bohr

γ (degrees)	E_1	E_2	E_3
60.001	2.793308	2.795131	5.873271
60.0015	2.793335	2.795104	5.873298
60.002	2.793362	2.795076	5.873298
60.003	2.793444	2.794995	5.873325
60.005	2.793580	2.794859	5.873407
60.007	2.793743	2.794723	5.873461
60.01	2.794070	2.794940	5.873543
60.015	2.794423	2.794587	5.873679
60.02	2.794233	2.794777	5.873842
60.03	2.793525	2.795512	5.874005
60.04	2.792818	2.796219	5.874305
60.05	2.792437	2.796927	5.874658
60.1	2.788926	2.800764	5.876182
60.2	2.781770	2.807893	5.879339
60.3	2.773661	2.814832	5.881597
60.4	2.766640	2.822207	5.885026
60.5	2.758939	2.829418	5.888020
61	2.723210	2.864576	5.903122
61.5	2.689303	2.901258	5.920266
62	2.655424	2.938729	5.935940
62.5	2.621627	2.972771	5.953954
63	2.585925	3.009044	5.970417
64	2.524344	3.081836	6.003725
65	2.459008	3.157540	6.039155
66	2.400230	3.228264	6.073497
67	2.343139	3.300975	6.109879
68	2.286974	3.374338	6.146860
69	2.233203	3.446586	6.183079
70	2.178833	3.520058	6.222183
71	2.129553	3.590293	6.258701
72	2.079156	3.660826	6.294540
73	2.031127	3.732802	6.332636

Table 12a: Nonadiabatic coupling elements in bohr^{-1} at $R_1 = R_2 = 1.97$ bohr

γ (degrees)	$\langle 1\|\frac{d}{d\gamma}\|2\rangle/R_1$	$\langle 1\|\frac{d}{d\gamma}\|3\rangle/R_1$	$\langle 2\|\frac{d}{d\gamma}\|3\rangle/R_1$
47	0.235185	0.164154	-0.01458
48	0.233484	0.154956	-1.33869
49	0.227702	0.158251	0.001818
50	0.22878	0.159789	-0.02642
51	0.233234	0.161472	-0.00344
52	0.233961	0.163101	-0.019
53	0.237976	0.164467	-0.01776
54	0.217007	0.165356	-0.06084
55	0.233608	0.165891	0.007804
56	0.244794	0.163668	0.0284
57	0.235129	0.163754	0.014694
57.5	0.160177	0.164622	0.000756
58	0.260784	0.16526	0.002725
58.5	0.224335	0.164913	-0.00874
59	0.074639	0.164172	-0.01314
59.5	0.216528	0.165206	-0.0115
59.6	0.226572	0.165069	-0.00101
59.7	0.585088	0.165313	-0.00102
59.8	0.66783	0.165318	0.00038
59.9	1.149598	0.165259	-0.00115
59.95	-0.10931	0.165871	-0.00149
59.96	19.60526	0.165912	-0.00818
59.97	5.320589	0.166472	-0.00889
59.98	-0.18763	0.166267	-0.00498
59.985	4.320716	0.164498	0.001206
59.99	-0.32299	0.016788	0.001269
59.993	-4.30353	0.167744	0.002099
59.995	6.719716	0.162563	-0.01294
59.997	-26.0188	0.15036	0.076327
59.998	59.1802	0.160441	-0.17539
59.999	-25549.4	11.01762	-1.68696
59.9995	25442.83	-3.334	-10.7384

Table 12b: Nonadiabatic coupling elements in bohr^{-1} at $R_1 = R_2 = 1.97$ bohr

γ (degrees)	$\langle 1 \vert \frac{d}{d\gamma} \vert 2 \rangle / R_1$	$\langle 1 \vert \frac{d}{d\gamma} \vert 3 \rangle / R_1$	$\langle 2 \vert \frac{d}{d\gamma} \vert 3 \rangle / R_1$
60.001	10.64692	-0.18636	0.153797
60.0015	-38.6709	-0.02011	0.162123
60.002	-10.2432	-0.05525	0.150242
60.003	-0.1925	-0.00312	0.165518
60.005	-1.90071	-0.00364	0.167602
60.007	-2.16098	-0.00163	0.164525
60.01	-0.21175	2.32E-05	0.016688
60.015	-2.52158	0.000856	0.165985
60.02	1.411407	0.004063	0.165467
60.03	4.966742	0.002288	0.165306
60.04	0.596585	-0.00216	0.166277
60.05	-0.16728	-0.0001	0.165727
60.1	-0.3673	-0.00193	0.165895
60.2	-0.26734	0.000749	0.165543
60.3	-0.48625	-0.00061	0.1654
60.4	-0.21665	-4.3E-05	0.165689
60.5	-0.2222	-2.3E-05	0.165702
61	-0.20104	-0.00242	0.16383
61.5	-0.23065	0.000754	0.163488
62	-0.23339	0.001349	0.16498
62.5	-0.22781	0.001891	0.165476
63	-0.22817	0.00368	0.153172
64	-0.22485	0.005157	0.166469
65	-0.22902	0.005973	0.167121
66	-0.23072	0.00446	0.171373
67	-0.22706	0.008224	0.201294
68	-0.23395	0.011788	0.361638
69	-0.23519	0.012955	0.207161
70	-0.21055	0.014512	0.145898
71	-0.22722	0.014209	0.18377
72	-0.22009	0.015463	0.151348
73	-0.22365	0.015357	0.203975

Table 13a: Nonadiabatic coupling elements in bohr^{-2} at $R_1 = R_2 = 1.97$ bohr

γ (degrees)	$< 1\|\frac{d^2}{d\gamma^2}\|2 > /R_1^2$	$< 1\|\frac{d^2}{d\gamma^2}\|3 > /R_1^2$	$< 2\|\frac{d^2}{d\gamma^2}\|3 > /R_1^2$
47			
48	495.5378	-13.0045	-828.733
49	412.1208	0.935195	401.5681
50	332.9519	5.841503	238.6233
51	412.2373	7.307592	1042.833
52	449.2008	0.007721	867.9464
53	592.587	-0.00292	-170.228
54	453.8245	-0.04218	445.1648
55	405.5708	0.017145	779.8679
56	544.3222	0.020835	401.4045
57	529.8943	0.01917	315.6224
57.5	445.142	0.021114	51.66721
58	440.3413	0.593507	203.9823
58.5	203.5229	-0.03419	1139.862
59	285.9409	0.023127	887.4871
59.5	-0.04288	0.021107	557.7151
59.6	0.297612	0.01924	9.519925
59.7	8.108931	0.02103	1.311111
59.8	7.922528	0.020927	9.039493
59.9	7.442281	-1.58899	1.885563
59.95	-15.9833	-1.41829	9.562716
59.96	1580.823	-127.351	293.1637
59.97	-704.159	-398.734	902.9014
59.98	-307.067	-343.348	359.3161
59.985	487.857	-298.115	357.9583
59.99	-472.051	-19.7485	5.383837
59.993	-853.764	-428.395	616.9783
59.995	2636.899	-342.811	779.9316
59.997	-8417.25	-441.526	355.7228
59.998	42887.53	-796.705	489.5093
59.999	-1.3E+07	212206.1	251271.9
59.9995	51804957	-543446	368481.9

Table 13b: Nonadiabatic coupling elements in bohr^{-2} at $R_1 = R_2 = 1.97$ bohr

γ (degrees)	$< 1\lvert\frac{d^2}{d\gamma^2}\rvert 2 > /R_1^2$	$< 1\lvert\frac{d^2}{d\gamma^2}\rvert 3 > /R_1^2$	$< 2\lvert\frac{d^2}{d\gamma^2}\rvert 3 > /R_1^2$
60.001	-8606205	890.5396	4480.647
60.0015	-49591.3	-715.709	857.0194
60.002	29172.65	-600.534	423.3196
60.003	5103.494	19.54533	11.29353
60.005	-146.93	-716.402	384.3689
60.007	-68.3057	-13.3087	3.175171
60.01	330.459	-7.05453	-19.4393
60.015	-308.76	-427.578	306.3522
60.02	469.0537	-265.174	362.2807
60.03	229.4741	-211.358	416.3267
60.04	-438.199	96.42331	137.6638
60.05	-40.443	1.092719	1.87745
60.1	-7.01593	-0.06544	0.771433
60.2	-3.2681	9.82755	0.017304
60.3	-8.31013	5.193687	0.017942
60.4	-2.64618	5.826297	0.020262
60.5	-2.34367	4.163434	0.023929
61	-1.51282	-6.49149	0.015187
61.5	-2.11447	0.461477	0.016505
62	-2.22649	1.545928	0.019725
62.5	-2.02705	2.71194	0.018862
63	-4.15911	8.014478	0.000592
64	-3.26355	5.090144	0.026648
65	-3.19983	6.671998	0.020516
66	-19.4243	420.5594	0.025394
67	-70.9604	259.2013	0.057563
68	-160.698	458.8634	8.051822
69	-175.511	502.7005	-27.8479
70	-130.873	384.6961	-0.00815
71	-121.605	397.2165	0.043659
72	-121.155	301.3369	0.006518
73	-101.42	302.2497	0.050594

Table 14a: Nonadiabatic coupling elements in bohr^{-1} at $R_1 = R_2 = 1.97$ bohr

γ (degrees)	$\langle 1\|\frac{d}{dR_1}\|2\rangle$	$\langle 1\|\frac{d}{dR_1}\|3\rangle$	$\langle 2\|\frac{d}{dR_1}\|3\rangle$
47	-0.8362	0.013233	-0.43011
48	-0.93232	0.010693	-0.40804
49	-1.04515	0.011416	-0.21228
50	-1.175	0.00961	-0.26526
51	-1.34116	0.008831	-0.24848
52	-1.53924	0.007447	-0.16909
53	-1.77677	0.006633	-0.10833
54	-2.11864	0.005923	-0.20724
55	-2.60566	0.004846	-0.15334
56	-3.07321	0.004095	-0.13655
57	-4.31123	0.001531	-0.11149
57.5	-5.18048	0.00287	-0.16805
58	-6.5971	0.002974	-0.18936
58.5	-9.2855	-0.0004	-0.1304
59	-13.7574	0.000975	-0.12694
59.5	-28.2372	0.000822	-0.09843
59.6	-35.5328	0.000959	-0.0813
59.7	-47.6866	0.001279	-0.05061
59.8	-72.492	0.002204	0.005188
59.9	-149.498	0.007297	0.175242
59.95	-311.487	0.025607	0.505835
59.96	-396.193	0.038897	0.67174
59.97	-540.791	0.065054	0.95132
59.98	-832.686	0.143928	1.49243
59.985	-1124.81	0.247549	2.025691
59.99	-1682.37	0.531878	3.016483
59.993	-2321.05	1.022566	4.131405
59.995	-3013.82	1.821622	5.307709
59.997	-4053	3.769281	6.76173
59.998	-4743	5.614655	7.236782
59.999	-5559.33	8.005369	6.698194
59.9995	-6003.11	9.227488	5.707428

Table 14b: Nonadiabatic coupling elements in bohr^{-1} at $R_1 = R_2 = 1.97$ bohr

γ (degrees)	$\langle 1\|\frac{d}{dR_1}\|2\rangle$	$\langle 1\|\frac{d}{dR_1}\|3\rangle$	$\langle 2\|\frac{d}{dR_1}\|3\rangle$
60.001	6089.434	-5.99017	-9.25837
60.0015	5274.858	-6.28385	-7.79472
60.002	4541.804	-6.28418	-6.51497
60.003	3411.254	-5.93383	-4.5107
60.005	2190.269	-4.78182	-2.28903
60.007	1609.415	-3.84461	-1.32214
60.01	1162.928	-2.90938	-0.6924
60.015	805.5412	-2.06283	-0.31934
60.02	621.169	-1.60787	-0.17919
60.03	428.9915	-1.14195	-0.07808
60.04	332.3406	-0.89845	-0.0441
60.05	270.489	-0.75521	-0.02858
60.1	141.4942	-0.40058	-0.05522
60.2	73.17326	-0.30643	-0.00069
60.3	49.32602	-0.2616	0.000278
60.4	37.32215	-0.23724	0.000748
60.5	29.97789	-0.22408	0.000929
61	15.29615	-0.19255	0.002111
61.5	10.22872	-0.1751	0.002555
62	7.72712	-0.16518	0.002316
62.5	6.242126	-0.15953	-0.00324
63	5.169724	-0.15681	-0.03297
64	3.892695	-0.15074	-0.13619
65	3.258485	-0.15536	0.005706
66	2.666709	-0.15828	-0.16826
67	2.372113	-0.00115	-0.23758
68	2.062728	-0.0972	-0.20175
69	1.851914	-0.10046	-0.12539
70	1.689015	-0.09851	-0.34959
71	1.556283	-0.09402	-0.75433
72	1.447456	-0.09102	-0.55794
73	1.408778	-0.09287	-0.43429

Table 15a: Nonadiabatic coupling elements in bohr^{-1} at $R_1 = R_2 = 1.97$ bohr

γ (degrees)	$\langle 1\|\frac{d}{dR_2}\|2\rangle$	$\langle 1\|\frac{d}{dR_2}\|3\rangle$	$\langle 2\|\frac{d}{dR_2}\|3\rangle$
47	0.841393	-0.01322	0.089183
48	0.93724	-0.01086	0.962048
49	1.058678	-0.01137	0.333333
50	1.184348	-0.00957	0.286006
51	1.35854	-0.00882	0.280024
52	1.557602	-0.00753	0.291511
53	1.800179	-0.00666	0.388236
54	2.148546	-0.00594	0.352072
55	2.632558	-0.00485	0.212429
56	3.109878	-0.0041	0.158517
57	4.372805	-0.00156	0.199609
57.5	5.254447	-0.00287	0.172354
58	6.694709	-0.00291	0.194554
58.5	9.375323	0.000418	0.144122
59	13.91677	-0.00096	0.141966
59.5	28.31284	-0.00082	0.108032
59.6	35.56393	-0.00096	0.089625
59.7	47.6803	-0.00127	0.05839
59.8	72.85622	-0.00219	0.00362
59.9	149.0936	-0.00721	-0.16986
59.95	312.4344	-0.0252	-0.49965
59.96	396.5515	-0.03828	-0.66506
59.97	540.0429	-0.06423	-0.94897
59.98	833.8708	-0.14103	-1.49632
59.985	1124.589	-0.24102	-2.03141
59.99	1683.142	-0.5232	-3.02929
59.993	2323.164	-1.00606	-4.15072
59.995	3014.31	-1.79246	-5.32326
59.997	4068.729	-3.71769	-6.8438
59.998	4763.13	-5.54919	-7.34846
59.999	5580.781	-7.99301	-6.86193
59.9995	6082.742	-9.14865	-6.10809

Table 15b: Nonadiabatic coupling elements in bohr^{-1} at $R_1 = R_2 = 1.97$ bohr

γ (degrees)	$\langle 1\vert \frac{d}{dR_2}\vert 2\rangle$	$\langle 1\vert \frac{d}{dR_2}\vert 3\rangle$	$\langle 2\vert \frac{d}{dR_2}\vert 3\rangle$
60.001	-6056.47	6.21404	9.18978
60.0015	-5271.64	6.385794	7.743032
60.002	-4531.49	6.375573	6.466506
60.003	-3405.37	5.968517	4.463932
60.005	-2190.73	4.80842	2.268985
60.007	-1611.11	3.845203	1.304557
60.01	-1162.84	2.922113	0.686248
60.015	-804.709	2.066459	0.313784
60.02	-620.083	1.612386	0.176561
60.03	-431.293	1.138139	0.078969
60.04	-330.004	0.903146	0.043716
60.05	-269.12	0.758167	0.028288
60.1	-141.327	0.405695	0.05513
60.2	-72.7602	0.306005	0.000677
60.3	-49.0547	0.262287	-0.00029
60.4	-37.0033	0.236844	-0.00074
60.5	-29.7389	0.225099	-0.00091
61	-15.0915	0.189276	-0.00209
61.5	-10.2199	0.17369	-0.00255
62	-7.72044	0.164734	-0.00232
62.5	-6.22189	0.158866	0.003152
63	-5.13036	0.152983	0.033015
64	-3.86447	0.14743	0.135872
65	-3.24402	0.154362	-0.00573
66	-2.66987	0.159618	0.168143
67	-2.36566	0.002888	0.237032
68	-2.05796	0.098263	0.201648
69	-1.84788	0.100959	0.125515
70	-1.68096	0.099054	0.347029
71	-1.55421	0.095492	0.755036
72	-1.44225	0.091287	0.557966
73	-1.40495	0.093434	0.434284

Table 16a: Energies in eV at $R_1 = R_2 = 1.973$ bohr

γ (degrees)	E_1	E_2	E_3
49	2.098476	3.744394	5.706869
50	2.147268	3.64273	5.706924
51	2.201719	3.543434	5.708502
52	2.259381	3.446722	5.714652
53	2.320363	3.354882	5.724367
54	2.382733	3.265517	5.741156
55	2.448178	3.180698	5.759171
56	2.513732	3.096177	5.780314
57	2.581054	3.019385	5.804098
58	2.649628	2.941123	5.82652
59	2.719808	2.867651	5.852943
59.1	2.726829	2.860793	5.855746
59.2	2.733931	2.853364	5.858658
59.3	2.740271	2.84599	5.861025
59.4	2.74819	2.839323	5.864808
59.5	2.755701	2.832275	5.867012
59.6	2.763075	2.825037	5.869924
59.7	2.770368	2.817744	5.873271
59.8	2.777552	2.810914	5.876264
59.9	2.785797	2.803539	5.879366
59.95	2.789199	2.800111	5.8807
59.97	2.790831	2.798696	5.881489
59.985	2.79192	2.797607	5.881924
59.99	2.792274	2.797253	5.88206
59.993	2.792491	2.797036	5.882305
59.995	2.792655	2.7969	5.882359
59.996	2.792709	2.796845	5.882387
59.997	2.792791	2.796764	5.882414
59.998	2.792845	2.796682	5.882468
59.9985	2.792899	2.796655	5.882468
59.999	2.792927	2.796627	5.882495
59.9992	2.792954	2.7966	5.882495
59.9994	2.792954	2.796573	5.882495
59.9995	2.792981	2.796573	5.882495

Table 16b: Energies in eV at $R_1 = R_2 = 1.973$ bohr

γ (degrees)	E_1	E_2	E_3
60.0002	2.793661	2.796464	5.882332
60.0004	2.793689	2.796437	5.882359
60.0005	2.793689	2.796437	5.882359
60.001	2.793716	2.79641	5.882359
60.0015	2.79377	2.796355	5.882387
60.002	2.793797	2.796328	5.882387
60.003	2.793852	2.796274	5.882414
60.004	2.793933	2.796192	5.882305
60.005	2.794015	2.79611	5.882332
60.007	2.794151	2.795974	5.882387
60.01	2.794369	2.795757	5.882332
60.015	2.794723	2.795403	5.882495
60.03	2.794287	2.795811	5.882931
60.05	2.792845	2.797308	5.883557
60.1	2.789362	2.80109	5.885434
60.2	2.781688	2.807757	5.887639
60.3	2.773606	2.815349	5.89104
61	2.722529	2.865773	5.912565
62	2.655751	2.938892	5.945573
63	2.586442	3.010051	5.979996
64	2.524562	3.083061	6.013086
65	2.459552	3.157676	6.048979
66	2.401645	3.229298	6.082749
67	2.343602	3.302362	6.119893
68	2.287437	3.375644	6.156384
69	2.234155	3.448545	6.193066
70	2.180248	3.521283	6.23236
71	2.130042	3.593041	6.268634
72	2.080027	3.662894	6.304662
73	2.032052	3.734026	6.342814

Table 17a: Nonadiabatic coupling elements in bohr^{-1} at $R_1 = R_2 = 1.973$ bohr

γ (degrees)	$\langle 1\|\frac{d}{d\gamma}\|2\rangle/R_1$	$\langle 1\|\frac{d}{d\gamma}\|3\rangle/R_1$	$\langle 2\|\frac{d}{d\gamma}\|3\rangle/R_1$
49	0.230688	0.157635	-0.00619
50	0.224289	0.159406	-0.04023
51	0.229356	0.161079	-0.038
52	0.217271	0.16244	0.02356
53	0.225566	0.164495	0.01133
54	0.22547	0.164864	-0.02887
55	0.253595	0.165541	-0.00314
56	0.214891	0.162462	0.008204
57	0.212525	0.16411	0.009858
58	0.229094	0.16474	-0.00053
59	0.013066	0.163751	-0.01728
59.1	0.257293	0.163908	-0.01089
59.2	0.441427	0.164269	-0.0092
59.3	0.134749	0.164431	-0.02157
59.4	0.101381	0.164703	0.017917
59.5	0.072927	0.164656	-0.01097
59.6	2.437538	0.165031	-0.00755
59.7	0.257772	0.165874	0.002095
59.8	1.379566	0.164791	-0.01364
59.9	2.403871	0.165181	-0.00584
59.95	-0.29547	0.16597	-0.00633
59.97	-0.6202	0.166233	-0.01668
59.985	2.77454	0.164235	0.006204
59.99	-1.93472	0.167775	-0.00722
59.993	-0.95755	0.167222	-0.00431
59.995	4.866093	0.160416	-0.00344
59.996	3.316369	0.16884	-0.03664
59.997	12.79525	0.151351	-0.04175
59.998	83.09346	0.161275	-0.24663
59.9985	132.797	0.170128	-0.46625
59.999	-25470.6	11.12574	-1.9335
59.9992	-28080	3.588443	-10.5817
59.9994	25825.41	-3.47912	-10.8585
59.9995	25841	-3.35325	-10.6999

Table 17b: Nonadiabatic coupling elements in bohr^{-1} at $R_1 = R_2 = 1.973$ bohr

γ (degrees)	$\langle 1 \vert \frac{d}{d\gamma} \vert 2 \rangle / R_1$	$\langle 1 \vert \frac{d}{d\gamma} \vert 3 \rangle / R_1$	$\langle 2 \vert \frac{d}{d\gamma} \vert 3 \rangle / R_1$
60.0002	36.72315	-0.61595	0.150521
60.0004	17.01851	-0.24895	0.148834
60.0005	18.73443	-0.26781	0.146
60.001	11.78063	-0.18169	0.154229
60.0015	-25.3442	-0.08598	0.161444
60.002	-9.92369	-0.04696	0.150245
60.003	-10.6428	0.014327	0.167413
60.004	-10.3203	0.016536	0.160905
60.005	-2.28091	-0.01081	0.167665
60.007	-6.85801	0.01912	0.167893
60.01	-6.43151	-0.00426	0.166823
60.015	0.565959	0.003291	0.165855
60.03	-2.82715	-0.00311	0.165101
60.05	-1.50642	-0.01136	0.38323
60.1	1.065356	-0.01038	0.165542
60.2	-0.48844	0.000406	0.16519
60.3	-0.72221	-0.00446	0.165137
61	-0.26364	-0.00258	0.162692
62	-0.2174	-0.00074	0.164797
63	-0.25844	-0.00399	0.20454
64	-0.24174	0.006542	0.168188
65	-0.22013	0.006341	0.164425
66	-0.23397	-0.00029	0.178565
67	-0.21095	0.010751	0.064899
68	-0.23914	0.012081	0.422068
69	-0.22571	0.014102	0.1581
70	-0.21844	0.014071	0.157581
71	-0.22134	0.014905	0.168028
72	-0.21167	0.015992	0.353835
73	-0.22283	0.015366	0.452771

Table 18a: Nonadiabatic coupling elements in bohr^{-2} at $R_1 = R_2 = 1.973$ bohr

γ (degrees)	$\langle 1\|\frac{d^2}{d\gamma^2}\|2\rangle/R_1^2$	$\langle 1\|\frac{d^2}{d\gamma^2}\|3\rangle/R_1^2$	$\langle 2\|\frac{d^2}{d\gamma^2}\|3\rangle/R_1^2$
49			
50	550.8229	-0.02899	51.56468
51	585.4386	-0.10135	247.9302
52	532.4969	0.017362	489.5007
53	409.2975	0.013418	562.9246
54	462.6931	0.047829	614.7625
55	661.7071	0.014479	5.867054
56	568.3911	0.016057	475.5547
57	602.2786	0.018471	279.962
58	429.6535	0.366492	133.9615
59	331.7526	0.024877	944.6799
59.1	44.45218	0.011244	964.3487
59.2	273.6813	0.031751	566.6396
59.3	499.7757	0.018215	78.06686
59.4	-111.975	0.025308	1294.905
59.5	-82.0899	0.026598	569.7656
59.6	678.1152	0.011704	87.51651
59.7	76.35495	-14.5689	1184.084
59.8	531.7783	-0.00305	-83.3941
59.9	353.1675	-47.6501	297.3525
59.95	58.6458	-203.937	747.7779
59.97	-5.33845	-423.077	919.6014
59.985	137.9489	-308.886	364.5925
59.99	-577.867	-478.146	546.4603
59.993	50.02403	-455.202	646.9286
59.995	1324.901	-343.712	701.2419
59.996	-946.748	-287.915	801.4275
59.997	4748.654	-444.47	368.8239
59.998	35217.46	-799.069	522.4282
59.9985	49765.04	-970.096	532.1431
59.999	-2.6E+07	218862.7	243855.2
59.9992	-6672599	522482.7	353302
59.9994	1.37E+08	-562470	382112.3
59.9995	129544.9	-537329	379174.4

Table 18b: Nonadiabatic coupling elements in bohr^{-2} at $R_1 = R_2 = 1.973$ bohr

γ (degrees)	$\langle 1 \vert \frac{d^2}{d\gamma^2} \vert 2 \rangle / R_1^2$	$\langle 1 \vert \frac{d^2}{d\gamma^2} \vert 3 \rangle / R_1^2$	$\langle 2 \vert \frac{d^2}{d\gamma^2} \vert 3 \rangle / R_1^2$
60.0002	-1.9E+07	1393.391	8906.053
60.0004	-50009	164.2425	1331.552
60.0005	8971.555	-554.964	915.2006
60.001	-6745.44	-84.6792	796.4797
60.0015	-37199.4	-784.78	849.5076
60.002	15947.23	-523.035	423.0065
60.003	-97.6672	-1026.61	300.6978
60.004	388.6444	-841.989	338.6805
60.005	4325.224	-714.238	388.1588
60.007	-954.618	-1110.3	525.0679
60.01	81.10061	-782.245	561.4138
60.015	751.8729	-319.311	302.437
60.03	-279.711	-203.152	441.3079
60.05	-494.308	105.7978	212.6286
60.1	-47.7881	-235.272	44.52478
60.2	-525.658	816.2548	-19.0991
60.3	-537.443	336.2875	0.024822
61	-510.903	503.0056	0.018653
62	-257.674	423.4761	0.018963
63	-385.378	377.0187	0.073107
64	-300.129	523.2092	0.003314
65	-254.69	560.1157	0.018042
66	-57.5792	375.4479	0.028655
67	-104.804	319.4334	-0.04968
68	-177.123	475.8889	0.554141
69	-185.257	583.7691	-56.0728
70	-111.325	357.2979	0.020415
71	-159.64	406.6506	0.106192
72	-148.155	382.1995	0.099713
73	-102.372	259.3797	0.037367

Table 19a: Nonadiabatic coupling elements in bohr^{-1} at $R_1 = R_2 = 1.973$ bohr

γ (degrees)	$\langle 1 \vert \frac{d}{dR_1} \vert 2 \rangle$	$\langle 1 \vert \frac{d}{dR_1} \vert 3 \rangle$	$\langle 2 \vert \frac{d}{dR_1} \vert 3 \rangle$
49	-1.04531	0.011165	-0.21311
50	-1.17052	0.009458	-0.25642
51	-1.34352	0.008974	-0.25569
52	-1.52895	0.007861	-0.18645
53	-1.76609	0.006842	-0.11421
54	-2.08752	0.005517	-0.21863
55	-2.59071	0.004427	-0.15404
56	-3.10865	0.003775	-0.12943
57	-4.2997	0.002135	-0.1011
58	-6.55586	0.002521	-0.18662
59	-13.7036	0.000979	-0.12607
59.1	-15.3241	0.000934	-0.12508
59.2	-17.3026	0.000955	-0.12325
59.3	-19.7796	0.000819	-0.11482
59.4	-23.277	0.000767	-0.10811
59.5	-28.2366	0.000747	-0.09839
59.6	-35.4144	0.000932	-0.08177
59.7	-47.6531	0.001442	-0.04962
59.8	-72.3252	0.002282	0.006507
59.9	-149.005	0.007139	0.169822
59.95	-311.648	0.024809	0.505136
59.97	-539.497	0.064746	0.948642
59.985	-1124.39	0.240762	2.014546
59.99	-1682.15	0.517881	3.001908
59.993	-2320.18	1.003326	4.115736
59.995	-3010.53	1.804876	5.286336
59.996	-3481.32	2.554106	6.03105
59.997	-4054.59	3.756628	6.757158
59.998	-4745.89	5.59201	7.236579
59.9985	-5133.05	6.757221	7.148508
59.999	-5556.2	7.996169	6.685428
59.9992	-5721.05	8.517725	6.325802
59.9994	-5910.84	8.988866	5.942518
59.9995	-6006.48	9.224707	5.688358

Table 19b: Nonadiabatic coupling elements in bohr^{-1} at $R_1 = R_2 = 1.973$ bohr

γ (degrees)	$\langle 1 \vert \frac{d}{dR_1} \vert 2 \rangle$	$\langle 1 \vert \frac{d}{dR_1} \vert 3 \rangle$	$\langle 2 \vert \frac{d}{dR_1} \vert 3 \rangle$
60.0002	7288.241	-4.71709	-11.6665
60.0004	7004.731	-5.2556	-11.0569
60.0005	6872.396	-5.38794	-10.782
60.001	6087.239	-6.02135	-9.26487
60.0015	5271.032	-6.29123	-7.80406
60.002	4539.798	-6.2887	-6.52531
60.003	3402.181	-5.95264	-4.51747
60.004	2668.061	-5.38711	-3.1786
60.005	2186.072	-4.79823	-2.29989
60.007	1605.653	-3.85805	-1.3234
60.01	1158.074	-2.91739	-0.69446
60.015	801.6525	-2.07037	-0.32326
60.03	429.4258	-1.1519	-0.08662
60.05	269.8358	-0.77952	-0.09954
60.1	141.2427	-0.44421	-0.00603
60.2	73.09263	-0.30746	-0.00045
60.3	49.27194	-0.26294	0.000308
61	15.24239	-0.19281	0.002285
62	7.720798	-0.16595	0.002343
63	5.156683	-0.15588	-0.01295
64	3.878987	-0.15002	-0.12834
65	3.227345	-0.15368	-0.06439
66	2.664162	-0.16488	-0.17474
67	2.353587	-0.04349	-0.10223
68	2.059806	-0.09861	-0.18479
69	1.850057	-0.10119	-0.10882
70	1.684481	-0.09762	-0.35292
71	1.557283	-0.09409	-0.71889
72	1.44727	-0.09093	-0.73509
73	1.59418	-0.109	-0.57324

Table 20a: Nonadiabatic coupling elements in bohr^{-1} at $R_1 = R_2 = 1.973$ bohr

γ (degrees)	$\langle 1\vert\frac{d}{dR_2}\vert 2\rangle$	$\langle 1\vert\frac{d}{dR_2}\vert 3\rangle$	$\langle 2\vert\frac{d}{dR_2}\vert 3\rangle$
49	1.056618	-0.01118	0.329458
50	1.186687	-0.00947	0.294056
51	1.362362	-0.00899	0.288859
52	1.554067	-0.00789	0.281002
53	1.782171	-0.00686	0.387389
54	2.124093	-0.00554	0.372822
55	2.616877	-0.00444	0.207752
56	3.147408	-0.00379	0.159109
57	4.366498	-0.00215	0.189428
58	6.666471	-0.00245	0.192506
59	13.91423	-0.00098	0.143792
59.1	15.38501	-0.00093	0.13654
59.2	17.35778	-0.00096	0.134046
59.3	20.03279	-0.00083	0.130235
59.4	23.36048	-0.00077	0.117117
59.5	28.29414	-0.00074	0.106591
59.6	35.56132	-0.00093	0.090872
59.7	47.69846	-0.00143	0.058665
59.8	72.56738	-0.00226	0.003704
59.9	149.1711	-0.00705	-0.16556
59.95	312.4604	-0.02446	-0.50031
59.97	540.6012	-0.06386	-0.94408
59.985	1124.286	-0.23507	-2.02216
59.99	1683.154	-0.51191	-3.01626
59.993	2321.674	-0.9886	-4.13029
59.995	3015.083	-1.76989	-5.31258
59.996	3485.699	-2.5098	-6.05101
59.997	4065.066	-3.70318	-6.81748
59.998	4755.665	-5.53523	-7.32041
59.9985	5150.504	-6.72614	-7.27461
59.999	5576.678	-7.97563	-6.84873
59.9992	5775.575	-8.47238	-6.60866
59.9994	5970.225	-8.93051	-6.26135
59.9995	6072.793	-9.14231	-6.09141

Table 20b: Nonadiabatic coupling elements in bohr^{-1} at $R_1 = R_2 = 1.973$ bohr

γ (degrees)	$\langle 1 \vert \frac{d}{dR_2} \vert 2 \rangle$	$\langle 1 \vert \frac{d}{dR_2} \vert 3 \rangle$	$\langle 2 \vert \frac{d}{dR_2} \vert 3 \rangle$
60.0002	-7217.99	5.297704	11.4502
60.0004	-6969.15	5.521802	10.97419
60.0005	-6815.44	5.725923	10.66273
60.001	-6056.42	6.220745	9.201067
60.0015	-5269.78	6.389306	7.762711
60.002	-4525.52	6.382977	6.470642
60.003	-3399.25	5.970177	4.466059
60.004	-2668.18	5.396672	3.13717
60.005	-2185.16	4.826072	2.273818
60.007	-1607.95	3.851242	1.308785
60.01	-1159.22	2.930779	0.690465
60.015	-801.535	2.07558	0.31674
60.03	-428.968	1.156885	0.085807
60.05	-268.311	0.784702	0.099223
60.1	-140.669	0.445743	0.005945
60.2	-72.4947	0.30736	0.000433
60.3	-48.974	0.261324	-0.00031
61	-15.045	0.189858	-0.00231
62	-7.70372	0.164639	-0.00235
63	-5.13108	0.15239	0.012992
64	-3.86187	0.147922	0.128082
65	-3.21078	0.152632	0.063592
66	-2.66474	0.166682	0.174566
67	-2.34063	0.044668	0.104623
68	-2.05562	0.099777	0.184778
69	-1.84183	0.100828	0.108157
70	-1.68145	0.098603	0.350798
71	-1.55024	0.094939	0.718818
72	-1.43793	0.091485	0.73513
73	-1.58967	0.109544	0.573236

Table 21a: Energies in eV at $\gamma = 59°$ and $R_1 = 1.97$ bohr

R_2 (bohr)	E_1	E_2	E_3
2.511904	1.947205	4.036297	6.863134
2.459328	2.008813	3.90734	6.757116
2.406406	2.072108	3.781239	6.64952
2.353134	2.14256	3.65484	6.54021
2.299507	2.217474	3.527052	6.427606
2.245519	2.2956	3.40321	6.318704
2.191166	2.380148	3.279858	6.216305
2.136443	2.469294	3.159309	6.119975
2.108941	2.515582	3.095932	6.070095
2.081344	2.564808	3.038352	6.023644
2.053653	2.613273	2.983383	5.976894
2.039771	2.637056	2.957314	5.954226
2.034212	2.646771	2.947763	5.944784
2.03143	2.651968	2.942457	5.939913
2.028648	2.656295	2.93764	5.935151
2.025865	2.661357	2.933041	5.930579
2.023081	2.665683	2.927844	5.925627
2.020296	2.670391	2.922837	5.920946
2.011935	2.683589	2.907489	5.908211
2.003566	2.693875	2.894373	5.894278
1.997981	2.701712	2.884413	5.885162
1.992393	2.70944	2.879842	5.876863
1.989597	2.710719	2.876495	5.872835
1.984003	2.714502	2.871923	5.864155
1.978405	2.717685	2.866889	5.855828
1.975604	2.718883	2.867324	5.851882
1.972803	2.719373	2.867896	5.848181
1.971121	2.719862	2.867079	5.84565

Table 21b: Energies in eV at $\gamma = 59°$ and $R_1 = 1.97$ bohr

R_2 (bohr)	E_1	E_2	E_3
1.970841	2.719917	2.867107	5.845215
1.970561	2.719563	2.86727	5.844752
1.969439	2.719618	2.867624	5.843528
1.969159	2.719618	2.86746	5.843283
1.968879	2.719835	2.867243	5.842902
1.967196	2.7191	2.86678	5.839854
1.964392	2.71872	2.866426	5.835528
1.961587	2.71842	2.866753	5.831337
1.955973	2.716189	2.871787	5.823582
1.950355	2.71042	2.875488	5.814112
1.947545	2.709522	2.879597	5.81022
1.941921	2.702801	2.885665	5.803989
1.936293	2.697603	2.894591	5.79675
1.927845	2.684487	2.908959	5.786818
1.913743	2.662418	2.935708	5.768668
1.899618	2.640158	2.961668	5.749755
1.885467	2.61643	2.988962	5.731904
1.85709	2.568455	3.051658	5.700121
1.828613	2.519473	3.114001	5.669589
1.800034	2.473621	3.185841	5.640281
1.771353	2.428939	3.257027	5.615138
1.74257	2.388665	3.336241	5.594239
1.728139	2.368773	3.376515	5.584551
1.684692	2.307818	3.501718	5.5667
1.626393	2.239979	3.671548	5.546645
1.567669	2.189528	3.862004	5.557203
1.508513	2.159431	4.071619	5.589776
1.448918	2.154397	4.305288	5.64752

Table 22a: Nonadiabatic coupling elements in bohr^{-1} at $\gamma = 59°$ and $R_1 = 1.97$ bohr

R_2 (bohr)	$\langle 1\|\frac{d}{d\gamma}\|2\rangle/R1$	$\langle 1\|\frac{d}{d\gamma}\|3\rangle/R1$	$\langle 2\|\frac{d}{d\gamma}\|3\rangle/R1$
2.511904	-0.82975	0.062678	0.16429
2.459328	-0.93405	0.067988	0.162642
2.406406	-1.06	0.073198	0.158605
2.353134	-1.22199	0.079401	0.154708
2.299507	-1.4356	0.085137	0.150577
2.245519	-1.74069	0.09198	0.145741
2.191166	-2.17441	0.099548	0.137475
2.136443	-2.87364	0.113042	0.121836
2.108941	-3.41072	0.12186	0.118754
2.081344	-4.10169	0.127954	0.110328
2.053653	-5.16964	0.137083	0.100913
2.039771	-5.84865	0.143153	0.094712
2.034212	-6.14161	0.146217	0.091673
2.03143	-6.29262	0.14777	0.088401
2.028648	-6.76145	0.156462	0.090363
2.025865	-6.58236	0.150225	0.088861
2.023081	-6.71988	0.151837	0.086134
2.020296	-6.85276	0.153512	0.084083
2.011935	-7.16301	0.158928	0.077751
2.003566	-7.24658	0.164411	0.069554
1.997981	-7.04034	0.166473	0.062867
1.992393	-6.48659	0.167826	0.054861
1.989597	-6.01728	0.167634	0.050218
1.984003	-4.76502	0.166782	0.040135
1.978405	-3.0254	0.165336	0.025959
1.975604	-2.00877	0.164971	0.017419
1.972803	-0.91874	0.164485	0.007944
1.971121	-0.23783	0.16423	0.002132

Table 22b: Nonadiabatic coupling elements in bohr^{-1} at $\gamma = 59°$ and $R_1 = 1.97$ bohr

R_2 (bohr)	$\langle 1\|\frac{d}{d\gamma}\|2\rangle/R1$	$\langle 1\|\frac{d}{d\gamma}\|3\rangle/R1$	$\langle 2\|\frac{d}{d\gamma}\|3\rangle/R1$
1.970841	-0.12117	0.164201	0.001325
1.970561	-0.0112	0.164147	0.000361
1.969439	0.452238	0.164195	0.003255
1.969159	0.566672	0.164217	0.004221
1.968879	0.678082	0.164208	0.005467
1.967196	1.363471	0.164362	0.011368
1.964392	2.463046	0.164933	0.020285
1.961587	3.484482	0.165107	0.029351
1.955973	5.242635	0.165299	0.043683
1.950355	6.498279	0.165321	0.05505
1.947545	6.968924	0.166026	0.059482
1.941921	7.512365	0.164059	0.067542
1.936293	7.690442	0.161503	0.074441
1.927845	7.580411	0.157207	0.082734
1.913743	6.901594	0.147101	0.094437
1.899618	6.12268	0.138207	0.098922
1.885467	5.426452	0.132171	0.105359
1.85709	4.320983	0.125027	0.118851
1.828613	3.572928	0.117019	0.128457
1.800034	3.011336	0.108699	0.138337
1.771353	2.609672	0.10044	0.14972
1.74257	2.302029	0.093785	0.154904
1.728139	2.173124	0.091377	0.154326
1.684692	1.867338	0.084165	0.161768
1.626393	1.559573	0.069086	0.178183
1.567669	1.345861	0.052562	0.198464
1.508513	1.178464	0.03704	0.216402
1.448918	1.047117	0.020538	0.237923

Table 23a: Nonadiabatic coupling elements in bohr^{-1} at $\gamma = 59°$ and $R_1 = 1.97$ bohr

R_2 (bohr)	$\langle 1 \vert \frac{d}{dR_1} \vert 2 \rangle$	$\langle 1 \vert \frac{d}{dR_1} \vert 3 \rangle$	$\langle 2 \vert \frac{d}{dR_1} \vert 3 \rangle$
2.511904	0.081744	0.09652	0.115438
2.459328	0.094278	0.098567	0.125697
2.406406	0.112992	0.100502	0.121418
2.353134	0.140307	0.102057	0.123996
2.299507	0.183293	0.103602	0.127223
2.245519	0.257968	0.104504	0.128709
2.191166	0.389657	0.103799	0.130793
2.136443	0.653435	0.103702	0.13538
2.108941	0.909118	0.10331	0.136905
2.081344	1.362781	0.100566	0.140316
2.053653	2.240275	0.096114	0.144654
2.039771	3.014417	0.092739	0.147256
2.034212	3.424567	0.091233	0.148798
2.03143	3.668156	0.088592	0.150867
2.028648	3.829793	0.089011	0.148729
2.025865	4.208769	0.088662	0.149456
2.023081	4.514934	0.087599	0.150437
2.020296	4.853989	0.086532	0.151314
2.011935	6.055932	0.083678	0.153029
2.003566	7.621853	0.08005	0.154181
1.997981	8.87399	0.075595	0.154868
1.992393	10.21999	0.069016	0.15492
1.989597	10.909	0.063729	0.154657
1.984003	12.15866	0.051888	0.149354
1.978405	13.08327	0.03681	0.142104
1.975604	13.50925	0.024465	0.140923
1.972803	13.82151	0.010973	0.136831
1.971121	13.92827	0.003285	0.134543

Table 23b: Nonadiabatic coupling elements in bohr^{-1} at $\gamma = 59°$ and $R_1 = 1.97$ bohr

R_2 (bohr)	$\langle 1 \vert \frac{d}{dR_1} \vert 2 \rangle$	$\langle 1 \vert \frac{d}{dR_1} \vert 3 \rangle$	$\langle 2 \vert \frac{d}{dR_1} \vert 3 \rangle$
1.970841	13.93406	0.002121	0.134144
1.970561	13.93659	0.001049	0.134069
1.969439	13.9362	0.003038	0.133865
1.969159	13.92616	0.004115	0.134146
1.968879	13.91278	0.0054	0.135177
1.967196	13.84479	0.013405	0.138078
1.964392	13.53113	0.026713	0.141153
1.961587	13.13099	0.037598	0.143549
1.955973	12.1181	0.053083	0.148841
1.950355	10.8216	0.063206	0.151919
1.947545	10.10983	0.069134	0.154203
1.941921	8.728143	0.075068	0.155102
1.936293	7.438465	0.079979	0.154301
1.927845	5.853466	0.085808	0.152362
1.913743	3.968065	0.090812	0.147769
1.899618	2.788213	0.094696	0.145095
1.885467	2.036428	0.097995	0.138821
1.85709	1.196312	0.104341	0.135846
1.828613	0.766997	0.108201	0.134616
1.800034	0.523812	0.109892	0.132632
1.771353	0.376019	0.112054	0.132893
1.74257	0.279451	0.112815	0.132892
1.728139	0.247825	0.114475	0.130513
1.684692	0.171035	0.113238	0.126582
1.626393	0.106184	0.110979	0.124768
1.567669	0.062197	0.108053	0.124295
1.508513	0.046568	0.102665	0.116392
1.448918	0.028786	0.09606	0.1145

Table 24a: Nonadiabatic coupling elements in bohr^{-1} at $\gamma = 59°$ and $R_1 = 1.97$ bohr

R_2 (bohr)	$\langle 1\vert\frac{d}{dR_2}\vert 2\rangle$	$\langle 1\vert\frac{d}{dR_2}\vert 3\rangle$	$\langle 2\vert\frac{d}{dR_2}\vert 3\rangle$
2.511904	-0.08218	0.067207	-0.07041
2.459328	-0.09368	0.070985	-0.08073
2.406406	-0.10907	0.075143	-0.08132
2.353134	-0.1315	0.079476	-0.08728
2.299507	-0.16758	0.083747	-0.09286
2.245519	-0.23469	0.088739	-0.09902
2.191166	-0.35695	0.094071	-0.10512
2.136443	-0.59729	0.098855	-0.1149
2.108941	-0.84812	0.097894	-0.11978
2.081344	-1.28156	0.094348	-0.12529
2.053653	-2.14387	0.091632	-0.13223
2.039771	-2.90461	0.089303	-0.13648
2.034212	-3.31418	0.088254	-0.13858
2.03143	-3.54879	0.087715	-0.14106
2.028648	-3.91502	0.089649	-0.13945
2.025865	-4.08175	0.086104	-0.14034
2.023081	-4.38554	0.085575	-0.14129
2.020296	-4.71989	0.084878	-0.14228
2.011935	-5.91314	0.082647	-0.1448
2.003566	-7.46627	0.080362	-0.14584
1.997981	-8.71177	0.076463	-0.14754
1.992393	-10.0571	0.070353	-0.14897
1.989597	-10.7582	0.064685	-0.14978
1.984003	-12.0564	0.052389	-0.14648
1.978405	-13.0833	0.03681	-0.1421
1.975604	-13.4665	0.026255	-0.13988
1.972803	-13.7958	0.01306	-0.13654
1.971121	-13.9157	0.005277	-0.1344

Table 24b: Nonadiabatic coupling elements in bohr^{-1} at $\gamma = 59°$ and $R_1 = 1.97$ bohr

R_2 (bohr)	$\langle 1\|\frac{d}{dR_2}\|2\rangle$	$\langle 1\|\frac{d}{dR_2}\|3\rangle$	$\langle 2\|\frac{d}{dR_2}\|3\rangle$
1.970841	-13.9272	0.004147	-0.13393
1.970561	-13.9351	0.003037	-0.13401
1.969439	-13.9368	0.001004	-0.13401
1.969159	-13.9329	0.002066	-0.1342
1.968879	-13.9271	0.003648	-0.13525
1.967196	-13.8655	0.011308	-0.13811
1.964392	-13.5762	0.024744	-0.14226
1.961587	-13.1909	0.03657	-0.14563
1.955973	-12.2206	0.053006	-0.15212
1.950355	-10.9684	0.063332	-0.15688
1.947545	-10.2619	0.069351	-0.15987
1.941921	-8.91212	0.075717	-0.16262
1.936293	-7.59934	0.081084	-0.16252
1.927845	-6.0064	0.087553	-0.16224
1.913743	-4.09658	0.09368	-0.15902
1.899618	-2.89806	0.097459	-0.15563
1.885467	-2.1297	0.100377	-0.15278
1.85709	-1.26855	0.114086	-0.15532
1.828613	-0.82725	0.123226	-0.16041
1.800034	-0.57114	0.129091	-0.16738
1.771353	-0.41305	0.134492	-0.17637
1.74257	-0.30434	0.138418	-0.18551
1.728139	-0.26808	0.141963	-0.18166
1.684692	-0.18492	0.147205	-0.18221
1.626393	-0.11742	0.154429	-0.19302
1.567669	-0.06262	0.16158	-0.21198
1.508513	-0.04155	0.165383	-0.22874
1.448918	-0.01735	0.170322	-0.25437

Table 25a: Nonadiabatic coupling elements in bohr^{-2} at $\gamma = 59°$ and $R_1 = 1.97$ bohr

R_2 (bohr)	$\langle 1\|\frac{d^2}{dR_2^2}\|2\rangle$	$\langle 1\|\frac{d^2}{dR_2^2}\|3\rangle$	$\langle 2\|\frac{d^2}{dR_2^2}\|3\rangle$
2.511904			
2.459328	0.249633	-0.09579	0.201921
2.406406	0.323458	-0.05546	0.007187
2.353134	0.453109	-0.05766	0.110074
2.299507	0.705759	-0.27098	0.049423
2.245519	1.273221	-0.06369	0.122118
2.191166	2.279507	-0.06609	0.133988
2.136443	4.421867	-0.03061	0.224991
2.108941	9.145985	0.12735	0.245985
2.081344	15.73985	0.279519	0.309915
2.053653	31.17845	0.365164	0.438041
2.039771	54.83979	0.551415	0.555388
2.034212	73.7741	7.307144	0.774458
2.03143	82.5754	26.19955	1.395333
2.028648	177.3665	-71.6884	-0.0974
2.025865	64.18636	-3.3822	0.724402
2.023081	109.0943	-7.27939	0.902604
2.020296	120.0959	0.934715	0.739334
2.011935	142.7605	1.109259	0.779399
2.003566	185.6256	1.348556	0.713861
1.997981	223.0577	1.970662	0.960529
1.992393	240.8008	2.580015	0.953184
1.989597	250.8182	3.628366	0.976304
1.984003	232.1015	3.960154	0.002656
1.978405	183.4777	4.641786	-0.31513
1.975604	136.8505	5.658512	-0.45681
1.972803	117.6075	6.605629	-1.02975
1.971121	61.96424	6.512496	-2.39594

Table 25b: Nonadiabatic coupling elements in bohr^{-2} at $\gamma = 59°$ and $R_1 = 1.97$ bohr

R_2 (bohr)	$\langle 1\|\frac{d^2}{dR_2^2}\|2\rangle$	$\langle 1\|\frac{d^2}{dR_2^2}\|3\rangle$	$\langle 2\|\frac{d^2}{dR_2^2}\|3\rangle$
1.970841	34.03747	5.882864	-2.49886
1.970561	23.57361	5.793332	-0.2775
1.969439	5.494137	3.640536	0.539115
1.969159	-7.91561	-1.94473	1.431972
1.968879	-12.9411	18.61727	20.18604
1.967196	-36.4678	17.07971	14.13778
1.964392	-103.162	-2.84274	1.114854
1.961587	-137.335	-2.28261	0.693632
1.955973	-172.834	-1.0616	0.489881
1.950355	-222.869	-0.11702	0.139773
1.947545	-251.39	-0.50447	0.3405
1.941921	-234.503	0.32328	0.434015
1.936293	-233.192	0.273953	-0.63804
1.927845	-188.554	0.199637	-0.56154
1.913743	-142.429	0.067768	-0.62797
1.899618	-86.4744	-0.16105	-0.52587
1.885467	-54.3033	0.10496	-0.41563
1.85709	-30.6323	-0.25241	-0.07631
1.828613	-15.5092	-0.19986	0.083849
1.800034	-8.98994	-0.11883	0.184467
1.771353	-5.49368	-0.12159	0.359281
1.74257	-3.79546	-0.08543	0.285173
1.728139	-2.52819	-0.20167	0.238915
1.684692	-1.89535	-0.10294	0.020779
1.626393	-1.13464	-0.11755	0.174297
1.567669	-0.90393	-0.12538	0.301651
1.508513	-0.32554	-0.47384	1.115815
1.448918	-0.36975	-0.09826	0.393644

Table 26a: Energies in eV at $\gamma = 60°$ and $R_1 = 1.973$ bohr

R_2 (bohr)	E_1	E_2	E_3
2.409243	2.077278	3.793947	6.693032
2.355991	2.149145	3.66616	6.584565
2.302384	2.223869	3.538563	6.477078
2.248416	2.303301	3.41034	6.36374
2.221296	2.344636	3.346827	6.310214
2.194084	2.387413	3.281273	6.260552
2.166779	2.435443	3.21972	6.210591
2.139381	2.47988	3.158901	6.15848
2.111889	2.528072	3.097647	6.111838
2.084303	2.575829	3.032419	6.063591
2.056622	2.624675	2.969886	6.015399
2.042745	2.653492	2.940198	5.991126
2.037188	2.664949	2.930075	5.981738
2.034407	2.670309	2.923789	5.976377
2.031626	2.675071	2.918047	5.971969
2.028844	2.680677	2.912061	5.967533
2.026061	2.686364	2.90572	5.963206
2.023277	2.69178	2.899434	5.959097
2.01492	2.707699	2.881447	5.946389
2.000971	2.734775	2.850943	5.923667
1.99259	2.752517	2.834643	5.911231
1.986997	2.764708	2.822833	5.902904
1.981401	2.775892	2.811594	5.894986
1.978602	2.782205	2.80607	5.890169
1.977202	2.785389	2.803294	5.8887
1.975801	2.788518	2.8006	5.886441
1.974961	2.790668	2.799158	5.884645
1.974401	2.792138	2.798478	5.883638
1.97384	2.793416	2.797389	5.882876
1.97356	2.793852	2.796655	5.882387
1.97342	2.794151	2.796274	5.882196

Table 26b: Energies in eV at $\gamma = 60°$ and $R_1 = 1.973$ bohr

R_2 (bohr)	E_1	E_2	E_3
1.97328	2.793689	2.795267	5.881978
1.973196	2.79377	2.794968	5.881978
1.97314	2.793879	2.794859	5.881897
1.97286	2.793852	2.794804	5.881625
1.972804	2.793797	2.794968	5.881407
1.97272	2.793689	2.795212	5.881298
1.97258	2.793906	2.79611	5.88108
1.972496	2.794015	2.796546	5.880972
1.971879	2.792791	2.79807	5.879747
1.971599	2.792328	2.79875	5.879665
1.971319	2.791321	2.798968	5.879257
1.970758	2.789988	2.799866	5.878495
1.970198	2.78909	2.80139	5.877625
1.968796	2.78577	2.803811	5.875529
1.967394	2.782559	2.806614	5.873298
1.96459	2.776355	2.812138	5.86927
1.958978	2.764245	2.823948	5.860209
1.953362	2.752136	2.834643	5.852562
1.944932	2.734639	2.85263	5.841269
1.916764	2.67733	2.91168	5.802002
1.888498	2.623858	2.976825	5.766844
1.860132	2.571938	3.039658	5.731986
1.831666	2.519473	3.105375	5.701536
1.803097	2.469594	3.17618	5.671983
1.774428	2.422054	3.250442	5.645615
1.745655	2.377617	3.329275	5.623247
1.716779	2.338078	3.408081	5.604198
1.687798	2.296825	3.493336	5.587545
1.629522	2.225502	3.662921	5.572714
1.57082	2.169772	3.855855	5.577639

Table 27a: Nonadiabatic coupling elements in bohr^{-1} at $\gamma = 60^\circ$ and $R_1 = 1.973$ bohr

R_2 (bohr)	$\langle 1\|\frac{d}{d\gamma}\|2\rangle/R_1$	$\langle 1\|\frac{d}{d\gamma}\|3\rangle/R_1$	$\langle 2\|\frac{d}{d\gamma}\|3\rangle/R_1$
2.409243	2.077278	3.793947	6.693032
2.355991	2.149145	3.66616	6.584565
2.302384	2.223869	3.538563	6.477078
2.248416	2.303301	3.41034	6.36374
2.221296	2.344636	3.346827	6.310214
2.194084	2.387413	3.281273	6.260552
2.166779	2.435443	3.21972	6.210591
2.139381	2.47988	3.158901	6.15848
2.111889	2.528072	3.097647	6.111838
2.084303	2.575829	3.032419	6.063591
2.056622	2.624675	2.969886	6.015399
2.042745	2.653492	2.940198	5.991126
2.037188	2.664949	2.930075	5.981738
2.034407	2.670309	2.923789	5.976377
2.031626	2.675071	2.918047	5.971969
2.028844	2.680677	2.912061	5.967533
2.026061	2.686364	2.90572	5.963206
2.023277	2.69178	2.899434	5.959097
2.01492	2.707699	2.881447	5.946389
2.000971	2.734775	2.850943	5.923667
1.99259	2.752517	2.834643	5.911231
1.986997	2.764708	2.822833	5.902904
1.981401	2.775892	2.811594	5.894986
1.978602	2.782205	2.80607	5.890169
1.977202	2.785389	2.803294	5.8887
1.975801	2.788518	2.8006	5.886441
1.974961	2.790668	2.799158	5.884645
1.974401	2.792138	2.798478	5.883638
1.97384	2.793416	2.797389	5.882876
1.97356	2.793852	2.796655	5.882387
1.97342	2.794151	2.796274	5.882196

Table 27b: Nonadiabatic coupling elements in bohr^{-1} at $\gamma = 60^\circ$ and $R_1 = 1.973$ bohr

R_2 (bohr)	$\langle 1\vert\frac{d}{d\gamma}\vert 2\rangle/R_1$	$\langle 1\vert\frac{d}{d\gamma}\vert 3\rangle/R_1$	$\langle 2\vert\frac{d}{d\gamma}\vert 3\rangle/R_1$
1.97328	2.793689	2.795267	5.881978
1.973196	2.79377	2.794968	5.881978
1.97314	2.793879	2.794859	5.881897
1.97286	2.793852	2.794804	5.881625
1.972804	2.793797	2.794968	5.881407
1.97272	2.793689	2.795212	5.881298
1.97258	2.793906	2.79611	5.88108
1.972496	2.794015	2.796546	5.880972
1.971879	2.792791	2.79807	5.879747
1.971599	2.792328	2.79875	5.879665
1.971319	2.791321	2.798968	5.879257
1.970758	2.789988	2.799866	5.878495
1.970198	2.78909	2.80139	5.877625
1.968796	2.78577	2.803811	5.875529
1.967394	2.782559	2.806614	5.873298
1.96459	2.776355	2.812138	5.86927
1.958978	2.764245	2.823948	5.860209
1.953362	2.752136	2.834643	5.852562
1.944932	2.734639	2.85263	5.841269
1.916764	2.67733	2.91168	5.802002
1.888498	2.623858	2.976825	5.766844
1.860132	2.571938	3.039658	5.731986
1.831666	2.519473	3.105375	5.701536
1.803097	2.469594	3.17618	5.671983
1.774428	2.422054	3.250442	5.645615
1.745655	2.377617	3.329275	5.623247
1.716779	2.338078	3.408081	5.604198
1.687798	2.296825	3.493336	5.587545
1.629522	2.225502	3.662921	5.572714
1.57082	2.169772	3.855855	5.577639

Table 28a: Nonadiabatic coupling elements in bohr^{-1} at $\gamma = 60^\circ$ and $R_1 = 1.973$ bohr

R_2 (bohr)	$\langle 1\vert\frac{d}{dR_1}\vert 2\rangle$	$\langle 1\vert\frac{d}{dR_1}\vert 3\rangle$	$\langle 2\vert\frac{d}{dR_1}\vert 3\rangle$
2.409243	-0.00191	0.102052	0.108354
2.355991	-0.00329	0.102869	0.11331
2.302384	-0.00377	0.10592	0.114492
2.248416	-0.00027	0.107951	0.114926
2.221296	-0.00104	0.10881	0.114601
2.194084	-0.01011	0.109351	0.114892
2.166779	-0.00922	0.109968	0.115702
2.139381	-0.015	0.10943	0.115882
2.111889	-0.01773	0.112811	0.115966
2.084303	-0.03068	0.112377	0.116245
2.056622	-0.0496	0.112314	0.11501
2.042745	-0.04266	0.112247	0.115125
2.037188	-0.03845	0.112584	0.115511
2.034407	-0.03735	0.112668	0.115525
2.031626	-0.03659	0.112821	0.115228
2.028844	-0.03651	0.112894	0.11529
2.026061	-0.03766	0.112599	0.115065
2.023277	-0.03582	0.112934	0.114887
2.01492	-0.02001	0.113598	0.114826
2.000971	-0.01063	0.11422	0.115526
1.99259	-0.04898	0.114897	0.115966
1.986997	-0.14512	0.115674	0.115494
1.981401	-0.49444	0.115573	0.115931
1.978602	-1.07332	0.11552	0.116071
1.977202	-1.87757	0.115574	0.115823
1.975801	-3.73091	0.114731	0.116235
1.974961	-6.46314	0.114427	0.117037
1.974401	-10.6111	0.114089	0.117147
1.97384	-18.9903	0.114472	0.123251
1.97356	-40.9884	0.331418	0.191432
1.97342	-35.4884	0.11644	0.122065

Table 28b: Nonadiabatic coupling elements in bohr^{-1} at $\gamma = 60^\circ$ and R_1 = 1.973 bohr

R_2 (bohr)	$\langle 1\lvert\frac{d}{dR_1}\rvert 2\rangle$	$\langle 1\lvert\frac{d}{dR_1}\rvert 3\rangle$	$\langle 2\lvert\frac{d}{dR_1}\rvert 3\rangle$
1.97328	45.0849	0.114199	0.122613
1.973196	53.07856	0.10419	0.123093
1.97314	63.39212	0.099118	0.108897
1.97286	50.18805	0.120168	0.120407
1.972804	44.8992	0.116907	0.12322
1.97272	37.74988	0.116336	0.125385
1.97258	29.81796	0.113096	0.122938
1.972496	26.20009	0.116092	0.125677
1.971879	12.20299	0.115331	0.1214
1.971599	9.295789	0.1149	0.120331
1.971319	7.305287	0.1149	0.120083
1.970758	4.793623	0.114656	0.11795
1.970198	3.40955	0.115081	0.117045
1.968796	1.856579	0.11508	0.11562
1.967394	1.011405	0.116086	0.112997
1.96459	0.437287	0.115492	0.11541
1.958978	0.125752	0.115955	0.11607
1.953362	0.046177	0.115775	0.11586
1.944932	0.009445	0.115637	0.116072
1.916764	0.018253	0.11445	0.116186
1.888498	0.023851	0.116289	0.116639
1.860132	0.001285	0.112819	0.113357
1.831666	0.010984	0.11485	0.116382
1.803097	0.015505	0.11625	0.11867
1.774428	0.016032	0.116095	0.120285
1.745655	0.015345	0.117105	0.1242
1.716779	0.013137	0.117416	0.11555
1.687798	0.010618	0.114543	0.112607
1.629522	0.016129	0.110334	0.116496
1.57082	0.024613	0.103908	0.114415

Table 29a: Nonadiabatic coupling elements in bohr^{-1} at $\gamma = 60°$ and $R_1 = 1.973$ bohr

R_2 (bohr)	$\langle 1\|\frac{d}{dR_2}\|2\rangle$	$\langle 1\|\frac{d}{dR_2}\|3\rangle$	$\langle 2\|\frac{d}{dR_2}\|3\rangle$
2.409243	0.016615	0.074249	-0.07672
2.355991	0.009693	0.079114	-0.08121
2.302384	0.007751	0.084627	-0.08568
2.248416	0.004998	0.090611	-0.08935
2.221296	0.001194	0.094221	-0.0918
2.194084	0.00972	0.097115	-0.09496
2.166779	-0.0037	0.095693	-0.09864
2.139381	-0.01443	0.095982	-0.10072
2.111889	-0.0157	0.108514	-0.10385
2.084303	-0.02104	0.107803	-0.1071
2.056622	-0.04317	0.106397	-0.10708
2.042745	-0.03963	0.106281	-0.10744
2.037188	-0.03715	0.106544	-0.10815
2.034407	-0.03648	0.106888	-0.1083
2.031626	-0.03752	0.10712	-0.10841
2.028844	-0.03767	0.10749	-0.10857
2.026061	-0.03801	0.107417	-0.10863
2.023277	-0.03617	0.107772	-0.10878
2.01492	-0.02265	0.108916	-0.10945
2.000971	-0.01906	0.111285	-0.11115
1.99259	-0.05194	0.113036	-0.11257
1.986997	-0.14318	0.114636	-0.11374
1.981401	-0.46818	0.114966	-0.11432
1.978602	-1.02595	0.115183	-0.11496
1.977202	-1.88677	0.11495	-0.1151
1.975801	-3.4708	0.114601	-0.11602
1.974961	-5.94316	0.109892	-0.11748
1.974401	-9.34759	0.114402	-0.11767
1.97384	-16.7788	0.113469	-0.1205
1.97356	-24.2053	0.117707	-0.12226
1.97342	-29.7748	0.116709	-0.12491

Table 29b: Nonadiabatic coupling elements in bohr^{-1} at $\gamma = 60°$ and $R_1 = 1.973$ bohr

R_2 (bohr)	$\langle 1\|\frac{d}{dR_2}\|2\rangle$	$\langle 1\|\frac{d}{dR_2}\|3\rangle$	$\langle 2\|\frac{d}{dR_2}\|3\rangle$
1.97328	-37.8106	0.119846	-0.1252
1.973196	-43.4833	0.114348	-0.12327
1.97314	-48.6998	0.11575	-0.13048
1.97286	-60.4505	0.118381	-0.12444
1.972804	-54.7542	0.117111	-0.11459
1.97272	-46.3552	0.117178	-0.1247
1.97258	-35.3868	0.111602	-0.12407
1.972496	-30.7156	0.113878	-0.12
1.971879	-13.678	0.113972	-0.11994
1.971599	-10.0213	0.114612	-0.12079
1.971319	-8.01144	0.114391	-0.11913
1.970758	-5.57912	0.115095	-0.11785
1.970198	-3.6426	0.114894	-0.1173
1.968796	-1.84587	0.115966	-0.11688
1.967394	-1.06531	0.115698	-0.11638
1.96459	-0.4566	0.116475	-0.1168
1.958978	-0.12646	0.116859	-0.11771
1.953362	-0.04313	0.117332	-0.1185
1.944932	-0.0042	0.117664	-0.11986
1.916764	-0.04041	0.118628	-0.12457
1.888498	-0.03219	0.123835	-0.12607
1.860132	-0.00978	0.12831	-0.12894
1.831666	-0.02135	0.133546	-0.13615
1.803097	-0.02057	0.137919	-0.14364
1.774428	-0.02361	0.142185	-0.155
1.745655	-0.03383	0.145468	-0.16839
1.716779	-0.03748	0.148486	-0.16416
1.687798	-0.03512	0.15041	-0.16947
1.629522	-0.03119	0.1549	-0.17246
1.57082	-0.04742	0.158706	-0.18962

Table 30a: Nonadiabatic coupling elements in bohr^{-2} at $\gamma = 60^\circ$ and $R_1 = 1.973$ bohr

R_2 (bohr)	$\langle 1\vert\frac{d^2}{dR_2^2}\vert 2\rangle$	$\langle 1\vert\frac{d^2}{dR_2^2}\vert 3\rangle$	$\langle 2\vert\frac{d^2}{dR_2^2}\vert 3\rangle$
2.409243	0.016615	0.074249	-0.07672
2.355991	0.009693	0.079114	-0.08121
2.302384	0.007751	0.084627	-0.08568
2.248416	0.004998	0.090611	-0.08935
2.221296	0.001194	0.094221	-0.0918
2.194084	0.00972	0.097115	-0.09496
2.166779	-0.0037	0.095693	-0.09864
2.139381	-0.01443	0.095982	-0.10072
2.111889	-0.0157	0.108514	-0.10385
2.084303	-0.02104	0.107803	-0.1071
2.056622	-0.04317	0.106397	-0.10708
2.042745	-0.03963	0.106281	-0.10744
2.037188	-0.03715	0.106544	-0.10815
2.034407	-0.03648	0.106888	-0.1083
2.031626	-0.03752	0.10712	-0.10841
2.028844	-0.03767	0.10749	-0.10857
2.026061	-0.03801	0.107417	-0.10863
2.023277	-0.03617	0.107772	-0.10878
2.01492	-0.02265	0.108916	-0.10945
2.000971	-0.01906	0.111285	-0.11115
1.99259	-0.05194	0.113036	-0.11257
1.986997	-0.14318	0.114636	-0.11374
1.981401	-0.46818	0.114966	-0.11432
1.978602	-1.02595	0.115183	-0.11496
1.977202	-1.88677	0.11495	-0.1151
1.975801	-3.4708	0.114601	-0.11602
1.974961	-5.94316	0.109892	-0.11748
1.974401	-9.34759	0.114402	-0.11767
1.97384	-16.7788	0.113469	-0.1205
1.97356	-24.2053	0.117707	-0.12226
1.97342	-29.7748	0.116709	-0.12491

Table 30b: Nonadiabatic coupling elements in bohr^{-1} at $\gamma = 60°$ and $R_1 = 1.973$ bohr

R_2 (bohr)	$\langle 1\vert\frac{d^2}{dR_2^2}\vert 2\rangle$	$\langle 1\vert\frac{d^2}{dR_2^2}\vert 3\rangle$	$\langle 2\vert\frac{d^2}{dR_2^2}\vert 3\rangle$
1.97328	-37.8106	0.119846	-0.1252
1.973196	-43.4833	0.114348	-0.12327
1.97314	-48.6998	0.11575	-0.13048
1.97286	-60.4505	0.118381	-0.12444
1.972804	-54.7542	0.117111	-0.11459
1.97272	-46.3552	0.117178	-0.1247
1.97258	-35.3868	0.111602	-0.12407
1.972496	-30.7156	0.113878	-0.12
1.971879	-13.678	0.113972	-0.11994
1.971599	-10.0213	0.114612	-0.12079
1.971319	-8.01144	0.114391	-0.11913
1.970758	-5.57912	0.115095	-0.11785
1.970198	-3.6426	0.114894	-0.1173
1.968796	-1.84587	0.115966	-0.11688
1.967394	-1.06531	0.115698	-0.11638
1.96459	-0.4566	0.116475	-0.1168
1.958978	-0.12646	0.116859	-0.11771
1.953362	-0.04313	0.117332	-0.1185
1.944932	-0.0042	0.117664	-0.11986
1.916764	-0.04041	0.118628	-0.12457
1.888498	-0.03219	0.123835	-0.12607
1.860132	-0.00978	0.12831	-0.12894
1.831666	-0.02135	0.133546	-0.13615
1.803097	-0.02057	0.137919	-0.14364
1.774428	-0.02361	0.142185	-0.155
1.745655	-0.03383	0.145468	-0.16839
1.716779	-0.03748	0.148486	-0.16416
1.687798	-0.03512	0.15041	-0.16947
1.629522	-0.03119	0.1549	-0.17246
1.57082	-0.04742	0.158706	-0.18962